

Springer Proceedings in Mathematics & Statistics

Jan Awrejcewicz *Editor*

Perspectives in Dynamical Systems III: Control and Stability

DSTA, Łódź, Poland December 2–5, 2019



Springer

**Springer Proceedings in Mathematics &
Statistics**

Volume 364

Springer Proceedings in Mathematics & Statistics

This book series features volumes composed of selected contributions from workshops and conferences in all areas of current research in mathematics and statistics, including operation research and optimization. In addition to an overall evaluation of the interest, scientific quality, and timeliness of each proposal at the hands of the publisher, individual contributions are all refereed to the high quality standards of leading journals in the field. Thus, this series provides the research community with well-edited, authoritative reports on developments in the most exciting areas of mathematical and statistical research today.

More information about this series at <http://www.springer.com/series/10533>


Jan Awrejcewicz
Editor

Perspectives in Dynamical Systems III: Control and Stability

DSTA, Łódź, Poland December 2–5, 2019

 Springer

Editor

Jan Awrejcewicz 
Department of Automation, Biomechanics
and Mechatronics
Lodz University of Technology
Lodz, Poland

ISSN 2194-1009 ISSN 2194-1017 (electronic)
Springer Proceedings in Mathematics & Statistics
ISBN 978-3-030-77313-7 ISBN 978-3-030-77314-4 (eBook)
<https://doi.org/10.1007/978-3-030-77314-4>

Mathematics Subject Classification: 28DXX, 34Cxx, 37-XX, 46LXX, 65-XX, 70-XX, 74-XX, 76-XX

© Springer Nature Switzerland AG 2021

This work is subject to copyright. All rights are reserved by the Publisher, whether the whole or part of the material is concerned, specifically the rights of translation, reprinting, reuse of illustrations, recitation, broadcasting, reproduction on microfilms or in any other physical way, and transmission or information storage and retrieval, electronic adaptation, computer software, or by similar or dissimilar methodology now known or hereafter developed.

The use of general descriptive names, registered names, trademarks, service marks, etc. in this publication does not imply, even in the absence of a specific statement, that such names are exempt from the relevant protective laws and regulations and therefore free for general use.

The publisher, the authors, and the editors are safe to assume that the advice and information in this book are believed to be true and accurate at the date of publication. Neither the publisher nor the authors or the editors give a warranty, expressed or implied, with respect to the material contained herein or for any errors or omissions that may have been made. The publisher remains neutral with regard to jurisdictional claims in published maps and institutional affiliations.

This Springer imprint is published by the registered company Springer Nature Switzerland AG
The registered company address is: Gewerbestrasse 11, 6330 Cham, Switzerland

Preface

15th International Conference “Dynamical Systems – Theory and Applications” (DSTA 2019) took place in Lodz, Poland, from December 2 to 5, 2019. It was the 15th edition in the series of conferences organized every 2 years in Lodz by the Department of Automation, Biomechanics and Mechatronics of the Lodz University of Technology.

For this edition, the scientific committee composed of 64 scientists had to review over 360 submitted topics to choose 200 that were to be presented during the DSTA 2019 by participants representing 40 countries from all over the world.

It resulted in the program of conference that covered both theoretical and experimental approaches to widely understood dynamical systems, including topics devoted to bifurcations and chaos, control in dynamical systems, asymptotic methods in nonlinear dynamics, stability of dynamical systems, lumped mass and continuous systems vibrations, original numerical methods of vibration analysis, nonsmooth systems, dynamics in life sciences and bioengineering, as well as to the engineering systems and differential equations.

All papers included in this book were submitted and presented during DSTA 2019. They contribute partially to the diverse approaches and topics covered by wide scope of dynamical systems.

A brief description of the book content is provided as follows.

The periodic solutions of governing system of motion obtained utilizing the Poincaré small parameter method up to the first order approximation for a rotational motion of a rigid body about a fixed point under the influence of Newtonian field and a gyro moment are addressed in chapter “[On the Spinning Motion of a Disc Under the Influence a Gyrostatic Moment](#)”.

Nishiyama and Yamashita in chapter “[Suppression of Impact Oscillations in a Railway Current Collection System with an Additional Oscillatory System](#)” conducted series of experiments to verify proposed model of pantograph and a conductor line in a railway current collection system. They investigated the effects of the added system on the impact oscillations between the main mass and the excitation source in the model consisting of a single-degree-of-freedom system.

Nakonechnyi et al. in chapter “[On Qualitative Analysis of Lattice Dynamical System of Two- and Three-Dimensional Biopixels Array: Bifurcations and Transition to “Chaos”](#)” analyzed the effect of the lattice type on the qualitative behavior of the model of the immunosensor. The model based on the system of lattice differential equations with time delay, describing interactions of biological species of neighboring pixels, is investigated numerically with a help of phase portraits, square and hexagonal lattice plots, and bifurcation diagrams as well as analytically by a comparison of the basic stability characteristics like basic reproductive numbers, through a comparison of the conditions for persistence (permanence), and extinction.

Chapter “[Response Sensitivity of Damper-Connected Adjacent Structural Systems Subjected to Fully Non-stationary Random Excitations](#)” is devoted to a new method for the evaluation the sensitivities of nongeometric spectral moments of the structural response of the non-classically damped coupled systems subjected to fully non-stationary zero-mean Gaussian excitation, through simple integrals in frequency domain.

New approach to optimization for non-isothermal chemical reactions with simultaneous modulation of the input concentration and the volumetric flow rate was proposed by Benner et al. in chapter “[Analysis of Switching Strategies for the Optimization of Periodic Chemical Reactions with Controlled Flow-Rate](#)”. Focusing on parametrization of optimal controls in terms of switching times in order to estimate the cost under different switching strategies, the authors considered control problem with non-convex for a class of nonlinear control systems with periodic boundary conditions.

In chapter “[Quaternion Based Free-Floating Space Manipulator Dynamics Modeling Using the Dynamically Equivalent Manipulator Approach](#)”, dynamical modeling approaches dedicated to freefloating spacecraft based on a modified dynamically equivalent manipulator method are developed, illustrated, and discussed. Applying space manipulators dynamics in quaternion parameterization instead Euler angles allowed to increase the computational efficiency of the dynamics modeling of space manipulators.

Numerical study of a quarter car vehicle-tank model by investigating motion of a linear pendulum model without baffles is presented in chapter “[Slosh Analyzes of a Full Vehicle-Tank Model with SDRE Control with a Hydraulic Damper](#)”. Results of this study indicated that the pendulum model can adequately map the fluid behavior in the tank and that state-dependent Riccati equation method can be used to calculate damping force necessary to stabilize the sloshing motion.

In chapter “[A Comparison of the Common Types of Nonlinear Energy Sinks](#)”, a numerical investigation, optimization, and comparison for energy transfer and dissipation for an impulsive excitation into a large-scale nine-story dynamical structure for three most common nonlinear energy sinks is presented.

Results of the simulation of the impact of driving speed on the lateral stability of the designed and developed prototype of a narrow, three-wheeled vehicle with electric drive designed as a delta type vehicle are reported in chapter “[Stability of Three Wheeled Narrow Vehicle](#)”.

Chapter “[Testing and Analysis of Vibration of a Tension Transmission with a Thermally Sealed Belt](#)” is focused on results of experimental investigations of vibration of a draw gear with a thermally sealed belt. Investigated was also the influence of the gearbox load on the value of the point measures of vibration signals, what yielded results useful for designers and technicians involved in the operation of drawstring drives with thermally weldable belts.

Model for computing motion resistance of double-flanged rollers while rolling over rubber tracks that can be used for the losses caused by the indentation of the rollers into the inner surface of the tracks as well as the sliding friction between the rollers and guide lugs of the tracks were proposed and experimentally validated in chapter “[Modeling and Experimental Tests on Motion Resistance of Double-Flanged Rollers of Rubber Track Systems Due to Sliding Friction Between the Rollers and Guide Lugs of Rubber Tracks](#)”.

Chapter “[Structural Dynamic Response of Coupling Between Transmission Line and Tower Under Random Excitation](#)” provides analyses of an overhead transmission line under different types of random wind excitation that simulate natural phenomena in situ represented by white noise. In addition, Kani-Tajimi and Firstorder filter spectrum using spectral element method to decrease computational time and simplify access to the model formulation are successfully employed.

Results of impact tests used to determine the values of the natural frequencies of the most stressed parts of the supporting structure for basic and reinforced support frame of the test station designed for gearing and belt transmissions testing are presented in chapter “[Experimental Assessment of the Test Station Support Structure Rigidity by the Vibration Diagnostics Method](#)”. Conducted experiment allowed to determine necessary design modifications for eliminating the danger of resonance and increasing the stiffness during vibration diagnostics.

In chapter “[Experimental Dynamical Analysis of a Mechatronic Analogy of the Human Circulatory System](#)”, results of an experimental test of the designed and constructed model of a human circulation system are presented. The conducted numerical simulation and mathematical description of an experimental model proved that while testing system solutions such as membrane tanks, control system and measurement method work correctly, but the dynamics of the system is not sufficiently convergent with real circulatory system.

Taylor et al. in chapter “[Robust Design of Inhibitory Neuronal Networks Displaying Rhythmic Activity](#)” developed a novel two-stage estimation method allowing to avoid associated with estimating all network parameters simultaneously in the artificial central pattern generators. This approach can be further utilized for a hardware implementation of artificial networks designed for integration with biological nervous systems.

In chapter “[Nonlinear Dynamics of the Industrial City’s Atmospheric Ventilation: New Differential Equations Model and Chaotic Ventilation](#)”, Khetselius et al. present a new generalized mathematical approach to analysis and modelling the characteristics of the chaotic atmospheric dynamical system, including natural air ventilation in the atmosphere of the industrial city based on the generalized model of the tensor equations for turbulent tensions.

Experimental study designed for exploration of the trajectory of the center of pressure in foot morphology control when maintaining an upright standing posture on a dynamic support surface with continuous periodical multidirectional perturbations is presented in chapter “[Biomechanical Analysis of Different Foot Morphology During Standing on a Dynamic Support Surface](#)”.

Birs et al. in chapter “[Comparison of Various Fractional Order Controllers on a Poorly Damped System](#)” focus on the issue of controlling a poorly damped system. In the study, two different fractional order control strategies are compared experimentally with the use of highly nonlinear experimental stand consisting of a vertical take-off and landing platform.

The physical parameters’ impact on the motion of the two-degrees-of-freedom model of a damped spring pendulum in an inviscid fluid flow is investigated in chapter “[Asymptotic Analysis of Submerged Spring Pendulum Motion in Liquid](#)”. The time histories of the achieved solutions, resonance cases, and steady-state solutions are discussed and illustrated graphically.

In chapter “[Parametric Identification of Nonlinear Structures Using Particle Swarm Optimization Based on Power Flow Balance Criteria](#)”, a novel concept of nonlinear parameter identification using instantaneous power flow balance objective function in time domain is introduced and implemented on a 10-DOF nonlinear system. Its simulation results show the accuracy of proposed method in nonlinear parameter identification procedure even at high noise contamination cases.

New approach based on applications of the R-functions theory and variational Ritz’s method for analysis of vibration and stability problems for laminated composite plates under non-uniform edge compressions are studied in chapter “[Vibration and Buckling of Laminated Plates of Complex form Under In-plane Uniform and Non-uniform Loading](#)”.

Material instability problems for non-local cases, when fractional derivatives are used to model non-locality in constitutive equations, are analyzed in chapter “[Dynamical Systems and Stability in Fractional Solid Mechanics](#)”. Presented research is concentrated on how the type of fractional derivatives effects the problems of stability investigation.

The methods based on results from graph theory, Lyapunov operator, Dini derivative, and some known inequality techniques are applied by Tojtovska and Ribarski in chapter “[Stability of Coupled Systems of Stochastic Cohen-Grossberg Neural Networks with Time Delays, Impulses and Markovian Switching](#)” to study the topic of the p th moment ($p \geq 2$) stability of coupled systems of stochastic Cohen-Grossberg neural networks with time delays, impulses, and Markovian switching. The obtained theoretical results are validated by a numerical example.

In chapter “[Stability of Steady States with Complex Behavior in Time](#)”, advantages and limitations of applying the numerical-analytical procedure based on the classical Lyapunov definition of stability and the Ince algebraization method to solve problem of stability of steady states are presented and discussed.

Chapter “[Modelling of Torsional Vibrations in a Motorcycle Steering System](#)” is focused on using mathematical modelling and computer simulation for identification of torsional vibrations of steering systems exhibited by motorcycles. The

authors applied Laplace transformation based on determination of the transfer functions, and frequency analysis combined with Bode plots allowed to reduce transfer functions and to carry out final calculation of state equations to synthesize the active damper control algorithm.

Szlachetka et al. in chapter “Free Vibration Frequencies of Simply Supported Bars with Variable Cross Section” described and experimentally validated new procedure based on Rayleigh method for determination of higher natural frequencies and derived formulas for frequencies of first three modes of free (transverse) vibrations of simply supported bars having the shape of truncated cone and truncated wedge.

For system consisting of a rigid block installed on a viscoelastic foundation, the influence of the system parameters as well as of the amplitude and frequency of the excitation upon characteristics of oscillations of the induced by horizontal harmonic motion of the foundation are studied in chapter “On Dynamics of a Rigid Block on Visco-Elastic Foundation”.

The DSTA Conferences are aimed to provide a common platform for exchange of new ideas and results of recent research in the field of scientific and technological advances in modern dynamical systems. Over the last 25 years, both approaches and understanding of sciences significantly evolved to include new ideas and trends, but the traditional views are still present and provide the basic understanding. Therefore, as both head of the organizing and scientific committees of DSTA 2019 and as the volume editor of Springer Proceedings, I hope this book will provide readers with both answers to their problems and ideas for their novel approaches to studying nonlinear dynamical systems.

I greatly appreciate the help of Springer Editor Dahlia Fisch, Springer Project Coordinators Murugesan Tamilsevan and Saveetha Balasundaram as well as project manager at SPi Global Kannan Sudha in publishing this volume in the Springer Proceedings in Mathematics and Statistics series. I would like also to express my gratitude to the scientific committee of DSTA 2019 and all reviewers for their help and professional support during book preparation.

Łódź, Poland

Jan Awrejcewicz

Contents

On the Spinning Motion of a Disc under the Influence a Gyrostatic Moment	1
M. A. Bek, Tarek Amer, and Yasser Gamiel	
Suppression of Impact Oscillations in a Railway Current Collection System with an Additional Oscillatory System	15
Naoto Nishiyama and Kiyotaka Yamashita	
On Qualitative Analysis of Lattice Dynamical System of Two- and Three-Dimensional Biopixels Array: Bifurcations and Transition to “Chaos”	23
Oleksandr Nakonechnyi, Vasyi Martsenyuk, Mikolaj Karpinski, and Aleksandra Klos-Witkowska	
Response Sensitivity of Damper-connected Adjacent Structural Systems Subjected to Fully Non-stationary Random Excitations	45
Giuseppe Muscolino, Federica Genovese, and Tiziana Alderucci	
Analysis of Switching Strategies for the Optimization of Periodic Chemical Reactions with Controlled Flow-Rate	59
Peter Benner, Andreas Seidel-Morgenstern, and Alexander Zuyev	
Quaternion Based Free-Floating Space Manipulator Dynamics Modeling Using the Dynamically Equivalent Manipulator Approach	71
Elżbieta Jarzębowska and Marcin Kłak	
Slosh Analyzes of a Full Vehicle-Tank Model with SDRE Control with a Hydraulic Damper	83
Wagner B. Lenz, Mauricio A. Ribeiro, Angelo M. Tusset, Jose M. Balthazar, and Elżbieta Jarzębowska	
A Comparison of the Common Types of Nonlinear Energy Sinks	95
Adnan S. Saeed and Mohammad A. AL-Shudeifat	

Stability of Three Wheeled Narrow Vehicle	105
Grzysztotf Weigel-Milleret and Witold Grzezożek	
Testing and Analysis of Vibration of a Tension Transmission with a Thermally Sealed Belt	117
Grzegorz M. Szymański and Piotr Krawiec	
Modeling and Experimental Tests on Motion Resistance of Double-Flanged Rollers of Rubber Track Systems Due to Sliding Friction Between the Rollers and Guide Lugs of Rubber Tracks	129
Piotr A. Dudziński and Jakub Chołodowski	
Structural Dynamic Response of Coupling Between Transmission Line and Tower Under Random Excitation	143
Yanne Marcela Soares Fernandes, Marcela Rodrigues Machado, and Maciej Dutkiewicz	
Experimental Assessment of the Test Station Support Structure Rigidity by the Vibration Diagnostics Method	161
Anna Šmeringaiová and Imrich Vojtko	
Experimental Dynamical Analysis of a Mechatronic Analogy of the Human Circulatory System	173
Paweł Olejnik, Fryderyk Wiądzkiewicz, and Jan Awrejcewicz	
Robust Design of Inhibitory Neuronal Networks Displaying Rhythmic Activity	187
Joseph D. Taylor, Kamal Abu-Hassan, Joanne J. A. van Bavel, Marc A. Vos, and Alain Nogaret	
Nonlinear Dynamics of the Industrial City’s Atmospheric Ventilation: New Differential Equations Model and Chaotic Ventilation	199
Olga Yu Khetselius, Alexander V. Glushkov, Sergiy M. Stepanenko, Andrey A. Svinarenko, and Vasily V. Buyadzhi	
Biomechanical Analysis of Different Foot Morphology During Standing on a Dynamic Support Surface	211
Yang Shu, Jan Awrejcewicz, and Bartłomiej Zagrodny	
Comparison of Various Fractional Order Controllers on a Poorly Damped System	219
Isabela Birs, Ioan Nascu, Eva Dulf, and Cristina Muresan	
Asymptotic Analysis of Submerged Spring Pendulum Motion in Liquid ...	233
T. S. Amer, M. A. Bek, and Asmaa Arab	
Parametric Identification of Nonlinear Structures Using Particle Swarm Optimization Based on Power Flow Balance Criteria	249
R. Anish and K. Shankar	

Vibration and Buckling of Laminated Plates of Complex Form under in-Plane Uniform and Non-uniform Loading 259
 Lidiya Kurpa, Victoriya Tkachenko, and Anna Linnik

Dynamical Systems and Stability in Fractional Solid Mechanics 269
 Péter B. Bédá

Stability of Coupled Systems of Stochastic Cohen-Grossberg Neural Networks with Time Delays, Impulses and Markovian Switching 285
 Biljana Tojtovska and Panche Ribarski

Stability of Steady States with Complex Behavior in Time 309
 Yuri V. Mikhlin and Nataliia S. Goloskubova

Modelling of Torsional Vibrations in a Motorcycle Steering System 327
 Andrzej Dębowski and Dariusz Żardecki

Free Vibration Frequencies of Simply Supported Bars with Variable Cross Section 339
 Olga Szlachetka, Jacek Jaworski, and Marek Chalecki

On Dynamics of a Rigid Block on Visco-Elastic Foundation 351
 Yury D. Selyutskiy, Rinaldo Garziera, and Luca Collini

On the Spinning Motion of a Disc under the Influence a Gyrostatic Moment



M. A. Bek, Tarek Amer, and Yasser Gamiel

Abstract This work outlines the motion of a disc about one of its fixed point different from its center of mass in the presence of a constant gyrostatic moment about the principal axes of inertia. The governing system of motion consists of six nonlinear differential equations and their first integrals are reduced to another quasilinear autonomous one of 2DOF besides one first integral. Initially, it is hypothesized that the body is rapidly spun about one of its principal axes. The method of small parameter of Poincaré is used to achieve the desired approximate solutions of the equations of motion. Euler's angles are used to interpret the motion of the body at any blink. The numerical solutions of autonomous system are investigated using the fourth order Runge-Kutta algorithms (RKA). The comparison between both two solutions reveals that the numerical solutions are in well agreement with the approximate ones and the deviation between them is very slightly. The importance of this work is focused on its great applications in many fields such as in engineering, physics and industrial applications for example ships stabilizers, racing cars, pointing devices for computer, satellites and like.

Keywords Spinning motion · Disk · Gyrostatic moment

M. A. Bek (✉)

Tanta University, Faculty of Engineering, Physics and Engineering Mathematics Department, Tanta, Egypt

Modern Sciences and Arts University, Faculty of Engineering/General Systems Engineering Department, October, Egypt

e-mail: y_egcglass@f-eng.tanta.edu.eg

T. Amer

Tanta University, Faculty of Science, Mathematics Department, Tanta, Egypt

Y. Gamiel

Tanta University, Faculty of Engineering, Physics and Engineering Mathematics Department, Tanta, Egypt

© Springer Nature Switzerland AG 2021

J. Awrejcewicz (ed.), *Perspectives in Dynamical Systems III: Control and Stability*,

Springer Proceedings in Mathematics & Statistics 364,

https://doi.org/10.1007/978-3-030-77314-4_1

1 Introduction

The rigid body motion about a fixed point had shed the interest of many researchers during the last six decades e.g. [1–10] because it is considered one of the important problems in theoretical classical mechanics due to its great artificial applications in life. In [1], the author studied this problem under the action of Newtonian field of force when the value of one of the principal moments of inertia equals to the sum of the other two ones. Hass case for the rigid body motion is studied in [2]. The method of small parameters is used in [3] to obtain the periodic solutions of a heavy solid body. It is considered in [4] that, the kinetic energy of asymmetric rigid body is greater than the potential one while in [5], the large angle theory is developed to solve the equations of motion without the requirement of solving any new integrals. The stability of the steady motions of this problem in a central gravitational field is studied in [6]. The authors considered that the body consists of a collection of point of mass. The small parameter method is used in [7] to investigate the solution of a disc when the natural frequency of motion equals unity. Burov in [7], studied the restricted motion of a heavy rigid body and investigated in [9] the existence of integrable case of the Euler-Poisson equations.

A great accuracy of the analytic solutions were obtained in [8, 9] for the problem of attitude motion of a self-excited rigid body. The analytical solution for asymmetric rigid body is studied in [10] when the third component of the gyro moment is acted addition to a Newtonian field using the small parameter method of Poincarè. On the other hand, the motion a symmetric rigid body is studied in [11] when the body is subjected under the influence of gravitational field and a constant gyro moment. The generalization of this problem, when the gyro rotates under external forces represented by the Newtonian field of force and the gyro moment, is investigated in [12]. The author determined Euler's angles through the geometric interpretation of motion. It is found that these angles depend on four arbitrary independent constants. Moreover, the graphical representations for the achieved analytical solutions are presented for the physical parameter of the gyro to reveal the good effect of both the Newtonian field and the gyro moment on the motion.

The method of Krylov-Bogoliubov-Mitropolski (KBM) [13, 14] is used in [15] and [16] to gain the periodic solutions for the motion of a heavy solid in a uniform field. Unfortunately, the obtained solutions have singular points when the natural frequency takes integer values or the multiple inverses of these values. This problem was generalized in [17] when the body moves under the presence of two components of the constant gyrostatic moment vector while the attained solutions don't have any singular points at all, due to that the authors used another frequency different from the used frequency in [15, 16] by a small quantity depends on the third component of the gyrostatic moment vector. Recently, KBM method is utilized in [18] to the solutions of the equations of motion of a rigid body in a general case, i.e. without any restrictions on the locations of the body center of mass and one the values of principal moments of inertia. The motion of a rigid body close to Kovalevskaya's

case is studied in [19] in the presence of gyro moment vector. The problem of rigid body is investigated in [20, 21] under the action of electromagnetic field due to a point charge located on the dynamic symmetry axis of the body and gyro moments. Some applications are presented in [21].

This work addresses the motion of a rigid body according to the disc case taking into consideration the effect of a gyro moment about the principal axes of inertia. It is assumed that the body has initially high speed about one these axes. One of the most common and important perturbation techniques namely; the Poincaré small parameter method is used to obtained the periodic analytical solutions of the equations of motion. These equations with their first integrals are reduced to a quasilinear autonomous system of two degrees of freedom (2-DOF) and one first integral. The attained solutions are considered generalization of the works included in [1] and [7], and represented graphically to reveal the physical different parameter of the body on the motion. The significant applications of this work in many different fields such as in Engineering, Physics and industrial applications gives an indication of its importance.

2 Modeling of the Problem

Consider the motion of a rigid body about a fixed point O , which will be taken as the origin of a dynamical model, subjected to the gyrostatic moment vector $\underline{\ell}$ about the principal axes of inertia. Two systems of reference are considered; a fixed one $OX_1X_2X_3$ and another moving one $Ox_1x_2x_3$, fixed in the disc, and whose axes are directed along the principal axes of inertia at O .

Initially, we assume that, the body rotates with a high angular velocity r_0 about x_3 -axis in which this axis makes an angle θ_0 close to $\pi/2$. Therefore, the governing system of motion corresponding to the disc case has the form [22].

$$\begin{aligned}
 \dot{p}_1 + q_1 r_1 + (A r_0)^{-1} q_1 \ell_3 &= \varepsilon a^{-1} x'_{20} \gamma''_1, \\
 \dot{q}_1 - p_1 r_1 - (B r_0)^{-1} p_1 \ell_3 &= -\varepsilon b^{-1} x'_{10} \gamma''_1, \\
 \dot{r}_1 &= \varepsilon^2 (x'_{10} \gamma'_1 - y'_0 \gamma_1 - C_1 p_1 q_1), \\
 \dot{\gamma}_1 - r_1 \gamma'_1 + \varepsilon q_1 \gamma''_1 &= 0, \\
 \dot{\gamma}'_1 + r_1 \gamma_1 - \varepsilon p_1 \gamma''_1 &= 0, \\
 \dot{\gamma}''_1 - \varepsilon (q_1 \gamma_1 - p_1 \gamma'_1) &= 0;
 \end{aligned} \tag{1}$$

where

$$\begin{aligned}
 \frac{p}{p_1} &= \frac{q}{q_1} = c \sqrt{\gamma''_0}, & r &= r_0 r_1, & (\cdot &\equiv d/d\tau), \\
 \frac{\gamma}{\gamma_1} &= \frac{\gamma'}{\gamma'_1} = \frac{\gamma''}{\gamma''_1} = \gamma''_0, & \tau &= r_0 t, & \gamma_0 > 0, & 0 < \gamma''_0 < 1;
 \end{aligned} \tag{2}$$

$$\begin{aligned}
A + B &= C, & C_1 &= (B - A) / C, & a &= A / C, & b &= B / C, \\
a + b &= 1, & \varepsilon &= c \sqrt{\gamma_0''} / r_0, & c^2 &= M g l / C, \\
x_{10} &= l x'_{10}, & x_{20} &= l x'_{20}, & l^2 &= x_{10}^2 + x_{20}^2.
\end{aligned} \tag{3}$$

Here, (A, B, C) represent the principal moments of inertia, (x_{10}, x_{20}, x_{30}) denote to the coordinates of the center of mass in which $x_{30} = 0$, $(\gamma, \gamma', \gamma'')$ refer to the components of the unit vector in the direction X_3 -axis, (p, q, r) are the angular velocity components, ℓ_3 is the third component of the gyrostatic moment vector acted along the principal axis Ox_3 , M is the mass of the body, g is the gravitational acceleration and $p_0, q_0, r_0, \gamma_0, \gamma_0'$ and γ_0'' are the initial values of the corresponding variables.

By virtue of system (1), the three first integrals for the considered motion take the form

$$r_1^2 = 1 + \varepsilon^2 S_1, \quad r_1 \gamma_1'' = 1 + \varepsilon S_2, \quad \gamma_1^2 + \gamma_1'^2 + \gamma_1''^2 = (\gamma_0'')^{-2}; \tag{4}$$

where

$$\begin{aligned}
S_1 &= a \left(p_{10}^2 - p_1^2 \right) + b \left(q_{10}^2 - q_1^2 \right) - 2 \left[x'_{10} \left(\gamma_{10} - \gamma_1 \right) + x'_{20} \left(\gamma'_{10} - \gamma'_1 \right) \right], \\
S_2 &= a \left(p_{10} \gamma_{10} - p_1 \gamma_1 \right) + b \left(q_{10} \gamma'_{10} - q_1 \gamma'_1 \right) + \left(c C \sqrt{\gamma_0''} \right)^{-1} \left[\ell_3 \left(1 - \gamma_1'' \right) \right];
\end{aligned} \tag{5}$$

Our principal aim now is to reduce the governing system of motion (1) and their first integrals (4) to another convenient system and one first integral. Therefore, we can express the variables r_1 and γ_1'' from (4) as

$$\begin{aligned}
r_1 &= 1 + \frac{1}{2} \varepsilon^2 S_1 + \dots, \\
\gamma_1'' &= 1 + \varepsilon S_2 - \frac{1}{2} \varepsilon^2 S_1 + \dots,
\end{aligned} \tag{6}$$

Differentiating both of the first and the fourth equations of system (1), using (6) and taking into account that r_0 is very large, therefore $r_0^{-2}, r_0^{-3}, \dots$ are neglected. Consequently, the four remaining equations of system (1) can be reduced to the following form

$$\begin{aligned}
\ddot{p}_1 + \omega^2 p_1 &= \varepsilon b^{-1} \left[x'_{10} + (A r_0)^{-1} x'_{10} \ell_3 \right] + \varepsilon^2 \left\{ \left[-\omega^2 S_1 p_1 + b^{-1} x'_{10} S_2 + C_1 p_1 q_1^2 \right. \right. \\
&\quad \left. \left. - q_1 \left(x'_{10} \gamma'_1 - x'_{20} \gamma_1 \right) + a^{-1} x'_{20} \left(q_1 \gamma_1 - p_1 \gamma'_1 \right) \right] - \frac{1}{2} r_0^{-1} \ell_3 p_1 (Ab)^{-1} S_1 \right. \\
&\quad \left. + (A b r_0)^{-1} x'_{10} S_2 \ell_3 \right\} - \frac{1}{2} \varepsilon^3 (Ab r_0)^{-1} x'_{10} S_1 \ell_3 + \dots,
\end{aligned} \tag{7}$$

$$\begin{aligned}
\ddot{\gamma}_1 + \gamma_1 &= -\varepsilon (B r_0)^{-1} \ell_3 p_1 + \varepsilon^2 \left\{ x'_{10} \left(\gamma_1'^2 + b^{-1} \right) - \gamma_1 \left[\left(x'_{20} \gamma'_1 + q_1^2 \right) + S_1 \right] \right\} \\
&\quad + \varepsilon^3 \left(2 b^{-1} x'_{10} \right) S_2 + \dots,
\end{aligned} \tag{8}$$

where

$$\omega'^2 = 1 + \frac{\ell_3}{A b r_0}.$$

On the other hand, the variables q_1 and γ_1' can be obtained from system (1) by solving the first and the fourth equations of this system, with the aid of the approximation form of r_1 and γ_1'' in (6), in the form

$$\begin{aligned} q_1 &= r_1^{-1} \left[1 - (A r_0 r_1)^{-1} \ell_3 + \dots \right] (-\dot{p}_1 + \varepsilon a^{-1} x'_{20} \gamma_1''), \\ \gamma_1' &= r_1^{-1} (\dot{\gamma}_1 - \varepsilon q_1 \gamma_1''). \end{aligned} \quad (9)$$

To accomplish our previous aim, we consider the following new variables

$$p_2 = p_1 - \varepsilon \chi, \quad \gamma_2 = \gamma_1 - \varepsilon a p_2, \quad (10)$$

where

$$\chi = \frac{x'_{10}}{b\omega'^2} \left(1 + \frac{\ell_3}{A r_0} \right), \quad y_3 = \left(c C \sqrt{\gamma_0''} \right)^{-1} \ell_3.$$

Therefore, the variables q_1 and γ_1' , in terms of these variables, have the form

$$\begin{aligned} q_1 &= X (a^{-1} y_2 - \dot{p}_2) + \varepsilon X a^{-1} x'_{20} + \frac{1}{2} \varepsilon^2 [(2X - 1) S_{11} \dot{p}_2 + 2X a^{-1} x'_{20} S_{21}] + \dots, \\ \gamma_1' &= \dot{\gamma}_2 + \varepsilon (a - X) \dot{p}_2 + \frac{1}{2} \varepsilon^2 [2X (a^{-1} x'_{20} - S_{21} \dot{p}_2) - S_{11} \dot{\gamma}_2] + \dots, \end{aligned} \quad (11)$$

where

$$X = 1 - \frac{\ell_3}{A r_0}.$$

Substituting (11) and (10) into (5), yields S_1 and S_2 in terms of power series of the small parameter ε as

$$S_i = S_{i1} + 2^{2-i} \varepsilon S_{i2} + \dots, \quad (i = 1, 2) \quad (12)$$

where

$$\begin{aligned} S_{11} &= a (p_{20}^2 - p_2^2) + b X^2 (\dot{p}_{20}^2 - \dot{p}_2^2) - 2 [x'_{10} (\gamma_{20} - \gamma_2) + x'_{20} (\dot{\gamma}_{20} - \dot{\gamma}_2)], \\ S_{12} &= a (\chi - x'_{10}) (p_{20} - p_2) - x'_{20} [a + X (b a^{-1} X - 1)] (\dot{p}_{20} - \dot{p}_2), \\ S_{21} &= a (p_{20} \gamma_{20} - p_2 \gamma_2) - b X [(\dot{p}_{20} \dot{\gamma}_{20} - \dot{p}_2 \dot{\gamma}_2)], \\ S_{22} &= a [a (p_{20}^2 - p_2^2) + \chi (\gamma_{20} - \gamma_2)] - b X [(a - X) (\dot{p}_{20}^2 - \dot{p}_2^2) \\ &\quad - a^{-1} x'_{20} (\dot{\gamma}_{20} - \dot{\gamma}_2)] - y_3 S_{21}. \end{aligned} \quad (13)$$

Substituting (12) and (13) into (6), gives

$$\begin{aligned} r_1 &= 1 + \frac{1}{2} \varepsilon^2 S_{11} + \varepsilon^3 S_{12} + \dots, \\ \gamma_1'' &= 1 + \varepsilon S_{21} + \varepsilon^2 \left(S_{22} - \frac{1}{2} S_{11} \right) - \varepsilon^3 S_{12} + \dots. \end{aligned} \quad (14)$$

The substitution from (10), (11), (12), (13) and (14) into (7), (8) and (4), gives the desired quasilinear autonomous system of two degrees of freedom and one first integral in the forms

$$\begin{aligned} \ddot{p}_2 + \omega'^2 p_2 &= \varepsilon^2 F(p_2, \dot{p}_2, \gamma_2, \dot{\gamma}_2, \varepsilon), \\ \dot{\gamma}_2 + \gamma_2 &= \varepsilon^2 \Phi(p_2, \dot{p}_2, \gamma_2, \dot{\gamma}_2, \varepsilon), \end{aligned} \quad (15)$$

$$\begin{aligned} \gamma_2^2 + \dot{\gamma}_2^2 + 2\varepsilon [a\gamma_2 p_2 + (a-X)\dot{p}_2 \dot{\gamma}_2 + S_{21}] + \varepsilon^2 [a^2 p_2^2 + (a-X)^2 \dot{p}_2^2 \\ + 2X\dot{\gamma}_2(a^{-1}x'_{20} - S_{21}\dot{p}_2) + S_{21}^2 + 2(S_{22} - \frac{1}{2}S_{11})] = (\gamma_0'')^{-2} - 1. \end{aligned} \quad (16)$$

where

$$F = f_1 + \varepsilon f_2 + \dots, \quad \Phi = \frac{A^2 r_0}{B \ell_3} \chi + \phi_1 + \varepsilon (\phi_2 - a f_2) + \dots,$$

$$\begin{aligned} f_1 &= x'_{10} b^{-1} S_{21} + C_1 X^2 p_2 (\dot{p}_2^2 - 2a^{-1} x'_{20} \dot{p}_2) - [x'_{20} X (1+a^{-1}) \gamma_2 \\ &\quad - x'_{10} X \dot{\gamma}_2] \dot{p}_2 - a^{-1} p_2 x'_{20} \dot{\gamma}_2 + \frac{1}{2} S_{11} p_2 [\ell_3 (Abr_0)^{-1} - 2], \\ \phi_1 &= -\gamma_2 S_{11} + x'_{10} (b^{-1} + \dot{\gamma}_2^2) - \gamma_2 (x'_{20} \dot{\gamma}_2 + X^2 \dot{p}_2^2) + 2S_{21} x'_{10} b^{-1}, \\ f_2 &= b^{-1} x'_{10} S_{22} - (2p_2 S_{12} + S_{11} \chi) + C_1 X^2 \chi \dot{p}_2 (\dot{p}_2 - 2a^{-1} x'_{20}) - a^{-1} X x'_{10} x'_{20} \dot{\gamma}_2 \\ &\quad - a X \dot{p}_2 [p_2 x'_{20} (1+a^{-1}) - x'_{10} \dot{p}_2] - a^{-1} x'_{20} p_2 (q_1 + a \dot{p}_2) - a^{-1} x'_{20} \chi \dot{\gamma}_2 \\ &\quad + \frac{1}{2} \ell_3 (Abr_0)^{-1} (S_{11} \chi + 2p_2 S_{12} - S_{11} x'_{10}), \\ \phi_2 &= 2x'_{10} [(a-X)\dot{p}_2 \dot{\gamma}_2 + b^{-1} S_{21}] - x'_{20} [(a-X)\gamma_2 \dot{p}_2 + a p_2 \dot{\gamma}_2] - (a p_2 S_{11} + 2\gamma_2 S_{12}) \\ &\quad + X^2 \dot{p}_2 (2a^{-1} x'_{20} \gamma_2 - a p_2 \dot{p}_2). \end{aligned} \quad (17)$$

3 Construction of Periodic Solutions

The goal of this section is to obtain the periodic solutions of the previous system (15). To accomplish this purpose we will rely that, system (15) is autonomous therefore the following conditions

$$p_2(0, 0) =, \quad \dot{p}_2(0, 0) = 0, \quad \dot{\gamma}_2(0, \varepsilon) = 0, \quad (18)$$

do not affect the generality of the solutions [19]. The generating system of (15) admits the following periodic solutions with period $T_0 = 2\pi n$ as

$$p_2^{(0)} = M_1 \cos \omega' \tau + M_2 \sin \omega' \tau, \quad \gamma_2^{(0)} = M_3 \cos \tau. \quad (19)$$

Here $(M_i; i = 1, 2, 3)$ are constants can be determined. Referring to the solutions (19), we suppose the required general periodic solutions take the form

$$\begin{aligned} p_2(\tau, \varepsilon) &= (M_1 + \beta_1) \cos \omega' \tau + (M_2 + \beta_2) \sin \omega' \tau + \sum_{k=1}^{\infty} \varepsilon^k G_k(\tau), \\ \gamma_2(\tau, \varepsilon) &= (M_3 + \beta_3) \cos \tau + \sum_{k=1}^{\infty} \varepsilon^k H_k(\tau), \end{aligned} \quad (20)$$

with period $T(\varepsilon) = T_0 + \alpha(\varepsilon)$.

The quantities $\beta_1, \omega' \beta_2$ and β_3 refer to the deviations of the initial values of p_2, \dot{p}_2 and γ_2 of system (15) from their initial values of its generating system; these deviations are functions of ε and vanish if $\varepsilon = 0$. Then the initial conditions of (20) can be expressed as

$$\begin{aligned} p_2(0, \varepsilon) &= M_1 + \beta_1, & \dot{p}_2(0, \varepsilon) &= \omega' (M_2 + \beta_2), \\ \gamma_2(0, \varepsilon) &= M_3 + \beta_3, & \dot{\gamma}_2(0, \varepsilon) &= 0. \end{aligned} \quad (21)$$

Now we define two functions namely $(G_k(\tau), H_k(\tau); k = 1, 2, 3, \dots)$ according to the following operator [23]

$$U = u + \frac{\partial u}{\partial M_1} \beta_1 + \frac{\partial u}{\partial M_2} \beta_2 + \frac{\partial u}{\partial M_3} \beta_3 + \frac{1}{2} \frac{\partial^2 u}{\partial M_1^2} \beta_1^2 + \dots, \quad \left(\begin{array}{l} U = G_k, H_k \\ u = g_k, h_k \end{array} \right) \quad (22)$$

in which the functions $g_k(\tau)$ and $h_k(\tau)$ have the form

$$\begin{aligned} g_k(\tau) &= \frac{1}{\omega'} \int_0^{\tau} f_k^{(0)}(t_1) \sin \omega' (\tau - t_1) dt_1, \\ h_k(\tau) &= \int_0^{\tau} \phi_k^{(0)}(t_1) \sin \omega' (\tau - t_1) dt_1; \quad (k = 1, 2, 3). \end{aligned} \quad (23)$$

In order to obtain the expressions of the functions $f_1^{(0)}$ and $\phi_1^{(0)}$, we can rewrite the periodic solutions (19) in the form

$$p_2^{(0)} = E \cos (\omega' \tau - \eta), \quad \gamma_2^{(0)} = M_3 \cos \tau, \quad (24)$$

where $E = \sqrt{M_1^2 + M_2^2}$ and $\eta = \tan^{-1} M_2/M_1$. Substituting (24) into (13) yields

$$\begin{aligned}
 S_{11}^{(0)} &= \frac{1}{2} E^2 \left[a (2 \cos^2 \eta - 1) + b X^2 \omega'^2 (2 \sin^2 \eta - 1) + (b X^2 \omega'^2 - a) \cos 2 (\omega' \tau - \eta) \right] \\
 &\quad - 2 M_3 \left[x'_{10} (1 - \cos \tau) + x'_{20} \sin \tau \right], \\
 S_{21}^{(0)} &= \frac{1}{2} M_3 E \left\{ 2a \cos \eta + (b \omega' X - a) \cos [(\omega' - 1) \tau - \eta] - (b \omega' X + a) \right. \\
 &\quad \left. \times \cos [(\omega' + 1) \tau - \eta] \right\}, \\
 S_{12}^{(0)} &= E \left\{ a X [\cos \eta - \cos (\omega' \tau - \eta)] - \omega' \left\{ a^{-1} b X^2 x'_{20} [\sin \eta + \sin (\omega' \tau - \eta)] \right. \right. \\
 &\quad \left. \left. - [a x'_{10} + (a - X) x'_{20}] [\sin \eta + \sin (\omega' \tau - \eta)] \right\} \right\}, \\
 S_{22}^{(0)} &= a \left\{ a E^2 [\cos^2 \eta - \cos^2 (\omega' \tau - \eta)] + \chi M_3 (1 - \cos \tau) \right\} \\
 &\quad + b X \left\{ a^{-1} x'_{20} M_3 \sin \tau - E^2 \omega'^2 (a - X) [\sin^2 \eta - \sin^2 (\omega' \tau - \eta)] \right\} - y_3 S_{21}^{(0)}
 \end{aligned} \tag{25}$$

Substituting (24) and (25) into formulas (17) gives

$$\begin{aligned}
 f_1^{(0)} &= L(\omega') (M_1 \cos \omega' \tau + M_2 \sin \omega' \tau) + \dots, \\
 \phi_1^{(0)} &= M_3 N(\omega') \cos \omega' \tau + \dots,
 \end{aligned} \tag{26}$$

where

$$\begin{aligned}
 L(\omega') &= -\frac{1}{4} \left[(a B r_0)^{-1} \ell_3 + 2\omega'^2 \right] \left\{ a (2M_1^2 - 1) + 2 \left[b \omega'^2 X^2 (2M_2^2 - 1) - M_3 x'_{10} \right] \right. \\
 &\quad \left. - (b \omega'^2 X^2 - a) (M_1^2 + M_2^2) \right\} + \dots, \\
 N(\omega') &= X^2 \omega'^2 \left[(1 + b) (M_1^2 + M_2^2) - b M_2^2 \right] + 2 x'_{10} M_3 - a M_1^2 + \dots.
 \end{aligned} \tag{27}$$

Substituting (26) and (27) into (23) gives

$$\begin{aligned}
 g_1(T_0) &= -\pi n (\omega')^{-1} M_2 L(\omega'), \quad \dot{g}_1(T_0) = \pi n M_1 L(\omega'), \\
 h_1(T_0) &= 0, \quad \dot{h}_1(T_0) = \pi n M_3 N(\omega').
 \end{aligned} \tag{28}$$

Making use of conditions (21) and the integral (16) for $\tau = 0$, we get

$$M_3^2 + 2 M_3 \beta_3 + \beta_3^2 + 2 a \varepsilon (M_1 + \beta_1) (M_3 + \beta_3) + \dots = (\gamma_0'')^{-2} - 1.$$

Assuming γ_0'' is independent of ε , we obtain M_3 and β_3 in the form

$$M_3 = \left(1 - \gamma_0''^2\right)^{\frac{1}{2}} (\gamma_0'')^{-1} \quad 0 < M_3 < \infty, \quad \beta_3 = -\varepsilon a (M_1 + \beta_1) + \dots. \tag{29}$$

The independent conditions for the periodicity of the solutions [19] lead to

$$\begin{aligned}
 -\pi n \beta_2 (\omega')^{-1} \left[L_1(\omega') - \omega'^2 N_1(\omega') \right] + \varepsilon [G_2(T_0) + \dots] &= 0, \\
 \pi n \beta_1 [L_1(\omega') + N_1(\omega') (b^{-1} y_1 - \omega' \beta_1)] + \varepsilon [\dot{G}_2(T_0) + \dots] &= 0, \\
 \varepsilon (M_3 + \beta_3)^{-1} [\dot{H}_1(T_0) + \varepsilon \dot{H}_2(T_0) + \varepsilon^2 \dot{H}_3(T_0) + \dots] &= \alpha(\varepsilon),
 \end{aligned} \tag{30}$$

Replacing M_1, M_2 and M_3 by β_1, β_2 and $M_3 + \beta_3$ into (28), we obtain $L_1(\omega')$ and $N_1(\omega')$. Therefore, we get

$$L_1(\omega') - \omega'^2 N_1(\omega') = (\beta_1^2 + \beta_2^2) W_1(\omega'), \tag{31}$$

where

$$W_1(\omega') = \frac{1}{4} \left[b(\omega' X)^2 - a \right] \left[2\omega'^2 - (aBr_0)^{-1} \ell_3 \right] - (1+b)(\omega'^2 X)^2.$$

From the condition that the z -axis has to be directed along the major or the minor axis of the ellipsoid of inertia of the body, it follows that $W_1(\omega') > 0$ for all ω' under consideration.

By use of (30), the expression of β_1 and β_2 are obtained in the form of a power series of integral powers of ε . These expansions begin with terms of order higher than ε^2 . Consequently, the first terms in the expansions of the periodic solutions and the quantity $\alpha(\varepsilon)$ are expressed in the following forms

$$\begin{aligned} p_1 &= \varepsilon x'_{10} (b\omega'^2)^{-1} (1 + (Ar_0)^{-1} \ell_3) + \dots, \\ q_1 &= \varepsilon a^{-1} x'_{20} X + \dots, \\ r_1 &= 1 - \varepsilon^2 M_3 [x'_{10} (1 - \cos \tau) + x'_{20} \sin \tau] + \dots, \\ \gamma_1 &= M_3 \cos \tau + \dots, \\ \gamma'_1 &= -M_3 \sin \tau + \varepsilon^2 X \{ a^{-1} x'_{20} - M_3^2 \sin \tau [x'_{10} (1 - \cos \tau) + x'_{20} \sin \tau] \} + \dots, \\ \gamma''_1 &= 1 + \varepsilon^2 M_3 [(a\chi + x'_{10})(1 - \cos \tau) + (Xba^{-1} + 1)x'_{20} \sin \tau] + \dots, \\ \alpha(\varepsilon) &= -2\varepsilon \pi n x'_{10} M_3 + \dots. \end{aligned} \tag{32}$$

An inspection of the previous solutions shows that there are no singular points at all owing to the introduction of Amer's frequency ω' [10–12] instead of ω . This means that these solutions are valid for all rational values of ω' and are considered as a general case of [1] and [7].

4 Discussion of the Results

This section is devoted to reveal the affection of different parameters on the body motion. Therefore, we consider the following data which determine the motion of the body

$$\begin{aligned} A &= 8.53 \text{ kg.m}^2, \quad B = 21.49 \text{ kg.m}^2, \quad r_0 = 1000 \text{ m}, \quad \gamma''_0 = 0.352, \\ M &= 300 \text{ kg}, \quad x_{10} = 1 \text{ m}, \quad x_{20} = 2 \text{ m}, \quad T = 12.566371, \\ \ell_3 &= (100, 150, 200, 300, 400, 500) \text{ kg.m}^2.\text{s}^{-1}. \end{aligned}$$

An inspection of Figs.1 and 2 shows that, they are calculated when $\ell_3 = (100, 150, 200) \text{ kg. m}^2. \text{ s}^{-1}$ and $\ell_3 = (300, 400, 500) \text{ kg. m}^2. \text{ s}^{-1}$ respectively, in which they are representing the variation of the solution p_1 via t . It clears that when the third component ℓ_3 of the gyro moment $\underline{\ell}$ increases, periodic waves are obtained, the amplitude of the waves decreases while the numbers of oscillations remain unchanged which give an induction about the motion is stable and free of chaos. On the other hand Figs.3 and 4 represent the variation of solution γ_1 against time t . It is evident that periodic waves are obtained when time goes on, the number numbers of fluctuations behaves a stable manner while the amplitudes increases to some extent when ℓ_3 increases. Figures 5, 6, 7, and 8 reveal the phase plane diagrams for the solutions p_1 and γ_1 via their corresponding velocities in which closed curves are obtained. They indicate the solutions p_1 and γ_1 behave a stable manner.

Fig. 1 Time history of the solution p_1 when $\ell_3 = (100, 150, 200)$

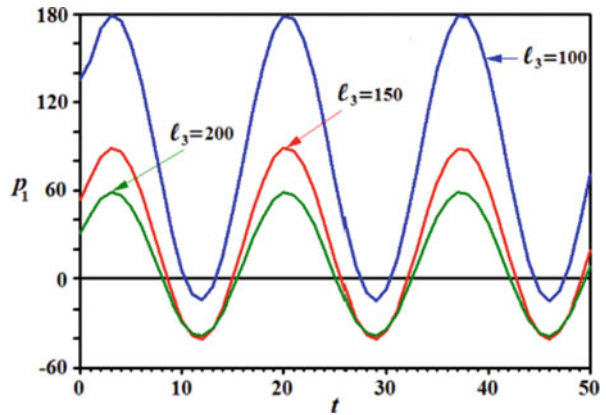


Fig. 2 Time history of the solution p_1 when $\ell_3 = (300, 400, 500)$

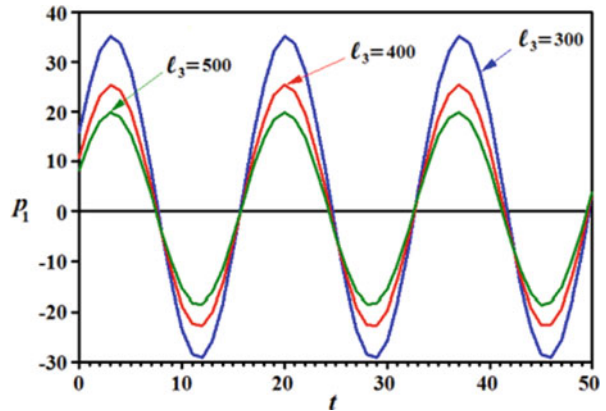


Fig. 3 Variation of the solution γ_1 when $\ell_3 = (100, 150, 200)$

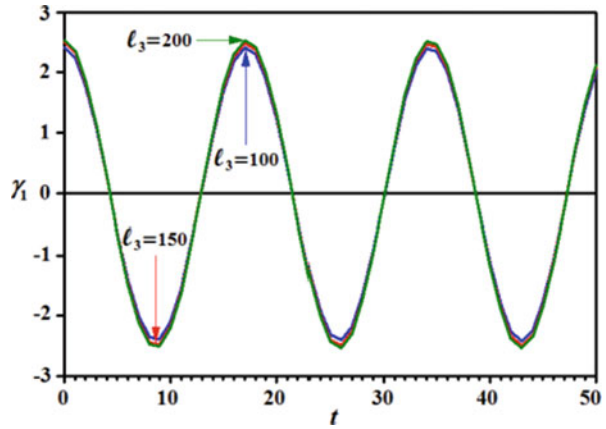


Fig. 4 Variation of the solution γ_1 when $\ell_3 = (300, 400, 500)$

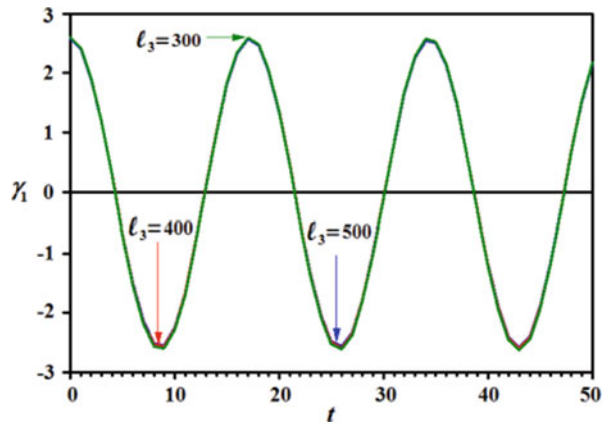


Fig. 5 Phase portrait of the p_1 at $\ell_3 = 100$

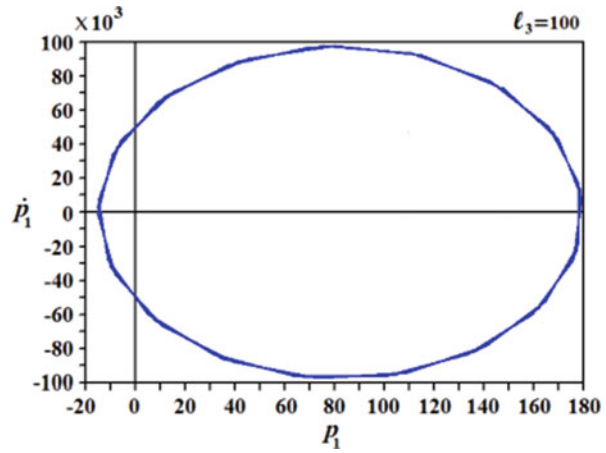


Fig. 6 Phase portrait of the p_1 at $\ell_3 = 400$

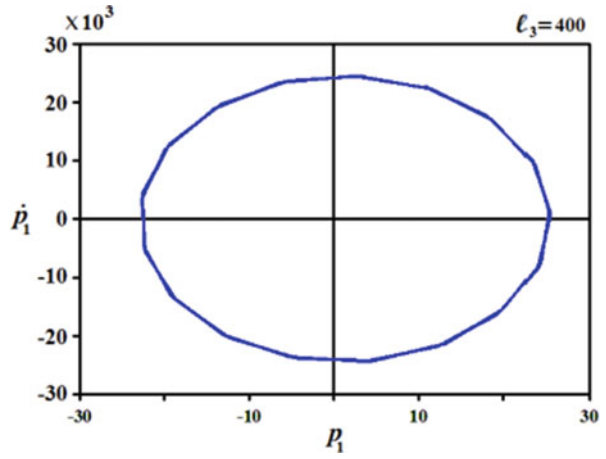


Fig. 7 Phase portrait of the γ_1 at $\ell_3 = 100$

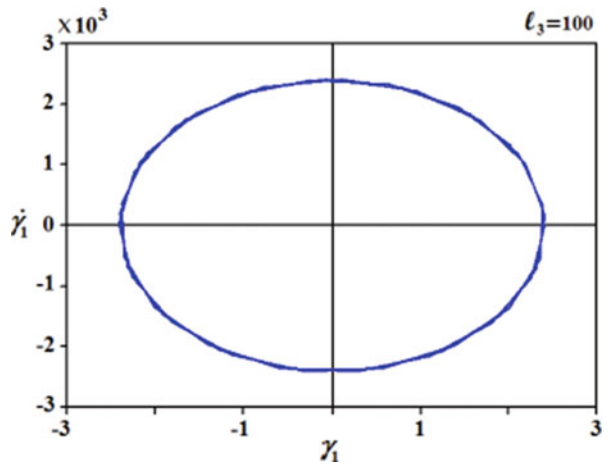
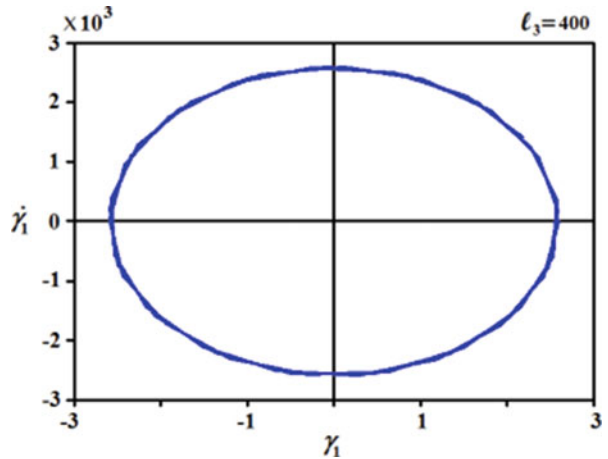


Fig. 8 Phase portrait of the γ_1 at $\ell_3 = 400$



5 Conclusion

The rotational motion of a rigid body about a fixed point under the influence of Newtonian field and a gyro moment about is investigated. The system of equations of motion and their first three integrals are reduced into a quasilinear autonomous one with 2DOF and one first integral. The periodic solutions of governing system of motion are obtained utilizing the Poincaré small parameter method up to the first order approximation. These solutions are considered as a generalization of some previous cases like [1] and [7]. The solutions and the correction of the period for the latter problems can be deduced from the attained solutions as limiting cases. These solutions do not have any singular points at all and are performed by computer codes to get their graphical representations.

References

1. Arkhangel'skii, I.A.: On a motion of a disk in a Newtonian force field. *J. Appl. Math. Mech.* **28**(4), 923–925 (1964)
2. Arkhangel'skii, I.A.: On the motion of the Hess gyroscope. *J. Appl. Math. Mech.* **34**(5), 934–938 (1970)
3. Vagner, E.A., Demin, V.G.: On a class of periodic motions of a solid body about a fixed point. *J. Appl. Math. Mech.* **39**(5), 890–893 (1975)
4. Bogaevskii, V.N., Ostrer, L.A.: On the fast rotation of a heavy rigid body about a fixed point. *J. Appl. Math. Mech.* **44**(6), 713–720 (1980)
5. Longuski, J.M., Tsiotras, P.: Analytic solution of the large angle problem in rigid body attitude dynamics. *J. Astronaut. Sci.* **43**(1), 25–46 (1995)
6. Abrarova, Y.V., Karapetyan, A.V.: Bifurcation and stability of the steady motions and relative equilibria of a rigid body in a central gravitational field. *J. Appl. Math. Mech.* **60**(3), 369–380 (1996)
7. Ismail, A.I.: The motion of a fast spinning disc which comes out from the limiting case $\gamma \neq 0 \approx 0$. *Comput. Methods Appl. Mech. Eng.* **161**, 67–76 (1998)
8. Longuski, J.M., Tsiotras, P.: Analytical solution of the large angle problem in the rigid body attitude dynamics. *J. Astronaut. Sci.* **43**, 25–46 (1995)
9. Longuski, J.M.: Real solutions for the attitude motion of a self-excited rigid body. *Acta Astronaut.* **25**, 131–139 (1991)
10. Ismail, A.I., Amer, T.S.: The fast spinning motion of a rigid body in the presence of a gyrostatic momentum ℓ_3 . *Acta Mech.* **154**, 31–46 (2002)
11. Amer, T.S.: On the motion of a gyrostat similar to Lagrange's gyroscope under the influence of a gyrostatic moment vector. *Nonlinear Dyn.* **54**, 249–262 (2008)
12. Amer, T.S.: On the dynamical motion of a gyro in the presence of external forces. *Adv. Mech. Eng.* **9**, 1–13 (2017)
13. Bogoliubov, N.N., Mitropolsky, Y.A.: *Asymptotic Methods in the Theory of Non-linear Oscillations*. Gordon and Breach, New York (1961)
14. Nayfeh, A.H.: *Perturbations Methods*, WILEY-VCH Verlag GmbH and co. Weinheim, KGaA (2004)
15. Ismail, A.I.: On the application of Krylov-Bogoliubov-Mitropolski technique for treating the motion about a fixed point of a fast spinning heavy solid. *ZFW.* **20**, 205–208 (1996)
16. Ismail, A.I.: Periodic solutions of equations of motion of a heavy solid applying Krylov-Bogoliubov-Mitropolski method. *J. Comput. Appl. Math.* **114**, 345–359 (2000)

17. Amer, T.S., Ismail, A.I., Amer, W.S.: Application of the Krylov-Bogoliubov-Mitropolski technique for a rotating heavy solid under the influence of a gyrostatic moment. *J. Aerospace Eng.* **25**, 421–430 (2012)
18. Amer, T.S., Abady, I.M.: On the application of KBM method for the 3-D motion of asymmetric rigid body. *Nonlinear Dyn.* **89**, 1591–1609 (2017)
19. Amer, T.S., Amer, W.S.: The rotational motion of a symmetric rigid body similar to Kovalevskaya's case. *Iran J Sci Technol Trans Sci.* **42**(3), 1427–1438 (2018)
20. Amer, T.S.: The rotational motion of the electromagnetic symmetric rigid body. *Appl. Math. Inf. Sci.* **10**(4), 1453–1464 (2016)
21. Amer, T.S., Abady, I.M.: On the motion of a gyro in the presence of a Newtonian force field and applied moments. *Math. Mech. Solids.* **23**(9), 1263–1273 (2018)
22. Leimanis, E.: *The General Problem of the Motion of Coupled Rigid Bodies about a Fixed Point.* Springer Verlag, Berlin (1965)
23. Arkhangel'skii, I.A.: *Construction of Periodic Solutions for the Euler-Poisson Equations by Means of Power Series Expansion Containing a Small Parameter.* Colloquia Mathematica Societatis Janos Bolyai, Keszthely (Hungary) (1975)

Suppression of Impact Oscillations in a Railway Current Collection System with an Additional Oscillatory System



Naoto Nishiyama and Kiyotaka Yamashita

Abstract A railway current collection system consists of a wire and a pantograph. The wave-like wear on the surface of an overhead rigid conductor line can cause contact loss between the conductor line and the pantograph. To explain the dynamical features of this problem, the essential model of the impact oscillations between the pantograph and the rigid conductor line has been previously proposed. This model consists of a single-degree-of-freedom system and an external excitation source that pushes against the system. In the present study, we add an oscillatory system is coupled to this model. We investigate the effects of the added system on the impact oscillations between the main mass and the excitation source. When the excitation frequency is near the second mode natural frequency, the impact oscillations are suppressed. In particular, a series of experiments are conducted with slowly increasing the excitation frequency to verify this theoretical result.

Keywords Impact oscillation · Nonlinear oscillation · Suppression · Experiments

1 Introduction

The impact oscillations between the mechanical elements are often produced by various reasons [1, 2]. In some cases, these impact oscillations are unacceptable and should be eliminated. A railway current collection system consists of a wire and a pantograph. The contact forces acting on the pantograph can fluctuate for various reasons. When the fluctuations become large, the pantograph will separate from the wire leading to contact loss and arching. Therefore, it is important to prevent contact loss to prolong service life and reduce maintenance.

N. Nishiyama (✉) · K. Yamashita
Fukui University of Technology, Fukui, Japan
e-mail: nishiyama@fukui-ut.ac.jp
<https://www.fukui-ut.ac.jp/laboratories/mechanical/entry-5956.html>

© Springer Nature Switzerland AG 2021
J. Awrejcewicz (ed.), *Perspectives in Dynamical Systems III: Control and Stability*,
Springer Proceedings in Mathematics & Statistics 364,
https://doi.org/10.1007/978-3-030-77314-4_2

A rigid conductor line is commonly used in tunnels. The wave-like wear on the surface of a conductor line forms over time and is one of the causes of contact loss. To explain the dynamical features of a pantograph after contact loss, Kawamura et al. [3] proposed an essential model of the impact oscillations between a pantograph and a rigid conductor line based on the results of experiments on an actual pantograph system. This model consists of a single-degree-of-freedom system and an external excitation source that pushes against the system. Nonlinear analyses showed periodic impact oscillations, periodic doubling motions and chaos. They conducted experiments and verified the theoretical results. In our previous study [4], we investigated the effects of the flexural vibrations of a pantograph on bifurcating motions. The pantograph was modeled as a flexural beam supported at the midpoint by a spring. When the excitation frequency is near the second mode natural frequency, we theoretically confirmed that the impact oscillations could be strongly suppressed.

For an undamped single-degree-of-freedom system, the application of dynamic vibration absorbers eliminates the forced excitation caused by a harmonic external force with constant frequency. In the present study, we couple a spring supported mass to the single-degree-of-freedom system (main mass) and construct a two-degree-of-freedom system. To examine the effects of the additional mass-spring system on the impact oscillations, we numerically investigate the bifurcating impact oscillations. We then conduct a series of experiments with slowly increasing the excitation frequency to confirm the bifurcating motions. When the excitation frequency is near the second mode natural frequency, the impact oscillations can be widely suppressed, as predicted by the numerical investigations.

2 Experiments

2.1 Experimental Apparatus

Figure 1 shows the experimental apparatus. Two aluminum blocks are used as the main mass m_1 and the added mass m_2 . Linear guides are used to restrict the motions of the two masses in the horizontal direction. A vibration generator periodically changes the displacement of the aluminum frame, which is used as the external excitation source that is pushed against the main mass. The main mass and the added mass are elastically supported by two coiled springs k_1 and k_2 . Experiments were carried out using the parameters determined for the system: $m_1 = m_2 = 0.52$ kg and $k_1 = k_2 = 750$ N/m. The displacements of the main mass, added mass, and excitation source are measured by three eddy current displacement sensors. The data are stored on a computer. The first and second mode natural frequencies are $\omega_1/2\pi = 3.8$ Hz and $\omega_2/2\pi = 9.8$ Hz, respectively.

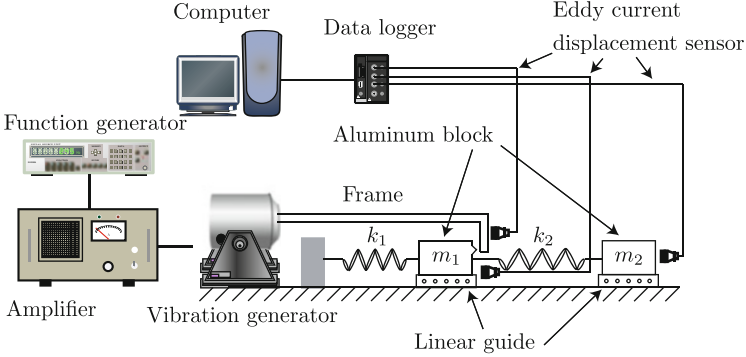


Fig. 1 Experimental apparatus

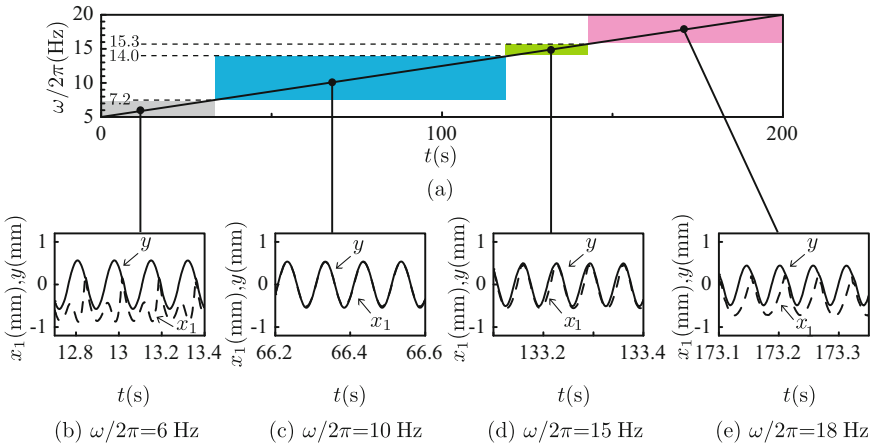


Fig. 2 Time histories of x_1 and y with slowly increasing ω . (a) Variation of ω and results for (b) $\omega/2\pi = 6$ Hz (impact oscillation), (c) $\omega/2\pi = 10$ Hz (no impact oscillation), (d) $\omega/2\pi = 15$ Hz (impact oscillation), and (e) $\omega/2\pi = 18$ Hz (periodic impact oscillation)

2.2 Experimental Results

In the experiments, the excitation frequency $\omega/2\pi$ was slowly varied from 5 Hz to 20 Hz. Figure 2 shows the time histories of the displacements of the main mass and the excitation source. y , x_1 , and x_2 are the displacements of the excitation source, main mass, and added mass, respectively. Figure 2a shows the variation of the excitation frequency $\omega/2\pi$. The solid and broken lines in Figs. 2b–e represent y and x_1 , respectively. For $5.0 \text{ Hz} \leq \omega/2\pi \leq 7.1 \text{ Hz}$, we observed impact oscillations, as shown in Fig. 2b. When ω is near the second mode natural frequency $\omega_2/2\pi = 9.8 \text{ Hz}$ ($7.2 \text{ Hz} \leq \omega/2\pi \leq 14.0 \text{ Hz}$), Fig. 2c shows that the impact oscillations between the main mass and the excitation source are suppressed and that the main mass is always in contact with the excitation source. When ω is increased further, the

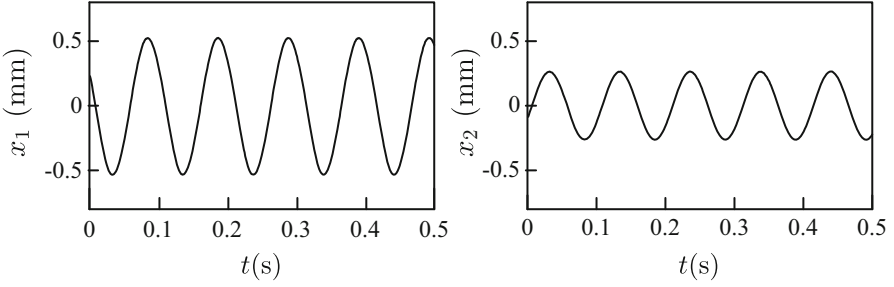


Fig. 3 Time histories of x_1 and x_2 . x_1 and x_2 move in opposite directions ($\omega/2\pi = 9.8$ Hz)

main mass gradually separates from the excitation source, as shown in Fig. 2d. For $\omega/2\pi > 15.3$ Hz, we observe periodic impact oscillations, as shown in Fig. 2e.

Figure 3 shows the time histories of x_1 and x_2 ($\omega/2\pi = 9.8$ Hz), respectively. In the region without contact loss (Fig. 2c), the main mass and the added mass move in opposite directions. Therefore, second mode vibration plays an important role in the suppression of impact oscillations.

3 Theoretical Analysis

3.1 Analytical Model and Basic Equation

Figure 4 shows the analytical model for impact oscillations between the sinusoidal excitation source and the main mass. m_1 and m_2 denote the main mass and the additional coupled mass, respectively. m_1 is connected to a fixed plane using a linear spring and is coupled to the additional mass m_2 . k_1 is the spring coefficient between the fixed plane and the main mass. k_2 is the spring coefficient between m_1 and m_2 . The origin of the coordinates is set where the springs do not expand. x_1 and x_2 denote the displacements of the main mass and added mass, respectively.

The excitation source is pushed against the main mass. The displacement of the excitation source y is written as $y = -d + y_0 \sin \omega t$, where d is the push up distance, y_0 is the excitation amplitude, and ω is the excitation frequency. When the main mass comes in contact with the excitation source ($x_1 = y$), the reaction force acts on the main mass. The reaction force at the n th impact time $t = t_n$ can be written in the form $F(t)\delta(t - t_n)$. The Dirac delta function $\delta(t - t_n)$ indicates that the reacting force is applied only at $t = t_n$.

With the introduction of non-dimensional variables $y^* = y/d$, $x_1^* = x_1/d$, $x_2^* = x_2/d$, and $t^* = \sqrt{k_1 t}/\sqrt{m_1}$, the non-dimensional governing equations for the two-degree-of-freedom spring-mass system can be written as follows:

$$\ddot{x}_1 + (1 + \alpha)x_1 - \alpha x_2 = - \sum_{n=1}^{\infty} f(t)\delta(t - t_n), \quad (1)$$

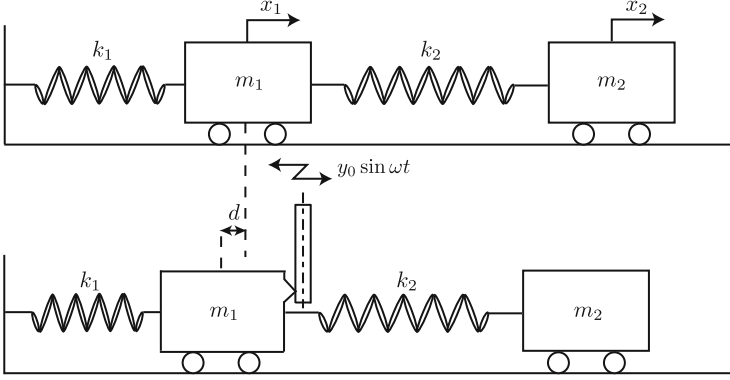


Fig. 4 Analytical model for impact oscillations between the excitation source and the main mass is coupled to the additional mass

$$\mu \ddot{x}_2 - \alpha x_1 + \alpha x_2 = 0. \tag{2}$$

The asterisks which indicate the non-dimensional variables are omitted in Eq. (1) and hereafter. The non-dimensional displacement of the excitation source is

$$y = -1 + \epsilon \sin \Omega t. \tag{3}$$

When we express the velocity of the main mass \dot{x}_1^- immediately before the n th impact time t_n , the velocity after impact \dot{x}_1^+ is given as

$$\dot{x}_{1n}^+ = -e \dot{x}_{1n}^- + (1 + e) \dot{y}(t_n), \tag{4}$$

where e is the coefficient of restitution and the subscript n indicates the n th impact. In Eqs. (1)–(4), the following four non-dimensional parameters are involved:

$$\alpha = \frac{k_2}{k_1}, \quad \epsilon = \frac{y_0}{d}, \quad \Omega = \omega \sqrt{\frac{m_1}{k_1}}, \quad e. \tag{5}$$

Letting $\mathbf{x} = P \mathbf{y}$, we rewrite the governing equations with the modal coordinates $\mathbf{y} = (y_1 \ y_2)^t$, where $\mathbf{x} = (x_1 \ x_2)^t$ and P is a transformation matrix. P is written as $P = (\mathbf{p}_1 \ \mathbf{p}_2)$, where $\mathbf{p}_1 = (\xi_{11} \ \xi_{12})$ and $\mathbf{p}_2 = (\xi_{21} \ \xi_{22})$ are the normalized first and second eigen-vectors, respectively. From the governing equations written in modal coordinates, we obtain the following velocity relationship during the n th impact:

$$\dot{y}_{1n}^+ = Z_1 \dot{y}_{1n}^- + Z_2 \dot{y}_{2n}^- + Z_3 \dot{y}(t_n), \quad \dot{y}_{2n}^+ = Z_4 \dot{y}_{1n}^- + Z_5 \dot{y}_{2n}^- + Z_6 \dot{y}(t_n), \tag{6}$$

where the coefficients Z_1 through Z_6 are given as follows

$$\begin{aligned} Z_1 &= \frac{\xi_{21}^2 - \xi_{11}^2 e}{\xi_{11}^2 + \xi_{21}^2}, & Z_2 &= \frac{-\xi_{11}\xi_{21}(1+e)}{\xi_{11}^2 + \xi_{21}^2}, & Z_3 &= \frac{\xi_{11}(1+e)}{\xi_{11}^2 + \xi_{21}^2}, \\ Z_4 &= \frac{-\xi_{11}\xi_{21}(1+e)}{\xi_{11}^2 + \xi_{21}^2}, & Z_5 &= \frac{\xi_{11}^2 - \xi_{21}^2 e}{\xi_{11}^2 + \xi_{21}^2}, & Z_6 &= \frac{\xi_{21}(1+e)}{\xi_{11}^2 + \xi_{21}^2}. \end{aligned} \quad (7)$$

3.2 Theoretical Results

Using Eqs. (1), (2), (3) and (6), we numerically investigate the effects of the additional mass on the impact oscillations between the main mass and the excitation source. Figure 5a shows the bifurcation diagram for the impact oscillations between the main mass and the excitation source. Ωt_n modulo 2π is the phase of y at the impact time t_n . Figures 5b,c and d show the time histories of x_1 and y . As seen in Figs. 5b and d, impact oscillations occur in the regions $0.88 \leq \Omega \leq 1.18$ and $2.37 \leq \Omega$. When Ω is near the second mode natural frequency $\omega_2 = 1.68$, the main

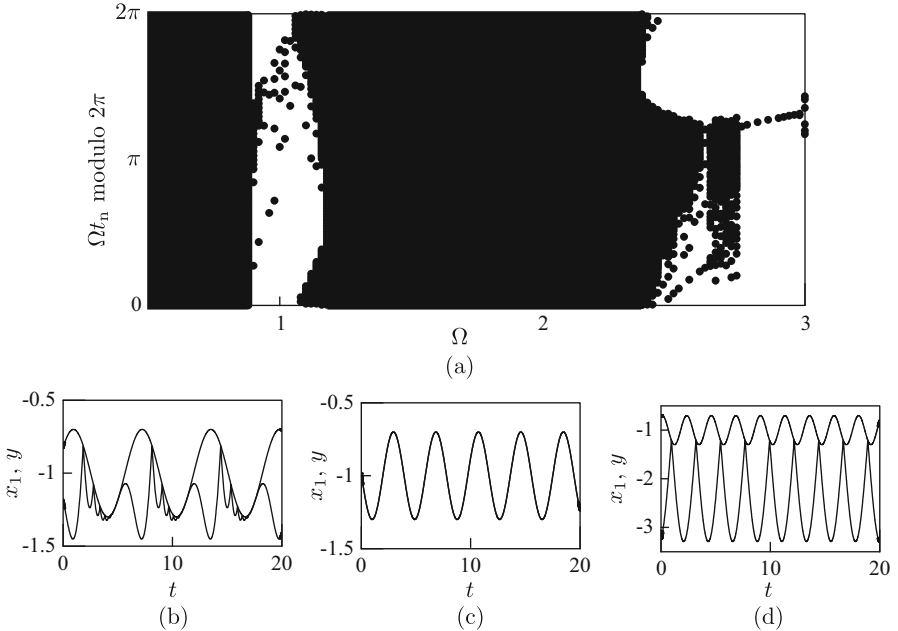


Fig. 5 Impact oscillations between the main mass and the excitation source. (a) Bifurcation diagram ($\alpha = 1$, $\mu = 1$, $e = 0.65$, $\epsilon = 0.3$), (b) time histories of x_1 and y ($\Omega = 1$), (c) time histories of x_1 and y ($\Omega = 1.68$), and (d) time histories of x_1 and y ($\Omega = 2.8$)

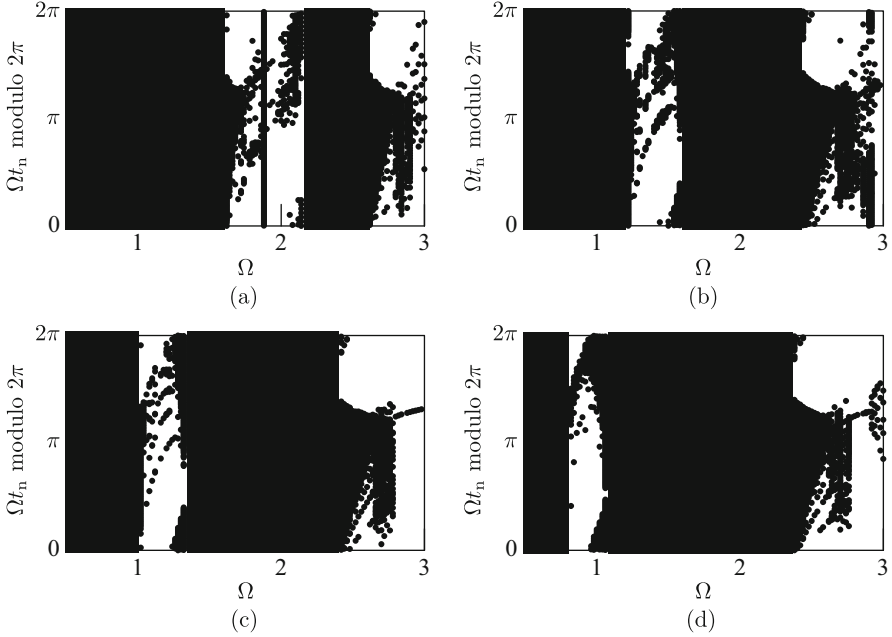


Fig. 6 Bifurcation diagrams ($\alpha = 1$, $\mu = 1$, $e = 0.65$, $\epsilon = 0.3$) for (a) $\mu = 0.25$, (b) $\mu = 0.5$, (c) $\mu = 0.75$ and (d) $\mu = 1.25$

mass is always in contact with the excitation source. $R_L = 1.18$ and $R_H = 2.37$ are the lower and upper limit excitation frequencies, respectively, in the contact region. Therefore, it is confirmed that the additional spring-mass system widely suppresses the impact oscillations between the main mass and the excitation source.

Next, we examine the effect of μ on the contact loss between the excitation source and the main mass. The bifurcation diagram for $\mu = 0.75$ is shown in Fig. 6c. R_L and R_H are 1.33 and 2.40, respectively. The impact oscillations are widely suppressed when ω is near ω_2 . Figure 6a and b shows the results for $\mu = 0.25$ and 0.50. μ decreases as the second mode natural frequency ω_2 becomes larger. Therefore, the contact zone ($R_L \leq \Omega \leq R_H$) shifts to higher frequency. Figure 6d shows the results for $\mu = 1.25$. In this case, R_L and R_H are 1.07 and 2.37, respectively.

4 Conclusions

The impact oscillations between a pantograph and a conductor line in a railway current collection system were investigated. The system was modeled as a mass-spring system subjected to a sinusoidal excitation source that pushed against the

mass. We numerically examined the effect of the additional mass-spring system couples to the main mass on the impact oscillations between the main mass and the excitation source. It was found that when the excitation frequency is near the second mode natural frequency, the impact oscillations are suppressed and contact loss does not occur. Finally, we conducted the experiments with slowly increasing the excitation frequency. We observed the suppression of the impact oscillations for the case where the excitation frequency is near the second mode natural frequency. In the region without contact loss, the main mass and the added mass move in opposite directions. The second mode vibration plays an important role in the suppression of the impact oscillations.

References

1. Bernardo, M., Budd, C., Champneys, A.R. Kowalczyk, P.: Piecewise-Smooth Dynamical Systems Theory and Applications. Springer, New York (2008)
2. Guckenheimer, J., Holmes, P.: Nonlinear Oscillations, Dynamical System, and Bifurcations of Vector Fields. Springer, New York (1983)
3. Kawamura, S., Kitajo, K., Horita, S., Yoshizawa, M.: Fundamental study on impact oscillations of rigid trolley-pantograph system. *Trans. Jpn. Soc. Mech. Eng.* **74**(742), 48–54 (2007)
4. Yamashita, K., Kitajo, K., Wada, S., Sugiura, T., Yabuno, H.: Impact oscillations with multiple modes between a pantograph and an overhead rigid conductor line in a railway current collection system. *J. Vibration Control* **18**(4), 499–508 (2012)

On Qualitative Analysis of Lattice Dynamical System of Two- and Three-Dimensional Biopixels Array: Bifurcations and Transition to “Chaos”



Oleksandr Nakonechnyi, Vasyl Martsenyuk, Mikolaj Karpinski,
and Aleksandra Klos-Witkowska

Abstract We consider the model of two- or three-dimensional biopixels array, which can be used for design of biosensors. The model is based on the system of lattice differential equations with time delay, describing interactions of biological species of neighbouring pixels. The qualitative analysis includes permanence and extinctions of solutions, stability investigation, bifurcations and transition to chaos. The stability conditions are obtained with help of the method of Lyapunov functionals. They are formulated in terms of the value of time necessary for immune response. Numerical research is presented with the help of phase portraits, square and hexagonal lattice plots and bifurcation diagrams.

Keywords Biopixels array · Delayed dynamic system · Qualitative analysis

1 Introduction

Nowadays, reaction-diffusion models are used in designing and studies of a lot of detecting, measuring and sensing devices. Immunosensor, which are studied here as an example, is kind of them. Such spatial-temporal models are described by the systems of partial or lattice differential equations.

O. Nakonechnyi

Department of Systems Analysis and Decision Making Theory, Taras Shevchenko National University of Kyiv, Kyiv, Ukraine

<https://csc.knu.ua/uk/person/nakonechniy>

V. Martsenyuk (✉) · M. Karpinski · A. Klos-Witkowska

Department of Computer Science and Automatics, University of Bielsko-Biala, Bielsko-Biala, Poland

e-mail: vmartsenyuk@ath.bielsko.pl; <http://www.kinf.ath.bielsko.pl/pl/vasyl-martsenyuk>;
mkarpinski@ath.bielsko.pl; <http://www.kinf.ath.bielsko.pl/pl/mikolaj-karpinski>;
awitkowska@ath.bielsko.pl; <http://www.kinf.ath.bielsko.pl/pl/aleksandra-klos-witkowska>

© Springer Nature Switzerland AG 2021

J. Awrejcewicz (ed.), *Perspectives in Dynamical Systems III: Control and Stability*,

Springer Proceedings in Mathematics & Statistics 364,

https://doi.org/10.1007/978-3-030-77314-4_3

The biosensor models are traditionally studied from the viewpoint of their qualitative analysis. Even in case of a small number of spatial elements they show complex behavior. In [1] it was shown that the model describing the chemical reaction of two morphogens (reactants), one of them diffusing within two compartments, results in “bi-chaotic” behavior. The origin of such chaotic phenomena¹ were also explained with help of statistics of topological defects [2].

When considering continuously distributed reaction-diffusion models described by nonlinear partial differential equations, Feigenbaum-Sharkovskii-Magnitskii bifurcation theory can be applied, which results in a subharmonic cascade of bifurcations of stable limit cycles [3].

The lattice differential equations describes the systems with the discrete spatial structure, which is more consistent with pixel devices. These equations were also called earlier by a series of authors as spatially discrete differential equations [4].

In [5] a lattice differential equation was presented in the form

$$\dot{u}_\xi = g_\xi(\{u_\zeta\}_{\zeta \in \Lambda}), \xi \in \Lambda, \quad (1)$$

where a lattice $\Lambda \subset \mathbb{R}^n$ can be determined as a discrete subset of \mathbb{R}^n , arranged in accordance with some regular spatial structure. Here u_ξ , $\xi \in \Lambda$ are the values of $u = \{u_\xi\}_{\xi \in \Lambda}$ at the points of the lattice, g_ξ are the right sides of the equations enabling us the existence of solution.

As a rule, without loss of generality, they consider $\Lambda = \mathbb{Z}^n$, which is the integer lattice in \mathbb{R}^n . The methods developed can be easily applied to a different type of lattices, namely, the planar rectangular and hexagonal lattice, the crystallographic lattices in \mathbb{R}^3 .

They pay an attention to the notion of delay in lattice differential equations, so-called delayed lattice differential equations. One of the application dealing with them is the investigation of traveling wave fronts and their stability [5]. The main results are applied to the delayed and discretely diffusive models for the population (see, e.g. [6, 7]).

Lattice differential equations are used as models in a lot of applications, for example, cellular neural networks, image processing, chemical kinetics, material science, in particular metallurgy, and biology [5, 8]. Lattice models are extremely attractive from viewpoint of population dynamics especially in case of spatially separated populations [5, 6, 8–11].

There are few reasons requiring consideration the hexagonal grid instead of rectangular ones (primarily in image and vision computing). Namely, the equal distances between neighboring pixels for hexagonal coordinate systems [12]; hexagonal points are packed more densely [13]; since the “hexagons are ‘rounder’ than squares”, the presentation of curves are more consistent with help of hexagonal systems [13]; hence, mathematical operations of edge detection and shape extraction are more successfully when applying hexagonal lattices [14].

¹They call it as “spiral turbulence” [2].

With the purpose of indexing hexagonal pixels, as a rule, they use two-² or three-³ element coordinate systems [15]. Our reasonings will be based on the last one. In contrary to skewed axes, the using of the cubic coordinates enables us symmetries with respect to all three axes.

2 Lattice Model of Antibody-Antigen Interaction for Two-Dimensional Biopixels Array

Let $V_{i,j}(t)$ be concentration of antigens, $F_{i,j}(t)$ be concentration of antibodies in biopixel (i, j) , $i, j = \overline{1, N}$ (Fig. 1).

The model is based on the following biological assumptions for arbitrary biopixel (i, j) .

1. We have some constant birthrate $\beta > 0$ for antigen population.
2. Antigens are detected, binded and finally neutralized by antibodies with some probability rate $\gamma > 0$.

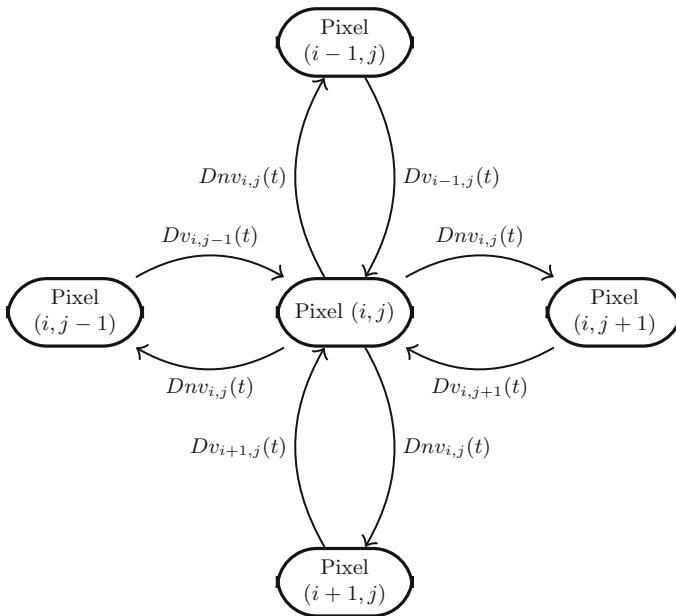


Fig. 1 Linear lattice interconnected four neighboring pixels model, $n > 0$ is disbalance constant

²So called “skewed-axis” coordinate system.

³It is also known as “cube hex coordinate system”.

3. We have some constant death rate of antibodies $\mu_f > 0$.
4. We assume that when the antibody colonies are absent, the antigen colonies are governed by the well known delay logistic equation:

$$\frac{dV_{i,j}(t)}{dt} = (\beta - \delta_v V_{i,j}(t - \tau))V_{i,j}(t), \quad (2)$$

where β and δ_v are positive numbers and $\tau \geq 0$ denotes delay in the negative feedback of the antigen colonies.

5. The antibody decreases the average growth rate of antigen linearly with a certain time delay τ ; this assumption corresponds to the fact that antibodies cannot detect and bind antigen instantly; antibodies have to spend τ units of time before they are capable of decreasing the average growth rate of the antigen colonies; these aspects are incorporated in the antigen dynamics by the inclusion of the term $-\gamma F_{i,j}(t - \tau)$ where γ is a positive constant which can vary depending on the specific colonies of antibodies and antigens.
6. In case of the lack of antigen colonies, the average growth rate of the antibody colonies decreases exponentially due to the presence of $-\mu_f$ in the antibody dynamics, and to incorporate the negative effects of antibody crowding, we have included the term $-\delta_f F_{i,j}(t)$ in the antibody dynamics.
7. The positive feedback $\eta\gamma V_{i,j}(t - \tau)$ in the average growth rate of the antibody has a delay since mature adult antibodies can only contribute to the production of antibody biomass; one can consider the delay τ in $\eta\gamma V_{i,j}(t - \tau)$ as a delay in antibody maturation.
8. While the last delay need not be the same as the delay in the hunting term and in the term governing antigen colonies, we have retained this for simplicity. We remark that the delays in the antibody term, antibody replacement term and antigen negative feedback term can be made different and a similar analysis can be followed.
9. We have some diffusion of antigens from four neighboring pixels $(i - 1, j)$, $(i + 1, j)$, $(i, j - 1)$, $(i, j + 1)$ (see Fig. 4) with diffusion $D > 0$. Here we consider only diffusion of antigens, because the model describes so-called “competitive” configuration of immunosensor [16]. When considering competitive configuration of immunosensor, the factors immobilized on the biosensor matrix are antigens, while the antibodies play the role of analytes or particles to be detected.
10. We consider surface lateral diffusion (movement of molecules on the surface on solid phase toward an immobilized molecules) [17]. Moreover, there are works [18, 19] which assume and consider surface diffusion as an entirely independent stage.
11. We extend definition of usual diffusion operator in case of surface diffusion in the following way. Let $n \in (0, 1]$ be a factor of diffusion disbalance. It means that only n th portion of antigens of the pixel (i, j) may be included into diffusion process to any neighboring pixel as a result of surface diffusion.

For the reasonings given we consider a very simple delayed antibody-antigen competition model for biopixels two-dimensional array which is based on well-known Marchuk model [20–23] and using spatial operator \hat{S} offered in [24] (Supplementary information, p.10)

$$\begin{aligned} \frac{dV_{i,j}(t)}{dt} &= (\beta - \gamma F_{i,j}(t - \tau) - \delta_v V_{i,j}(t - \tau))V_{i,j}(t) + \hat{S}\{V_{i,j}\}, \\ \frac{dF_{i,j}(t)}{dt} &= (-\mu_f + \eta\gamma V_{i,j}(t - \tau) - \delta_f F_{i,j}(t))F_{i,j}(t) \end{aligned} \quad (3)$$

with given initial functions

$$\begin{aligned} V_{i,j}(t) = V_{i,j}^0(t) \geq 0, \quad F_{i,j}(t) = F_{i,j}^0(t) \geq 0, \quad t \in [-\tau, 0), \\ V_{i,j}(0), F_{i,j}(0) > 0. \end{aligned} \quad (4)$$

For a square $N \times N$ array of traps, we use the following discrete diffusion form of the spatial operator [24]

$$\hat{S}\{V_{i,j}\} = \begin{cases} D[V_{1,2} + V_{2,1} - 2nV_{1,1}] & i, j = 1 \\ D[V_{2,j} + V_{1,j-1} + V_{1,j+1} - 3nV_{i,j}] & i = 1, j \in \overline{2, N-1} \\ D[V_{1,N-1} + V_{2,N} - 2nV_{1,N}] & i = 1, j = N \\ D[V_{i-1,N} + V_{i+1,N} + V_{i,N-1} - 3nV_{i,N}] & i \in \overline{2, N-1}, j = N \\ D[V_{N-1,N} + V_{N,N-1} - 2nV_{N,N}] & i = N, j = N \\ D[V_{N-1,j} + V_{N,j-1} + V_{N,j+1} - 3nV_{N,j}] & i = N, j \in \overline{2, N-1} \\ D[V_{N-1,1} + V_{N,2} - 2nV_{N,1}] & i = N, j = 1 \\ D[V_{i-1,1} + V_{i+1,1} + V_{i,2} - 3nV_{i,1}] & i \in \overline{2, N-1}, j = 1 \\ D[V_{i-1,j} + V_{i+1,j} + V_{i,j-1} + V_{i,j+1} - 4nV_{i,j}] & i, j \in \overline{2, N-1} \end{cases} \quad (5)$$

Each colony is affected by the antigen produced in four neighboring colonies, two in each dimension of the array, separated by the equal distance Δ . We use the boundary condition $V_{i,j} = 0$ for the edges of the array $i, j = 0, N + 1$. Further we will use the following notation of the constant

$$k(i, j) = \begin{cases} 2 & i, j = 1; \quad i = 1, j = N; \quad i = N, j = N; \quad i = N, j = 1, \\ 3 & i = 1, j \in \overline{2, N-1}; \quad i \in \overline{2, N-1}, j = N; \quad i = N, j \in \overline{2, N-1}; \\ & i \in \overline{2, N-1}, j = 1 \\ 4 & i, j \in \overline{2, N-1} \end{cases} \quad (6)$$

which will be used in manipulations with the spatial operator (5).

Results of modeling (3) are presented further. It can be seen that qualitative behavior of the system is determined mostly by the time of immune response τ (or time delay), diffusion D and constant n .

2.1 Stability Investigation

Steady States The steady states of the model (3) are the intersection of the nullclines $dV_{i,j}(t)/dt = 0$ and $dF_{i,j}(t)/dt = 0$, $i, j = \overline{1, N}$.

Antigen-Free Steady State If $V_{i,j}(t) \equiv 0$, the free antigen equilibrium is at $\mathcal{E}_{i,j}^0 \equiv (0, 0)$, $i, j = \overline{1, N}$ or $\mathcal{E}_{i,j}^0 \equiv (0, -\frac{\mu_f}{\delta_f})$, $i, j = \overline{1, N}$. The last solution does not have biological sense and can not be reached for nonnegative initial conditions (4).

When considering endemic steady state $\mathcal{E}_{i,j}^* \equiv (V_{i,j}^*, F_{i,j}^*)$, $i, j = \overline{1, N}$ for (3) we get algebraic system:

$$\begin{aligned} (\beta - \gamma F_{i,j}^* - \delta_v V_{i,j}^*) V_{i,j}^* + \hat{S} \{V_{i,j}^*\} &= 0, \\ (-\mu_f + \eta\gamma V_{i,j}^* - \delta_f F_{i,j}^*) F_{i,j}^* &= 0, \quad i, j = \overline{1, N}. \end{aligned} \quad (7)$$

The solutions $(V_{i,j}^*, F_{i,j}^*)$ of (7) can be found as a result of solving lattice equation with respect to $V_{i,j}^*$, and using relation $F_{i,j}^* = \frac{-\mu_f + \eta\gamma V_{i,j}^*}{\delta_f}$

Then we have to differ two cases.

Identical Endemic State for All Pixels Let's assume there is a solution of (7) $V_{i,j}^* \equiv V^*$, $F_{i,j}^* \equiv F^*$, $i, j = \overline{1, N}$, i.e., $\hat{S} \{V_{i,j}^*\} \equiv 0$. Then $\mathcal{E}_{i,j}^* = (V^*, F^*)$, $i, j = \overline{1, N}$ can be calculated as

$$V^* = \frac{-\beta\delta_f - \gamma\mu_f}{\delta_v\delta_f - \eta\gamma^2}, \quad F^* = \frac{\delta_v\mu_f - \eta\gamma\beta}{\delta_v\delta_f - \eta\gamma^2}. \quad (8)$$

provided that $\delta_v\delta_f - \eta\gamma^2 < 0$.

Nonidentical Endemic State for Pixels In general case we have endemic steady state which is different from (8). It is shown numerically in Appendix B that it appears as a result of diffusion between pixels D .

At absence of diffusion, i.e. $D = 0$, we have only identical endemic state for pixels of external layer. At presence of diffusion $D > 0$ nonidentical endemic states tends to identical one (8) at internal pixels, which can be observed at numerical simulation. This phenomenon is clearly appeared at bigger amount of pixels.

Basic Reproduction Numbers Here we define the basic reproduction number for antigen colony which is localized in pixel (i, j) . When considering epidemic models, the basic reproduction number, \mathcal{R}_0 , is defined as the expected number of secondary cases produced by a single (typical) infection in a completely susceptible population. It is important to note that \mathcal{R}_0 is a dimensionless number [25]. When applying this definition to the pixel (i, j) , which is described by the equation (3), we get

$$\mathcal{R}_{0,i,j} = \mathcal{T}_{i,j} \bar{c}_{i,j} d_{i,j}$$

where $\mathcal{T}_{i,j}$ is the transmissibility (i.e., probability of binding given constant between an antigen and antibody), $\bar{c}_{i,j}$ is the average rate of contact between antigens and antibodies, and $d_{i,j}$ is the duration of binding of antigen by antibody till deactivation.

Unfortunately, the lattice system (3) doesn't include all parameters, which allow to calculate the basic reproduction numbers in a clear form. Firstly, let's consider pixel (i^*, j^*) without diffusion, i.e., $\hat{S}\{V_{i^*,j^*}\} \equiv 0$. In this case the non-negative equilibria of (3) are

$$\mathcal{E}_{i^*,j^*}^0 = (V^0, 0) := \left(\frac{\beta}{\delta_v}, 0\right), \quad \mathcal{E}_{i^*,j^*}^* = (V^*, F^*).$$

Due to the approach which was offered in [26] (in pages 4 for ordinary differential equations, 5 for delay model), we introduce the basic reproduction number for pixel (i^*, j^*) without diffusion, which is given by expression

$$\mathcal{R}_{0,i^*,j^*} := \frac{V^0}{V^*} = \frac{\beta}{\delta_v V^*} = \frac{\beta(\eta\gamma^2 - \delta_v\delta_f)}{\delta_v(\beta\delta_f + \gamma\mu_f)}.$$

Its biological meaning is given as being the average number of offsprings produced by a mature antibody in its lifetime when introduced in a antigen-only environment with antigen at carrying capacity.

Following the approach of population dynamics it has to be shown that antibody-free equilibrium \mathcal{E}_{i^*,j^*}^0 is locally asymptotically stable if $\mathcal{R}_{0,i^*,j^*} < 1$ and it is unstable if $\mathcal{R}_{0,i^*,j^*} > 1$ (see, e.g. [27]). It can be done with help of analysis of the roots of characteristic equation (similarly to [26], p.5). Thus, $\mathcal{R}_{0,i^*,j^*} > 1$ is sufficient condition for existence of the endemic equilibrium \mathcal{E}_{i^*,j^*}^* .

We can consider the expression mentioned above for the general case of the lattice system (3), i.e., when considering diffusion. In this case we have the "lattice" of the basic reproduction numbers $\mathcal{R}_{0,i,j}$, $i, j = \overline{1, N}$ satisfying to

$$\mathcal{R}_{0,i,j} := \frac{V_{i,j}^0}{V_{i,j}^*}, \quad i, j = \overline{1, N}, \quad (9)$$

where $\mathcal{E}_{i,j}^0$, $i, j = \overline{1, N}$ are nonidentical steady states, which are found as a result of solution of the algebraic system

$$\left(\beta - \delta_v V_{i,j}^0\right) V_{i,j}^0 + \hat{S} \left\{ V_{i,j}^0 \right\} = 0, \quad i, j = \overline{1, N}, \quad (10)$$

endemic states $\mathcal{E}_{i,j}^* = \left(V_{i,j}^*, F_{i,j}^*\right)$, $i, j = \overline{1, N}$ are found using (7).

It is worth to say that due to the principles of population dynamics the conditions

$$\mathcal{R}_{0,i,j} > 1, \quad i, j = \overline{1, N} \quad (11)$$

have to be sufficient for the existence of endemic state $\mathcal{E}_{i,j}^*$. We will check it only with help of numerical simulations.

2.2 Persistence of the Solutions

We will use the following definition which generalizes [28] for lattice differential equations.

Definition 1 System (3) is said to be uniformly persistent if for all $i, j = \overline{1, N}$ there exist compact regions $\mathcal{D}_{i,j} \subset \text{int}\mathbb{R}^2$ such that every solution $(V_{i,j}(t), F_{i,j}(t))$, $i, j = \overline{1, N}$ of (3) with the initial conditions (4) eventually enters and remains in the region $\mathcal{D}_{i,j}$.

Theorem 1 Let $(V_{i,j}(t), F_{i,j}(t))$, $i, j = \overline{1, N}$ be the solutions of (3) with initials conditions (4). If

$$\beta\eta\gamma - \mu_f\delta_v > 0, \quad (12)$$

then

$$0 < V_{i,j}(t) \leq M_v, \quad 0 < F_{i,j}(t) \leq M_f \quad (13)$$

for some large values of t . Here

$$M_v = \frac{\beta}{\delta_v} e^{\beta\tau}, \quad M_f = \frac{1}{\delta_f} \left(\eta\gamma M_v - \mu_f \right). \quad (14)$$

Proof Firstly, we can prove that there exists some large instant of time T_1 that $\hat{S}\{V_{i,j}(t)\} \leq 0$, $i, j = \overline{1, N}$, $t > T_1$.

Let's assume the contrary, i.e. there is $i^*, j^* \in \overline{1, N}$, that $\hat{S}\{V_{i,j}(t)\} > 0$ at $t > T_1$, which is a contradiction with a balance principle.

Since the solutions of the system (3), (4) are positive, then

$$\frac{dV_{i,j}(t)}{dt} \leq \left(\beta - \delta_v V_{i,j}(t - \tau) \right) V_{i,j}(t). \quad (15)$$

Further we can apply the basic steps of proof of Lemma 3.1 [29] which is proved in nonlattice case (i.e. without spatial operator).

Remark 1 Conditions of uniform persistence of system (3) in nonlattice case were obtained in [30]. They resulted in inequality (12) provided that

$$\beta \delta_f + \mu_f \gamma > 0 \quad (16)$$

holds.

2.3 Extinction Research

The next result introduces a sufficient condition for the underlying grid size ensuring that the solution of (3) is non-vanishing.

Theorem 2 *Let for the system (3) the positive orthant Ω be positive invariant. Besides that, let N be such that $f_{\text{extnc}}(N) < 1$ holds, where*

$$f_{\text{extnc}}(N) = \max_{k,l=1,N} \left| \beta - \frac{4D}{\Delta^2} \left(1 + \cos \frac{\pi(k+l)}{2(N+1)} \cos \frac{\pi(k-l)}{2(N+1)} \right) \right|. \quad (17)$$

Then $\lim_{t \rightarrow \infty} V_{i,j}(t) = 0$, $i, j = \overline{1, N}$.

Proof It requires a comparison principle for differential equations.

The following inequalities hold for $V_{i,j}(t)$

$$\frac{V_{i,j}(t)}{dt} < \beta V_{i,j}(t) + \hat{S} \{V_{i,j}(t)\}.$$

Consider N^2 -vector of the form

$$V(n) = \left(V_{1,1}(t), V_{1,2}(t), \dots, V_{1,N}(t), V_{2,1}(t), \dots, V_{2,N}(t), \dots, \right. \\ \left. V_{N,1}(t), \dots, V_{N,N}(t) \right)^\top.$$

We compare $\frac{V(t)}{dt} \leq CV(t)$, where $C = I_N \otimes A + B \otimes I_N$,

$$A = \begin{bmatrix} \beta - \frac{4D}{\Delta^2} & \frac{D}{\Delta^2} & & & & \\ \frac{D}{\Delta^2} & \beta - \frac{4D}{\Delta^2} & \frac{D}{\Delta^2} & & & \\ & \frac{D}{\Delta^2} & \ddots & & & \\ & & & \ddots & & \\ & & & & \beta - \frac{4D}{\Delta^2} & \frac{D}{\Delta^2} \\ & & & & \frac{D}{\Delta^2} & \beta - \frac{4D}{\Delta^2} \end{bmatrix} \in \mathbb{R}^{N \times N},$$

$$B = \begin{bmatrix} 0 & \frac{D}{\Delta^2} & & & & \\ \frac{D}{\Delta^2} & 0 & \frac{D}{\Delta^2} & & & \\ & \frac{D}{\Delta^2} & \ddots & & & \\ & & & \ddots & & \\ & & & & 0 & \frac{D}{\Delta^2} \\ & & & & \frac{D}{\Delta^2} & 0 \end{bmatrix} \in \mathbb{R}^{N \times N},$$

I_N is $N \times N$ identity matrix. The N^2 eigenvalues of C are of the form (see [31], Theorem 8.3.1) $\lambda_{k,l}(C) = \lambda_k(A) + \lambda_l(B)$, $k, l = \overline{1, N}$, where the eigenvalues of A

$$\lambda_k(A) = \beta - \frac{4D}{\Delta^2} - \frac{2D}{\Delta^2} \cos(\pi k / (N + 1)), \quad k = \overline{1, N},$$

the eigenvalues of B

$$\lambda_l(B) = -\frac{2D}{\Delta^2} \cos(\pi l / (N + 1)), \quad l = \overline{1, N}.$$

The comparison system $\frac{Z(t)}{dt} = CZ(t)$ tends asymptotically to zero if $|\lambda_{k,l}| < 1$. That is,

$$\max_{k,l=\overline{1,N}} \left| \beta - \frac{4D}{\Delta^2} - \frac{2D}{\Delta^2} \left(\cos \frac{\pi k}{N+1} + \cos \frac{\pi l}{N+1} \right) \right| < 1.$$

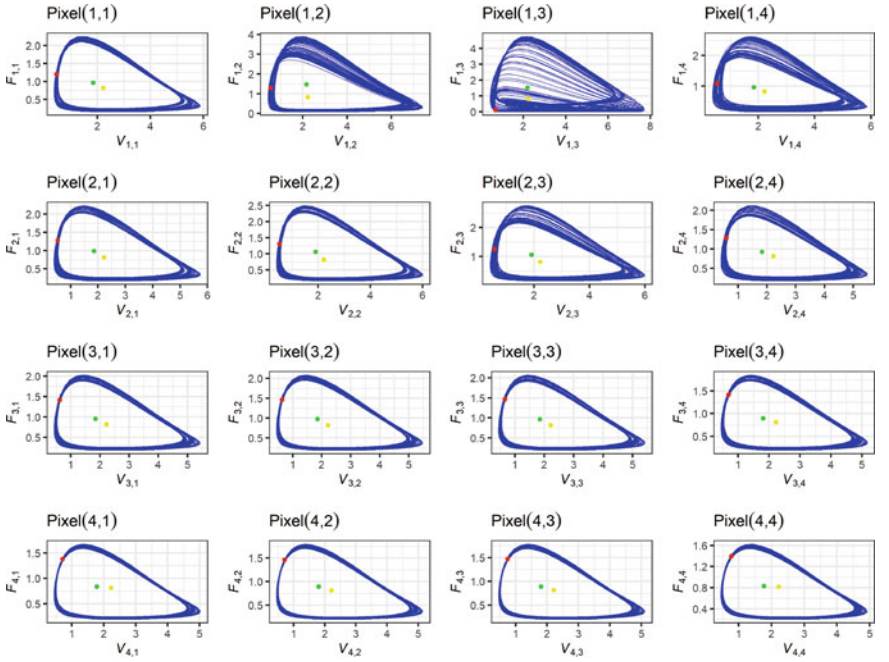
2.4 Numerical Simulation of Square 4×4 Pixels Array

First of all we calculate the basic reproductive numbers $\mathcal{R}_{0,i,j}$, $i, j = \overline{1, 4}$ due to (9) (See Table 1). We see that the conditions (11) hold. Thus, equilibrium without antibodies $\mathcal{E}_{i,j}^0$, $i, j = \overline{1, 4}$ is unstable and there exists endemic equilibrium $\mathcal{E}_{i,j}^*$, $i, j = \overline{1, 4}$.

Table 1 The values of $R_{0,i,j}$, $i, j = \overline{1, 4}$

$R_{0,i,j}^*$	1	2	3	4
1	3.218727	3.425273	3.474323	3.224824
2	3.171270	3.235043	3.236289	3.126438
3	3.092287	3.107824	3.096617	3.040443
4	2.997269	3.020902	3.012915	2.971442

Table 2 The phase plane plots of the system (3) for antibody populations $F_{i,j}$ versus antigen populations $V_{i,j}$, $i, j = \overline{1, 4}$. Numerical simulation of the system (3) at $n = 0.9$, $\tau = 0.28725$. Here ● indicates identical steady state, ● indicates nonidentical steady state. Trajectories are constructed for $t \in [550, 800]$. The solution behavior looks chaotic



The numerical simulations were implemented at different values of $n \in (0, 1]$. Here we can see that when changing the value of τ we have changes of qualitative behavior of pixels and entire immunosensor. We considered the parameter value set given above and computed the long-time behavior of the system (3) for $\tau = 0.05, 0.22, 0.23, 0.2865$, and 0.28725 . The phase diagrams of the antibody vs. antigen populations for the pixel (1, 1) are shown in Table 2.

For example, at $\tau \in [0, 0.22]$ we can see trajectories corresponding to stable node for all pixels.

For $\tau = 0.23$, the phase diagrams show that the solution is a limit cycle with two local extrema (one local maximum and one local minimum) per cycle. Then for $\tau = 0.2825$ the solution is a limit cycle with four local extrema per cycle, and, for $\tau = 0.2868, 0.2869, 0.28695$ the solutions are limit cycles with 8, 16 and 32

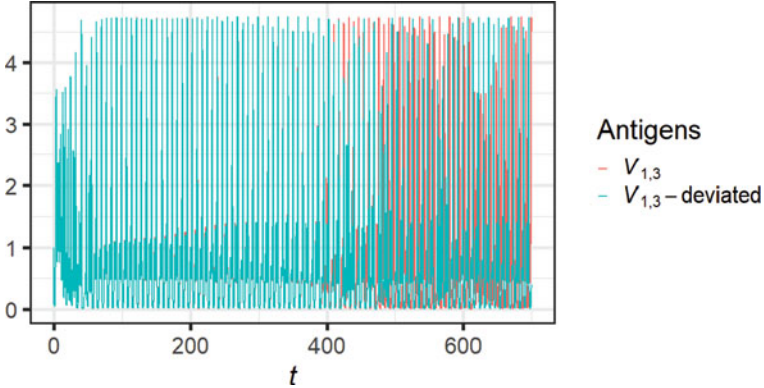


Fig. 2 The time series of the solutions to the system (3) for the antigen population $V_{1,3}$ from $t = 0$ to 700 with $\tau = 0.28725$ for initial conditions $V_{1,3}(t) = 1$ and $V_{1,3}(t) = 1.001$ (deviated), $t \in [-\tau, 0]$, and identical all the rest ones. At the beginning the two solutions appear to be the same, but as time increases there is a marked difference between the solutions supporting the conclusion that the system behavior is chaotic

local extrema per cycle, respectively. Finally, for $\tau = 0.28725$, the behavior shown in Table 2 is obtained which looks like chaotic behavior. In this paper, we have regarded behavior as chaotic if no periodic behavior could be found in the long-time behavior of the solutions.

The divergence of nearby trajectories in phase space is one of the most striking properties of chaotic behavior of deterministic systems [32]. In order to evaluate that the solution is chaotic for $\tau = 0.28725$, we perturbed the initial conditions to test the sensitivity of the system. Figure 2 presents two trajectories (in red and blue) starting from initial conditions with a small deviation (0.001). It can be seen that till the moment about $t = 400$ there is no significant difference between the trajectories, whereas further nearby trajectories are being deviated. The divergence of the trajectories with the small initial deviation evidences numerically the chaotic behavior at $\tau = 0.28725$.

We have also checked numerically that the solutions for the limit cycles are periodic and computed the periods for each of the local maxima and minima in the cycles. In the chaotic solution region, the numerical calculations (not shown in this paper) confirmed that no periodic behavior could be found.

A bifurcation diagram showing the maximum and minimum points for the limit cycles for the antigen population $V_{1,3}$ as a function of time delay is given in Fig. 3. The Hopf bifurcation from the stable equilibrium point to a simple limit cycle and the sharp transitions at critical values of the time delay between limit cycles with increasing numbers of maximum and minimum points per cycle can be clearly seen.

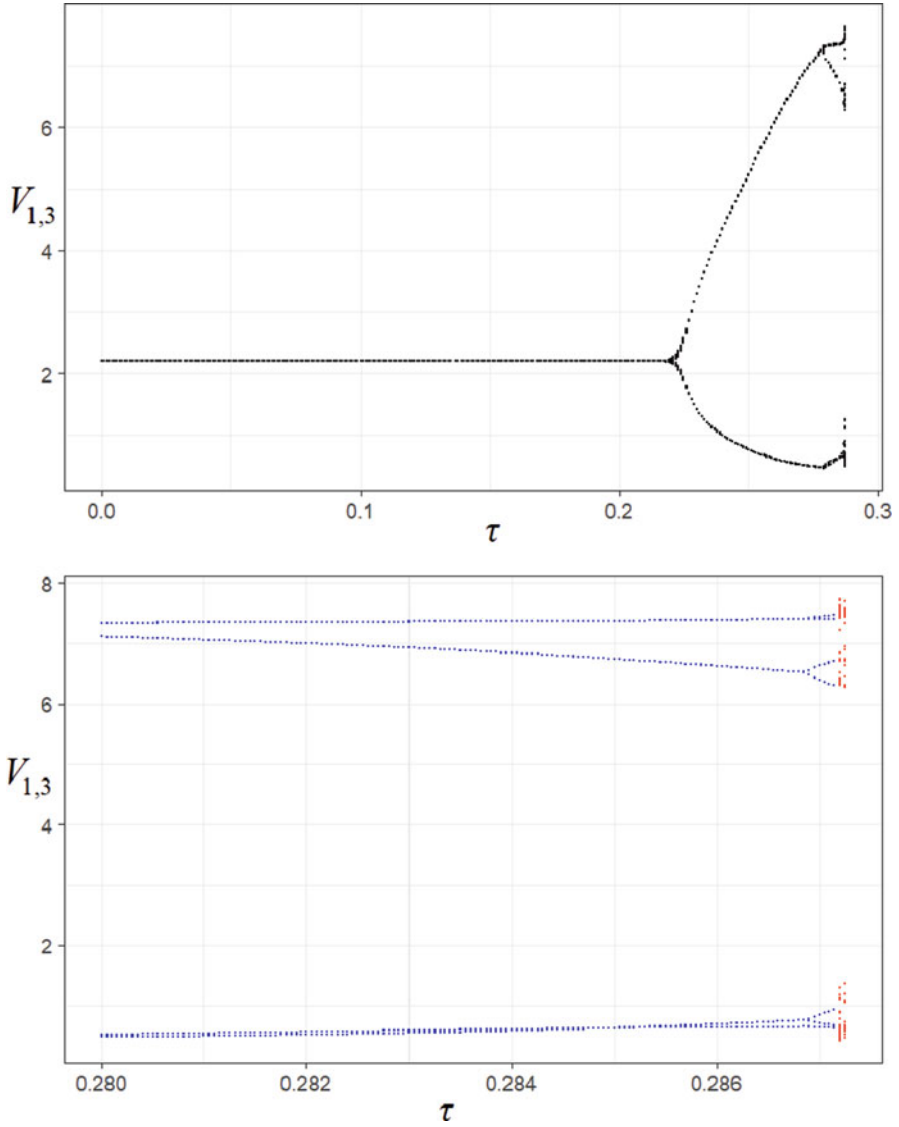


Fig. 3 A bifurcation diagram showing the “bifurcation path to chaos” as the time delay is increased. The points show the local extreme points per cycle for the $V_{1,3}$ population. Chaotic-type solutions occur at $\tau \approx 0.28725$ and are indicated in red in the figure with value 0 for the number of extreme points

3 Three-Dimensional Biopixels Array

When modeling three-dimensional pixels array it is natural way to apply the model based on the hexagonal lattice. Such model may use the following assumption. Namely, antigens are assumed to diffuse from six neighboring pixels, $(i + 1, j, k - 1)$, $(i + 1, j - 1, k)$, $(i, j - 1, k + 1)$, $(i - 1, j, k + 1)$, $(i - 1, j + 1, k)$, $(i, j + 1, k - 1)$ (see Fig. 4), with diffusion rate $D\Delta^{-2}$, where $D > 0$ and $\Delta > 0$ is distance between pixels.

Taking into account prerequisites mentioned above, we get a simplified antibody-antigen competition model with delay for a hexagonal array of biopixels, which uses Marchuk model of the immune response [20–23] and using spatial operator \hat{S} which is constructed similarly to [24] (Supplementary information, p.10)

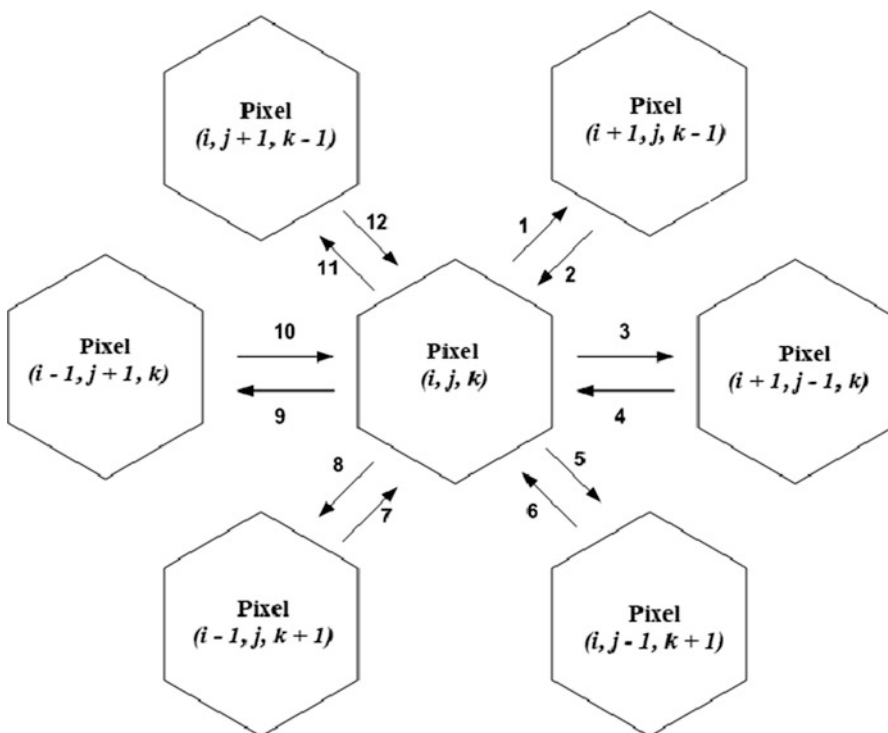


Fig. 4 Diffusion of antigens for the hexagonal lattice model. Antigens from six neighboring pixels interact, $n > 0$ is the constant of disbalance. Here ‘1’, ‘3’, ‘5’, ‘8’, ‘9’, ‘11’ have to be replaced with $D\Delta^{-2}V_{i,j,k}(t)$, ‘2’ with $D\Delta^{-2}V_{i+1,j,k-1}(t)$, ‘4’ with $D\Delta^{-2}V_{i+1,j-1,k}(t)$, ‘6’ with $D\Delta^{-2}V_{i,j-1,k+1}(t)$, ‘7’ with $D\Delta^{-2}V_{i-1,j,k+1}(t)$, ‘10’ with $D\Delta^{-2}V_{i-1,j+1,k}(t)$, ‘12’ with $D\Delta^{-2}V_{i,j+1,k-1}(t)$

$$\begin{aligned} \frac{dV_{i,j,k}(t)}{dt} &= (\beta - \gamma F_{i,j,k}(t - \tau) - \delta_v V_{i,j,k}(t - \tau)) V_{i,j,k}(t) + \hat{S}\{V_{i,j,k}\}, \\ \frac{dF_{i,j,k}(t)}{dt} &= (-\mu_f + \eta\gamma V_{i,j,k}(t - \tau) - \delta_f F_{i,j,k}(t)) F_{i,j,k}(t) \end{aligned} \quad (18)$$

with given initial functions

$$\begin{aligned} V_{i,j,k}(t) &= V_{i,j,k}^0(t) \geq 0, \quad F_{i,j,k}(t) = F_{i,j,k}^0(t) \geq 0, \quad t \in [-\tau, 0), \\ V_{i,j,k}(0), F_{i,j,k}(0) &> 0. \end{aligned} \quad (19)$$

We use the following spatial operator of discrete diffusion for a hexagonal array of pixels⁴

$$\begin{aligned} \hat{S}\{V_{i,j,k}\} &= D\Delta^{-2} \left[V_{i+1,j,k-1} + V_{i+1,j-1,k} + V_{i,j-1,k+1} + V_{i-1,j,k+1} + V_{i-1,j+1,k} \right. \\ &\quad \left. + V_{i,j+1,k-1} - 6nV_{i,j,k} \right] \\ i, j, k &\in \overline{-N+1, N-1}, \quad i+j+k=0. \end{aligned} \quad (20)$$

Each pixel is affected by the antigens flowing out six neighboring pixels, two in each of three directions of the hexagonal array. The adjoint pixels are separated by the distance Δ .

Boundary conditions $V_{i,j,k} = 0$ for the edges of the hexagonal array, i.e. if $i \vee j \vee k \in \{-N-1, N+1\}$, are used.

We can present analytical results with respect to the model (18) in the form of restrictions for the parameters, enabling us persistence and global asymptotic stability. Moreover, we executed numerical research of the system qualitative behavior in dependence of changes of the time of immune response τ (delay of time), diffusion rate $D\Delta^{-2}$ and factor n .

3.1 Persistence and Extinction of the Solutions

Concerning persistence, for the hexagonal lattice can be obtained similar result as for square one (Theorem 1), just adding the third index.

Unfortunately, we didn't manage to present such clear condition of extinction as in Theorem 2. We can check it only numerically in an experimental way.

⁴Without loss of generality we consider spatial operator for internal pixels only.

3.2 Numerical Study

For numerical simulation we consider model (18) of hexagonal pixels array at $N = 4$, $\beta = 2 \text{ min}^{-1}$, $\gamma = 2 \frac{\text{mL}}{\text{min} \cdot \mu\text{g}}$, $\mu_f = 1 \text{ min}^{-1}$, $\eta = 0.8/\gamma$, $\delta_v = 0.5 \frac{\text{mL}}{\text{min} \cdot \mu\text{g}}$, $\delta_f = 0.5 \frac{\text{mL}}{\text{min} \cdot \mu\text{g}}$, $D = 0.2 \frac{\text{nm}^2}{\text{min}}$, $\Delta = 0.3 \text{ nm}$. Numerical modeling was implemented at different values of $n \in (0, 1]$. For this purpose we used RStudio environment.

Using local bifurcation plot, dynamics of the system (18) was analysed for different values of $n \in (0, 1]$. We have concluded that oscillatory and then chaotic behavior starts for smaller values of τ at smaller values of n . Further, increasing the values of n we can observe asymptotically stable steady solutions for wider range of τ .

Numerical integration of the system has shown the influence of time delay τ . Namely, as it is agreed with the analytical results, we observe the stable focuses at pixel-dependent endemic states for small delays $\tau \in [0, 0.18)$. At $\tau \approx 0.18 \text{ min}$ the stable focus is transformed into a stable limit cycle of tiny radius, which corresponds to Hopf bifurcation. A deeper study of this phenomenon requires obtaining the condition of the appearance of the pair of purely imaginary roots of the characteristic quasipolynomial of the linearized system. The limit cycles of ellipsoidal form are observed till $\tau \approx 0.285 \text{ min}$. Pay attention that when increasing τ , near $\tau = 0.285$ we get period doubling (see Fig. 5).⁵

Qualitative behavior of immunosensor model can be analyzed with help of hexagonal tiling plots also. For this purpose we can use both plots for antigens (Fig. 6), antibodies (Fig. 7) and probabilities of binding antigens by antibodies (Fig. 8).

4 Conclusions

In the work a reaction-diffusion models of two- and three-dimensional immunopixels array were considered. Mathematically it is described by the system of lattice delayed differential equations on rectangular or hexagonal grids. The systems include the spatial operator describing diffusion of antigenes between five and seven neighboring pixels respectively.

The main results are dealing with qualitative investigation of the model. The conditions of persistence were obtained. Also we have managed to get the result dealing with the extinction of the solutions. Namely, it can be seen that the amount of pixels determines their non-vanishing. In two-dimensional case this dependence can be presented in a clear form.

The conditions of local or global asymptotic stability can be obtained using construction of the Lyapunov functional. Because of cumbersome of evidence, we

⁵It can be approximately seen from local bifurcation plot also.

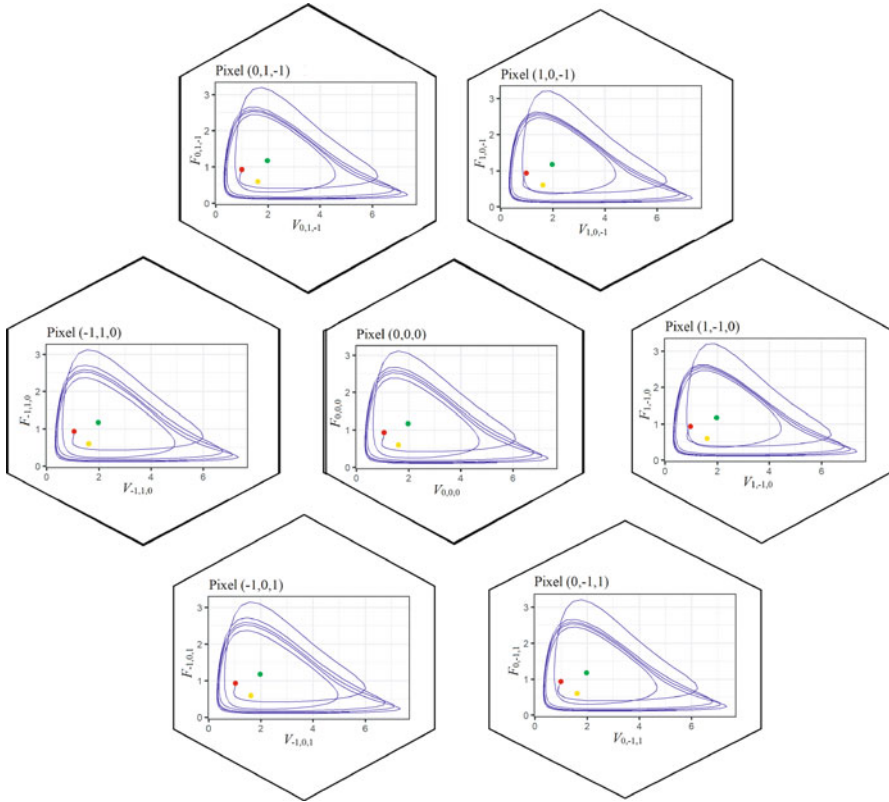


Fig. 5 Phase plots of the system (18) at $\tau = 0.287$. Here \bullet indicates initial state, \bullet indicates pixel-independent endemic state, \bullet indicates pixel-dependent endemic state. The solution tends to a stable limit cycle with six local extrema per cycle

didn't include it here. They results in inequality including the system parameters and delay. So, estimation of the delay enabling us local or global asymptotic stability can be obtained.

Numerical analysis of the model qualitative behavior is performed with the help of the bifurcation diagram, phase trajectories, and rectangular or hexagonal tile portraits. It has shown the changes in qualitative behavior with respect to the growth of time delay. Namely, starting from the stable focus at small delay values, then through Hopf bifurcation to limit cycles, and finally through period doublings to deterministic chaos. It is agreed with the results on spatial-temporal chaos for reaction-diffusion systems, which were previously obtained in [1–3].

As compared with rectangular lattice model, for hexagonal model we observe Hopf bifurcation at smaller values of τ . That is hexagonal lattice accelerates changes in qualitative behavior.

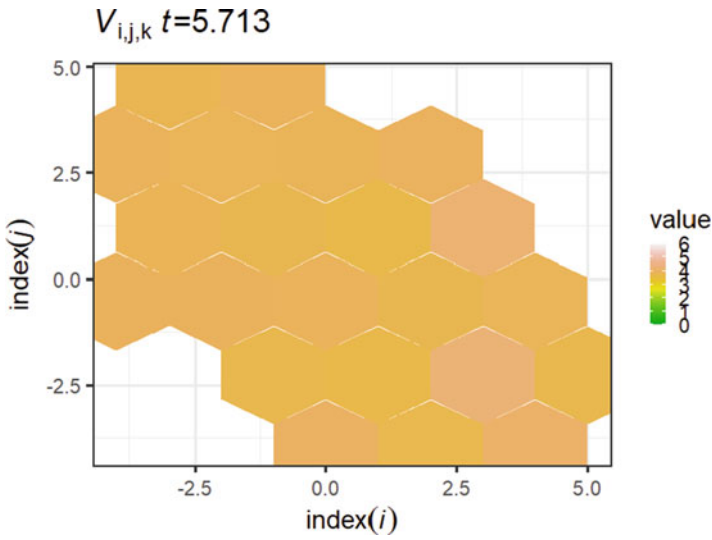


Fig. 6 Example of hexagonal tiling plot for V

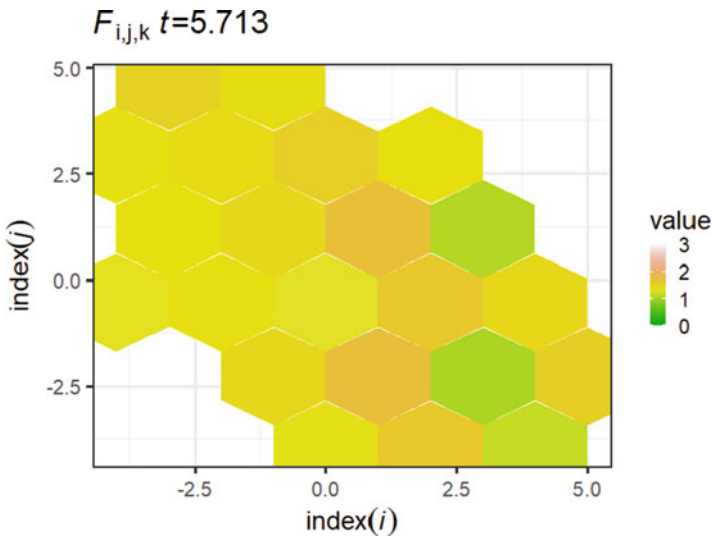


Fig. 7 Example of hexagonal tiling plot for F

Note, that model can be applied for an arbitrary amount of pixels determined by natural $N \geq 1$. However, it can be numerically seen that qualitative behavior of the entire immunosensor is determined by 5 or 7 pixels array for square and hexagonal lattices respectively.

The results of the work differ from the results presented earlier since here we try to show a comparative study of the model of biopixels array both in square

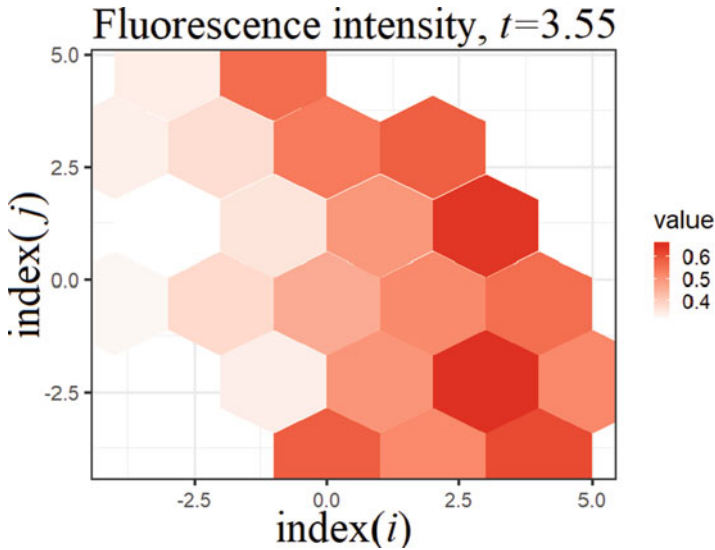


Fig. 8 Example of hexagonal tiling plot for probabilities of binding antigens by antibodies, i.e. $V \times F$. In case of optical immunosensor it is fluorescence intensity

and hexagonal lattices. Such a comparative study is based on both analytical and numerical results. Analytical outcomes include a comparison of the basic stability characteristics like basic reproductive numbers, a comparison of the conditions for persistence (permanence), and extinction. Numerical analysis use phase portraits and bifurcation plots which are constructed on the basis of local extremes. Earlier such studies were executed focusing on some type of the lattice. So, here we investigate the effect of the lattice type on the qualitative behavior of the model.

References

1. Rössler, O.E.: Chemical turbulence: Chaos in a simple reaction-diffusion system. *Zeitschrift für Naturforschung A* **31**(10), (1976). <https://doi.org/10.1515/zna-1976-1006>
2. Hildebrand, M., Bär, M., Eiswirth, M.: Statistics of topological defects and spatiotemporal chaos in a reaction-diffusion system. *Phys. Rev. Lett.* **75**(8), 1503–1506 (1995). <https://doi.org/10.1103/physrevlett.75.1503>
3. Zaitseva, M.F., Magnitskii, N.A.: Space-time chaos in a system of reaction-diffusion equations. *Differential Equations* **53**(11), 1519–1523 (2017). <https://doi.org/10.1134/s0012266117110155>
4. Cahn, J.W., Chow, S.N., Van Vleck, E.S.: Spatially discrete nonlinear diffusion equations. *Rocky Mount. J. Math.* **25**(1), 87–118 (1995)
5. Chow, S.-N., Mallet-Paret, J., Van Vleck, E.S.: Dynamics of lattice differential equations. *Int. J. Bifur. Chaos* **6**(09), 1605–1621 (1996)
6. Pan, S.: Propagation of delayed lattice differential equations without local quasimonotonicity. Preprint (2014). ArXiv:1405.1126.

7. Huang, J., Lu, G., Zou, X.: Existence of traveling wave fronts of delayed lattice differential equations. *J. Math. Anal. Appl.* **298**(2), 538–558 (2004)
8. Niu, H.: Spreading speeds in a lattice differential equation with distributed delay. *Turkish J. Math.* **39**(2), 235–250 (2015)
9. Hoffman, A., Hupkes, H., Van Vleck, E.: Entire Solutions for Bistable Lattice Differential Equations with Obstacles. American Mathematical Society, Rhode Island (2017)
10. Wu, F.: Asymptotic speed of spreading in a delay lattice differential equation without quasimonotonicity. *Electron. J. Differ. Equ.* **2014**(213), 1–10 (2014)
11. Zhang, G.-B.: Global stability of traveling wave fronts for non-local delayed lattice differential equations. *Nonlinear Anal. Real World Appl.* **13**(4), 1790–1801 (2012)
12. Luczak, Ed., Rosenfeld, A.: Distance on a hexagonal grid. *IEEE Trans. Comput.* **25**(5), 532–533 (1976). <https://doi.org/10.1109/TC.1976.1674642>
13. Hexagonal Coordinate Systems.: https://homepages.inf.ed.ac.uk/rbf/CVonline/LOCAL_COPIES/AV0405/MARTIN/Hex.pdf. Accessed: 2019-05-12
14. Middleton, L., Sivaswamy, J.: Edge detection in a hexagonal-image processing framework. *Image Vis. Comput.* **19**(14), 1071–1081 (2001)
15. Fayas, A., Nisar, H., Sultan, A.: Study on hexagonal grid in image processing. In: The 4th International Conference on Digital Image Processing, pp. 7–8 (2012)
16. Cruz, H.J., Rosa, C.C., Oliva, A.G.: Immunosensors for diagnostic applications. *Parasitology Research* **88**, S4–S7 (2002)
17. Paek, S.-H., Schramm, W.: Modeling of immunosensors under nonequilibrium conditions: I. mathematic modeling of performance characteristics. *Analytical Biochemistry* **196**(2), 319–325 (1991)
18. Bloomfield, V.A., Prager, S.: Diffusion-controlled reactions on spherical surfaces. application to bacteriophage tail fiber attachment. *Biophysical Journal* **27**(3), 447–453 (1979)
19. Berg, O.G.: Orientation constraints in diffusion-limited macromolecular association. the role of surface diffusion as a rate-enhancing mechanism. *Biophysical Journal* **47**(1), 1–14 (1985)
20. Marchuk, G.I., Petrov, R.V., Romanyukha, A.A., Bocharov, G.A.: Mathematical model of antiviral immune response. i. data analysis, generalized picture construction and parameters evaluation for hepatitis b. *J. Theor. Biol.* **151**(1), 1–40 (1991). [https://doi.org/10.1016/S0022-5193\(05\)80142-0](https://doi.org/10.1016/S0022-5193(05)80142-0). <https://www.scopus.com/inward/record.uri?eid=2-s2.0-0025819779&doi=10.1016%2fS0022-5193%2805%2980142-0&partnerID=40&md5=f850637085913dc18f8e52c5b3f28600> Cited By 38
21. Foryś, U.: Marchuk’s model of immune system dynamics with application to tumour growth. *J. Theor. Med.* **4**(1), 85–93 (2002). <https://doi.org/10.1080/10273660290052151>. <https://www.tandfonline.com/doi/abs/10.1080/10273660290052151>
22. Nakonechnyi, A.G., Marzeniuk, V.P.: Uncertainties in medical processes control. *Lect. Notes Econ. Math. Syst.* **581**, 185–192 (2006). https://doi.org/10.1007/3-540-35262-7_11. https://www.scopus.com/inward/record.uri?eid=2-s2.0-53749093113&doi=10.1007%2f3-540-35262-7_11&partnerID=40&md5=03be7ef103cbbc1e94cacbb471daa03f Cited By 2
23. Marzeniuk, V.P.: Taking into account delay in the problem of immune protection of organism. *Nonlinear Anal. Real World Appl.* **2**(4), 483–496 (2001). [https://doi.org/10.1016/S1468-1218\(01\)00005-0](https://doi.org/10.1016/S1468-1218(01)00005-0). <https://www.scopus.com/inward/record.uri?eid=2-s2.0-0041331752&doi=10.1016%2fS1468-1218%2801%2900005-0&partnerID=40&md5=9943d225f352151e77407b48b18ab1a9>. Cited By 2
24. Prindle, A., Samayoa, P., Razinkov, I., Danino, T., Tsimring, L.S., Hasty, J.: A sensing array of radically coupled genetic ‘biopixels’. *Nature* **481**(7379), 39–44 (2011). <https://doi.org/10.1038/nature10722>
25. Jones, J.H.: Notes on R_0 . California: Department of Anthropological Sciences (2007)
26. Yang, J., Wang, X., Zhang, F.: A differential equation model of hiv infection of cd t-cells with delay. *Discrete Dynamics in Nature and Society* (2008)
27. Elaiw, A.M., Almatrafi, A.A., Hobiny, A.D.: Effect of antibodies on pathogen dynamics with delays and two routes of infection. *AIP Advances* **8**(6), 065104 (2018). <https://doi.org/10.1063/1.5029483>.

28. Kuang, Y.: Delay Differential Equations with Applications in Population Dynamics. Academic Press, New York (1993)
29. zhong He, X.: Stability and delays in a predator-prey system. *J. Math. Anal. Appl.* **198**(2), 355–370 (1996). <https://doi.org/10.1006/jmaa.1996.0087>
30. Wendi, W., Zhien, M.: Harmless delays for uniform persistence. *J. Math. Anal. Appl.* **158**(1), 256–268 (1991). [https://dx.doi.org/10.1016/0022-247X\(91\)90281-4](https://dx.doi.org/10.1016/0022-247X(91)90281-4)
31. Lancaster, P., Tismenetsky, M.: *The Theory of Matrices: With Applications*. Elsevier (1985)
32. Persson, P.B., Wagner, C.D.: General principles of chaotic dynamics. *Cardiovascular Research* **31**, 332–341 (1996). <https://cardiovascres.oxfordjournals.org/content/31/3/332.full-text.pdf>

Response Sensitivity of Damper-connected Adjacent Structural Systems Subjected to Fully Non-stationary Random Excitations



Giuseppe Muscolino , Federica Genovese , and Tiziana Alderucci 

Abstract In the last decades, due to the growing population, civil engineers faced with the problem of the design of adjacent buildings in limited areas; this could lead to mutual pounding if those structures are subjected to dynamic excitation such as ground motion accelerations. Among the possible solutions to this problem, the connection with vibration control devices, such as dampers, could be an innovative way. The sensitivity analysis represents a powerful tool in the optimization procedure, especially when the design of vibration control devices is required; in fact, it is possible to determine the alterations of the structural response with the reference structural parameters changes. In this paper a method for the evaluation of the sensitivity of the response of two adjacent buildings connected through fluid dampers is presented; the sensitivity of the structural response statistics is obtained through very simple frequency domain integrals. The proposed approach requires the evaluation of explicit closed form solutions of the derivatives of time-frequency response vector functions with respect to the parameters, that define the modified structural model.

Keywords Sensitivity analysis · Adjacent buildings · Non-stationary processes

1 Introduction

Interconnecting adjacent buildings with supplemental active or passive devices is a practical and effective approach to get dual advantage of avoiding pounding and response reduction if the parameters of devices are select properly. Notice also that adjacent buildings connected by discrete viscoelastic dampers form a non-classically damped system. Moreover, it is well known that the most realistic representation of seismic excitations is as fully non-stationary zero-mean Gaussian

G. Muscolino · F. Genovese (✉) · T. Alderucci
Department of Engineering, University of Messina, Messina, Italy
e-mail: gmuscolino@unime.it; fedgenovese@unime.it; talderucci@unime.it

stochastic process. The analysis of adjacent structures has been an active research area in recent years. In particular Gurley et al. [1] investigated the possibility of using a passively damped elastic link to couple adjacent buildings for control of response to wind. Luco et al. [2] determined the optimal values for the distribution of passive dampers minimizing the peak amplitudes of the transfer functions for the response at the top of the taller structure in the vicinity of the first and second modes of the structure. Xu et al. [3] investigated earthquake resistant performance of adjacent buildings connected by a number of damped elastic links. They found the optimum parameters of dampers through extensive numerical parametric studies. Zhang and Xu [4] proposed an analytical method, combining the complex mode superposition method with the pseudo-excitation method, for investigating both dynamic characteristic and seismic response of adjacent buildings connected by viscoelastic dampers. Zhu et al. [5] evaluate for 2-DOF coupled system analytical formula of optimal parameters of devices (Kelvin-Voigt and Maxwell models are analyzed), then they verified the relationships for multi degree of freedom (MDOF) systems.

The sensitivity analysis represents a powerful tool in the optimization procedure when it is possible to determine the alterations of the structural response once the reference structural parameters changes. The main limit in using the sensitivity approach is the cumbersome analytical and the numerical effort especially for non-classically structural systems subjected to seismic excitations modeled as fully non-stationary zero-mean Gaussian processes.

In this study, the sensitivities of nodal time-frequency varying response (*TFR*) vector function of the nodal structural response of the non-classically damped coupled system subjected to fully non-stationary zero-mean Gaussian excitation processes are evaluated in explicitly closed form. Then, performing simple integrals in frequency domain it is possible to evaluate the sensitivities of non-geometric spectral moments of response. The main steps of this study are: (i) to determine, for the non-classically dynamic structure composed of two adjacent buildings linked by viscoelastic dampers represented by the Kelvin-Voigt model, the *TFR* vector function of the nodal response; (ii) to evaluate the sensitivity of *TFR* vector function of the nodal response; (iii) to find the optimal parameters of dampers through parametric studies, analyzing the sensitivity of nodal response for both stationary and non-stationary zero-mean Gaussian stochastic process.

2 Equations of Motion

Let us consider two adjacent linear structures of n_1 and n_2 stories, respectively, connected by viscous dampers at some stories. It is assumed that the two structures are symmetric, with their symmetric planes coincident with each other. The two structures are subjected to a seismic acceleration assumed in the direction of the symmetric planes. Therefore, the problem can be regarded as a one-dimensional

problem and the structures can be simply modeled by two plane frames. Furthermore, the two structures are assumed to be subjected to the same seismic acceleration, so the spatial variability of the ground motion is herein not considered. The equations of motion of the coupled quiescent structural system, can be written as:

$$\mathbf{M}_S \ddot{\mathbf{U}}(\boldsymbol{\alpha}, t) + [\mathbf{C}_S + \mathbf{C}_D(\boldsymbol{\alpha}_c)] \dot{\mathbf{U}}(\boldsymbol{\alpha}, t) + [\mathbf{K}_S + \mathbf{K}_D(\boldsymbol{\alpha}_k)] \mathbf{U}(\boldsymbol{\alpha}, t) = -\mathbf{M}_S \boldsymbol{\tau} \ddot{u}_g(t), \quad (1)$$

where \mathbf{M}_S , \mathbf{C}_S and \mathbf{K}_S are the $n \times n$ ($n = n_1 + n_2$) mass, damping and stiffness matrices of the system without coupling damping devices, whose mathematical form can be found in [3], $\mathbf{U}(\boldsymbol{\alpha}, t)$ is the n -dimensional vector of nodal displacements relative to the ground; $\boldsymbol{\tau}$ is the n -dimensional array listing the influence coefficients of the ground shaking; $\ddot{u}_g(t)$ is the seismic acceleration which is modeled as a zero-mean Gaussian stochastic process; a dot over a variable denotes differentiation with respect to time. Moreover, in Eq. (1) $\mathbf{C}_D(\boldsymbol{\alpha}_c)$ and $\mathbf{K}_D(\boldsymbol{\alpha}_k)$ are the $n \times n$ additional damping and stiffness matrices due to the installation of the damping devices. Finally, the vector $\boldsymbol{\alpha}^T = [\boldsymbol{\alpha}_c^T \ \boldsymbol{\alpha}_k^T]$, of order r ($r = r_c + r_k$), collects the dimensionless parameter which must be evaluated by the design procedure, the superscript T denotes the transpose operator. Obviously, the structural response depends on vector $\boldsymbol{\alpha}$. Since the structural modifications, due to the introduction of damping devices, leads to a non-classically damped structural system, the equations of motion of the quiescent structural system are written in state variables:

$$\dot{\mathbf{Z}}(\boldsymbol{\alpha}, t) = \mathbf{D}(\boldsymbol{\alpha}) \mathbf{Z}(\boldsymbol{\alpha}, t) + \mathbf{w} F(t), \quad (2)$$

where $\mathbf{Z}(\boldsymbol{\alpha}, t)$ is the state variable vector of order $2n$, $\mathbf{D}(\boldsymbol{\alpha})$ is a matrix, of order $2n \times 2n$, and the \mathbf{w} is a vector, of order $2n$, respectively defined as:

$$\mathbf{Z}(\boldsymbol{\alpha}, t) = \begin{bmatrix} \mathbf{U}(\boldsymbol{\alpha}, t) \\ \dot{\mathbf{U}}(\boldsymbol{\alpha}, t) \end{bmatrix}; \quad \mathbf{D}(\boldsymbol{\alpha}) = \begin{bmatrix} \mathbf{O}_{n,n} & \mathbf{I}_n \\ -\mathbf{M}_S^{-1} [\mathbf{K}_S + \mathbf{K}_D(\boldsymbol{\alpha}_k)] & -\mathbf{M}_S^{-1} [\mathbf{C}_S + \mathbf{C}_D(\boldsymbol{\alpha}_c)] \end{bmatrix}; \quad \mathbf{w} = \begin{bmatrix} \mathbf{0}_n \\ -\boldsymbol{\tau} \end{bmatrix} \quad (3)$$

where \mathbf{I}_n and $\mathbf{O}_{n,n}$ are respectively the identity and the zero matrices of $n \times n$ order while $\mathbf{0}_n$ stands for a n -dimensional zero vector. In order to evaluate the structural response, the $2n \times 2n$ transition matrix $\Theta(\boldsymbol{\alpha}, t)$ has to be introduced, this matrix for non-classically damped systems can be evaluated as:

$$\begin{aligned} \Theta(\boldsymbol{\alpha}, t) &= \exp[\mathbf{D}(\boldsymbol{\alpha}) t] = \boldsymbol{\Psi}(\boldsymbol{\alpha}) \exp[\boldsymbol{\Lambda}(\boldsymbol{\alpha}) t] \boldsymbol{\Psi}^T(\boldsymbol{\alpha}) \mathbf{A}(\boldsymbol{\alpha}) \\ &\equiv \boldsymbol{\Psi}^*(\boldsymbol{\alpha}) \exp[\boldsymbol{\Lambda}^*(\boldsymbol{\alpha}) t] \boldsymbol{\Psi}^{*T}(\boldsymbol{\alpha}) \mathbf{A}(\boldsymbol{\alpha}) \end{aligned} \quad (4)$$

in which $\mathbf{D}(\boldsymbol{\alpha})$ has been defined in Eq. (3). In Eq. (4) $\boldsymbol{\Lambda}(\boldsymbol{\alpha})$, is a complex matrix, of order $2m \times 2m$, and $\boldsymbol{\Psi}(\boldsymbol{\alpha})$ is complex matrix, of order $2n \times 2m$, collecting the $m \leq n$ eigenvalues and eigenvectors respectively. These matrices, depending on uncertain

parameters α , are evaluated by formally solving the following algebraic complex eigenproblem:

$$\mathbf{D}^{-1}(\alpha) \Psi(\alpha) = \Psi(\alpha) \Lambda^{-1}(\alpha); \quad \Psi^T(\alpha) \mathbf{A}(\alpha) \Psi(\alpha) = \mathbf{I}_{2m} \quad (5)$$

Notice that $\Lambda(\alpha)$ is a diagonal matrix and

$$\mathbf{A}(\alpha) = \mathbf{A}_S + \mathbf{A}_D(\alpha_c) = \begin{bmatrix} \mathbf{C}_S & \mathbf{M}_S \\ \mathbf{M}_S & \mathbf{O}_{n,n} \end{bmatrix} + \begin{bmatrix} \mathbf{C}_D(\alpha_c) & \mathbf{O}_{n,n} \\ \mathbf{O}_{n,n} & \mathbf{O}_{n,n} \end{bmatrix}. \quad (6)$$

3 Dynamic Response Sensitivity for Fully Non-stationary Stochastic Load Processes

3.1 Closed Form Solutions for the Time-frequency Varying Response Vector Function

In the framework of non-stationary analysis of structures, the non-geometric spectral moments can be evaluated in compact form by introducing the *pre-envelope covariance (PEC)* matrix. This matrix, in nodal space, is a $2n \times 2n$ Hermitian matrix, that, for non-classically damped systems, can be evaluated formally as [6, 7]:

$$\Sigma_{ZZ}(\alpha, t) = E \left\langle \mathbf{Z}(\alpha, t) \mathbf{Z}^{*T}(\alpha, t) \right\rangle = \begin{bmatrix} \Lambda_{0, \text{UU}}(\alpha, t) & i\Lambda_{1, \text{UU}}(\alpha, t) \\ -i\Lambda_{1, \text{UU}}^*(\alpha, t) & \Lambda_{2, \text{UU}}(\alpha, t) \end{bmatrix} \quad (7)$$

where $i = \sqrt{-1}$ is the imaginary unit, $\mathbf{Z}(\alpha, t)$ is the nodal state variable vector solution of Eq. (2), while the matrices $\Lambda_{i, \text{UU}}(\alpha, t)$ collect the *non-geometric spectral moments (NGSM)* [6, 8, 9]. Introducing the following coordinate transformation:

$$\mathbf{Z}(\alpha, \omega, t) = \Psi(\alpha) \mathbf{X}(\alpha, \omega, t) \quad (8)$$

where $\mathbf{Z}(\alpha, \omega, t)$ is the *time-frequency varying response (TFR)* vector function of the nodal response of order $2n \times 1$, and $\mathbf{X}(\alpha, \omega, t)$ is the *TFR* vector function of the modal response, of order $2m \times 1$, defined as [10]:

$$\mathbf{X}(\alpha, \omega, t) = \int_{t_0}^t \exp[\mathbf{A}(\alpha, t - \tau)] \exp(i\omega\tau) a(\omega, \tau) d\tau \mathbf{v}(\alpha), \quad \mathbf{v}(\alpha) = \Psi^T(\alpha) \mathbf{A}(\alpha) \mathbf{w}. \quad (9)$$

It follows that, after few mathematical steps, the nodal *PEC* matrix, can be evaluated in time-domain, for quiescent structural systems as [10]:

$$\Sigma_{ZZ}(\boldsymbol{\alpha}, t) = \Psi^*(\boldsymbol{\alpha}) \left[\int_0^\infty G_0(\omega) \mathbf{X}^*(\boldsymbol{\alpha}, \omega, t) \mathbf{X}^T(\boldsymbol{\alpha}, \omega, t) d\omega \right] \Psi^T(\boldsymbol{\alpha}) \quad (10)$$

where the one-sided *evolutionary power spectral density (EPSD)* [11, 12] $G_{FF}(\omega, t) = |a(\omega, t)|^2 G_0(\omega)$ is introduced, with $a(\omega, t) \equiv a^*(-\omega, t)$ the modulating function, that for *fully non-stationary processes* depends on both time and frequency, and $G_0(\omega)$ is the one-sided *PSD* function of the stationary counterpart of the fully not stationary input process. It has been demonstrated that for the following modulating function:

$$a(\omega, t) = \varepsilon(\omega) \exp[-\alpha_a(\omega) t]; \quad t > 0 \quad (11)$$

the vector $\mathbf{X}(\boldsymbol{\alpha}, \omega, t)$, of the quiescent structural systems ($\mathbf{X}_0(\boldsymbol{\alpha}, \omega) = \mathbf{0}$) can be evaluated in explicit form as [10, 13]:

$$\mathbf{X}(\boldsymbol{\alpha}, \omega, t) = - \left\{ \exp[-\beta(\omega) t] \left[\Gamma^2(\boldsymbol{\alpha}, \omega) + t \Gamma(\boldsymbol{\alpha}, \omega) \right] - \exp[\Lambda(\boldsymbol{\alpha}) t] \Gamma^2(\boldsymbol{\alpha}, \omega) \right\} \times \varepsilon(\omega) \mathbf{v}(\boldsymbol{\alpha}); \quad t > 0 \quad (12)$$

where $\beta(\omega) = \alpha_a(\omega) - i\omega$ and $\Gamma(\boldsymbol{\alpha}, \omega)$ is a diagonal matrix, defined as:

$$\Gamma(\boldsymbol{\alpha}, \omega) = [\Lambda(\boldsymbol{\alpha}) + \beta(\omega) \mathbf{I}_{2m}]^{-1}. \quad (13)$$

3.2 Closed Form Solutions for the Sensitivity of Time-Frequency Varying Response Vector Function

In order to evaluate the optimal parameters a *sensitivity analysis* is performed. The *sensitivity analysis* consists in the evaluation of the change in the system response due to system parameter variations in the neighborhood of prefixed values, $\boldsymbol{\alpha} = \boldsymbol{\alpha}_0$, called “nominal parameter”. By differentiating the *PEC* matrix, defined in Eq. (10), it is possible to evaluate its sensitivity with respect to the i -th parameter, as follows:

$$\begin{aligned} \Sigma_{s_{Z,i}}(\boldsymbol{\alpha}_0, t) &= \left. \frac{\partial \Sigma_{ZZ}(\boldsymbol{\alpha}, t)}{\partial \alpha_i} \right|_{\boldsymbol{\alpha}=\boldsymbol{\alpha}_0} = \frac{\partial}{\partial \alpha_i} \left[\begin{array}{cc} \Lambda_{0,UU}(\boldsymbol{\alpha}, t) & i\Lambda_{1,UU}(\boldsymbol{\alpha}, t) \\ -i\Lambda_{1,UU}^{*T}(\boldsymbol{\alpha}, t) & \Lambda_{2,UU}(\boldsymbol{\alpha}, t) \end{array} \right] \Bigg|_{\boldsymbol{\alpha}=\boldsymbol{\alpha}_0} = \\ &= E \left\langle \mathbf{Z}^*(\boldsymbol{\alpha}_0, t) \frac{\partial \mathbf{Z}^T(\boldsymbol{\alpha}, t)}{\partial \alpha_i} \Bigg|_{\boldsymbol{\alpha}=\boldsymbol{\alpha}_0} \right\rangle + E \left\langle \mathbf{Z}^*(\boldsymbol{\alpha}_0, t) \frac{\partial \mathbf{Z}^T(\boldsymbol{\alpha}, t)}{\partial \alpha_i} \Bigg|_{\boldsymbol{\alpha}=\boldsymbol{\alpha}_0} \right\rangle^{*T} \end{aligned} \quad (14)$$

The elements of this matrix are the sensitivities of *the non-geometric spectral moments* of the response. It has been recently demonstrated that the following relationship holds [14]:

$$E \left\langle \mathbf{Z}^* (\boldsymbol{\alpha}_0, t) \frac{\partial \mathbf{Z}^T (\boldsymbol{\alpha}, t)}{\partial \alpha_i} \Big|_{\boldsymbol{\alpha}=\boldsymbol{\alpha}_0} \right\rangle = \boldsymbol{\Psi}_0^* \left\{ \int_0^\infty \mathbf{X}^* (\boldsymbol{\alpha}_0, \omega, t) \mathbf{Y}_i^T (\boldsymbol{\alpha}_0, \omega, t) G_0 (\omega) d\omega \right\} \boldsymbol{\Psi}_0^T \quad (15)$$

where $\boldsymbol{\alpha}_0$ is the “nominal parameter vector”, and $\mathbf{Y}_i (\boldsymbol{\alpha}_0, \omega, t)$ is the *sensitivity* of *TFR* vector function with respect to the parameter α_i , given as:

$$\mathbf{Y}_i (\boldsymbol{\alpha}_0, \omega, t) = \int_0^t \exp [\mathbf{A}_0 (t - \tau)] \mathbf{B}_{i,0} \mathbf{X} (\boldsymbol{\alpha}_0, \omega, \tau) d\tau; \quad \mathbf{B}_{i,0} \equiv \mathbf{B}_i (\boldsymbol{\alpha}_0) = \boldsymbol{\Psi}_0^T \mathbf{A}_0 \mathbf{D}'_{i,0} \boldsymbol{\Psi}_0; \quad (16)$$

with \mathbf{A}_0 and $\boldsymbol{\Psi}_0$ evaluated by solving the eigenproblem (5) for the “nominal system”, in which $\boldsymbol{\alpha} = \boldsymbol{\alpha}_0$; $\mathbf{A}_0 = \mathbf{A} (\boldsymbol{\alpha}_0)$ and

$$\mathbf{D}'_{i,0} = \frac{\partial}{\partial \alpha_i} \mathbf{D} (\boldsymbol{\alpha}) \Big|_{\boldsymbol{\alpha}=\boldsymbol{\alpha}_0} = \begin{bmatrix} \mathbf{O}_{n,n} & \mathbf{O}_{n,n} \\ -\mathbf{M}_S^{-1} \frac{\partial \mathbf{K}_D (\boldsymbol{\alpha}_k)}{\partial \alpha_i} \Big|_{\boldsymbol{\alpha}=\boldsymbol{\alpha}_0} & -\mathbf{M}_S^{-1} \frac{\partial \mathbf{C}_D (\boldsymbol{\alpha}_c)}{\partial \alpha_i} \Big|_{\boldsymbol{\alpha}=\boldsymbol{\alpha}_0} \end{bmatrix} \quad (17)$$

The *sensitivity* of *TFR* vector function, given in Eq. (16), can be evaluated as solution of the following differential equation with zero start conditions:

$$\dot{\mathbf{Y}}_i (\boldsymbol{\alpha}_0, \omega, t) = \mathbf{A}_0 \mathbf{Y}_i (\boldsymbol{\alpha}_0, \omega, t) + \mathbf{B}_{i,0} \mathbf{X} (\boldsymbol{\alpha}_0, \omega, \tau); \quad t > 0, \quad \mathbf{Y}_i (\boldsymbol{\alpha}_0, \omega, 0) = \mathbf{0}. \quad (18)$$

To perform the solution of this set of differential equations the vector $\mathbf{X} (\boldsymbol{\alpha}_0, \omega, t)$, defined in Eq. (12), is rewritten as [14]:

$$\mathbf{X} (\boldsymbol{\alpha}_0, \omega, t) = \mathbf{X}_1 (\boldsymbol{\alpha}_0, \omega, t) + \mathbf{X}_2 (\boldsymbol{\alpha}_0, \omega, t) \quad (19)$$

where:

$$\begin{aligned} \mathbf{X}_1 (\boldsymbol{\alpha}_0, \omega, t) &= -\varepsilon (\omega) \exp [-\beta (\omega) t] \left[\boldsymbol{\Gamma}_0^2 (\omega) + t \boldsymbol{\Gamma}_0 (\omega) \right] \mathbf{v}_0; \quad t > 0 \\ \mathbf{X}_2 (\boldsymbol{\alpha}_0, \omega, t) &= \varepsilon (\omega) \exp [\mathbf{A}_0 t] \boldsymbol{\Gamma}_0^2 (\omega) \mathbf{v}_0; \quad t > 0. \end{aligned} \quad (20)$$

In the previous equations $\boldsymbol{\Gamma}_0 (\omega)$ and \mathbf{v}_0 are evaluated by Eq. (13) and the last relationship of Eq. (9), respectively, for the “nominal system” ($\boldsymbol{\alpha} = \boldsymbol{\alpha}_0$).

It follows that it is possible to split the vector solution of Eq. (18) as the sum of two vectors, solutions of the following two sets of differential equations, with zero start initial conditions:

$$\begin{aligned}\mathbf{X}_1(\boldsymbol{\alpha}_0, \omega, t) &= -\varepsilon(\omega) \exp[-\beta(\omega) t] [\boldsymbol{\Gamma}_0^2(\omega) + t \boldsymbol{\Gamma}_0(\omega)] \mathbf{v}_0; \quad t > 0 \\ \mathbf{X}_2(\boldsymbol{\alpha}_0, \omega, t) &= \varepsilon(\omega) \exp[\boldsymbol{\Lambda}_0 t] \boldsymbol{\Gamma}_0^2(\omega) \mathbf{v}_0; \quad t > 0.\end{aligned}\quad (21)$$

Then, the *sensitivity TFR's* vector function can be evaluate in closed form solution as:

$$\begin{aligned}\mathbf{Y}_i(\boldsymbol{\alpha}_0, \omega, t) &= \mathbf{Y}_{i,1}(\boldsymbol{\alpha}_0, \omega, t) + \mathbf{Y}_{i,2}(\boldsymbol{\alpha}_0, \omega, t) = \{\mathbf{Y}_{i,1,p}(\boldsymbol{\alpha}_0, \omega, t) + \mathbf{Y}_{i,2,p}(\boldsymbol{\alpha}_0, \omega, t) \\ &\quad - \exp[\boldsymbol{\Lambda}_0 t] [\mathbf{Y}_{i,1,p}(\boldsymbol{\alpha}_0, \omega, 0) + \mathbf{Y}_{i,2,p}(\boldsymbol{\alpha}_0, \omega, 0)]\}; \quad t > 0\end{aligned}\quad (22)$$

where the particular solution vectors of Eqs. (21), can be evaluated, after some algebra, as:

$$\begin{aligned}\mathbf{Y}_{i,1,p}(\boldsymbol{\alpha}_0, \omega, t) &= \varepsilon(\omega) \exp[-\beta(\omega) t] \boldsymbol{\Gamma}_0(\omega) [\boldsymbol{\Gamma}_0(\omega) \mathbf{B}_{i,0} + \mathbf{B}_{i,0} \boldsymbol{\Gamma}_0(\omega) + t \mathbf{B}_{i,0}] \boldsymbol{\Gamma}_0(\omega) \mathbf{v}_0 \\ \mathbf{Y}_{i,2,p}(\boldsymbol{\alpha}_0, \omega, t) &= \varepsilon(\omega) \mathbf{P}_{i,0}(\boldsymbol{\alpha}_0, t) \exp[\boldsymbol{\Lambda}_0 t] \boldsymbol{\Gamma}_0^2(\omega) \mathbf{v}_0;\end{aligned}\quad (23)$$

where $\mathbf{P}_i(\boldsymbol{\alpha}_0, t)$ is a matrix of order $2m \times 2m$ whose elements, $P_{i,jk}(\boldsymbol{\alpha}_0, t)$, are defined as:

$$P_{i,jj}(\boldsymbol{\alpha}_0, t) = t B_{i,jj}(\boldsymbol{\alpha}_0); \quad P_{i,jk}(\boldsymbol{\alpha}_0, t) = \frac{B_{i,jk}(\boldsymbol{\alpha}_0)}{\lambda_k - \lambda_j}, \quad j \neq k \quad (24)$$

with $B_{i,jk}(\boldsymbol{\alpha}_0)$ elements of the matrix $\mathbf{B}_{i,0}$ defined in the last of Eq. (16).

Note that, the *sensitivity of non-geometrical spectral moments*, with respect to the parameter α_i , which are elements of *sensitivity of PEC* matrix defined in Eq. (14), can be evaluated by substituting Eqs. (20) and (23) into Eq. (15).

3.3 Sensitivity of Frequency Response Vector Function for Stationary Excitations

Notice that the sensitivities of spectral moments of structural response, for zero-mean stationary Gaussian excitation stochastic process can be evaluated particularizing Eqs. (9) and (16). In fact, assuming the modulating function equal to *unit step function* (Heaviside function, $a(\omega, t) = 1; t > 0$), and taking the limit as $t \rightarrow \infty$, the first of Eq. (9) leads to:

$$\mathbf{X}(\boldsymbol{\alpha}, \omega) = \lim_{t \rightarrow \infty} \mathbf{X}(\boldsymbol{\alpha}, \omega, t) = \exp(i \omega t) [i \omega \mathbf{I}_{2m} - \boldsymbol{\Lambda}(\boldsymbol{\alpha})]^{-1} \mathbf{v}(\boldsymbol{\alpha}) \quad (25)$$

while the first of Eqs. (16) leads to:

$$\mathbf{Y}(\boldsymbol{\alpha}_0, \omega) = \lim_{t \rightarrow \infty} \mathbf{Y}(\boldsymbol{\alpha}_0, \omega, t) = \exp(i \omega t) [\mathbf{i} \omega \mathbf{I}_{2m} - \mathbf{A}_0]^{-1} \mathbf{B}_{i,0} [\mathbf{i} \omega \mathbf{I}_{2m} - \mathbf{A}_0]^{-1} \mathbf{v}_0 \quad (26)$$

It follows that the *sensitivity of PEC* matrix, with respect to the i -th parameter, is not a time-dependent matrix and can be evaluated as:

$$\begin{aligned} \boldsymbol{\Sigma}_{s_{Z,i}}(\boldsymbol{\alpha}_0) &= \left. \frac{\partial \boldsymbol{\Sigma}_{ZZ}(\boldsymbol{\alpha})}{\partial \alpha_i} \right|_{\boldsymbol{\alpha}=\boldsymbol{\alpha}_0} = \frac{\partial}{\partial \alpha_i} \left[\begin{array}{cc} \mathbf{A}_{0,UU}(\boldsymbol{\alpha}) & \mathbf{i} \mathbf{A}_{1,UU}(\boldsymbol{\alpha}) \\ -\mathbf{i} \mathbf{A}_{1,UU}^{*T}(\boldsymbol{\alpha}) & \mathbf{A}_{2,UU}(\boldsymbol{\alpha}) \end{array} \right] \Bigg|_{\boldsymbol{\alpha}=\boldsymbol{\alpha}_0} = \\ &= \mathbf{E} \left\langle \mathbf{Z}^*(\boldsymbol{\alpha}_0, t) \frac{\partial \mathbf{Z}^T(\boldsymbol{\alpha}, t)}{\partial \alpha_i} \Bigg|_{\boldsymbol{\alpha}=\boldsymbol{\alpha}_0} \right\rangle + \mathbf{E} \left\langle \mathbf{Z}^*(\boldsymbol{\alpha}_0, t) \frac{\partial \mathbf{Z}^T(\boldsymbol{\alpha}, t)}{\partial \alpha_i} \Bigg|_{\boldsymbol{\alpha}=\boldsymbol{\alpha}_0} \right\rangle^{*T} \end{aligned} \quad (27)$$

which gives the *sensitivity of PEC* matrix for stationary excitations, with respect to the parameter α_i , whose elements are the *sensitivity of spectral moments*. Eq. (27), according to Eq. (15), gives:

$$\begin{aligned} \mathbf{E} \left\langle \mathbf{Z}^*(\boldsymbol{\alpha}_0, t) \frac{\partial \mathbf{Z}^T(\boldsymbol{\alpha}, t)}{\partial \alpha_i} \Bigg|_{\boldsymbol{\alpha}=\boldsymbol{\alpha}_0} \right\rangle &= \\ = \boldsymbol{\Psi}_0^* \left\{ \int_0^\infty G_0(\omega) [\mathbf{i} \omega \mathbf{I}_{2m} - \mathbf{A}_0^*]^{-1} \mathbf{v}_0 \mathbf{v}_0^T [\mathbf{i} \omega \mathbf{I}_{2m} - \mathbf{A}_0]^{-1} \mathbf{B}_{i,0}^T [\mathbf{i} \omega \mathbf{I}_{2m} - \mathbf{A}_0]^{-1} d\omega \right\} \boldsymbol{\Psi}_0^T. \end{aligned} \quad (28)$$

4 Numerical Results

In order to verify the applicability of the proposed approach, a numerical application has been conducted on two adjacent buildings, connected each other through fluid dampers devices. The connected three-storey structures have the same floor elevations (see Fig. 1).

The buildings have a global floor stiffness equal to 4×10^9 N/m and 2×10^9 N/m, respectively for building 1 and building 2, and the same tributary mass per storey, equivalent as 1.29×10^6 kg. The same damping ratio $\xi = 0.02$ has been assumed for all the modes of vibrations of the two unlinked structures. The main characteristics, circular frequency ω_i , period T_i and modal participating mass ratio ε_i , of the unlinked structures, together with the global one, are summarized in Table 1.

The global structure undergoes to a seismic input modeled as a stationary and fully non-stationary stochastic model; the stationary *PSD* is defined according to the Tajimi-Kanai filter:

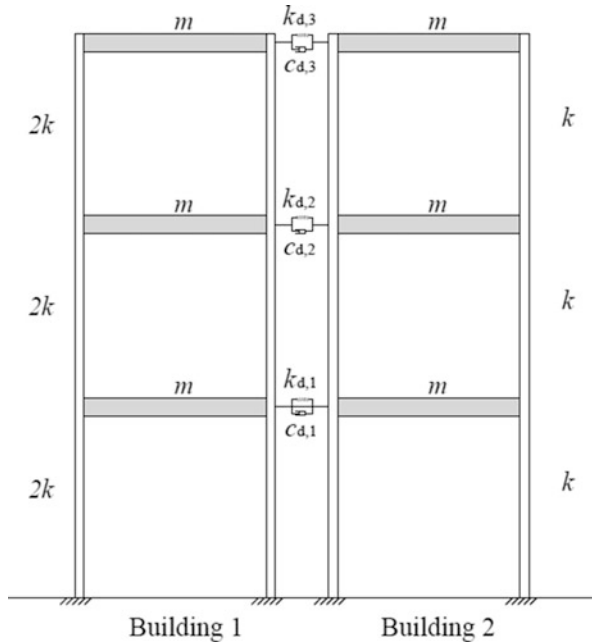


Fig. 1 Geometric configuration of the analyzed system

Table 1 Modal information of the analyzed buildings

Building 1			Building 2			Global system		
ω_i [rad/s]	T_i [s]	ε_i [%]	ω_i [rad/s]	T_i [s]	ε_i [%]	ω_i [rad/s]	T_i [s]	ε_i [%]
24.782	0.254	91.408	17.524	0.359	91.408	17.524	0.359	47.704
69.438	0.090	7.488	49.099	0.128	7.488	24.782	0.254	47.704
100.340	0.063	1.104	70.951	0.089	1.104	49.099	0.128	3.744

$$G_0(\omega) = G_W \frac{4 \zeta_K^2 \omega_K^2 \omega^2 + \omega_K^4}{(\omega_K^2 - \omega^2)^2 + 4 \zeta_K^2 \omega_K^2 \omega^2} \tag{29}$$

where $G_W = 0.1 \text{ m}^2/\text{s}^3$, $\omega_K = 4 \pi \text{ rad/s}$ is the filter frequency that determines the dominant input frequency and $\zeta_K = 0.6$ is the filter damping coefficient that indicates the sharpness of the PSD function.

The fluid dampers are modeled as a combination of a linear spring and a linear dashpot; the parameters of each fluid damper device, stiffness k_d and damping coefficient c_d , have been chosen to obtain the optimal system, for dynamic performances and costs. First, a parametric cost benefit analysis has been conducted to define the optimal stiffness value k_d . As evidenced from Fig. 2, in order to have the greater reduction of the variance of the displacement of the topper floor λ_{0,u_3} ,

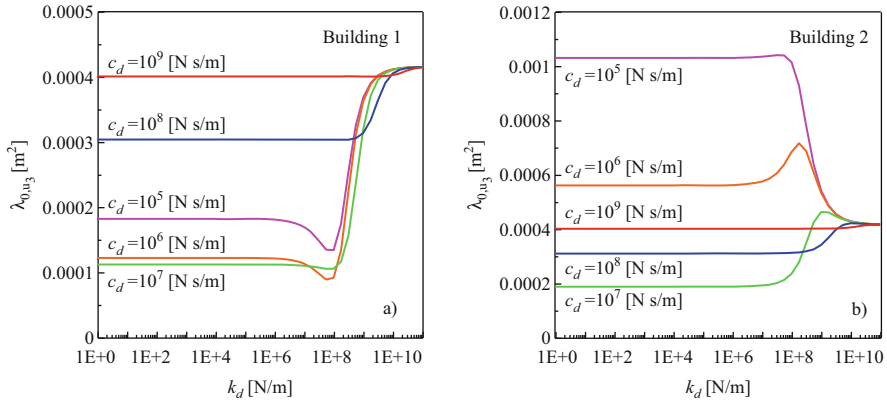


Fig. 2 Trend of the first spectral moment of the topper floor λ_{0,u_3} [m²] versus damper device stiffness k_d [N/m]: (a) Building 1; (b) Building 2

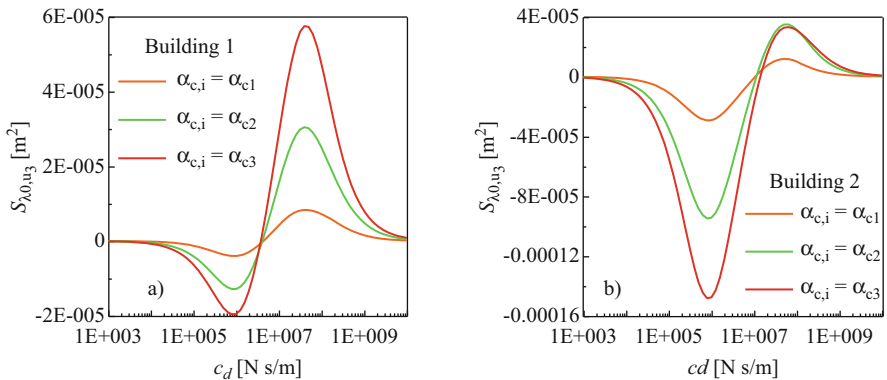


Fig. 3 Sensitivity of the first spectral moment of the third floor with respect to the damping coefficient: (a) Building 1; (b) Building 2

the best value of the stiffness of the damper devices should be chosen as 10^8 N/m; although, it has to be highlighted that this reduction is insignificant if compared to the other devices, in front of a higher cost. For this reason, the stiffness k_d for all the devices has been set equal to 30 N/m.

Then, in order to define the best damping coefficient value, a parametric study has been conducted, analyzing the sensitivity of nodal response for both stationary and non-stationary zero-mean Gaussian stochastic process. It is necessary to remember that a positive sensitivity indicates an increment of the corresponding *NGSM*, when the parameter α changes, while a negative sensitivity means that the *NGSM* decreases when the parameter changes. Then, the best parameter to choose in design phase is the corresponding to the minimum of the sensitivity parameter. Figure 3

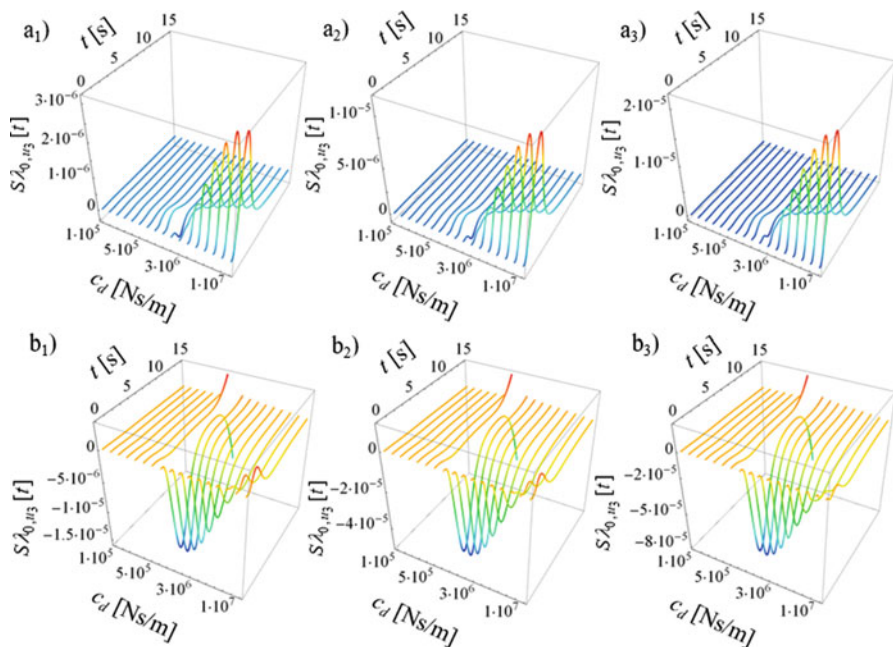


Fig. 4 Time-varying sensitivity of the first spectral moment of the third floor with respect to the dissipation parameter of i -th floor, $S\lambda_{0,u_3}$ [t] [m^2], versus damping coefficient c_d [N s/m]: (a) Building 1; (b) Building 2

shows, for both buildings, the trend of the sensitivity of the first spectral moment of the top floor displacement $S\lambda_{0,u_3} = \left. \frac{\partial \lambda_{0,u_3}}{\partial \alpha_i} \right|_{\alpha=\alpha_0}$, with respect to the dissipation parameter of i -th floor $\alpha_{c,i}$, versus the damping coefficient c_d .

As evidenced from Fig. 3, the greatest influence on the reduction of the system response is caused by the device positioned at the top (red line); for both buildings, the best parameter for the viscous damping is equal to $c_d = 10^6$ [N s/m] where the sensitivity reaches its lower value for all the three elevations. For the fully non-stationary seismic input, according to [11, 12] the stationary counterpart of the *EPSD* $G_0(\omega)$ has been defined in Eq. (29) and the modulating function has been chosen according to Eq. (11), where $\alpha_a(\omega) = \frac{1}{2} \left(0.15 + \frac{\omega^2}{25\pi^2} \right)$, $\varepsilon(\omega) = \frac{\sqrt{2}}{5\pi} \omega$ [15].

As evidenced from Fig. 4, the optimal value of the damping coefficient c_d , where the sensitivity with respect to the dissipation parameter of i -th floor $S\lambda_{0,u_3}$ [t] = $\left. \frac{\partial \lambda_{0,u_3}}{\partial \alpha_i} \right|_{\alpha=\alpha_0}$ assumes its lower value, is very close to the one of the stationary case.

This important result leads to the immediate consequence that, in the design phase of plane frames it is sufficient to analyze the stationary model, with a remarkable gain in terms of computational time.

5 Conclusions

During last decades, among the various proposed solutions for the mutual pounding, connecting structures through dampers could be the right innovative way. So, the engineers have to face to the problem of the design of these vibration control devices, taking into account also the modeling of the dynamics loads as fully non-stationary zero-mean Gaussian stochastic process; in this framework the sensitivity analysis represents a powerful tool in the optimization procedure.

This work dealt with a new method for the evaluation the sensitivities of non-geometric spectral moments of the structural response of the non-classically damped coupled systems subjected to fully non-stationary zero-mean Gaussian excitation, through simple integrals in frequency domain. The main steps of this study are: i) to determine, for the non-classically dynamic structure composed of two adjacent buildings linked by viscoelastic dampers represented by the Kelvin-Voigt model, the *TFR* vector function of the nodal response; ii) to evaluate the *sensitivity of TFR* vector function of the nodal response in explicit closed form; iii) to find the optimal parameters of dampers through parametric studies, analyzing the sensitivity of nodal response for both stationary and non-stationary zero-mean Gaussian stochastic process.

A numerical application has been conducted in order to optimize a damping system; from the analysis of the results it can be stated that: (a) the system stiffness does not play a central role in the reduction of the relative displacements of the studied structure; (b) since stationary and non-stationary input conducted to the same optimal value of the damping coefficient, during the design phase of plane frames it could be sufficient to take into account only the results of the stationary analysis, with a remarkable gain in terms of computational time.

References

1. Gurley, K., Kareem, A., Bergman, L.A., Johnson, E.A., Klein, E.: Coupling tall buildings for control of response to wind. In: Schueller, Shinozuka, Yao (eds.) *Structural Safety & Reliability*, pp. 1553–1560. Balkema, Rotterdam (1994)
2. Luco, J.E., De Barros, F.C.: Optimal damping between two adjacent elastic structures. *Earthq. Eng. Struct. Dyn.* **27**, 649–659 (1998)
3. Xu, Y.L., He, Q., Ko, J.M.: Dynamic response of damper-connected adjacent buildings under earthquake excitation. *Eng. Struct.* **21**, 135–148 (1999)
4. Zhang, W.S., Xu, Y.L.: Dynamic characteristics and seismic response of adjacent buildings linked by discrete dampers. *Earthq. Eng. Struct. Dyn.* **28**, 1163–1185 (1999)
5. Zhu, H.P., Ge, D.D., Huang, X.: Optimum connecting dampers to reduce the seismic responses of parallel structures. *J. Sound Vib.* **9**, 1931–1949 (2011)
6. Di Paola, M., Petrucci, G.: Spectral moments and pre-envelope covariances of nonseparable processes. *J. Appl. Mech. (ASME)*. **57**, 218–224 (1990)
7. Muscolino, G.: Nonstationary: pre-envelope Covariances of nonclassically damped systems. *J. Sound Vib.* **149**, 107–123 (1991)

8. Muscolino, G.: Nonstationary envelope in random vibration theory. *J. Eng. Mech. (ASCE)*, **114**, 1396–1413 (1988)
9. Michaelov, G., Sarkani, S., Lutes, L.D.: Spectral characteristics of nonstationary random processes – a critical review. *Struct. Saf.* **21**, 223–244 (1999)
10. Alderucci, T., Muscolino, G.: Time–frequency varying response functions of non-classically damped linear structures under fully non-stationary stochastic excitations. *Probab. Eng. Mech.* **54**, 95–109 (2018)
11. Priestley, M.B.: Evolutionary spectra and non-stationary processes. *J. Royal Stat. Soc. Series B Methodol.* **27**, 204–237 (1965)
12. Priestley, M.B.: Power spectral analysis of non-stationary random processes. *J. Sound Vib.* **6**, 86–97 (1967)
13. Muscolino, G., Alderucci, T.: Closed-form solutions for the evolutionary frequency response function of linear systems subjected to separable or non-separable non-stationary stochastic excitations. *Probab. Eng. Mech.* **40**, 75–89 (2015)
14. Alderucci, T., Genovese, F. and Muscolino, G.: Response sensitivity of structural systems subjected to fully non-stationary random processes, UNCECOMP 2019, Proceedings of the 3rd International Conference on Uncertainty, Quantification in Computational Sciences and Engineering (Eds. M. Papadrakakis, V. Papadopoulos and G. Stefanou), pp. 75–89 (2019)
15. Spanos, P., Solomos, G.P.: Markov approximation to transient vibration. *J. Eng Mech. (ASCE)*, **109**, 1134–1150 (1983)

Analysis of Switching Strategies for the Optimization of Periodic Chemical Reactions with Controlled Flow-Rate



Peter Benner, Andreas Seidel-Morgenstern, and Alexander Zuyev

Abstract An isoperimetric optimal control problem with non-convex cost is considered for a class of nonlinear control systems with periodic boundary conditions. This problem arises in chemical engineering as the maximization of the product of non-isothermal reactions by consuming a fixed amount of input reactants. It follows from the Pontryagin maximum principle that the optimal controls are piecewise constant in the considered case. We focus on a parametrization of optimal controls in terms of switching times in order to estimate the cost under different switching strategies. We exploit the Chen-Fliess functional expansion of solutions to the considered nonlinear system with bang-bang controls to satisfy the boundary conditions and evaluate the cost analytically for small periods. In contrast to the previous results in this area, the system under consideration is not control-affine, and the integrand of the cost depends on the state. This approach is applied to non-isothermal chemical reactions with simultaneous modulation of the input concentration and the volumetric flow-rate.

Keywords Isoperimetric optimal control problem · Bang-Bang controls · Chen–Fliess series · Nonlinear chemical reactions

P. Benner · A. Seidel-Morgenstern
Max Planck Institute for Dynamics of Complex Technical Systems, Magdeburg, Germany
e-mail: benner@mpi-magdeburg.mpg.de; seidel@mpi-magdeburg.mpg.de

A. Zuyev (✉)
Max Planck Institute for Dynamics of Complex Technical Systems, Magdeburg, Germany
Otto von Guericke University Magdeburg, Germany
Institute of Applied Mathematics & Mechanics, National Academy of Sciences of Ukraine,
Sloviansk, Ukraine
e-mail: zuyev@mpi-magdeburg.mpg.de

© Springer Nature Switzerland AG 2021
J. Awrejcewicz (ed.), *Perspectives in Dynamical Systems III: Control and Stability*,
Springer Proceedings in Mathematics & Statistics 364,
https://doi.org/10.1007/978-3-030-77314-4_5

1 Introduction

Strategies for the dynamic optimization of chemical reaction models have been studied in the mathematical literature by using the Pontryagin maximum principle [1, 15], vibrational control technique [2], frequency-domain methods [9–11], center manifold theory [7], flatness-based approach and extremum seeking [5], model predictive control methodology [4], and other approaches.

A remarkable result in this area was formulated for a mathematical model of an isothermal reaction the type “ $v_1 A_1 + v_2 A_2 \rightarrow \text{Product}$ ” with the power law rate $r = k C_1^{n_1} C_2^{n_2}$ in [6]. Namely, it was shown that the conversion of A_1 and A_2 to the product cannot be improved by using time-varying controls if $0 < n_1 < 1$, $0 < n_2 < 1$, and $n_1 + n_2 \leq 1$. In the non-isothermal case, it turns out that it is possible to improve the performance of first-order reactions of the type “ $A \rightarrow \text{Product}$ ” by using sinusoidal periodic inputs [9]. For a realistic non-isothermal reaction of this type, it was shown that the optimal controls are bang-bang, and periodic switching strategies have been described by applying the Pontryagin maximum principle in [15]. An analytic approach for computing the switching parameters of τ -periodic controls has been developed in [3] for the case of small periods τ .

Note that the above papers deal with reaction models with a constant flow-rate, while the periodic flow-rate modulation is shown to be an important ingredient for improving the reaction performance [8]. The corresponding isoperimetric optimal control problem is rigorously formulated in [16] for a non-isothermal mathematical model with two independent inputs: the inlet concentration and the flow-rate. As in the case of constant flow-rate, it is shown in [16] that the optimal controls are piecewise constant, and their switching times are defined in terms of zeros of certain auxiliary functions. However, the structure of switching controllers has not been analyzed so far. This paper aims at developing an efficient approach for computing periodic bang-bang controls and evaluating the cost for the isoperimetric optimal control problem introduced in [16].

2 Optimization Problem

Consider a nonlinear control system describing non-isothermal chemical reactions of the type “ $A \rightarrow \text{Product}$ ” and order \bar{n} [8, 16]:

$$\dot{x} = f_0(x) + v_1 v_2 g_1(x) + v_2 g_2(x), \quad x = (x_1, x_2)^T \in \mathbb{R}^2, \quad (1)$$

where x_1 is the dimensionless concentration of A in the reactor, x_2 is the dimensionless temperature,

$$\begin{aligned} f_0(x) &= \begin{pmatrix} -k_1(1+x_1)^{\bar{n}} \exp\left(-\frac{\gamma}{x_2+1}\right) \\ \delta - St(1+x_2) - k_2(1+x_1)^{\bar{n}} \exp\left(-\frac{\gamma}{x_2+1}\right) \end{pmatrix}, \\ g_1(x) &= \begin{pmatrix} 1 + k_1 \exp(-\gamma) \\ 0 \end{pmatrix}, \quad g_2(x) = \begin{pmatrix} -1 - x_1 \\ k_2 \exp(-\gamma) + St - \delta - x_2 \end{pmatrix}, \end{aligned} \quad (2)$$

and k_1 , k_2 , St , γ , and δ are physical parameters (cf. [8]). The dimensionless control variables $v_1 \in [v_1^{\min}, v_1^{\max}]$ and $v_2 \in [v_2^{\min}, v_2^{\max}]$ correspond to the inlet concentration of A and the flow-rate, respectively. We assume that $0 < v_i^{\min} \leq 1$ and $v_i^{\max} \geq 1$ for $i = 1, 2$. Then it is easy to see that $x_1 = x_2 = 0$ is an equilibrium of system (1) that corresponds to a steady-state operation of the considered chemical reactor with $v_1 = v_2 = 1$.

System (1) can be transformed to the control-affine form with respect to the inputs $u_1 = v_1 v_2$ and $u_2 = v_2$ as follows [16]:

$$\dot{x} = f_0(x) + u_1 g_1(x) + u_2 g_2(x), \quad x \in \mathbb{R}^2, \quad u = (u_1, u_2)^T \in U = \text{Conv } U_b, \quad (3)$$

where

$$U_b = \left\{ \begin{pmatrix} u_1^{\min} \\ u_2^{\min} \end{pmatrix}, \begin{pmatrix} u_1^{\max} \\ u_2^{\max} \end{pmatrix}, \begin{pmatrix} u_1^- \\ u_2^{\max} \end{pmatrix}, \begin{pmatrix} u_1^+ \\ u_2^{\min} \end{pmatrix} \right\},$$

$$u_1^{\min} = v_1^{\min} v_2^{\min}, \quad u_1^- = v_1^{\min} v_2^{\max}, \quad u_1^+ = v_1^{\max} v_2^{\min}, \quad u_1^{\max} = v_1^{\max} v_2^{\max}.$$

As maximizing the conversion of A to the product over a given time period $t \in [0, \tau]$ can be treated in the sense of minimizing the remaining mass of A in the outgoing stream, our goal is to minimize the cost

$$J = \frac{1}{\tau} \int_0^\tau (x_1(t) + 1) u_2(t) dt. \quad (4)$$

We also assume that the consumption of A over the period is fixed as

$$\frac{1}{\tau} \int_0^\tau u_1(t) dt = \bar{u}_1,$$

which yields the following isoperimetric optimal control problem.

Problem 2.1 ([16]) *Given $\tau > 0$, $\bar{u}_1 \in \mathbb{R}$, and $x^0 \in \mathbb{R}^2$, the goal is to find an admissible control $\hat{u} \in L^\infty([0, \tau]; U)$ that minimizes the cost J along the*

trajectories of (3) corresponding to the admissible controls $u \in L^\infty([0, \tau]; U)$ such that

$$\frac{1}{\tau} \int_0^\tau u_1(t) dt = \bar{u}_1 \quad \text{and} \quad x(0) = x(\tau) = x^0. \quad (5)$$

If $\hat{u}(t)$ ($0 \leq t \leq \tau$) is an optimal control for Problem 2.1, then it follows from the results of [16] that $\hat{u}(t) \in U_b$ almost everywhere on $[0, \tau]$, and the switching times of $\hat{u}(t)$ are related to zeros of the following functions: $I_1(t)$ $I_2(t)$, $\frac{u_1^- - u_1^{\min}}{u_2^{\max} - u_2^{\min}} I_1(t) + I_2(t)$, $\frac{u_1^{\max} - u_1^+}{u_2^{\max} - u_2^{\min}} I_1(t) + I_2(t)$, where $I_1(t)$ and $I_2(t)$ are defined by solutions of the associated Hamiltonian system. It should be noted that $I_1(t)$ and $I_2(t)$ are parameterized by initial values of the adjoint variables. In this paper, we will not use any information on the behavior of adjoint variables and define the switching parameters directly from (5). Then the cost (4) will be approximated analytically to estimate the performance improvement for the considered class of bang-bang controllers.

3 Computation of the Switching Controls

Assuming that a bang-bang control $\hat{u}(t) \in U_b$ ($0 \leq t \leq \tau$) has a finite number of switchings, we enumerate the switching times

$$0 = t_0 < t_1 < \dots < t_N = \tau \quad \text{with some } N \in \mathbb{N} \quad (6)$$

and denote

$$u^j = \hat{u}(t) \in U_b \quad \text{for } t \in S_j = (t_{j-1}, t_j), \quad j = 1, 2, \dots, N. \quad (7)$$

Our goal is to analyse the cost J on the trajectories of system (3) with piecewise-constant controls of the form (7) depending on the parameters

$$(t_1, t_2, \dots, t_N), \quad (u^1, u^2, \dots, u^N).$$

A straightforward computation of $\int_0^\tau \hat{u}_1(t) dt$ for the piecewise-constant control (7) shows that the isoperimetric constraint in (5) is equivalent to

$$\sum_{j=1}^N \alpha_j u_1^j = \bar{u}_1 \quad \text{with} \quad \alpha_j = \frac{t_j - t_{j-1}}{\tau} > 0. \quad (8)$$

In order to satisfy the periodic boundary condition $x(0) = x(\tau)$ and estimate the cost (4) analytically for small τ , we exploit the Chen–Fliess expansion of solutions to system (3) with the initial value $x(0) = x^0$ and control $u = \hat{u}(t)$ (see, e.g., [14]):

$$x = x^0 + \sum_{i=0}^2 g_i(x^0)V_i(t) + \sum_{i,j=0}^2 (L_{g_j}g_i)(x^0)V_{ij}(t) + \sum_{i,j,l=0}^2 (L_{g_l}L_{g_j}g_i)(x^0)V_{ijl}(t) + O(t^4), \quad (9)$$

where we assume that $g_0(x) = f_0(x)$, $L_{g_i}g_j(x) = \frac{\partial g_j(x)}{\partial x}g_i(x)$ is the directional derivative of $g_j(x)$ along $g_i(x)$, and

$$V_i(t) = \int_0^t u_i(s)ds, \quad u_0(t) \equiv 1, \quad V_{ij}(t) = \int_0^t \int_0^s u_i(s)u_j(p)dp ds, \\ V_{ijl}(t) = \int_0^t \int_0^s \int_0^p u_i(s)u_j(p)u_l(r)dr dp ds, \quad t \in [0, \tau].$$

The remainder of formula (9) is of order $O(t^4)$ for small $t > 0$ if the vector fields $g_j(x)$ are of class C^3 in a neighborhood of x^0 .

As in [3], we restrict our analysis to the cases $N \leq 4$, motivated by the estimate of the number of switchings in isoperimetric problems proposed in [15]. The main analytical result of our study is summarized as follows.

Proposition 3.1 *Let $\hat{u}(t)$, $t \in [0, \tau]$ be a bang-bang control represented by (7) with the parameters $0 < t_1 \leq t_2 \leq t_3 \leq t_4 = \tau$ and $u^1, u^2, u^3, u^4 \in U_b$, and let $x(t)$, $t \in [0, \tau]$ be the corresponding solution of (3) such that $x(0) = x^0 \in \mathbb{R}^2$. Then the isoperimetric constraint (8) is equivalent to*

$$\sum_{j=2}^4 \alpha_j (u_1^j - u_1^1) = \bar{u}_1 - u_1^1, \quad \alpha_1 = 1 - \alpha_2 - \alpha_3 - \alpha_4, \quad (10)$$

and the periodic boundary condition $x(0) = x(\tau)$ reduces to

$$\sum_{j=1}^4 \alpha_j f_j + \frac{\tau}{2} \{ \alpha_1^2 L_{f_1} f_1 + \alpha_2^2 L_{f_2} f_2 - \alpha_3^2 L_{f_3} f_3 - \alpha_4^2 L_{f_4} f_4 + 2\alpha_1 \alpha_2 L_{f_1} f_2 - 2\alpha_3 \alpha_4 L_{f_4} f_3 \} \\ + \frac{\tau^2}{6} \{ \alpha_1^3 L_{f_1}^2 f_1 + \alpha_2^3 L_{f_2}^2 f_2 + \alpha_3^3 L_{f_3}^2 f_3 + \alpha_4^3 L_{f_4}^2 f_4 + 3\alpha_1 \alpha_2 L_{f_1} (\alpha_1 L_{f_1} + \alpha_2 L_{f_2}) f_2 \\ + 3\alpha_3 \alpha_4 L_{f_4} (\alpha_4 L_{f_4} + \alpha_3 L_{f_3}) f_3 \} = O(\tau^3), \quad (11)$$

where $f_i(x) = f_0(x) + u_1^i g_1(x) + u_2^i g_2(x)$, $i = 1, 2, 3, 4$. Moreover, the cost (4) evaluated for $x(t)$ admits the representation $J = \bar{u}_2 + X_1$, where

$$\bar{u}_2 = \frac{1}{\tau} \int_0^\tau \hat{u}_2(t)dt = u_2^1 + \sum_{j=2}^4 \alpha_j (u_2^j - u_2^1) \quad (12)$$

and X_1 is the first component of the vector $X \in \mathbb{R}^2$:

$$\begin{aligned} X &= \frac{1}{\tau} \int_0^\tau x(t) \hat{u}_2(t) dt = \bar{u}_2 x^0 + \frac{\tau}{2} \left(\alpha_1^2 u_2^1 f_1 - (1 - \alpha_1)^2 u_2^2 f_2 \right) \\ &\quad + \frac{\tau^2}{6} \left(\alpha_1^3 u_2^1 L_{f_1} f_1 + (1 - \alpha_1)^3 u_2^2 L_{f_2} f_2 \right) \\ &\quad + \frac{\tau^3}{24} \left(\alpha_1^4 u_2^1 L_{f_1} L_{f_1} f_1 - (1 - \alpha_1)^4 u_2^2 L_{f_2} L_{f_2} f_2 \right) + O(\tau^4). \end{aligned} \quad (13)$$

The vector fields $f_i(x)$ and their directional derivatives in (11), (13) are evaluated at $x = x^0$.

The assertion of Proposition 3.1 is obtained from the Chen–Fliess expansion (9) for the solution $x(t)$ of system (3) with $u = \hat{u}(t)$.

Note that the cases with $N < 4$ can be considered as particular cases of $N = 4$ with some of the α_j being zero. In particular, the case $N = 2$ is treated by assuming $\alpha_3 = \alpha_4 = 0$ in (8). In this case, the Eqs. (10), (11), and (12) are reduced, respectively, to

$$\alpha_1 = \frac{\bar{u}_1 - u_1^2}{u_1^1 - u_1^2} \in (0, 1), \quad \alpha_2 = 1 - \alpha_1 \quad \text{if } u_1^1 \neq u_1^2, \quad (14)$$

$$\alpha_1(f_1 - f_2) + f_2 + \frac{\tau}{2} (\alpha_1^2 L_{f_1} f_1 - (1 - \alpha_1)^2 L_{f_2} f_2) + \frac{\tau^2}{6} (\alpha_1^3 L_{f_1}^2 f_1 + (1 - \alpha_1)^3 L_{f_2}^2 f_2) = O(\tau^3), \quad (15)$$

and

$$\bar{u}_2 = \frac{1}{\tau} \int_0^\tau \hat{u}_2(t) dt = \alpha_1 u_2^1 + (1 - \alpha_1) u_2^2. \quad (16)$$

4 Simulation Results

We take the following parameters for numerical simulations for the first-order ($\bar{n} = 1$) adiabatic reaction considered in [3] with $\delta = St = 0$:

$$\gamma = \frac{E_A}{RT} = 17.77, \quad k_1 = k_0 \bar{C}_A^{\bar{n}-1} \frac{V}{F} = 5.819 \cdot 10^7, \quad k_2 = \frac{\Delta H_R k_0 \bar{C}_A^{\bar{n}} V}{\rho c_p \bar{T} F} = -8.99 \cdot 10^5.$$

The above dimensionless parameters are computed with the gas constant $R = 8.3144598 \frac{\text{J}}{\text{K} \cdot \text{mol}}$ and the activation energy $E_A = 44.35 \frac{\text{kJ}}{\text{mol}}$, the collision factor $k_0 = 1.4 \cdot 10^5 \text{ s}^{-1}$, the reaction heat $\Delta H_R = -55.5 \frac{\text{kJ}}{\text{mol}}$, and $\rho c_p = 4.186 \frac{\text{kJ}}{\text{K} \cdot \text{l}}$ being the product of the density and the heat capacity. This model corresponds to the chemical reaction $(\text{CH}_3\text{CO})_2\text{O} + \text{H}_2\text{O} \rightarrow 2 \text{CH}_3\text{COOH}$ in the CSTR of volume

$V = 0.2981$ with the steady-state outlet concentration $\bar{C}_A = 0.3498 \frac{\text{mol}}{\text{l}}$ and the steady-state temperature $\bar{T} = 300.17 \text{ K}$. We assume that the flow-rate and the inlet concentration can be controlled around their steady-state values $\bar{F} = 7.17 \cdot 10^{-4} \frac{\text{l}}{\text{s}}$ and $\bar{C}_{Ai} = 0.74 \frac{\text{mol}}{\text{l}}$, respectively, within the range of 85%, i.e. $v_i^{\min} = 0.15$, $v_i^{\max} = 1.85$, $i = 1, 2$. This choice of control constraints corresponds to the following components of the points in U_b :

$$u_1^{\min} = 0.0225, u_1^{\max} = 3.4225, u_1^+ = u_1^- = 0.2775, u_2^{\min} = 0.15, u_2^{\max} = 1.85. \quad (17)$$

In the sequel, we impose the isoperimetric constraint (5) with $\bar{u}_1 = 1$. The constraint $\bar{u}_1 = 1$ is satisfied, in particular, by the constant controls $u_1 = u_2 = 1$ for system (3) (or, equivalently, $v_1 = v_2 = 1$ for system (1)). As it was already mentioned, system (3) admits the equilibrium $x_1 = x_2 = 0$ with $u_1 = u_2 = 1$, and this equilibrium corresponds to the cost $\bar{J} = 1$ in (4). In this section, we will compare the steady-state value \bar{J} with the values of J for the periodic trajectories corresponding to controls (7). As the goal of Problem 2.1 is to minimize the cost J , we will treat the periodic trajectories with $J < \bar{J}$ as improving the reactor performance in comparison with its steady-state operation. The results of numerical simulations with controls of the form (7) are summarized in Figs. 1, 2 and Table 1 for the following switching strategies:

$$N = 2, u^1 = \begin{pmatrix} u_1^{\max} \\ u_2^{\max} \end{pmatrix}, u^2 = \begin{pmatrix} u_1^{\min} \\ u_2^{\min} \end{pmatrix}, \quad (18)$$

$$N = 2, u^1 = \begin{pmatrix} u_1^{\max} \\ u_2^{\max} \end{pmatrix}, u^2 = \begin{pmatrix} u_1^+ \\ u_2^{\min} \end{pmatrix}, \quad (19)$$

$$N = 3, u^1 = \begin{pmatrix} u_1^{\max} \\ u_2^{\max} \end{pmatrix}, u^2 = \begin{pmatrix} u_1^{\min} \\ u_2^{\min} \end{pmatrix}, u^3 = \begin{pmatrix} u_1^- \\ u_2^{\max} \end{pmatrix}, \quad (20)$$

$$N = 3, u^1 = \begin{pmatrix} u_1^{\max} \\ u_2^{\max} \end{pmatrix}, u^2 = \begin{pmatrix} u_1^{\min} \\ u_2^{\min} \end{pmatrix}, u^3 = \begin{pmatrix} u_1^+ \\ u_2^{\min} \end{pmatrix}, \quad (21)$$

$$N = 3, u^1 = \begin{pmatrix} u_1^{\max} \\ u_2^{\max} \end{pmatrix}, u^2 = \begin{pmatrix} u_1^+ \\ u_2^{\min} \end{pmatrix}, u^3 = \begin{pmatrix} u_1^- \\ u_2^{\max} \end{pmatrix}, \quad (22)$$

$$N = 3, u^1 = \begin{pmatrix} u_1^{\max} \\ u_2^{\max} \end{pmatrix}, u^2 = \begin{pmatrix} u_1^- \\ u_2^{\max} \end{pmatrix}, u^3 = \begin{pmatrix} u_1^+ \\ u_2^{\min} \end{pmatrix}, \quad (23)$$

$$N = 4, u^1 = \begin{pmatrix} u_1^{\max} \\ u_2^{\max} \end{pmatrix}, u^2 = \begin{pmatrix} u_1^+ \\ u_2^{\min} \end{pmatrix}, u^3 = \begin{pmatrix} u_1^{\min} \\ u_2^{\min} \end{pmatrix}, u^4 = \begin{pmatrix} u_1^- \\ u_2^{\max} \end{pmatrix}, \quad (24)$$

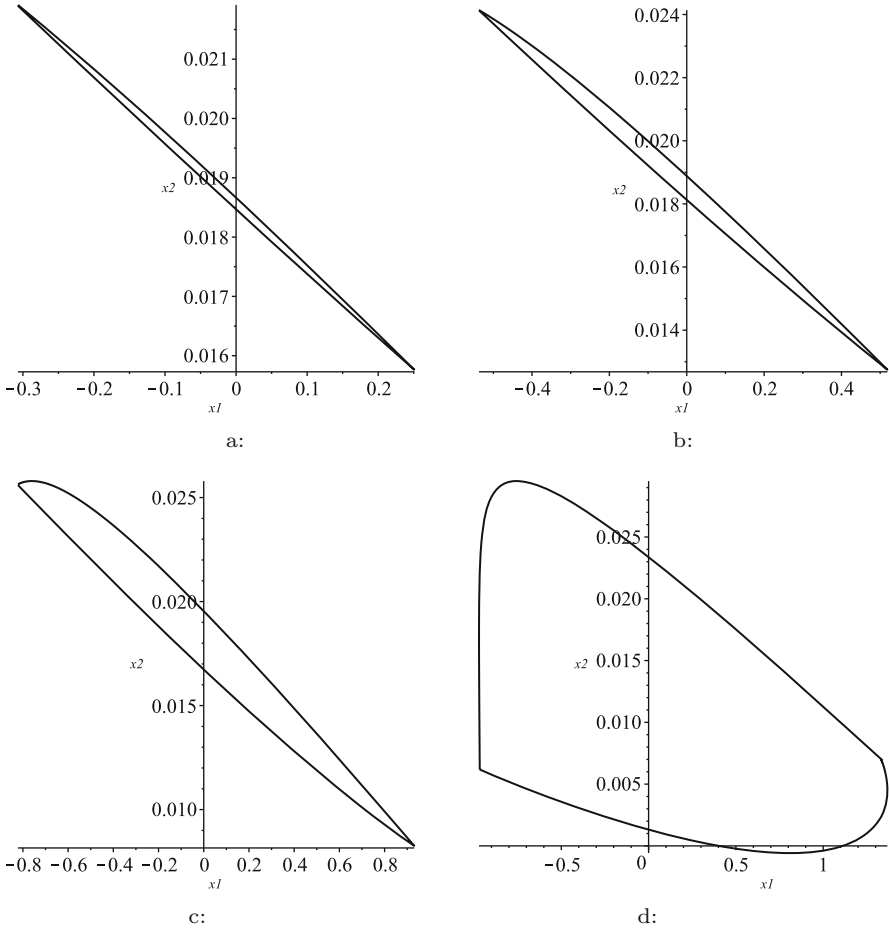


Fig. 1 Periodic trajectories of system (3) with $N = 2$. (a) Strategy (18), $\tau = 0.5$. (b) Strategy (18), $\tau = 1$. (c) Strategy (18), $\tau = 2$. (d) Strategy (19), $\tau = 10$

$$N = 4, \quad u^1 = \begin{pmatrix} u_1^{max} \\ u_2^{max} \end{pmatrix}, \quad u^2 = \begin{pmatrix} u_1^- \\ u_2^{max} \end{pmatrix}, \quad u^3 = \begin{pmatrix} u_1^{min} \\ u_2^{min} \end{pmatrix}, \quad u^4 = \begin{pmatrix} u_1^+ \\ u_2^{min} \end{pmatrix}. \quad (25)$$

Note that we only keep the switching strategies compatible with the constraint $\bar{u}_1 = 1$ in formulas (18)–(25), given the numerical values of controls in (17). These formulas also allow the analysis of strategies obtained by cyclic permutations of (u^1, u^2, u^3, u^4) because of the periodic nature of the considered control problem. In Table 1, the switching parameters $\alpha_j = \frac{t_j - t_{j-1}}{\tau}$ are chosen according to the initial value x^0 of system (3) by solving the algebraic equations (10), (11) in Proposition 3.1.

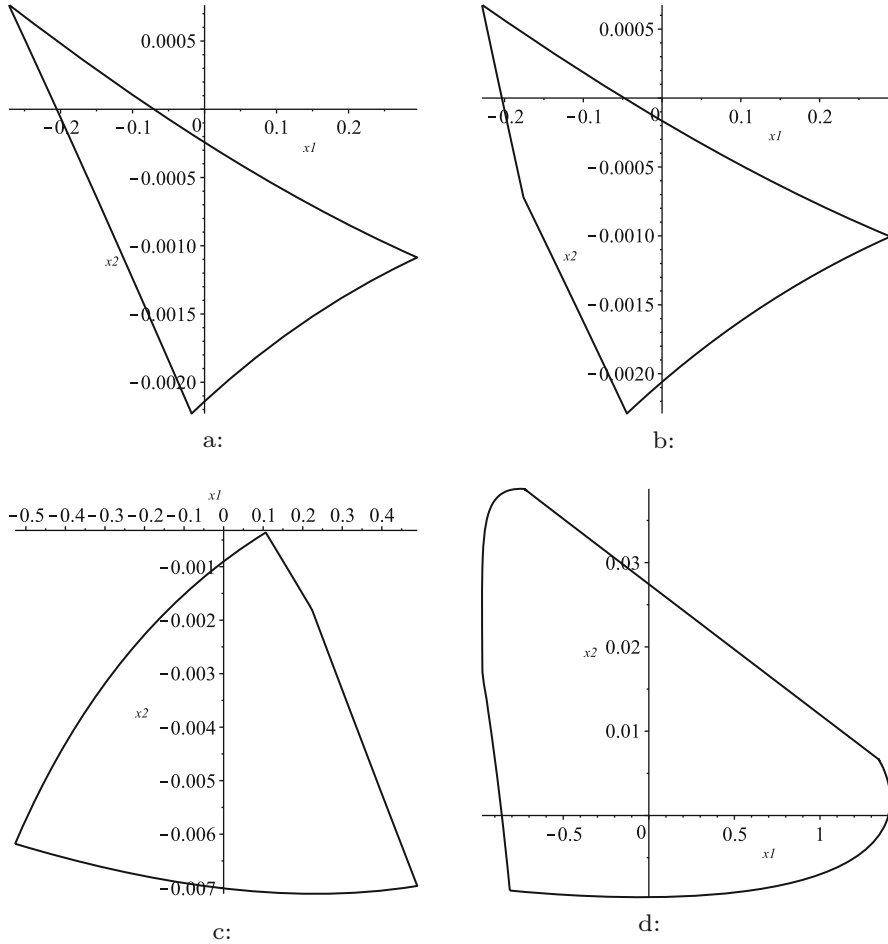


Fig. 2 Periodic trajectories of system (3) with $N = 3$ and $N = 4$. (a) Strategy (23), $\tau = 0.5$. (b) Strategy (25), $\tau = 0.5$. (c) Strategy (24), $\tau = 1$. (d) Strategy (24), $\tau = 10$

5 Conclusions

The presented simulation results confirm that the best performance improvement in the sense of the cost (4) is achieved by bang-bang controls of the form (7) in the case (19) (up to a permutation of u^1 and u^2). In contrast to the previous works [3, 15], we have considered the case of variable flow-rate in this paper. Note that the periodic trajectories in Figs. 1 and 2 are obtained as numerical solutions of system (3), (7), and their orbital stability (or partial stability [12, 13]) remains to be verified in future work to justify the practical relevance of the proposed discontinuous control strategies.

Table 1 Simulation results for system (3) with controls (7), $\tau = 0.5$

Control strategy	Parameters	Initial data	Cost
	$\alpha_j = (t_j - t_{j-1})/\tau$	x^{0T}	J
(18)	$\alpha_1 = 0.2875, \alpha_2 = 0.7125$	(-0.307, 0.0219)	0.6293
(19)	$\alpha_1 = 0.2297, \alpha_2 = 0.7703$	(-0.3259, 0.0325)	0.4883
(20)	$\alpha_1 = 0.2365, \alpha_2 = 0.0833, \alpha_3 = 0.6802$	(-0.2413, 0.017)	0.653
(21)	$\alpha_1 = 0.2703, \alpha_2 = 0.5, \alpha_3 = 0.2297$	(-0.198, 0.00078)	1.055
(22)	$\alpha_1 = 0.2297, \alpha_2 = 0.0833, \alpha_3 = 0.6870$	(-0.3305, 0.0312)	0.502
(22)	$\alpha_1 = 0.2297, \alpha_2 = 0.1667, \alpha_3 = 0.6036$	(-0.3326, 0.0299)	0.5169
(22)	$\alpha_1 = 0.2297, \alpha_2 = 0.25, \alpha_3 = 0.5203$	(-0.332, 0.0287)	0.5326
(22)	$\alpha_1 = 0.2297, \alpha_2 = 0.3333, \alpha_3 = 0.4370$	(-0.3306, 0.0273)	0.5488
(22)	$\alpha_1 = 0.2297, \alpha_2 = 0.4167, \alpha_3 = 0.3536$	(-0.3269, 0.026)	0.5659
(22)	$\alpha_1 = 0.2297, \alpha_2 = 0.5, \alpha_3 = 0.2703$	(-0.323, 0.0249)	0.5828
(23)	$\alpha_1 = 0.2297, \alpha_2 = 0.5, \alpha_3 = 0.2703$	(-0.271, 0.00076)	1.0591
(24)	$\alpha_1 = 0.264, \alpha_2 = 0.083, \alpha_3 = 0.417, \alpha_4 = 0.236$	(-0.329, -0.0056)	1.1259
(24)	$\alpha_1 = 0.237, \alpha_2 = 0.417, \alpha_3 = 0.083, \alpha_4 = 0.263$	(-0.263, 0.0133)	0.7179
(24)	$\alpha_1 = \alpha_2 = \alpha_3 = \alpha_4 = 0.25$	(-0.266, 0.00066)	0.9465
(25)	$\alpha_1 = 0.264, \alpha_2 = 0.083, \alpha_3 = 0.417, \alpha_4 = 0.236$	(-0.2077, 0.0007)	1.057
(25)	$\alpha_1 = 0.237, \alpha_2 = 0.417, \alpha_3 = 0.083, \alpha_4 = 0.263$	(-0.256, 0.0007)	1.0604
(25)	$\alpha_1 = \alpha_2 = \alpha_3 = \alpha_4 = 0.25$	(-0.228, 0.00067)	1.0616

Acknowledgments This work was supported in part by the German Research Foundation (DFG), project ZU 359/2-1.

References

- Bailey, J., Horn, F.: Comparison between two sufficient conditions for improvement of an optimal steady-state process by periodic operation. *J. Optim. Theory Appl.* **7**(5), 378–384 (1971). <https://doi.org/10.1007/BF00934000>
- Bellman, R., Bentsman, J., Meerkov, S.: Vibrational control of systems with Arrhenius dynamics. *J. Math. Anal. Appl.* **91**(1), 152–191 (1983). [https://doi.org/10.1016/0022-247X\(83\)90099-9](https://doi.org/10.1016/0022-247X(83)90099-9)
- Benner, P., Seidel-Morgenstern, A., Zuyev, A.: Periodic switching strategies for an isoperimetric control problem with application to nonlinear chemical reactions. *Appl. Math. Model.* **69**, 287–300 (2019). <https://doi.org/10.1016/j.apm.2018.12.005>
- Ellis, M., Liu, J., Christofides, P.: *Economic Model Predictive Control: Theory, Formulations and Chemical Process Applications*. Springer, Cham (2017). <https://doi.org/10.1007/978-3-319-41108-8>
- Guay, M., Dochain, D., Perrier, M., Hudon, N.: Flatness-based extremum-seeking control over periodic orbits. *IEEE Trans. Automatic Control* **52**, 2005–2012 (2007). <https://doi.org/10.1109/TAC.2007.904255>
- Hoffmann, U., Schädlich, H.-K.: The influence of reaction orders and of changes in the total number of moles on the conversion in a periodically operated CSTR. *Chem. Eng. Sci.* **41**, 2733–2738 (1986). [https://doi.org/10.1016/0009-2509\(86\)80004-5](https://doi.org/10.1016/0009-2509(86)80004-5)

7. Kravaris, C., Dermitzakis, I., Thompson, S.: Higher-order corrections to the pi criterion using center manifold theory. *Eur. J. Control* **18**(1), 5–19 (2012). <https://doi.org/10.3166/ejc.18.5-19>
8. Nikolić, D., Seidel-Morgenstern, A., Petkovska, M.: Nonlinear frequency response analysis of forced periodic operation of non-isothermal cstr using single input modulations. Part I: Modulation of inlet concentration or flow-rate. *Chem. Eng. Sci.* **117**, 71–84 (2014). <https://doi.org/10.1016/j.ces.2014.06.013>
9. Petkovska, M., Seidel-Morgenstern, A.: Evaluation of periodic processes. In: Silveston, P., Hudgins, R. (eds.) *Periodic Operation of Chemical Reactors*, p. 387–413. Butterworth-Heinemann (2013)
10. Shi, H., Lang, Z., Zhu, Y., Yuan, D., Wang, W.: Optimal design of the inlet temperature based periodic operation of non-isothermal CSTR using nonlinear output frequency response functions. *IFAC-PapersOnLine* **51**(18), 620–625 (2018). <https://doi.org/10.1016/j.ifacol.2018.09.355>
11. Sterman, L., Ydstie, B.: Periodic forcing of the cstr: An application of the generalized π -criterion. *AIChE J.* **37**(7), 986–996 (1991). <https://doi.org/10.1002/aic.690370704>
12. Zuyev, A.: On Brockett's condition for smooth stabilization with respect to a part of the variables. In: *Proc. 1999 European Control Conference (ECC)*, pp. 1729–1732 (1999). <https://doi.org/10.23919/ecc.1999.7099564>
13. Zuyev, A.: Stabilization of non-autonomous systems with respect to a part of variables by means of control Lyapunov functions. *J. Automat. Inf. Sci.* **32**(10), 18–25 (2000). <https://doi.org/10.1615/JAutomatInfScien.v32.i10.30>
14. Zuyev, A., Grushkovskaya, V.: Motion planning for control-affine systems satisfying low-order controllability conditions. *Int. J. Control* **90**, 2517–2537 (2017). <https://doi.org/10.1080/00207179.2016.1257157>
15. Zuyev, A., Seidel-Morgenstern, A., Benner, P.: An isoperimetric optimal control problem for a non-isothermal chemical reactor with periodic inputs. *Chem. Eng. Sci.* **161**, 206–214 (2017). <https://doi.org/10.1016/j.ces.2016.12.025>
16. Zuyev, A., Seidel-Morgenstern, A., and Benner, P.: Optimal periodic control of nonlinear chemical reactions with a time-varying flow rate. *PAMM Proc. Appl. Math. Mech.* **19**, e201900146 (2019). <https://doi.org/10.1002/pamm.201900146>

Quaternion Based Free-Floating Space Manipulator Dynamics Modeling Using the Dynamically Equivalent Manipulator Approach



Elżbieta Jarzębowska  and Marcin Kłak

Abstract The paper presents a dynamics modeling method dedicated to free-floating spacecraft, e.g. manipulators, based on a modified Dynamically Equivalent Manipulator (DEM) method. DEM enables dynamics modeling of space manipulators by their suitable substitution by ground fixed manipulator models. This provides attractive modeling and control design tools. It enables carrying tests and experiments for space manipulators in Earth labs multiple times what contributes to mission cost and failure reductions. Originally, DEM is developed in Euler angles. The paper contribution is the modification of DEM to present space manipulators dynamics in quaternion parameterization. Quaternions do not share Euler angles' drawbacks and they are computationally more efficient, but their implementation reveals challenges due to nonlinear relations for space manipulator angular velocities and a constraint equation they add to its dynamics. The motivation for DEM modification is to make dynamic models suitable for description of arbitrary space manipulator maneuvers and missions like debris removal, servicing, space mining and on-orbit docking and assemblies. The development of DEM in quaternion parameterization is illustrated by an example of space manipulator attitude dynamics and reorientation control.

Keywords Dynamically equivalent manipulator · Quaternion-based dynamics · Space robot attitude · Free-floating maneuvers

E. Jarzębowska (✉)
Warsaw University of Technology, Warsaw, Poland
e-mail: elajarz@meil.pw.edu.pl

M. Kłak
Warsaw University of Technology, Warsaw, Poland
GMV Innovating Solutions, Warsaw, Poland

1 Introduction

Servicing dedicated spacecraft equipped with robotic manipulators become more widely used in variety of applications like on-orbit servicing, asteroid mining, active space debris removal and space mining. Examples of such missions can be found in [1] and references there. Operating a robotic manipulator on a spacecraft results in a complex system falling into disciplines of robotics and aerospace engineering. The dynamics between the manipulator and the base-spacecraft are coupled, the system requires nonlinear control systems to meet the capture or manipulation goals and ensure mission completion. The effects of manipulator operations on the orientation and position of the base were studied in many works, e.g [2]. Specifically, effects of fast-moving manipulators mounted on small base-spacecraft were critical to position and orientation disturbances of the base as discussed in [3, 4]. There are thus many reasons, like the already mentioned, increasing needs for spacecraft applications and understanding their complex dynamics and control behaviors, for which engineers developing spacecraft control and sensor systems, communications systems and operation plans have to understand the complex dynamics. However, dynamics modeling and control of space manipulators (SM) are not part of a typical robotics, aerospace and control activities. Literature dedicated to dynamics modeling, control and application and performance analysis of SM is vast, see example an overview in [5]. Generally, two commonly used methods for modeling SM are based on the recursive Newton-Euler and the Lagrangian methods. In [6] presentation of the Newton-Euler dynamics for developing motion equations of SM is provided. When SM is equipped with flexible links, equations of motion can be developed using the direct path method [7]. The Lagrangian method based upon a system kinetic and potential energies uses a set of generalized coordinates describing link positions. However, the most often Euler angles are used for SM reorientation description.

When controlling motion of a SM system, the dynamic coupling between its base and the manipulator may become dominant. The base may not be actuated and then any manipulator motion will cause its rotation and translation. From the point of view of most servicing tasks it is not desirable. A detailed overview of methods of how to take into account dynamic coupling in SM systems in control applications can be found in [8]. Our paper is not focused directly on control, however, the new modeling method, which we present is intended to serve controller designs. The developed methods, worth listing are the Virtual Manipulator (VM) approach, the Dynamically Equivalent Manipulator (DEM) approach, and the Generalized Jacobian Matrix (GJM) approach. The VM approach, which is purely kinematic computational model, replaces a physical SM system with a dynamically consistent VM system, see [9] for details. There, the base of the VM is a spherical joint located at the center of mass of the physical space manipulator system. The orientation of this joint is the orientation of the base of SM in the inertial frame. In absence of external forces, the system center of mass remains fixed and the free-floating SM is replaced by a dynamically consistent fixed-base system. The VM cannot be

represented by a physical manipulator but in the DEM approach it can be done [10]. In the DEM approach the base joint is also a spherical joint at the system center of mass, and geometry of the SM system is the same in the DEM and VM methods. The difference is that DEM takes link masses and inertia into account rescaling them appropriately. DEM can then be used in experimental tests on the ground. One more widely used method is the GJM approach originally proposed in [11] and modifying the dynamic analysis previously introduced in [12]. The GJM method was successfully used in developing control algorithms for the ETSVII demonstrator mission [13].

The paper presents a dynamic modeling method dedicated to free-floating spacecraft, specifically SM systems, based on the modified DEM method. Considering free SM rotation in space, quaternions are the more suitable parameters for attitude description. Not only they do not share Euler angles' drawbacks, but they are also computationally more efficient. However, implementation of quaternions reveals other challenges due to nonlinear relations with respect to SM angular velocities and a constraint equation they add to the SM dynamics. Introduction of quaternion parameterization to the Lagrange based dynamics modeling can be found in some works but the derivation procedure was developed for ground fixed manipulators subjected to position constraints only [14]. Preliminary studies, including the best method selection for derivation the SM dynamics in quaternion parameterization, and simulation tests are presented in [15].

The paper contribution is the application of the modified DEM method to enable SM kinematics and dynamics presentation in quaternions. The modified DEM method delivers a tool for conducting reliable simulation studies and tests for various maneuvers and mission scenarios for SM and it offers an attractive control design tool.

The paper is organized as follows. After Introduction, Sect. 2 presents the SM dynamics modeling using the DEM method in quaternion parameterization. The application of the DEM quaternion based method is illustrated by an example of SM reorientation maneuver in Sect. 3. The paper closes with conclusions and the reference list.

2 Space Manipulator Dynamics Modeling Using the DEM Method Modified for Quaternion Parameterization

2.1 Quaternion Parameterization Properties for Attitude Dynamics Description

Attitude dynamics of SM is of a special interest due to its reorientation maneuvers inherent to most of its operations. Attitude can be described in various ways. The most popular representations are rotation matrices, Euler angles and quaternions.

The quaternion originates in Euler's rotation theorem and it describes attitude as a single rotation about a vector in 3D space.

A unit quaternion consists of four elements constrained by its norm. Thus, a quaternion has 3 degrees of freedom and it is not the minimum representation, as for instance in the case of Euler angles. Quaternions come in different conventions and in this paper the Hamilton convention is adopted, see [16] for details. Specifically, the quaternion is represented as:

$$\mathbf{q} = \begin{bmatrix} q_0 \\ \mathbf{q}_v \end{bmatrix} = [q_0 \quad q_1 \quad q_2 \quad q_3]^T \quad (1)$$

The scalar part of the quaternion is a function of rotation magnitude only. The latter elements describe direction of the rotation axis, preserving the unit norm. Describing the rotation magnitude as θ and the unit vector of the rotation axis as \bar{e} the formula for the quaternion yields:

$$\mathbf{q} = \begin{bmatrix} \cos\left(\frac{\theta}{2}\right) \\ \bar{e} \sin\left(\frac{\theta}{2}\right) \end{bmatrix} \quad (2)$$

Quaternions can be easily related to the more intuitive SM angular velocity vector $\boldsymbol{\omega}$ expressed in its body frame (x, y, z). These relations yield:

$$\dot{\mathbf{q}} = \frac{1}{2} \mathbf{q} \otimes \begin{bmatrix} 0 \\ \boldsymbol{\omega} \end{bmatrix} = \frac{1}{2} \begin{bmatrix} 0 & -\omega_x & -\omega_y & -\omega_z \\ \omega_x & 0 & \omega_z & -\omega_y \\ \omega_y & -\omega_z & 0 & \omega_x \\ \omega_z & \omega_y & -\omega_x & 0 \end{bmatrix} \mathbf{q} \quad (3)$$

Equation (3) applies the quaternion product described with the operator \otimes and zero is appended to the velocity vector to form the so-called pure quaternion making the multiplication possible. However, a matrix multiplication form is also applicable. The quaternion multiplication can be written in following form:

$$\mathbf{q} \otimes \mathbf{p} = \begin{bmatrix} q_0 p_0 - \mathbf{q}_v \mathbf{p}_v \\ q_0 \mathbf{p}_v + p_0 \mathbf{q}_v + \mathbf{p}_v \times \mathbf{q}_v \end{bmatrix} \quad (4)$$

In comparison to other parameterizations, quaternions possess a couple of advantages:

- They are intuitive, unlike Euler angles where the sequential nature is more difficult to comprehend than a single rotation.
- The representation is not susceptible to gimbal lock as for the Euler angles.
- Any rotation can be presented as a continuous trajectory of quaternions.
- Quaternion algebra does not use trigonometric functions, just basic operations on numbers and thus is usually more computationally efficient than Euler angles.

- Any rotation represented by quaternions can be linearly interpolated by efficient methods [16].
- Four elements construct a more compact representation than the 9-element rotation matrix.

There are also some disadvantages of adopting quaternion description, e.g.:

- The attitude is not represented uniquely, in particular \mathbf{q} and $-\mathbf{q}$ describe the same rotation.
- Algebra behind quaternions requires some preprocessing work to start with this representation.

Another useful formula can be applied to guidance and control design and analysis of SM quaternion based dynamics. The rotation of a vector is more complex than using the rotation matrix. The relation between vectors in two different reference frames, say A and B, is as follows:

$$\mathbf{v}^B = \mathbf{q}_A^B \otimes \mathbf{v}^A \otimes \mathbf{q}_A^{B*} \quad (5)$$

In Eq. (5) the subscript “*” stands for quaternion conjugate, which is simultaneously the quaternion inverse, i.e.:

$$\mathbf{q}^* = \begin{bmatrix} q_0 \\ -\mathbf{q}_v \end{bmatrix} = \begin{bmatrix} q_0 & -q_1 & -q_2 & -q_3 \end{bmatrix}^T \quad (6)$$

$$\mathbf{q}\mathbf{q}^* = \mathbf{q}^*\mathbf{q} = \begin{bmatrix} 1 & 0 & 0 & 0 \end{bmatrix}^T \quad (7)$$

$$\mathbf{q}_A^{B*} = \mathbf{q}_B^A \quad (8)$$

Composition of consecutive rotations can be written as:

$$\mathbf{q}_A^C = \mathbf{q}_B^C \otimes \mathbf{q}_A^B \quad (9)$$

For attitude control applications, the convenient description of a control error in quaternions takes the form:

$$\mathbf{q}_{err} = \mathbf{q}_{ref}^* \otimes \mathbf{q}_{est} \quad (10)$$

The vector part of the error quaternion computed in Eq. (10) can be used as a direct input to a controller. The error does not change linearly due to trigonometric relations, however, it behaves monotonically, and in most applications additional operations are not required. Note that the sequence of quaternions in Eq. (10) may differ with respect to the selected convention [16]. Since the quaternions are based on half angles, see Eq. (2), the quaternion error is often multiplied by two to align the values with the angular rates.

2.2 The DEM Method for Space Manipulators Modeling

As described in introduction the concept of mapping a free-floating SM equivalent fixed base manipulator has been introduced by Liang, Xu and Bergerman [10].

To map a free-floating SM into a fixed-base robotic one, the base is replaced by another link. To reproduce unconstrained attitude of the base, the link is fixed with a spherical joint. It can be either passive or actuated if the SM's attitude is controlled. The latter joints are actuated according to the original SM design. In Fig. 1 modeling structures of (a) Space Manipulator (SM) and (b) Dynamically Equivalent Manipulator (DEM) are shown. There (ϕ, θ, ψ) are Euler's angles, θ_i are joint angles, \mathbf{u}_i is a vector of a rotation axis. \mathbf{L}_i is a vector connecting joint J_i to the center of its mass C_i and \mathbf{R}_i connects C_i to joint J_{i+1} . \mathbf{W}_i is a vector from J_i to J_{i+1} . All variables with a superscript "prime" refer to DEM.

Mass, inertia and centers of masses of the DEM structure are scaled by transformations provided in [10]. Specifically:

$$m'_1 = m_1 \quad (11)$$

$$m'_i = \frac{M_i^2 m_i}{\sum_{k=1}^{i-1} m_k \sum_{k=1}^i m_k}, i = 2, \dots, n+1 \quad (12)$$

$$\mathbf{I}_i = \mathbf{I}_i, i = 1, \dots, n+1 \quad (13)$$

$$\mathbf{W}_1 = \mathbf{r}_1 \quad (14)$$

$$\mathbf{W}_i = \mathbf{r}_i + \mathbf{L}_i, i = 2, \dots, n+1 \quad (15)$$

$$\mathbf{l}_{c1} = 0 \quad (16)$$

$$\mathbf{l}_{ci} = \frac{\sum_{k=1}^{i-1} m_k}{M_i} \mathbf{L}_i, i = 2, \dots, n+1 \quad (17)$$

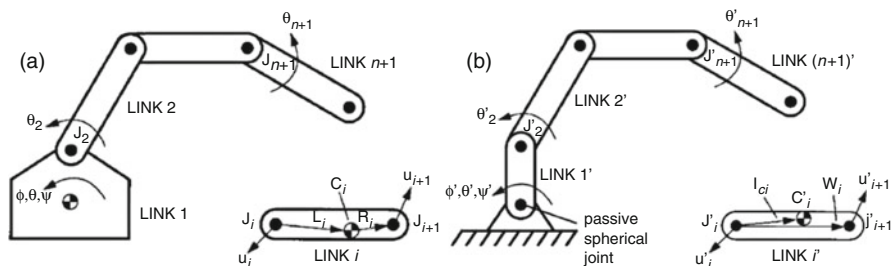


Fig. 1 Model structures of (a) Space Manipulator and (b) Dynamically Equivalent Manipulator [10]

In Eq. (12) $M_t = \sum_i m_i$ is a total mass of SM.

Equations of motion for SM are derived in [10] using Euler's angles for attitude representation. Due to the reasons emphasized in Introduction, this description is not the most suitable for SM system missions. Therefore, authors have introduced the quaternion representation to the DEM approach. Two concepts have been researched. The first attempt was to develop the Lagrange equations using quaternions and then derive SM equations of motion. This approach, however, occurred to be computationally inefficient for increasing number of manipulator links. Due to poor scalability, authors decided to model SM as a set of links, which for modeling purposes are considered separate bodies subjected to position constraints. In this formulation each link has 6 degrees of freedom and its state is described by the following 13-element state vector. In notation that follows, time dependency is skipped for clarity.

$$x_i = \begin{bmatrix} r_i^T & v_i^T & q_i^T & \omega_i^T \end{bmatrix}^T \quad (18)$$

where:

r_i are global, translational coordinates of the center of mass of a body i ,

$v_i = \dot{r}_i$ is global translational velocity,

$q_i = q_{iB}^1$ is a quaternion rotating from the body to the inertial.

ω_i is the angular velocity determined in the i -th body frame.

The Lagrange multipliers method is adopted then and equations governing DEM composed of b rigid bodies are of the following form:

$$\begin{bmatrix} M & B^T \\ B & O \end{bmatrix} \begin{bmatrix} \dot{x} \\ \lambda \end{bmatrix} = \begin{bmatrix} f \\ \mu \end{bmatrix} \quad (19)$$

In Eq. (19) $M = \text{diag} \begin{bmatrix} m_1 I_1 & \dots & m_b I_b \end{bmatrix}$ is a mass matrix, B is a matrix satisfying the equation:

$$\dot{\phi} = Bw + \phi_t = O \quad (20)$$

where:

ϕ represents the position constraint equation,

$$w = \begin{bmatrix} v_i^T & \omega_i^T \end{bmatrix}^T,$$

- λ is a vector of Lagrange multipliers,
- f is a vector of forces and torques,
- μ satisfies the equation:

$$\ddot{\phi} = B\dot{w} - \mu = O \quad (21)$$

Each two consecutive links of SM are connected by two constraint equations that describe a revolute joint. A position constraint of the form:

$$\phi_1 = r_i + s_{1i}^P - r_j - s_{1j}^P = \mathbf{O} \quad (22)$$

is needed to connect extremities of links i and j . s_{1i}^P and s_{1j}^P are vectors from the centers of mass of links i and j to the joint location.

Another equation is required to constrain the rotational motion to a single axis. It has the form:

$$\phi_2 = s_{2i}^P \times s_{2j}^P = \mathbf{O} \quad (23)$$

The vectors s_{2i}^P and s_{2j}^P describe joint rotation vectors of links i and j . Equation (23) preserves that those axes are parallel. Combined Eqs. (22) and (23) force revolute joint connection between links i and j .

Constrained mechanical system models when solved numerically, tend to exhibit unstable solutions and instabilities increase with simulation time. To stabilize the solution the Baumgarte numerical stabilization method is used [17]. It requires that the differentiated constraint Eq. (20) is augmented as follows:

$$\ddot{\phi} + 2\alpha\dot{\phi} + \beta^2\phi = \mathbf{O} \quad (24)$$

In (24) α and β are gains which must be selected. The constraint equation in the form (24) secures the constraints satisfaction during the SM model simulation. With the Baumgarte method introduced, Eqs. (19) turn into:

$$\begin{bmatrix} M & B^T \\ B & O \end{bmatrix} \begin{bmatrix} \dot{x} \\ \lambda \end{bmatrix} = \begin{bmatrix} f \\ \mu - 2\alpha\dot{\phi} - \beta^2\phi \end{bmatrix} \quad (25)$$

The system of Eqs. (25) is the final form of the SM motion equations in the quaternion parameterization.

3 Space Manipulator Reorientation Using the Quaternion Based DEM Method

An experimental simulation study has been performed to verify, evaluate and compare the correctness and possible applicability of the modified, quaternion based DEM method. An example of a planar manipulator model using the original DEM method is presented in [10]. However, it was meaningless to verify a quaternion based dynamics model on a plane. Thus, a spatial model was prepared for the simulation experiment and a 2-link SM model has been selected. Firstly, the

Table 1 Space manipulator properties

Link number	$L_i[m]$	$R_i[m]$	$m_i[kg]$	$I_i[kg\ m^2]$
1	–	0.75	4	$1 * \mathbf{I}_3$
2	0.75	0.75	1	$0.2 * \mathbf{I}_3$
3	0.75	0.75	1	$0.2 * \mathbf{I}_3$

Table 2 DEM properties

Link number	$W_i[m]$	$l_{ci}[m]$	$m_i[kg]$	$I_i[kg\ m^2]$
1	0.5	0	4	$1 * \mathbf{I}_3$
2	1.125	0.5	1.8	$0.2 * \mathbf{I}_3$
3	1.375	0.625	1.2	$0.2 * \mathbf{I}_3$

properties of the SM must be mapped to DEM. These are presented in Tables 1 and 2.

To demonstrate the quaternion based DEM method to SM maneuvers, a control system needs to be applied. A complex maneuver for SM composed of a base and two arms is selected. Attitude of the base is also controlled. The maneuver consists of two simultaneous tasks:

1. Rotation of the SM base by 90 degrees around two axes
2. Folding the manipulator arms

In the initial configuration the SM arms are straighten, i.e. all angles as in Fig. 1 are equal to zero. Velocities and angular rates are also null. The reference state of the SM base is described by base quaternion $q = [0.5\ 0.5\ 0.5\ 0.5]^T$. The quaternion corresponds to the subsequent 90 degrees rotations around z and x axes in base body frame. The quaternion description allows for smooth attitude change. The arm reference positions are 90 and -90 degrees respectively for the first and second joint. The angles are specified with respect to base attitude.

To perform the maneuver, PD controllers are used. The controller selection may not be optimal for highly nonlinear systems, however it is sufficient for this simulation experiment.

Figure 2 shows diagram of the SM model evolving in time. Thin, solid lines show trajectories of links’ centers of masses. Circles mark the joints. On the left hand side of the figure the initial configuration is shown. The final state for the folded arms can be seen on the right hand side of the figure.

In Fig. 3 quaternion control errors are shown. The unit on vertical axis is $2q_{err}$, so that for small angles it provides results in radians. Three error functions in time are for the base and the latter two are for the joint angles. The experiment has demonstrated that the quaternion description is convenient for control application. The quaternion control error does not expose problems with large and complex slews. In contrast, the Euler angles can exhibit problems due to the sequential nature of rotation description.

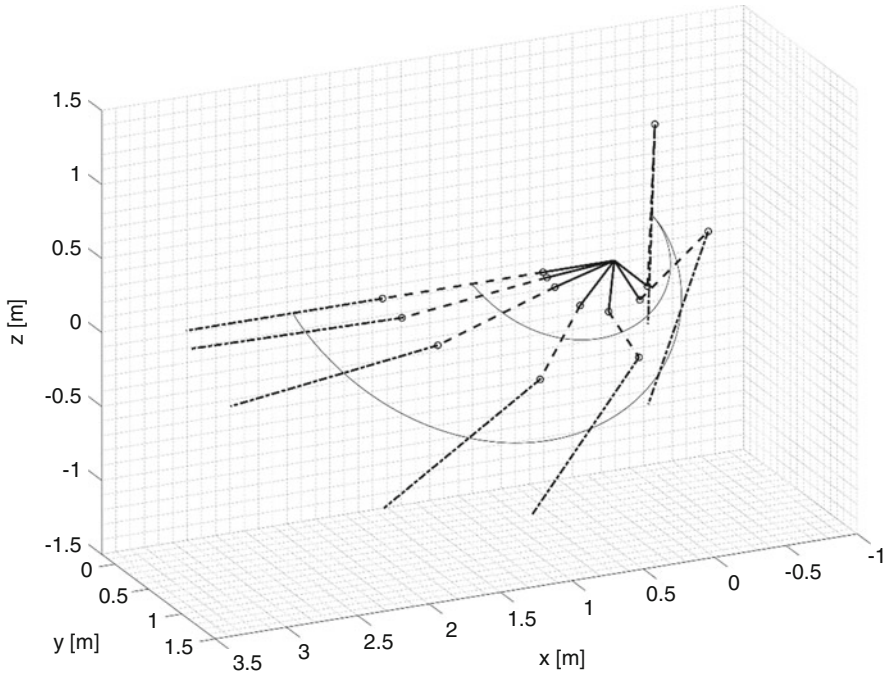


Fig. 2 Diagram of DEM referring to the base and two links of SM

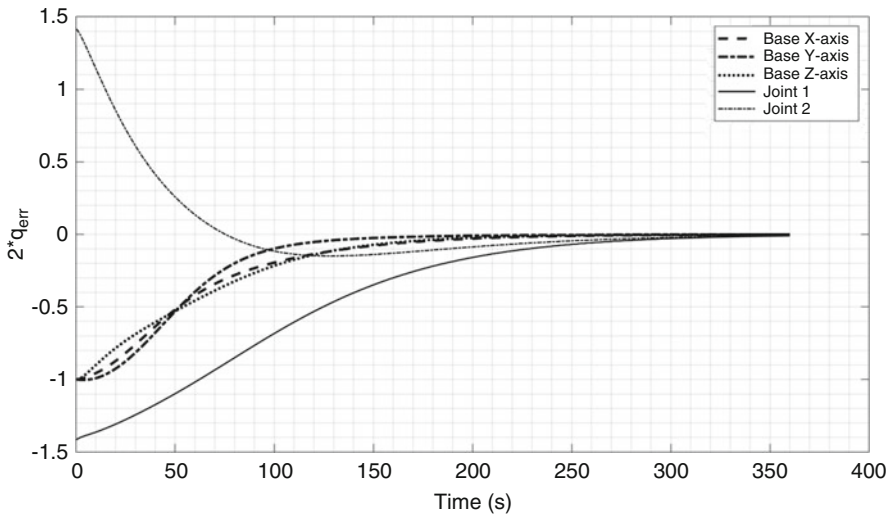


Fig. 3 Control errors of quaternions

4 Conclusions

The paper presented a dynamic modeling method dedicated to free-floating spacecraft, specifically manipulators, based on the modified DEM method. DEM enables dynamics modeling of space manipulators, e.g. free-floating maneuvers, via their suitable substitution by ground fixed manipulator models. As a result, the SM dynamics is equivalent to the ground one. This provides attractive modeling and control design tools since it enables conducting tests and experiments for SM in earth laboratories. The basic motivation for the DEM modification was to make dynamic and kinematic models suitable for description of arbitrary space manipulators maneuvers and their missions like debris removal, servicing, space mining and on-orbit docking and assemblies. It may also support SM attitude controller designs. The paper contribution was the modification of DEM to enable space manipulator kinematics and dynamics representation in quaternions. The modified DEM method delivers a tool for conducting reliable simulation studies and tests for various maneuvers and mission scenarios for SM and it offers a promising control design tool. The application of DEM to a complex reorientation maneuver of the SM model and simulation of its controlled motion using PD controllers was demonstrated in the paper. Future works are planned to include elastic links into SM modeling and development of nonlinear control systems for them.

References

1. Wilde, M., Kwook, C.S., Grompone, A., Romano, M.: Equations of motion of free-floating spacecraft-manipulator systems: an engineer's tutorial. *Front. Robot. AI.* (2018). <https://doi.org/10.3389/frobt.2018.00041>
2. Sargent, D.G.: The impact of remote manipulator structural dynamics on shuttle on-orbit flight control. In: *Proceedings of 17th Fluid Dynamics, Plasma Dynamics, and Lasers Conference.* AIAA, Seattle (1984)
3. Oda, M.: Experiences and lessons learned from the ETS-VII robot satellite. In: *Proceedings of the 2000 IEEE Int. Conf. Robot. Automat.*, pp. 914–919. IEEE, San Francisco (2000)
4. Kennedy, F.G.: Orbital express: accomplishments and lessons learned. In: *Proceedings of the AAS Guidance and Control Conference*, pp. 575–586. Univelt, Breckenridge (2008)
5. Moosavian, S.A.A., Papadopoulos, E.: Free-flying robots in space: an overview of dynamics modeling, planning and control. *Robotica.* **25**, 537–547 (2007). <https://doi.org/10.1017/S0263574707003438>
6. STONEKING, Eric: Newton-Euler dynamic equations of motion for a multi-body spacecraft. In: *Proceedings of AIAA Guidance, Navigation and Control Conference and Exhibit*, p. 6441. Hilton Head, South Carolina (2007)
7. Ho, J.Y.L.: Direct path method for flexible multibody spacecraft dynamics. *J. Spacecr. Rocket.* **14**, 102–110 (1977)
8. Flores-Abad, A., Ma, O., Pham, K., Ulrich, S.: A review of space robotics technologies for on-orbit servicing. *Prog. Aerosp. Sci.* **68**, 1–26 (2014). <https://doi.org/10.1016/j.paerosci.2014.03.002>
9. Vafa, Z., Dubowsky, S.: On the dynamics of manipulators in space using the virtual manipulator approach. In: *Proceedings of IEEE International Conference on Robotics and Automation.* Raleigh, IEEE. (1987)

10. Liang, B., Xu, Y., Bergerman, M.: Mapping a space manipulator to a dynamically equivalent manipulator. *J. Dyn. Syst. Meas. Control.* **120**, 1–7 (1998)
11. Yoshida, K., Umetani, Y.: Control of space manipulators with generalized Jacobian. In: Xu, Y., Kanade, T. (eds.) *Space Robotics: Dynamics and Control*, pp. 165–204. Springer, Boston (1993)
12. Dubowsky, S., Papadopoulos, E.: The kinematics, dynamics, and control of free-flying and free-floating space robotics systems. *IEEE Trans. Robot. Autom.* **9**, 531–543 (1993)
13. Yoshida, K.: Engineering test satellite VII flight experiments for space robot dynamics and control: theories on laboratory test beds ten years ago, now in orbit. *Int. J. Robot. Res.* **22**, 321–335 (2003). <https://doi.org/10.1177/0278364903022005003>
14. Nikravesh, P.E., Kwon, O.K., Wehage, R.A.: Euler parameters in computational kinematics and dynamics. Part 2. *J. Mech. Transm. Autom. Des.* **107**(3), 366–369 (1985)
15. Jarzębowska, E., Kłak M.: Quaternion-Based Spacecraft Dynamic Modeling and Reorientation Control Using the Dynamically Equivalent Manipulator Approach. *Advances in Spacecraft Attitude Control*. IntechOpen. (2020)
16. Sola, J.: Quaternion kinematics for the error-state KF. In: *Laboratoire d'Analyse et d'Architecture des Systemes-Centre national de la recherche scientifique (LAAS-CNRS)*. Tech. Rep, Toulouse (2012)
17. Baumgarte, J.: Stabilization of constraints and integrals of motion in dynamical systems. *Comput. Methods Appl. Mech. Eng.* **1**(1), 1–16 (1972)

Slosh Analyzes of a Full Vehicle-Tank Model with SDRE Control with a Hydraulic Damper



Wagner B. Lenz , Mauricio A. Ribeiro , Angelo M. Tusset ,
Jose M. Balthazar , and Elzbieta Jarzebowska 

Abstract Slosh has been one of the main concerns for transportation vehicles, specifically with partially filled tanks trucks. The liquid movement due to changes of vehicle velocity magnitude and direction as well as external excitation can be the source of instability problems in trucks and passenger vehicles. Due to intrinsic characteristics, the natural frequency of sloshing is similar to the human input frequency, wind excitation and road displacement. Thus, managing and controlling the vehicle-tank system dynamics is required to maintain the desired safety standards. In this paper a numerical study of a quarter car vehicle-tank model is conducted by investigating motion of a linear pendulum model without baffles. A numerical analyses of the roll dynamics, bifurcation diagram and 0–1 test, is performed and a controller based upon the State-Dependent Riccati Equation method controlling the movement on the damper. The results demonstrate that the pendulum model adequately maps the fluid behavior in the tank. Nevertheless, due to low dissipation of slosh motion, around the natural frequency the displacement increases significantly and the vehicle motion can cause loss of control and roll over. In this case, the passive control is unable to significantly reduce the slosh. Nevertheless, it significantly reduce the pendulum motion and avoids the overturn and improving the drivability and safety.

Keywords Slosh motion · Control · Nonlinear dynamics

W. B. Lenz · M. A. Ribeiro · A. M. Tusset
Federal University of Technology, Ponta Grossa, Brazil

J. M. Balthazar (✉)
Sao Paulo State University - Bauru, Federal University of Technology, Sao Paulo, Brazil

E. Jarzebowska
Warsaw University of Technology, Warsaw, Poland
e-mail: elajarz@meil.pw.edu.pl

1 Introduction

Slosh is the interaction between liquid and the surrounding vessel during a forced excitation. This interaction creates waves and changes the behaviour compared with a solid structure. It is a complex phenomena and it commonly study as a damper [1, 2].

It can be used to dissipate energy as Tunnel Liquid Damper, where tanks are tuned for a specific frequency to allow waves to grow and dissipate energy as it impact itself [3–5]. As shown, on [3] have a optimum ration of mass of water and anchoring mass, and have a slow frequency, usually below 2 Hz.

In addition, slosh can be dangerous, creating huge moving waves and shifting the center of mass. Thus, surges on lateral forces leads can lead lateral instability. Especially on rockets and liquid transportation, such as tank trucks and liquid cargo vessels. Slosh has been a concern on tank truck since the invention of the fire truck. To avoid overturn, slow speed were recommend on the first fire truck that did not have baffles [2, 6]. Recently, the main focus is on proving mechanical models with Computational Fluid Dynamics (CFD) [7, 8]. In addition, lateral stability in rockets or trucks. In this case, the slosh can be self induced by the controller. As the fuel is consumed, the liquid height decrease and the system has a different frequency [9, 10].

The current model of road transport allows tank truck to carry different partial loads of different liquids. The lateral slosh on truck is connected to two main factors, partial loads and slow natural frequencies. The partial loads are responsible to allow the liquid movement. The slow natural frequencies are due to the large amount of mass moving and the characteristics of the vessel. The slows frequency match the same response frequency of the drives input. Thus, a self induce slows can occur on a tank truck as the drivers avoid a pothole, or an overtaking maneuver. Thus, the linear slosh is where the liquid surface is intact, at this stage the mechanical simplification as pendulum or mass is equivalent [1]. As excitement, the displacement of water begins to change the continuity of the surface. At this stage, the mechanical representation is no longer valid. However, in nonlinear mode, there is no continuous surface of the liquid, movements begin to have impacts and large waves hit each other, which we must consider as nonlinear equations.

2 Mathematical Model

The mathematical model of truck is considering a single pendulum and the interaction with a quarter-car model. As describe on [1, 11] the main division on the slosh modeling is the orientation of the characteristic length (C_l) in relation to wave propagation. For rockets, the gravity is in the same direction of the (C_l) , know as cylindrical slosh. For tank trucks, the (C_l) is a perpendicular to gravity, in this cases most shapes of tanks can be approximate as a rectangular slosh

[11]. Both models can be converted to mass-spring-damper models or pendulum-spring-damper models. Seamlessly, they are interchangeable. Nevertheless, it is recommend to use pendulum for rotational movement as in rocket, and mass to linear displacement for break and acceleration models [12]. In this paper, the pendulum half a car interaction was modeled to investigate the effects of a rough terrain on the roll movement.

2.1 Truck Dynamics with Pendulum

The truck dynamics with a pendulum is a complex coupling between the vertical acceleration \ddot{x} , roll acceleration $\ddot{\alpha}_2$, rotation acceleration $\ddot{\beta}_2$ [1]. The coupling is shown on Fig. 1.

where: s is the distance of center of mass (c_m), z_l is the excitation on the left tire, z_r is the excitation on the right tire, β_2 is the angle of pendulum, α_2 is the roll angle of the chassis, h_a is the height of the pendulum until it attachment. h_1 the distance between attachment and free surface, l_{wp} is the length of the pendulum, m_{wp} is the mass of free flowing liquid, m_0 is the stationary fluid, I_0 is the moment of inertia of stationary fluid. Using the same methodology as [1].

$$\begin{cases} (m_0 + m_{wp} + m_T)\ddot{x}_T + m_{wp}l_{wp} \sin(\beta_2)\ddot{\beta}_2 + m_{wp}l_{wp} \cos(\beta_2)\dot{\beta}_2^2 + \sum F_{S_{usp}} = 0 \\ (I_T + m_{wp}h_a^2 + I_T)\ddot{\alpha}_2 + m_{wp}l_{wp}h_a \cos(\beta_2)\ddot{\beta}_2 - m_{wp}l_{wp}h_a \sin(\beta_2)\dot{\beta}_2^2 + \sum M_{S_{usp}} = 0 \\ m_{wp}l_{wp} \sin(\beta_2)\ddot{x}_T + m_{wp}l_{wp}h_a \cos(\beta_2)\ddot{\alpha}_2 + m_{wp}(l_{wp}^2 \sin(\beta_2)^2 + l_{wp}h_a \cos(\beta_2)^2)\ddot{\beta}_2 \dots \\ + 2m_{wp}l_{wp} \cos(\beta_2)\dot{x}_T\dot{\beta}_2 - 2m_{wp}l_{wp}h_a \sin(\beta_2)\dot{\alpha}_2\dot{\beta}_2 + l_{wp} \sum F_{S_{usp}} + l_{wp}g \sin \beta_2 = 0 \end{cases} \quad (1)$$

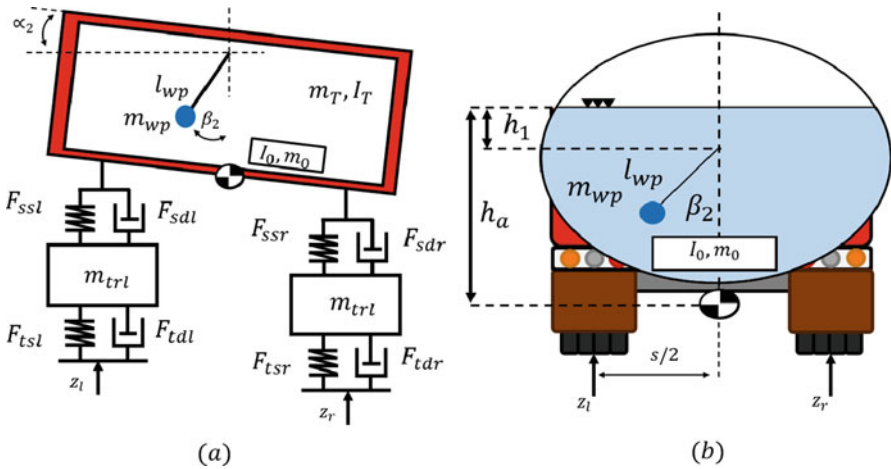


Fig. 1 Half-car model coupled with slosh pendulum model, (a) the body diagram, (b) the schematic representation for the tank truck

where: $F_{Susp} = -(F_{ssl} + F_{sdl} + F_{ssr} + F_{sdr})$, and $M_{Susp} = \frac{\delta}{2}(-F_{ssl} - F_{sdl} + F_{ssr} + F_{sdr})$.

2.2 Pendulum Slosh

The unsprung masses can be calculate by the 2nd Newton Law. The Pendulum slosh mechanical model divide the bulk mass (m_l) of the liquid in two masses, a fraction of the mass is static to roll (m_0) and a part swings with the roll motion (m_{wp}). Thus, the mass of the liquid is divided in a static and Moment of Inertia (I_0), and another part has a mass a known length (l_{wp}), with a specific point of attachment (h_a). The pendulum analogy can be further improve by creating n more pendulums. Nevertheless, it is not recommend more than 1 pendulum [11]. The main parameters are describe on the equation [1, 11].

2.3 Tire Dynamics

Tire dynamics is a complex subject,that involves the angles of suspension, tire manufacturing, air pressure. The mechanical modeling is It is a important issues when aquaplane is involve. Tire can be represented as a simple tire spring, a non-linear spring to avoid [13, 14]. Nevertheless, when including the suspension angles a common representation is the magic formula that incorporates the relation between angles of the suspension, material saturation [15], it is shown as Eq. (2):

$$F_{tm}(x_r) = P_1 \sin(P_2 \operatorname{atan}(P_3 x_r - P_4 (P_3 x_r - \operatorname{atan}(P_3 x_r))))); \quad (2)$$

where: x_r is the relative displacement, and parameter P_1, P_2, P_3, P_4 related to the tire and suspension orientation presented on [15].

2.4 Damper Dynamics

The damper is the element that dissipate the energy of the vertical motion of the car. The common models are shown in Fig. 2.

As shown in Fig. 2a dynamics is commonly express a linear function. Nevertheless, Fig. 2b, the non linearity associate with the shaft and hydrodynamic were mitigate by center relief channels. In (c), the relief channels are at the end travel. Figure 2d shows an damper model where the pressure on the lower chamber can be used to create a restriction patch and further dissipate energy. This patch can be fully controlled by activating a valve that transfer fluid and it assume massless. Thus operating between all the position between close and open. In this paper, the

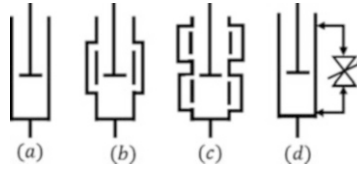


Fig. 2 Models of damper (a) Without relief channels (b) Center relief channels (c) Extremity Center relief channels (d) External valve relief pressure Adapted from: [16, 17]

parameter c_4 will be used as variable parameter on the Eq. (3) that describes the dampers dynamics [18–20].

$$F_d(\dot{x}) = c_1\dot{x} - c_2\dot{x}\text{sign}|\dot{x}| + c_3c_4\sqrt{|\dot{x}|} \quad (3)$$

where: $|\dot{x}|$ is the relative speed on the damper.

2.5 Spring Dynamics

The spring is the element that maintains the contact and of the tire on the soil, by applying a constant pressure. Usually is model as linear e proportional to the relative displacement. However, the more realist modeling is a nonlinear modeling, with an additional cubic factor, to take in account the vary pitch, that is a desire increase on stiffness. Thus, the spring force is

$$F_s(x_r) = k_1x_r + k_2x_r^3 \quad (4)$$

where, k_1 is the linear factor, k_2 is the nonlinear factor.

2.6 Road Profile and External Forces

The external forces such as lateral forces or slope contribute to slosh movement. Usually, lateral forces are the main concerns because it can alternate sides and have a consider magnitude with a similar frequency as slosh natural frequency [1]. The slope or road inclination is a contribution because moves the angle of the liquid slowly in on direction. Thus, increasing the speed of the traveling fluid. The road profile could have a significant impact on the car dynamics. It can be model as white noise, sine or sign wave with specific amplitude.

$$\begin{cases} z_l(t) = a_{mp}\text{sign}[\sin(2\pi ft)] \\ z_r(t) = a_{mp}\text{sign}[\sin(2\pi ft + \beta)] \end{cases} \quad (5)$$

2.7 Simplified Controllers

Before the advent of Multiple Input Multiple Output, many strategies of control were elaborated based on states of the car. The three more used are On/off, sky hook and ground hook [13, 21]. The On/off control has only two states, on and off. Thus, to optimize the energy consumption it is only activate when the force is maximum, and on stand-by during other period, shown on equation

$$c_{\text{On}} = \begin{cases} \text{if } (V_1 > 0 \wedge V_1 > V_2) \vee (V_1 < 0 \wedge V_1 < V_2) \rightarrow c_{\text{max}} \\ c_{\text{min}} \end{cases} \quad (6)$$

where V_1 is the upper mass, and V_2 is the lower mass.

The sky-off methodology aims to reduce the vibration on the chassis. Thus, virtually connecting the sprung mass to a damper to a ground reference. Thus, the logic of actuation is shown on Eq. (8)

$$F_{\text{sky}} = c_{\text{sky}} V_1 = \begin{cases} \text{if } V_1(V_1 - V_2) > 0 \rightarrow c_{\text{max}} \\ c_{\text{min}} \end{cases} \quad (7)$$

On the other hand, the ground hook virtually connects the unsprung masses to a ground reference. Thus, reducing the displacement of the wheels.

$$F_{\text{gr}} = c_{\text{gr}} V_2 = \begin{cases} \text{if } -V_2(V_1 - V_2) > 0 \rightarrow c_{\text{max}} \\ c_{\text{min}} \end{cases} \quad (8)$$

2.8 State-Dependent Riccati Equation Control

The State-Dependent Riccati Equation (SDRE) control consists in a variable adaptive control that relies on an adaptive state matrix ($\mathbf{A}(\mathbf{x})$). This means that $\mathbf{A}(\mathbf{x})$ is a function of states and varies along with the simulation, where the \mathbf{B} , \mathbf{Q} , \mathbf{R} usually remain constant over time. The employment of SDRE control has been investigate for [13], using the methodology allows to a refine control. Nevertheless, some step must be taken on account to assure contrability and a define control matrix (\mathbf{K}), thus the same methodology used on[13] was deployed calculate the amount of force required. After that the coefficient c_4 of the damper was calculated by bisection method. Using the following equation.

$$c_4 = \begin{cases} c_3 \sqrt{|\dot{x}|} \times F_{\text{control}} \leq 0 \rightarrow c_4 = 0 \\ 0 < c_3 \sqrt{|\dot{x}|} \times F_{\text{control}} < 1 \rightarrow c_4 = \frac{F_{\text{control}}}{c_3 \sqrt{|\dot{x}|}} \\ c_3 \sqrt{|\dot{x}|} \times F_{\text{control}} \leq 1 \rightarrow c_4 = 1 \end{cases} \quad (9)$$

3 Methodology

The parameters utilized on tire magic dynamic are $p1 = 190 \times 10^2$, $p2 = 1.9$, $p3 = 13$, $p4 = 0.97$. The parameters utilized on the damper dynamics are $k_1 = 238(10^2)$, $k_3 = 238(10^4)$, $m_T = 4000$, $m_{wp} = 2128.9$, $h_1 = 0.3$, $I_0 = 250$, $l_{wp} = 0.75$, $c_p1 = 0.0557$, $\frac{s}{2} = 3$, $m_0 = 2089.5$, $c_1 = 700$, $c_2 = 400$, $c_3 = 200$, $c_4 = 0.1$, where c_4 is the control parameter that varies according to opening of the valve. In this paper the road profiles has the following parameters, $a_{mp} = 0.05$ m, $\alpha_l = 0^\circ$, $\alpha_r = 180^\circ$, the frequency is variable. The numerical integration was made with a fixed step of 10^{-3} .

4 Results and Conclusions

The dynamic analyses was made by the bifurcation diagram and Scalograms for the X_T .

As Shown on Fig. 3 there is burst of displacement that have multiple periods. Thus, the square waves enter in resonance with the system and can damage, roll the vehicle. The roll movement α_2 shows similar behavior with multiple periods and large oscillations.

As shown on Fig. 4, the roll moment of the car is compressed lower than 10° . Nevertheless, at regions close to the natural frequency of the fluid the roll movement is exacerbate by the road profile. Despite the linear dynamics been used the big displacements indicates the natural frequencies, similar analyses should be compared and contrast to further investigate the dynamics using the nonlinear slosh models. Analyzing the displacement of the pendulum on Fig. 5.

The pendulum dynamics it was extremely coupled with the vertical motion, and induced the roll over presented on Fig. 3. Due to square wave to simulate the road

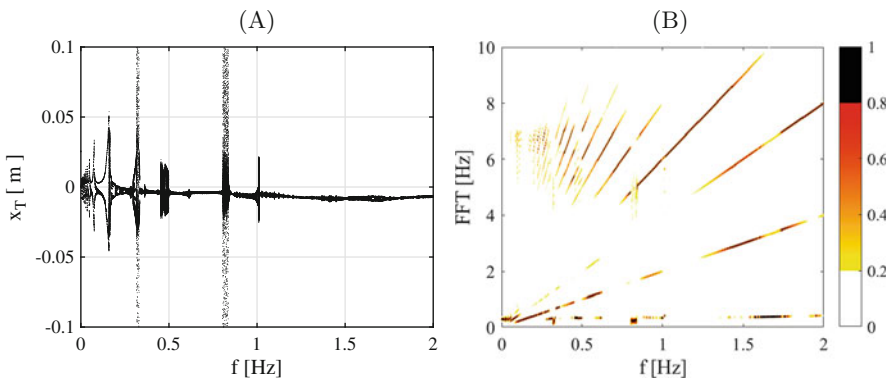


Fig. 3 Dynamic state of X_T (a) Bifurcation (b) Scalograms

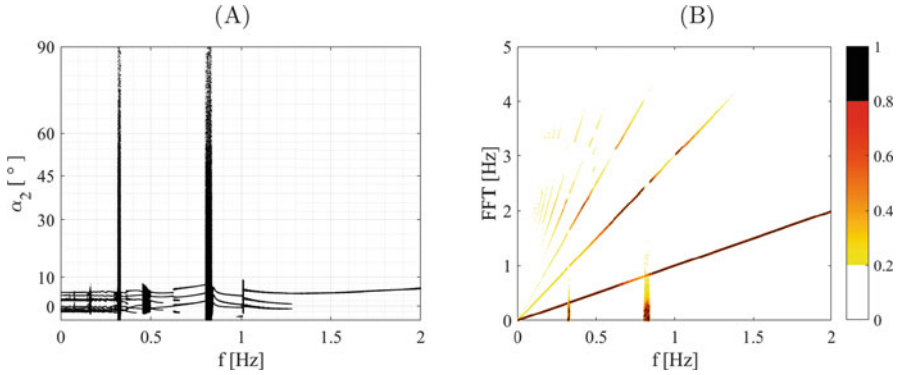


Fig. 4 Dynamic state of α_2 (a) Bifurcation (b) Scalograms

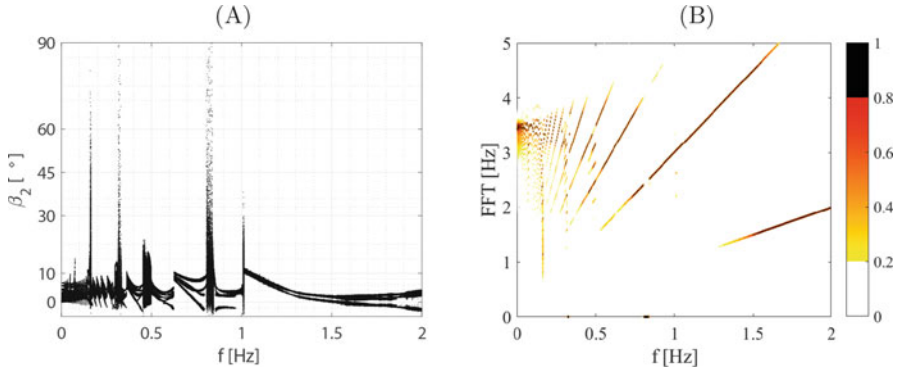


Fig. 5 Dynamic state of β_2 (a) Bifurcation (b) Scalograms

at lower frequencies the pendulum swing freely at the natural frequency, after the impact. Thus, analyzing the temporal displacement for $f = 0.8124$ [Hz].

As shown in Fig. 6, before 200s of simulation the rollover event occur. The lateral movement start to violent swing and the pendulum start to rotate. Nevertheless, all the four control technique stabilized the motion. The first two present are the On/Off and the Sky in Fig. 7.

Similarly, the SDRE and Ground are presented on Fig. 8.

To further elucidate the improvement the Table 1 summarizes the Rms values and Max values for $t = 500$ s.

Because the system is constantly excited, the effectiveness of the controllers should not just be reflected on the displacement of the selected variables. The amount of force constantly been demand and applied by the variable c_4 , must be taken in account as well. This values are summarized on Table 2.

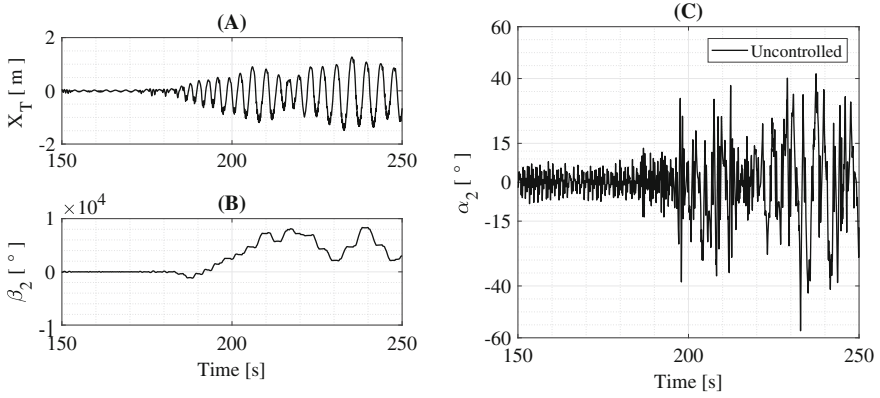


Fig. 6 Temporal analyses for $f = 0.8124$ [Hz] without control (a) X_T (b) β_2 (c) α_2

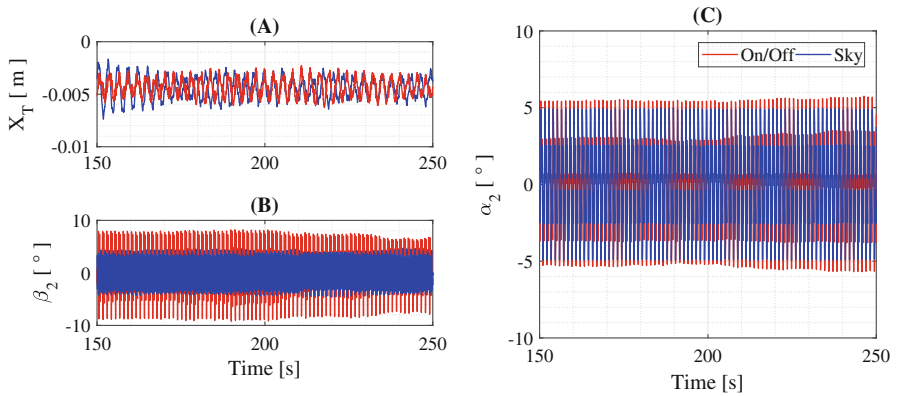


Fig. 7 Temporal analyses for different controllers $f = 0.8124$ [Hz] (a) X_T (b) β_2 (c) α_2

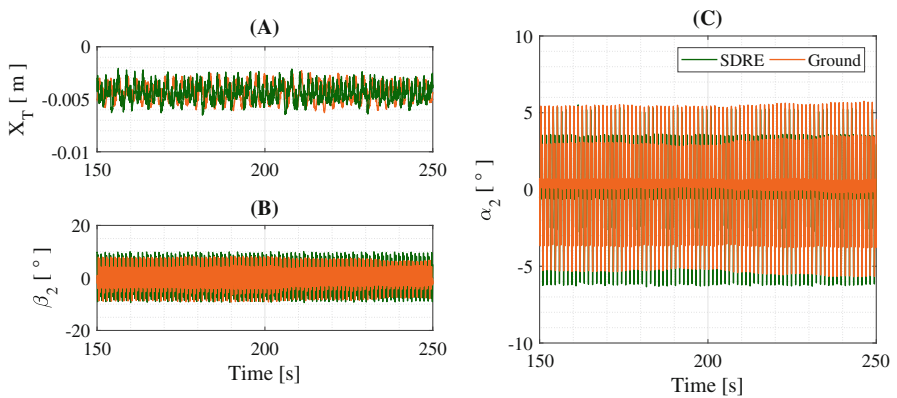


Fig. 8 Temporal analyses for different controllers $f = 0.8124$ [Hz] (a) X_T (b) β_2 (c) α_2

Table 1 Summary of selected parameters

Var.	Rms					Max				
	Sky	On	Ground	Sdre	Unco.	Sky	On	Ground	Sdre	Unco.
\dot{X}_T	0.004	0.004	0.004	0.004	0.591	0.007	0.006	0.006	0.006	1.621
\dot{X}_T	0.004	0.009	0.009	0.012	1.424	0.013	0.026	0.026	0.032	6.766
α_2	2.58	2.82	2.82	2.84	14.17	5.01	5.83	5.83	6.35	65.41
$\dot{\alpha}_2$	29.39	36.58	36.58	36.90	90.99	74.83	98.43	98.43	95.88	496.59
β_2	2.37	4.24	4.24	5.21	4886	4.82	9.31	9.31	10.14	15162
$\dot{\beta}_2$	44.83	76.77	76.77	95.60	848	91.26	173.81	173.81	189.29	5227

Table 2 Summary of applied forces by controllers

	Sky	On	Ground	SDRE
rmsleft	430.30	532.91	532.91	339.23
maxlet	1703.75	1701.55	1701.55	1723.03
rmsright	431.65	528.81	528.81	419.87
maxrighth	1710.14	1674.33	1674.33	1689.97

5 Conclusions

The linear dynamics of the pendulum slosh model is a good representation and is a very good tool to determinate and show the regions of instability. Nevertheless, after 200s of excitation the pendulum motion is no longer available to be passive control. All the controller proposed were able to reduce significantly the vertical and roll motion. Nevertheless, due to internal logic, some controller required more Rms force because there is periods without actuation. Whereas the SDRE control can uses this moments as and advantage and further reduce the energy levels. Thus, having a lower RMS force.

Acknowledgments The authors acknowledge the support by CNPq, CAPES, FAPESP and FA, all Brazilian research agencies.

References

1. Ibrahim, R.A., Pilipchuk V.N., Ikeda, T.: Recent advances in liquid sloshing dynamics. *Appl. Mech. Rev.* **54**(2) 133 (2001)
2. Ranganathan, R., Rakheja, S., Sankar, S.: Influence of liquid load shift on the dynamic response of articulated tank vehicles. *Ve. Syst. Dyn.* **19**(4), 177–200 (1990)
3. JYu, J.K., Wakahara, T., Reed, D.A.: A non-linear numerical model of the tuned liquid damper. *Earthq. Eng. Struct. Dyn.* **28**(6), 671–686 (1999)
4. Tusset, A.M., Rocha, R.T., Janzen, F.C., Balthazar, J.M., Lenz, W.B.: On a liquid tuned damper and nonlinear mass tuned damper passive application in a building to reduce high vibrations. In: *Proceedings of the 24th ABCM International Congress of Mechanical Engineering.* ABCM (2017)

5. Das, S., Choudhury, S.: Seismic response control by tuned liquid dampers for low-rise RC frame buildings. *Aust. J. Struct. Eng.* **18**(2), 135–145 (2017)
6. Turner, M.R., Bridges, T.J., Ardakani, H.A.: The pendulum-slosh problem: Simulation using a time-dependent conformal mapping. *J. Fluids Struct.* **59**, 202–223 (2015)
7. Green, S.T.: A comparison of methods for estimating Slosh model parameters from CFD simulations. In: 2018 Joint Propulsion Conference, 4758 (2018)
8. Benson, D.J., Ng, W.: Validation of Slosh Modeling Approach Using STAR-CCM+ (2018)
9. Coulter, N.: Design of an Attitude Control System for a Spacecraft with Propellant Slosh Dynamics (2018)
10. Wie, B.: Space vehicle dynamics and control. *Am. Inst. Aeronaut. Astronaut.* (2008)
11. Dodge, F.T.: The New Dynamic Behavior of Liquids in Moving Containers 111–116. Southwest Research Inst., San Antonio, TX (2000)
12. Xu, L., Dai, L., Dong, M., Setiawan, B.: Influence of liquid slosh on ride quality of liquid cargo tank vehicles. *Proc. Inst. Mech. Eng. D J. Automob. Eng.* **218**(7), 675–684 (2004)
13. Lenz, W.B., Tusset, A.M., Rocha, R.T., Janzen, F.C., Kossoski, A., Ribeiro, M.A., Balthazar, J.M.: A note on anti-roll bar effectiveness full-car dynamics with magnetorheological damper control. *Int. Rev. Mech. Eng.* 47–57 (2019)
14. Jazar, R.N.: *Vehicle Dynamics: Theory and Application*. Springer (2017)
15. Pacejka, H.B.: *Tire and Vehicle Dynamics*. Tire and Vehicle Dynamics, 3rd edn. Butterworth-Heinemann, Oxford (2012)
16. Zhang, Y., Zhang, X., Zhan, M., Guo, K., Zhao, F., Liu, Z.: Study on a novel hydraulic pumping regenerative suspension for vehicles. *J. Franklin Inst.* **352**(2), 485–499 (2015)
17. Nie, S., Zhuang, Y., Wang, Y., Guo, K.: Velocity displacement-dependent damper: A novel passive shock absorber inspired by the semi-active control. *Mec. Syst. Signal Process.* **99**, 730–746 (2018)
18. Matheus Alves, M.A.: *Matheus: Análise comparativa de estratégias para suspensão semiativa em um modelo de 1/4 de veículo*, UNB, (2018)
19. Milliken, W.F., Milliken, D.L.: *Race Car Vehicle Dynamics* (Vol. 400, p. 16). Society of Automotive Engineers, Warrendale, PA (1995)
20. Gaspar, P., Szaszi, I., Bokor, J.: Active suspension design using LPV control. *IFAC Proc.* **37**(22), 565–570 (2004)
21. Tusset, A.M.: Controle ótimo aplicado em modelo de suspensão veicular não-linear controlada através de amortecedor magneto-reológico. UFRGS (2008)

A Comparison of the Common Types of Nonlinear Energy Sinks



Adnan S. Saeed  and Mohammad A. AL-Shudeifat

Abstract Real life dynamical structures are subjected to different sources of excitations such as earthquakes, blasts, collisions, fluid-structure interaction, impacts, etc. that may induce high vibration levels and increase the risk of system failure. Hence, linear vibrations absorbers have been employed to protect such dynamical structures from collapse. However, these are only effective at a specified primary structure natural frequencies and their performance significantly deteriorates as the frequency changes. The newly proposed vibration absorbers, usually referred to as Nonlinear Energy Sinks (NESs) incorporate the essential nonlinear property that enables efficient and rapid vibration mitigation for wide frequency-energy domain. Consequently, many types of NESs have been proposed in literature and those are classified by the method of nonlinearly attaching the NES to the associated floor of the primary structure into stiffness-based, rotary-based and impact-based NESs. This paper presents a numerical investigation in which the most common NES types: cubic-stiffness NES, rotary NES, double-sided and single-sided vibro-impact (SSVI) NESs, are optimized, discussed and compared for energy transfer and dissipation for an impulsive excitation into a large-scale nine-story dynamical structure. The system description and governing equations of each coupled system are given first followed by a numerical optimization to maximize energy transfer and dissipation. It is found that an optimized SSVI NES gives the best performance to achieve highly efficient targeted energy transfer (TET).

Keywords Targeted Energy Transfer · Nonlinear Energy Sink · Shock Mitigation

A. S. Saeed (✉) · M. A. AL-Shudeifat
Aerospace Engineering, Khalifa University of Science and Technology, Abu Dhabi, UAE

© Springer Nature Switzerland AG 2021
J. Awrejcewicz (ed.), *Perspectives in Dynamical Systems III: Control and Stability*,
Springer Proceedings in Mathematics & Statistics 364,
https://doi.org/10.1007/978-3-030-77314-4_8

1 Introduction

To account for shock and seismic hazards, it is essential to avoid the inelastic response by integrating structural control systems that rapidly suppress the high vibration amplitudes and therefore prevent human and economic losses. To this end, these structural control systems, which must not significantly increase the weight, size or complexity of the system, can be classified into: active, semi-active, passive and hybrid systems. However, despite the promising shock and seismic mitigation performance of hybrid, active and semi-active control systems, factors such as the complexity of the design, increased capital and maintenance costs and requirement of constant power source limited the full-scale implementation in real-world structures. As a result, passive control systems are widely implemented due to their application simplicity and comprehensive theoretical development.

Passive linear vibration absorbers, such as tuned mass damper, require careful tuning of the parameters to a specific natural frequency to enable efficient energy transfer and vibration absorption. The maximum mitigation capacity is obtained when the natural frequency of the linear vibration absorber is equivalent to the frequency of a particular mode of the primary structure. Because of this equivalence, the absorber engages in resonance capture with that mode which increases the amplitude of oscillations of the absorber leading to localization and dissipation of energy. However, the performance of passive linear vibration absorbers deteriorate significantly if the natural frequency slightly fluctuates which might occur due to aging, unexpected practice, extreme loading conditions, or poor estimation. Consequently, this very narrow dissipation bandwidth ignited interest in finding new methods to passively dissipate the induced energy into the primary structures to protect them from damage. Accordingly, the passive Targeted Energy Transfer (TET) or nonlinear energy pumping concept was developed for nonlinear energy transfer and dissipation [1]. It refers to the process of transferring energy in a nearly one-way irreversible manner from a primary structure to a nonlinear attachment known as Nonlinear Energy Sink (NES). As per the definition, the NES possesses essentially nonlinear coupling element which enables it to interact with a primary structure in relatively broad range of frequency-energy domain by engagement in single or cascade of resonance captures with the nonlinear normal modes (NNMs) branches and backbones of the whole system in the frequency-energy plot [1]. As a result, unlike linear vibration absorbers, the nonlinear nature of the NES indicates that it does not have a preferential frequency and can tune itself to nonlinear frequencies of the whole system in the vicinity of the primary system frequencies. Therefore, the NESs are capable of passive energy transfer by dissipating vibration energy induced into a primary structure for a broadband frequency-energy domain. Accordingly, recent studies showed that properly designed essentially nonlinear vibration absorbers known as NESs are capable of providing efficient TET.

Based on different kinds of nonlinear coupling elements, the three most common types of NESs can be named as stiffness-based NESs [1–5], rotary-based NESs [5–9], and impact-based NESs [10–18]. Stiffness-based NESs employ a nonlinear

coupling spring of cubic stiffness which is usually realized by transversely coupled linear stiffness springs. Being the first studied NES in the literature, this set has three subtypes, the most common of which is Type I which employs a nonlinear restoring stiffness force accompanied with linear viscous damping element. A freely rotating rigid arm forms the nonlinear inertial coupling element of the rotary NESs. The NES mass freely rotates about a vertical axis perpendicular to the direction of motion of the primary structure. Similar to TMDs, the impact-based NESs are composed of linear stiffness and viscous damping coupling elements. However, the nonlinear element is introduced by vibro-impacts (VIs) between the NES mass and the associated floor of the primary structure via rigid barriers fixed to the floor of primary structure. Impact-based NESs are categorized into two subtypes known as Double-Sided Vibro-Impact (DSVI) and Single-Sided Vibro-Impact (SSVI). In the DSVI NES, two rigid barriers are fixed symmetrically with respect to the initial position of the NES. This will engage the NES mass in consecutive impacts with the associated floor of the primary linear structure. In the SSVI NES, one rigid barrier is removed and the NES impacts with the associated floor on one side only (asymmetrically). The goal of this paper is to demonstrate a comparison of the aforementioned common types of NESs to engage in efficient TET when employed to a large-scale nine-story primary structure under impulsive loading. In addition, their robustness to changes in the magnitude of the impulse is compared.

2 System Description and Governing Equations

The nine-story structure analyzed in [8, 15–16, 18] is considered as the primary structure in this investigation as shown in Fig. 1(a) where the displacement of the j th mass is denoted by x_j . The 9-by-9 mass, stiffness and damping matrices of the structure denoted by \mathbf{M} , \mathbf{K} and \mathbf{C} respectively can be found in [8, 15–16, 18]. Type I, rotary, DSVI and SSVI NESs are attached to the top floor ($j = 1$) of the structure separately as shown in Fig. 1 to investigate the capability of each absorber to significantly reduce the shock response of the structure by dissipating initial induced energy through its local damping and scattering energy from low- to high- frequency structural modes. In this study, a constant NES mass of 500kg is considered which corresponds to approximately 5% of the total mass of the structure. All NESs are designed to be nonparasitic (i.e. they do not add mass to the structure, their mass is taken from the floor to which it is attached). The governing equation of motion of the primary system is given as

$$\mathbf{M}\ddot{\mathbf{x}} + \mathbf{C}\dot{\mathbf{x}} + \mathbf{k}\mathbf{x} = \mathbf{f}_{\text{nes}} \quad (1)$$

where $\mathbf{x} = [x_1 \ x_2 \ \dots \ x_j \ \dots \ x_9]^T$ and \mathbf{f}_{nes} is the 9-by-1 force vector acting on the primary structure due to the addition of the NES. This force varies for different types of NESs and is discussed next.

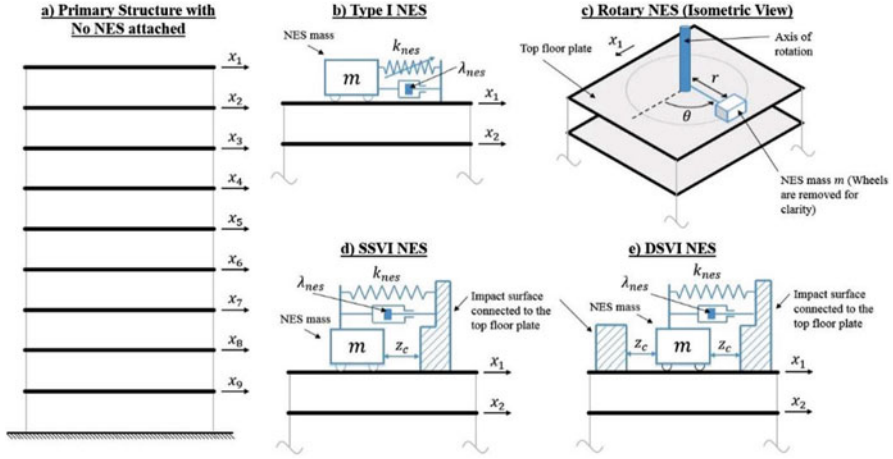


Fig. 1 (a) Illustration of the nine-story structure with a schematic of (b) Type I NES, (c) Rotary NES, (d) SSVI NES, and (e) DSVI NES on the top floor of the structure

Type I NES as shown in Fig. 1 consists of a cubic nonlinear stiffness and linear viscous damping elements given by k_{nes} and d_{nes} respectively. Consequently, the force \mathbf{f}_{nes} is given as

$$\mathbf{f}_{nes} = \left[k_{nes}(x_{nes} - x_1)^3 + \lambda_{nes} (\dot{x}_{nes} - \dot{x}_1) \ 0 \ \dots \ 0 \right]^T \quad (2)$$

where x_{nes} denotes the displacement of the NES mass. The added governing equation describing Type I NES mass motion is given by

$$m\ddot{x}_{nes} + \lambda_{nes}(\dot{x}_{nes} - \dot{x}_1) + k_{nes}(x_{nes} - x_1)^3 = 0 \quad (3)$$

As shown in Fig. 1(c), the rotary NES mass rotates about a vertical axis perpendicular to the direction of motion and on a plane parallel to the floor plate. This inertial coupling causes the essential nonlinear property required by the NESs to extract and scatter induced impulsive energies to the high-frequency structural modes of the primary structure. The nonlinear force vector \mathbf{f}_{nes} for this type of NES is given as

$$\mathbf{f}_{nes} = \left[m\ddot{x}_1 + mr(\ddot{\theta} \sin\theta + \dot{\theta}^2 \cos\theta) \ 0 \ \dots \ 0 \right]^T \quad (4)$$

and the added governing equation describing the rotary NES mass motion is given by

$$mr^2\ddot{\theta} - mr\ddot{x}_1 \sin\theta + d_{nes}\dot{\theta} = 0 \quad (5)$$

where θ defines the angular rotation of the NES mass from the positive horizontal displacement of the top floor, r is the length of coupling arm from the vertical axis to the NES mass and d_{nes} is the torsional viscous damping associated with the NES mass rotary motion. Impact-based NESs consist of linear stiffness and viscous damping elements analogous to a tuned mass damper. However, in addition to that, they incorporate rigid barriers fixed to the top floor of the primary structure to cause consecutive vibro-impacts generating nonsmooth strongly nonlinear coupling between the NES and the structural modes of the primary structure. This causes energy scattering from the low-frequency structural mode of the primary structure to higher frequency structural modes and to the NES itself leading the energy dissipation through the NES's viscous damping element, inelastic collisions and the structures inherent damping. For DSVI and SSVI NESs, the force \mathbf{f}_{nes} is given as

$$\mathbf{f}_{nes} = \left[k_{nes} (x_{nes} - x_1) + \lambda_{nes} (\dot{x}_{nes} - \dot{x}_1) \ 0 \ \dots \ 0 \right]^T \quad (6)$$

the added governing equation describing the NES mass motion between the impacts is given by

$$m\ddot{x}_{nes} + \lambda_{nes} (\dot{x}_{nes} - \dot{x}_1) + k_{nes}(x_{nes} - x_1) = 0 \quad (7)$$

The numerical integration of the governing equations is continued until the impact condition is satisfied. As shown in Fig. 1(d), for SSVI NES where the motion is constraint asymmetrically in one direction, the impact condition is given as

$$x_{nes} - x_1 \geq z_c \quad (8)$$

and for DSVI NES where the motion is constrained on both directions of motion symmetrically, the impact condition is given as

$$|x_{nes} - x_1| \geq z_c \quad (9)$$

Then, the velocities of the NES and top floor after the impact are derived from the conservation of momentum and Newtonian concept for the coefficient of restitution as

$$\dot{x}_1^+ = \frac{m\dot{x}_{nes}^- + M_1\dot{x}_1^- - mr_c(\dot{x}_1^- - \dot{x}_{nes}^-)}{m + M_1} \quad (10)$$

$$\dot{x}_{nes}^+ = \dot{x}_1^+ + r_c(\dot{x}_1^- - \dot{x}_{nes}^-) \quad (11)$$

where M_1 and m are the masses of the top floor and NES respectively and the superscripts $+$ and $-$ indicate the velocities after and before the impacts respectively.

One way to quantify the performance of an NES-coupled system for achieving efficient TET is by measuring the enhancement in the damping of the respective effective modal oscillators. This is quantified by the time-independent averaged effective modal damping measures $\lambda_{eff,i}$ expressed as

$$\lambda_{eff,i} = \frac{\dot{q}_i(T_0)^2 - \dot{q}_i(T_f)^2 + \omega_i^2 \left(\dot{q}_i(T_0)^2 - \dot{q}_i(T_f)^2 \right)}{2 \int_{T_0}^{T_f} \dot{q}_i^2 dt} = \frac{E(T_0) - E(T_f)}{\int_{T_0}^{T_f} \dot{q}_i^2 dt} \quad (12)$$

where \dot{q}_i is the modal velocity of the i -th mode, T_0 and T_f are the initial and final simulation times, E is the instantaneous energy and ω_i^2 is the effective modal stiffness. The nominal modal damping λ_i of the i -th structural mode can be obtained using Eq. 12 by considering the modal response of a linear primary structure without the NES leading to energy scattering between the structural modes. The nonlinear interaction of the NES causes energy exchange between the structural modes and therefore the energy in each mode is not conserved. The normalized weighted-averaged effective damping measures $\hat{\lambda}_{eff,i}$ is defined as the ratio of the time-independent averaged effective damping measures $\lambda_{eff,i}$ to the nominal modal damping λ_i of the NES-free system. If $\hat{\lambda}_{eff,i} > 1$, then energy is transferred out of the i -th mode in the given time interval and it is eventually dissipated by the NES's local damping and other modes and vice versa.

3 Results and Discussion

The parameters of each type of NES are optimized to obtain the maximum value of normalized weighted-averaged effective mode 1 damping measure $\hat{\lambda}_{eff,1}$ which indicates the maximum amount of energy transferred out from the lowest fundamental (highly-energetic) mode to be dissipated locally by the NES or by the inherent structural damping of the higher frequency structural modes. For the optimization purposes, the simulation time T_f is set to 5 seconds to ensure efficient and rapid TET. The initial impulsive energy is input through an identical initial velocity of 0.25m/s induced equally to all floors of the primary structure with zero initial displacements. The clearance z_c of DSVI and SSVI NESs is fixed to 0.020m to ensure non-smooth vibro-impacts will occur and the coefficient of restitution during the inelastic impacts is assumed to be 0.7 which corresponds to steel-to-steel impacts. The initial angle of the rotary NES is taken as $\pi/2$ to excite it with the maximum possible angular velocity. The linear or nonlinear stiffness coefficient and linear viscous damping coefficient are the optimizing parameters for Type I,

DSVI and SSVI NESs. The length of the coupling arm and the angular damping coefficient are the optimizing parameters for the rotary NES. The contour plots showing the normalized weighted-averaged effective mode 1 damping measures for varying parameters of each NES type is shown in Fig. 2.

The optimal normalized weighted-averaged effective mode 1 damping measures resulting from the optimization in Fig. 2 (indicated by black crosses) are compared in Fig. 3. Type I and SSVI NESs engage in the most effective frequency-energy scattering to transfer energy out of the fundamental mode. Although the rotary and DSVI NESs show poorer performance in energy transfer and dissipation, they still result in $\hat{\lambda}_{eff,1}$ that are greater than unity indicating that significant energy has been transferred from the fundamental to the NES or other modes. Additionally, the performance of the optimized NESs at an initial velocity of 0.25m/s are compared in Fig. 4(a) for varying initial velocities applied equally to all floors. The optimized SSVI NES showed very robust performance over a wide range of initial input shock loadings signifying its capability to engage efficient TET even for severe loadings

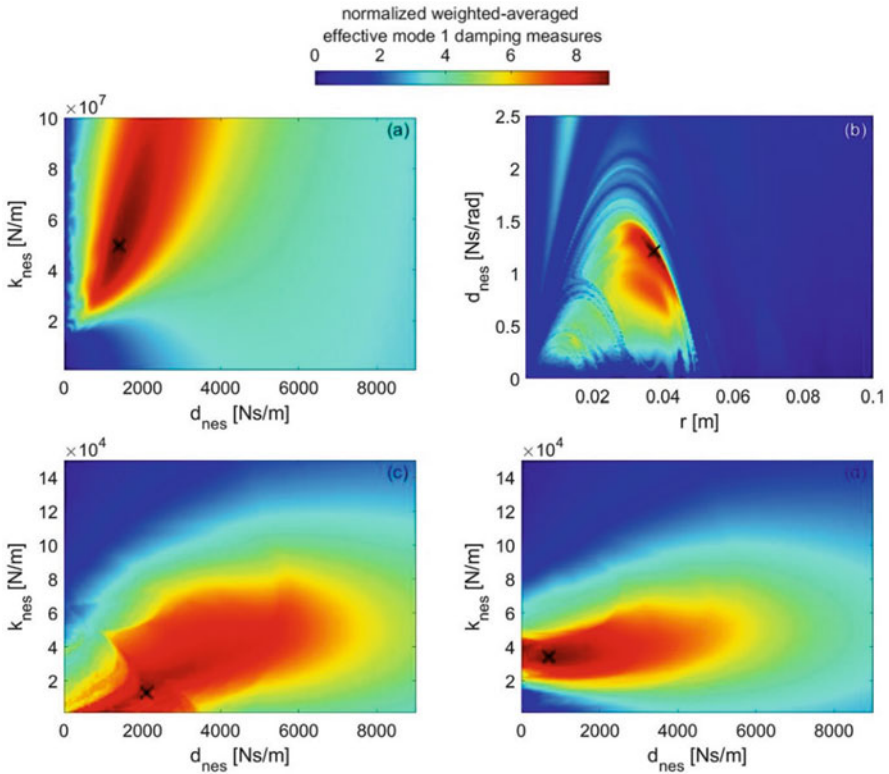


Fig. 2 Contour plots of $\hat{\lambda}_{eff,1}$ by the Type I NESin (a), rotary NES in (b), DSVI NES in (c) and SSVI NES in (d) for varying parameters for the nine-story primary structure; identical initial velocity 0.25 m/s is considered for each floor; black crosses indicate optimal system parameters

Fig. 3 The resulting optimum $\hat{\lambda}_{eff,1}$ for each type of NES; indicated by black crosses in Fig. 2

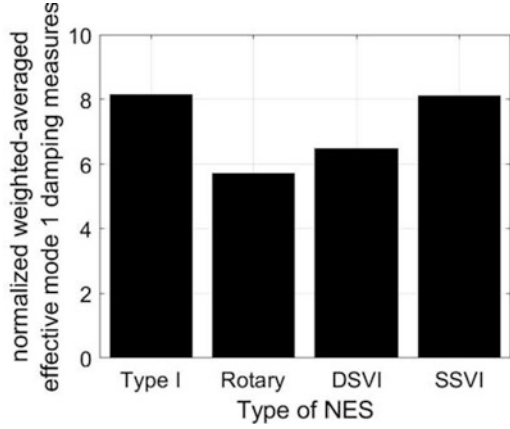
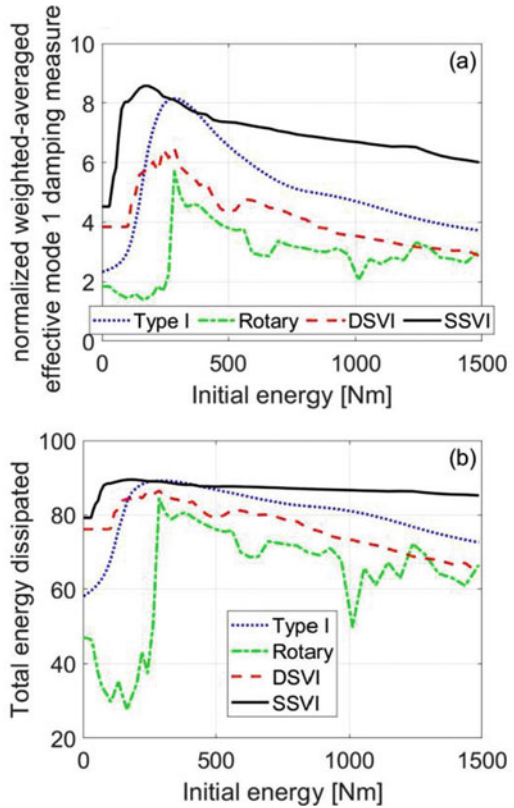


Fig. 4 The performance of the optimized NESs for varying initial impulsive energies induced by identical velocities to all floors



unlike other types whose performance deteriorate drastically. This outcome can also be seen from Fig. 4(b) which shows the corresponding energy dissipated by each NES for varying input energies. The enhanced performance of the SSVI NES makes it eligible for efficiently protecting structures under severe seismic or blast loadings as well.

4 Conclusions

The NES performs rapid and passive energy transfer and dissipation for a significant portion of the induced vibration energy into primary structures. Therefore, it can be utilized in a wide variety of aerospace, mechanical and civil engineering applications since vibration absorption is a major aspect of such small- and large-scale dynamical structures. An optimized design of the NES when attached to a dynamic structure is expected to significantly protect the structure from impacts, blast loadings, earthquakes, wind gusts, typhoons, etc. which saves human life as well as the structure itself. A thorough comparison of the common types of NESs is carried here for an impulsively loaded large-scale nine-story real physical structure. It was found that the SSVI NES provides the most energy transfer from the first fundamental (destructive) mode to be dissipated locally by the NES itself or through the inherent structural damping of the higher modes for a wide range of impulsive energies. Consequently, it can be said that the SSVI NES is the most efficient passive structural control device.

References

1. Vakakis, A.F., Gendelman, O.V., Bergman, L.A., McFarland, D.M., Kerschen, G., Lee, Y.S.: *Nonlinear Targeted Energy Transfer in Mechanical and Structural Systems*. Springer Science & Business Media, Dordrecht (2008)
2. Sapsis, T.P., Quinn, D.D., Vakakis, A.F., Bergman, L.A.: Effective stiffening and damping enhancement of structures with strongly nonlinear local attachments. *J. Vib. Acoust.* **134**(1), 011–016 (2012)
3. Saeed, A.S., AL-Shudeifat, M.A.: Vibration suppression in two-dimensional oscillation dynamical systems. In: *Proceedings of the ASME 2018. International Mechanical Engineering Congress and Exposition (IMECE)*, Pittsburgh (2018)
4. AL-Shudeifat, M.A., Saeed, A.S.: Frequency-energy dependence of the bistable nonlinear energy sink. In: *Proceedings of the ASME 2017. International Design Engineering Technical Conferences and Computers and Information in Engineering Conference (IDETC-CIE)*, Cleveland (2017)
5. AL-Shudeifat, M.A., Saeed, A.S.: Analytical treatment for bistable nonlinearly coupled oscillator. In: *Proceedings of the ASME 2017. International Design Engineering Technical Conferences and Computers and Information in Engineering Conference (IDETC-CIE)*, Cleveland (2017)

6. Sigalov, G., Gendelman, O., Al-Shudeifat, M.A., Manevitch, L., Vakakis, A.F., Bergman, L.A.: Resonance captures and targeted energy transfers in an inertially-coupled rotational nonlinear energy sink. *Nonlinear Dynam.* **69**(4), 1693–1704 (2012)
7. Gendelman, O., Sigalov, G., Manevitch, L., Mane, M., Vakakis, A.F., Bergman, L.A.: Dynamics of an eccentric rotational nonlinear energy sink. *J. Appl. Mech.* **79**(1), 011012 (2012)
8. Saeed, A.S., Al-Shudeifat, M.A.: Rotary-oscillatory nonlinear energy sink of robust performance. *Int. J. Non Linear Mech.* **177**, 103249
9. Saeed, A.S., AL-Shudeifat, M.A.: A new type of NES: rotary vibro-impact. In *Proceedings of the ASME 2017. International Design Engineering Technical Conferences and Computers and Information in Engineering Conference (IDETC-CIE)*, Cleveland (2017)
10. Gendelman, O.V.: Analytic treatment of a system with a vibro-impact nonlinear energy sink. *J. Sound Vib.* **331**(21), 4599–4608 (2012)
11. Li, T., Seguy, S., Berlioz, A.: Dynamics of cubic and vibro-impact nonlinear energy sink: analytical, numerical, and experimental analysis. *J. Vib. Acoust.* **138**(3), 031010 (2016)
12. Gendelman, O.V., Alloni, A.: Dynamics of forced system with vibro-impact energy sink. *J. Sound Vib.* **358**(1), 301–314 (2015)
13. Li, T., Seguy, S., Berlioz, A.: On the dynamics around targeted energy transfer for vibro-impact nonlinear energy sink. *Nonlinear Dynam.* **87**(3), 1453–1466 (2017)
14. Al-Shudeifat, M.A., Wierschem, N., Quinn, D.D., Vakakis, A.F., Bergman, L.A., Spencer, B.F.: Numerical and experimental investigation of a highly effective single-sided vibro-impact nonlinear energy sink for shock mitigation. *Int J Nonlinear Mech.* **52**(1), 96–109 (2013)
15. AL-Shudeifat, M.A., Vakakis, A.F., Bergman, L.A.: Shock mitigation by means of low-to high frequency nonlinear targeted energy transfers in a largescale structure. *J. Comput. Nonlinear Dyn.* **11**(2), 021006 (2016)
16. Wierschem, N.E., Hubbard, S.A., Luo, J., Fahnestock, L.A., Spencer, B.F., McFarland, D.M., Quinn, D.D., Vakakis, A.F., Bergman, L.A.: Response attenuation in a large-scale structure subjected to blast excitation utilizing a system of essentially nonlinear vibration absorbers. *J. Sound Vib.* **389**(1), 52–72 (2017)
17. Li, W., Wierschem, N.E., Li, X., Yang, T.: On the energy transfer mechanism of the single-sided vibro-impact nonlinear energy sink. *J. Sound Vib.* **437**(1), 166–179 (2018)
18. Luo, J., Wierschem, N.E., Hubbard, S.A., Fahnestock, L.A., Quinn, D.D., McFarland, D.M., Spencer, D.F., Vakakis, A.F., Bergman, L.A.: Large-scale experimental evaluation and numerical simulation of a system of nonlinear energy sinks for seismic mitigation. *Eng. Struct.* **77**(1), 34–48 (2014)

Stability of Three Wheeled Narrow Vehicle



Krzysztof Weigel-Milleret  and Witold Grzegózek 

Abstract A serious problem in modern cities are congestions and a lack of parking space, especially in cities centers. The narrow, three-wheeled vehicles seems to be solution to these problems. The work presents a description of the designed and developed urban individual mean of transport. The implemented prototype is a narrow, three-wheeled vehicle with electric drive designed as a delta type vehicle. Road tests of controllability were performed — a constant radius of turn and constant steering angle tests and stability of the vehicle using the single lane change maneuver. A mathematical vehicle model with three degrees of freedom (3DOF) was arranged, including lateral displacement, roll and yaw angle rotation. These road tests were used to validate parameters in the vehicle model. A vehicle motion simulation was performed in accordance with the NHTSA J-turn maneuver procedure. The results of the simulation allowed the assessment of the impact of driving speed on the lateral stability of the vehicle by the determination of the dynamic roll angle.

Keywords Narrow vehicle · Torque Vectoring · Active Roll Mitigation

Nomenclature

m	mass of the vehicle [kg],
δ_1	steering angle of the front wheels [rad],
δ_2	steering angle of the rear wheels [rad],
l_1	distance from front axle to centre of mass [m],
l_2	distance from rear axle to centre of mass [m],
h	height of a center of mass [m],
b	track width [m],

K. Weigel-Milleret (✉) · W. Grzegózek
Cracow University of Technology, Krakow, Poland
e-mail: krzysztof.weigel-milleret@pk.edu.pl

© Springer Nature Switzerland AG 2021
J. Awrejcewicz (ed.), *Perspectives in Dynamical Systems III: Control and Stability*,
Springer Proceedings in Mathematics & Statistics 364,
https://doi.org/10.1007/978-3-030-77314-4_9

M_{ext}	additional yaw moment [Nm],
F_{ext}	additional horizontal force [N],
K_1	cornering stiffness of the front axle [N/rad],
K_2	cornering stiffness of the front axle [N/rad],
c	rolling stiffness of a vehicle [Nm/rad],
k	torsion damping factor [Nm/rad/s].

1 Introduction

Designing today's vehicles forces manufacturers to create more fuel-efficient structures. One of the ideas is to build smaller, with more aerodynamic shapes or tailored to specialized tasks vehicles. The idea of personal transportation especially at urban agglomerations leads to introducing the three wheel platform and narrow vehicles.

The narrow cars are a special kind of microcars. These are small-dimension vehicles with limited range. The range of several dozen kilometers is enough on one tank or charging is sufficient for most residents of modern cities. They are designed for only driver or a driver with one passenger with a small luggage. Due to their small dimensions, high maneuverability, dynamic driving performance and lower fuel consumption the narrow cars perform perfectly in the urban agglomeration spaces. A lack of parking space, traffic jams and road congestions are a serious problem in modern cities. In academic papers it is estimated that more than 5 billion hours are annually spent waiting on freeways in traffic congestions [1]. The efficient utilization of existing infrastructure (e.g. roads, parking places) seems to be good solution. Especially since the costs of road construction are rising [2]. The design of small vehicles, with a better weight/load relation, has been proposed in several studies, e.g. [3–5].

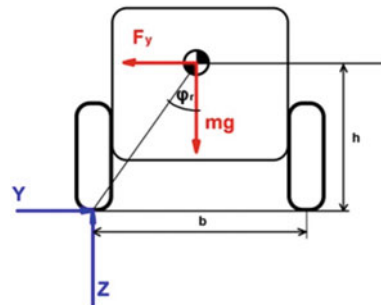
Vehicle rollover should be consider as an important safety problem. Accidents involving vehicle rollover often have fatal consequences [6]. The narrow cars are very susceptible to rollover, because they have a small track and a high center of gravity.

In this paper the MIST car was chosen for tests. This narrow car was designed and developed in Institute of Automobiles and Internal Combustion Engines of the Cracow University of Technology. MIST body is made as a welded space frame with a front suspension subframe. This design provides high rigidity and torsional stiffness of the body. Vehicle body has enough space for the driver and a small luggage. It is driven by two electric motors built in the rear wheel hubs. Its basic technical data is presented in Table 1 [7]. The combination of trailing-arm and pushed-arm suspension causes the rolling axis of the vehicle body to be located in the plane of the road. That increase the rolling stiffness of the vehicle. MIST is a four-wheeled vehicle, however, the short wheelbase and parallel suspension movement of the front axle means that the vehicle can be considered a three-wheeler.

Table 1 MIST technical data

Frame	steel, welded space frame
Front suspension	dependent suspension with parallel wheel movement, doubled pushed arm
Rear suspension	semi-independent twist beam with towed arms
Motor	2 × Brushless DC motor (3.5 kW peak power)
Brakes	Hydraulic, disc brakes
Vehicle mass	197 kg unloaded; 268 kg with driver
Wheelbase	1560 mm
Track width	470 mm front axle, 870 mm rear axle

Fig. 1 Balance of forces acting on a car in a curve



2 Narrow Vehicle Stability

In automotive industries the vehicle, developing the dynamics control (VDC) system was considered important. The VDC system improves the vehicle response in critical cornering situations. It is achieved by distributing asymmetric brake forces to the wheels. Due to its significant benefit the VDC system installed on top of the ABS/TCS system have already been commercialized. The systems are nowadays installed in passenger vehicles. Some researchers proposed PID controls or LQ-optimal controls to compensate the error between the actual state and desired state of the vehicle [8, 9]. The most common approach at VDC systems is to use vehicle brakes to create the deflection or tilting moment of the vehicle. However, each activation of the vehicle’s brakes dissipates a portion of kinetic energy of the vehicle as heat. Therefore, each operation of the vehicle’s stabilization system contributes to reducing the range of the electric vehicle. The range of the vehicle is limited due to the weight and dimensions limitation of narrow vehicle, which limits the size of the battery.

The vehicle resistance to overturning is called a rollover stability. It is assumed that the vehicle loses rollover stability when the normal reaction under at least one wheel on the vehicle’s side drops to zero. This case is showed in Fig. 1. It should be noticed that the vehicle is considered as a rigid body (impact of the suspension of the vehicle is not taken into account).

The quotient of lateral force and vehicle's weight must be less than tangent of the line between the center of mass and rolling axis [10]:

$$\frac{F_y}{mg} \leq \tan \varphi_r \quad (1)$$

$$F_y \leq \frac{b}{2h} mg \quad (2)$$

For short maneuvers lateral acceleration may exceed the value described above, and do not cause the vehicle rollover. The limitation of lateral acceleration in roll mitigation systems may reduce the possibility of cornering while traveling at high longitudinal velocity and significantly reduces maneuverability of the vehicle. That approach is highly inadequate for narrow vehicles. On the other hand more complicated maneuvers undertaken to defend against an obstacle may lead to lateral swinging of the vehicle and, as a result, its overturning. Based on own research, it has been noticed that a single lane change is often the driver's basic defensive maneuver. Interestingly, this maneuver is often undertaken too vigorously, which can cause the vehicle to rollover. The function of the active roll control system, which is developed by the authors, described in this paper allows to change the vehicle's steerability characteristics in order to reduce the risk of rollover.

Development of active roll mitigation systems have been described in the literature. Nowadays the roll mitigation systems based on static or steady-state rollover models are widely used in the automotive industry [11]. Less commonly used dynamic models are presented in academic papers [12]. The roll mitigation systems for dynamics are usually based on continuous normal load force calculation. It is difficult to measure the value of the vertical load of particular wheel, so the lateral load transfer ratio during maneuvers parameter is commonly used. However, the dynamic model should take into account changes in the mass of the vehicle that are difficult to measure or predict. Therefore, the use of dynamic models is complicated. For microcars with low payloads, which are designed only for the driver, it is easier to predict the total weight and its distribution in the vehicle. The distribution of driving forces on individual wheels of the driven axle can be used to prevent rolling over and to stabilize the vehicle motion. Such solution can be implemented only in vehicles with independent power supply for electric motors, which drive a single wheel. It causes the increase of the energy efficiency of the vehicle, which makes increasing the maximum range of the vehicle possible. Currently, active torque vectoring control systems are mainly used to limit the yaw rate and vehicle slip angle [11, 12].

3 Vehicle Dynamics Model

In order to manage the active roll mitigation system a model with three-degrees of freedom (3DOF) including yaw, roll (around the rollover axis) and lateral motion of vehicle is used [13]. The model consider the suspension stiffness and damping

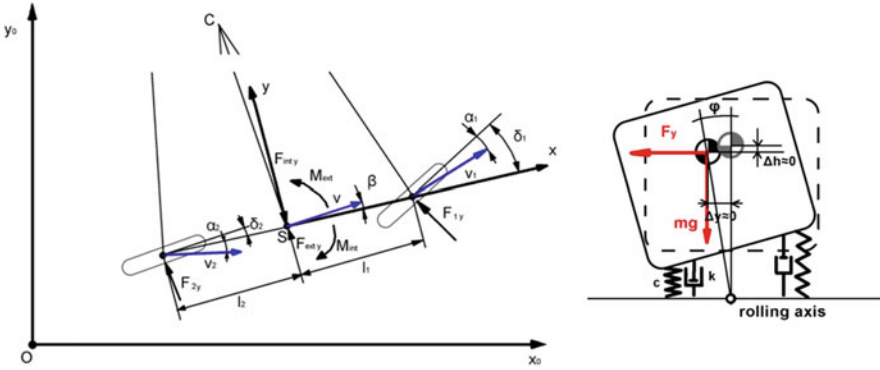


Fig. 2 3DOF model used for simulations

to predict vehicle movement. Because one of the assumption is the a constant longitudinal speed ($v_x = \text{const}$) the x-axis motion of the vehicle is not taken into account. Fig. 2. shows the vehicle's motion in two perpendicular planes. The forces and moments acting on the vehicle can be calculated as:

$$\begin{cases} \sum F_y = m\ddot{y} \\ \sum M_z = I_z\ddot{\psi} \\ \sum M_\varphi = I_\varphi\ddot{\varphi} \end{cases} \quad (3)$$

Where F_y , M_z and M_φ are lateral force and the moments around z and rolling axis; I_z and I_φ represent the moment of inertia around vertical and rolling axels. y , ψ , φ denote lateral position, yaw and roll angles. Suspension model is taken into account as presented in Fig. 2.

The equations of forces and moments acting on the vehicle take the form:

$$-F_{\text{int } y} + F_{1y} \cos \delta_1 + F_{2y} \cos \delta_2 + F_{\text{ext } y} = 0 \quad (4)$$

$$-M_{\text{int } z} + F_{1y} \cos \delta_1 l_1 - F_{2y} \cos \delta_2 l_2 + M_{\text{ext } z} = 0 \quad (5)$$

$$-M_{\text{int } \varphi} + F_y h \cos \varphi + mgh \sin \varphi - c\varphi - k\dot{\varphi} + M_{\text{ext } \varphi} = 0 \quad (6)$$

Moment of inertia around the rolling axis:

$$I_\varphi = I_x + mh^2 \quad (7)$$

One of the simpler mathematical models of the tire is the linear model. When the magnitude of the wheel slip is small, the tire forces generated by the wheel are proportional to the slip:

$$F_{ix} = k_x \bullet \lambda \quad (8)$$

$$F_{iy} = k_y \bullet \alpha \quad (9)$$

These forces are proportional to the longitudinal slip of the wheel and the wheel drift angle. The coefficients of slip resistance and wheel drift k_x and k_y are constant values. This model is accurate for wheel slip $\lambda < 0.15$ and wheel drift angle $\alpha < 0.1$ rad. For larger values of wheel slip or drift angle, the forces calculated from the real model are higher than the real forces at the contact point of the tire and the road. For narrow cars, the linear tire model gives sufficient compatibility over the entire speed range with which the vehicle moves.

The lateral forces of the front and rear axles can be determined as:

$$F_{1y} = K_1 \alpha_1 \quad (10)$$

$$F_{2y} = K_2 \alpha_2 \quad (11)$$

After taking into account other assumptions: $\delta_2 = 0$; $\cos \delta_1 \approx 1$; $\cos \beta \approx 1$ and $\beta = \frac{\dot{y}}{x}$ the equations take form:

$$m\ddot{y} = K_1 \delta_1 - \frac{K_1 + K_2}{v} \dot{y} - \frac{K_1 l_1 - K_2 l_2 + m v^2}{v} \dot{\psi} \quad (12)$$

$$I_z \ddot{\psi} = K_1 l_1 \delta_1 - \frac{K_1 l_1 - K_2 l_2}{v} \dot{y} - \frac{K_1 l_1^2 + K_2 l_2^2}{v} \dot{\psi} + M_{\text{ext } z} \quad (13)$$

$$I_\varphi \ddot{\varphi} = F_y h \cos \varphi + m g h \sin \varphi - c \varphi - k \dot{\varphi} \quad (14)$$

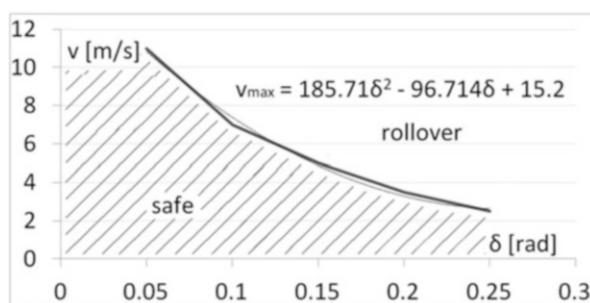
4 Preliminary Simulations

Matlab R2015b software was selected for the motion simulation. The geometric and mass parameters of the vehicle were determined at preliminary tests. Previously determined [14] cornering stiffness for the front and rear axles were used in the 3DOF model. Basic model parameters are presented in Table 2. The input to the model was the steering angle as a function of time. The result of the simulation is the lateral movement of a vehicle $y(t)$, $y'(t)$ in local CS, yaw angle $\psi(t)$, yaw rate $\dot{\psi}(t)$, roll angle $\varphi(t)$ and roll rate $\dot{\varphi}(t)$ as a function of time.

In the preliminary simulations, limit values for the vehicle speed and steering angle were determined, exceeding which for a single lane change maneuver results

Table 2 Model parameters

Parameter	Unit	Value
m – mass of the vehicle	kg	305
l_1 – distance from front axle to centre of mass	m	1.03
l_2 – distance from rear axle to centre of mass	m	0.53
h – height of a center of mass	m	0.8
K_1 – cornering stiffness of the front axle	N/rad	15000
K_2 – cornering stiffness of the rear axle	N/rad	25000
I_z – moment of inertia around vertical axis	kg m ²	80
I_φ – moment of inertia around rolling axis	kg m ²	370
c – rolling stiffness of a vehicle	Nm/rad	5000
k – torsion damping factor	Nm/rad/s	3000

Fig. 3 Speed and steering angle limit function

in loss of stability by raising one of the wheels from the surface. The maximum safe roll angle range of the car body is $\varphi = 14^\circ \approx 0.25$ rad. At this angle the inner wheel of the vehicle is detached from the road surface. For safety reasons, the determination of the vehicle speed and the steering angle limit was based only on simulation. The adopted vehicle model needs a lot of computing power and cannot be used in an active real-time system based on simple controller. For this reason from the calculated limits, a function combining the speed and the steering angle was created. The function combining the speed and steering angle is presented in Fig. 3.

5 Controller Design

To improve the vehicle handling and stability velocity, yaw rate of the vehicle and steering wheel angle are controlled not to exceed their maximum value and to calculate the limit function. The controller block diagram is shown in Fig. 4.

While driving without the risk of overturning the vehicle, the controller performs the functions of an electronic differential. When driving in an arc, the current supplying the engines is divided in proportion to the steering wheel angle. Normally,

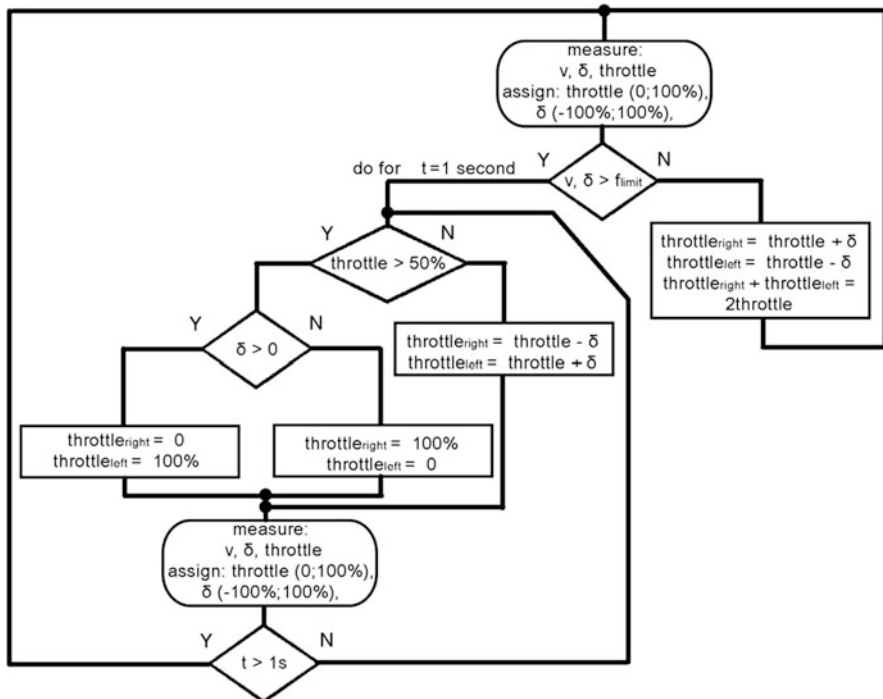


Fig. 4 Block diagram of Active roll control system

when driving in an arc, the inner wheel rotates at a lower speed than the outer wheel of the vehicle. Earlier studies showed that this action reduces understeer of the vehicle, even to neutral steering characteristic, which increases its maneuverability and the vehicle’s response to movement of the steering wheel becomes faster. When the function limit is exceeded, the program reverses the drive torque distribution sign of the electronic differential for a set time. Greater driving force is created under the inner wheel to the arc.

In addition, the controller continuously monitors the vehicle’s roll angle. If the value of the roll angle exceeds the set maximum, the controller shuts off power to the propulsion engines.

The Arduino platform was chosen to support active control of electric motors. It is a platform created for embedded systems based on Open Hardware. The programming language used by Arduino is based on the Wiring environment and on the C / C ++ language.

The Arduino Mega board used consists of an 8-bit Atmel AVR microcontroller. On the Arduino driver board most of the microcontroller input / output pins are derived for use by other systems.

The following sensors are installed in the vehicle:

- Honeywell RTY 270HVNAX Hall-Effect rotary position sensor measuring the steering angle,
- MPU-6050 integrated 6-axis MotionTracking device that combines a 3-axis gyroscope, 3-axis accelerometer, and a Digital Motion Processor™ (DMP) measuring lateral, longitudinal yaw and roll accelerations. The device is used to calculate the roll angle of the vehicle.

6 Simulations and Road Tests

The 3DOF model described above was used in simulations. The only modification was the additional yaw moment implemented in the model as a function of the steering angle (and time). Other input data was the steering angle as a function of time and vehicle velocity. Steering angle function was obtained from real road tests. The result of the simulation is the lateral movement of a vehicle $y(t)$, $y'(t)$ in local CS, yaw angle $\psi(t)$, yaw rate $\psi'(t)$, roll angle $\phi(t)$ and roll rate $\phi'(t)$ as a function of time.

Except the sensors used to controller following test equipment was installed in the vehicle:

- Datron Correvit apparatus measuring the longitudinal and lateral velocities of the vehicle,
- Crossbow measuring velocities and lateral, longitudinal and rolling accelerations,

Road tests were conducted with an active roll limitation system built according to the assumptions described in point 5. The tests and the simulations included a single turn and single lane change maneuver performed at different driving velocities. The road tests of a single lane change were carried out on a track adapted to the dimensions and speeds of the tested vehicle. The diagram of the test track is shown in Fig. 5.

Simulations were carried out at multiple vehicle velocities for the equal driving torque distribution, for use of the electronic differential which minimizes the vehicle understeer and for use of the active roll control system. The obtained data of the roll angle was compared with the value measured during the tests. Figures 6 and 7. show examples of simulation result examples carried out at vehicle speed 3,5 m/s.

The above simulations results coincide with the results obtained during road tests. For the presented maneuvers minimization of understeer by driving torque

Fig. 5 Single line change track

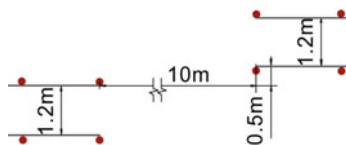


Fig. 6 Steering angle function δ , calculated and measured roll angle φ for different torque distribution. Single turn maneuver

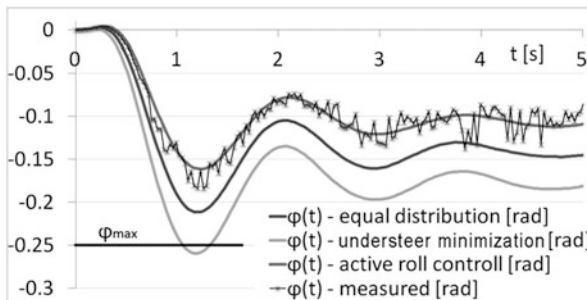
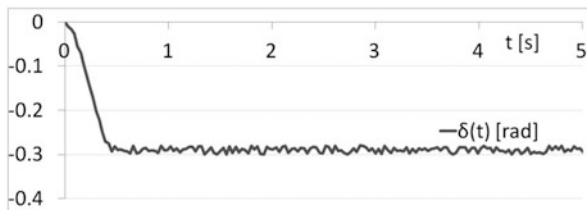
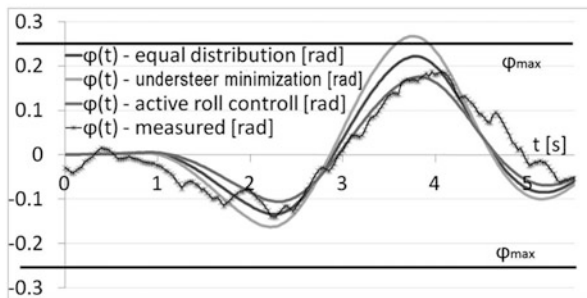
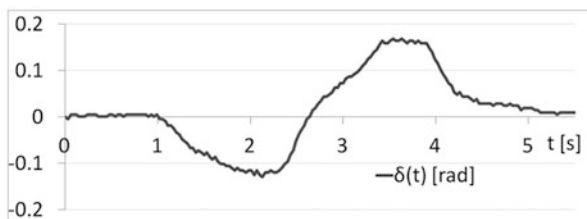


Fig. 7 Steering angle function δ , calculated and measured roll angle φ for different torque distribution. Single line change maneuver



distribution leads to the safe value of vehicle roll angle being exceed. Active roll angle control system reduces the roll angle which remained in safe value.

7 Conclusion

- A. Studies have shown the need to use an active roll angle reduction system. The absence of such a system results in exceeding the rollover limit of the narrow vehicle under test. A single lane change maneuver can be considered a frequent defensive maneuver against an unexpected obstacle.

- B. Due to the developed system, the tested narrow vehicle achieved a reduction of the roll angle by about 21%.
- C. The basic limitation of narrow vehicles is rollover.
- D. The conducted tests are consistent with the tests carried out for typical passenger cars. The results indicate the usefulness of the developed system that allows proper torque distribution for different values of v and δ so that the vehicle remains stable.
- E. The subjective feelings of drivers of a vehicle equipped with an active roll limitation system are positive.

References

1. Rajamani, R., Gohl, J., Alexander, L., Starr, P.: Dynamics of narrow tilting vehicles. In: *Math. Comput. Model. Dyn. Syst.* **9**(2), 209–231 (2003)
2. Michalek, J., Papalambros, P., Skerlos, S.: A study of fuel efficiency and emission policy impact on optimal vehicle design decisions. *J. Mech. Des.* **126**(6), 1062–1070 (2004)
3. Ashmore, C.: Through the eyes of Colin Ashmore. *Eng. Manag. J.* **16**, 10 (2006)
4. Brink, C., Kroonen, H.: Dvct m - the banking technology driving the carver. In: *7th International Symposium on Advanced Vehicle Control* (2004)
5. Vieira, R., Nicolazzi, L., Roqueiro, N., Padilha, R.: Dynamic model of a leaning three-wheeled vehicle. In: *XVI Congresso e exposicao internacionais da tecnologia da mobilidade*. SAE, Sao Paulo (2007)
6. Yoon, J., Yi, K.: A Rollover Mitigation Control Scheme Based on Rollover Index. In: *Proceeding of the 2006 American Control Conference* (2006)
7. Grzegożek, W., Weigel-Milleret, K.: Torque vectoring for improving stability of small electric vehicles. In: *IOP Conference Series: Materials Science and Engineering* (2016)
8. Koibuchi, K., Yamamoto, M., Fukuda, Y., Inagaki S.: Vehicle stability control in limit cornering by active brake. In: *SAE 960187* (1996)
9. Alleyne, A.: A comparison of alternative intervention strategies for unintended roadway departure (URD) control. In: *Proceedings of AVEC*, pp. 485–506 (1996)
10. Reński, A.: Automotive active safety. *Oficyna Wydawnicza Politechniki Warszawskiej*, pp. 247–268 (2011)
11. Kiencke, U., Nielsen, L.: *Drivetrain Control Automotive Control Systems – For Engine, Driveline and Vehicle*. Springer (2005)
12. De Novellis, L., Sorniotti, A., Gruber, P.: Wheel torque distribution criteria for electric vehicles with torque-vectoring differentials. *IEEE Trans. Veh. Technol.* **63**(4), 1593–1602 (2013)
13. Grzegożek, W., Weigel-Milleret, K.: Wheel torque distribution for narrow cars. In: *11th International Science and Technical Conference Automotive Safety, AUTOMOTIVE SAFETY 2018 5 June 2018*, pp. 1–6 (2018)
14. Grzegożek, W., Weigel-Milleret, K.: Modelling and simulation of narrow car dynamic. In: *IOP Conference Series: Materials Science and Engineering* (2018)

Testing and Analysis of Vibration of a Tension Transmission with a Thermally Sealed Belt



Grzegorz M. Szymański  and Piotr Krawiec 

Abstract The advantages of heat-sealable belts include: the possibility of welding of their ends (allows obtaining a strip of any length and a quick replacement in case of damage), excellent resistance to abrasion, resistance to oil, grease, dirt and some chemicals, resistance to temperatures from $-30\text{ }^{\circ}\text{C}$ to $+80\text{ }^{\circ}\text{C}$, significant elasticity at a relatively low level of stretching, high value of the friction coefficient (thus very good anti-slip properties even at load changes), safety when in contact with food. There are few publications devoted to these belts, therefore the authors have built a test stand for experimental studies of such drives. The analysis of vibration of a draw gear with a thermally sealed belt was carried out in accordance with the assumptions of an active experiment. The following input parameters were adopted: belt tension force, torque loading the gearbox, rotational speed of the drive shaft. The following output parameters were adopted: the values of vibration acceleration of selected elements of the test stand (the transducers are mounted on the bearing housings of the drive and the driven shafts). During the research, the load of the gearbox was changed and the influence of its impact on the value of the point measures of vibration signals was observed. The following point measures were analyzed: the RMS value, the peak value and the kurtosis. The results of the research will certainly be useful for designers and technicians involved in the operation of drawstring drives with thermally weldable belts.

Keywords Vibration. Tension. Transmission. Thermally Sealed Belt

G. M. Szymański (✉)

Poznan University of Technology, Faculty of Civil and Transport Engineering, Institute of Transport, Poznan, Poland

e-mail: grzegorz.m.szymanski@put.poznan.pl

P. Krawiec

Poznan University of Technology, Faculty of Mechanical Engineering, Institute of Machine Design, Poznan, Poland

e-mail: piotr.krawiec@put.poznan.pl

© Springer Nature Switzerland AG 2021

J. Awrejcewicz (ed.), *Perspectives in Dynamical Systems III: Control and Stability*,

Springer Proceedings in Mathematics & Statistics 364,

https://doi.org/10.1007/978-3-030-77314-4_10

1 Introduction

The causes of vibration and its influence on selected machine drives were thoroughly discussed in [1–4]. Multiple examples of analytical assessments of the vibration in belt transmissions [5–13] can be found, however, the attempts to evaluate them through experiment are scarce [14–16]. This paper will present the results of proprietary research concerning the gearing with the PU 75 A belt. Figures 1.a and 1.b present the test stand for the measurements of the vibration of the transmission with the polyurethane belt. The source of mechanical vibration may be as follows: inaccuracies in the manufacturing and assembly process of the machines and devices [17–19], unbalanced components in rotational motion [20, 21], component wear [22, 23], slider-crank components, reciprocating components.

2 Research Methodology

The analysis of the belt transmission fitted with a heat-sealable belt was carried out according to the assumptions of the active experiment. It was assumed that the input parameters were: the tensile force of the belt, the precise loading moment of the transmission and the rotational speed of the transmission shaft, whereas the output parameters were the values of the vibration acceleration of individual components (the transducers were mounted on the housings of the bearings of the transmission and the driven shafts). The measurement system shown in Fig. 1a

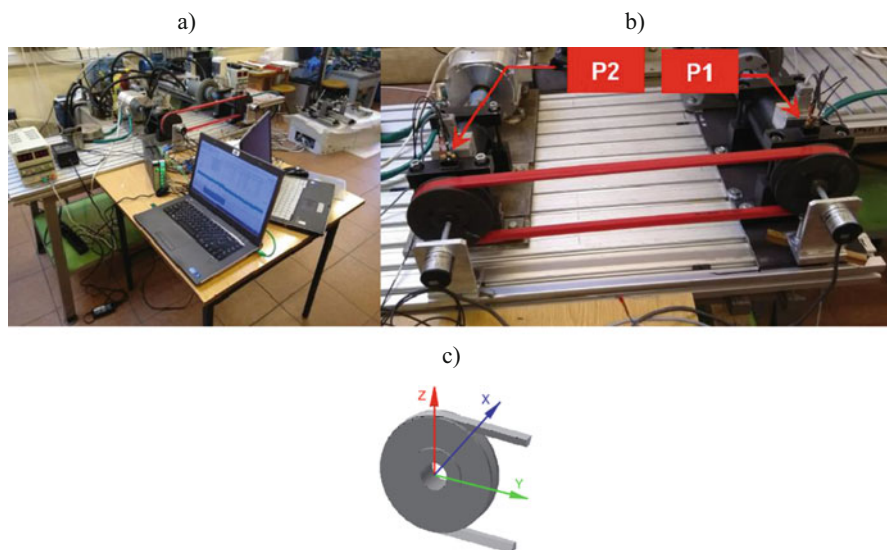


Fig. 1 The examination of the transmission with the PU 75 A belt; (a) view of the test stand, (b) location of the vibration transducers, (c) directions of vibration measurements

allows a simultaneous recording of fast-varying time tracings in 12 measurement channels with the dynamics of up to 160 dB. The 4504 Brüel & Kjær vibration transducers described in [1] were selected based on the guidelines provided in [12]. The linear frequency range of the selected transducers was 0.1 Hz to 18 kHz. During the investigations, the signals in the range from 0.1 Hz to 25 kHz were recorded. The sampling frequency was set to 65,536 Hz. A principle was adopted that the accelerometer should be placed as close to the precise point of the source of the vibration signal as possible [1]. Two triaxial transducers (P1, P2) connected to the measurement module were used to record the signals. The directions of the measurement of the vibration signals were set as: X – parallel to the axes of both shafts, Z – radial (vertical), Y – perpendicular to the other two (Fig. 1c).

3 Broadband Analysis of the Point Measures

Using point measures is one of the ways to describe the signals such as: displacement, velocity or acceleration of the vibration signals. The point measures allow characterizing the vibration signal using a single number, therefore, the changes of the vibroacoustic signal resulting from the current state of an object can be easily detected. Throughout the investigations, the load on the transmission was changed in order to observe its impact on the value of the point measures of the vibration signal. The point measures that were analyzed were: the RMS value, the peak value and the kurtosis. Filtration was not used in the analysis process. The speed of the transmission shaft was set at 500 rpm. The authors adopted a principle that the results of the measurements obtained on the transmission shaft were referred to as ‘the motor’ and the results of the measurements obtained on the driven shaft were referred to as ‘the brake’.

Figure 2 presents the changes of the kurtosis of the vibration acceleration signals depending on the load on the belt drive. Based on the said analyses, it was observed that the value of the kurtosis falls when the load on the transmission increases.

Those relations are not monotonic in the case of the signals recorded on the driven wheel along the X and Z axes, whereas in the case of the wheel driven along the X and Z axes, the changes can be approximated by the exponential curve. It is noteworthy that the dynamics of the changes of the kurtosis is similar for the X and Z axes, which is approximately 30 dB.

In order to examine the influence of the changes of the belt drive speed on the point measures of the signals of vibration acceleration, an experiment was carried out. During this experiment, the shaft load was changed by applying two different speed values of the transmission shaft (500 rpm and 1000 rpm). The following point measures were analyzed: the rpm value, the peak value and the kurtosis. Figure 3 shows the shifts in the rpm value of the vibration acceleration signals in relation to the load on the belt. Based on the analysis of these results it was determined that increasing the speed of the shaft results in an increase in the rpm value of the vibration signals recorded along all the axes both on the transmission and the driven

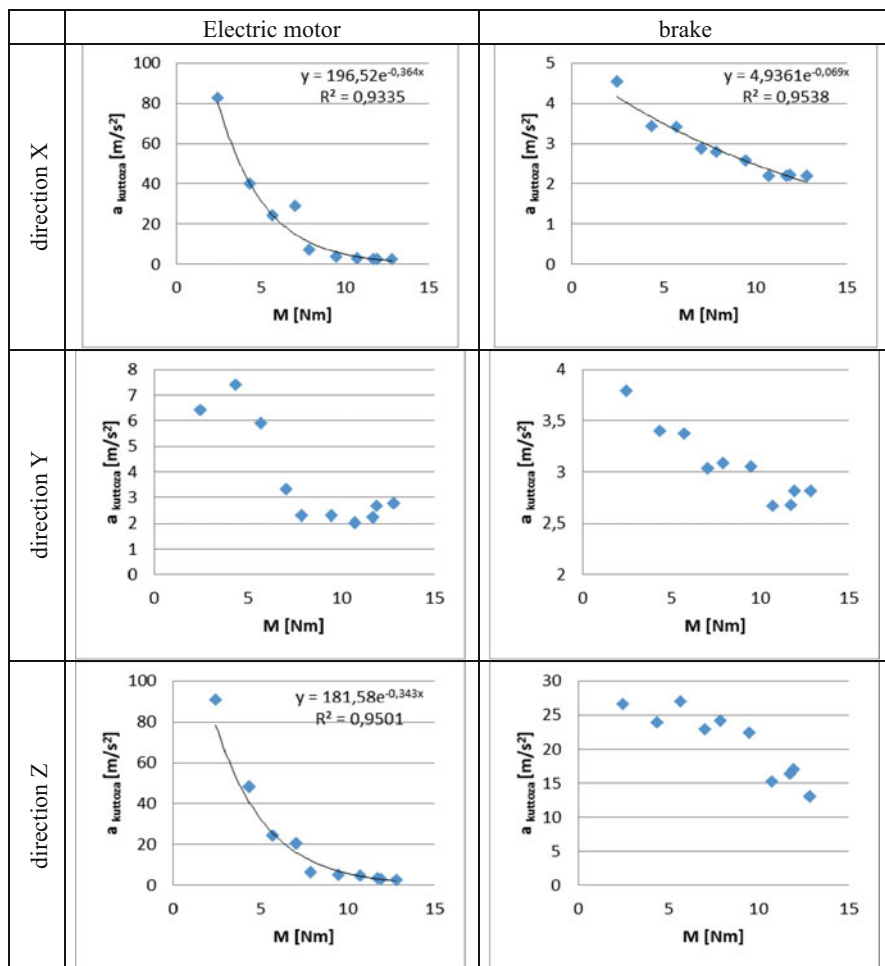


Fig. 2 Relation of the kurtosis of the signals of vibration acceleration and the load applied to the belt with the shaft speed of 500 rpm

shafts. A correlation was observed between the results recorded along the Z axis at the motor and along the X and Z axes at the brake.

Figure 4. shows the changes in the peak value of the vibration acceleration signals in relation to the load on the belt. As a result, it was determined that increasing the speed of the shafts results in an increase in the peak value of the vibration signals recorded at the driven shaft along all the axes. The peak values of the vibrations recorded at the driven wheel decreased when small loads on the belt were applied.

Figure 5. presents the changes of the kurtosis of the vibration acceleration signals in relation to the load on the transmission. As a result, it was determined that increasing the rpm of the transmission shafts results in a decrease of the kurtosis

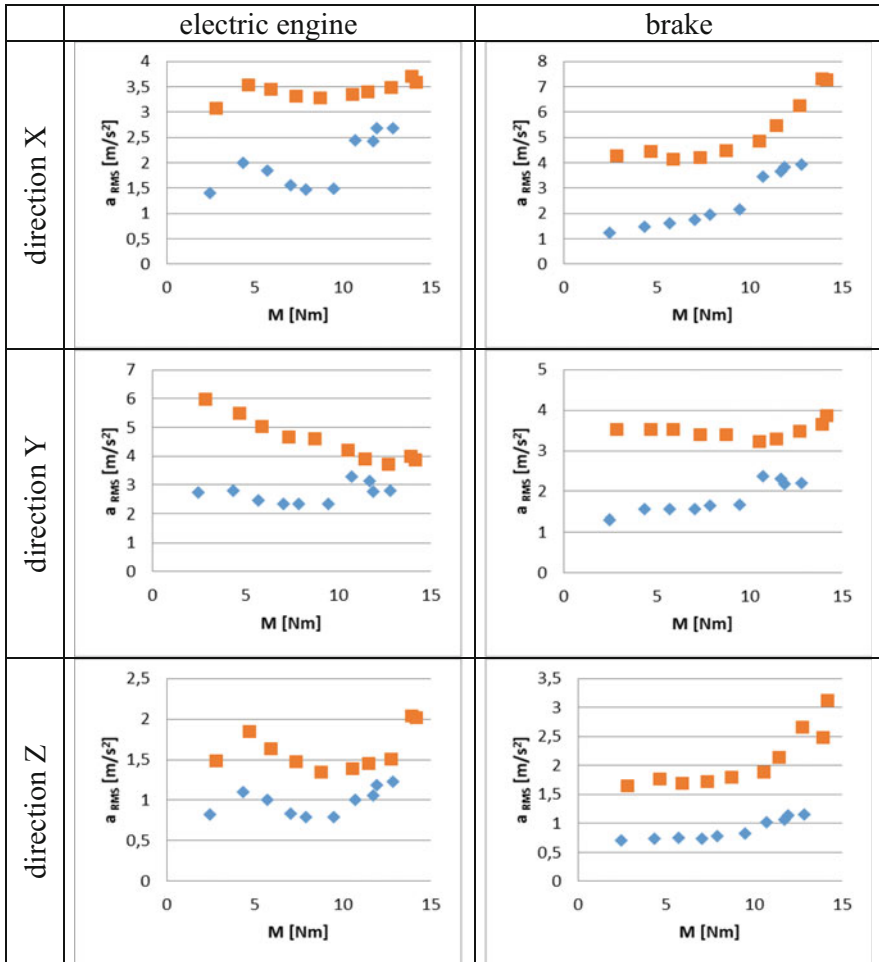


Fig. 3 Relation between the rpm value of vibration acceleration signals and the load on the belt, with the speed of 500 rpm (blue) and 1000 rpm (orange)

of the vibration signals along all the axes, for both the transmission and the driven shaft, with small loads applied to the transmission.

4 Results of the Analysis of the Influence of the Change in the Belt Tension on Selected Point Measures

In order to assess the influence of the change in the belt tension on the values of the point measures of vibration accelerations, an experiment was conducted consisting in changing the transmission load by applying two values of the belt tension. Three

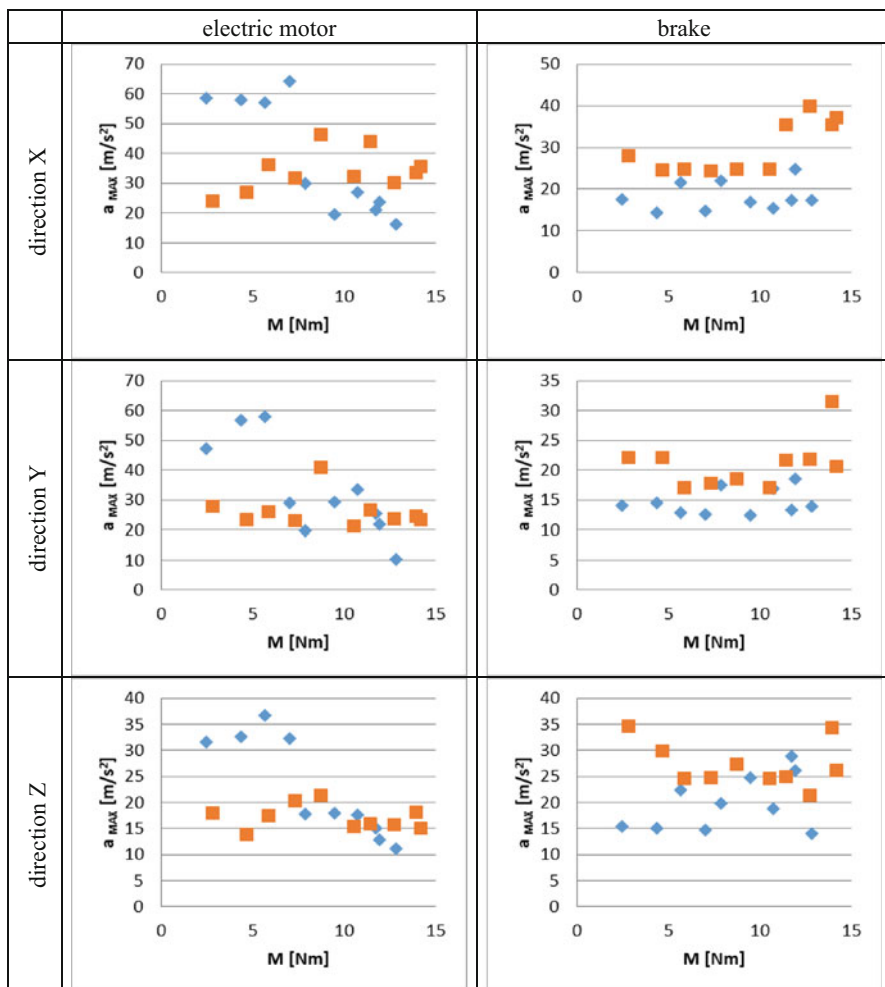


Fig. 4 Relation between the peak value of the vibration acceleration signals and the load on the transmission with the speed of 500 rpm (blue) and 1000 rpm (orange)

point measures were analyzed: the rpm value, the peak value and the kurtosis (for reasons of brevity, this paper discusses only the relation of the kurtosis of the signal acceleration and the load on the transmission with different belt tensions).

Figure 6 shows the changes of the kurtosis in the vibration acceleration signals in relation to the belt load. From the figure it can be determined that increasing the belt tension by 40 N results in an increase of the kurtosis of the vibration signals along the Z (recorded along the transmission shaft) and X axes.

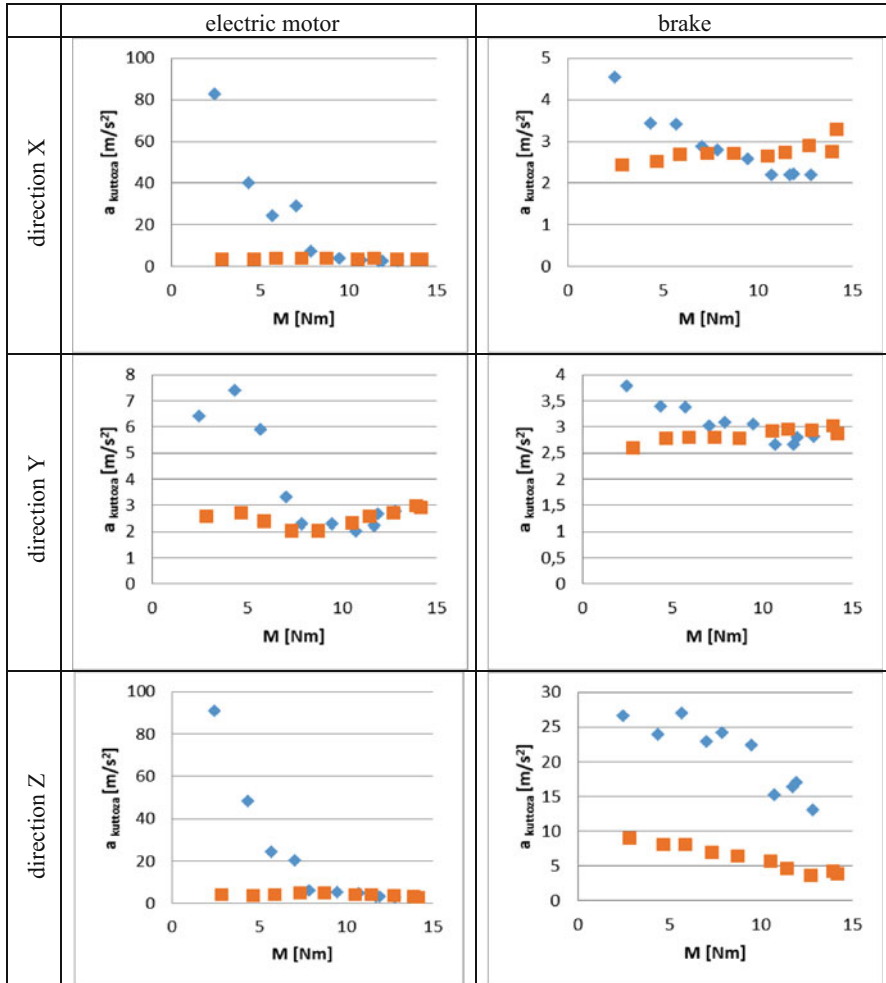


Fig. 5 Relation between the kurtosis of the vibration acceleration signals and the load on the transmission with the speed of 500 rpm (blue) and 1000 rpm (orange)

5 Determining the Vibration Frequency Generated by the Belt Drive

Based on the geometry of the belt drive and using kinematic relationships (e.g. belt transmission ratio), the hypothetical values of vibration frequencies can be assumed, which may later be searched for in the amplitude or envelope spectra. They were determined assuming the belt diameter (when formed in a circle) of 112 mm, and it's length 1420 mm. The vibration frequency caused by the interaction of the shaft and the belt has been shown in Table 1.

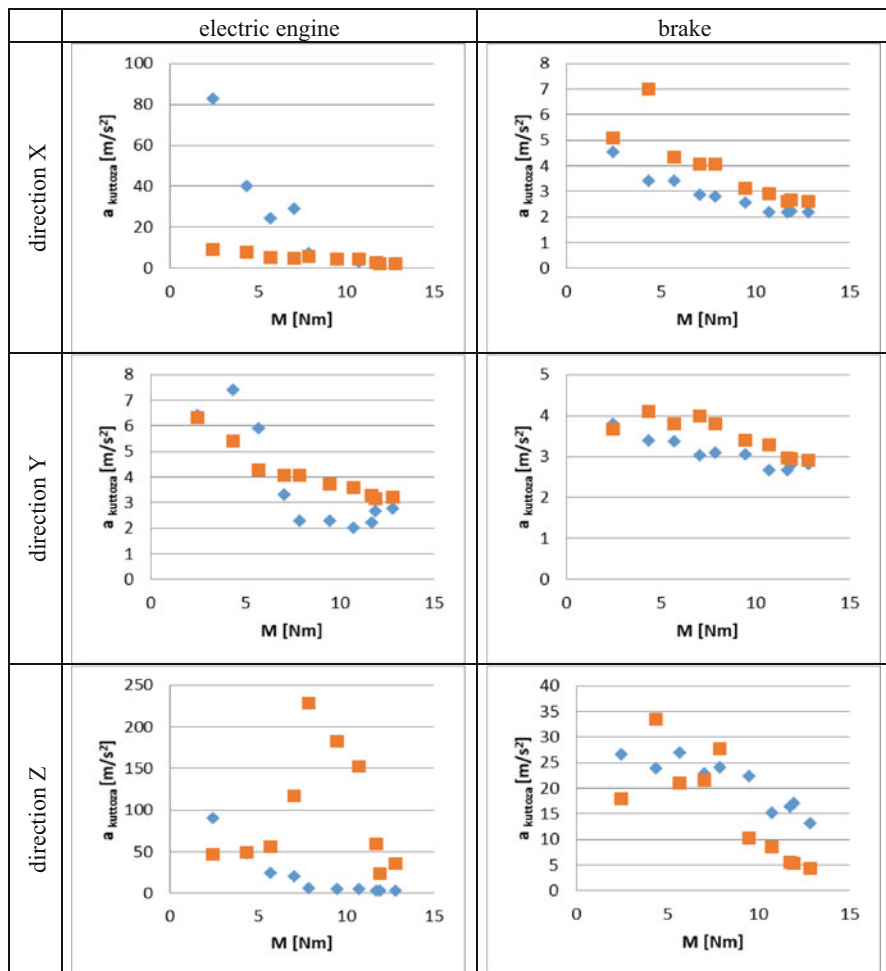


Fig. 6 Relation between the value of the kurtosis of the vibration acceleration signals and the load applied to the belt of two values (belt tension): 120 N (blue) and 80 N (orange)

6 Analysis of the Spectra of the Vibration Signal

Important for the vibration analysis is the assessment of the influence of the input parameters (speed of the shafts, load on the transmission, belt tension) on the spectra of the vibration acceleration signals. Figure 7a presents the influence of the changes in the load applied to the transmission on the vibration spectra measured on the housing of the of the transmission shaft bearing (the shaft speed of 500 rpm and the belt tension of 80 N). Figure 7b presents the changes in the vibration spectra with the shaft speed of 500 rpm and the belt tension of 120 N. The blue line in both

Table 1 Characteristic vibration frequencies related to the interaction between the transmission shaft and the belt

n [rpm]	f_{w-p} [Hz]	$2f_{w-p}$ [Hz]	$3f_{w-p}$ [Hz]	$4f_{w-p}$ [Hz]
500	17.06	34.13	51.19	68.25
495	16.72	33.45	50.17	66.89
490	16.39	32.78	49.16	65.55
485	16.05	32.11	48.16	64.22
480	15.73	31.45	47.18	62.90
475	15.40	30.80	46.20	61.60
470	15.08	30.15	45.23	60.31
465	14.76	29.52	44.27	59.03
460	14.44	28.88	43.33	57.77
455	14.13	28.26	42.39	56.52
450	13.82	27.64	41.46	55.29

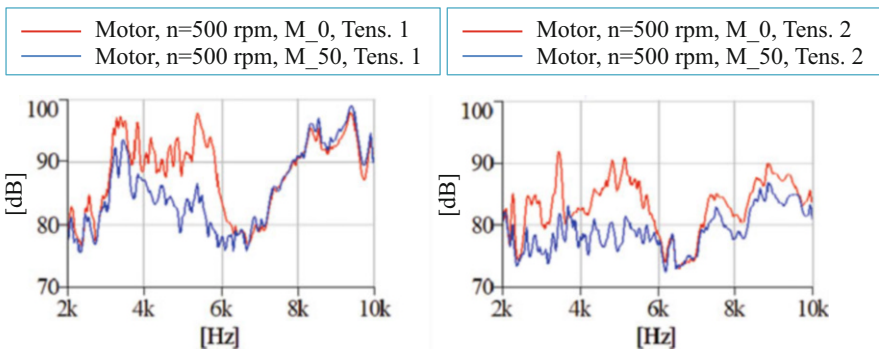


Fig. 7 The spectra of the vibration signal recorded on the belt transmission; (a) $n = 500$ rpm. Tension 1 = 80 N. (b) $n = 500$ rpm. Tension 2 = 120 N

figures indicates the spectra for the minimum load applied to the transmission and the red line - the spectra for the maximum load applied to the transmission.

The analysis of Fig. 7 leads to the following conclusions: when the belt tension equals 80 N, an increase in the vibration acceleration in the 2.8÷6 kHz band is observed with the maximum load on the transmission compared to the minimum load.

When the tension equals 120 N, the values of vibration acceleration increase in a wider band of 2.8÷6 kHz and 7÷10 kHz for the maximum load on the transmission compared to the minimum load. When comparing the frequency characteristics for the same loads, an increase is observed in the vibration activity in the 2.8–10 kHz band.

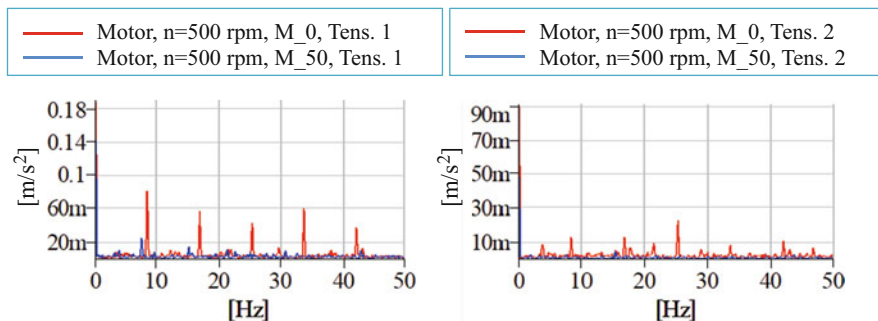


Fig. 8 Spectra from the envelope of the transmission vibration signals: (a) $n = 500$ rpm, tension 1 = 80 N. (b) $n = 500$ rpm, tension 2 = 120 N

7 Analysis of the Spectra in the Envelope of the Vibration Signal

During the final stage of the vibration assessment, the signal was filtered through a band-pass filter equivalent to the range of the resonance frequency. Then, the signal was demodulated in order to extract the signal envelope.

These signals could contain low-frequency modulations corresponding to the cyclical impulse phenomena resulting from the possible interaction of the belt contact with the pulley. Later on in this paper, the Hilbert's Transform was implemented for the time signals $a(t)$.

Figure 8a shows the influence of the changing load on the transmission on the vibration spectra measured for the transmission shaft with the shaft speed of 500 rpm and the belt tension of 80 N. Figure 8b presents the changes in the amplitude spectra with the shaft speed of 500 rpm and the belt tension of 120 N.

The analysis of Fig. 8 allows a conclusion that for smaller belt tension forces higher values are observed in the spectrum from the vibration acceleration envelope. Irrespective of the belt tension, with the increase in the load applied to the belt drive, a decrease in the values of the characteristic vibrations occurs.

8 Conclusions

This paper presented an analysis of the heat-sealed PU75A belt drive vibration. One of the belt's multiple advantages is the possibility of its heat-sealing at its ends, which allows making up a belt of any length, should a quick replacement become necessary. Based on the conducted research and its analysis, it was determined that the value of the kurtosis decreases along with the increase in the transmission load. An increase in the speed of the transmission shafts resulted in an increase in both the RMS and the peak values of the vibration signals recorded in all axes along

the transmission shaft as well as the driven shaft, with simultaneous increases of the kurtosis for the vibration signals along all axes along the transmission as well as the driven shafts with small loads applied to the transmission. An increase of tension by 40 N results in the elevated kurtosis along the Z axis (recorded along the transmission shaft) and along the X and Y axes (recorded along the driven shaft). It was also observed that the level of vibration acceleration in the $2.8 \div 6$ kHz band increased when using the maximum transmission load compared to the minimum load and when the applied belt tension force was 120 N, the level of vibration acceleration increased in a wider band, i.e. $2.8 \div 6$ kHz and $7 \div 10$ kHz for the maximum transmission load compared to the minimum load. With the increase in belt load, the values of the characteristic frequencies decrease regardless of the belt tension. The test results will certainly be useful for designers and people involved in the operation of belt transmissions where modern transport belts are applied.

Acknowledgments The presented research has been subsidized by the Ministry of Science and Higher Education 05/52/SBAD/0295 and 0416/SBAD/0001

References

1. Żóltowski, B., Ćwik, Z.: *Lexicon of Technical Diagnostics* (Original Title in Polish: *Leksykon Diagnostyki Technicznej*). ATR, Bydgoszcz (1996)
2. Osiński, Z.: *Vibration Damping* (Original Title in Polish: *Tłumienie drgań*). PWN, Warszawa (1997)
3. Bajkowski, J.: *Theorie Des Vibrations*. Office des Publications Universitaires, Oran (1989)
4. Bała, B., Sonmez, F.O., Cengiz, A.: Speed losses in V-ribbed belt drives. *Mech. Mach. Theory*. **86**, 1–14 (2015). <https://doi.org/10.1016/j.mechmachtheory.2014.11.016>
5. Gutowski, R., Swietlicki, Z.: *Dynamics and vibration of mechanical systems* (original title in Polish: *Dynamika i drgania układów mechanicznych*). s. (1986)
6. Krasieński, M., Stachoń, S.: Parametric vibration of transmission belts. *Mach. Dyn. Probl.* **22**, 65–75 (1998)
7. Abrate, S.: Vibrations of belts and belt drives. *Mech. Mach. Theory*. **27**(6), 645–659 (1992). [https://doi.org/10.1016/0094-114X\(92\)90064-O](https://doi.org/10.1016/0094-114X(92)90064-O)
8. Cepon, G., Manin, L., Boltežar, M.: Validation of a flexible multibody belt-drive model. *Strojniški vestnik. J. Mech. Eng.* **57**(7–8), 539–546 (2011)
9. Incerti, G.A.: Model for Analyzing the Startup Dynamics of a Belt Transmission Driven by a DC Motor. *Int. J. Mech. Mechatron. Eng.* **8**(9), 1537–1542 (2014)
10. Serridge, M., Licht, T.R.: *Piezoelectric accelerometers and vibration preamplifiers*. Brüel Kjær, Glostrup (1987)
11. Kumar, B., Kiran, G., Satyanarayana, S.: Determination of unbalance in rotating machine using vibration signature analysis. *Int. J. Mod. Eng. Res.* **2**(5), 3415–3421 (2012)
12. Cepon, G., Manin, L., Boltežar, M.: Introduction of damping into the flexible multi-body belt-drive model: a numerical and experimental investigation. *J. Sound Vib.* **324**, 283–296 (2009)
13. Ojha, S., Sarangi, D., Pal, B.K., Biswal, B.B.: Performance monitoring of vibration in belt conveyor system. *J. En. Res. Appl.* **4**(7), 22–31 (2014)
14. Hassan, A.R., Ali, K.M.: Dignosis of pulley-belt system faults using vibration analysis technique. *J. Univ. Babylon Eng. Sci.* **26**(2), 67–180 (2018)
15. Kubas, K.: A research stand for measuring friction parameters in a belt transmission. *Arch. Automot. Eng.* **75**(1), 69–83 (2017)

16. Ruijun, Z., Xinxin, S., Weiwei, Y., Nannan, W.: Analysis of resonance reliability for synchronous belt transmission with transverse vibration. *J. Vibroeng.* **16**(2), 891–900 (2014)
17. Krawiec, P.: Numerical analysis of geometrical characteristics of machine elements obtained through CMM scanning. In: *Progress in industrial mathematics*, pp. 925–930. Springer-Verlag, Berlin–Heidelberg (2010)
18. Kujawski, M., Krawiec, P.: Analysis of generation capabilities of noncircular cog belt pulleys on the example of a gear with an elliptical pitch line. *J. Manuf. Sci. E. T. ASME.* **133**(5), 051006 (2011)
19. Krawiec, P., Grzelka, M., Krocak, J., Domek, G., Kołodziej, A.: A proposal of measurement methodology and assessment of manufacturing methods of nontypical cog belt pulleys. *Measurement.* **132**, 182–190 (2019)
20. Krawiec, P., Marlewski, A.: Profile design of noncircular belt pulleys. *J. Theor. Appl. Mech.* **54**(2), 561–570 (2016)
21. Krawiec, P.: Analysis of selected dynamic features of a two-whwled transmission system. *J. Theor. Appl. Mech.* **55**(2), 461–467 (2017)
22. Krawiec, P., Waluś, K., Warguła, Ł., Adamiec, J.: Wear evaluation of elements of V-belt transmission with the application of optical microscope. In: *MATEC web of conferences 157*, pp. 01009–1–01009–8 (2018). <https://doi.org/10.1051/mateconf/201815701009>
23. Krawiec, P., Warguła, Ł., Waluś, K., Adamiec, J.: Wear evaluation study of the multiple grooved pulleys with optical method. In: *MATEC web of conferences 254*, pp. 01004–1–01004–8 (2019). <https://doi.org/10.1051/mateconf/201925401004>

Modeling and Experimental Tests on Motion Resistance of Double-Flanged Rollers of Rubber Track Systems Due to Sliding Friction Between the Rollers and Guide Lugs of Rubber Tracks



Piotr A. Dudziński  and Jakub Chołodowski 

Abstract Modern off-road vehicles are often equipped with rubber tracked undercarriages. While designing a rubber tracked crawler, an issue of high importance is to distinguish a power unit whose performance corresponds well with the actual power demand of the vehicle. In order to do so, algorithms for determination of external and internal motion resistance of rubber tracked vehicles are required. The Department of Off-Road Machine and Vehicle Engineering (DORMVE, Wrocław University of Science and Technology) conducts theoretical and experimental research aimed at development of advanced computational models of this type. Motion resistance of rollers (road wheels) is one of the factors affecting the energy consumption of rubber tracked undercarriages. Firstly, since the rollers are loaded with vertical force, they indent into rubbery envelope of the track. Consequently, some amount of energy is lost due to mechanical hysteresis of rubber. Secondly, motion resistance of rollers is attributed to sliding friction between the rollers and guide lugs of the track. Energy losses caused by this phenomenon are noticeable if rollers are loaded with high lateral force, i.e. while turning or operating a vehicle on a slope inclined along the lateral axis of the vehicle. The article presents a model for estimation of motion resistance of double-flanged rollers of rubber tracked undercarriages allowing for both abovementioned phenomena. The results of exemplary model computations will be compared with experimental data.

Keywords Rubber tracked undercarriage · Rollers · Internal motion resistance

P. A. Dudziński · J. Chołodowski (✉)

Wrocław University of Science and Technology, Department of Off-Road Machine and Vehicle Engineering, Wrocław, Poland

e-mail: jakub.cholodowski@pwr.edu.pl

© Springer Nature Switzerland AG 2021

J. Awrejcewicz (ed.), *Perspectives in Dynamical Systems III: Control and Stability*,

Springer Proceedings in Mathematics & Statistics 364,

https://doi.org/10.1007/978-3-030-77314-4_11

1 Introduction

Undercarriages of modern earthmoving and agricultural machinery as well as other commercial vehicles are often fitted with rubber tracks nowadays. On the other hand, the literature review does not bring any comprehensive model summarizing motion resistance of the most common rubber tracked vehicles, enabling detailed analyses of the phenomena leading to losses in rubber track systems, e.g. interaction between rollers (road wheels) and tracks, repetitive bending of the tracks while passing over drive and idler wheels of track systems, transverse vibrations of the tracks, etc. [1]. Consequently, while designing a rubber tracked vehicle, it is hard to distinguish a power unit of performance meeting the actual power demand of the vehicle. It is also challenging to optimize the undercarriage design so that its energy consumption were possibly small. Therefore, The Department of Off-Road Machine and Vehicle Engineering (DORMVE, Wrocław University of Science and Technology) has been conducting extensive theoretical and experimental research contributing to development of the abovementioned models.

The research conducted by DORMVE includes considerations on the losses caused by the interaction between road wheels and rubber tracks. These losses are attributed to two phenomena. Firstly, since the rollers indent into the rubbery surface of the tracks, some amount of energy is lost due to mechanical hysteresis of rubber. Secondly, sliding friction between the rollers and guide lugs of the tracks occurs. The authors of the article have already carried out the experiments on exemplary double-flanged rollers for “pure rolling” case, i.e. where the losses are caused only by the indentation of rollers into the track surface, as well as in the load conditions where sliding friction between the rollers and the guide lugs occurs [2, 3].

According to the results obtained in [2, 3] and the literature data [4], the indentation losses can be successfully calculated with the models derived as a result of the theoretical considerations on the resistance caused by indentation of idlers into conveyor belts, discussed e.g. in [5, 6]. In [3] the authors of the article estimated the parameters of these models for exemplary double-flanged rollers coupled with rubber tracks. Furthermore, in [2, 7], they carried out experiments and presented a theoretical-empirical model illustrating the influence of non-uniform contact pressure distribution between a double-flanged roller and inner track surface on rolling resistance coefficient.

The resistance attributed to sliding friction between road wheels and guide lugs of rubber tracks has not been discussed in the literature in many details. Any analogies cannot be also found in the literature pertaining to belt conveyors. On the other hand, the research done in this field by the authors [2] indicates that in the conditions where sliding friction between rollers and the guide lugs occurs, the overall motion resistance of the rollers is higher by 1.5 ... 7.7 times than the resistance noted in the “pure rolling” case. The magnitude of the increase depends basically on the vertical load of the rollers. Thus, a strong need to formulate a model representing motion resistance of rollers in these conditions was revealed. In the previous papers the authors presented a simplified, empirical model whose only parameter was the

roller vertical load. The following article presents an upgraded one, which allows for the roller vertical and lateral load as well as geometrical dimensions of the track and sliding friction coefficient for roller-guide lug contact surface.

2 Model Assumptions

Figure 1 illustrates a double-flanged roller, a rubber track and forces acting on both of them. The scheme was involved in formulating the model representing motion resistance of a double-flanged roller in the conditions where sliding friction between the roller and guide lugs of the track occurs. The vertical and lateral load of the roller, represented by G and F_s , equal the ground vertical and lateral reaction forces F_z and F_y . Considering the equilibrium of forces acting on the roller, it was assumed that forces acting from the track on the roller are: the normal reaction force acting from the guide lug on the roller F_n , the reaction force tangent to the roller-guide lug contact surface T attributed to sliding friction and the F_v which represents the overall vertical reaction force acting from the inner track surface on the circumference of the roller. According to the assumptions, the roller lateral load F_s is balanced completely by the forces acting from the guide lug on the roller. A lateral reaction force that could occur in the contact area between the inner track surface and the roller circumference was neglected. The only force acting from the inner track surface on the roller is the F_v , which counteracts the roller vertical load G . Since some fraction of the roller vertical load is balanced by the roller-guide lug contact reaction forces, the G and F_v forces do not equal each other.

In the load conditions described above the overall roller motion resistance force F_R is given with Eq. 1. Namely, it is a sum of the F_{Roll} (Eq. 2) and F_μ (Eq. 3) forces that represent the losses caused by the indentation of the roller into the inner track surface and the sliding friction between the roller and the guide lugs, respectively.

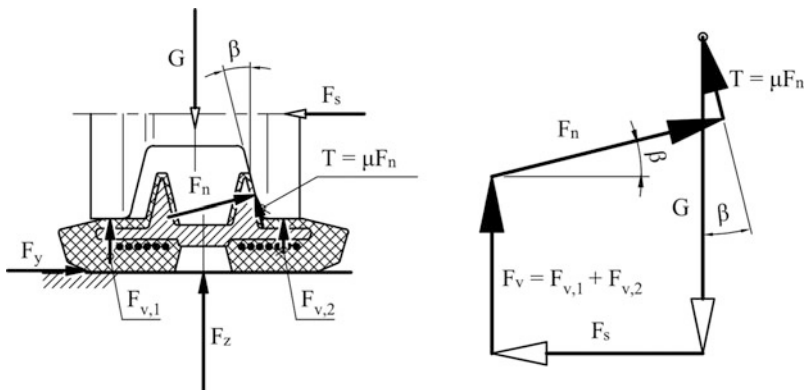


Fig. 1 A drawing illustrating the main assumptions of the model

Equations 5 and 6, representing forces F_n and F_v , were derived on the basis of equations of equilibrium of forces acting on the roller. The reaction force T tangent to the roller-guide lug contact surface is given with Eq. 4.

$$F_R = F_{Roll} + F_\mu \quad (1)$$

$$F_{Roll} = A \bullet F_v^q \quad (2)$$

$$F_\mu = \mu F_n \quad (3)$$

$$T = \mu F_n \quad (4)$$

$$F_n = \frac{F_s}{\cos \beta - \mu \sin \beta} \quad (5)$$

$$F_v = G - F_n (\sin \beta + \mu \cos \beta) \quad (6)$$

- A [$1/N^{q-1}$] – a coefficient representing the indentation losses – depends on elasticity modulus and damping properties of the rubber track as well as radius and width of the roller,
- q [-] – an exponent representing the indentation losses – is defined by the shape of the roller and track surface,
- μ [-] – sliding friction coefficient for contact surface between the roller and guide lugs,
- β [$^\circ$] – an angle representing the slope of side surface of the guide lug (vide Fig. 1)

3 Experimental Tests and Model Verification

3.1 Course of the Experiment

The model was verified on the basis of the data collected during the experiments carried out on the double-flanged roller and the 72 mm pitched rubber track with transverse stiffening metal molds depicted in Fig. 2. The roller and the track are commercially available spare parts of the mini dump truck IHIMER Carry 107.

The test stand depicted in Fig. 3 was involved in the experiments. It is fitted with a measurement plate for measuring vertical, lateral and longitudinal force acting on the upper surface of the plate. Referring to the Fig. 1, these forces correspond to the vertical and lateral load of the roller and the force representing roller motion

Fig. 2 Dimensions of the roller and the rubber track involved in verification of the model

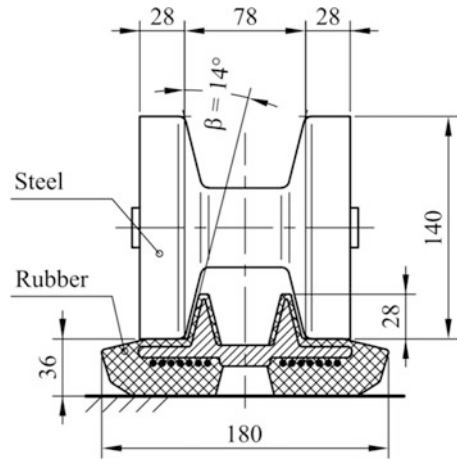


Fig. 3 The test stand involved in the experimental tests on motion resistance of double-flanged rollers carried out in the laboratory of DORMVE at Wrocław University of Science and Technology

resistance. The investigated track was aligned along the plate and fixed to its upper surface. On the other hand, the roller was connected with an upper arm of the stand with a revolute joint and pressed against the inner track surface by the gravity force acting on the upper arm and weights optionally attached to the arm. The roller rolls over the track when the measurement plate is moved along the stand. During the tests being in the scope of the article the axis of symmetry of the track was intentionally misaligned with respect to the axis of symmetry of the roller so that sliding friction between the roller and guide lugs of the track occurred. The experiments conducted herein were divided into two sessions. In the first one the misalignment between the axes of symmetry of the roller and the track was kept at constant, whereas the vertical load of the roller was set at various values. On the other hand, in the second session the tests were carried out at constant vertical load and variable amount

of the misalignment. Consequently, a variety of load conditions, including roller vertical loads of 150 N ... 2500 N and lateral load varying from 0 N to 360 N, was considered. Every dataset acquired during the experiments consisted of three values representing the average value of roller vertical and lateral load as well as roller motion resistance.

3.2 A Method for Estimation of Model Parameters

Before the model was verified, its parameters had been estimated for the considered roller and track. The values of the A and q parameters were estimated at the ones determined in [3], where the experiments on the same roller and track in the “pure rolling” case were carried out. The β angle was calculated on the basis of geometrical dimensions of the guide lugs measured with a caliper. Eventually, sliding friction coefficient μ was estimated involving the assumed values of the A , q and β parameters as well as selected datasets obtained as a result of the first session of the experiments. Namely, the μ coefficient was estimated at a value minimizing the Eq. 7.

$$err_{\mu}(\hat{\mu}) = \sum_{i=1}^N \left(\left[\frac{F_{s,exp,i}}{\cos \beta - \hat{\mu} \sin \beta} \hat{\mu} + A \left(G_{exp,i} - F_{s,exp,i} \frac{\sin \beta + \hat{\mu} \cos \beta}{\cos \beta - \hat{\mu} \sin \beta} \right)^q - F_{R,exp,i} \right]^2 \right) \quad (7)$$

- $\hat{\mu}$ [-] – the estimate of sliding friction coefficient for contact surface between considered double-flanged roller and rubber track guide lug,
- $G_{exp,i}$ [N] – average roller vertical load determined in i -th experiment involved in sliding friction coefficient estimation,
- $F_{s,exp,i}$ [N] – average roller lateral load determined in i -th experiment,
- $F_{R,exp,i}$ [N] – average roller motion resistance determined in i -th experiment.

The function given with the Eq. 7 was obtained by squaring the left-hand side of Eq. 8, which was derived by substituting the formulas Eqs. 2, 3, 5 and 6 into the Eq. 1 and performing further transformations.

$$\frac{F_s}{\cos \beta - \mu \sin \beta} \mu + A \left(G - F_s \frac{\sin \beta + \mu \cos \beta}{\cos \beta - \mu \sin \beta} \right)^q - F_R = 0 \quad (8)$$

If the model properly reproduces the phenomenon discussed in the paper and the model parameters are correct, the equality given with the Eq. 8 is true for every experimental dataset. However, if at least one of these conditions is not fulfilled, the Eq. 7 represents the overall estimation error for a specific set of model parameters and N experimental datasets.

3.3 Verification of the Model and Model Computations

The model parameters for the roller and the track shown in Fig. 2 were estimated at the following values:

- $A = 0.0034 \text{ N}^{-0.35}$,
- $q = 1.35$,
- $\beta = 14^\circ$,
- $\mu = 0.21$.

The results of the first and the second measurement session are presented in Figs. 4 and 6, respectively. Motion resistance of the investigated roller was expressed with a coefficient of motion resistance f calculated according to Eq. 9.

$$f = \frac{F_R}{G} \quad (9)$$

Referring to the results of the first measurement session, the model was verified using only the experimental data that were not involved in μ parameter estimation discussed in the Sect. 3.2. At medium and high roller vertical loads, i.e. $G > 450 \text{ N}$, the estimation error did not exceed the values determined in the experiments by no more than 12%, whereas the average error was not higher than 2.2%. The estimation error did not indicate any specific trend.

A significant overestimation of roller motion resistance was noted at small vertical loads. For example, in the load conditions defined by $G = 172 \text{ N}$ and $F_s = 218 \text{ N}$ the coefficient of motion resistance computed with the model exceeded the experimental value by 85%. This discrepancy might be explained by the fact that the actual character of the interaction between the roller and the track does not strictly follow the model assumptions.

The model assumes that while the roller is rolling over the track, it always makes contact with the inner track surface as well as it slides against at least one guide lug of the track. During the experiments some specific load conditions could have been distinguished where the roller did not touch the guide lugs continuously. In order to represent roller motion resistance in these conditions, the relationship Eq. 10 should be used instead of the Eq. 1.

$$F_R = \lambda \bullet (F_n \mu + A \bullet F_v^q) + (1 - \lambda) \bullet A \bullet G^q \quad (10)$$

$$\lambda = s_{sf} / s_{ovl} \quad (11)$$

- s_{sf} [m] – a distance covered by the roller while rolling over the track and sliding against the surface of the guide lugs,
- s_{ovl} [m] – the overall distance covered by the roller while rolling over the track.

The λ parameter introduced in the Eq. 10 is a dimensionless coefficient that changes its value from 0 to 1, depending on the roller load conditions. Equation 10

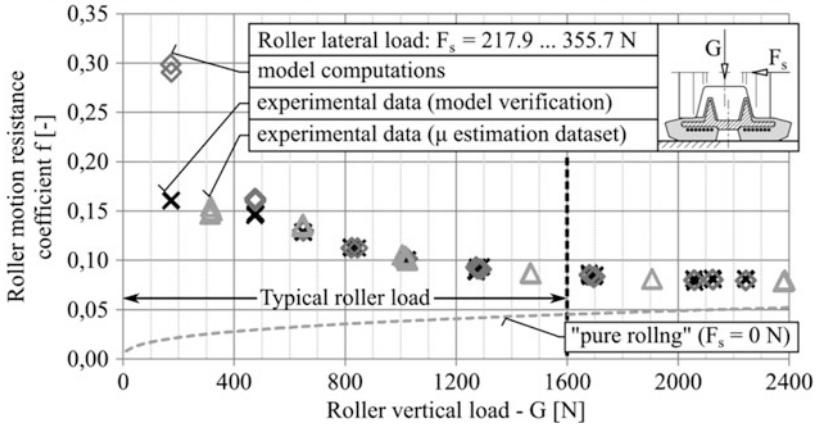


Fig. 4 Coefficient of motion resistance of the roller depicted in Fig. 3 as a function of roller vertical load – experimental results of the first measurement session compared with the results of the model computations

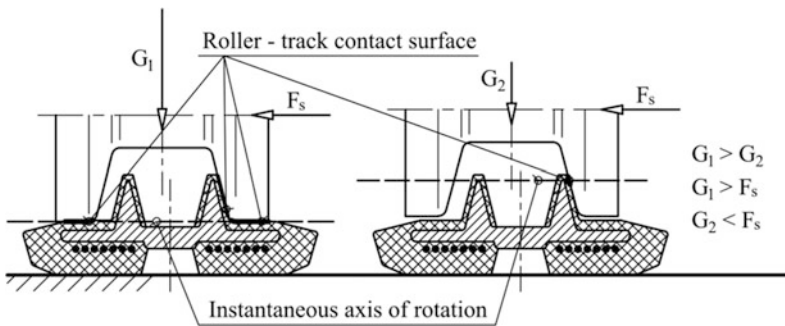


Fig. 5 The character of interaction between the roller and rubber track observed in the experiments conducted herein depending on load conditions of the roller

allows for the fact that if the roller does not make contact with any guide lug while rolling over the track, the entire roller vertical load is counteracted by the vertical reaction force acting from the inner track surface on the roller circumference. Value of the λ parameter was computed for every dataset presented in Fig. 4, assuming sliding friction coefficient $\mu = 0.21$. The λ parameter was equal to 1 at roller vertical loads exceeding 478 N, whereas at smaller loads it was smaller than 1. For example, in the load conditions defined by $G = 320 \text{ N}$ and $F_s = 290 \text{ N}$ the λ parameter was estimated at 0.64.

Furthermore, during the experiments in the conditions where $G \leq F_s$, the circumferential surface of the roller lost contact with the inner track surface, whereas the contact area between the roller and the guide lugs was so small that it resembled a single point (vide Fig. 5). This also does not correspond well with the model assumptions discussed in Sect. 2.

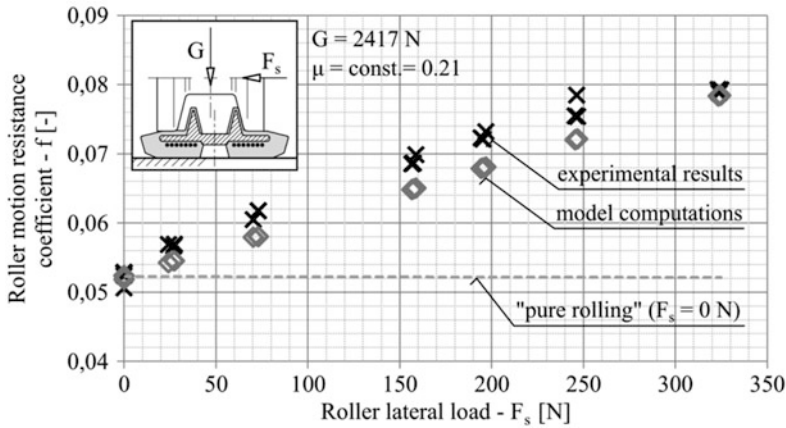


Fig. 6 Coefficient of motion resistance of the roller depicted in Fig. 3 as a function of roller lateral load – experimental results of the second measurement series compared with the results of the model computations

The model was also verified with reference to all the data obtained in the second measurement session. Assuming a constant value of sliding friction coefficient $\mu = 0.21$, the maximum estimation error was not higher than 8.1%, whereas the average one did not exceed 4.2%. The magnitude of the error was acceptable, however, the results of the model computations generally underestimated the experimental data. For this reason, in order to improve the model accuracy, the following approach was embodied in the model. Firstly, friction coefficient μ was estimated individually for various combinations of the roller vertical and lateral load considered in the experiments, according to the method discussed in the Sect. 3.2. Afterwards, the relationship between the μ coefficient and the normal reaction force acting from the guide lugs on the roller F_n was found (vide Fig. 7) and implemented in the model. This approach improved the performance of the model. The maximum estimation error was decreased to 2.5%, whereas the average one was 0.8%.

Every value of the μ coefficient shown in Fig. 7 was estimated on the basis of the results obtained in three separate experiments conducted in particular load conditions. The values of the F_n forces were calculated according to the Eq. 5, using the averaged results of the experiments. The relationship presented in Fig. 7 might be claimed to be reliable. A decrease in the normal reaction force acting from the guide lug on the roller resulted in an increase in sliding friction coefficient μ . Moreover, the relationship can be successfully approximated with a power function whose exponent equals $-1/9 \dots -1/3$, which corresponds well with the literature [8–10] where sliding friction between rigid bodies against surfaces made from rubber was broadly discussed. It should be underlined, that while estimating the μ values presented in the Fig. 7, $\lambda = 1$ was assumed (vide Eq. 10). If smaller values of the λ parameter were involved in the considerations, the estimated sliding friction coefficient μ would be higher.

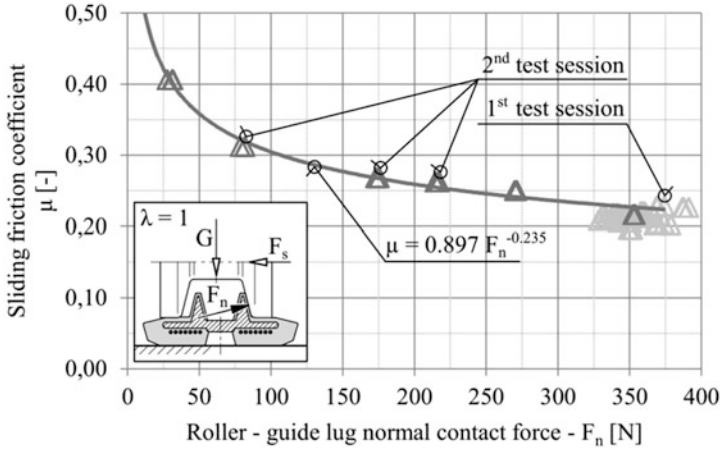


Fig. 7 The estimated values of sliding friction coefficient for roller-guide lug contact surface as a function of normal reaction force acting on the roller from the guide lugs

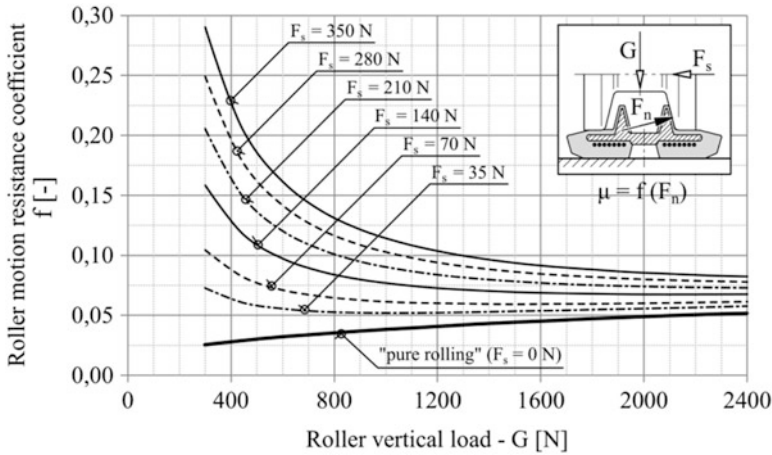


Fig. 8 Exemplary results of model computations of motion resistance for the roller depicted in Fig. 3 in load conditions defined by various vertical and lateral loads

Figure 8 summarizes the considerations presented in the paper. It shows the results of exemplary model computations of motion resistance coefficient carried out for the roller and the track investigated in the article in various load conditions. The results allow for the relationship represented by the Fig. 7, however, $\lambda = 1$ was assumed.

The biggest increase in roller motion resistance due to sliding friction between the rollers and the guide lugs was observed at relatively small roller vertical loads. For example, if lateral load of 35 N were applied to the roller loaded with a vertical

load $G = 400$ N, motion resistance of the roller would increase by up to 2.3 times in comparison with the resistance to motion manifested by the roller while rolling with no contact with the guide lugs. On the other hand, if the same lateral load were applied to the roller loaded with a vertical load of 1200 N, the analogous increase would be 1.28 times. Using the model formulated in the paper, a ratio of the roller motion resistance attributed to sliding friction between the roller and the guide lugs to the overall roller motion resistance might be calculated. According to the computations performed herein, the smaller the roller vertical load, the higher the ratio is. For example, in the load conditions defined by the roller lateral load of 35 N and vertical load of 400 N the ratio was estimated at 60%. On the other hand, at the same lateral force and vertical load of 1200 N it was as small as 24%. The ratio also increases with increasing lateral load of the roller.

The situation discussed above arises from the fact that the relationship between the force representing losses due to the roller indentation into the inner track surface and the force F_v which causes the indentation is approximated by a power function whose exponent is greater than 1. In practice, the F_v force is close to the roller vertical load. The fraction of the roller vertical load balanced by the reaction forces acting from the guide lugs on the roller is relatively small because sliding friction coefficient μ and the β angle representing the slope of the side surface of the guide lugs are very limited.

4 Summary and Conclusions

The article presents a model for computing motion resistance of double-flanged rollers while rolling over rubber tracks. The model represents the losses caused by the indentation of the rollers into the inner surface of the tracks as well as the sliding friction between the rollers and guide lugs of the tracks. It allows for the vertical and lateral load of the rollers.

The model might be successfully applied in engineering computations of the internal motion resistance of double-flanged rollers in rubber track systems. At medium and high vertical loads and high lateral load of the roller involved in model verification, motion resistance of the roller was correctly estimated with a basic version of the model, i.e. assuming that sliding friction coefficient for the roller-guide lugs contact surface could have been approximated with a constant value. However, it is advisable to implement in the model the relationship between the sliding friction coefficient for roller-guide lugs contact surface and the normal reaction force acting on the roller from the guide lugs. Otherwise, at small roller lateral loads the model would underestimate motion resistance of the roller. The results of model computations given in Fig. 8 allow for this relationship.

The model verification carried out herein revealed that if the vertical load of the roller investigated in the article is small, the model overestimates the roller motion resistance. This was caused by the differences between model assumptions and the actual character of the interaction between the roller and the track – mainly by the

fact that in some load conditions the roller did not maintain an unbroken contact with the guide lugs while rolling over the track. In order to solve this problem, an improved formula for determination of motion resistance of rollers was proposed (Eq. 10). The formula involves the λ coefficient representing the ratio of the distance covered by a roller while rolling over a track and sliding against the surface of guide lugs to the overall distance covered by the roller. The forthcoming research by the authors will be focused on developing a method for predicting the λ coefficient depending on the roller load conditions. The results of the model computations presented herein (Fig. 8) were obtained assuming that the investigated roller made continuous contact with at least one guide lug while rolling over the track ($\lambda = 1$).

The experiments and the model calculations performed in the paper indicate that sliding friction between double-flanged rollers and guide lugs of rubber tracks leads to significant increase in motion resistance of the rollers. The increase is exceptionally high at small vertical and high lateral loads of the rollers. Sliding friction between the rollers and the guide lugs may arise while a vehicle performs turning maneuvers or negotiates a terrain inclined along the vehicle's lateral plane. Thus, the problem highlighted in the paper cannot be neglected in engineering computations pertaining to energy consumption of rubber tracked vehicles.

The forthcoming research by the authors will be focused on integrating the model presented herein with the one derived in [7] in order to formulate a comprehensive model for determination of motion resistance of double-flanged rollers over rubber tracks.

References

1. Chołodowski, J., Dudziński P.: A method for experimental identification of bending resistance of reinforced rubber belts. In: Computational technologies in engineering (TKI 2018): proceedings of the 15th Conference on Computational Technologies in Engineering, pp. 1–8. AIP Publishing, Melville, NY (2019)
2. Dudziński, P., Chołodowski, J.: Energy efficiency of rubber tracked chassis. *Journal of KONES*. **23**(2), 97–104 (2016)
3. Dudziński, P., Chołodowski, J., Ketting, M.: Experimental tests on rolling resistance of road wheels in rubber tracked undercarriages. In: Engineering Mechanics 2018: 24th international conference, pp. 197–200. Czech Academy of Sciences, Prague (2018)
4. Rehorn, I.: Entwicklung eines Tiefseeraupenfahrzeugs und Untersuchung seiner inneren Fahrwiderstände (Ph.D. thesis supervised by Univ.-Prof. Dr.-Ing. W. Schwarz). Universität-Gesamthochschule Siegen, Verlag Shaker, Aachen (1994)
5. Gładysiewicz, L.: Belt Conveyers: Theory and Design Computations. Wrocław University of Science and Technology Publishing House, Wrocław (2003) (in Polish)
6. Lachmann, H.-P.: Der Walkwiderstand von Gummigurtt Förderern. *Forschung auf dem Gebiete des Ingenieurwesens*. **20**(4), 97–107 (1954)
7. Chołodowski, J., Dudziński, P.: Method for estimation of road wheels rolling resistance in rubber track systems. In: Engineering Mechanics 2018: 24th international conference, pp. 161–164. Czech Academy of Sciences, Prague (2018)
8. Dudziński, P., Konieczny, A.: An innovative vehicle of adaptive mobility for locomotion along cables. *Transport Przemysłowy i Maszyny Robocze*. **25**(3), 74–80 (2014) (in Polish)

9. Greenwood, J.A., Tabor, D.: The friction of hard slider on lubricated rubber: the importance of deformation loss. *Proc. Phys. Soc.* **71**(pt. 6), 989–1002 (1957)
10. Schallamach, A.: The load dependence of rubber friction. *Proc. Phys. Soc.* **65**(pt. 9-B), 657–661 (1952)

Structural Dynamic Response of Coupling Between Transmission Line and Tower Under Random Excitation



Yanne Marcela Soares Fernandes, Marcela Rodrigues Machado ,
and Maciej Dutkiewicz 

Abstract The study of the dynamic behaviour of the overhead transmission line is highly relevant when the objective is to ensure its stability and maintenance. This paper aims to analyse an overhead transmission line under different types of random wind excitation that simulate natural phenomena in situ represented by white noise, Kani-Tajimi and First-order filter spectrum. The numerical model regards the Spectral Element Method (SEM) to overcome the dynamic analysis from low to high frequencies and simple implementation. The numerical analysis performed through the SEM investigates the overhead transmission receptance and natural frequency and compares with the results obtained by the Finite Element Method (FEM). Since SEM is an exact method of solution, there is no need for discretised continuous elements, which means less computational time-consuming and easy access to the model formulation. The vibration responses of the system suffered greater variations when the overhead transmission is under random wind excitation, which leads in challenging to design vibration control devices and performs its health monitoring. SEM model performed satisfactorily and accurate results in comparison with FEM. It shows to be an alternative tool for analysing the dynamics of structures.

Keywords Overhead transmission tower-line system · Vibration analysis · Random excitation · Wind loads

Y. M. S. Fernandes · M. R. Machado (✉)
Faculdade de Tecnologia, University of Brasília, Brasília, Brazil
e-mail: marcelam@unb.br

M. Dutkiewicz
University of Science and Technology, Bydgoszcz, Poland

© Springer Nature Switzerland AG 2021
J. Awrejcewicz (ed.), *Perspectives in Dynamical Systems III: Control and Stability*,
Springer Proceedings in Mathematics & Statistics 364,
https://doi.org/10.1007/978-3-030-77314-4_12

1 Introduction

In many countries, as well as in Brazil, electric energy travels large distances from the generation points to the final consumer, increasing the demand for energy transmission systems. In this context, overhead transmission lines (OTL) appear as a widely used solution. Theoretical and experimental studies on overhead transmission lines are presented in [1–4]. As the high and extension of the transmission systems increase, the demand for safety and reliability of these structures increases with the high and extension of the transmission systems [5]. Transmission towers are responsible for supporting their weight, resisting the effects of conductor cables, wind and rain loads that enhance the complexity of dynamic analysis of the system. Leon and Smith [6] analysed the transmission lines with cross suspension through experimental and numerical tests employing FEM. McClure and Lapointe [7] presented the OTL dynamic analysis using the software ADINA and performed studies about failures in the OTL. Dua et al. [8], and Desai et al. [9] carried out a dynamic analysis of the OTL using FEM to demonstrate the vibrational amplitudes behave at different OTL intervals and showed the interaction of the cables-towers by adding equivalent stiffness and fixed supports. Fu and Li [10] presented a study on OTL with the effect of random excitation of wind and rain forces and compared the results of experimental and numerical tests. Generally, the structural and dynamic analyses are usually performed using FEM, although this method in medium and high frequencies or structures with high modal density presents a high computational cost. In this way, a fast and easy method that considers all the loads and uncertainties necessary for an accurate study is required.

SEM is a mesh method similar to FEM, where the functions of approximate forms of the element are replaced by functions of the exact solution of differential equations of government. Therefore, a single element is enough to model any continuous and uniform part of the structure. This feature significantly reduces the number of elements required in the structure model and improves the accuracy of the dynamic system solution. An extensive study of the fundamentals and a variety of new applications of SEM, such as composite laminates, periodic structure, damage detection was presented in [11]. The behaviour of the waves in composites and non-homogeneous media are studied in [12–14]. Theory of elementary and high order bars was performed in [15–17], and in a conductor cable of transmission line in [1, 18–21]. However, SEM has some disadvantages when compared to FEM as the unavailability of exact wave solutions for more complex 3D structures. In these cases, approximate spectral element modelling can be used and can still provide very accurate solutions. Besides, SEM guarantees an accurate response in the frequency domain, and for time-domain solutions, which require special attention is needed to obtain the inverse DFT. Dynamic excitations arise from natural phenomena such as impacts, gusty winds, rain, earthquake ground motion, sea waves. There are situations where devices are operating under unknown or random excitations. In structural analysis, random excitation is generally modelled as a white noise which is a Gaussian stochastic process [22]. However, random excitation is better

represented by other spectrum types such as first-order filter (FOF) and Kanai–Tajimi models. Several approaches have been proposed to treat with the challenging problem of characterizing the random response of a structural system under stochastic excitation [23–25]. The random excitation is usually specified regarding its power spectral density (PSD), which is a function that describes the power content distribution of a quantity over a given frequency band. This paper treats the dynamic analysis of an overhead transmission span composed by tower and conductor-cable under random wind excitation. The tower is a massive structure compared with the conductor. However, both component presents its local and global vibration characteristic. Therefore, the dynamic coupling behaviour between tower and cable structural is analysed. The SEM is used to model the whole system under random excitation that represents the wind force action. Numerical analyses showed that the efficiency to use SEM in such application.

2 Spectral Element Theory

2.1 Beam Spectral Element with Axial Load

By considering a simplified cable model as illustrate in Fig. 1, the governing differential equation for the undamped free vibration is given by [15, 26],

$$EI \frac{\partial^4 v(x, t)}{\partial x^4} + \rho A \frac{\partial^2 v(x, t)}{\partial t^2} - T \frac{\partial^2 v(x, t)}{\partial x^2} = 0 \tag{1}$$

For a simply supported beam under axial force, the natural frequency expressed as

$$\omega_n = \frac{\pi^2}{L^2} \sqrt{\frac{EI}{\rho A}} \left(n^4 + \frac{n^2 T L^2}{\pi^2 EI} \right) \tag{2}$$

where ρA is mass per unit length, EI the uniform bending rigidity, L cable length, T is tension force, and $v(x, t)$ is the cable displacement as a function of the position x and time t .

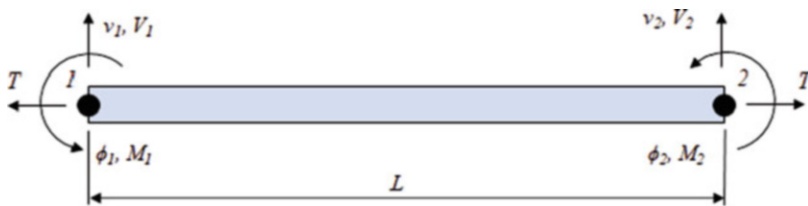


Fig. 1 Two-node cable spectral element

Structural internal damping is introduced into the beam formulation by adding into Young's modulus weighted by a complex damping factor $i\eta, i = \sqrt{-1}$, η is the hysteretic structural loss factor, to obtain $E = E(1 + i\eta)$. By considering a constant coefficient, the displacement solution can be written as,

$$v(x, t) = v_0 e^{-i(kx - \omega t)} \quad (3)$$

where v_0 is a amplitude, ω is the frequency and k is the wave number. Substituting Eq. (3) into Eq. (1), yields a fourth-order characteristic polynomial equation in k

$$k^4 EI + k^2 T - \omega^2 \rho A = 0 \quad (4)$$

The solution of Eq. (4) leads to four roots solution representing two sets of wave mode pairs, which are the two pairs of wave modes, in the positive and negative directions,

$$k_1 = \pm \sqrt{\frac{-T + \sqrt{T^2 + 4EI\rho A\omega^2}}{2EI}} \quad (5)$$

$$k_2 = \pm i \sqrt{\frac{-T - \sqrt{T^2 + 4EI\rho A\omega^2}}{2EI}} \quad (6)$$

where k_1 is the real part of the wavenumber and k_2 the imaginary part [21]. The general solution for the Euler-Bernoulli beam spectral element subjected to axial load of length L , can be expressed in the form as

$$\widehat{v}(x, \omega) = a_1 e^{-ik_1 x} + a_2 e^{-k_2 x} + a_3 e^{ik_1(L-x)} + a_4 e^{k_2(L-x)} = \mathbf{s}(x; \omega) \mathbf{a} \quad (7)$$

where

$$\mathbf{s}(x, \omega) = [e^{-ik_1 x}, e^{-k_2 x}, e^{ik_1(L-x)}, e^{k_2(L-x)}]$$

$$\mathbf{a} = [a_1, a_2, a_3, a_4]^T$$

The spectral nodal displacements and slopes of the beam element are related to the displacement field at node 1 ($x=0$), and node 2 ($x=L$) are represented in a matrix form by

$$\mathbf{d} = \begin{Bmatrix} \widehat{v}_1 \\ \widehat{\phi}_1 \\ \widehat{v}_2 \\ \widehat{\phi}_2 \end{Bmatrix} = \begin{Bmatrix} \widehat{v}(0) \\ \widehat{v}'(0) \\ \widehat{v}(L) \\ \widehat{v}'(L) \end{Bmatrix} \quad (8)$$

By substituting Eq. (7) into the right-hand side of Eq. (8) and written in a matrix form gives

$$\mathbf{d} = \begin{Bmatrix} s(0, \omega) \\ s'(0, \omega) \\ s(L, \omega) \\ s'(L, \omega) \end{Bmatrix} \mathbf{a} = \mathbf{G}(\omega)\mathbf{a} \quad (9)$$

where

$$\mathbf{G}(\omega) = \begin{bmatrix} 1 & 1 & e^{-ikL} & e^{-kL} \\ -ik & -k & -ike^{-ikL} & -ke^{-kL} \\ e^{-ikL} & e^{-kL} & 1 & 1 \\ -ike^{-ikL} & -ke^{-kL} & -ik & -k \end{bmatrix} \quad (10)$$

The frequency-dependent displacement within an element is interpolated from the nodal displacement vector \mathbf{d} , by eliminating the constant vector \mathbf{a} from Eq. (7) and using Eq. (10) it is expressed as

$$v(x, \omega) = \mathbf{g}(x, \omega)\mathbf{d} \quad (11)$$

where the shape function is

$$\mathbf{g}(x, \omega) = \mathbf{s}(x, \omega)\mathbf{G}^{-1}(\omega) \quad (12)$$

The dynamic stiffness matrix for the spectral beam element under axial tension can be determined as:

$$\mathbf{S}_c = EI \left[\int_0^L \mathbf{g}''(x)^T \mathbf{g}''(x) dx - k^4 \int_0^L \mathbf{g}(x)^T \mathbf{g}(x) dx \right] + T \int_0^L \mathbf{g}'(x)^T \mathbf{g}'(x) dx \quad (13)$$

where ' express the spatial partial derivative. By solving the integral, the dynamic stiffness matrix. As far as cable structure is uniform without any sources of discontinuity, it can be represented by a single spectral element with very accurate solutions. However, if there exist sources of discontinuity such as the point loads the beam should be spatially discretised into spectral elements. Analogous to the FEM [27], the spectral elements can be assembled to form a global structure matrix system [11].

2.2 Bar Elementar Spectral Element

The elementar bar model showed in Fig. 2 used to build up the tower considers only axial loads and unidimensional deformations.

Since E is the elastic modulus of the material, A is the cross section of the element, ω is the circular frequency, u is the longitudinal displacement, and q is the excitation force, the undamped bar equation of motion is given by,

$$EA \frac{\partial^2 u(x, t)}{\partial x^2} - \rho A \frac{\partial^2 u(x, t)}{\partial t^2} = 0 \quad (14)$$

In the spectral form, the equation can be described as

$$E_c A \frac{\partial^2 \hat{u}}{\partial x^2} + \omega^2 \rho A \hat{u} = 0 \quad (15)$$

where $\hat{\cdot}$ is used to indicate that it is the result of the Fourier transform, $E_c = E(1 + i\eta)$ represents the structural damping model introduced in the Young's modulus, and η is a loss factor. The homogeneous solution of the displacement regarding the wave propagation into the bar is given by

$$\hat{u}(x, \omega) = a_1 e^{-ikx} + a_2 e^{-ik(L-x)} \quad (16)$$

Amplitude a_1 and a_2 are constants, L is the length of the bar and k is the wave numbers expressed as

$$k = \omega \sqrt{\frac{\rho}{E_c}} \quad (17)$$

By applying the boundary conditions, it is assumed $x = 0$ and $x = L$, so that

$$\hat{u}(0) = a_1 + a_2 e^{-ikL} = \hat{u}_1 \quad (18)$$

$$\hat{u}(L) = a_1 e^{-ikL} + a_2 = \hat{u}_2 \quad (19)$$

The axial force given to the bar is given as

$$\hat{F}_x = EA \frac{\partial \hat{u}}{\partial x} \quad (20)$$



Fig. 2 Two-node bar spectral element

The frequency-dependent dynamic stiffness matrix, S_b , which relates the nodal spectral forces with the nodal spectral displacements as $\hat{F} = S_b \hat{u}$ and expressed by

$$\begin{Bmatrix} \hat{F}_0 \\ \hat{F}_L \end{Bmatrix} = \underbrace{\frac{E_c A}{L} \frac{ikL}{(1 - e^{-2kL})} \begin{bmatrix} 1 + e^{-i2kL} & -2e^{-i2kL} \\ -2e^{-i2kL} & 1 + e^{-i2kL} \end{bmatrix}}_{S_b} \begin{Bmatrix} \hat{u}_1 \\ \hat{u}_2 \end{Bmatrix} \quad (21)$$

2.3 Spectral Elements in Global Coordinate

The cable and bar spectral elements are formulated in the local coordinate system, defined referencing the axial and transverse directions terms of the element axis [28]. As the tower were built up with bars connected at different angles, it is necessary to transform the local coordinates into global coordinates.

The nodal displacements in the truss as showed in Fig. 3 are given by u_2 and v_2 and the corresponding global displacements given by U_3 and U_4 relating to the θ angle. As the global and local displacements must be the same, it has $u_2 = U_3 \cos(\theta) + U_4 \sin(\theta)$, and $v_2 = -U_3 \sin(\theta) + U_4 \cos(\theta)$. The rotational matrix used for the elementar bar that has one-degree of freedom per node is given as,

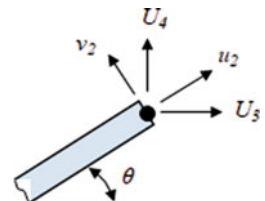
$$\tau = \begin{bmatrix} \cos(\theta) & \sin(\theta) & 0 & 0 \\ \sin(\theta) & \cos(\theta) & 0 & 0 \\ 0 & 0 & \cos(\theta) & \sin(\theta) \\ 0 & 0 & \sin(\theta) & \cos(\theta) \end{bmatrix} \quad (22)$$

and the dynamic stiffness matrix for the truss is written as $S_t(\omega) = \tau' S_b \tau$. For the cable the rotational matrix is of the form,

$$\tau = \begin{bmatrix} \cos(\theta) & \sin(\theta) & 0 & 0 & 0 & 0 \\ \sin(\theta) & \cos(\theta) & 0 & 0 & 0 & 0 \\ 0 & 0 & 1 & 0 & 0 & 0 \\ 0 & 0 & 0 & \cos(\theta) & \sin(\theta) & 0 \\ 0 & 0 & 0 & \sin(\theta) & \cos(\theta) & 0 \\ 0 & 0 & 0 & 0 & 0 & 1 \end{bmatrix} \quad (23)$$

and the stiffness matrix for the cable is $S_t(\omega) = \tau' S_c \tau$.

Fig. 3 Single node element global displacements



3 Wind Force and Random Spectra

The determination of the acting force of the wind takes into account several factors such as transmission line height, terrain relief, wind turnaround time and many other factors that are determined in specific standards. In these standards are found formulas for calculating wind speed, given by:

$$V_h = V_b \left(\frac{h}{10} \right)^{\frac{1}{n}} K_r K_D \quad (24)$$

where V_h is the wind speed at a height h , V_b the basic wind speed, n the coefficient depending on the roughness of the terrain, K_r the coefficient of roughness, K_D the correction coefficient of the integration period to 10 min. The dynamic wind pressure is determined with the following ratio.

$$q_0 = \frac{1}{2} \rho V_h^2 \quad (25)$$

where ρ is the specific mass of air, given in kg/m^3 , so that the dynamic action as a result of applying wind to the cable can be determined as follows:

$$A_0 = q_0 C_{xc} \alpha d \left(\frac{z}{2} \right) \sin^2 \beta \quad (26)$$

The coefficient C_{xc} is the drag coefficient, d the cable diameter, α the dimensionless effectiveness factor obtained by the specified standards, and β the angle of incidence of the wind. In the literature there are several spectra that represent random wind loads as highly dynamic excitations. However, wind spectra describe the distribution of the wind energy fluctuating in the frequency domain, and there are large differences between fluctuations in wind speeds generated by different wind spectra. In this paper we chose the white noise, Kanai-Tajimi, and First order filter spectrum.

The Wiener–Khinchin theorem relates the autocorrelation function $R(\tau)$ to a frequency domain Power Spectral Density (PSD) by a Fourier transform pair [25]. The time series can be numerically generated by a Fast Fourier Transform (FFT)-based algorithm by taking the inverse discrete Fourier transform (IDFT) of the discretized target PSD. Therefore, the spectra amplitude is estimated as the square root of the discretized PSD ($\sqrt{S_f}$), and a random phase is generated from a uniform distribution within the interval $[0, 2\pi]$.

The white noise PSD model is given by $S_f(\omega) = S_0$, where S_0 has zero mean and unitary standard deviation [29]. It is an idealization in which the signal frequency content is equally distributed over the frequency band (band-limited white noise). This assumption is not physically sound and other PSD models can be used like as the First Order Filter (FOF),

$$S_f(\omega) = \frac{S_0}{v^2 + (2 * \pi * \omega)^2} \tag{27}$$

or the Kanai-Tajimi model, a second order type of filter given by

$$S_f(\omega) = \frac{1 + 4\xi_g^2(\omega/\omega_g)S_0}{(1 + (\omega/\omega_g)^2 + 4\xi_g^2(\omega/\omega_g)^2)} \tag{28}$$

where the constant v , ξ and ω_g are adjusted according to specific features of the random load. An important relations used in the analysis of the dynamic response of any system to random excitation is that the PSD of the response of a system to an input PSD is given by the following expression:

$$PDS_{out}(\omega) = |\mathbf{H}(\omega)|^2 \cdot S_f(\omega) \tag{29}$$

where the function $\mathbf{H}(\omega) = \mathbf{S}_t^{-1}(\omega)$ is the transfer function.

4 Numerical Analysis

The numerical study presents four analyses regarding on tower, cable, coupling cable-tower model and coupling subject to random wind force load.

Tower

The tower is modelled as a steel structure whose mechanical properties are, modulus of elasticity E of 210 GPa, density equal to $\rho = 7860 \text{ kg/m}^3$, the area is A 0.01 m, and the tower high is 26 m. Figure 4 shows a span transmission line of 100 m used in this study. Receptances responses are obtained at (a), (b) tower (red dot), (c) coupling point (yellow dot), (d) cable at 1 m from coupling point (blue dot), (e) middle of the cable (blue dot), and (f) end of the cable (blue dot).

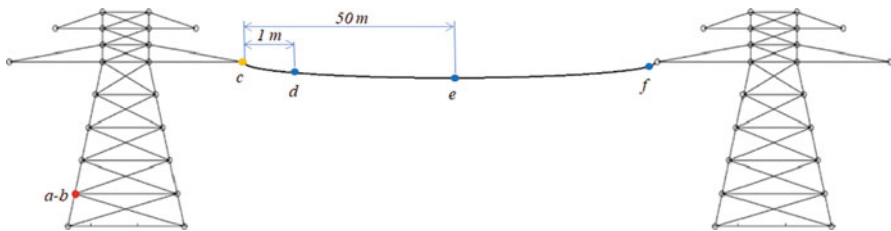


Fig. 4 Overhead transmission line with 100 m spam

Table 1 Tower’s resonance frequency

Mode	Resonance frequency [Hz] per meshed size [m]					
	SEM	FEM				
	N/A	N/A	1	0.5	0.1	0.01
1	5.58	4.1221	5.17	5.35	5.53	5.572
2	30.69	18.864	27.24	28.72	30.25	30.64
3	39.79	28.388	36.88	38.18	39.45	39.76
4	61.24	40.776	55.79	58.17	60.56	61.17
5	107.1	63.538	94.10	100.45	105.68	106.92

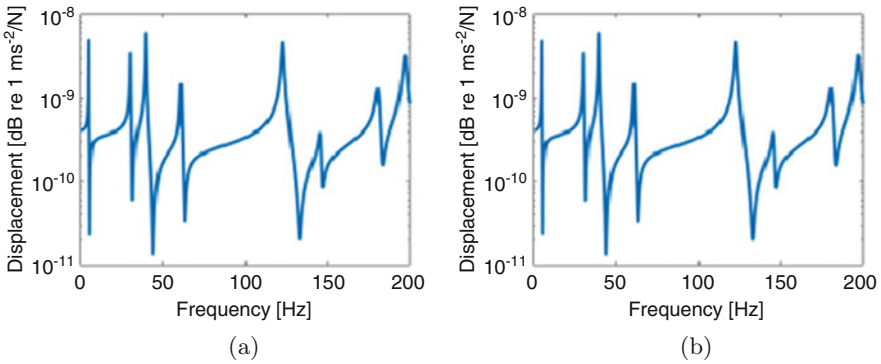


Fig. 5 FRF of the tower obtained at point ‘a’ (red dot) by: (a) SEM, and (b) FEM with meshed element sizing 0.01 m

The vibrational frequency range goes up to 200 Hz. SEM and FEM by the software ANSYS modelled tower and cable. In the tower modelled with SEM, there is no discretisation in the bars of the tower. It has 22 nodes, and 48 continuous bar elements, the boundary condition is assumed to be fixed in its base. For the model using ANSYS, the bar is meshed in different levels of discretisation to improve the accuracy of the structural dynamic response. Each bar element has meshed with elements sizing 1, 0.5, 0.1, and 0.01 m. Table 1 presents the firsts five-tower resonance frequencies calculated by SEM and FEM without and meshed elements.

By comparing SEM and FEM resonance frequencies, the best approximation was achieved with the FEM meshed element size of 0.01m. Thus, Fig. 5a and b show the FRF obtained with FEM (mesh sizing 0.01m length) and SEM at point ‘a’ (red dot) by unitary excitation at the same position. Both methods presented a similar number of resonant frequencies and close mode shapes. The FRF curves have good approximation in the whole frequency range, which validated the SEM model.

Cable

The cable is made of aluminum with mechanical properties of $E = 74$ GPa, $\rho = 2700$ kg/m³, $\eta = 0.01$; and geometrical characteristics: area of $A = 0.005$ mm²,

Table 2 Cable conductor’s resonance frequency

Mode	Resonance frequency					
	SEM	Analytical	FEM (N ^o elements)			
			10	20	50	100
1	0.43	0.43	0.42	0.43	0.43	0.43
2	0.86	0.86	0.83	0.85	0.86	0.86
3	1.29	1.29	1.18	1.28	1.29	1.29
4	1.72	1.72	1.21	1.69	1.72	1.72

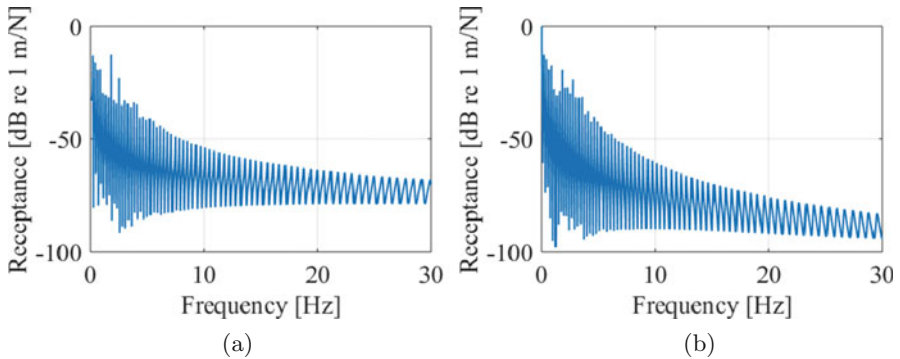


Fig. 6 Receptance FRF of the cable using: (a) SEM, (b) FEM with 20 elements

length $L = 100$ m and a tension load of 1000 kN. Table 2 shows the resonance frequencies of the cable estimated by analytical solution [30], SEM, and FEM with a different number of elements. The SEM presented the same resonance frequencies values of the analytical solution showing the accuracy of the method. As in the Tower study, FEM solution improves the approximation with the solution estimated by SEM and analytical as the number of elements increases, which implies in high computational cost.

The cable presented a good approximation of the results obtained with FEM by comparing with SEM from up to 20 elements in the discretization and lower computational effort by comparing the 50 and 100 elements. Thus, the tests performed using the FEM model considered 20 elements in the cable discretization. The cable presented a good approximation of the results from the discretization in 20 elements, Fig. 6a and b show the acceptance FRFs obtained at the left end of the cable with SEM and FEM with 20 elements, respectively. The resonance frequencies up to 10 Hz are similar, from 10Hz the resonances have a small difference due to the assumed discretization. The mode shapes are close in the whole frequency range.

Coupling Interaction Tower-Cable

A unitary excitation is adopted at node ‘a’ and measured in six points over the overhead transmission. The interaction between cable and tower are demonstrated in Fig. 7a–f. The receptance responses obtained in the tower shown in Fig. 7a–c, the

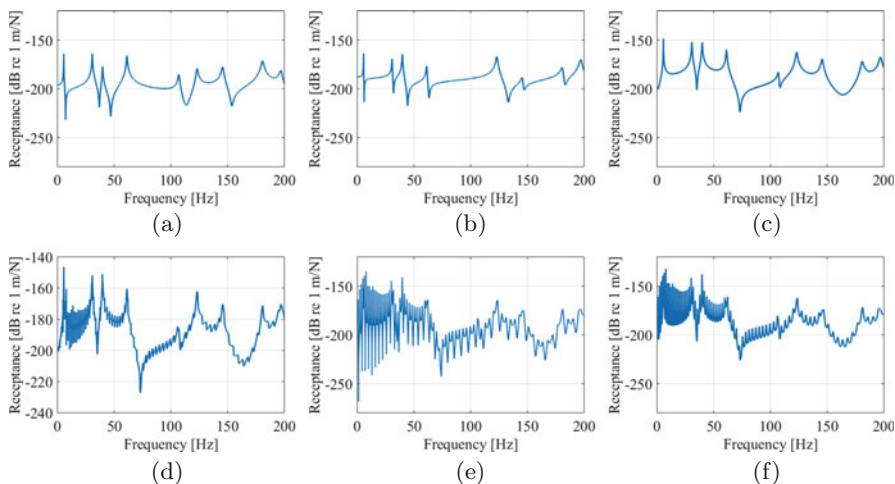


Fig. 7 Receptances obtained at: (a), (b) tower; (c) coupling point, (d) cable at 1 m from coupling point; (e) middle of the cable; (f) end of the cable

Table 3 Resonance frequencies of the system

Mode	Resonance frequency			
	Tower	Connection	Cable (1 m)	Cable (50 m)
1	5.7	5.7	5.7	1.4
2	31.5	31.5	9.4	4.1
3	40.8	40.8	12.1	5.7
4	62.7	62.7	14.8	6.8
5	108.7	108.7	17.5	9.4

system coupling point, Fig. 7b,c, the FRF has only the influence of the tower. The receptance obtained on the cable at 1 m of the connection from the tower coupling points is shown in Fig. 7d, in this point it is observed the cable and tower interaction, where is possible to recognise some mode shape of the tower and the cable. The receptance FRFs obtained in the middle of the cable and end presented in Fig. 7e,f, respectively, the cable has great influence in the vibration, and the vibrational response of the tower is difficult to identify. Therefore the cable presented a high modal density, the measured FRFs at the cable points are modulated by the tower response.

Table 3 presented the list of the firsts fifth-resonance frequencies obtained in the tower, at the connection point, in the cable from 1 m of the connection, and in the middle of the cable. As in the receptance response analyses, it is also possible to identify the interaction between the tower and cable by the resonance peaks.

4.1 Effect of the Wind Random Excitation in the Transmission Line

In general, wind load acting throughout the cable. In all cases, the wind PSD was applied at point ‘c’ and the PSD responses measured along the transmission line (Fig. 8). Wind parameters adopted are: basic speeds of the wind equal to 20 m/s, ground clearance $h = 244$ m, coefficient $n = 12$ (Fig. 9). The terrain assumed as category D, which correspond to urban areas and land with high trees, applies $K_r = 0.67$ and $K_D = 1.6$ for a 10 s integration period. To obtain the specific mass of air was adopted at a temperature of 25°C at sea elevation. $C_{xc} = 1$, $\alpha = 0.65$, and z being the span length considered the total length of the transmission line thus $z = 100$ m. Since the wind has random behaviour, it is compared to different wind spectra as white noise spectra shown in Fig. 10, FOF Fig. 11 and Kanai-Tajimi Fig. 12.

The Power Spectral Density of tip excitation force for each signal is shown in Fig. 8. The white noise spectra presented as continuous line, that means a good level and constant excitation in the whole frequency range. It is noticed that Kanai-Tajimi and FOF spectra show more dominant low-frequency components and since Kanai-Tajimi is a second-order filter, the formation of a peak near its characteristic frequency. Both spectra presented a decay along with the frequency band, limiting the excitation level to low frequencies.

Figure 9 shows the random wind load spectrum in the time domain modelled with the three theories. The white noise spectra maintain a no correlated dispersion around the mean value in the whole time range. Kanai-Tajimi spectra has a large correlated distribution and behaves irregularly around the mean value. The FOF has

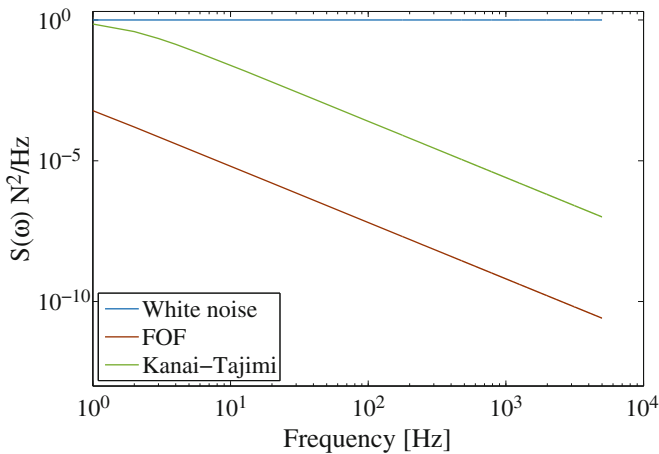


Fig. 8 Power Spectral Density of tip excitation force for white noise (blue), First Order Filter (red) and Kanai-Tajimi (green)

Fig. 9 Time domain white noise, Kanai-Tajimi, and FOF wind spectrum

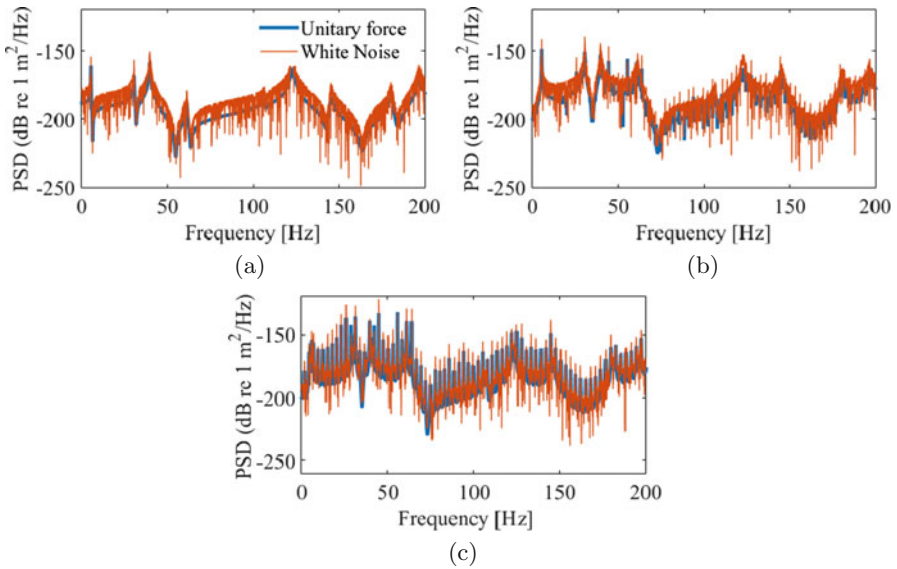
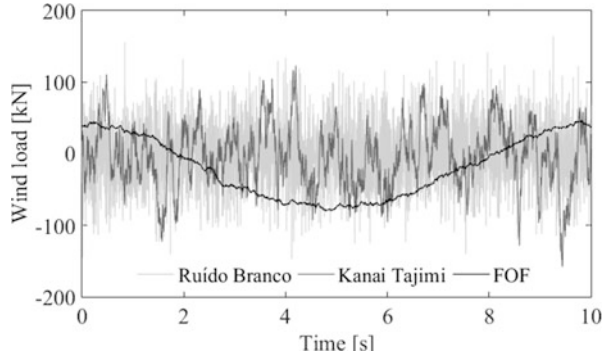


Fig. 10 PSD calculated with white noise excitation spectrum: (a) obtained in points of the tower; (b) in the cable at 1 m from the tower fixture;c)obtained at 50m

small variability and follows the mean value; however, FOF’s PSD has a higher correlation variable.

The knowledge about how the structure will behave under a specific excitation is crucial, for example, for the vibration control, structure reliability or fatigue analyses. Thus, in all case, the effect of the random excitation has a great influence on the FRFs. The conductor PSDs presented a random vibration following the input spectrum. It caused difficulties in estimate the resonances in some points. The PSDs obtained from a white noise input showed constant amplitude in the whole frequency range, and similar amplitude of the FRFs obtained using unitary excitation, see Fig. 10. PSD calculated with input as FOF spectrum and Kanai-Tajimi decay its energy along of he frequency in reason of the input PSD phenomena.

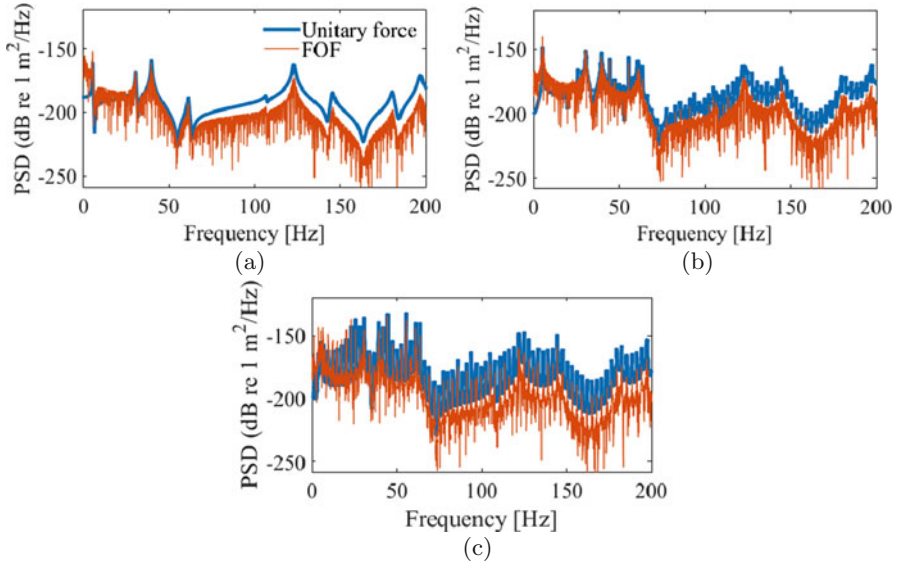


Fig. 11 PSD calculated with FOF spectrum: (a) obtained in points of the tower; (b) in the cable at 1 m from the tower fixture; (c) obtained at 50m

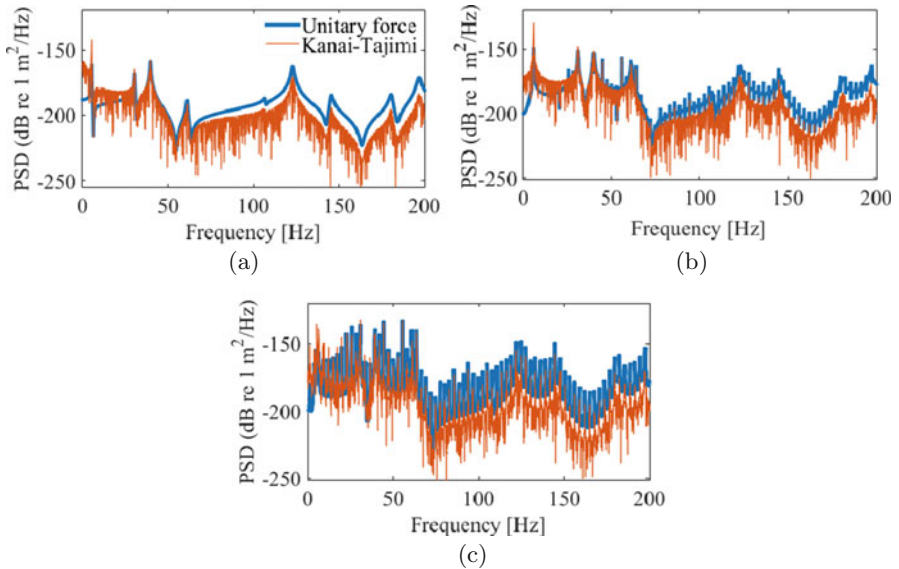


Fig. 12 PSD calculated with Kanai-Tajimi excitation: (a) obtained in points of the tower; (b) in the cable at 1 m from the tower fixture; (c) obtained at 50m

5 Conclusion

This paper presents a numerical model of overhead transmission line towers and their interaction through the Spectral Element Method. Responses obtained with the SEM is compared with the vibrational responses obtained analytically and via the FEM to validate the proposed model. SEM accuracy and efficiency are observed when comparing the discretisation number required by the FEM method. The cable tower is shown to have a dynamic interaction coupling at some points that should be taken into account. Different results were also obtained due to wind excitation spectra. The vibration responses of the system suffered greater variations when the overhead transmission is under random wind excitation, which leads in challenging to design vibration control devices and performs its health monitoring. SEM shows to be an alternative tool for analysing the dynamics of complex structures.

References

1. Dutkiewicz, M., Machado M.R.: Measurements in situ and spectral analysis of wind flow effects on overhead transmission lines. *Sound Vibration* **53**, 161–175 (2019)
2. Vecchiarelli, J., Curie, I.G., Havard, D.G.: Computational analysis of aeolian conductor vibration with a stockbridge-type damper. *J. Fluids Struct.* **14**, 489–509 (2000)
3. Meynen, H., Verma, P., Hagedorn, P., Schafer, M.: On the numerical simulation of vortex-induced vibrations of oscillating conductors. *J. Fluids Struct.* **21**(1), 41–48 (2005)
4. Kiessling, E., Nefzger, P., Nolasco, J.E., Kaintzyk, U.: *Overhead Power Lines - Planning, Design, Construction*. Springer, Berlin, Heidelberg (2003)
5. Yasui, H., Marukawa, H., Momomura, Y., Ohkuma, T.: Analytical study on wind-induced vibration of power transmission towers. *J. Wind Eng. Ind. Aerodyn.* **83**, 431–441 (1999)
6. Leon, K., Smith, S.: Cross-rope transmission tower-line dynamic analysis. *J. Struct. Eng.* **110**(6), 1321–1335 (1984)
7. McClure, G., Lapointe, M.: Modeling the structural dynamic response of overhead transmission lines. *Comput. Struct.* **81**(8–11), 852–834 (2003)
8. Dua, A., Clobes, M., Höbbel, T., Matsagar, V.: Dynamic analysis of overhead transmission line under turbulent wind loading. *Open J. Civil Eng.* **5**, 359–371 (2015)
9. Desai, Y.M., Yu, P., Popplewell, N., Shah, A.H.: Finite element modelling of transmission line galloping. *Comput. Struct.* **57**, 407–420 (1995)
10. Fu, X., Li, H.N.: Dynamic analysis of transmission tower-line system subjected to wind and rain loads. *J. Wind Eng. Ind. Aerodyn.* **157**, 95–103 (2016)
11. Lee, U.: *Spectral Element Method in Structural Dynamics*. Inha University Press (2004)
12. Gopalakrishnan, S., Chakraborty, A., Mahapatra, D.R.: *Spectral Finite Element Method*. Springer, New York, USA (2007)
13. Machado, M.R., Khalij, L., Fabro, A.T.: Dynamic analysis of a composite structure under random excitation based on the spectral element. *Int. J. Non. Sci. Numeri. Simul.* **20**(2), 179–190 (2019)
14. Machado, M.R., Adhikari, S., Dos Santos, J.M.C.: Spectral element-based method for a one-dimensional damaged structure with distributed random properties. *J. Braz. Soc. Mech. Sci. Eng.* **40**, 415 (2018)
15. Clough, R., Penzien, J.: *Dynamics of Structures*, McGraw Hill, New York (1995)
16. Doyle, J.F.: *Wave Propagation in Structures: Spectral Analysis Using Fast Discrete Fourier Transforms*. Springer, New York (1997)

17. Mei, C.: Comparison of the four rod theories of longitudinally vibrating rods. *J. Vib. Cont.* **21**(8), 1639–1656 (2015)
18. Dutkiewicz, M., Machado, M.R.: Spectral approach in vibrations of overhead transmission lines. *IOP Confer. Ser. Mat. Sci. Eng.* **471**, 052029 (2019)
19. Dutkiewicz, M., Machado, M.R.: Dynamic response of overhead transmission line in turbulent wind flow with application of the spectral element method. *IOP Confer. Ser. Mat. Sci. Eng.* **471**, 052031 (2019)
20. Dutkiewicz, M., Machado, M.R.: Spectral element method in the analysis of vibrations of overhead transmission line in damping environment. *Struct. Eng. Mech.* **71**(3), 291–303 (2019)
21. Machado, M.R., Dutkiewicz, M., Matt, C.F.T., Castello, D.C.: Dynamic response of overhead transmission line in turbulent wind flow with application of the spectral element method. *Mech. Syst. Sig. Proc.* **136**, 106483 (2020)
22. Papoulis, A., Pillai, S.U.: *Probability, Random Variables and Stochastic Processes*. McGraw-Hill, Boston (2002)
23. Li, J., Chen, J.: *Structural Dynamics and Probabilistic Analyses for Engineers*. Wiley, England (2009)
24. Maymon, G.: *Stochastic Dynamics of Structures*. Butterworth-Heinemann, Oxford (2008)
25. Newland, D.E.: *An Introduction to Random Vibrations, Spectral & Wavelet Analysis*. Courier Corporation (2012)
26. Yu, B.Y.J., Soliman, M.: Estimation of cable tension force independent of complex boundary conditions, *ASCE J. Eng. Mech.* **60**, 1–8 (2014)
27. Zienkiewicz, O.C. , Taylor, R.L.: *The Finite Element Method*. McGraw-Hill, London (1991)
28. Hutton, D.V.: *Fundamentals of Finite Element Analysis*. McGraw-Hill (2004)
29. Shin, K., Hammond, J.K.: *Fundamentals of Signal Processing for Sound and Vibration Engineers*. Wiley, England (2008)
30. Rao, S.S.: *Mechanical Vibration*. Person Prentice-Hall (2008)

Experimental Assessment of the Test Station Support Structure Rigidity by the Vibration Diagnostics Method



Anna Šmeringaiová  and Imrich Vojtko 

Abstract The paper presents the results of the impact test. The test has been done to assess the rigidity of the test station support frame. Test station was designed and constructed to test different types of gearing and belt transmissions. The test station allows to simulate different operating conditions. The procedure of the tests can be both short-term and long-term with different load levels. The basic support frame structure of the test station was evaluated as insufficient based on the results of measurement and processing of the measured low and high frequency vibration values in the verification series of experimental tests. The basic failure of the original design were the significant resonance actions that were the results of the dominant sources of vibration being near the natural frequencies of the vertical and horizontal beams of the test station base. A structural design of the test station supporting frame was designed and implemented. The impact tests were used to determine the values of the natural frequencies of the most stressed parts of the supporting structure - vertical and horizontal beams, before and after implementation of structural modifications. The comparability of the impact test results was determined by adherence to identical measurement conditions.

Keywords Test Station · Impact test · Natural frequency

1 Testing Station for Dynamic Testing of Toothed and Belt Gear Drives

When designing the gearbox, it is appropriate to know its dynamic characteristics. With improperly selected gearbox parameters, especially in transient states, there can be a high dynamic stress on their functional parts. There was designed and built a

A. Šmeringaiová (✉) · I. Vojtko

Faculty of Manufacturing Technologies of the Technical University of Košice with a seat in Prešov, Prešov, Slovakia

e-mail: anna.smeringaiova@tuke.sk; imrich.vojtko@tuke.sk

© Springer Nature Switzerland AG 2021

J. Awrejcewicz (ed.), *Perspectives in Dynamical Systems III: Control and Stability*,

Springer Proceedings in Mathematics & Statistics 364,

https://doi.org/10.1007/978-3-030-77314-4_13

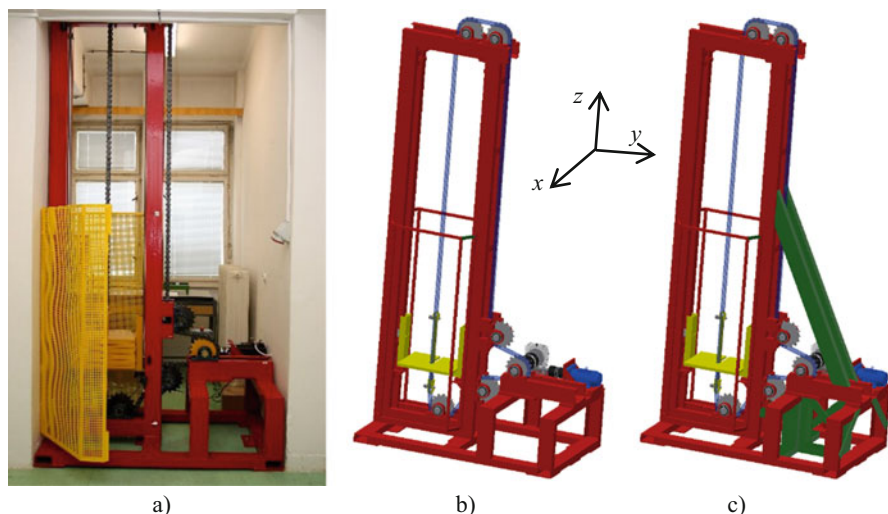


Fig. 1 Dynamic Transmission Testing Station. (a) Real testing station, 3D stand model (b) before and (c) after the structural modification

test station to realize the dynamic tests of gears at Department of Technical Systems Design and Monitoring, Faculty of Manufacturing Technologies of the Technical University of Košice with the seat in Prešov (see Fig. 1a). Designed test station allows to realize both, short and long-term comparative tests of various types of gearboxes. It is possible to test gearboxes with various design and technological modifications, to reduce their dynamic load in order to improve their parameters and increase their service life. The principle scheme and functional description of the test station is shown in [10].

1.1 Functional Testing of the Test Station and Verification of the Proposed Methodology for Dynamic Testing

The basic requirement for functional use of the test station was the achievability of objective and comparable results of the experiments. The main goal of the tests first stage was to verify the functionality of the test station and of used measuring instruments and equipment. From this point of view, the selection of methods for measuring the wear of the functional parts of gears and diagnostic methods to assess their technical condition were also considered. Commonly manufactured Z80-J-010-P single-stage worm gear units were used as a test object. During the experimental operation, the technical conditions of the worm gear units were monitored in two different operating modes. The operating conditions have been according to recommendations [9] deliberately designed to achieve a maximum of 70 ÷ 80% of the nominal transmission power guaranteed by the manufacturer and to stabilize the oil temperature below the limit. The following parameters (dynamic characteristics) were measured and evaluated for the tested worm gear

units: load amplitude magnitudes and frequency, oil temperature, worm gear teeth wear. A detailed description of the preparation and course of a series of validation experimental measurements are described in [10, 11].

1.2 Verification Test Results Evaluation

According to [11], results of measurements of dynamic quantities (temperature, vibration, ultrasound) were found:

- significant difference in measured parameters depending on transmission load,
- significant changes in the measured parameters during heating, the effect of thermal expansion on the clearance in the teeth of the worm gear, bearings and chain, until the temperature has stabilized,
- significant resonance events, high mechanical vibrations above the Alarm 2 recommended limit (hazard according to Vibration Severity Standard [3]) especially in area of the vertical beam and the horizontal frame under the sprocket, the transmission of these vibrations to the gearbox and a significant deterioration of the meshing conditions on the gears,
- unfavorable operating conditions when starting the engine (gearbox), mainly due to higher load, oscillation and insufficient chain guidance, and again transfer of vibrations to the gearbox.

The elementary structure of the test station was evaluated as unsatisfactory based on the results of measurement and processing of measured values of low-frequency and high-frequency vibrations in the verification series of experimental tests. The main drawback of the original design were significant resonance events, which were due to the fact that the dominant sources of vibration were close to the natural frequencies of the vertical and horizontal beam of the test station base structure.

In order to ensure acceptable measurement results of the tested gearboxes, it was necessary to prevent the occurrence of adverse resonance events and the occurrence of high mechanical vibrations inside the mechanical system (testing facility). The issue of objective experimental results is discussed also in [5] and [6].

2 Solving Adverse Resonance Events

In vibrodiagnostics and when performing rotating machine failures identification, in addition to common failures, we occasionally encounter a special error that is not actually a malfunction [1]. It is a feature of a device that, in a given configuration, adversely affects the operation of the device. It is a resonance, resonance phenomenon or operation at critical speed. The problem arises with devices in which the excitation force frequency is identical to the intrinsic resonant frequency. For example, if the electric motor speed is the same as the natural resonant frequency of the mechanical system. In this case, even a small imbalance

causes a high response in the system and high vibrations are generated. In order to eliminate this phenomenon, it is first of all necessary to identify it and to determine its intrinsic resonant frequencies. Usually, the natural frequencies are determined by the impact tests (Bump Test). Several studies offer valuable insights on research and response to adverse resonance events (see in particular [2], [4], [8] and [12]).

In general, there are two options how to solve resonant phenomena:

1. changing the frequency of the driving force, (engine shaft revolutions),
2. tuning the system, that means moving the resonant band to a frequency range where there is no excitation.

Generally for resonant frequency f_r :

$$f_r = \frac{1}{2\pi} \sqrt{\frac{k}{m}} [\text{Hz}], \quad (1)$$

where k is force constant (stiffness) [N.m-1] and m is weight [kg]. From the Eq. (1) it follows that as the rigidity (k) increases, the resonance frequency increases and with the increase in mass (m) the resonance frequency decreases.

In this case, the option 2. – optimization of the structure of the supporting frame was chosen for the solution of resonance phenomena. The aim is to increase the rigidity of the test station base structure. Frame reinforcement and other measures, such as chain guiding and adequate fastening of weights, should have a positive effect on eliminating vibrations and shifting the resonant band of the base structure beyond the frequency range of the driving forces. The design of the supporting frame of the testing station was developed and implemented. The 3D model of the test station with the designed structural modification is shown in Fig. 1c. By measuring and comparing the natural frequencies of the basic design of the test station before and after the design changes, the control of the fulfillment of the expected target was performed.

3 Impact Test (Bump Test)

The natural frequencies of the mechanical system were determined by the bump test in the resting state of the mechanical system:

1. Before design of the test station, after completion of the functional tests described in [11].
2. After modification of the test station frame support design.

The natural frequencies of the most stressed parts of the supporting structure (vertical and horizontal beam) and of the tested worm gearbox before and after the design modifications were determined. The comparability of the bump test results was conditioned by observing identical measurement conditions.

3.1 Description of the Bump Test Conditions

Used measuring instruments and aids:

- measurement system OKTALON, graphical programming software LabVIEW with measurement algorithms – recording and processing of the measured signal,
- vibration acceleration sensor – ACC-100 mV/g, fixing - flat magnet,
- impact hammer.

3.2 Measurement Procedure

- Calculation of expected excitation force frequencies (operating frequencies values) – Table 1.
- Preparation of measuring system and vibration measuring aids.
- Choice of united coordinate system – Fig. 1.
- Determination of measuring points, location of sensors, direction and sense of impact – Fig. 2a, 5a, 7a and 9a.
- Measurement at selected measurement locations: vibration acceleration sensor mounting, bump hammer strike near the sensor, vibration acceleration dumping time recording.
- Signal processing: vibration velocity waveform as a result of vibration acceleration time wave integration, FFT vibration velocity time waveform analysis, graphical and tabular processing of dominant frequencies.
- Comparison of bump test results before and after design – Table 2.

Table 1 Expected frequency – basic calculation [11]

Structural Node	Frequency	
	Cycles / min	Hz
Engine, input into gearbox, Clutch, Worm	1400	23,3
Output of the Gearbox, Sprocket	45,16	0,753
Transmission chain, frequency of chain links	768	12,80

Table 2 Frequencies with dominant vibration values before and after design

	Frequency [Hz]			
	Measurement 1	Measurement 2	Measurement 3	Measurement 4
Condition before design change	34,5	32,9	6,6	33,7
	45,5	36,5	10,4	78,6
	89,3	88,9	55,7	88,4
Condition after design change	797,6	137,5	68,2	68,3
	865,5	800,4	162,7	100,9
	896,2	902,6	326,59	226,2

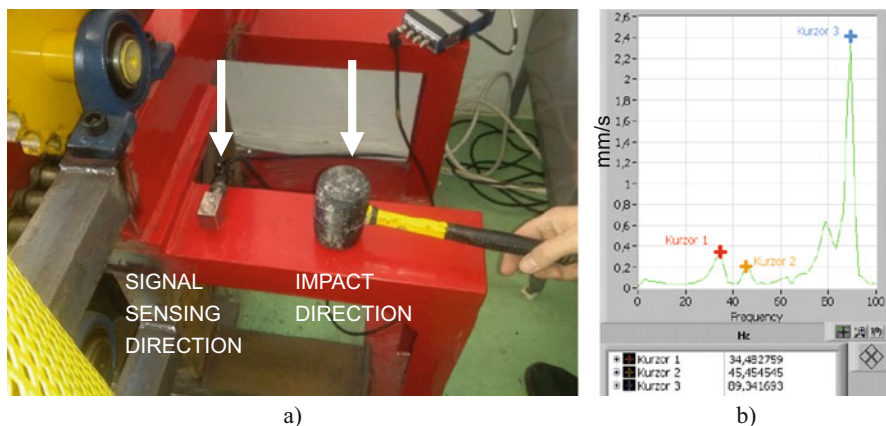


Fig. 2 Measurement 1. Measurement of the natural frequency in vertical direction: (a) measurement execution, (b) frequency spectre before the design change

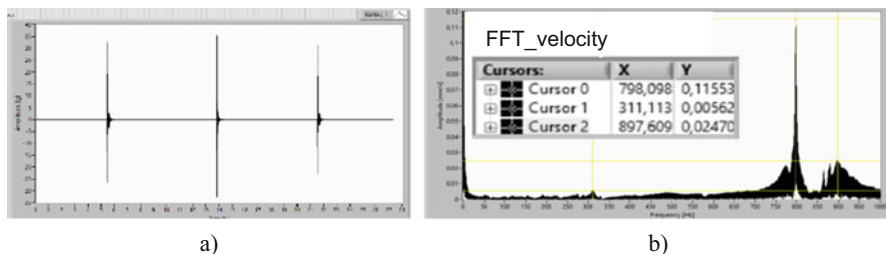


Fig. 3 Measurement 1. (a) time course of vibration acceleration, (b) FFT velocity after design change

3.3 Bump Test – Measurements Results

At Figs. 2a, 5a, 7a and 9a the location and course of the bump test at selected locations are shown. The direction of sensing the vibration signal and the direction of the modal hammer bump are indicated. After bumping in the indicated direction, the vibrations generated were recorded by a vibration acceleration sensor.

Measurement 1 Measurement of the natural frequency in vertical direction.

Figure 2b is shown details of frequency analysis of the shock damping time course with the indication of the dominant frequencies obtained from the measurement before test station redesign and at Figs. 3 and 4 are shown the results of a frequency analysis time course of the shock damping after design changes have been made.

Regarding the determination of natural frequencies, it does not matter whether the spectrum is calculated from the ACCELERATION or VELOCITY time course. The frequencies in the spectrum are in the same positions on the “x” axis. The only

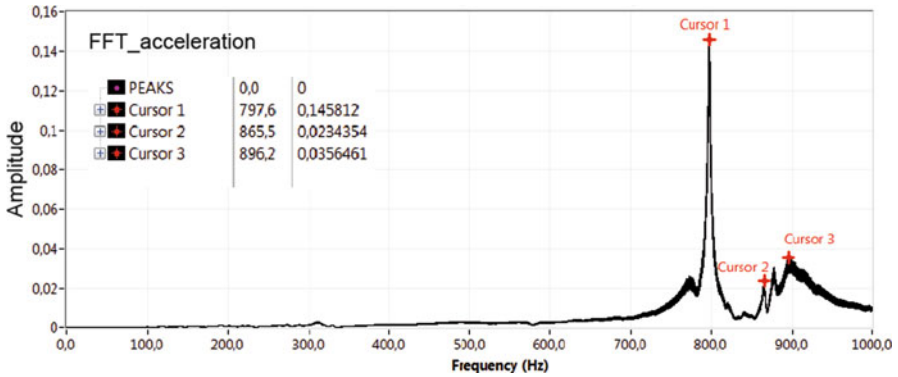


Fig. 4 Measurement 1. Frequency spectre after design modification

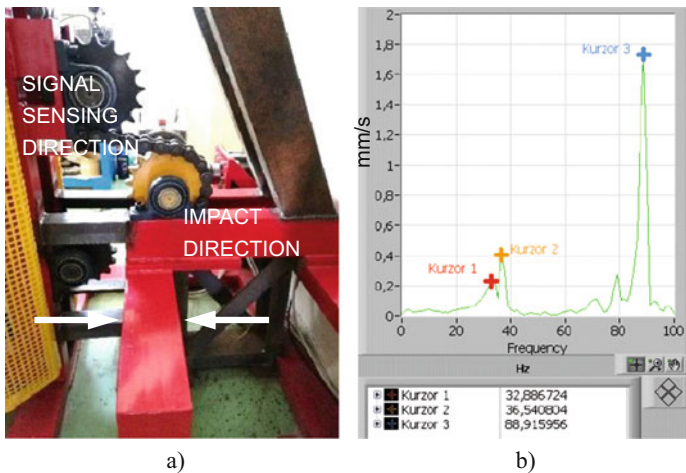


Fig. 5 Measurement 2. Measurement of natural frequency of the table in horizontal direction: (a) measurement execution, (b) frequency spectre before the design

difference is that VELOCITY is calculated from acceleration by integration. This proportionally amplifies the lower frequencies and suppresses the higher frequencies (see Fig. 3b and 4).

Measurement 2 Measurement of natural frequency of the table with drive mechanism in horizontal direction (Figs. 5 and 6).

Measurement 3 Measurement of natural frequency of vertical frame (Figs. 7 and 8).

Measurement 4 Measurement of the natural frequency of worm gear – horizontally in worm gear axis direction (Figs. 9 and 10)

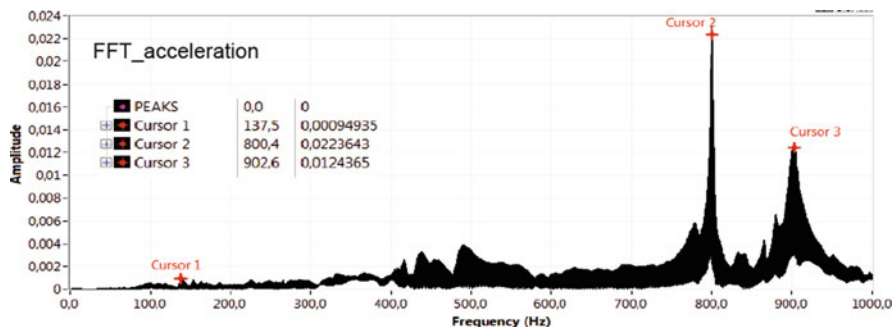


Fig. 6 Measurement 2. Measurement of natural frequency of the table in horizontal direction. Dominant frequencies identified after the design change

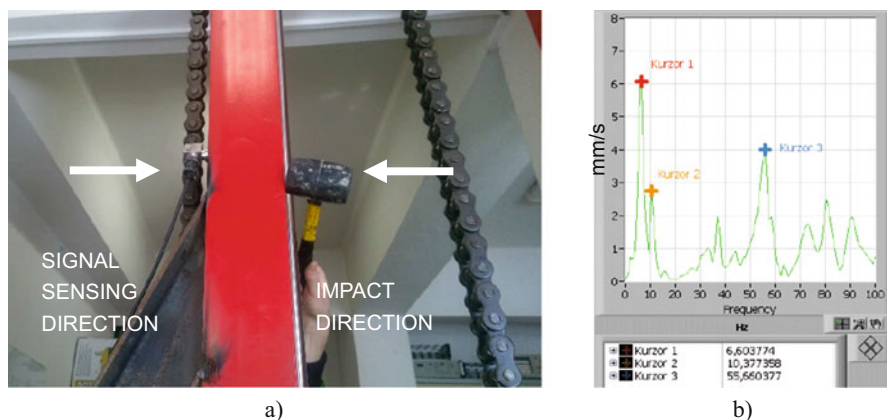


Fig. 7 Measurement 3. Measurement of natural frequency of the vertical frame: (a) measurement execution, (b) frequency spectre before the design modification

4 Evaluation of Natural Frequency Measurement Results

To suppress possible resonance events in the process of experimental operation of the tested gearboxes, we chose to tune the system by changing the rigidity of the base frame of the test station. Based on the analysis of the results of the above described functional tests of the worm gears and results of the bump test, there were found high mechanical vibrations of mainly vertical “lift” beams and horizontal table beam under the sprocket were found. The transmission of these vibrations to the gearbox during operation in the short term significantly worsened the meshing conditions in the worm gear. The aim of the design modifications was to increase the stiffness of the basic structure, especially the vertical frame and table base on which the machine drive mechanism is mounted.

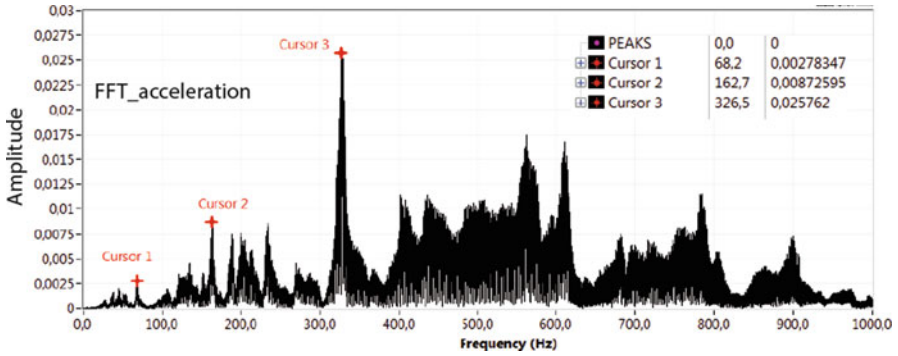


Fig. 8 Measurement 3. Measurement of natural frequency of vertical frame. Dominant frequencies identified after the design change

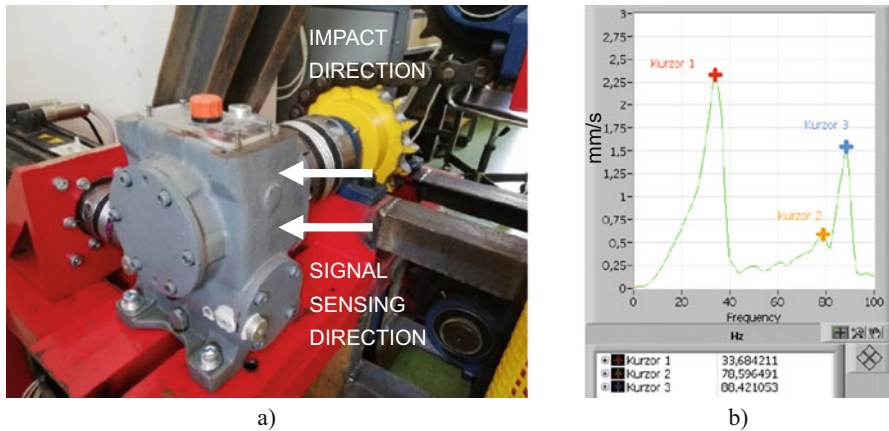


Fig. 9 Measurement 4. Measurement of the natural frequency of the worm gearbox: (a) measurement execution, (b) frequency spectre before the design change of the frame

A repeated bump test revealed a significant shift of the natural frequencies of both vertical and horizontal beams in the frequency spectrum (see Table 2). After the frame has been reinforced, there has been a significant decrease in the vibration velocity amplitude and a shift of the dominant frequencies far beyond the operating values of the excitation forces frequencies. This occurrence had happened in both the vertical and horizontal directions. For example, in the case of a horizontal table beam, the dominant frequencies have shifted from the range from 30 Hz to 90 Hz to near 800 Hz. This is a prerequisite for obtaining objective results of planned experimental measurements also for other transmissions and other operating conditions.

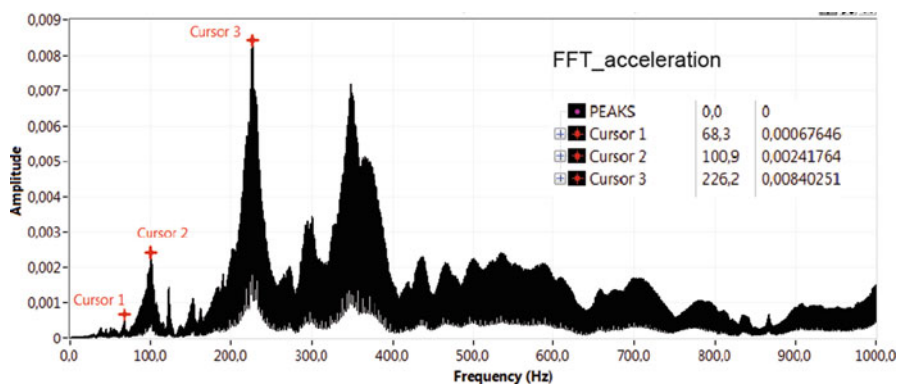


Fig. 10 Measurement 4. Measurement of gearbox natural frequency in worm gear axis direction. Dominant frequencies identified after the design change

The natural frequencies of the worm gear housing were also measured repeatedly. The drift of dominant frequency values with significant amplitude peaks can be explained as a result of gearbox disassembly and reattachment on a reinforced table.

5 Conclusions

Vibration diagnostics belongs to modern methods of non-destructive technical diagnostics, by means of which it is possible to determine the current technical state of various production machines and equipment directly in the process of operation [7]. The aim of the design modifications of the testing station for dynamic testing of toothed and belt drives was to eliminate the danger of resonance and increase the stiffness of the basic stand structure. A bump test performed under the same conditions before and after frame reinforcement confirmed that by the structural modification of the testing facility was achieved a higher rigidity of the base frame. Shifting the natural frequencies, especially of the vertical and horizontal beam, outside the operating frequencies of the tested transmissions is a necessary condition for achieving objective results of the planned experiments.

Acknowledgments The authors would like to thank the Slovak Research and Development Agency under contract no. APVV 18-0316.

References

1. Biloš, J., Bilošová, A.: Applied Mechanics as Part of a Team of Designers and Developers: Vibration Diagnostics (in Czech). VŠB TU, Ostrava (2012)
2. Çakar, O.: A method for shifting natural frequencies of a dynamic system to desired values with concentrated mass modifications. *J. Vibroeng.* **20**(1) 1–12 (2018)

3. ISO 10816-3:2009 Mechanical vibration. Evaluation of machine vibration by measurements on non-rotating parts — Part 3
4. Krenický, T., Ružbarský, J., Panda, A.: Operation and diagnostics of machines and production systems operational states III. In: Key Engineering Materials, vol. 669, p. 596. Trans Tech Publications, Switzerland (2016)
5. Maščenik, J., Vojtko, I.: Experimental monitoring and diagnostics of belt gears in testing device. *MM Sci J.* **2016**(September), 964–968 (2016)
6. Molnár, V., Michalik, P.: Design modification of test device for analyzing of conveyor belt samples. In: Applied Mechanics and Materials: LOGI 2015, vol. 803, pp. 179–184. Trans Tech Publications, Switzerland (2015)
7. Murčinková, Z., Murčinko, J., Adamčík, P.: The multi-parameter on-line monitoring system applied for rotating machinery. *Rev. Ind. Eng. Letters.* **3**(2), 19–28 (2016)
8. Murčinková, Z., et al.: Damping properties of fibre composite and conventional materials measured by free damped vibration response. *Adv. Mech. Eng.* **11**(5), 1–11 (2019)
9. Pavlenko, S., Maščenik, J., Krenický, T.: Worm Gears: General Information, Calculations, Dynamics and Reliability. RAM-Verlag, LÜdenscheid (2018)
10. Šmeringaiová, A., Vojtko, I., Monková, K.: Experimental analysis of the dynamics of gear boxes I (in German). *Tech. Mess.* **82**(2), 57–64 (2015)
11. Šmeringaiová, A., Vojtko, I., Monková, K.: Experimental analysis of the dynamics of gear boxes II (in German). *Tech. Mess.* **82**(4), 224–232 (2015)
12. Žiaran, S.: Low-Frequency Noise and Vibration (in Slovak). STU, Bratislava (2016)

Experimental Dynamical Analysis of a Mechatronic Analogy of the Human Circulatory System



Paweł Olejnik , Fryderyk Wiądkowicz, and Jan Awrejcewicz 

Abstract The purpose of the work is to numerically simulate and mathematically describe an experimental model of a mechatronic analogy of a human circulation system. The examined laboratory system consists of pneumatic elements to model the blood circulation system. Two containers with rubber membranes model heart ventricles, another four similar containers model the capacity and elasticity of arteries and veins. Two pneumatic valves are used to control the pressure in main chambers. To analyze the dynamics of the system, four digital pressure sensors are used to measure the system pressures. The step and ascending linear input signal responses were examined.

Keywords Circulation system · Mechatronic analogy · Experimental station

1 Introduction

The human circulatory system is a complex system that performs a number of key functions in the body. This system transports oxygen throughout the body, ensures a constant supply of nutrients to its organs, distributes vitamins and minerals, also participates in the removal of metabolic products from cells, transporting them to the excretory organs. The proper functioning of the circulatory system is crucial for the functioning of the whole organism. Therefore, it is extremely important to create an artificial circulatory system that could replace the biological system in the case of its inability to continue functioning. The circulatory system is exposed to many threats, such as: diseases, mechanical damage to the most important organs, inefficiency, incorrect functioning and many more.

P. Olejnik (✉) · F. Wiądkowicz · J. Awrejcewicz
Department of Automation, Biomechanics and Mechatronics, Faculty of Mechanical Engineering,
Lodz University of Technology, Lodz, Poland
e-mail: pawel.olejnik@p.lodz.pl

© Springer Nature Switzerland AG 2021
J. Awrejcewicz (ed.), *Perspectives in Dynamical Systems III: Control and Stability*,
Springer Proceedings in Mathematics & Statistics 364,
https://doi.org/10.1007/978-3-030-77314-4_14

The main elements of the circulatory system, the construction and functioning of which will be described in the following chapters are: heart, blood vessels, blood, spleen.

The heart is the key organ of the circulatory system. It ensures constant blood flow throughout the body. From a mechanical point of view, the heart is a pump. In many non-technical studies, the heart is presented as an embossing and suction pump. This is a mistaken belief. In the event that the heart would be a pressing-sucking pump in our bodies, a negative pressure would be created at each blow, which would destroy the blood vessels and ultimately lead to immediate death. From the biological point of view, the heart is an organ constructed of transversely striated muscle. The shape resembles a distorted cone, pointing vertically downwards. The heart reaches its normal size in relation to the rest of the body at the age of 18–20.

The most important elements of the heart's construction are the two left and right vestibules and the right and left chambers. Through the upper and lower main vein, the un-oxygenated blood from the body goes to the right vestibule. Through the contraction of the vestibule, the blood gets into the right ventricle, then after the contraction of the right ventricle it is pumped through the lungs to the lungs where it oxygenates. Oxygenated blood returns to the left atrium via pulmonary veins, where it is passed to the left ventricle after its contraction. Due to left ventricular contraction, the already oxygenated blood is thrown further through the aorta to all organs in the human body.

1.1 Mechanical Operation of the Heart

The mechanical activities of the heart are limited to contraction and relaxation of the chambers and atria. Ventricular spasm occurs alternately with atrial contraction. During ventricular contraction, blood is ejected into the small blood circulation from the right ventricle and into the large blood circulation from the left ventricle. However, during atrial contraction, blood gets from the atria into the chambers. All phases are cyclic and repeat at rest with a frequency of about 1.2 Hz. The duration of a single cycle (total duration of ventricular contraction and diastole) is approx. 800 ms. Time of duration of main phases of the heart cycle is as follows (in ms): ventricular contraction (270), ventricular diastole (530).

1.2 The Time History of Blood Pressure

In this work, main emphasis was placed on the pressure measurement in the system under examination. Sensors are located in four places of the system for in-depth analysis of its operation. The approximate course of pressure, depending on the blood vessel and the place in the human body can be encountered, as it follows (mm Hg): left atrium (about 4), left ventricle (0–120), aorta (80–120), large arteries

(70–130), small arteries (55–110), arterioles (20–60), capillaries (4–20), veins and atriums (constant, about 5), right ventricle (0–27), pulmonary arteries (5–27).

Both in the left and right atrium the pressure is low and its fluctuations are minimal. The largest pressure amplitudes occur in the left ventricle, from 0 to 120 mm Hg. Pressure in the aorta is the blood pressure measured, e.g., when visiting a doctor. In an adult, a healthy person ranges from 80 to 120 mm Hg. In the large arteries, the pressure values are close to the pressure in the aorta. In small arteries, the course is similar to large but the average pressure values and its amplitude are smaller. A similar situation occurs in arterioles. In capillaries and veins, the blood flows under a small, constant pressure, about 10 mm Hg. In the right ventricle the amplitude of the pressure increases and amounts to 20 mm Hg. In pulmonary arteries, the pressure is about 20 mm Hg, while its amplitude is relatively small.

2 Concepts and Implementation of Model Circulatory Systems

Creation of circulatory systems and simulation of the main pump behavior, i.e., heart pulsation, involves many mechanisms and biophysical phenomena, which interact in many ways. One encounters, between others [1]: tissue fluids, heart rate and stroke volume, oxygen in non-muscle, oxygen in muscle, local autoregulation in muscle, vascular stress relaxation, kidney dynamics, capillary system, angiotensin control, aldosterone control, autonomic control, electrolytes and cell water, pulmonary dynamics.

After analyzing the literature related to the subject of artificial heart a few interesting solutions of the artificial heart model were selected.

A very interesting solution of the mechatronic model of the circulatory system is the model proposed in [2] by Shi and Chew. In contrast to the model studied in this work, they modeled the circulatory system using electrical components. For the modeling of atria and chambers, capacitors were used. The diodes model the valves which correspond to the check valves in the tested system. Throttling valves, i.e., lungs in an electric circuit, are modeled using resistors. In addition, the coils used in the circuit are used to model the inertia of the fluid flowing through the vessels, and additional capacitors are the equivalent of tanks that model the capacities of veins and arteries and their elasticity.

An electrical network analog of a human cardiovascular system has been also simulated in [3]. The results of the numerical simulations performed by the authors are confirmed in this work, i.e., in the mechatronic pneumo-hydraulic model by registration of similar shapes time histories of pressures in the pulmonary veins and aorta.

A ventricular assist device proposed in [4] can model the characteristics of the natural human blood circulatory system, including the pressure and flow of the aortic root, as well as mathematical model of the system has been established. A

new mock circulatory system has been established using basic hydraulic elements. Numerical computation has been employed on the basis of modelling of fluid dynamics and ideal gas flow by means of mechatronic devices, such as: centrifugal pump, electromagnetic switch valve, vessels with a certain volume and a throttling valve. Other attempts of building of mock circulatory systems for testing pediatric rotary blood pumps [5], and ventricular assist device differ in the realization of the cardiac function [6–8].

Numerical simulations of circulatory systems are widely used, allowing a medical physicist for a better understanding of the mechanisms and the functions thereof. In this context, a systemic circulation simulator developed in Automation Studio is considered in [9]. The work describes a computational approach for a mechanical model of the systemic circulation. It reproduces with high accuracy the physiological hemodynamic function. Quite universal model allows for changing of the vascular parameters and the construction of pressure-blood flow curves in various components of the system at a physiological conditions.

Dynamic behavior of the cardiovascular system was simulated in [2] with the use of a mechanical simulator. The simulator including the coronary circulation modelled by a nonlinear hydraulic resistance device, the aorta modelled by different wall thickness rubber tubes, the arterial vascular resistance modelled by a thin, variable length tube and other was mainly created for teaching purposes.

Electric equivalent as a net has been used in [10] to develop a model of greater of the human circulatory system. The designed model allows to simulate the biological vascular system and to analyze the greater circulation in physiological and pathological cases.

Application of a PExSim for modeling a POLVAD artificial heart and the human circulatory system with left ventricle assistance is considered in [11]. There are presented simulation results of the physiological conditions, left ventricle failure and pathological conditions with parallel assistance.

3 Laboratory Station

3.1 Analogy to Reality

It was inevitable that some simplifications were applied to reality in order to allow the construction of the system under examination. As a consequence, in the system shown in Fig. 1, the atria and their contraction are not explicitly modeled, and water that simulates blood enters the chambers due to the elasticity of the membranes used in the system.

The thesis was also made that blood circulates throughout the body due to the elasticity of the blood vessel system. In order to reproduce this assumption, two tanks were built, equipped with membranes that represent the elasticity of blood vessels. In addition, veins and arteries in the human body have an unmatched volume.

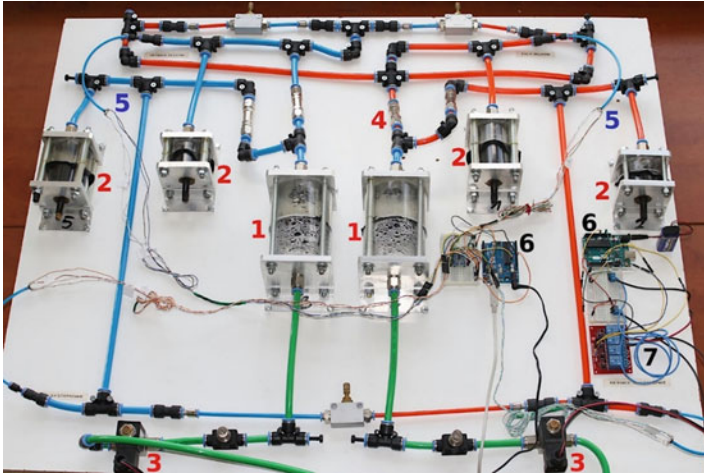


Fig. 1 View of the experimental station modelling the mechatronic circulatory system: 1 heart chambers, 2 artery capacity and veins, 3 electromagnetic valves, 4 non-return valve, 5 pressure sensors, 6 microcontrollers, 7 electric relays

To make the model realistically, two more tanks were added, the volume of which corresponds to the amount of blood in the veins and arteries in the human body. The throttling valves used in the system are used to model the throttling of blood flow in organs in the human body. In the analogy, one of the throttling valves models the throttling in the capillaries of all organs (except the lungs), while the other two model the choking in the capillaries in the left and right lung. However, it is nowhere described how exactly the blood flow on the organs is suppressed, in addition, in each of the organs the choking is different. Simplifying the heart cycle is also simplified. In the examined system, the heart cycle consists of two phases: valve opening, during which the pressure in the chamber increases and the liquid is thrown onto the circulation, corresponds to ventricular contraction, and phases when the valves are closed, chambers are vented and thanks to elasticity, the membranes return to the original shape and the liquid fills the chambers again, it is a phase similar to the atrial contraction and the rest of the heart. The heart cycle consists of many different phases that differ from each other by pressures, valve status, duration and blood ejection. It is also worth mentioning that the valves present in the heart in the system under test correspond to check valves.

3.2 Construction and Components

In order to model the heart chambers, special tanks (1) made of two fragments of a Plexiglas tube with a diameter of 84 mm, a height of 65 mm and a thickness of 3 mm were used. Both pieces of pipe were connected with silicone with aluminum flat bars

serving as covers. A rubber membrane about 1 mm thick was inserted between the combined halves of the tanks. The whole was screwed using threaded rods and nuts. The reservoirs modeling artery capacity and veins were made in the same way (2). Both tanks have a diameter of 32 mm, and their height in the case of a venous tank is 40 mm and in the case of an arterial reservoir is 22 mm.

Pneumatic parts are used as PU wire connections: $\text{Ø}10/8$ mm – red, green, blue; $\text{Ø}6/4$ mm – red, blue; $\text{Ø}4/2$ mm – blue.

Connectors are created by three-way joint $\text{Ø}10$ mm and $\text{Ø}6$ mm; four-way joint $\text{Ø}10$; angular connector $\text{Ø}10$ mm; reducing connectors $\text{Ø}10/6$ mm, $\text{Ø}6/4$ mm and $\text{Ø}8/6$ mm screw-in straight connector with thread G1/4" to the line $\text{Ø}10$ mm.

The system includes control valves: shut-off electromagnetic valve 3/2 G1/4" (3), directly controlled, normally closed (flow: 300 l/min, working pressure range: 0–1.0 MPa) and throttle valves: G1/4" valve restricting input; Trunking check valve $\text{Ø}10$ mm; non-return valve (4).

The pressure measurement was carried out using the Honeywell digital pressure sensor ABPDANN005PG2A3 (5).

In order to activate the valves and to read measurement signals from the sensors and write data in a form allowing their subsequent processing, it was decided to use the Arduino UNO microcontroller (6). The selected platform is used to control valves, download data from 4 digital pressure sensors and send downloaded data by means of UART transmission to a PC. Control is carried out indirectly, i.e., a logic signal from the microcontroller is sent to two separate relays (7) (after each on the valve), which after receiving the high signal short circuit to ground, which results in the required voltage on the valves controlling the air flow. The voltage required to control the valves is provided by an additional pulse power supply (8) set to 24 V.

4 Control System

Figure 2 shows the block diagram of the tested system, including pneumatic and electronic parts.

Looking at the diagram at the very bottom there are the elements responsible for controlling the pneumatic valves. The dotted line in the schematic indicates the digital signal. A high or low signal is required to control the valves, and a 14-bit digital signal is sent in the case of sensors. The diagram includes the division into the left and right parts of the heart and the veins and arteries connected directly to the heart. A small and large blood circulation was also distinguished. At the top of the diagram you can see a set of elements responsible for the acquisition and analysis of the data collected by the sensors. From the constructed diagram it also follows that this system is an open control system. Based on the diagram shown, the operation of the entire system can be described. When there is a high signal on the Arduino output pins on the relays, a voltage of 3.3 V will flow, thanks to which the relays will be shorted to ground, which will cause the valves to be 24 V, which will open them.

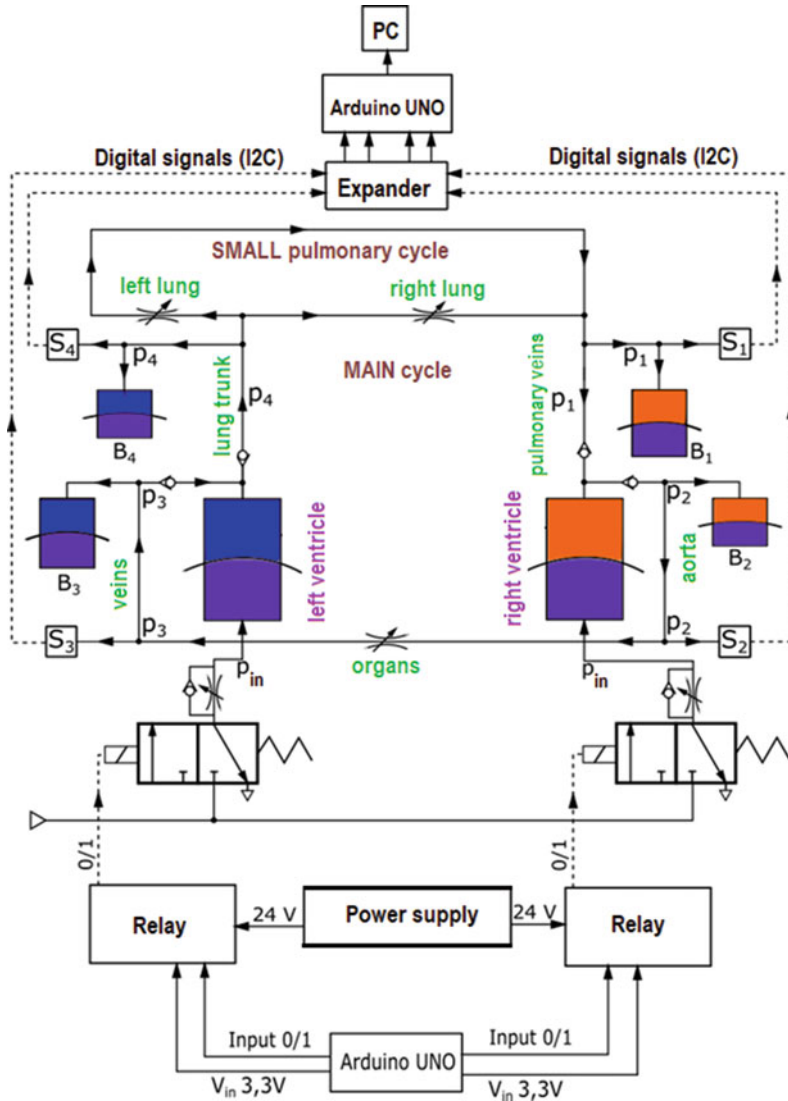


Fig. 2 Block diagram of the laboratory experimental system station modelling the mechatronic circulatory system

Then, the air will flow through the valves at the pressure set on the compressor. It will deform the membranes in the main tanks, which will make it similar to reality, the water will be pushed into the small and main circuit. This corresponds to the ventricular contraction phase. When the high signal on the Arduino output pins disappears, the valves will close and the atrial and resting phase will start, which will fill the tanks again.

5 Measurements and Analysis of Time Characteristics of Dynamic Responses

5.1 Sensor Characteristics and Signal Processing

Four digital sensors from the Honeywell series of ABPs were used to measure the pressure. Selected models are 14-bit sensors operating in the 0–5 PSI range, communicating with the microcontroller using the I2C bus. The problem encountered during the installation of the sensors were the identical bit addresses of all 4 sensors, which is why it was decided to use the I2C bus expander, which makes it possible to distinguish up to 8 devices on the address bus. Before the measurements were made, the static characteristics of all sensors were removed. To do this, a 1.5 m long PU wire 10/8 pneumatic conduit was attached to an even and flat surface, which was filled with water using a syringe. The whole system was set vertically and then the height of the liquid column in the transparent conduit was measured to determine the pressure. The hydrostatic pressure was calculated $p = \rho gh$, where: p – hydrostatic pressure [Pa], g – acceleration of gravity [m/s^2], ρ – the density of the liquid used during the measurement [kg/m^3], h – the height of the liquid column [m].

Pressures $p_{1..4}$ versus voltage readings by sensors 1–4 are experimentally estimated as follows: $p_1(v) = 0.0265v - 45.227$, $p_2(v) = 0.0264v - 44.376$, $p_3(v) = 0.0272v - 48.091$, $p_4(v) = 0.0262v - 42.766$. The sensors are connected to the expander ports 6, 3, 2, 7, respectively. The formulas of functions for each sensor describe the obtained relationships between the sensor's indications and the pressure value in mm Hg.

The characteristics $p_{1..4}(v)$ were obtained by measuring at several points and then the obtained results were approximated with a straight line. The correlation coefficient (R_2) for each sensor is greater than 99%, so it can be concluded that each sensor has a linear static characteristic. In order to collect data from the sensors, a program for the Arduino platform was written, the task of which is to communicate with the sensors, process the signal and further transfer of data to the computer. Communication with sensors takes place on the I2C bus through an expander separating signals from 4 sensors into 4 different addresses. The microcontroller downloads data at a frequency of 20 Hz. Then, programmatically using the analytical relations obtained during the identification of the sensors, the received values are converted into pressure values in mm Hg. The last stage of the program's operation is sending the converted values to the PC computer via UART communication. One can view the received values on the computer in the serial port monitor.

5.2 Measurement Method

Sensors have been incorporated into the system in four places. Sensor 1 measures the pressure corresponding to the pressure in the pulmonary veins, delivering

oxygenated blood to the left atrium. The pressure of water corresponding to the pressure in the main veins entering the right atrium is measured by the sensor 4. The sensor 3 examines the pressure in the pulmonary trunk that goes directly from the right ventricle and delivers blood to the lungs. An important factor, from the point of view of comparison between the model and the reality, is sensor 2. It measures the water pressure in the place corresponding to the aorta. The blood pressure is measured in the aorta at the left ventricular output.

5.3 Results

First, the system response to linear excitation was investigated. The measurement was made by reading the data from the sensors while increasing the pressure reference value from 0 to 3 bar (0–2250 mm Hg). The response of 4 sensors was obtained as a function of time, which is shown in Fig. 3. The set point signal was generated by a compressor whose output signal was manually regulated by a reducing valve.

According to the observed response, the system can be used at a set pressure of not more than approx. 800 mmHg which corresponds to 1 bar on the pressure gauge connected to the reducing valve of the used compressor. Above this value each of the sensors will show the maximum of its range.

It can be seen that the system’s response has a certain inertia due to the elasticity of the membranes used. Unfortunately, the inertia when venting the space under the membrane is so large that it disturbs the heart cycle. This is evident during the operation of the system when the valves are reopened before the pressure under the membrane equalizes with the atmospheric one then measurements were made during the normal work cycle. Forcing pressure was 1 bar, valve opening time corresponding to ventricular contraction was 600 ms, while valve closing time, corresponding to atrial contraction and cardiac rest phase, was 1000 ms. It was

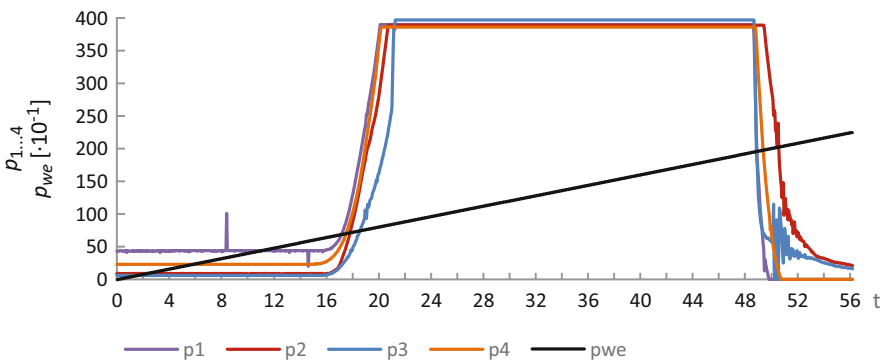


Fig. 3 System response to the ascending linear input p_{we} (in mm Hg)

decided to increase the heart's working time twice as much as the real one due to the inertia of the air. With a shorter opening and closing time, diaphragm deflections were observed (Fig. 4).

The graphs shown below in Figs. 5, 6, 7, and 8 present the data collected by each of the sensors. The measurement was made every 0.05 s.

The time history of pressure shown in Fig. 5 corresponds to the pressure in the pulmonary veins delivering oxygenated blood to the left atrium. The pressure value varies from about 15 to 275 mm Hg.

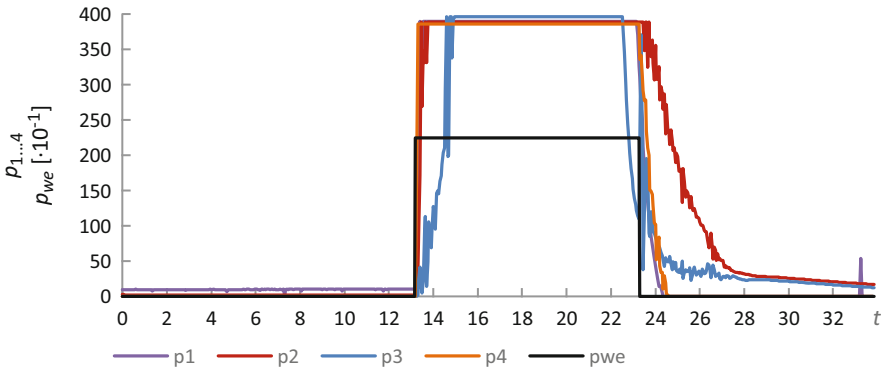


Fig. 4 System response to the step input p_{we} (in mm Hg)

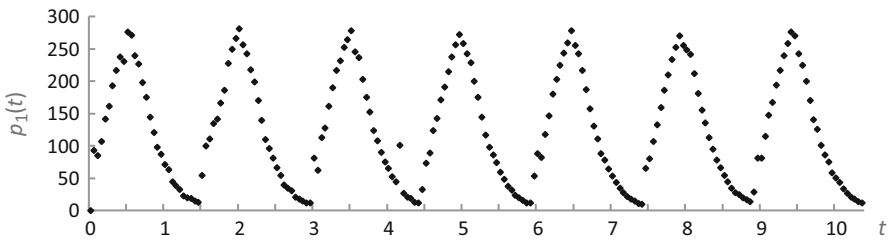


Fig. 5 Time history of pressure (in mm Hg) read by sensor 1

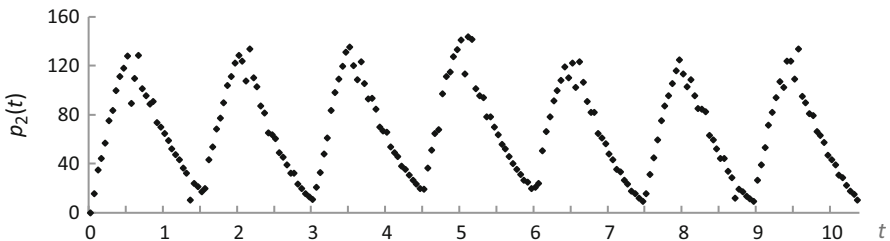


Fig. 6 Time history of pressure (in mm Hg) read by sensor 2

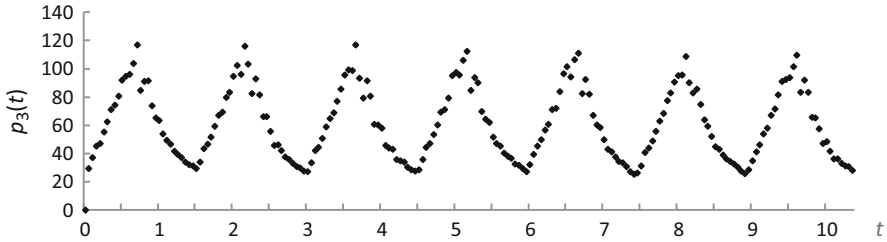


Fig. 7 Time history of pressure (in mm Hg) read by sensor 3

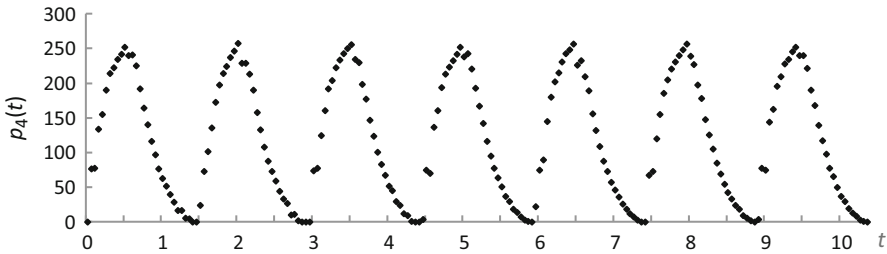


Fig. 8 Time history of pressure (in mm Hg) read by sensor 4

The value read by sensor 2 is the arterial pressure present in the aorta. In an adult, the average upper (systolic) pressure is about 120 mm Hg, while the lower (diastolic) pressure is about 80 mm Hg. In the tested system, the value of the upper pressure is about 130 mm Hg, while the lower pressure is about 30 mm Hg.

Sensor 3 collects data behind the throttling valve, modeling the organs. The pressure values collected correspond to the blood pressure flowing into the right atrium. The pressure ranges from 30 to about 115 mm Hg.

The data from sensor 4 corresponds to blood pressure after lung ejection from the right ventricle. The read pressure varies from 0 to approx. 250 mm Hg.

The obtained pressure waveforms show a certain periodicity and regularity. This means that the system under test works correctly and smoothly.

6 Conclusions

After examining the response of the system to an increasing signal, it can be noticed that when the forced force exceeds 1 bar, the pressure in the system exceeds the measuring range of the sensors.

During the experiment, the system's response to a step signal of 3 bar was also tested. Despite the high pressure, it can be seen that in the case of sensor 3, the pressure has settled after almost a second. This is due to the fact that the sensor 3 is

located farthest from the source of pressure, which in the system appears first in the main tanks.

The readings from the sensor 2, showing the arterial pressure are not consistent with the reality. Their values range from 15 to 130 mm Hg. It is similar to the course of pressure in the left ventricle.

Sensors 1 and 3 show the blood pressure in the veins. The waveforms deviate significantly from reality, which should be almost linear. This may indicate that both the system under test and the proposed simulation model incorrectly reflect the mechanics of the circulatory system.

When analyzing the graphs, there is a large similarity between pressure 1 and 4 and between pressure 2 and 3. This is due to the layout of the system, which sensors 1 and 4 are in one circuit (pulmonary circuit), while sensors 2 and 3 in the other circuit (main circuit).

The pressure values in the main circulation are close to the real ones, while those from the pulmonary circulation exceed more than twice the values observed in the human body. This is due to the fact that the work of non-return valves, as opposed to valves, depends on the pressure behind the valve. Valves may not open properly or remain closed for some time. This problem could be solved by separating these roads or by explicit modeling of the atria.

A drawback of the system is the fact that it has been adapted to work horizontally. In fact, the circulatory system works most of the time in many different positions. It can affect the correlation between read and real values. In addition, the capacity of the system should be about 2 liters of water, since it was more than twice less than the amount of blood in an adult human.

Finally, it can be concluded that in the tested system solutions such as membrane tanks, control system and measurement method work correctly, however, after analyzing the dynamics of the system it can be stated that it does not sufficiently well maps the real circulatory system.

Acknowledgements The authors would like to thank Professor Donat Lewandowski for valuable remarks and discussion.

References

1. Dittrich, K., Riesenber, A.: A model of the human circulatory system with an extended pulse simulator as a basis for artificial heart monitoring. *Biomed. Eng.* **30**(6), 385–361 (1996)
2. Zannoli, R., Corazza, I., Branzi, A.: Mechanical simulator of the cardiovascular system. *Phys. Med.* **25**, 94–100 (2009)
3. Formaggia, L., Nobile, F., Quarteroni, A., Veneziani, A.: Multiscale modelling of the circulatory system: a preliminary analysis. *Comput. Vis. Sci.* **2**, 75–83 (1999)
4. Ferrari, G., Delazzari, C., Mimmo, R., Ambrosi, D., Tosti, G.: Mock circulatory-system for in-vitro reproduction of the left-ventricle, the arterial tree and their interaction with a left-ventricular assist device. *J. Med. Eng. Technol.* **18**(3), 87–95 (1994)
5. Telyshev, D.V., Pugovkin, A.A., Selishchev, S.V.: A mock circulatory system for testing pediatric rotary blood pumps. *Biomed. Eng.* **51**(2), 83–87 (2017)

6. Zannoli, R., Corazza, I., Branzi, A.: Mechanical simulator of the cardiovascular system. *Phys. Med.* **25**(2), 94–100 (2009)
7. Timms, D., Hayne, M., McNeil, K., Galbraith, A.: A complete mock circulation loop for the evaluation of left, right, and biventricular assist devices. *Artif. Organs.* **29**(7), 564–572 (2005)
8. Colacino, F., Arabia, M., Moscato, F., Danieli, G.: Modeling, analysis, and validation of a pneumatically driven left ventricle for use in mock circulatory systems. *Med. Eng. Phys.* **29**(8), 829–839 (2007)
9. Lemos, D., Nunes, A., Machado, J., Barros, C., Leão, C.P., Soares, F., Minas, G.: Mechanical simulation model of the systemic circulation. *Measurement.* **66**, 212–221 (2015)
10. Pustelny, T., Struk, P., Nawrat, Z., Gawlikowski, M.: Design and numerical analyses of the human greater circulatory system. *Eur. Phys. J. Special Topics.* **154**, 171–174 (2008)
11. Siewnicka, A., Fajdek, B., Janiszowski, K.: Application of a PExSim for modeling a POLVAD artificial heart and the human circulatory system with left ventricle assistance. *Polish J. Med. Phys. Eng.* **16**(2), 107–124 (2010)

Robust Design of Inhibitory Neuronal Networks Displaying Rhythmic Activity



Joseph D. Taylor, Kamal Abu-Hassan, Joanne J. A. van Bavel, Marc A. Vos, and Alain Nogaret

Abstract Central pattern generators (CPGs) are neuronal networks that autonomously produce patterns of phase-locked activity. The need for bioelectronic implants that adapt to physiological feedback calls for novel methods for designing synthetic CPGs that respond identically to their biological counterparts. Here, we consider optimization-based parameter estimation for identifying network parameters that give rise to activity with specific temporal properties. We demonstrate that reducing a network to the phase resetting curves (PRCs) of its component neurons allows for the sequential parameter estimation of each single neuron separately. In this way, the challenges associated with estimating all network parameters simultaneously may be avoided. We highlight a possible application of our approach by estimating parameters of a CPG emulating the phase-locked activity associated with ECG data. This work paves the way for the design of synthetic networks which may be interfaced with nervous systems.

Keywords Parameter estimation · Central pattern generators · Neuronal networks

1 Introduction

Synchronization in networks of coupled oscillators is a phenomenon which holds particular importance in the central nervous system. The onset of synchrony and phase-locking has long been studied in the context of smaller networks known as central pattern generators (CPGs), circuits of neurons whose synaptic interactions

J. D. Taylor (✉) · K. Abu-Hassan · A. Nogaret
Department of Physics, University of Bath, Bath, United Kingdom
e-mail: j.taylor@bath.ac.uk

J. J. A. van Bavel · M. A. Vos
Department of Medical Physiology, Division of Heart and Lungs, University Medical Center
Utrecht, Utrecht, Netherlands

can autonomously produce rhythmic patterns of activity in which the component neurons burst with fixed phasic relationships [4]. The precise phasic timing of CPG networks depends sensitively on the interplay between the intrinsic dynamics of the component neurons and the strength and time-dependent properties of the synapses which connect them. This nonlinear dependence makes estimating all parameters of a network model a formidable problem. Nonlinear optimization has previously been used to estimate single neuron model parameters [6], but such methods quickly become intractable when optimizing large network models composed of complex neurons. In this paper, we propose a solution to this challenge by describing a novel two-stage estimation method. We first reduce the network oscillators to their individual phase resetting curves (PRCs). We show that these curves can be used to determine how each oscillator must behave individually for the network to generate specific rhythmic patterns. This allows each oscillator to be optimized entirely separately, enabling the estimation of all neuron and synapse parameters of the network while avoiding the challenges associated with searching the high-dimensional parameter space of a whole-network model. We apply our approach to the problem of estimating synaptic conductances for a four-cell CPG designed to predict the sequence of heart chamber contractions in an ECG recording. This work paves the way for the development of bioelectronic implants that adapt appropriately to physiological feedback [7]. The rest of the paper is organised as follows: Sect. 2 describes the model system used throughout this work, and Sect. 3 shows examples of the limit cycle dynamics available to multistable CPGs; Sect. 4 demonstrates that the PRCs of the constituent neurons contain all the information necessary to predict these network dynamics; Sect. 5 explains how the shape of neuron PRCs determines the existence and character of phase-locked modes; Sect. 6 describes the optimization-based method that we use to estimate network parameters, which we use in Sect. 7 to construct a four-cell CPG. Finally, we conclude with possible directions for future work.

2 Model System

In this paper, we consider networks of identical neurons coupled by inhibitory chemical synapses (Fig. 1a). The neurons are described by an extended Morris-Lecar (ML) model that includes a Ca^{2+} -dependent K^+ current that allows them to be parameterized in a bursting regime [5]. In isolation, each individual neuron displays periodic bursting with period T_0 in response to a fixed stimulation current. The membrane voltages obey the current balance equation:

$$C_m \frac{dV}{dt} = -I_{\text{Ca}} - I_{\text{K}} - I_{\text{KCa}} - I_L - I_{\text{syn}} + I_{\text{stim}}, \quad (1)$$

where $C_m = 20 \mu\text{F}/\text{cm}^2$ is the neuron membrane capacitance and $I_{\text{stim}} = 45 \mu\text{A}/\text{cm}^2$ is the injected current. The leak current $I_L = g_L(V - E_L)$ has a

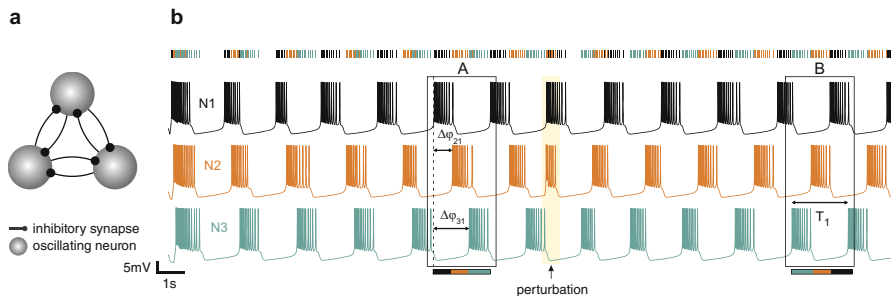


Fig. 1 (a) Bursting Morris-Lecar neurons were interconnected with mutually inhibitory synapses, $g_{\text{syn}} = 10\mu\text{S}/\text{cm}^2$. (b) The network initially converged towards a steady-state mode (N1→N2→N3) labeled A. The application of a brief depolarizing current pulse to neuron N2 switches the circuit to a second steady-state mode, labeled B, in which the neurons burst in a different order. Both modes of activity are stable solutions of the network dynamics with a cycle period of $T = T_1$

conductance $g_L = 2.0 \text{ mS}/\text{cm}^2$; $E_L = -60 \text{ mV}$. The spike-generating Ca^{2+} and K^+ voltage-dependent ionic currents (I_{Ca} and I_{K}) are of the Hodgkin-Huxley type. The transient calcium current is given by $I_{\text{Ca}} = g_{\text{Ca}}m(V - E_{\text{Ca}})$, where the activation variable m is assumed to respond instantaneously to changes in membrane voltage and has a steady-state response given by $m_{\infty} = 0.5[1 + \tanh((V + 1.2)/18)]$. The delayed rectifier current is given by $I_{\text{K}} = g_{\text{K}}n(V - E_{\text{K}})$, where the activation variable obeys the first-order kinetics: $dn/dt = \psi(0.5[1 + \tanh((V - 12)/17.4)] - n)/\tau_n$; $\tau_n = 1/\cosh((V - 12)/34.8)$; $\psi = 0.23$, $g_{\text{K}} = 8.0 \text{ mS}/\text{cm}^2$, $E_{\text{K}} = -84 \text{ mV}$. For bursting dynamics, we include $I_{\text{KCa}} = g_{\text{KCa}}z(V - E_{\text{K}})$, where $z = \text{Ca}/[\text{Ca} + 1]$ and Ca is the intracellular calcium concentration which obeys $d\text{Ca}/dt = \epsilon(-\mu I_{\text{Ca}} - \text{Ca})$; $\epsilon = 0.006$, $\mu = 0.02$, $g_{\text{KCa}} = 0.25 \text{ mS}/\text{cm}^2$.

The synaptic currents are given by $I_{\text{syn}} = g_{\text{syn}}s(V - E_{\text{syn}})$, where g_{syn} is the maximal synaptic conductance and $E_{\text{syn}} = -75\text{mV}$ is the synaptic reversal potential. The gating variable s represents the fraction of docked synaptic neurotransmitters and obeys the first-order kinetics $ds/dt = \alpha F(V_{\text{pre}})(1 - s) - s/\tau_{\text{syn}}$, where $\alpha = 6.25\text{ms}^{-1}$, $\tau_{\text{syn}} = 100\text{ms}$, and $F(V_{\text{pre}}) = 1/(1 + \exp(-(V_{\text{pre}} - \theta_{\text{syn}})/2))$. The threshold parameter θ_{syn} is the value that the presynaptic membrane voltage must exceed for neurotransmitter release to occur. Setting $\theta_{\text{syn}} = 0\text{mV}$ ensures that postsynaptic inhibition occurs only when the presynaptic cell spikes [8].

3 Network Configuration and Dynamics

The interplay of mutual synaptic inhibition in CPG circuits leads to stable patterns of oscillation in which the neurons phase-lock one another, bursting with fixed phasic relationships. In designing artificial CPG networks, we are interested in tailoring

the precise timings of these bursts relative to one another. We first demonstrate this type of behaviour by interconnecting three identical ML neurons with reciprocally inhibitory synapses. We plot the membrane voltage of the three interconnected cells over thirteen cycle periods, with the raster plot representing neuronal spike times (Fig. 1b). This network initially stabilises in a steady-state mode labeled A, in which the bursting of N1 is followed by N2, which is followed by N3. In this stable mode the bursting of N2 and N3 are delayed relative to that of N1 by $\Delta\Phi = \frac{1}{3}T_1$ and $\Delta\Phi = \frac{2}{3}T_1$, respectively. We refer to these delays as *phase lags*. The network will maintain this stable mode unless it receives additional input. ‘Multistable’ CPG circuits can simultaneously support several stable modes, and transient perturbations to a such a circuit may induce a shift from one stable pattern of behavior to another. We demonstrate this property by allowing the network to stabilize and applying a brief current pulse to neuron N2 (Fig. 1b). This perturbation switches the network to a second stable mode, labeled B, in which the neurons fire in a different order.

In order to simplify the circuit analysis, following references [3, 9], we show how the full network dynamics may be visualized in two-dimensional return maps. We begin with some useful notation. First, we explicitly define the phase lag $\Delta\Phi_{i1}$ for each neuron i as the time delay in burst initiation relative to that of the reference neuron N1, normalised by the bursting period T_1 (see Fig. 1). Let the onset of bursting in N1 define the start of a new cycle. The state of the system in any given cycle may be defined as the the phase lag pair $\Delta\Phi = (\Delta\Phi_{21}, \Delta\Phi_{31})$. We can initialize the network in a particular phase lag state by staggering the onset of stimulation I_{stim} for each cell. The phase lags in successive cycles can then be measured as the system tends towards a stable mode of oscillation and this set of evolving lags can be plotted as a trajectory in a 2D $(\Delta\Phi_{21}, \Delta\Phi_{31})$ coordinate system. Figure 2a shows the phase portrait of trajectories for a reciprocally-coupled network with homogenous synaptic strengths $g_{\text{syn}} = 1\mu\text{S}/\text{cm}^2$, where each trajectory emanates from a different initialization of $\Delta\Phi$. The state trajectories converge towards five attracting fixed points (or attractors) in the phase map, each corresponding to a different stable mode of oscillation. Each attractor has a color-coded ‘basin of attraction’, the set of initial phase lags for which the network arrives in the corresponding stable mode. Figure 2b shows the phase lag map for a ring network, similar to the reciprocal CPG, but with the conductances of the counterclockwise synapses set to $g_{\text{syn}} = 0\mu\text{S}/\text{cm}^2$. This CPG is still multistable, but a smaller range of dynamics is observed, with only two attractors present. By generating these phase lag maps, the full dynamics available to their respective networks may be visualized. Our goal of designing CPGs with particular stable rhythms can now be viewed as a question of finding network parameters which give rise to particular attractor positions in the network phase portraits.

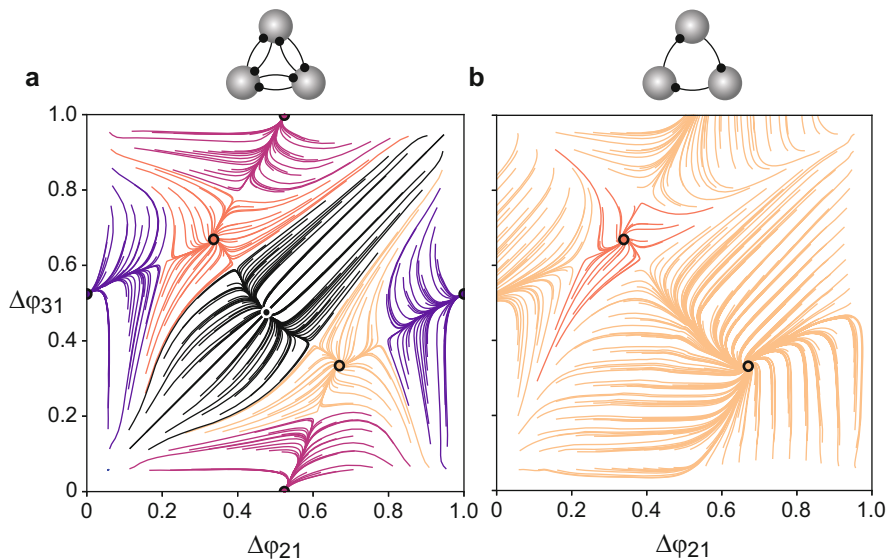


Fig. 2 (a) Phase lag map for the reciprocal network revealing five stable fixed points (FPs) at $(\Delta\Phi_{21}, \Delta\Phi_{31}) = (\frac{1}{2}, \frac{1}{2}), (0, \frac{1}{2}), (\frac{1}{2}, 0), (\frac{1}{3}, \frac{2}{3}),$ and $(\frac{2}{3}, \frac{1}{3})$. The basins of attraction of the FPs are color coded to match the color of the FP. (b) Phase lag map for the ring network showing the disappearance of the three partially-synchronous attractors, leaving only two attractors at $(\Delta\Phi_{21}, \Delta\Phi_{31}) = (\frac{1}{3}, \frac{2}{3}),$ and $(\frac{2}{3}, \frac{1}{3})$

4 PRCs Determine Network Dynamics

It has recently been demonstrated that the existence of synchronous modes of a network can be predicted by an analysis of the PRCs of the constituent neurons [1]. Here, we demonstrate that the PRCs of the constituent neurons contain sufficient information to predict both the stable *and* transient network dynamics presented in the previous section by reproducing the phase lag map shown in Fig. 2a. In doing so, we justify our subsequent use of the PRC for estimating neuron and synapse parameters. We start by describing the method of generating a PRC, which is schematically illustrated in Fig. 3a. In short, a single-oscillator PRC encodes the transient effect of synaptic inhibition on the cycle period of a running oscillator. Specifically, we wish to determine the effect of synaptic inhibition on a bursting ML neuron. To this end, two bursting ML neurons are connected as shown, with a presynaptic neuron N2 inhibiting a postsynaptic neuron N1. Initially, N1 is stimulated with $I_{\text{stim}} = 45\mu\text{A}/\text{cm}^2$ and exhibits intrinsic bursting with a cycle period T_0 . This constitutes our running oscillator. Subsequently, N2 is momentarily stimulated such that it produces a single burst that arrives at some phase $\varphi \in [0, 1]$ into the bursting cycle of N1. The synaptic inhibition from N2 then acts to perturb N1, temporarily lengthening or shortening its cycle period by some time ΔT , causing its next burst to occur later or earlier than it otherwise would have. We

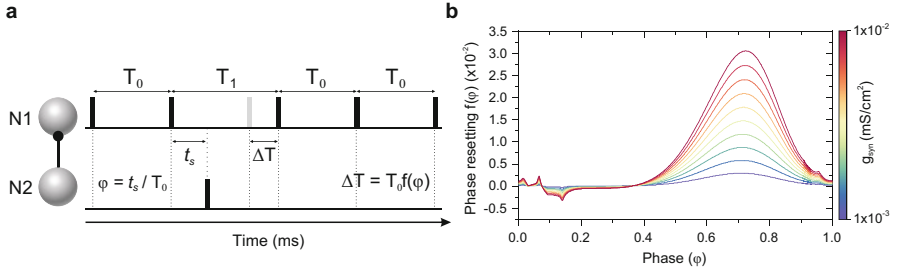


Fig. 3 Generation of the phase resetting curve. **(a)** Solid vertical bars indicate the bursting times of the neurons to their left. N1 represents a regular bursting ML model neuron with intrinsic period T_0 . A burst in the N2 causes N1 to burst later or earlier than it otherwise would have (grey bar), depending on when it occurs. The change ΔT in the period as a result of the perturbation received at a phase φ is used to generate the phase-resetting curve. T_1 represents the period of the cycle in which the stimulus is received. **(b)** Example phase resetting curves $f(\varphi)$ for an ML neuron at increasing synaptic strengths g_{syn} . Induced delays correspond to positive regions in the PRC and advances correspond to negative regions

denote the transiently adjusted period in which this perturbation is received as T_1 . By expressing this delay as a fraction of the typical cycle period T_0 , and repeating this process for multiple phases φ , the phase resetting curve $f(\varphi) = (T_1(\varphi) - T_0) / T_0$ of the neuron can be plotted. Figure 3b shows the PRC calculated for the Morris-Lecar neuron at increasing synaptic strengths g_{syn} .

We now briefly describe a model-free algorithm that we use to extract information from the PRC, and show that it can successfully predict the full dynamics of our CPG network [2]. The only inputs to the iterative algorithm are the PRCs of the component neurons, the initial phase of each neuron, and the intrinsic bursting period of each neuron. The iterator begins by determining which neuron(s) will burst next (i.e. whichever oscillator has the shortest time remaining before reaching a phase of one). Any oscillators that do not burst at this time have their phases incremented by the (normalised) time to this bursting event. Next, any phase resetting occurring as a result of the bursting neuron is subtracted from these phases. Then, the phase of the bursting oscillator is reset to zero. This completes one iteration of the algorithm. Once the program has iterated over $N_B = 1000$ bursting events, we can calculate the associated phase lags in each cycle period and plot these evolving phase lags as a trajectory on a return map. By initialising this algorithm with a host of different initial neuron phases, we can probe the entire phase space of the network, as before (see Sect. 2). This phase lag map is shown in Fig. 4, which shows a remarkable likeness to the observed dynamics (Fig. 2a). This is strong evidence in favour of our hypothesis that the PRC may be used to effectively analyse the behaviour of CPG networks.

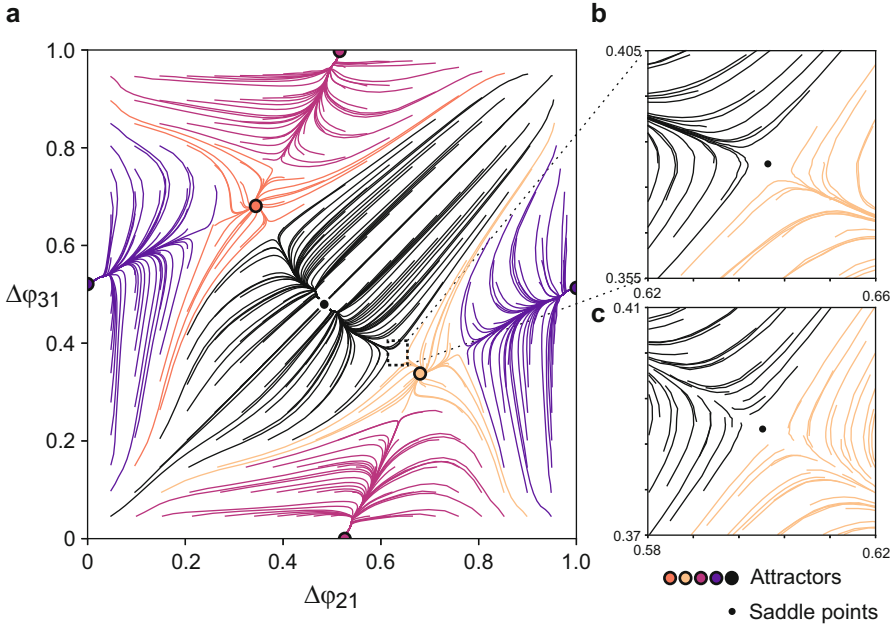


Fig. 4 (a) PRC-generated phase lag map for the reciprocal network. Just as in the observed network phase-lag map, there are five stable FPs at $(\Delta\Phi_{21}, \Delta\Phi_{31}) = (0.5, 0.5), (0, 0.5), (0.5, 0), (0.33, 0.66),$ and $(0.66, 0.33)$. In addition to correctly predicting the attractor locations, the PRC-generated map displays a strikingly similar trajectory flow globally. (b) Enlarged area of the PRC-generated phase lag map corresponding to a saddle point and its environment. (c) Enlarged area of the same saddle point in the observed network phase lag map. Note the slight repositioning of the saddle point

5 Stable Modes Correspond to Specific PRC Shapes

Recall that our aim is to estimate parameters for a CPG network which displays specific rhythmic patterns. It is useful to briefly derive the necessary criteria for the existence of stable oscillatory modes. We simplify our analysis by considering a ring network of N *identical* oscillators in which each neuron is inhibited by the preceding neuron in the ring, though a more detailed analysis is possible if these assumptions are relaxed. In any phase-locked oscillatory mode, by definition, the relative phases of the oscillators have ceased to change (Fig. 1b). This is only possible if the cycle period of all neurons in the network are equal *after* the phase resetting effects of synaptic inhibition are taken into account [2]. Therefore, if each neuron i receives synaptic inhibition from the preceding neuron at a phase φ_i , then the new entrained cycle period of all neurons must be equal to $T_1 = T_0 + f_i(\varphi_i)$

in the stable phase-locked mode. In our system, all (identical) cells have the same intrinsic period T_0 , and so our first existence criterion for phase-locked modes is:

$$f_1(\varphi_1) = f_2(\varphi_2) = \dots = f_n(\varphi_n) = \dots = f_N(\varphi_N). \quad (2)$$

In other words, all neurons must have equal values of $f_i(\varphi_i)$ in order to possess the same entrained period after phase resetting. The second criterion is the trivial fact that since an oscillator must be in phase with itself, the sum of all the phase differences around the ring must add up to the common entrained period (or some integer multiple thereof). Our second existence criterion for a phase-locked mode is therefore:

$$\sum_{i=1}^N \varphi_i = m[1 + f_n(\varphi_n)], \quad (3)$$

for some integer $m \in [0, N]$. So, if we desire an N -cell network that displays a particular stable mode, these criteria inform us that: (1) each oscillator i must possess a particular PRC which passes through a specific $(\varphi_i, f_i(\varphi_i))$ coordinate, and that (2) all $f_i(\varphi_i)$ must be equal. We can then use this insight to perform N individual parameter estimations, each one optimizing the parameters of a single neuron to produce a model cell with particular PRC characteristics. By analysing the network in terms of individual cells in this way, we are able to avoid difficulties associated with estimating parameters of an entire network simultaneously. In the next section, we demonstrate how this estimation is performed.

6 Parameter Estimation Procedure

In order to estimate parameters for a single neuron which possesses a desired phase resetting characteristics, we begin by designing artificial ‘target data’ $V_{\text{data}}(t)$ resembling the membrane voltage of a neuron whose PRC would pass through the desired $(\varphi, f(\varphi))$ coordinate. Recall that $f_i(\varphi_i)$ encodes the delay induced in the cycle period of a neuron i which receives a synaptic perturbation $I_{\text{syn}}(t)$ at phase φ_i . The target data therefore consists of a bursting ML neuron waveform with intrinsic period T_0 receiving a synaptic perturbation (blue) at phase φ . We use linear interpolation of duration $f(\varphi)$ to artificially tune the inter-burst interval to the required delay (Fig. 5b). To reiterate, this data is what would be observed in an ML neuron which possessed the desired PRC. Next, we use an optimization-based parameter estimation method to fit a neuron model to the target data. Here, we use nonlinear optimization software IPOPT, which seeks to minimize a least-squares mismatch between the membrane voltage $V(t)$ of a neuron model and the target data $V_{\text{data}}(t)$ by adjusting the model neuron parameters \mathbf{p} described in Sect. 2. The

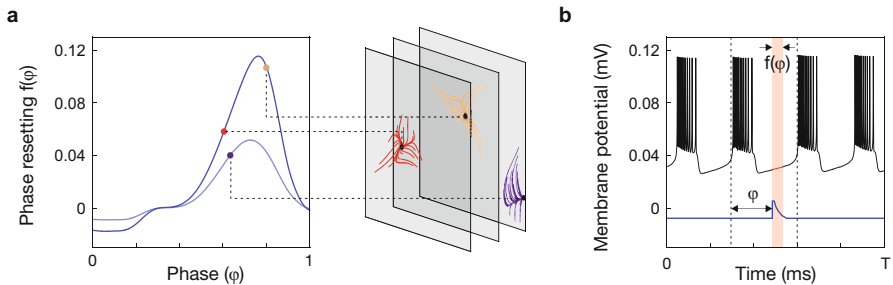


Fig. 5 Schematic of estimation procedure. **(a)** Attractors in a CPG phase portrait correspond to phase-locked modes, and the precise rhythms are determined by points on the PRCs of the constituent neurons. **(b)** Using equations (2) and (3), we can calculate the necessary PRC properties ($\varphi, f(\varphi)$) which will give rise to a desired attractor. We then generate an artificial time series $V_{\text{data}}(t)$ in which a neuron burst is delayed for a duration $f(\varphi)$ by synaptic inhibition $I_{\text{syn}}(t)$ received at phase φ . Established parameter estimation methods can be used to extract the neuronal and synaptic parameters which would give rise to $V_{\text{data}}(t)$

mismatch is represented by the following cost function: $C(\mathbf{p}) = \sum_{t=0}^T [V_{\text{data}}(t) - V(t)]^2$. This cost function is minimized subject to the neuron model equations of motion (Eq. 1), which are held as constraints on the optimization procedure (see [6] for more details on the optimization method). When the minimization has been performed, the adjusted set of K free parameters $\mathbf{p} = [p_0, p_1, \dots, p_K]$ should correspond to those of a neuron which matches the target data, producing a completed neuron model which possesses the desired PRC. Recall that a PRC is a function of both intrinsic neuron parameters and the strength g_{syn} of the synaptic perturbation $I_{\text{syn}}(t)$ (see Fig. 3b). Thus, by choosing which parameters may be adjusted by the optimization procedure, one can use this approach to estimate intrinsic neuron parameters, synaptic parameters, or some combination of the two.

7 Application to ECG Recordings

We now demonstrate how this approach can be used to design functional networks by successfully fitting the phases of a four-cell ring CPG to particular features of an ECG recording. In the neuron model optimizations performed in this section, we only allow one parameter g_{syn} to vary, holding all other neuron parameters fixed (Sect. 2, Eq. 1). Our approach, however, is sufficiently general to allow for the estimation of any chosen neuron and synaptic network parameters. It requires only that these chosen parameters also be left free during the optimization procedure. In order to fit the phasic timings of the ECG recording in Fig. 6b, we must first determine the relative phases of the four target features of the ECG: the start (P_i) and end (P_f) of the P wave, corresponding to atrial depolarization (black and

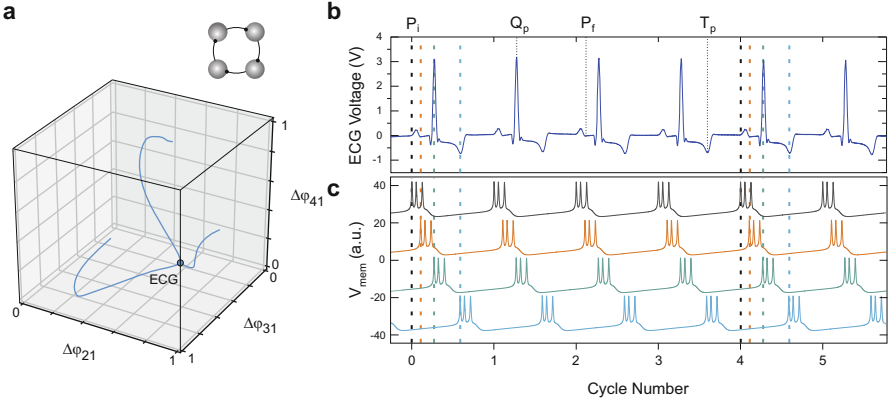


Fig. 6 (a) Three-dimensional phase lag portrait displaying trajectories converging to the ECG ‘target’ attractor for a four-cell ring network CPG. The target attractor corresponds to the four-phase ECG rhythm shown in the top-right panel. (b) Stable ECG recording obtained from an anaesthetised dog. We attempt to match four target features: the start (P_i) and end (P_f) of the P wave, corresponding to atrial depolarization; the peak of the QRS complex (Q_p), corresponding to ventricular depolarization; and the peak of the T wave (T_p), representing ventricular repolarization. (c) Stable four-phase rhythm of the ‘completed’ CPG. The onset of bursting in the four cells aligns exactly with the onset of the four target features of the ECG recording

orange dashed lines, respectively); the peak of the QRS complex (green line, Q_p), corresponding to ventricular depolarization; and, finally, the peak of the T wave (blue line, T_p), representing ventricular repolarization. Taking $P_i \equiv N1$ as the zero-phase reference, the phase lags of the three other features (in the notation of Sect. 2) are as follows: $\Delta\Phi_{P_f, P_i} = \Delta\Phi_{41} = 0.137$, $\Delta\Phi_{Q_p, P_i} = \Delta\Phi_{31} = 0.296$, and $\Delta\Phi_{T_p, P_i} = \Delta\Phi_{21} = 0.614$. Now, we begin by assuming $g_{syn}^{4 \rightarrow 1} = 1 \mu\text{S}/\text{cm}^2$ and note that in the stable mode N1 receives perturbations from N4 at a phase $\varphi = 0.137$. The PRC for the ML cell generated with $g_{syn} = 1 \mu\text{S}/\text{cm}^2$ (Fig. 3b) gives us a value of $f_1(\varphi_1 = 0.137) = -0.00321$. Since N2 receives perturbations from N1 at a phase of $\varphi_2 = (1 - 0.614) = 0.386$, we must ensure that the PRC of N2 also possesses a value of $f_2(0.386) = -0.00321$, in order to satisfy Eq. (2). By generating the appropriate target data (Fig. 5b), we can minimize the cost function $C(\mathbf{p})$ to obtain an estimated optimum synaptic weight $g_{syn}^{1 \rightarrow 2} = 4.94 \mu\text{S}/\text{cm}^2$. Continuing this process around the ring, ensuring Eq. (2) is satisfied for each cell, we obtain estimates for all remaining synapses, thus completing our network model (see Table 1).

By forward-integrating the model completed with the estimated synaptic parameters, we can see whether the network predicts the ECG rhythm as desired. Figure 6c shows that the network exhibits stable bursting precisely aligned with the ECG targets. It is important to note that while the phase-locked mode estimated here is clearly dynamically stable (Fig. 6a), the criteria in Eqs. (2) and (3) only guarantee that such a mode will *exist*. It is possible that such an estimation procedure would result in the existence a mode which is unstable to dynamical perturbations and

Table 1 Synapse parameters for the four-cell identical neuron CPG estimated using the PRC-based optimization method. Forward integrating the completed network model with these parameters gives rise to a phase-locked mode that precisely matches the sequence of heart chamber contractions as recorded in the ECG data

Parameter	Value ($\mu\text{S}/\text{cm}^2$)
$g_{\text{syn}}^{1 \rightarrow 2}$	4.94
$g_{\text{syn}}^{2 \rightarrow 3}$	7.53
$g_{\text{syn}}^{3 \rightarrow 4}$	2.80
$g_{\text{syn}}^{4 \rightarrow 1}$	1.00

noise. Future work should address this issue by deriving further *stability* criteria that may be used when generating target data.

8 Conclusion

Biological CPGs exhibit rhythmic behaviour with precise phasic delays between the onset of activity in each constituent neuron. The ability to design artificial CPGs for integration with biological nervous systems requires robust methods for estimating parameters giving rise to this rhythmic behaviour. We have demonstrated that reducing the network dynamics to the PRCs of its constituent neurons enables the estimation of network parameters one neuron at a time, avoiding the prohibitive computational costs associated with the optimization of whole-network models. By fitting a network rhythm to four target features of an ECG recording, we have demonstrated how this method can be used for the development of artificial CPGs with desired phasic timings. This work paves the way for a hardware implementation of artificial networks designed for integration with biological nervous systems. The CPG networks considered in this work were composed of identical neurons. Future work may seek to relax this assumption, which could enable the building of networks composed of different neuron types, further expanding the range of dynamics available to artificial CPG designs.

Acknowledgments This work was supported by the European Union’s H2020 Future Emerging Technologies programme under Grant No. 732170.

References

1. Achuthan, S., Canavier, C.C.: Phase-resetting curves determine synchronization, phase locking, and clustering in networks of neural oscillators. *J. Neurosci.* **29**(16), 5218–5233 (2009)

2. Canavier, C.C., Baxter, D.A., Clark, J.W., Byrne, J.H.: Control of multistability in ring circuits of oscillators. *Biological Cybernetics* **80**(2), 87–102 (1999)
3. Chauhan, A.S., Taylor, J.D., Nogaret, A.: Dual mechanism for the emergence of synchronization in inhibitory neural networks. *Scientific Reports* **8**(1), 11431 (2018)
4. Marder, E., Bucher, D.: Central pattern generators and the control of rhythmic movements. *Current Biology* **11**(23), R986–R996 (2001)
5. Moye, M.J., Diekman, C.O.: Data assimilation methods for neuronal state and parameter estimation. *J. Math. Neurosci.* **8**(1), 11 (2018)
6. Nogaret, A., Meliza, C.D., Margoliash, D., Abarbanel, H.D.: Automatic construction of predictive neuron models through large scale assimilation of electrophysiological data. *Scientific Reports* **6**, 32749 (2016)
7. Nogaret, A., Zhao, L., Moraes, D.J., Paton, J.F.: Modulation of respiratory sinus arrhythmia in rats with central pattern generator hardware. *J. Neurosci. Methods* **212**(1), 124–132 (2013)
8. Wang, X.-J., Buzsáki, G.: Gamma oscillation by synaptic inhibition in a hippocampal interneuronal network model. *J. Neurosci.* **16**(20), 6402–6413 (1996)
9. Wojcik, J., Schwabedal, J., Clewley, R., Shilnikov, A.L.: Key bifurcations of bursting polyrhythms in 3-cell central pattern generators. *PloS One* **9**(4), e92918 (2014)

Nonlinear Dynamics of the Industrial City's Atmospheric Ventilation: New Differential Equations Model and Chaotic Ventilation



Olga Yu Khetselius, Alexander V. Glushkov, Sergiy M. Stepanenko, Andrey A. Svinarenko, and Vasily V. Buyadzhi

Abstract We present a new generalized mathematical approach to analysis and modelling the characteristics of the chaotic atmospheric dynamical system, including natural air ventilation in the atmosphere of the industrial city. The approach is based on the Arakawa-Schubert model of calculation of cloud convection, modified to calculate the current involvement of the ensemble of clouds, and hydrodynamical prediction model (with correct quantitative accounting for the turbulence in an atmosphere of the urban zone) and theory of a complex geophysical field. The method for computing a turbulence spectra inside the city's (urban) zone is based on the generalized model of the tensor equations for turbulent tensions. The velocity components of an air flux over the city area are determined in an approximation of "shallow water" and found on the basis of the advanced spectral series expansion approach. The results of the PC simulation experiments for an chaotic air ventilation and a chaotic heat transfer in atmosphere of industrial city, including the data of modelling ventilation (mesocirculation) parameters over territory of Odessa are presented. The numerical data on a current function and velocity potential are computed and analyzed presented for a few hydrodynamic (synoptic) situations in the Odessa city.

Keywords Nonlinear dynamics · Chaotic ventilation · Atmosphere system

1 Introduction

The intensive development of the effective methods of the theory of dynamic systems and chaos theory made it possible to achieve quite substantial progress not only in the study of, say, classical dynamic (mechanical) systems, but to provide

O. Y. Khetselius · A. V. Glushkov · S. M. Stepanenko · A. A. Svinarenko · V. V. Buyadzhi (✉)
Odessa State Environmental University, Odessa, Ukraine

breakthrough solutions in the theory of chemical, physical, biological, economic and other systems.

Moreover, the application of modern methods of a chaos theory allows us to describe the most complex nonlinear and chaotic processes in many dynamical systems from a new point of view. The aim of our work is a quantitative study of nonlinear, chaotic phenomena in the nonequilibrium atmosphere of industrial cities based on the methods of the theory of dynamical systems, classical models with systems of hydrodynamic differential equations, generalized to the case of taking into account the chaos phenomenon, as well as the characteristics of chaotic (vortex) ventilation [1–14].

Investigation of regular and chaotic energy-, heat-, mass-transfer in continuous mediums and systems is very actual and complex problems of the modern physics of dynamical systems, computational hydrodynamics and atmosphere physics etc. At present time one could remind about different simplified models that allow to estimate the temporal and spatial structure of chaotic air ventilation in an atmosphere. However, these approaches are based on the known classical laws of molecular diffusion, as well as the known regression relations models [1–5]. It explains a number of disadvantages; for example, these models do not work if the atmosphere contains elements of chaotic convective instability.

More sophisticated approaches such as different versions of the Lagrangian particle dispersion models and similar one (e.g., [1–3]) provide significantly more accurate results, however, such approaches require very complicated simulation and, as minimum, very correct input data.

Over the past decade, a new class of dynamical atmospheric models has emerged, namely, chemical and physical, cybernetic and other weather forecasting models, fueled by the rapid build-up of supercomputer capabilities (e.g., [1, 2]).

As recognized by the authors of the above cited models, along with their advantages associated with the rapid growth of supercomputer capabilities and the operational availability of high-resolution digital weather forecast data (as input to atmospheric transport models) and others, and significant shortcomings are mainly related to the insufficiently adequate level of consideration of the non-linear, chaotic features of low-frequency atmospheric processes and atmospheric macro-circulation, atmospheric macro-turbulence (including the eddy-diffusion, stochastic, chaos-dynamical mechanisms) and other factors.

An effective approach to a number of these nonlinear problems can be found by using efficient methods and algorithms of a modern theory of dynamical systems and a chaos theory.

In this chapter we present an elaborated advanced approach to the simulation of chaotic heat and air ventilation in atmosphere of an industrial region. It is based on the Arakawa-Schubert model of calculation of cloud convection, modified to calculate the current involvement of the ensemble of clouds, and hydrodynamical prediction model (with correct quantitative accounting for the turbulence in an atmosphere of the urban zone) [2–14]. The key moment of the total approach is linked with using complex geophysical plane field method. Very complicated topic of the approach is connected with computing the turbulence spectra inside the urban

(or city's) zone. The standard method for this calculation is based on the advanced tensor equations for turbulent tensions. The velocity components of an air flux over the city area are determined in a generalized model of "shallow water" and firstly determined by means of the advanced, relatively efficient spectral series expansion method (see details in Ref. [14]).

2 Nonlinear Dynamics of Chaotic Atmospheric Ventilation

We present a new generalized mathematical approach to analysis and modelling the natural air ventilation in the atmosphere of the industrial city, which is based on the new methods of plain complex field theory combined with the Arakawa-Schubert generalized model (its generalization is in a possibility of computing a current involvement of the clouds ensembles) and nonlinear hydrodynamical forecast model (with correct quantitative accounting for the turbulence in an atmosphere of the urban zone) [2–4].

The modified by us Arakawa-Schubert method [13] allows computing the cumuli convection and shifting cumulus cloud ensemble from surrounding city regions and computing a cloud work for situation of the city's landscape. Firstly we have developed a generalized mathematical model for air masses circulation at the urban zone. The plain complex geophysical field theory methods have been used for computing the atmospheric (air) masses circulation and also for computing the main criteria of non-stationary turbulence in a medium. The balance relation's calculations for the inside-urban zone turbulence have been carried out for turbulent regime kinetic energy equation.

We present a new effective scheme for calculation of the ventilation potential and stream's function of winds in the urban zone. We present the key principles of the cloud convection phenomenon and corresponding air circulation to calculate the ventilation potentials for any industrial city in different periods of year. To calculate the involving streams (the real involving masses effect is created due to misbalance of vertical and down-running streams), reaching the territory of city, the modified Arakawa-Schubert equations system [13] for humidity and warm flow equations are solved [14]. Scheme of ventilation of the urban zone by air flows in a presence of the chaotic cloud's convection is presented in Ref. [7].

The physical and mathematical aspects of the chaotic ventilation processes in an atmosphere of the industrial city are described in ref. [2, 7–10]. Speech is about effect of the ventilation currents as the Couette flows, characteristics of the ventilation currents and so called dry thermions in a standard atmosphere.

It should be noted that in principle, any typical city area is characterized by sufficiently complex relief from the geometric viewpoint. A simplified approach to describing the dynamics of the origin and evolution of thermions can be described in the framework of the Boussinesq fine convection theory [7]. Indeed, a turbulent convective layer is formed over a flat surface by uniform heating of the medium. Then the known Boussinesq fine convection theory equation with a given neutral

stratified potential temperature profile works and one can get different turbulent moments of the convective layer.

From the atmospheric-physical viewpoint, the known convective thermions originate in a relatively thin surface layer near the heated surface, and then rise up under the action of the standard Archimedes force. It is also very important to note that the process of thermions creation is associated with the instability of the surface layer, and is significantly stochastic (chaotic), as well as the interaction of convective vortices with each other and with their environment.

That is, for further consideration, it is important to keep in mind that the thermion system is a stochastic ensemble. A significant part of the convective layer is the so-called layer of intensive mixing, in which the value of the second turbulent moment of the vertical velocity is almost constant. This analogy between the thermostat and the mixing layer allows to use a system of thermions and an ensemble of Brownian particles random forces of the same structure in the known Langevin equations (see [7–12]).

The most effective method of comprehensive empirical study of turbulent convection in the atmosphere of an industrial city is actually measurement using laboratory aircraft, as well as the use of lidars and Doppler radars. The typical size of atmospheric thermions varies from a few tens of centimetres to several tens of meters. Typical values of velocity and positive temperature ripple of atmospheric thermions are of the order of $0.5 \text{ m} \times \text{s}^{-1}$ and $0.3 \text{ }^\circ\text{C}$ respectively.

It is fundamentally important that when using the known K-form of the stochastic Fokker-Planck equation with variable coefficients, the nonstationary distributions of vertical velocities converge to the known Maxwell distribution at large times. This point is usually significantly used in the further consideration at formation of the generalized Arakawa-Schubert model. Note that the possibility of extending the methods of physical kinetics to turbulent flows of a homogeneous fluid is discussed in detail in monographs [2, 14].

The standard methods proved to be effective in describing homogeneous isotropic turbulence, but when generalizing turbulent convection to academic problems, the methods require a significant complication. At the same time, in the case of considering these processes in the atmosphere of industrial cities, as a rule, the classical concepts seem too simplistic and in fact at the present time are still not adequately developed. In fact, at the fundamental and quantitative level, this is done by us here for the first time.

It is important to note that since the meaning of the studied process is to correctly describe the process of stabilization of turbulent vortices, divergent at different intervals of the spectrum, the linear theory naturally only distorts the solution without introducing useful information. According to the linear theory, the diffusion from the source spreads evenly by the spot in the isotropic space, while in the real diffusion the impurities are captured by large vortices and carried away by the flow over much greater distances. This process is called a wave or vortex diffusion. It should be noted that this very clear aspect is still ignored in most papers on the modelling atmospheric ventilation and computing a distribution of pollutants in atmosphere of industrial cities.

Indeed the redistribution of energy over the spectrum of vortex sizes is usually called spectral transformation, the study of which is possible only if there is a real introduction of nonlinearity in the equation of turbulent motion. In principle, the phenomenon of vortex diffusion must be described in the framework of an adequate nonlinear theory. This, however, provokes a significant complication of the mathematical apparatus. In the case of collision of flows with real urban relief, this process of transformation is the main one (not the dissipation of energy into the spectrum of micro- pulsations). Such dissipation is justified by a long movement of the flow over the uniform surface roughness (for example, over the forest, sea or field). In the urban conditions, impurities from the source of pollution can be transported over much greater distances than in conventional diffusion, which introduces ambiguities and creates known problems in the development of recreational activities.

As a rule, the application of linear theories of turbulence for the typical industrial city is hopeless. This explains why there is still no scientifically sound program for the theoretical study of the processes of spread of harmful impurities in the atmosphere of industrial cities. Moreover, at present, in the conditions of growth and emergence of new modern megacities, as a rule, a sophisticated analysis of possible atmospheric ventilation taking into account geographical, climatic and other factors is especially necessary.

Below we will realize a computing the velocity field, which consists of the total picture of the involvement of air masses in convective thermions (ensemble of thermions, “urban thermion island”). The physics of these processes in details is described in Refs. [2–14]). Here it is important to remind that turbulent vortices over the urban area should be in the interaction of resonant contact with turbulent vortices of cloud masses. This condition provides an effective (excellent) air ventilation. These physical points provide the corresponding generalization of the Arakawa-Schubert model, which results in a few budget equations for total water content, mass, energy, namely (e.g.) [13, 14]:

$$\begin{aligned}
 E\tilde{s} - Ds_c - \frac{\partial M_c s_c}{\partial z} + pLc &= 0, \\
 E\tilde{q} - Dq_c - \frac{\partial M_c q_c}{\partial z} + pc &= 0, \\
 E - D - \frac{\partial M_c}{\partial z} &= 0,
 \end{aligned}
 \tag{1}$$

$$M_c = \sum pw_i \sigma_i = pw_c \sigma,$$

$$w_c, s_c = c_p T + gz,$$

Here w_i , c are velocity and horizontal cross-section square for i -th cloud, E is an inflow, D is an outflow, M_c is a vertical air mass flow in a cloud; p - air density; c is an amount of the condensed moisture; q_c , \tilde{s} , \tilde{q} - weighted average values of vertical speed, statistical energy and the ratio of the mixture of water vapor. Then one could with the corresponding equations of heat and moisture influx (e.g. [2, 7, 14]).

The spectral representation of E in an ensemble of clouds is as follows:

$$E(z) = \int \varepsilon(z, \lambda) m_A(\lambda) d\lambda \quad (2)$$

and analogous expression for quantity D (Eq. (1)). The standard balance relations for the convection cloud work A and work of down falling streams in the neighbourhood of cloud with using definition of an air mass $m_A(\lambda)$ are as follows:

$$\begin{aligned} \frac{dA}{dt} &= \frac{dA}{dt_c} + \frac{dA}{dt_{down}} = 0 \\ \frac{dA}{dt_{down}} &= \int_0^{\lambda_{max}} m_A(\lambda') G(\lambda, \lambda') d\lambda', \end{aligned} \quad (3)$$

Here λ is a velocity of drawing, $G(\lambda, \lambda')$ is a kernel of the Eq. (3); the latter determines the dynamical interaction between neighbour clouds. As a new element we introduce a parameter δ into Eq. (3) and it determines the imbalance of the cloud due to the return of part of the cloud energy on the organization of the wind field in their vicinity, and additionally introduces a balance ratio that regulates the contribution of the cloud with the weather process. Namely, the imbalance of vertical and descending currents should create the effect of the mass of the real retraction. Taking into account $\frac{dA}{dt_{downstr}} = T(\lambda)$, the mass balance equation in the convective thermion is as follows:

$$\delta \int_0^{\lambda_{max}} G(\lambda, \lambda') m_A(\lambda') d\lambda' + T(\lambda) = m_A(\lambda) \quad (4)$$

A detailed expressions for kernel functions are given in Ref. [13]. It easily to write a general solution of the modified Arakawa-Shubert equation with accounting for air streams superposition of some synoptic process as:

$$m_A(\lambda) = T(\lambda) + \delta \int_0^{\lambda_{max}} G(s) R(\lambda, t : \delta) dt, \quad (5)$$

Here R is a resolvent of the Eq. (5), which is usually defined as follows:

$$R(\lambda, t : \delta) = \sum_{m=1}^{\infty} \delta^{m-1} G_m(\lambda, t) \quad (6)$$

According to Refs. [2, 7], the quantity R is further determined in the form of the Laurent expansion $R = \sum_{n=-\infty}^{\infty} a_n (\xi - c)^n$ in a complex plane ξ (its centre is a centre of urban heating island and internal cycle coincides with its periphery).

The next important point is using the known “shallow water” model in order to describe an atmosphere circulation above a city’s zone [2, 3]. Let us note that an effective algorithm to solution of the problem is connected with using methods of the plane geophysical complex field theory [2, 14]. The cloud masses on the urban periphery can be defined in the wind field as follows (complex velocity potential):

$$v_x - i v_y = \frac{df}{d\xi},$$

$$\frac{df}{d\xi} = \frac{\Gamma}{2\pi i} \left[\frac{1}{\zeta - \zeta_0} + \sum_{k=1}^{\infty} \left(\frac{1}{\zeta - \zeta_0 - kr} + \frac{1}{\zeta - \zeta_0 + kr} \right) \right] + \frac{d}{d\zeta} \left[\sum_{k=1}^n \Gamma_k \ln (\zeta - c_k) \right]. \tag{7}$$

The system of parameters in Eq. (7) is described in Ref. [7]. Here we shortly note that quantities Γ_k, Γ are circulations on the atmospheric vortex and Carman chain elements respectively; c_k – co-ordinates of this forming; r – distance between standard Carman chain vortices; $\zeta, \zeta - kr$ and $\zeta + kr$ are a centre co-ordinate, co-ordinate of beginning and co-ordinate of end for the convective perturbation line respectively.

At last it is important block of the whole approach is conned with computing the turbulence spectra inside the city’s (urban) zone. Here one could apply the standard tensor equations of turbulent tensions (see details in Refs. [14]). Computing balance relationships for inside-urban zone is fulfilled on the basis of equation for kinetic energy of turbulent regime.

Equating the velocity components determined in the model (7) and the corresponding components of the “shallow water” model one could obtain the spectral matching between the wave numbers that define the functional elements in the Fourier-Bessel series with source element of a the plane geophysical complex field theory. More details are in Refs. [2–10, 14–17]. All computing is carried out with using the PC codes “Geomath”, “Quantum Chaos”, “ScanPoints” [18–34].

3 Some Numerical Results and Conclusions

As application of a new approach, some illustrative PC simulation results on modelling an air ventilation field for the Odessa region are presented. As usually, arbitrary vector field, say $v = \nabla\psi + v_\chi$, has the rotational and divergent components; in a case of the horizontal wind, ψ is a current function (rotational component) and χ is a velocity potential (divergent one).

Below these components are computed for a concrete synoptic process in the Odessa region with input data parameters (such as cloudiness and convection intensities) from [2, 3] and listed in Figs. 1 and 2.

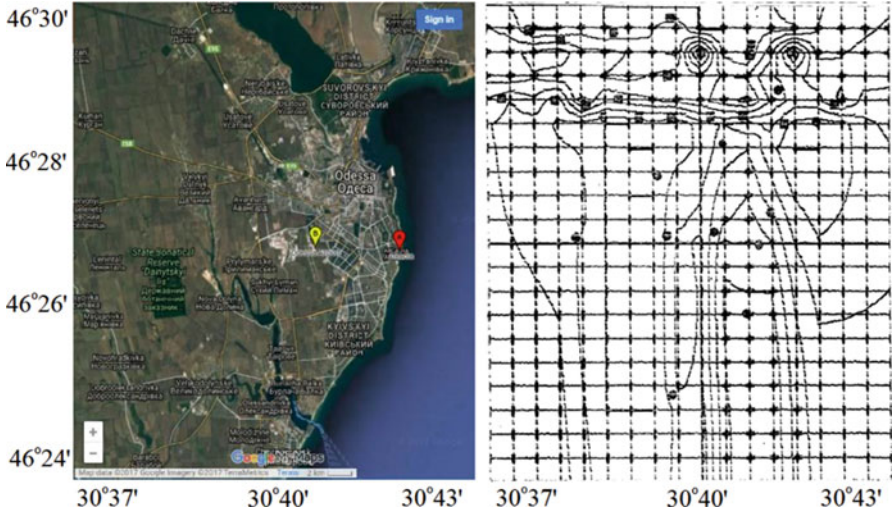


Fig. 1 Potential of ventilation χ for atmospheric situation (Odessa city; see text)

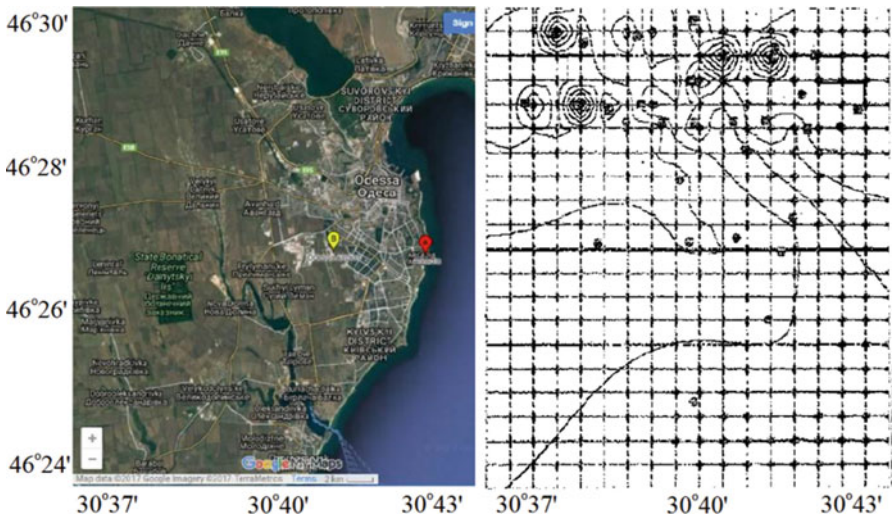


Fig. 2 Current function ψ for the atmospheric situation, presented in Fig. 1 (Odessa city)

The key basic assumptions and numerical parameters are as follows: the clouds (black squares in Figs. 1, 2) with distance between them 500–700 m are coming to the city by a few lines of convective instability and penetrate deep into the Gulf of Odessa and the city with some distribution of the dry thermions (black circles in Figs. 1, 2). The latter create their involvement currents and support a heat circulation in the urban zone. The velocity field variation in time is about 0.5 m/s and the density

of current lines is about 1 m/s to 0.5 cm of gradient in Fig. Obviously, if, say, $v_x > 0$, then the velocity increases in the direction of positive foci (and similarly on y) that is marked with sign “+” (sign “-”). Figure 1 shows the picture of penetration of air ventilation for most of the city, but the penetration of ventilation is expressed more weakly for a current function field (Fig. 2).

References

1. Pinault, J.-L., Baubron, J.-C.: Signal processing of diurnal and semidiurnal variations in radon and atmospheric pressure: a new tool for accurate in situ measurement of soil gas velocity, pressure gradient, and tortuosity. *J. Geophys. Res.* **102**(b8), 101–120 (1997)
2. Bunyakova, Y.Y., Glushkov, A.V.: Analysis and forecast of the impact of anthropogenic factors on air base in of an industrial city. Ecology, Odessa (2010)
3. Khetselius, O.Y., Glushkov, A.V., Bunyakova, Y.Y., Buyadzhi, V.V., Bondar, O.I., Vaschenko, V.N., Bykowszczenko, N.: New approach and microsystem technology to modelling dynamics of atmosphere ventilation of industrial city and elements of the “Green-City” construction technology. *Sensor Electr. Microsyst. Techn.* **14**(4), 37–46 (2017)
4. Buyadzhi, V.V., Glushkov, A.V., Khetselius, O.Y., Ternovsky, V.B., Serga, I.N., Bykowszczenko, N.: An advanced analysis and modelling the air pollutant concentration temporal dynamics in atmosphere of the industrial cities: Odessa city. *IOP Conf. Series Earth Environm. Sci.* **92**, 012006 (2017)
5. Glushkov, A.V., Khetselius, O.Y., Bunyakova, Y.Y., Prepelitsa, G.P., Solyanikova, E.P., Serga, E.N.: Non-linear prediction method in short-range forecast of atmospheric pollutants: low-dimensional chaos. In: *Dynamical Systems - Theory and Applications*, vol. LIF111. Lodz University Press, Lodz (2011)
6. Buyadzhi, V.V., Glushkov, A.V., Khetselius, O.Y., Bunyakova, Y.Y., Florco, T.A., Agayar, E.V., Solyanikova, E.P.: An effective chaos-geometric computational approach to analysis and prediction of evolutionary dynamics of the environmental systems: atmospheric pollution dynamics. *J. Phys. Conf. Ser.* **905**, 012036 (2017)
7. Glushkov, A., Khetselius, O.Y., Agayar, E.V., Buyadzhi, V.V., Romanova, A.V., Mansarliysky, V.F.: Modelling dynamics of atmosphere ventilation and industrial city's air pollution analysis: new approach. *IOP Conf. Series Earth Environ. Sci.* **92**, 012014 (2017)
8. Khetselius, O.Y.: Forecasting evolutionary dynamics of chaotic systems using advanced non-linear prediction method. In: Awrejcewicz, J., Kazmierczak, M., Olejnik, P., Mrozowski, J. (eds.) *Dynamical Systems Applications*, T2, pp. 145–152. Lodz University Press, Lodz (2013)
9. Stepanenko, S.N., Shnaidman, V.N.: Comparison of the results of a generalization of experimental data with calculations from a three-parameter model of the atmospheric boundary layer. *Fluid Mech. Soviet Res.* **12**, 123–131 (1983)
10. Bunyakova, Y.Y., Glushkov, A.V., Khetselius, O.Y., Ignatenko, A.V., Bykowszczenko, N., Buyadzhi, V.V.: New approach and microsystem technology of advanced analysis and forecasting the air pollutant concentration temporal dynamics in atmosphere of the industrial cities. *Sensor Electr. Microsyst. Technol.* **14**(3), 65–78 (2017)
11. Glushkov, A.V., Khetselius, O.Y., Bunyakova, Y.Y., Grushevsky, O.N., Solyanikova, E.P.: Studying and forecasting the atmospheric and hydroecological systems dynamics by using chaos theory methods. In: Awrejcewicz, J., Kazmierczak, M., Olejnik, P., Mrozowski, J. (eds.) *Dynamical Systems Theory*, T1, pp. 249–258. Lodz University Press, Lodz (2013)
12. Glushkov, A.V., Vaschenko, V.N., Gerasimenko, G., Bunyakova, Y.Y.: Atmospheric pollutants concentrations temporal dynamics for the industrials ukrainian cities: low-dimensional chaos. In: Awrejcewicz, J., Kazmierczak, M., Olejnik, P., Mrozowski, J. (eds.) *Dynamical Systems Applications*, T2, pp. 241–250. Lodz University Press, Lodz (2013)

13. Arakava, A., Shubert, W.H.: Interaction of cumulus cloud ensemble with the large-scale environment. *J. Atm. Sci.* **31**, 674–701 (1974)
14. Glushkov, A.V.: *Methods of a Chaos Theory*. Astroprint, Odessa (2012)
15. Glushkov, A.V., Bunyakova, Y.Y., Buyadzhi, V.V., Dubrovskaya, Y.V., Kuznetsova, A.A., Khetselius, O.Y.: New approach and microsystem technology of advanced non-linear analysis and modelling chaotic environmental radioactivity dynamics. *Sensor Electr. Microsyst. Technol.* **14**(3), 24–37 (2017)
16. Bunyakova, Y.Y., Ternovsky, V.B., Dubrovskaya, Y.V., Ignatenko, A.V., Svinarenko, A.A., Vitavetskaya, L.A.: Analysis of the beryllium-7 activity concentration dynamics in the atmospheric environment time series after the Fukushima Daiichi nuclear power plants emergency. *Sensor Electr. Microsyst. Technol.* **14**(4), 73–82 (2017)
17. Glushkov, A.V., Safranov, T.A., Khetselius, O.Y., Ignatenko, A.V., Buyadzhi, V.V., Svinarenko, A.A.: Analysis and forecast of the environmental radioactivity dynamics based on methods of chaos theory: general conceptions. *Environ. Prob.* **1**(2), 115–120 (2016)
18. Glushkov, A.V., Malinovskaya, S.V., Loboda, A.V., Shpinareva, I.M., Gurnitskaya, E.P., Korchevsky, D.A.: Diagnostics of the collisionally pumped plasma and search of the optimal plasma parameters of x-ray lasing: calculation of electron-collision strengths and rate coefficients for Ne-like plasma. *J. Phys. Conf. Ser.* **11**, 188–198 (2005)
19. Glushkov, A.V., Malinovskaya, S.V., Prepelitsa, G.P., Ignatenko, V.M.: Manifestation of the new laser-electron nuclear spectral effects in the thermionized plasma: QED theory of cooperative laser-electron-nuclear processes. *J. Phys. Conf. Ser.* **11**, 199–206 (2005)
20. Svinarenko, A.A.: Study of spectra for lanthanides atoms with relativistic many-body perturbation theory: Rydberg resonances. *J. Phys. Conf. Ser.* **548**, 012039 (2014)
21. Florko, T.A., Ambrosov, S.V., Svinarenko, A.A., Tkach, T.B.: Collisional shift of the heavy atoms hyperfine lines in an atmosphere of the inert gas. *J. Phys. Conf. Ser.* **397**, 012037 (2012)
22. Glushkov, A.V., Ambrosov, S.V., Ignatenko, A.V., Korchevsky, D.A.: DC strong field stark effect for nonhydrogenic atoms: consistent quantum mechanical approach. *Int. J. Quant. Chem.* **99**, 936–939 (2004)
23. Glushkov, A.V.: Oscillator strengths of Cs and Rb-like ions. *J. Appl. Spectrosc.* **56**(1), 5–9 (1992)
24. Malinovskaya, S.V., Glushkov, A.V.: Calculation of the spectra of potassium-like multicharged ions. *Russ. Phys. J.* **35**(11), 999–1004 (1992)
25. Glushkov, A.V., Efimov, V.A., Gopchenko, E.D., Dan'kov, S.V., Polishchuk, V.N., Goloshchak, O.P.: Calculation of spectroscopic characteristics of alkali-metal dimers on the basis of a model perturbation theory. *Optics Spectr.* **84**(5), 670–678 (1998)
26. Glushkov, A.V., Malinovskaya, S.V., Loboda, A.V., Shpinareva, I.M., Prepelitsa, G.P.: Consistent quantum approach to new laser-electron-nuclear effects in diatomic molecules. *J. Phys. Conf. Ser.* **35**, 420–424 (2006)
27. Glushkov, A.V., Malinovskaya, S.V., Filatov, V.V.: S-Matrix formalism calculation of atomic transition probabilities with inclusion of polarization effects. *Sov. Phys. J.* **32**(12), 1010–1014 (1989)
28. Glushkov, A.V.: Relativistic multiconfiguration time-dependent self-consistent-field theory for molecules. *Sov. Phys. J.* **34**(10), 871–876 (1991)
29. Glushkov, A.V., Malinovskaya, S.V., Chernyakova, Y.G., Svinarenko, A.A.: Cooperative laser-electron-nuclear processes: QED calculation of electron satellites spectra for multi-charged ion in laser field. *Int. J. Quantum Chem.* **99**, 889–893 (2004)
30. Glushkov, A.V., Ambrosov, S.V., Loboda, A.V., Gurnitskaya, E.P., Prepelitsa, G.P.: Consistent QED approach to calculation of electron-collision excitation cross sections and strengths: Ne-like ions. *Int. J. Quantum Chem.* **104**, 562–569 (2005)
31. Glushkov, A.V.: QED theory of radiation emission and absorption lines for atoms and ions in a strong laser field. *AIP Conf. Proc.* **1058**, 134–136 (2008)
32. Glushkov, A.V., Loboda, A.V.: Calculation of the characteristics of radiative multiphoton absorption and emission lines when an atom interacts with pulsed laser radiation. *J. Appl. Spectr.* (Springer). **74**(305–309) (2007)

33. Glushkov, A.V.: Multiphoton spectroscopy of atoms and nuclei in a laser field: relativistic energy approach and radiation atomic lines moments method. In: Jenkins, S., Kirk, S.R., Maruani, J., Brändas, E. (eds.) *Advances in Quantum Chemistry*, vol. 78, pp. 253–285. Elsevier, Cambridge (2019)
34. Glushkov, A.V., Khetselius, O.Y., Svinarenko, A.A., Buyadzhi, V.V.: *Methods of computational mathematics and mathematical physics*. P.1. TES, Odessa (2015)

Biomechanical Analysis of Different Foot Morphology During Standing on a Dynamic Support Surface



Yang Shu, Jan Awrejcewicz , and Bartłomiej Zagrodny

Abstract Foot is a significant element during the balance as the main organ that connects with surface. From the research of habitually barefoot people and habitually shod people, there were significant differences in distance between the hallux and the interphalangeal joint of the second toe. Habitually shod males had a high risk of injury because of the lack of toes function. Based on these differences in foot morphology and importance of hallux during activities, expanding the distance between the hallux and other toes could increase the ability of hallux, especially the balance. In order to analyse the influence of hallux during balance tests, three conditions were set with light silica instruments: (1) normal toes, (2) expanding toes, (3) binding toes. During the experiments, the 6-DOF transportation vibration platform had continuous sinusoidal translation in the anterior-posterior and medial-lateral directions with a sine wave. From the results, binding toes showed larger movement of centre of pressure than normal toes and expanding toes. In addition, people with normal toes also indicated larger sway than expanding toes. It could conclude that control the toes function causes instability during static balance but improve the hallux function can increase the balance ability.

Keywords Foot morphology · Toes · Hallux function · Balance

Y. Shu (✉)
China Institute of Sport Science, Beijing, China
e-mail: shuyang@ciss.cn

J. Awrejcewicz · B. Zagrodny
Lodz University of Technology and Department of Automation, Biomechanics and Mechatronics,
Lodz, Poland

1 Introduction

Balance is an important ability in dynamic and static features of human in biomechanics, and it maintains the line of gravity (vertical line from centre of mass) of a body within the base of support with minimal postural sway [1]. The factors influencing balance ability including: (1) internal adjustment including somatosensory, visual and vestibular systems and motor response [2], and (2) the mechanical factors which could disrupt the orientation information. The perturbation or change of center of Mass needs somatosensory to main balance. The influence of support surface, such as support area and instability of support, would affect the somatosensory and visual inputs.

Different ethnicities, pathological factors and different forms of sport participation could bring about foot morphology differences [3–5]. Treating foot as a lever, fulcrum of Habitually shod people was forefoot but hallux and forefoot for habitually barefoot people. Habitually barefoot people have more loading under the hallux rather than the medial forefoot, could reduce the loading of the fulcrum. The functions of the remaining toes balance control under static and dynamic conditions [6]. Some studies found that tactile information feedback could be a benefit to the postural control and balance [7]. plantar perception exercises contribute to controlling balance [8]. My research of foot morphology indicated that hallux angle and the minimal distance between the hallux and the interphalangeal joint of the second toe were the main morphological differences between habitually shod people and habitually barefoot people [9, 10]. However, most normal people are habitually shod. It is convenient to expand the angle and distance forwardly. On the other hand, decreasing hallux grip force was associated with weakening and worsened balance [11]. In addition, it concluded that the active function of toes could prevent foot injuries based on the research between running between binding toes and normal toes, such as metatarsal fracture and plantar fasciitis [12]. This study is to explore the trajectory of the COP in foot morphology control when maintaining an upright standing posture on a dynamic support surface with continuous periodical multidirectional perturbations.

2 Methods

Eighteen healthy young male students volunteered to attend the experiment (see Table 1). All participants were free of lower limb pain and injury and had no history of major surgery on the lower back or lower limbs for the past 12 months. They were informed of the experimental procedure and gave written consent.

For this study, the light silica instrument was used to set the position of hallux in three conditions: (1) Normal Toes; (2) Expending Toes; (3) Binding Toes (see Fig. 1). The experiments tested 3 days in every foot condition. It aimed to prevent the

Table 1 Participant demographics

	Total
Participants	18
Age (years)	25 ± 2.1
Height (cm)	176 ± 2.3
Weight (kg)	64 ± 5.5
Right leg length (cm)*	88.3 ± 2.8
Body mass index	22.4 ± 2.0
LEFS score	81.0 ± 1.0
Tegner activity score	6.0 ± 1.0
VAS	0.0 ± 0.0

Note: Right leg length, the measurement from right anterior superior iliac spine to the medial malleolus

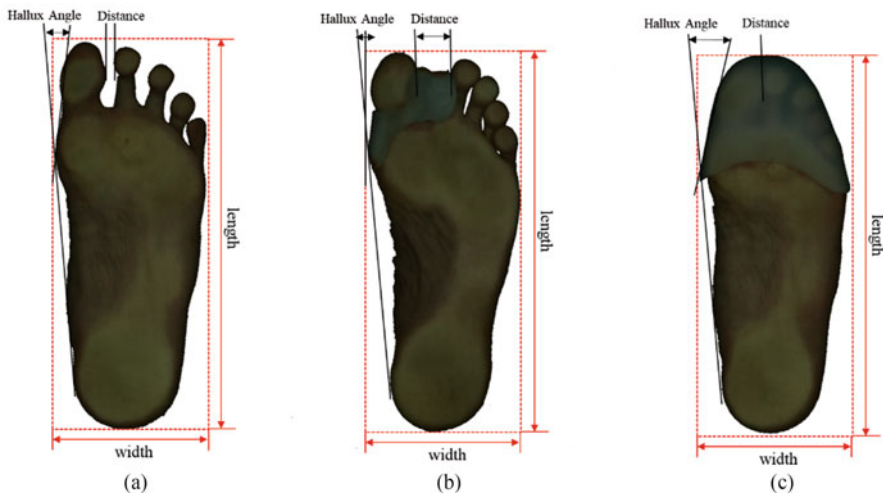


Fig. 1 2D foot print image of Natural Toes (a), Expanding Toes (b) and Binding Toes (c)

influence of wearing instruments. Before the experiments, participants wore these instruments and socks for both feet. Then they had free activities for 1 hour to adapt.

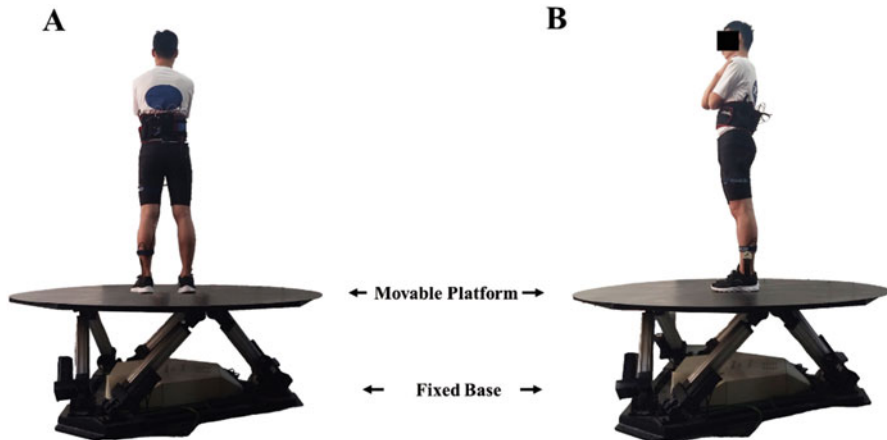
The Easy-Foot-Scan (EFS), OrthoBaltic (Kaunas, Lithuania) was used to scan the foot of participants. From the results of foot scan after wearing instruments, length of foot was 261.4 ± 12.3 mm, width was 119.8 ± 15.0 mm. Table 2 showed the hallux angle and distance between three different conditions:

A six degrees of freedom (6-DOF) transportation vibration platform is a motion simulation technology that can generate an infinite floor with various surfaces. Users could use this interface to experience life-like movements in multidirectional perturbations even virtual environment with various terrains. This research used the 6-DOF transportation vibration platform (MTD 6.0, TARCH, Wuhan, China). which consists of a movable platform (diameter: 2 m), six servo valves and pistons and a

Table 2 One-way analysis of variance of hallux angle and distance between Natural Toes, Expanding Toes and Binding Toes people

	Natural Toes	Expanding Toes	Binding Toes
Hallux angle (deg)	10.20 ± 5.33*,#	6.54 ± 3.05*,&	16.87 ± 4.65#,&
Distance (mm)	3.56 ± 2.31*,#	24.00 ± 5.74*,&	0.00 ± 0.12#,&

*, #, and & indicate significant differences ($p < 0.05$) for comparison between Natural Toes and Expanding Toes, between Natural Toes and Binding Toes, and between Expanding Toes and Binding Toes, respectively

**Fig. 2** Structure of the 6-DOF transportation movable platform (a: back, b: side)

fixed base. The movable platform can move in three linear movements (vertical, longitudinal and lateral), three rotations (pitch, roll, and yaw), and any combination movements in space. Each participant performed on the 6-DOF platform (see Fig. 2).

The PEDAR insole system (Novel, GmbH, Munich, Germany) was used to measure the plantar pressure distribution and the trajectory of the COP. The insoles are approximately 2.6 mm thick and contain 99 sensors which are able to measure pressures up to 120 N/cm².

During the experiments, the 6-DOF transportation vibration platform had continuous sinusoidal translation in the anterior-posterior (AP) and medial-lateral (ML) directions with a sine wave (frequency: 1 rad/s; amplitude: 3, see Fig. 3):

$$y = 3 \sin 2\pi x, \quad (1)$$

All trials were obtained from the right lower limbs of each participant, the in-shoe data recorded by the PEDAR system included the coordinates and trajectory of the COP. In the coordinates (C_x , C_y) of COP trajectory, C_x is coordinated in the ML direction and C_y is coordinated in the AP direction. COP excursion was defined as

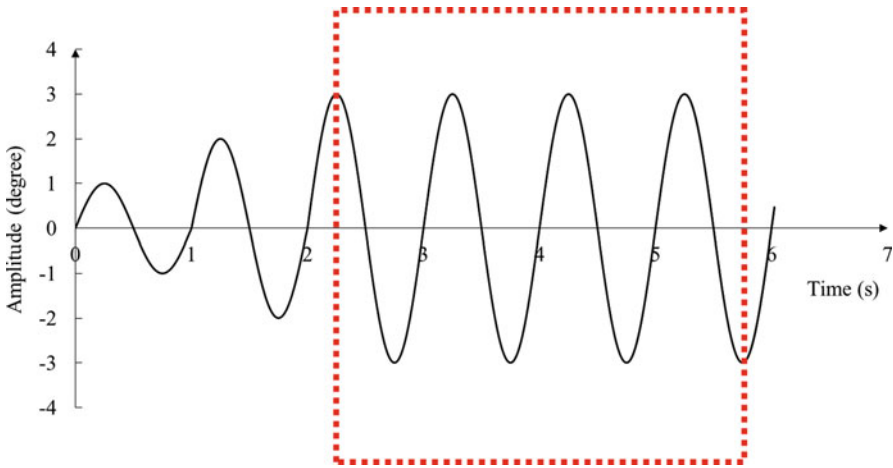


Fig. 3 6-DOF transportation vibration platform undergoing continuous sinusoidal translation. Data were collected when the amplitude of the platform reached an integral sine wave

the distance between the furthest points in the A-P and M-L directions of the COP in each sine wave.

The statistical measures were performed with SPSS 19.0 software. One-way analysis of variance with post hoc Bonferroni correction was performed to investigate the variation tendency among different weight of loads. If $p < 0.05$, statistical results were considered significant.

3 Results and Discussion

From Fig. 4, in M-L Direction, A-P Direction and COP Excursion, the length of binding toes was significantly higher than normal toes and expending toes; Moreover, the length of normal toes was also significantly higher than expending toes.

Stability is generally defined as the ability of a person to maintain or restore the equilibrium state of an upright posture without changing the support base [13]. The increase of COP parameters, such as excursion, conclude the increase of instability [14]. Recent studies indicated that lateral balance is more challenging than in the A-P direction [15, 16]. From this experiment, Binding Toes showed large postural sway in not only M-L direction, but also A-P direction and Excursion. It indicated that control the toes function would cause instability. Conversely, Expending Toes has less postural sway and instability than normal toes and binding toes. It suggested that the balance ability would increase with the increasing of toes function.

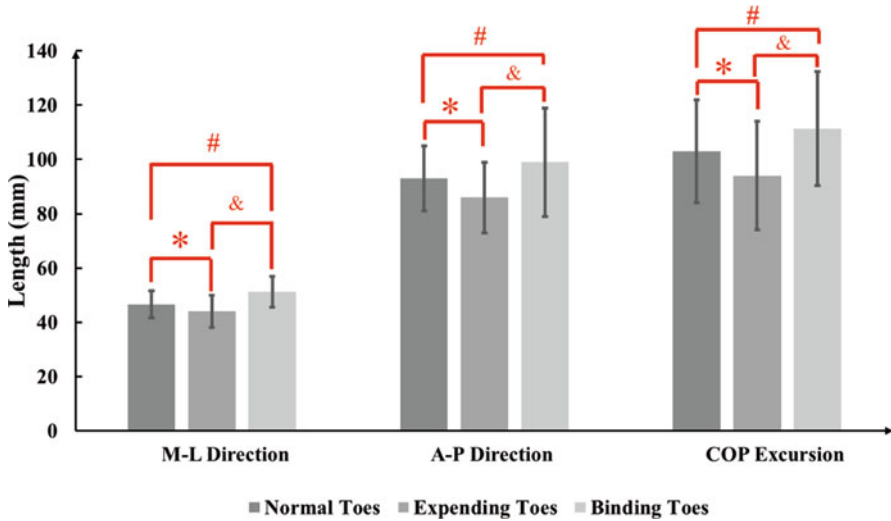


Fig. 4 6-DOF transportation vibration platform undergoing continuous sinusoidal translation. Data were collected when the amplitude of the platform reached an integral sine wave

4 Conclusions

Balance ability is crucial for movement in daily life. There were many factors could affect the performance of stability. Foot is a significant element during the balance as the main organ that connects with surface. From the research of habitually barefoot people and habitually shod people, there were significant differences in distance between the hallux and the interphalangeal joint of the second toe. Habitually shod males had a high risk of injury because of the lack of toes function. Based on these differences in foot morphology and importance of hallux during activities, expanding the distance between the hallux and other toes could increase the ability of hallux, especially the balance.

During standing on the dynamic support surface, binding toes showed larger movement of centre of pressure than normal toes and expending toes. In addition, people with normal toes also indicated larger sway than expending toes. It could conclude that control the toes function causes instability during static balance but improve the hallux function can increase the balance ability. Finding of this study provides detailed and important information for further studies on improving human movement ability.

References

1. Shumwaycook, A., Anson, D., Haller, S.: Postural sway biofeedback - its effect on reestablishing stance stability in hemiplegic patients. *Arch. Phys. Med. Rehabil.* **69**(6), 395–400 (1988)
2. Nashner, L.M., Black, F.O., Wall, C.: Adaptation to altered support and visual conditions during stance - patients with vestibular deficits. *J. Neurosci.* **2**(5), 536–544 (1982). <https://doi.org/10.1523/JNEUROSCI.02-05-00536>
3. Mauch, M., Grau, S., Krauss, I., Maiwald, C., Horstmann, T.: A new approach to children's footwear based on foot type classification. *Ergonomics.* **52**(8), 999–1008 (2009). <https://doi.org/10.1080/00140130902803549>
4. Gurney, J.K., Kuch, C., Rosenbaum, D., Kersting, U.G.: The Maori foot exhibits differences in plantar loading and midfoot morphology to the Caucasian foot. *Gait Posture.* **36**(1), 157–159 (2012). <https://doi.org/10.1016/j.gaitpost.2012.01.013>
5. Guiotto, A., Sawacha, Z., Guarneri, G., Cristoferi, G., Avogaro, A., Cobelli, C.: The role of foot morphology on foot function in diabetic subjects with or without neuropathy. *Gait Posture.* **37**(4), 603–610 (2013). <https://doi.org/10.1016/j.gaitpost.2012.09.024>
6. Ku, P.X., Abu Osman, N.A., Yusof, A., Wan Abas, W.A.: The effect on human balance of standing with toe-extension. *PLoS One.* **7**(7), e41539 (2012). <https://doi.org/10.1371/journal.pone.0041539>
7. Meyer, P.F., Oddsson, L.I., De Luca, C.J.: The role of plantar cutaneous sensation in unperturbed stance. *Exp. Brain Res.* **156**(4), 505–512 (2004). <https://doi.org/10.1007/s00221-003-1804-y>
8. Morioka, S., Fujita, H., Hiyamizu, M., Maeoka, H., Matsuo, A.: Effects of plantar perception training on standing posture balance in the old old and the very old living in nursing facilities: a randomized controlled trial. *Clin. Rehabil.* **25**(11), 1011–1020 (2011). <https://doi.org/10.1177/0269215510395792>
9. Shu, Y., Mei, Q., Fernandez, J., Li, Z., Feng, N., Gu, Y.: Foot morphological difference between habitually shod and unshod runners. *PLoS One.* **10**(7), e0131385 (2015). <https://doi.org/10.1371/journal.pone.0131385>
10. Gu, Y., Shu, Y., Feng, N.: Foot morphological characteristic of habitually unshod runners. *Osteoporos. Int.* **26**, S481–S481 (2015)
11. Chatzistergos, P.E., Healy, A., Naemi, R., Sundar, L., Ramachandran, A., Chockalingam, N.: The relationship between hallux grip force and balance in people with diabetes. *Gait Posture.* **70**, 109–115 (2019). <https://doi.org/10.1016/j.gaitpost.2019.02.020>
12. Wang, S., Shu, Y., Gu, Y.: A pilot analysis of external binding manipulation on toes function. *Osteoporos. Int.* **26**, S485–S485 (2015)
13. Maki, B.E., Holliday, P.J., Fernie, G.R.: Aging and postural control: a comparison of spontaneous-and induced-sway balance tests. *J. Am. Geriatr. Soc.* **38**(1), 1–9 (1990). <https://doi.org/10.1111/j.1532-5415.1990.tb01588.x>
14. Hertel, J., Buckley, W.E., Denegar, C.R.: Serial testing of postural control after acute lateral ankle sprain. *J. Athl. Train.* **36**(4), 363–368 (2001)
15. Vistamehr, A., Kautz, S.A., Bowden, M.G., Neptune, R.R.: Correlations between measures of dynamic balance in individuals with post-stroke hemiparesis. *J. Biomech.* **49**(3), 396–400 (2016). <https://doi.org/10.1016/j.jbiomech.2015.12.047>
16. Bauby, C.E., Kuo, A.D.: Active control of lateral balance in human walking. *J. Biomech.* **33**(11), 1433–1440 (2000). [https://doi.org/10.1016/s0021-9290\(00\)00101-9](https://doi.org/10.1016/s0021-9290(00)00101-9)

Comparison of Various Fractional Order Controllers on a Poorly Damped System



Isabela Birs, Ioan Nascu, Eva Dulf, and Cristina Muresan

Abstract Poorly damped systems exhibit a high oscillatory behavior making them harder to control. The paper explores the possibilities of controlling a poorly damped system using different fractional order control approaches such as the Fractional Order Internal Model Control (FOIMC) and the Fractional Order Proportional Integral (FOPI) controllers. The case study is chosen to be a highly nonlinear experimental platform consisting of a vertical take-off and landing platform. The performances of the closed loops with the two fractional order controllers are compared experimentally by analyzing reference tracking, disturbance rejection and robustness.

Keywords Fractional order control · Internal model control · Fractional order proportional integral control · Poorly damped process

1 Introduction

The classical Proportional Integral Derivative (PID) controller is dominant in most industrial control applications based on feedback control loops. Among the years, multiple tuning strategies have been developed for the PID, satisfying different process requirements [5, 19]. However, as the processes became more complex or the specifications more demanding, other control options have emerged for process

I. Birs (✉)

Automation Department, Technical University of Cluj-Napoca, Cluj-Napoca, Romania

Dynamical Systems and Control Research Group, Ghent University, Ghent, Belgium

Core Lab EEDT, Flanders Make Consortium, Ghent, Belgium

e-mail: Isabela.Birs@aut.utcluj.ro

I. Nascu · E. Dulf · C. Muresan

Automation Department, Technical University of Cluj-Napoca, Cluj-Napoca, Romania

e-mail: Ioan.Nascu@aut.utcluj.ro; Eva.Dulf@aut.utcluj.ro; Cristina.Muresan@aut.utcluj.ro

© Springer Nature Switzerland AG 2021

J. Awrejcewicz (ed.), *Perspectives in Dynamical Systems III: Control and Stability*,

Springer Proceedings in Mathematics & Statistics 364,

https://doi.org/10.1007/978-3-030-77314-4_18

control such as the Internal Model Control (IMC) approach. Applications for IMC strategies are mostly abundant in controlling processes with dead time, proving superior to the PID controller [20]. Comparisons between the two strategies show that the PID is easier to understand than the IMC, but the tuning of the IMC controller is easier for dead time processes [8].

Poorly damped processes feature a high-oscillatory response in the time domain with the presence of resonance peaks in the frequency domain representation of the process, increasing the difficulty of the control task. The transfer function of the classical PID controller has a single pair of zeros to compensate the poorly damped process, motivating the need of a higher order controller to compensate for the poorly damped characteristics of the plant [6]. Hence, the development of more complex tuning procedures is needed for controlling processes with poorly damped dynamics.

One of the most popular extensions of the traditional PID controller represents its generalization based on the fractional calculus theory. A popular approach for modern control engineering, fractional order control gives the differentiation operation an infinite dimension. The PID controller features integration and differentiation operations of order 1. Its fractional order generalization, known as the Fractional Order Proportional Integral Derivative (FOPID) controller, allows any rational order for the integral and derivative terms. Hence, the obtained FOPID controller can simultaneously satisfy more constraints than the classical PID approach as well as providing increased stability of the closed loop system [11, 12, 17, 21, 22].

Variations of the FOPID controller such as the Fractional Order Proportional Derivative (FOPD) and Fractional Order Proportional Integral (FOPI) controllers have been tuned with the purpose of controlling poorly damped systems. A poorly damped mass-spring-damper system expressed through a second order transfer function is controlled using the FOPI controller in [6]. The paper also compares the FOPI with the integer order PI controller, showing the superiority of the FOPI controller. FOPD controllers are developed by [2, 15, 18] for high-oscillatory vibration suppression processes with low damping ratios. The controllers are validated experimentally proving once more the superiority of the fractional approach for poorly-damped processes. In [13], the FOPID controller is compared to the traditional PID for a high-oscillatory thyristor controlled series capacitor process.

The Internal Model Control (IMC) approach also has a generalization in the fractional calculus field, known as the Fractional Order Internal Model Control (FOIMC). This implies the usage of a fractional order filter in favor of the integer order one for integer order processes [14] or inverting a fractional order model [23]. The available research surrounding the FOIMC controller is focused on time delay plants, where the superiority of this approach has been widely proven [7, 10, 24–26]. However, the development of FOIMC controllers for poorly damped time delay systems has been neglected.

The novelty of the present study lies in the development of an FOIMC control strategy for a poorly damped process with time delay. In addition, an FOPI is developed for the same process with the purpose of comparing the two methods. Both control strategies are implemented on a real life platform and the validation

of both methods is realized experimentally. Ultimately, the best approach will be determined by analyzing the closed loop response of the poorly damped system in terms of steady state error, settling time, overshoot, robustness and disturbance rejection performance.

The paper is structured as follows: Sect. 2 details the tuning methodology of the FOPI controller, Sect. 3 presents the mathematical background of the FOIMC approach; Sect. 4 presents the case study with an in-depth analysis of the process, system identification; controller tuning and experimental results; while Sect. 5 concludes the study.

2 Fractional Order Proportional Integral Control

The negative feedback control structure with the FOPI controller is presented in Fig. 1.

Several approaches are available for the tuning of an FOPI controller spanning from graphical tuning methodologies [3, 27] to optimization techniques [4]. The chosen design strategy of the FOPI controller is based on imposing frequency domain requirements of the open loop system given by

$$H_{ol}(s) = H_{FOPI}(s)H_p(s), \tag{1}$$

where $H_p(s)$ is the transfer function of a poorly damped process with time delay

$$H_p(s) = \frac{k}{s^2 + 2\zeta\omega_n s + \omega_n^2} e^{-\tau s} \tag{2}$$

and $H_{FOPI}(s)$ is the FOPI controller

$$H_{FOPI}(s) = k_p + \frac{k_i}{s^\lambda}. \tag{3}$$

The process' poorly damped dynamics is given by the low value of the damping ratio ζ . The time delay amount is expressed through τ , while the process' gain and natural frequency are enclosed in k and ω_n .

The FOPI controller is characterized by the proportional and integral gains k_p and k_i , respectively, and by the fractional order of differentiation which is denoted by λ . The fractional order λ can be any rational number from the (0, 2) interval. For

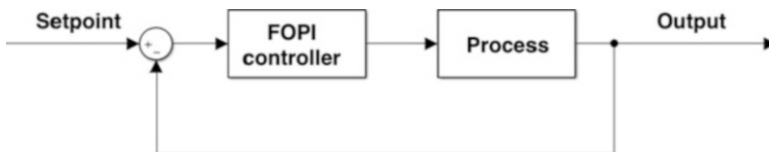


Fig. 1 FOPI control structure

the particular case of $\lambda = 1$, the transfer function from Eq. (3) becomes the classical, integer order, PI controller.

The tuning of the FOPI controller consists in determining k_p , k_i and λ . For this purpose, a set of frequency domain constraints are imposed targeting gain crossover frequency ω_{gc} , phase margin ϕ_m and the iso-damping property. This is one of the most popular methods for tuning FOPID-type controllers [4]. One of the main advantages of this method is its suitability on multiple processes such as the time delay family.

Replacing $s = j\omega$ gives the frequency domain representation of the open loop transfer function from Eq. (1). The first two constraints regarding gain crossover frequency and phase margin influence the damping ratio and the settling time of the closed loop system. The mathematical representation of the first two constraints can be written as

$$|H_{ol}(j\omega_{gc})| = 1 \quad (4)$$

$$\angle(H_{ol}(j\omega_{gc})) = -\pi + \phi_m. \quad (5)$$

The iso-damping property is the closed loop system's robustness to gain variations. The specification translates into a straight line of the phase representation around the gain crossover frequency. This means that for a certain range of gain changes, the phase remains constant, guaranteeing a robust behavior. The iso-damping equation is given by the derivative of the phase which is known to be zero for a constant line [1].

$$\left. \frac{d(\angle H_{ol}(j\omega_{gc}))}{d\omega} \right|_{\omega=\omega_{gc}} = 0 \quad (6)$$

The three equations from Eqs. (4), (5) and (6) form a system of nonlinear transcendental equations. The system is solved by imposing the desired gain crossover frequency ω_{gc} and phase margin ϕ_m . Reference [16] presents a set of guidelines for choosing adequate values for ω_{gc} and ϕ_m such that the obtained controller has physical meaning. There are multiple possibilities to solving the system of equations such as classical graphical approaches or more complex optimization techniques using MATLAB's Optimization Toolbox with constraints regarding $\lambda \in (0, 2)$ and $k_p, k_i > 0$.

3 Fractional Order Internal Model Control

Figure 2 shows the control scheme of the FOIMC controller applied to a time delayed process. The IMC control strategy uses the process in an explicit manner, while the FOPI structure from Fig. 1 uses it in an implicitly. The FOPI parameters are tuned based on the process model, without always knowing how the process will

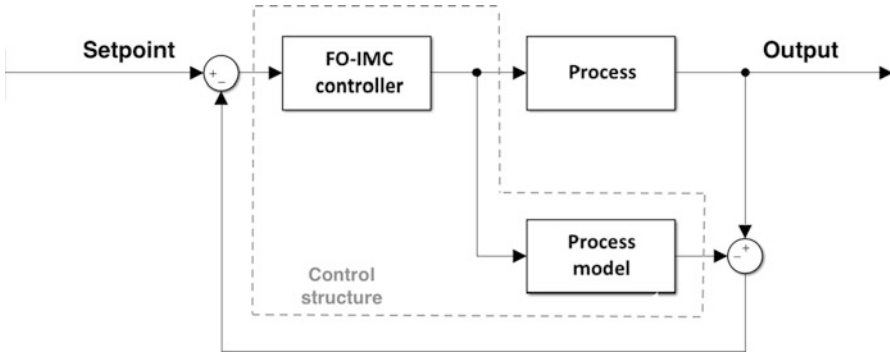


Fig. 2 FOIMC control structure

influence the control parameters. The FOIMC control structure is based directly on the process transfer function. For the integer order IMC case, there is one parameter that needs to be determined, usually denoted by λ , representing the filter coefficient [20]. It is important to specify that the parameters λ has different meanings for the FOPI and FOIMC.

In order to develop the tuning methodology of the FOIMC controller, the time delay τ from Eq. (2) is approximated using the series approach

$$e^{-\tau s} \approx 1 - \tau s, \tag{7}$$

giving the approximated process model

$$H_m(s) = \frac{k(1 - \tau s)}{s^2 + 2\zeta\omega_n s + \omega_n^2}. \tag{8}$$

The FOIMC controller from Fig. 1 is expressed as

$$H_{FOIMC}(s) = \frac{s^2 + 2\zeta\omega_n s + \omega_n^2}{k} \frac{1}{\lambda s^\alpha + 1}, \tag{9}$$

where λ is the filter coefficient and $\alpha \in (0, 2)$ is the filter's fractional order. The control structure with the FOIMC controller can be written as

$$H_c(s) = \frac{H_{FOIMC}(s)}{1 - H_{FOIMC}(s)H_m(s)} = \frac{s^2 + 2\zeta\omega_n s + \omega_n^2}{k(\lambda s^\alpha + \tau s)} \tag{10}$$

obtaining the open loop system

$$H_{ol}(s) = \frac{1}{\lambda s^\alpha + \tau s} e^{-\tau s}. \tag{11}$$

The FOIMC controller from Eq. (9) has two parameters that need to be determined: α and λ . A similar approach as for the tuning of the FOPI controller from Sect. 2 can be employed based on the gain crossover and phase equations

from Eqs. (4) and (5). A gain crossover frequency ω_{gc} and a phase margin ϕ_m are imposed for the open loop system in Eq. (11), resulting in a system of two nonlinear transcendental equations. Solving the system can be performed in a similar fashion as for the FOPI controller, obtaining α and λ .

The experimental implementation of the FOIMC controller is realized by splitting the control structure transfer function from Eq. (10) in an integer order PID controller and a fractional order filter

$$H_{FO}(s) = \frac{1}{\lambda s^{\alpha-1} + \tau}. \quad (12)$$

4 The Poorly Damped Case Study

4.1 Process Description

An oscillating, highly nonlinear process, consisting of a Vertical Take-Off and Landing (VTOL) platform has been chosen as the experimental case study. The platform is manufactured by Quanser for didactic purposes and is compatible with NIElvis boards from National Instruments. The VTOL process is displayed in Fig. 3.

The red cantilever beam is attached to a rotating component allowing angular movements on a single axis around the pivot point. The beam is equipped with

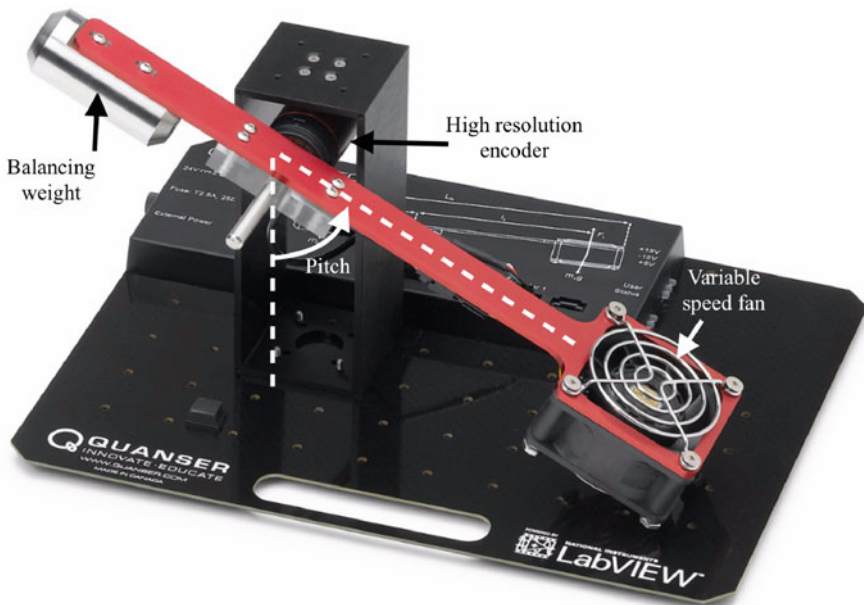


Fig. 3 VTOL platform

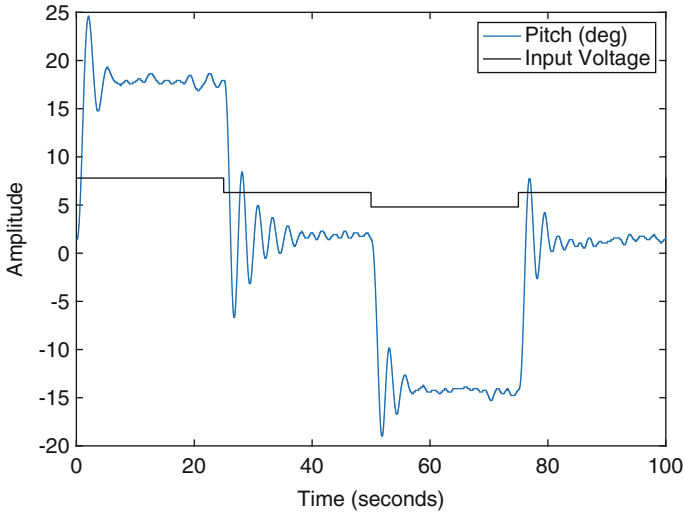


Fig. 4 Non-linearity and poor damping of the VTOL process

a balancing weight (left) and with a fan (right) that thrusts the cantilever beam upwards through its rotation. The input of the process is considered the voltage (V) applied to the motor connecting to the fan, while the output is the angular displacement of the beam. The displacement is measured with respect to the 0 deg position which is considered to be parallel to the base platform of the experimental setup. The maximum movement interval is $[-26, 60]$ deg due to construction limitations.

The experimental test presented in Fig. 4 proves the high oscillating and nonlinear nature of the process. The test implies stabilizing the platform at the 0 position using a 6.3 V input and changing the value by 1.5 V and -1.5 V.

The desired closed loop system behavior is to impose a setpoint position for the beam which is honored with a short settling time and minimum overshoot. A discrete control law is computed and sent to the platform with a sampling time of 0.005 s using LabVIEW graphical programming and the NIElvis microcontroller. The control loop is closed using built-in encoders to measure the real-time position of the beam used as feedback.

The process is described by a second order transfer function with time delay. The system identification is based on a step input of amplitude 6.3 V that stabilizes the beam at the 0 position. The experimentally obtained model based on Eq. (2) is given by

$$H_p(s) = \frac{22.24}{s^2 + 0.6934s + 5.244} e^{-0.8s}. \tag{13}$$

The damping ratio $\zeta = 0.1514$ suggests a poorly damped process response which is also confirmed by Fig. 4.

4.2 Tuning of the Fractional Order Controllers

The main requirement of the process described in the previous section is the zero steady state error, motivating the choice of the FOPI controller. The parameters are determined by imposing the gain crossover frequency $\omega_{gc} = 0.4$ rad/s and a phase margin $\phi_m = 75$ deg. The system of equations formed by Eqs. (4), (5) and (6) is translated into a minimization problem and is handled using optimization routines provided by MATLAB. The obtained controller

$$H_{FOPI}(s) = 0.0422 + \frac{20.7745}{s^{0.9288}} \quad (14)$$

has a fractional order of differentiation $\lambda = 0.9288$.

For the experimental implementation of the FOPI controller on the VTOL unit, the discrete control law has been computed based on the method detailed in [9]. The method provides a direct mapper between the fractional transfer function and the discrete domain using frequency domain approximations, without the need of the intermediary step where the fractional order transfer function is approximated to a high order integer order model. The discrete controller is obtained using a fifth order approximation and a sampling time $T_s = 0.005$ s.

The same frequency domain specification as for the case of the FOPI tuning are imposed in order to determine the FOIMC controller, $\omega_{gc} = 0.4$ rad/s and $\phi_m = 75$ deg. Solving the system of equations formed by Eqs. (4) and (5) with the open loop system from Eq. (11) gives the following FOIMC controller

$$H_{FOIMC}(s) = \frac{s^2 + 0.6934s + 5.244}{k} \frac{22.24}{1.09s^{0.8536} + 1}. \quad (15)$$

Note the fractional order of the filter that has been obtained as $\alpha = 0.8536$.

Furthermore, the control structure is obtained as

$$H_c(s) = \frac{s^2 + 0.6934s + 5.244}{22.24(1.09s^{0.8536} + 0.8s)} \quad (16)$$

A first order filter with the time constant $T_f = 0.1$ s is added to the equivalent controller from Eq. (16).

The discrete form of the FOIMC control structure with the added filter is obtained using the same approximation method and the same parameters as the FOPI controller.

4.3 Experimental Results and Comparisons

Both FOIMC and FOPI controllers are implemented on the experimental VTOL platform using the same discrete time approximation. For the physical implementation, the command signal applied to the platform is saturated in the $[0,10]$ V interval.

A set of steps with different amplitudes is applied as reference values and the behavior of both control strategies are disseminated in Fig. 5. The test involves applying the step references $r = (-15, -10, -15, -23)$ deg at times $t = (0, 30, 45, 60)$ s. The settling time obtained with the FOPI controller is $t_{s-FOPI} \approx 10$ s, while the FOIMC performance is $t_{s-FOIMC} \approx 6$ s. It is clear that for every step change, the FOIMC controller is the better choice. The FOIMC causes a spike of 30 V, at the beginning of the test which leads to a reduced time delay of the closed loop system, compared to the FOPI command which is smoother and has no abrupt changes (Figs. 6 and 7).

For the disturbance rejection test scenario, a setpoint of -15 deg is imposed for the duration of the test. After the closed loop systems stabilize at the desired position, an input disturbance of -0.5 V is introduced at $t_1 = 30$ s which is further removed at $t_2 = 60$ s. The FOIMC controller is the better choice for this test also, due to its reduced overshoot and settling time.

The last test involves adding a 50 g weight to the right end of the rotating beam with the purpose of slightly altering the process. The robustness is assessed by

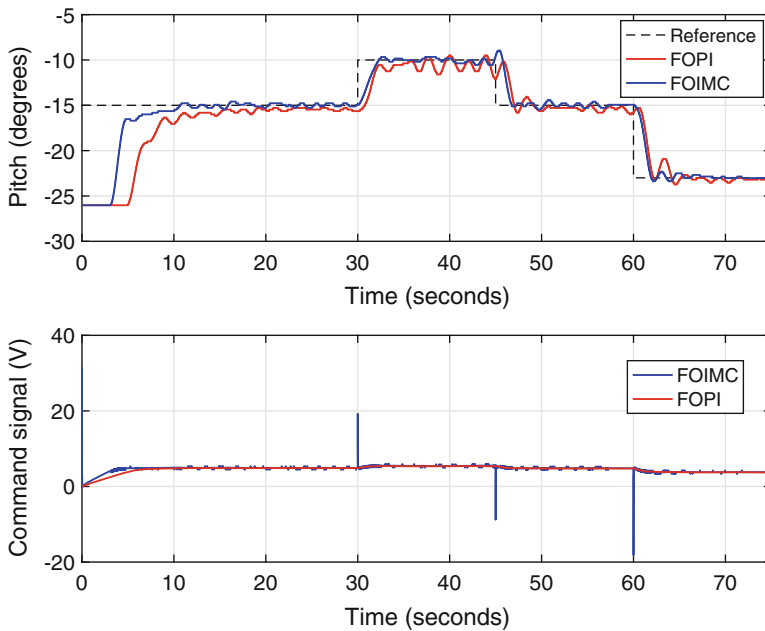


Fig. 5 Experimental reference tracking

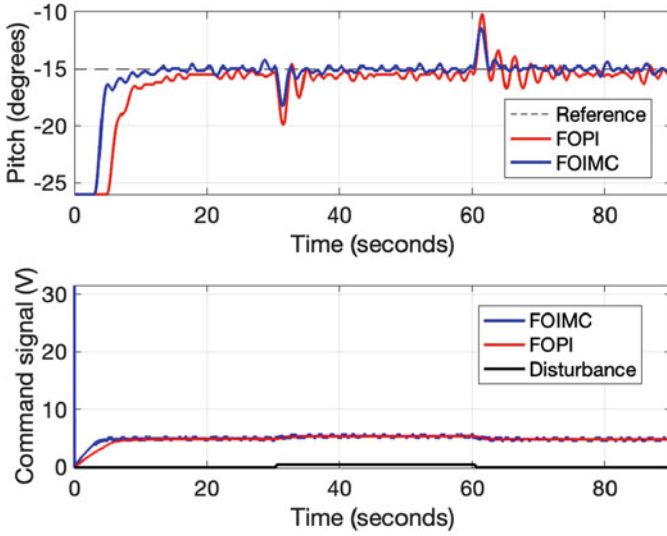


Fig. 6 Experimental disturbance rejection

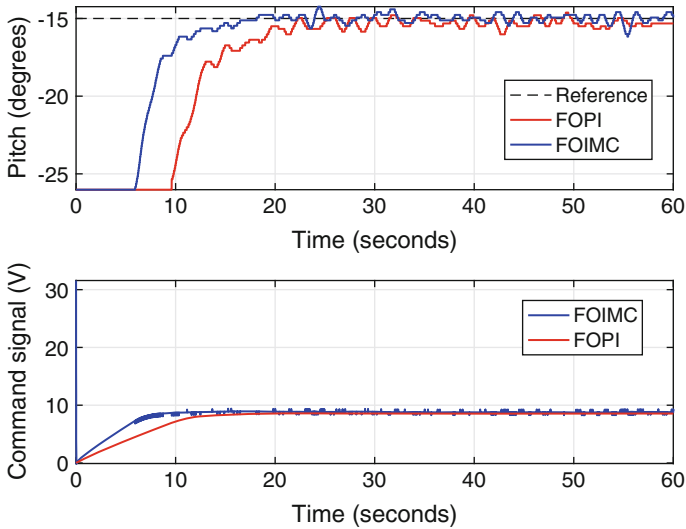


Fig. 7 Experimental robustness assessment

applying a single step reference of -15 V to the process. Both controllers produce 0 overshoot, but the FOIMC provides a smaller settling time and reduced time delay. The initial command spike is also present for the FOIMC controller.

5 Conclusions

Two different control strategies are developed and experimentally validated on a poorly damped process representing by a VTOL platform. The first strategy involves the tuning of an FOPI controller, while the second targets an FOIMC approach. Both controllers are tuned using the same frequency domain specifications: gain crossover frequency and phase, while the FOPI uses an extra robustness requirement. In addition, physical implementation of the control law uses the same discretization procedure with identical parameters. The two controllers are tested experimentally and their performance is assessed in terms of step reference tracking, disturbance of the input signal and robust behavior. For every test, the performance of the FOIMC control is superior to the FOPI. However, regardless of the performance of the two strategies for this particular process, the paper proves that fractional order controllers can be successfully applied to real life poorly damped processes.

Acknowledgments This work was supported by a mobility grant of the Romanian Ministry of Research and Innovation, CNCS—UEFISCDI, project number PN-III-P1-1.1-MC-2019-0357, within PNCDI III and by a grant of the Romanian Ministry of Education and Research, CNCS-UEFISCDI, project number PN-III-P1-1.1-TE-2019-0745, within PNCDI III. This research was also supported by Research Foundation Flanders (FWO) under grant 1S04719N.

References

1. Barbosa, R.S., Machado, J.A., Ferreira, I.M.: Tuning of PID controllers based on bode's ideal transfer function. *Nonlinear Dynamics* (2004). <https://doi.org/10.1007/s11071-004-3763-7>
2. Birs, I.R., Folea, S., Muresan, C.I.: An optimal fractional order controller for vibration attenuation. In: 2017 25th Mediterranean Conference on Control and Automation, MED 2017 (2017). <https://doi.org/10.1109/MED.2017.7984221>
3. Birs, I., Copot, D., Muresan, C.I., Keyser, R.D., Ionescu, C.M.: Robust fractional order pi control for cardiac output stabilisation. *IFAC-PapersOnLine* **52**(1), 994–999 (2019). <https://doi.org/10.1016/j.ifacol.2019.06.192>. <https://www.sciencedirect.com/science/article/pii/S2405896319302800>. In: 12th IFAC Symposium on Dynamics and Control of Process Systems, including Biosystems DYCOPS 2019
4. Birs, I., Muresan, C., Nascu, I., Ionescu, C.: A survey of recent advances in fractional order control for time delay systems. *IEEE Access* **7**, 30,951–30,965 (2019). <https://doi.org/10.1109/ACCESS.2019.2902567>
5. Blevins, T.L.: PID advances in industrial control. In: *IFAC Proceedings Volumes (IFAC-PapersOnline)* (2012)
6. Chevalier, A., Copot, C., Copot, D., Ionescu, C.M., de Keyser, R.: Fractional-order feedback control of a poorly damped system. In: 2014 IEEE International Conference on Automation, Quality and Testing, Robotics, pp. 1–4 (2014)
7. Hanane, B., Charef, A.: IMC based fractional order control design for automatic voltage regulator system. In: *Proceedings of 2015 7th International Conference on Modelling, Identification and Control, ICMIC 2015* (2016). <https://doi.org/10.1109/ICMIC.2015.7409476>

8. Hung, J.C.: Internal model control. Control and Mechatronics, 2nd edn. CRC Press (2016)
9. Keyser, R.D., Muresan, C.I., Ionescu, C.M.: An efficient algorithm for low-order direct discrete-time implementation of fractional order transfer functions. ISA Transactions **74**, 229–238 (2018). <https://doi.org/10.1016/j.isatra.2018.01.026>. <https://www.sciencedirect.com/science/article/pii/S0019057816306887>
10. Maâmar, B., Rachid, M.: IMC-PID-fractional-order-filter controllers design for integer order systems. ISA Transactions (2014). <https://doi.org/10.1016/j.isatra.2014.05.007>
11. Monje, C.A., Vinagre, B.M., Feliu, V., Chen, Y.: Tuning and auto-tuning of fractional order controllers for industry applications. Control Eng. Pract. **16**(7), 798–812 (2008). <https://doi.org/10.1016/j.conengprac.2007.08.006>. <https://www.sciencedirect.com/science/article/pii/S0967066107001566>
12. Monje, C.A., Chen, Y., Vinagre, B.M., Xue, D., Feliu-Battle, V.: Fractional-Order Systems and Controls Fundamentals and Applications: Fundamentals of Fractional-order Systems. Springer-Verlag, London (2010)
13. Morsali, J., Zare, K., Hagh, M.T.: Applying fractional order pid to design tscs-based damping controller in coordination with automatic generation control of interconnected multi-source power system. Eng. Sci. Technol. Int. J. **20**(1), 1–17 (2017). <https://doi.org/10.1016/j.jestch.2016.06.002>. <https://www.sciencedirect.com/science/article/pii/S2215098616300878>
14. Muresan, C.I., Dutta, A., Dulf, E.H., Pinar, Z., Maxim, A., Ionescu, C.M.: Tuning algorithms for fractional order internal model controllers for time delay processes. Int. J. Control (2016). <https://doi.org/10.1080/00207179.2015.1086027>
15. Muresan, C.I., Birs, I.R., Folea, S., Dulf, E.H., Prodan, O.: Experimental results of a fractional order PD λ controller for vibration suppression. In: 2016 14th International Conference on Control, Automation, Robotics and Vision, ICARCV 2016 (2017). <https://doi.org/10.1109/ICARCV.2016.7838715>
16. Muresan, C.I., Birs, I.R., Ionescu, C.M., Keyser, R.D.: Tuning of fractional order proportional integral/proportional derivative controllers based on existence conditions. Proc. Inst. Mech. Eng. I J. Syst. Control Eng. **233**(4), 384–391 (2019). <https://doi.org/10.1177/0959651818790809>
17. Podlubny, I.: Fractional-order systems and PI λ D μ -controllers. IEEE Trans. Autom. Control (1999). <https://doi.org/10.1109/9.739144>
18. Prodan, O., Birs, I.R., Folea, S., Muresan, C.I.: Seismic mitigation in civil structures using a fractional order PD controller. Int. J. Struct. Civil Eng. Res. (2016). <https://doi.org/10.18178/ijscer.5.2.93-96>
19. Rigelsford, J.: Advances in PID control. Assembly Automation (2001). <https://doi.org/10.1108/aa.2001.03321aad.010>
20. Saxena, S., Hote, Y.V.: Advances in internal model control technique: A review and future prospects. IETE Tech. Rev. **29**(6), 461–472 (2012). <https://doi.org/10.4103/0256-4602.105001>
21. Shah, P., Agashe, S.: Review of fractional PID controller (2016). <https://doi.org/10.1016/j.mechatronics.2016.06.005>
22. Sondhi, S., Hote, Y.V.: Fractional order controller and its applications: A review. In: Proc. of AsiaMIC (2012)
23. Tavakoli-Kakhki, M., Haeri, M.: Fractional order model reduction approach based on retention of the dominant dynamics: Application in IMC based tuning of FOPI and FOPID controllers. ISA Transactions (2011). <https://doi.org/10.1016/j.isatra.2011.02.002>
24. Titouche, K., Mansouri, R., Bettayeb, M., Al-Saggaf, U.M.: Internal model control-proportional integral derivative-fractional-order filter controllers design for unstable delay systems. J. Dyn. Syst. Measur. Control Trans. ASME (2016). <https://doi.org/10.1115/1.4032131>
25. Vinopra, T., Sivakumaran, N., Narayanan, S.: IMC based fractional order PID controller. In: Proceedings of the IEEE International Conference on Industrial Technology (2011). <https://doi.org/10.1109/ICIT.2011.5754348>

26. Vinopraba, T., Sivakumaran, N., Narayanan, S., Radhakrishnan, T.K.: Design of internal model control based fractional order PID controller. *J. Control Theory Appl.* (2012). <https://doi.org/10.1007/s11768-012-1044-4>
27. Wang, C., Jin, Y., Chen, Y.: Auto-tuning of fopi and fo[pi] controllers with iso-damping property. In: *Proceedings of the 48th IEEE Conference on Decision and Control (CDC) held jointly with 2009 28th Chinese Control Conference*, pp. 7309–7314 (2009). <https://doi.org/10.1109/CDC.2009.5400057>

Asymptotic Analysis of Submerged Spring Pendulum Motion in Liquid



T. S. Amer , M. A. Bek , and Asmaa Arab 

Abstract In the current work, the response of two degrees of freedom nonlinear dynamical model represented by the motion of a damped spring pendulum in an inviscid fluid flow is investigated. Lagrange's equations are utilized to deduce the descriptive equations of motion. The approximate solution up to the second order is obtained using the multiple scales perturbation technique. Classifications of different resonance cases were presented along with the modulation equations. The resonance curves, steady-state solution, and time history are presented. These types of models are essential as it represents several engineering applications.

Keywords Non-linear dynamics · Multiple scales technique · Fixed points · Stability

1 Introduction

The parametrical non-linear systems such as spring pendulum motion are of great interest for many types of research. These models have several industrial applica-

T. S. Amer (✉)

Tanta University, Faculty of Science, Mathematics Department, Tanta, Egypt
e-mail: tarek.saleh@science.tanta.edu.eg

M. A. Bek

Tanta University, Faculty of Engineering, Physics and Engineering Mathematics Department,
Tanta, Egypt

Mathematics Department, Faculty of Advanced Basic Sciences, Galala University, New Galala
City, Egypt

e-mail: m.ali@f-eng.tanta.edu.eg

A. Arab

Tanta University, Faculty of Engineering, Physics and Engineering Mathematics Department,
Tanta, Egypt

e-mail: asmaa-arab@f-eng.tanta.edu.eg

© Springer Nature Switzerland AG 2021

J. Awrejcewicz (ed.), *Perspectives in Dynamical Systems III: Control and Stability*,

Springer Proceedings in Mathematics & Statistics 364,

https://doi.org/10.1007/978-3-030-77314-4_19

tions such as swaying buildings, sieves, and roto dynamics [1–6]. These models provided a rich source for many applications, such as controlling the vibrations caused by external forces. A few researchers have investigated the pendulum motion in a fluid, see [7–9]. The multiple scales (MS) perturbation technique is used widely to obtain the systems' asymptotic solutions governing motion equations, as presented in [10–12].

Similarly, the small parameter method was used, and the fourth-order Rung-Kutta method is used in [13–15] to obtain the approximate and numerical solutions. The model investigated in the paper can represent various engineering applications or can simulate the motion of an autonomous underwater vehicle (AUV). The used MS method allows for identifying the system's harmful parameters due to the resonance. Also, the steady-state solution's stability can be carried out after transferring the modulation equations into an autonomous form. The modulation system of both amplitudes and modified phases in terms of time scales parameter is obtained. The time histories for the gained solutions are represented graphically to describe these solutions' behavior at any instant. Fixed points are calculated from the intersection of the curves in each plot. The stabilities of the steady-state solutions are checked through the Routh-Hurwitz criterion.

In this work, we will investigate the 2DOF dynamical model's behavior consists of the motion of a pendulum in a fluid flow. The equations of motion are obtained using Lagrange's equations up to the second-order approximation using the MS perturbation technique. Classifications of different resonance cases were presented in light of the obtained modulation equations. Time histories of these solutions are represented graphically to reveal the physical parameters' impact on the motion of the considered model. The importance of this model is due to its various applications, which centric on engineering vibrating systems.

2 Dynamical Model Description

The considered model represents the planar motion of a damped massless spring pendulum moving in a liquid with stiffness k .

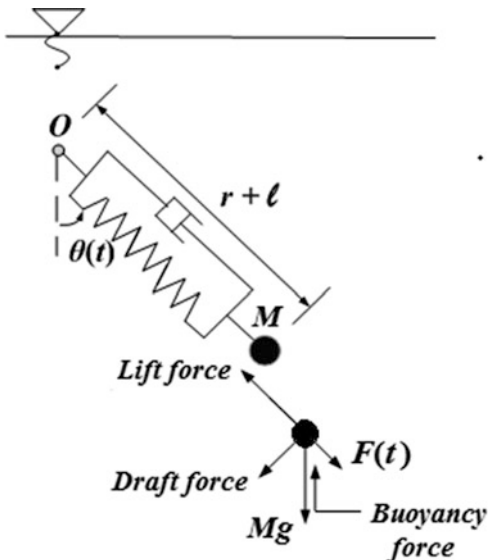
The spring is hinged at a fixed point O , and the other side is attached with a mass M as presented in Fig. 1. The pendulum arm is subjected to an external harmonic force $F(t) = F_0 \cos(\Omega t)$. Where Ω and F_0 are the frequency and the force amplitude. The spring initial length and elongation are denoted as ℓ , r where θ denotes the inclination angle on the vertical downward axis OY .

Therefore the kinetic and potential energies can be written in the form

$$\begin{aligned} V &= (Mg - F_B)(\ell + r)(1 - \cos \theta) + \frac{1}{2}kr^2, \\ T &= \frac{1}{2}M[(\ell + r)^2\dot{\theta}^2 + \dot{r}^2], \end{aligned} \quad (1)$$

where g are the gravitational acceleration.

Fig. 1 The dynamical model



Now, let us consider ρ as the liquid density, v refers to the velocity of the pendulum, A represents the cross-sectional area, V_{ol} is the mass volume, C_L is a lift coefficient and C_D is a drag one.

Therefore, the applied forces on the dynamical are:

1. The external force $F(t) = F_0 \cos(\Omega t)$,
2. The buoyancy force $F_B = \rho g V_{ol}$,
3. The drag force $F_D = \frac{1}{2} \rho v^2 A C_D$ represents the resistance force due to the motion of a mass through a liquid. Therefore, it acts in the opposite direction of the movement,
4. the lift force $F_L = \frac{1}{2} \rho v^2 A C_L$, clarifies a net force that acts perpendicular to the direction of the relative motion. It is created by different pressures on opposite sides of a mass due to the motion.

It is also worth mentioning that the motion of the system is damped by viscous force $c_1 \dot{r}$ of the damper and viscous rotation force $c_2 \dot{\theta}$; where c_1 and c_2 are the damping coefficients.

Using the above, we can obtain directly the Lagrangian $L = T - V$, and according to Lagrange's equations [16] of the second type, one gets the governing equations of motion as follow:

$$\begin{aligned}
 M \left[\ddot{r} - (\ell + r) \dot{\theta}^2 \right] + (Mg - F_B) (1 - \cos \theta) + kr \\
 = F_0 \cos(\Omega t) - c_1 \dot{r} - \frac{1}{2} \rho A C_L [(\ell + r)^2 \dot{\theta}^2 + \dot{r}^2], \\
 M \left\{ \ddot{\theta} (\ell + r)^2 + (\ell + r) \left[2 \dot{\theta} \dot{r} + \left(g - \frac{F_B}{M} \right) \sin \theta \right] \right\} \\
 = -\frac{1}{2} \rho A C_D \times [(\ell + r)^2 \dot{\theta}^2 + \dot{r}^2] - c_2 \dot{\theta}.
 \end{aligned} \tag{2}$$

The above system (2) consists of two non-linear second order differential equations of r and θ .

Let us use the following parameters

$$\begin{aligned} \frac{r}{\ell} &= \varepsilon \tilde{r}, & \theta &= \varepsilon \tilde{\theta}, & F_0 &= \varepsilon^3 \tilde{f}, & F_B &= \varepsilon^2 \tilde{f}_B, \\ \omega_1^2 &= \frac{k}{M}, & \omega_2^2 &= \frac{g}{\ell}, & f &= \frac{\tilde{f}}{\ell M}, & \frac{c_1}{M} &= \varepsilon^2 \tilde{c}_1, \\ f_B &= \frac{\tilde{f}_B}{\ell M}, & G_1 &= \frac{g}{2\ell}, & \frac{c_2}{M} &= \varepsilon^2 \tilde{c}_2, \\ H_D &= \frac{\rho A C_D \ell}{2M\varepsilon}, & H_L &= \frac{\rho A C_L \ell}{2M\varepsilon}. \end{aligned} \tag{3}$$

where ε is a small parameter.

Approximating the trigonometric functions $\sin\theta$ and $\cos\theta$ up to third order and according to (3), the governing system (2) is converted into

$$\begin{aligned} \ddot{\tilde{r}} + \omega_1^2 \tilde{r} &= \varepsilon \left(\dot{\tilde{\theta}}^2 - G_1 \tilde{\theta}^2 \right) + \varepsilon^2 \left(\tilde{r} \dot{\tilde{\theta}}^2 - c_1 \dot{\tilde{r}} \right) \\ &+ \varepsilon^2 \left[f \cos(\Omega t) + f_B + H_L \left(\dot{\tilde{\theta}}^2 + \dot{\tilde{r}}^2 \right) \right], \\ \ddot{\tilde{\theta}} + \omega_2^2 \tilde{\theta} &= -\varepsilon \left(2\dot{\tilde{\theta}}\dot{\tilde{r}} + 2\tilde{r}\ddot{\tilde{\theta}} - \omega_2^2 \tilde{r}\tilde{\theta} - f_B \tilde{\theta} \right) - \varepsilon^2 \left[2\dot{\tilde{\theta}}\tilde{r}\dot{\tilde{r}} + \tilde{r}^2 \ddot{\tilde{\theta}} - \frac{\omega_2^2}{3!} \tilde{\theta}^3 \right. \\ &\left. + c_2 \dot{\tilde{\theta}} + H_D \left(\dot{\tilde{\theta}}^2 + \dot{\tilde{r}}^2 \right) + f_B \tilde{r}\tilde{\theta} \right]. \end{aligned} \tag{4}$$

3 The Proposed Method

In order to obtain the asymptotic solutions of the governing system (4) and to get the modulation equations, we utilize the multiple scales method [12]. Therefore, let us assume the desired asymptotic uniform solutions r and θ have the forms of power series of a non-dimensional bookkeeping small parameter, say $0 < \varepsilon \ll 1$, as

$$\begin{aligned} r &= \sum_{k=0}^2 \varepsilon^k r_k(T_0, T_1, T_2) + O(\varepsilon^3), \\ \theta &= \sum_{k=0}^2 \varepsilon^k \theta_k(T_0, T_1, T_2) + O(\varepsilon^3), \end{aligned} \tag{5}$$

where $T_n = \varepsilon^n T$; ($n = 0, 1, 2$) are independent different time scales, in which T_0 and T_1, T_2 are the fast and slow time scales respectively.

It is convenient to express the general solutions of equations in the following complex form

$$\begin{aligned} r_0 &= A_1 e^{i\omega_1 T_0} + \overline{A_1} e^{-i\omega_1 T_0}, \\ \theta_0 &= A_2 e^{i\omega_2 T_0} + \overline{A_2} e^{-i\omega_2 T_0}. \end{aligned} \tag{6}$$

Here A_i ($i = 1, 2$) are defined as unknown complex functions of T_1 and T_2 can be determined later while \bar{A}_i denotes to their complex conjugate.

Substituting the above solutions (6) into the system equations, then eliminating terms that lead to secular terms, we have the first-order approximation solution in the forms

$$\begin{aligned}
 r_1 &= -\frac{(G_1 + \omega_2^2)}{(\omega_1^2 - 4\omega_2^2)} A_2^2 e^{2i\omega_2 T_0} + \frac{(2\omega_2^2 - 2G_1)}{\omega_1^2} A_2 \bar{A}_2 + c.c., \\
 \theta_1 &= -\frac{\omega_2 (2\omega_1 + \omega_2)}{\omega_1 (\omega_1 + 2\omega_2)} A_1 A_2 e^{i(\omega_1 + \omega_2) T_0} + \frac{\omega_2 (2\omega_1 - \omega_2)}{\omega_1 (\omega_1 - 2\omega_2)} \\
 &\quad \times A_1 \bar{A}_2 e^{i(\omega_1 - \omega_2) T_0} + c.c.
 \end{aligned}
 \tag{7}$$

The conditions for the elimination of secular terms for the first approximation required that

$$\begin{aligned}
 2i\omega_1 \frac{dA_1}{dT_1} &= 0; \\
 2i\omega_2 \frac{dA_2}{dT_1} &= 0.
 \end{aligned}
 \tag{8}$$

Consequently,

$$\begin{aligned}
 r_2 &= \frac{1}{2(\omega_1^2 - \Omega)} f e^{iT_0 \Omega} + \frac{1}{\omega_1^2} f_B + H_L \left[\frac{2\omega_2^2}{\omega_1^2} (A_2 \bar{A}_2 + A_1 \bar{A}_1) \right. \\
 &\quad \left. + \frac{A_1^3}{3} e^{2i\omega_1 T_0} - \frac{\omega_2^2 A_2}{(\omega_1^2 - 4\omega_2^2)} e^{2i\omega_2 T_0} \right] \\
 &\quad + \frac{\omega_2^2 A_1 A_2^2}{4\omega_2 (\omega_1 - \omega_2)} e^{i(\omega_1 + 2\omega_2) T_0} + c.c., \\
 \theta_2 &= \frac{\omega_1 \omega_2 A_1^2}{2\omega_1} \left[\frac{A_2}{(\omega_1 + \omega_2)} e^{i(2\omega_1 + \omega_2) T_0} - \frac{\bar{A}_2}{(\omega_1 - \omega_2)} e^{i(2\omega_1 - \omega_2) T_0} \right] \\
 &\quad - \frac{\omega_2^2 A_2}{2\omega_1} \times \left[\frac{A_1^2}{(\omega_1 + \omega_2)} e^{i(2\omega_1 + \omega_2) T_0} + \frac{\bar{A}_1^2}{(\omega_1 - \omega_2)} e^{i(\omega_2 - 2\omega_1) T_0} \right] \\
 &\quad - \frac{A_2^3}{64} e^{3i\omega_2 T_0} - H_D \left[2A_2 \bar{A}_2 + \frac{A_2^2}{3\omega_2^2} e^{2i\omega_2 T_0} - \frac{\omega_1^2 A_1^2}{\omega_2^2 - 4\omega_1^2} e^{2i\omega_2 T_0} \right. \\
 &\quad \left. + 2 \frac{\omega_1^2}{\omega_2^2} A_1 \bar{A}_1 \right] + f_B \left(\frac{A_1 A_2 e^{i(\omega_1 + \omega_2) T_0}}{\omega_1 (\omega_1 + 2\omega_2)} + \frac{\bar{A}_1 A_2 e^{i(\omega_2 - \omega_1) T_0}}{\omega_1 (\omega_1 - 2\omega_2)} \right) + c.c.
 \end{aligned}
 \tag{9}$$

Eliminating the terms that lead to secular ones form the second approximation demands that

$$\begin{aligned}
 2\omega_2^2 A_2 \bar{A}_2 A_1 - \frac{d^2 A_1}{dT_1^2} - i\omega_1 \left(c_1 A_1 + 2 \frac{dA_1}{dT_2} \right) &= 0, \\
 2\omega_2 A_1 A_2 (\omega_2 \bar{A}_1 - \omega_1 \bar{A}_1) - i\omega_2 \left(c_2 A_2 + 2 \frac{dA_2}{dT_2} \right) &= 0.
 \end{aligned}
 \tag{10}$$

As mentioned before, the unknown functions $A_i (i = 1, 2)$ can be determined from the removing conditions of the secular terms.

There are many resonance cases, primary external and internal secondary cases. The Primary external resonance occurs at $\Omega = \omega_1$, while the Internal or secondary resonance occurs at $\omega_1 = \pm \omega_2, \omega_1 = 2\omega_2, \omega_1 = 0, \omega_2 = 0$. Hence a complicated dynamical behaviour is expected.

4 Stability of the System

The following part contains the system stability investigation at the two resonance cases. Where, $\Omega \approx \omega_1$ and $\omega_2 \approx \omega_1$ are satisfied. This means that Ω and ω_2 are closer to ω_1 . Therefore, the detuning parameters $\sigma_i (i = 1, 2)$ are introduced according to the following form

$$\Omega = \omega_1 + \sigma_1, \quad \omega_2 = \omega_1 + \sigma_2.
 \tag{11}$$

These new parameters σ_i can be looked as a distance of the oscillations from the strict resonance, and then we can write σ_i as

$$\sigma_i = \varepsilon \tilde{\sigma}_i \overleftarrow{\leftarrow} \overleftarrow{\leftarrow} \overleftarrow{\leftarrow} \overleftarrow{\leftarrow} \quad (i = 1, 2).
 \tag{12}$$

By using conditions (11) and (12) and eliminating terms that lead to secular terms in order to obtain the solvability conditions:

$$\begin{aligned}
 \frac{1}{2} f e^{i\sigma_1 T_1} + 2\omega_2^2 A_2 \bar{A}_2 A_1 - 2i\omega_1 \frac{\partial A_1}{\partial T_2} - i\omega_1 c_1 A_1 &= 0, \\
 \frac{\omega_2^2}{2} A_2^2 \bar{A}_2 - 2i\omega_2 \frac{\partial A_2}{\partial T_2} + (2\omega_2^2 - 2\omega_1 \omega_2) A_1 \bar{A}_1 A_2 & \\
 - i c_2 \omega_2 A_2 + H_D \omega_1^2 A_1^2 e^{-i\sigma_2 T_1} &= 0.
 \end{aligned}
 \tag{13}$$

It is noticed from (13) that these functions depend on T_2 only and then we can express them as follow:

$$A_i = \frac{\tilde{a}_i(T_2)}{2} e^{i\tilde{\psi}_i T_2}, \quad a_i = \varepsilon \tilde{a}_i; \quad i = 1, 2.
 \tag{14}$$

Here \tilde{a}_i and ψ_i ($i = 1, 2$) represent the real functions amplitudes and phases for the solutions of r, θ .

The functions A_i can be expressed in the form

$$\frac{\partial A_i}{\partial T} = \varepsilon^2 \frac{\partial A_i}{\partial T_2} \quad (i = 1, 2). \quad (15)$$

Therefore Eq. (13) mutate into ordinary differential equations. The following modified phases can be introduced to transform these equations into autonomous ones

$$\begin{aligned} \theta_1(T_1, T_2) &= T_1 \tilde{\sigma}_1 - \psi_1(T_2), \\ \theta_2(T_1, T_2) &= -T_1 \tilde{\sigma}_2 - \psi_2(T_2) + 2\psi_1(T_2). \end{aligned} \quad (16)$$

Using (13), (14), (15), and (16) and identifying real parts and imaginary ones, we obtain the following system of four first-order ordinary differential equations (modulation) of the amplitudes a_i and the modified phases θ_i ($i = 1, 2$) for the examined resonance cases

$$\begin{aligned} \frac{da_1}{dT} &= \frac{f}{2\omega_1} \sin \theta_1 - \frac{1}{2} a_1 c_1, \\ a_1 \frac{d\theta_1}{dT} &= a_1 \sigma_1 - \frac{f}{2\omega_1} \cos \theta_1 - \frac{\omega_2^2}{\omega_1} \frac{a_1 a_2^2}{4}, \\ \frac{da_2}{dT} &= -\frac{a_2 c_2}{2} - H_D \frac{a_1^2 \omega_1^2}{4\omega_2} \sin \theta_2, \\ a_2 \frac{d\theta_2}{dT} &= \frac{a_1^2 a_2}{8} (\omega_2 - \omega_1) + \omega_2 \frac{a_2^3}{16} \\ &\quad - H_D \frac{a_1^2 \omega_1^2}{4\omega_2} \cos \theta_2 - a_2 \sigma_2. \end{aligned} \quad (17)$$

An inspection of the above system, we can conclude that this system has the solutions a_i and θ_i which describe the amplitudes and phases modulation in terms of the time scale T . These solutions are demonstrated graphically as in Figs. 2, 3, 4, and 5 using the following parameters:

$$\begin{aligned} \omega_1 &= (1.5, 2.5, 3.5) \text{ rad.s}^{-1}, \quad f = 10^{-3} \text{ M} = 10 \text{ kg}, \\ c_1 &= (0.004, 0.012, 0.02) \text{ kg.m}^2.\text{s}^{-1}, \quad g = 9.8 \text{ kg.s}^{-2}, \\ c_2 &= (0.001, 0.008, 0.03) \text{ kg.m}^2.\text{s}^{-1}, \quad c_D = 0.47, \\ \ell &= (1.2, 1.3, 1.5) \text{ m}, \quad R = 0.113 \text{ m}, \quad \varepsilon = 0.005 \\ \tilde{\sigma}_2 &= 0.01 \text{ rad.s}^{-1}, \quad \tilde{\sigma}_1 = 0.005 \text{ rad.s}^{-1}, \quad c_L = 0.25. \end{aligned}$$

Fig. 2 Represents the time history of the amplitude a_1 versus T when $\omega_1 = (1.5, 2.5, 3.5)\text{rad. s}^{-1}$

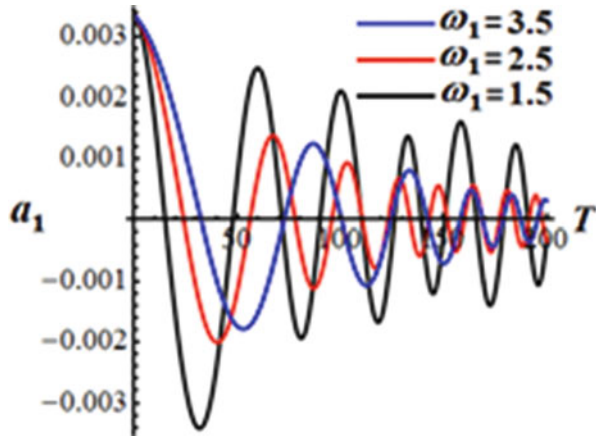


Fig. 3 Represents the influence of variance of T on the amplitude a_2 when $\omega_1 = (1.5, 2.5, 3.5)\text{rad. s}^{-1}$

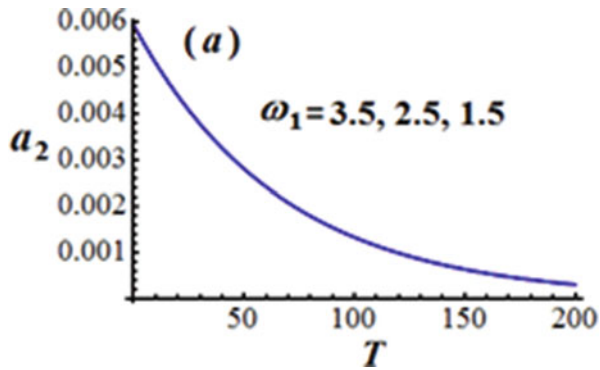
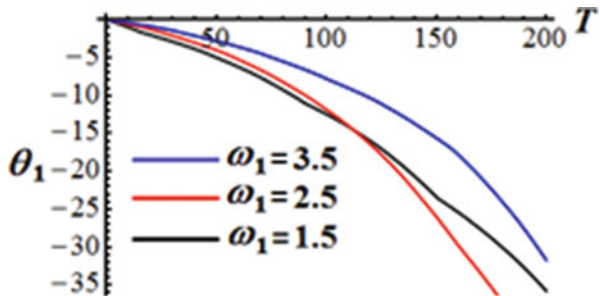
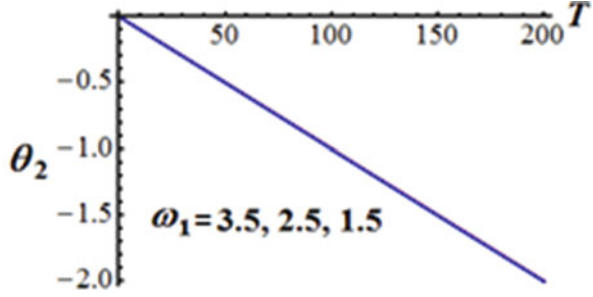


Fig. 4 Examines the variance of the modified phase θ_1 with T when $\omega_1 = (1.5, 2.5, 3.5)\text{rad. s}^{-1}$



It is of interest to continue studying the shapes of Fig. 2 that represent the variance of a_1 via T where Fig. 2 illustrates the progressive wave amplitude variance of a_1 with time using different values of ω_1 . The oscillation amplitude shows gradual decrement with the increase of ω_1 values. Moreover, the change of the waves becomes tiny when ω_1 , c_1 and c_2 have different values, as seen in Fig. 3. However, Figs. 4 and 5 represent the effects of changing ω_1 on the behavior of the modified phases θ_1 and θ_2 respectively. It is clear that these drawings indicate that

Fig. 5 Explores the effects of time T on the modified phase θ_2 when $\omega_1 = (1.5, 2.5, 3.5)\text{rad. s}^{-1}$



the monotonic decrease of the behaviour of the modified phases, as shown in Eqs. (24) and (26).

5 Steady-State Solutions

In order to study the steady-state vibration, we assume $\frac{d\theta_i}{dT} = \frac{da_i}{dT} = 0$ ($i = 1, 2$) in (17) to obtain the following system of four algebraic equations of the unknowns a_i and θ_i ; $i = 1, 2$

$$\begin{aligned} \frac{f}{2\omega_1} \sin \theta_1 - \frac{1}{2} a_1 c_1 &= 0, \\ \frac{f}{2\omega_1} \cos \theta_1 + \frac{\omega_2^2}{\omega_1} \frac{a_1 a_2^2}{4} - a_1 \sigma_1 &= 0, \\ \frac{a_2 c_2}{2} + H_D \frac{a_1^2 \omega_1^2}{4\omega_2} \sin \theta_2 &= 0, \\ \frac{a_1^2 a_2}{4} (\omega_2 - \omega_1) + \omega_2 \frac{a_2^3}{16} - H_D \frac{a_1^2 \omega_1^2}{4\omega_2} \cos \theta_2 - a_2 \sigma_2 &= 0. \end{aligned} \quad (18)$$

After eliminating the modified phases θ_1 and θ_2 , from Eq. (18), we have a system of two implicit non-linear algebraic equations of amplitudes a_i and frequencies ω_i besides the detuning parameters σ_i .

$$\begin{aligned} \frac{f^2}{4\omega_1^2} &= \frac{1}{4} a_1^2 c_1^2 + \left(a_1 \sigma_1 - \omega_2^2 \frac{a_1 a_2^2}{4} \right)^2, \\ H_D^2 \frac{a_1^4 \omega_1^4}{16\omega_2^2} &= \frac{a_2^2 c_2^2}{4} + \left(\frac{a_1^2 a_2}{4} (\omega_2 - \omega_1) + \omega_2 \frac{a_2^3}{16} - a_2 \sigma_2 \right)^2. \end{aligned} \quad (19)$$

Figure 6 represents the variance of a_1 via σ_1 when $\omega_1 = (1.5, 2.5)\text{rad. s}^{-1}$. and the variance of a_1 via σ_1 when $c_1 = (0.004, 0.02)\text{kg. m}^2. \text{s}^{-1}$ is shown in Fig. 7, however, Fig. 8 displays the variance of a_2 via σ_1 when $c_2 = (0.001, 0.03)\text{kg. m}^2. \text{s}^{-1}$. It is concluded the steady-state amplitudes are decreased monotonically with

Fig. 6 Displays the resonance curves a_1 via σ_1 when $\omega_1 = (1.5, 2.5, 3.5)\text{rad. s}^{-1}$

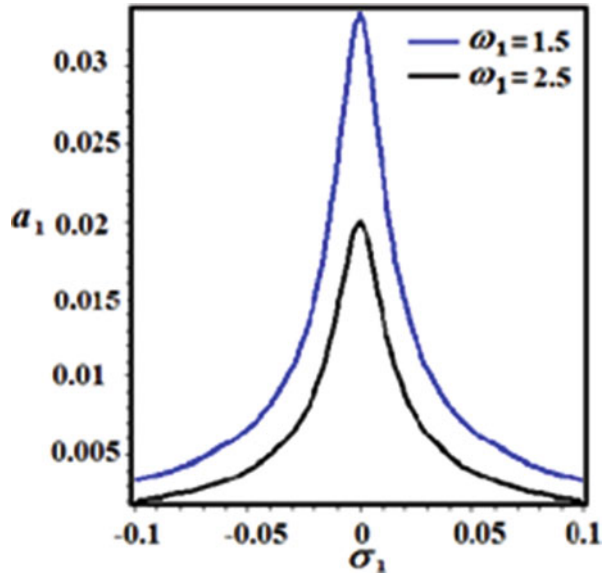
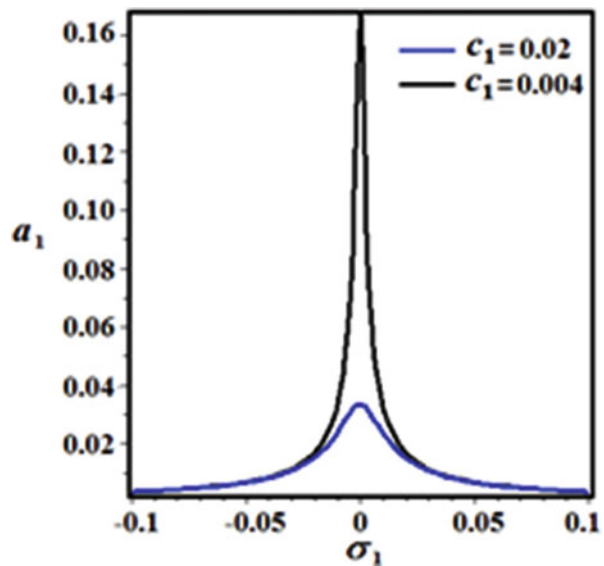


Fig. 7 Illustrate of the resonance curves a_1 via σ_1 when $c_1 = (0.004, 0.02)\text{kg. m}^2. \text{s}^{-1}$

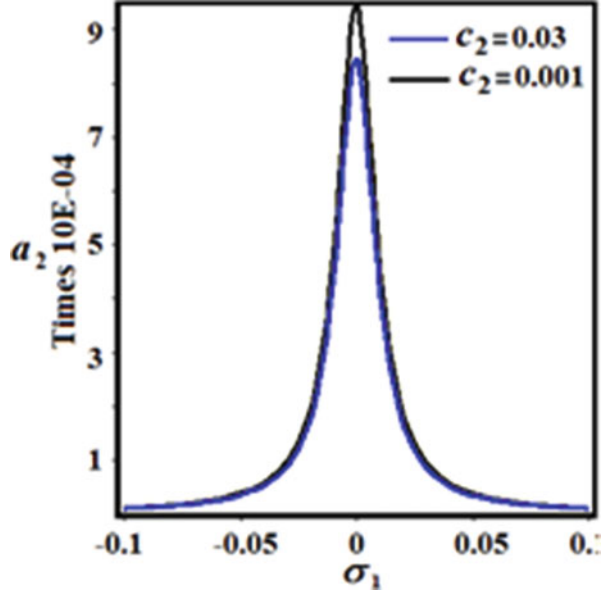


the increasing of the value of ω_1 . While the higher value of c_2 the lower readings of a_1 .

In order to further investigate the stability near fixed points, we consider:

$$\begin{aligned} a_1 &= a_{10} + a_{11}, & a_2 &= a_{20} + a_{21}, \\ \theta_1 &= \theta_{10} + \theta_{11}, & \theta_2 &= \theta_{20} + \theta_{21}, \end{aligned} \tag{20}$$

Fig. 8 Illustrate the resonance curves a_2 via σ_1 when $c_2 = (0.001, 0.03)\text{kg. m}^2. \text{s}^{-1}$



where $a_{10}, \theta_{10}, a_{20}$ and θ_{20} are the steady-state solutions of (17) and $a_{11}, \theta_{11}, a_{21}$ and θ_{21} are the assumed corresponding small perturbations. Substituting (20) into (17), one obtains the linearized equations in the form

$$\begin{aligned} \frac{da_{11}}{dT} &= \frac{f}{2\omega_1} \cos \theta_{10}\theta_{11} - \frac{1}{2}a_{11}c_1, \\ a_{10} \frac{d\theta_{11}}{dT} &= \frac{f}{2\omega_1} \sin \theta_{10}\theta_{11} - \frac{\omega_2^2}{4} (2a_{10}a_{20}a_{21} + a_{11}a_{20}^2) + a_{11}\sigma_1, \\ \frac{da_{21}}{dT} &= -H_D \frac{\omega_1^2}{4\omega_2} a_{10}^2 \cos \theta_{20}\theta_{21} - \frac{1}{2}a_{21}c_2, \\ a_{20} \frac{d\theta_{21}}{dT} &= \frac{3}{16} \omega_2 a_{20}^2 a_{21} + \frac{\omega_1^2}{2\omega_2} a_{10}^2 H_D \sin \theta_{20}\theta_{21} + \frac{1}{4} (\omega_2 - \omega_1) \\ &\quad \times [a_{10}^2 a_{21} + 2a_{10}a_{20}a_{11}] + a_{21}\sigma_2. \end{aligned} \tag{21}$$

Bearing in mind that $a_{11}, \theta_{11}, a_{21}$ and θ_{21} are unknown perturbation functions. Each function can be expressed as a linear combination of $k_i e^{\lambda\tau}$, in which k_i ($i = 1, 2, 3, 4$) are constants and λ is the eigenvalue corresponding to the unknown perturbation. In this regards, if the steady-state solutions (fixed points) $a_{10}, \theta_{10}, a_{20}$ and θ_{20} are asymptotically stable, then the real parts of the roots of the following characteristic equation of the set of Eq. (21)

$$\lambda^4 + \Gamma_1 \lambda^3 + \Gamma_2 \lambda^2 + \Gamma_3 \lambda + \Gamma_4 = 0, \tag{22}$$

must be negative.

Here $\Gamma_1, \Gamma_2, \Gamma_3, \Gamma_4$ depend on $a_{10}, \theta_{10}, a_{20}, c_1, c_2, f$ and take the forms

$$\Gamma_1 = \frac{c_1 + c_2}{2} - \frac{f \sin(\theta_{10})}{2a_{10}\omega_1} - \frac{\sin(\theta_{20}) a_{10}^2 H_D \omega_1^2}{2a_{20}\omega_2},$$

$$\Gamma_2 = \frac{1}{32a_{10}a_{20}\omega_1\omega_2^2} \left\{ 8f a_{10}^2 H_D \omega_1^2 \omega_2 \sin \theta_{10} \sin \theta_{20} - 8f a_{20} \left[(c_1 + c_2) \sin \theta_{10} \right. \right. \\ \left. \left. + 2\sigma_1 \cos \theta_{10} \right] \omega_2^2 + 8a_{10}a_{20}c_1c_2\omega_1\omega_2^2 + 4f a_{10}^3 \omega_2^4 \times \cos \theta_{10} \right. \\ \left. + 4a_{10}^5 H_D \omega_1^3 \omega_2 (\omega_2 - \omega_1) \cos \theta_{20} + a_{10}^3 H_D \omega_1^3 \left[\omega_2 \right. \right. \\ \left. \left. \times (16\sigma_2 + 3a_{20}^2 \omega_2) \cos \theta_{20} - 8\omega_2 (c_1 + c_2) \sin \theta_{20} \right] \right\},$$

$$\Gamma_3 = \frac{1}{64a_{10}a_{20}\omega_1\omega_2^2} \left\{ 4a_{10}^2 H_D \omega_1^2 \omega_2 \sin \theta_{20} \left[2f (c_1 + c_2) \sin \theta_{10} \right. \right. \\ \left. \left. - 2a_{10}c_1c_2\omega_1 - a_{10}^2 H_D \omega_1^2 \cos \theta_{20} (f \sin \theta_{10} - a_{10}c_1\omega_1) \right. \right. \\ \left. \left. + f (4\sigma_1 - a_{20}^2 \omega_2^2) \cos \theta_{10} \right] + 4f a_{20}c_2\omega_2^2 \left[(-4\sigma_1 + a_{20}^2 \omega_2^2) \right. \right. \\ \left. \left. \times \cos \theta_{10} - 2c_1 \sin \theta_{10} \right] \left[16\sigma_2 + 3a_{20}^2 \omega_2 + 4a_{10}^2 (\omega_2 - \omega_1) \right] \omega_2 \right\},$$

$$\Gamma_4 = \frac{1}{256 a_{20} \omega_2^2} f a_{10} H_D \omega_1 \left\{ 8 c_1 \sin \theta_{10} + 16 \sigma_1 \cos \theta_{10} \left[2 c_2 \right. \right. \\ \left. \left. \times \sin \theta_{20} + \cos \theta_{20} (-4 \sigma_2 + a_{10}^2 \omega_1) \right] - 2 \cos \theta_{20} (4a_{10}^2 + 3a_{20}^2) \right. \\ \left. \times (c_1 \sin \theta_{10} + 2\sigma_1 \cos \theta_{10} \omega_2) + 4a_{20}^2 \omega_2^2 \cos \theta_{10} \left[(4\sigma_2 \right. \right. \\ \left. \left. + 3a_{10}^2 \omega_1) \cos \theta_{20} - 2c_2 \sin \theta_{20} \right] + 3 \cos \theta_{10} \cos \theta_{20} a_{20}^2 \omega_2^3 \right. \\ \left. \times (a_{20}^2 - 4a_{10}^2) \right\}. \tag{23}$$

Therefore, one can obtain the essential conditions for the stability of the steady-state solutions according to the Routh-Hurwitz criterion in the form

$$\begin{aligned} \Gamma_1 > 0, \quad \Gamma_3 (\Gamma_1 \Gamma_2 - \Gamma_3) - 34 \Gamma_1^2 > 0, \\ \Gamma_1 \Gamma_2 - \Gamma_3 > 0, \quad \Gamma_4 > 0. \end{aligned} \tag{24}$$

The stability of the solutions is tested according to the graphical representations of the system of Eq. (19). The results are displayed in Figs. 9 and 10 to show the variance of a_2 versus a_1 for different values of c_2 and σ_2 . These figures are calculated according to the following parameters:

$$\begin{aligned} \omega_1 &= (1.5, 2.5, 3.5) \text{ rad.s}^{-1}, c_1 = 0.012 \text{ kg.m}^2.\text{s}^{-1}, \\ c_2 &= (0.001, 0.008, 0.03) \text{ kg.m}^2.\text{s}^{-1}, \ell = 1.2 \text{ m}, \\ f &= 0.0001, \sigma_1 = 0.005 \text{ rad.s}^{-1}, M = 10 \text{ kg}, \\ \sigma_2 &= (0.01, 0.04, 0.05, 0.09) \text{ rad.s}^{-1}. \end{aligned}$$

Fig. 9 Clarifies the intersection of the amplitudes a_1 and a_2 in order to obtain the fixed points: eight fixed points in which four of them are stable, and the others are unstable when $c_2 = 0.03\text{kg.m}^2.\text{s}^{-1}$

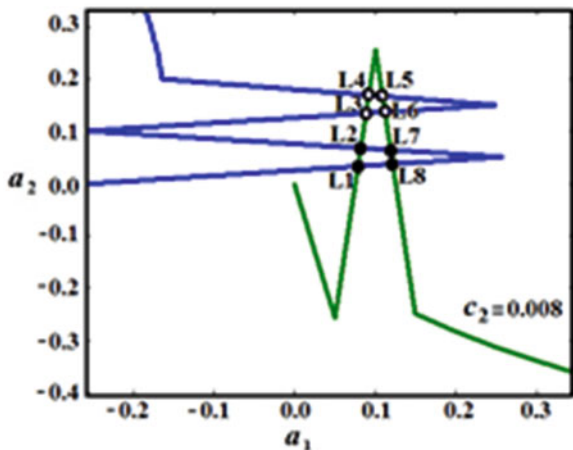
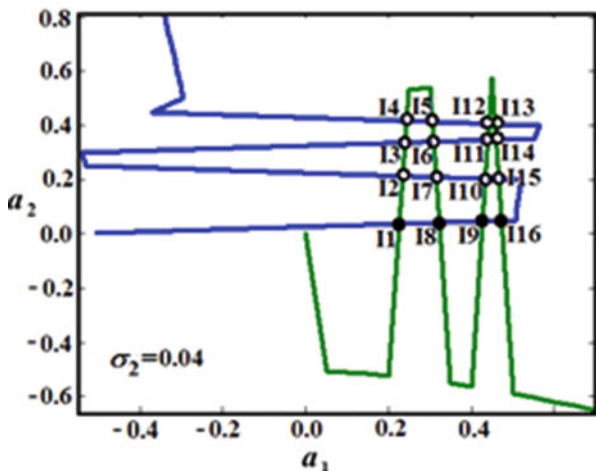


Fig. 10 Clarifies the intersection of the amplitudes a_1 and a_2 in order to obtain the fixed points: 16 fixed points in which four of them are stable, and the others are unstable when $\sigma_2 = 0.04$.



The intersection between the two curves gives the fixed points where small black circles mark the stable fixed points, satisfies all of the conditions (24), while hollow circles characterise the unstable ones. Figures 9 and 10 present the location of the fixed points eight and sixteen, respectively, with the following data: $c_2 = 0.03$ with only four stable fixed points that meet the conditions (23) out of eight. Finally, Fig. 10 has been calculated when $\sigma_2 = 0.04$ with the constancy of other values to produce 16 fixed points. Eight of the fixed points meets the conditions (23) and tends to be stable.

6 Conclusion

This work discusses the analysis of the damped spring pendulum, which is moving in liquid. The equation of motion is obtained using Lagrange's equations in the presence of external forces acting on the system. The MS method is successfully used to get the approximate solution to the second-order and to gain the modulation equations in the frame work of the solvability conditions. Two cases of resonance cases are introduced as primary external resonance and the internal one. The possible fixed points are determined, and then their stability is checked out according to the Routh–Hurwitz criterion. The time histories of the achieved solutions, resonance cases and steady-state solutions are represented graphically. The importance of this work is to go back to its direct applications in the fields of shipbuilding, submarines and engineering machines which have damping to deal with vibrations.

References

1. Thomsen, J.J.: *Vibrations and Stability: Advanced Theory, Analysis, and Tools*. Springer-Verlag, Berlin Heidelberg (2003)
2. Lee, W.K., Hsu, C.S.: A global analysis of a harmonically excited spring-pendulum system with internal resonance. *J. Sound Vib.* **171**, 335–359 (1994)
3. Lee, W.K., Park, H.D.: Chaotic dynamics of a harmonically excited spring-pendulum system with internal resonance. *Nonlinear Dyn.* **14**, 211–229 (1997)
4. Eissa, M., Sayed, M.: Vibration reduction of a three DOF non-linear spring pendulum. *Commun Nonlinear Sci.* **13**, 465–488 (2008)
5. Amer, T.S., Bek, M.A., Abouhmr, M.K.: On the vibrational analysis for the motion of a harmonically damped rigid body pendulum. *Nonlinear Dyn.* **91**, 2485–2502 (2018). <https://doi.org/10.1007/s11071-017-4027-7>
6. Amer, T.S., Bek, M.A., Abouhmr, M.K.: On the motion of a harmonically excited damped spring pendulum in an elliptic path. *Mech. Res. Commun.* **95**, 23–34 (2019). <https://doi.org/10.1016/j.mechrescom.2018.11.005>
7. Ibrahim, R.A., Pilipchuk, V.N., Ikeda, T.: Recent advances in liquid sloshing dynamics. *Appl. Mech. Rev.* **54**, 133–199 (2001)
8. Ikeda, T.: Non-linear parametric vibrations of an elastic structure with a rectangular liquid tank. *Nonlinear Dyn.* **33**, 43–70 (2003)

9. Martins, D.A., Silveira-Neto, A., Steffen Jr., V.: A pendulum-based model for fluid structure interaction analysis. *Engenharia Térmica (Thermal Engineering)*. **6**, 76–83 (2007)
10. Eng, Y.H., Lau, W.S., Low, E., Seet, G.L.: Identification of the hydrodynamics coefficients of an underwater vehicle using free decay pendulum motion. In: *International MultiConference of Engineers and Computer Scientists*, vol. 2, pp. 423–430, Hong Kong (2008)
11. Nayfeh, A.H.: *Perturbations Methods*. Wiley-VCH Verlag GmbH and Co. KGaA, Weinheim (2004)
12. Nayfeh, A.H.: *Problems in Perturbation*. Willey-Interscience, New York (1985)
13. Gilat, A.: *Numerical Methods for Engineers and Scientists*. Wiley, New York (2013)
14. Ismail, A.I.: Relative periodic motion of a rigid body pendulum on an ellipse. *J. Aerosp. Eng.* **22**, 67–77 (2009)
15. Amer, T.S.: The dynamical behavior of a rigid body relative equilibrium position. *Adv. Math. Phys.* **2017**, 13 pages (2017). <https://doi.org/10.1155/2017/8070525>
16. Chernousko, F.L., Akulenko, L.D., Leshchenko, D.D.: *Evolution of Motions of a Rigid Body about its Center of Mass*. Springer International Publishing AG, Cham (2017). <https://doi.org/10.1007/978-3-319-53928-7>

Parametric Identification of Nonlinear Structures Using Particle Swarm Optimization Based on Power Flow Balance Criteria



R. Anish  and K. Shankar 

Abstract This paper discusses a novel approach for nonlinear parameter identification of structures. An inverse problem was formulated as an optimization problem, using two objective functions in time domain. The first objective function is formulated as an error between measured acceleration and predicted acceleration of the model. While the second objective function minimizes the substructure Instantaneous Power Flow Balance, which is the sum of input power, dissipated power, transmitted power and time rate of kinetic and strain energy to zero. Here a cubic nonlinearity in spring (Duffing equation) and a quadratic nonlinearity in damper are used to model the nonlinear system. Numerical simulations were performed on a 10-DOF nonlinear system under harmonic excitation using Particle Swarm Optimization tool under noise-free and 5% noisy cases. Identified results are compared in terms of mean absolute percentage error, with other methods in nonlinear parameter identification available in literature. Simulation results show the accuracy of proposed method in nonlinear parameter identification even at high noise contamination cases.

Keywords Parameter identification · Power flow balance · Substructure · Particle swarm optimization

1 Introduction

Structural identification problems are inverse analysis problems, which are concerned with system modeling from input output information. Most commonly used parameter identification problems are vibration-based identification techniques, because of many reasons like, it is simple, reasonably accurate and cheaper compared to other methods. It is also possible to do analysis on running machines

R. Anish (✉) · K. Shankar

Machine Design Section, Department of Mechanical Engineering, Indian Institute of Technology Madras, Chennai, India

© Springer Nature Switzerland AG 2021

J. Awrejcewicz (ed.), *Perspectives in Dynamical Systems III: Control and Stability*,

Springer Proceedings in Mathematics & Statistics 364,

https://doi.org/10.1007/978-3-030-77314-4_20

using vibration-based methods. In recent years many of the researchers are more biased towards the area of nonlinear structural parameter identification with the objective to develop more accurate mathematical model. One such attempt is carried out in this paper using substructure acceleration matching objective function and a novel instantaneous power flow balance criteria.

Nonlinear parameter identification problems are more generic in nature and there exists no common analysis procedure that can be applied to all nonlinear problems at all instances. An extensive number of literatures are available in nonlinear parameter identification. Kerschen et al. [1] reviewed the state of art nonlinear structural parameter identification techniques, to understand the theoretical backgrounds, assets, limitations and the possible applications of various methods. Noel and Kerschen [2] conducted a detailed survey on key developments in nonlinear parameter estimation methods over the last decade. It also explains different stages in identification process like detection, localization and estimation of nonlinearities. Timlison and Woden [3] described various identification techniques in time and frequency domain. A number of experimental case studies are also discussed to demonstrate the nonlinear system identification methods.

Koh et al. [4, 5] used the substructure technique to decomposes a large system to small manageable subsystems to improve the convergence of structural parameter identification and computational time. Varghese and Shankar [6] developed a Multi Objective (MO) optimization formulation to detect and quantify the crack damage parameters in beam structure at various locations in substructure level. Koh and Shankar [7] suggested a new methodology for system parameter identification of substructure without the need of interface measurement, which are difficult to get in certain cases like beam or frame rotational response. Power flow analyses, which describe the energy interaction between various subsystems, are studied by many researchers. Mace [8] used the wave approach to study the power flow between two point coupled wave bearing subsystems under time harmonic excitation and work by Stephen [9] to explain the theory behind the base excitation concepts of harvesting and dissipation of energy of elastically mounted system are notable contributions in this field. Varghese and Shankar [6] introduced an inverse identification technique, which investigates the application of substructural power flow to linear structural parameter estimation.

Kapaniya [10] introduced a two-step identification process using Time Finite element Method (TFM) for the structural parameter identification of both linear and nonlinear terms separately. Kumar and Shankar [11] worked on structural parametric identification with cubic nonlinearity in springs and quadratic nonlinearities in dampers. They treated the problem as inverse using substructure acceleration matching objective function with Genetic Algorithms (GA) optimization search tool. Eberhart and Kennedy [12] were the first to propose a population-based optimization technique called Particle Swarm Optimization (PSO). Thereafter, several studies conducted by a number of researchers revealed the superiority of the Particle Swarm Optimization Algorithm over other non-classical algorithms like Genetic Algorithm in terms of its convergence speed, simplicity in coding, computational inexpensiveness etc. Perez and Behdinan [13] successfully implemented the particle

swarm optimization into constraint structural optimization problems. Xue et al. [14] used a modified PSO algorithm with a feasibility strategy to deal with various constraints of the problem. It also discusses the influences of the availability of limited response measurements on the performance of PSO for parameter identification.

2 Objective Functions

The optimization problems were formulated separately by using the conventional acceleration matching and instantaneous power flow balance objective functions. The substructure identification method used in this work, allows the researchers to concentrate, the sensor measurements to a smaller zone of interest and thereby reducing the computational time.

2.1 Substructure Acceleration Matching

The concept of sub structuring is based on the ‘divide and conquer’ rule, in which the global structure is divided into substructures so that the number of unknown parameters to be identified is reduced into manageable ones. The first fitness function is formulated by comparing the measured and estimated acceleration as weighted error cost function as [15].

$$f_1 = \sum_{i=1}^M \sum_{j=1}^T \frac{(\ddot{x}_m - \ddot{x}_e)^2}{T * M} \quad (1)$$

Where, the subscripts ‘*m*’ and ‘*e*’ represents the measured and estimated acceleration response for fitness evaluation. ‘*M*’ is the number of measurement points or sensor locations and ‘*L*’ is the number of time steps. Here the measured acceleration response was simulated numerically and noise has been added to compensate the measurement error.

2.2 Instantaneous Power Flow Balance

Power flow balance is another form of law of conservation of energy. The power balance criteria states that within a substructure the net sum of power that is net sum of input, damping and transferred power is zero. The main purpose of instantaneous power study is to formulate an objective function in terms of instantaneous power flow balance as

$$f_2 = \frac{1}{T} \sum_{i=1}^T (IP_e^b)^2 \quad (2)$$

Where, ‘ T ’ is the number of time steps and superscript ‘ e ’ denotes the estimated instantaneous power balance for objective function evaluation.

Thus, the two objective functions are combined together to form a multi objective optimization problem using weighted aggregation approach. The combined objective function can be represented as [16].

$$f = w_1 f_1 + w_2 f_2 \quad (3)$$

Where, w_1 and w_2 are non-negative weighting factors, which takes values between 0 and 1, such that $\sum w_i = 1$, where ‘ i ’ is the number of objective functions. For this particular study, weighting factors of {0.5,0.5} was chosen as explained in [6].

3 Numerical Modeling

The substructure nonlinear parameter identification is explained through a numerical model of 10DOF lumped mass model in Kumar and Shankar [11] was selected with different excitation load conditions. The global and substructure considerations are as shown in Fig. 1. All masses were considered as unity (1 kg). The values of all linear springs and linear dampers considered are taken as 25 N/m and 1Ns/m respectively. The nonlinear spring damper pairs are attached to fourth and seventh DOF. A cubic nonlinearity (Duffing equation) in spring and quadratic nonlinearity in damper were selected for the analysis and the nonlinear relations are as follows.

$$K_n \delta_n = a_n \delta_n + b_n \delta_n^3 \quad (4)$$

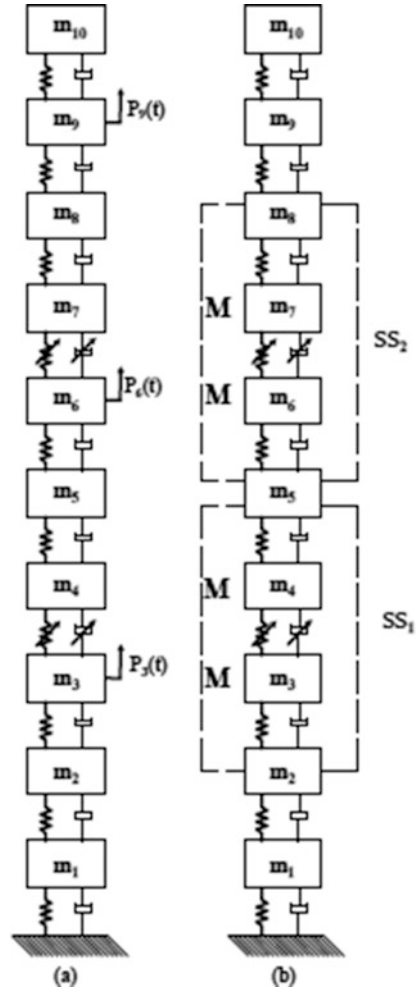
$$C_n (\delta_n, \dot{\delta}_n) = c_n \dot{\delta}_n (1 + \delta_n^2) \quad (5)$$

Where, a_n is the linear coefficient term in nonlinear spring, b_n and c_n are the coefficients of nonlinear spring force and nonlinear damper force corresponding to nth (say 4th and 7th) node/DOF of the structure to be analyzed. $\delta_n, \dot{\delta}_n$ are the relative displacement and relative velocity corresponding to nth node.

4 Parameter Identification

The substructure method without overlap is chosen for parameter identification study. The global structure is sub-divided into substructures and is shown in Fig. 1. The first substructure (SS1) is considered here for demonstration purpose. It has two interface nodes (2 and 5 in global structure) and two interior nodes (3 and

Fig. 1 Global structure and substructure classifications



4). The masses correspond to interface nodes are not considered for substructure formulation. The nonlinear elements are placed between the interior nodes as shown in Fig. 1. The responses for internal DOF of the substructures are simulated using the time span of 0–1 seconds and sampling time step of 0.0002 seconds using the Runge Kutta 4th order numerical integration method in MATLAB®. In the substructure parameter identification procedure, the coefficients of nonlinear spring and damper terms (a_4 , b_4 and c_4 in SS1) are assumed as unknown parameters. A Particle Swarm Optimization (PSO) with population size of 30, generation of 125, acceleration coefficients ($c_1 = c_2 = 2$) and an inertia weight 0.9 has been used for identification. Analysis was conducted with and without the application of noise to study the robustness of the proposed approach in noise contamination cases.

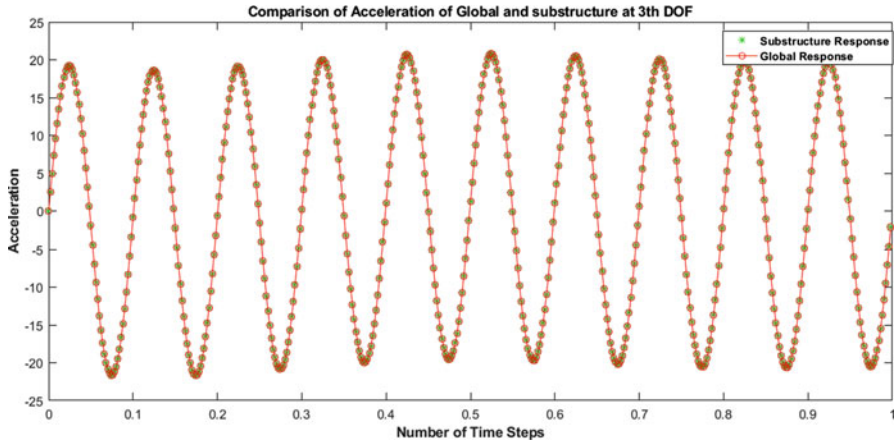


Fig. 2 Comparison of acceleration response of global structure and substructure at third DOF of 10 DOF nonlinear System

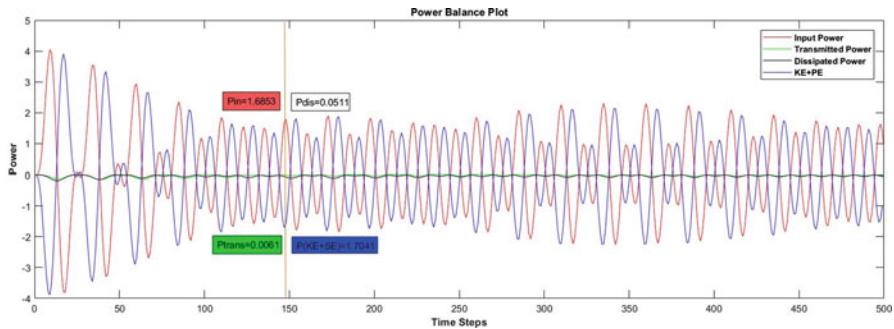


Fig. 3 Components of Instantaneous Power Flow balance for Substructure-1 without noise

The acceleration response obtained through substructure formulation and global structure at measurement location (M) corresponding substructure-1, are as shown in Fig. 2. From the plot it can be observed that both the global (actual) and substructure responses match very closely and hence the accuracy of the substructure formulation is verified. The components of instantaneous power flow such as input power, transmitted power, dissipated power and power due to kinetic and strain energies in substructure (SS1) without the noise case are shown in Fig. 3. From the plot it is clear that at each sampling point the system satisfies the power balance criteria as stated earlier.

In this study both the nonlinear springs are considered to be Hardening Springs for numerical analysis. Table 1 gives the mean results of identified nonlinear coefficients using a harmonic load of 1.5 N magnitude and 20 Hz excitation frequency under noise free and noise contamination cases. The loads are applied on third, sixth and ninth nodal positions as shown in Fig. 1. The identified results obtained

Table 1 Identified substructure parameters of 10DOF nonlinear system using Acceleration Matching (AM) and IPFB objective functions under harmonic load

Type of problem	Nonlinear coefficients	Actual value	Single objective (AM) with multiple measurement sensors		Multi objective (AM + IPFB) with multiple measurement sensors	
			Without noise (% error)	With 5% noise (%error)	Without noise (% error)	With 5% noise (%error)
Substructure SS1	a₄	25	24.893 (0.429)	24.673(1.309)	24.999(0.004)	23.692(5.232)
	b₄	1	1.057 (-5.72)	1.061(-6.109)	0.9891(1.088)	0.975(2.471)
	c₄	1	1.017 (-1.68)	1.056(-5.559)	0.9998(0.020)	1.002(-0.164)
Maximum % error			-5.72	-6.109	1.088	5.232
Mean absolute % error			2.61	4.326	0.371	2.622

Table 2 Comparison of Identification results of 10DOF nonlinear system with literature

Substructure SS1	Without noise		With 5% noise	
	Kumar and Shankar [11]	Present method	Kumar and Shankar [11]	Present method
Maximum % error	-7.81	-3.412	-9.55	8.82
Mean absolute % error	3.61	0.933	3.99	3.077

using acceleration matching with multiple sensors and combined objective of both acceleration matching and instantaneous power flow balance method are shown in Table 1. In terms of mean absolute error for substructure-1, the identification results are found to be with 2.61% and 4.326%, respectively for acceleration matching objective, noise free and 5% noisy cases. For the same cases the respective errors are reduced to 0.371% and 2.622% in multi objective of both acceleration matching and IPFB objective approach. That means, a significant reduction in mean absolute error of 85.78% (noise free) and 39.39% (noisy case) were observed in multi objective case, compared with single objective of acceleration matching case in substructure-1. A convergence study of two methods of identification process was also conducted. It was found that the multi objective of both Acceleration Matching (AM) and IPFB method convergence faster than the single objective Acceleration Matching with multiple sensor method. For brevity, the convergence plot is not shown here.

The analysis was repeated with increased number of unknown variables (all 7 parameters in SS1) and an impulsive load of 10 N applied in the form of initial velocity on mass m_1 . The identified results are compared with those from the original research paper [11] from which the example was taken, and is furnished in Table 2. There, the estimated nonlinear parameters have a mean absolute error of 3.61% (noise free case) was noted on Substructure-1, with only acceleration matching objective function using Genetic Algorithm (GA) search tool. In the present study using PSO, the mean absolute error is reduced to 0.933% (noise free). That is, a reduction of 74.15% in mean absolute error was achieved using the proposed multi objective approach. Similarly, for 5% noise case, the reduction is 22.88%.

5 Conclusions

A novel concept of nonlinear parameter identification using instantaneous power flow balance objective function in time domain has been introduced. The proposed method was successfully implemented on a 10DOF nonlinear system. Comparing the Mean Absolute % Error, a reduction of 85.78% and 39.39% in noise free and noisy cases are obtained for substructure-1, using the proposed multi objective method. The convergence study on parameter identification reveals the effect of instantaneous power flow balance objective function method on parameter identification.

References

1. Kerschen, G., et al.: Past, present and future of nonlinear system identification in structural dynamics. *Mech. Syst. Signal Process.* **20**(3), 505–592 (2006)
2. Noel, J.-P., Kerschen, G.: Nonlinear system identification in structural dynamics: 10 more years of progress. *Mech. Syst. Signal Process.* **83**, 2–35 (2017)
3. Tomlinson, G.R., Worden, K.: *Nonlinearity in Structural Dynamics: Detection, Identification and Modelling*. CRC Press (2000)
4. Koh, C.G., See, L.M., Balendra, T.: Estimation of structural parameters in time domain: a substructure approach. *Earthq. Eng. Struct. Dyn.* **20**(8), 787–801 (1991)
5. Koh, C.G., Hong, B., Liaw, C.Y.: Sub structural and progressive structural identification methods. *Eng. Struct.* **25**(12), 1551–1563 (2003)
6. Varghese, C.K., Shankar, K.: Damage identification using combined transient power flow balance and acceleration matching technique. *Structural Control and Health Monitoring.* **21**(2), 135–155 (2014)
7. Koh, C.G., Shankar, K.: Substructural identification method without interface measurement. *J. Eng. Mech.* **129**(7), 769–776 (2003)
8. Mace, B.R.: Power flow between two continuous one-dimensional subsystems: a wave solution. *J. Sound Vib.* **154**(2), 289–319 (1992)
9. Stephen, N.G.: On energy harvesting from ambient vibration. *J. Sound Vib.* **293**(1–2), 409–425 (2006)
10. Varghese, C.K., Shankar, K.: Identification of structural parameters using combined power flow and acceleration approach in a substructure. *Int. J. Eng. Technol. Innov.* **1**(1), 65–79 (2016)
11. Kumar, R.K., Shankar, K.: Parametric identification of structures with nonlinearities using global and substructure approaches in the time domain. *Adv. Struct. Eng.* **12**(2), 195–210 (2009)
12. Eberhart, R., Kennedy, J.: A new optimizer using particle swarm theory, *Micro Machine and Human Science, 1995. MHS'95, Proceedings of the Sixth International Symposium on*. IEEE, 1995
13. Perez, R.L., Behdinan, K.: Particle swarm approach for structural design optimization. *Comput. Struct.* **85**(19–20), 1579–1588 (2007)
14. Xue, S., Tang, H., Zhou, J.: Identification of structural systems using particle swarm optimization. *J. Asian Archit. Build. Eng.* **8**(2), 517–524 (2009)
15. Clough, R.W., Penzien, J.: *Dynamics of Structures*, Second edn. McGraw-Hill, New York, USA, New York (1993)
16. Rao, S.S.: *Engineering Optimization, Theory and Practice*, Fourth edn. Wiley, New York (2009)

Vibration and Buckling of Laminated Plates of Complex Form under in-Plane Uniform and Non-uniform Loading



Lidiya Kurpa , Victoriya Tkachenko, and Anna Linnik 

Abstract The vibration and buckling analysis of symmetrically laminated plates with complex form subjected to in-plane uniform and non-uniform loading is performed using variational Ritz's method and the R-functions theory. First order shear deformations theory of Timoshenko's type are adopted. Each ply is assumed to be an orthotropic homogeneous one without slip at interfaces. The developed approach includes several stages: determination of the heterogeneous subcritical state of the plate; finding buckling critical load; solving linear vibration problem. Ritz's method is applied on each stage. Systems of the admissible functions, that satisfy at least main (kinematic) boundary conditions have been built by the R-functions method. Validation of the proposed method and created software is confirmed by comparison of buckling load and frequencies vibration with known results for square laminated plates with free circular or rectangular cut-outs. Buckling loads for laminated clamped plates with complex form under non-uniform edge compressions have been obtained. It is assumed that plates can be made of different materials and have the different ply orientations. The effect of the cut-outs sizes on critical load and frequencies values are studied. Number of layers, degree of orthotropic, boundary conditions, type of loading (uniform and non-uniform) on buckling critical load and frequencies value are investigated.

Keywords Buckling · Laminate plates · Non-uniform load · R-functions theory · Rayleigh-Ritz method

1 Introduction

Many elements of modern structures are made of composite materials in order to reduce its weight and make structure stronger. So, it is important to develop methods

L. Kurpa · V. Tkachenko · A. Linnik (✉)

The Kharkov State Technical University, Department of Applied Mathematics, Kharkiv, Ukraine
e-mail: Kurpa@kpi.kharkov.ua

© Springer Nature Switzerland AG 2021

J. Awrejcewicz (ed.), *Perspectives in Dynamical Systems III: Control and Stability*,

Springer Proceedings in Mathematics & Statistics 364,

https://doi.org/10.1007/978-3-030-77314-4_21

and software to calculate dynamical behavior of such structural elements. One of the important components of this calculation is determination of the natural frequencies and values of the critical load.

The study of the stability and oscillation of loaded multilayer plates is significantly complicated when the plates have a complex shape and non-uniform loading. It is connected with occurrence of inhomogeneous subcritical state of the plate. Many theories and methods for solving the stability and vibration problems have been proposed today. Review of research in analysis of composite plates can be found in the works [1–3], and others. It should be noted that these problems are usually solved by approximate methods due to the complexity of mathematical models. One of the more universal and popular approaches is the finite element method. Despite the large number of publications concerning the stability and vibration problems of loaded multilayer plates, most of them consider the simply supported or clamped rectangular plates. There is essentially small number of works dealing with plates of another geometric shape or loaded non-uniformly according to some law (for example, linear, parabolic, etc.) [3, 4], that is subcritical state of the laminated plate is inhomogeneous. As it was shown in works [5, 6] the R-functions method (RFM) can take into account the complex shape, type of the boundary conditions and inhomogeneous subcritical state. In the present work RFM is applied to the problems of the stability and vibration of the loaded in plane composite plates under uniform and non-uniform loading.

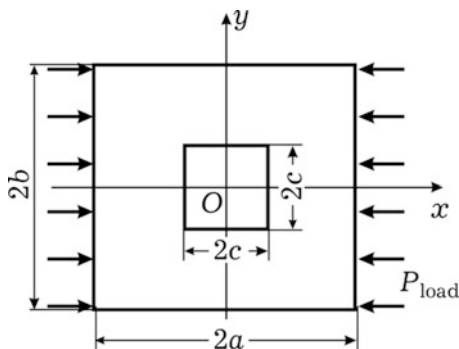
2 Problem Formulation

Consider a symmetrically laminated plate subjected to uniaxial uniform (see Fig. 1) or non-uniform (see Figs. 3 and 5) varying in plane loading. In general case plate can have an arbitrary planform. It is supposed that symmetrically laminated plate is equivalent to an anisotropic plate with mechanical characteristics calculated by a special way. We will assume that the subcritical stress state is heterogeneous and described by the relations of linear elasticity theory. All external loads are proportional to a parameter λ . Within the framework of the refined first-order layered plate theory, based on the straight line hypothesis, the complete system of motion equations in displacements has the following form [6].

$$\begin{aligned} L_{11}u + L_{12}v &= 0, \\ L_{21}u + L_{22}v &= 0; \end{aligned} \tag{1}$$

$$\begin{aligned} L_{33}w + L_{34}\psi_x + L_{35}\psi_y &= m_1w_{,tt} - \lambda \left(N_{11}^0 \frac{\partial^2 w}{\partial x^2} + N_{22}^0 \frac{\partial^2 w}{\partial y^2} + 2N_{12}^0 \frac{\partial^2 w}{\partial x \partial y} \right) \\ L_{43}w + (L_{44} - C_{55})\psi_x + (L_{45} - C_{54})\psi_y &= m_2\psi_{x,tt}, \\ L_{53}w + (L_{54} - C_{45})\psi_x + (L_{55} - C_{44})\psi_y &= m_2\psi_{y,tt}. \end{aligned} \tag{2}$$

Fig. 1 Plan form of the plate



The unknown functions u, v, w coincide with the displacements of the points of the middle surface in the directions of the axes, Ox, Oy, Oz respectively, and the functions ψ_x, ψ_y determine the angles of rotation of the normal to the middle surface relatively to the axes Oy and Ox . Linear operators L_{ij} ($i, j = \overline{1, 5}$) are presented in [6].

The coefficients C_{ij}, D_{ij} ($ij = 11, 22, 12, 16, 26, 66$) which are included in linear operators L_{ij} ($i, j = \overline{1, 5}$) and m_1, m_2 are defined as

$$(C_{ij}, D_{ij}) = \sum_{s=1}^N \int_{h_s}^{h_{s+1}} B_{ij}^s(1, z^2) dz, \quad m_{1,2} = \sum_{s=1}^n \int_{h_s}^{h_{s+1}} \rho_0^{(s)}(1, z^2) dz, \quad (3)$$

where $\rho_0^{(s)}$ is the material density of the s -th layer. These coefficients are matrix elements $C = [C_{ij}]$, $D = [D_{ij}]$:

$$C = \begin{pmatrix} C_{11} & C_{12} & C_{16} \\ C_{21} & C_{22} & C_{26} \\ C_{16} & C_{26} & C_{66} \end{pmatrix} \quad D = \begin{pmatrix} D_{11} & D_{12} & D_{16} \\ D_{21} & D_{22} & D_{26} \\ D_{16} & D_{26} & D_{66} \end{pmatrix} \quad (4)$$

The systems of Eqs. (1)–(2) are supplemented by the corresponding boundary conditions, which depend on the way of edge fixing of the plate and its loading way. In Eq. (2), the forces $N_{11}^0, N_{22}^0, N_{12}^0$ correspond to the value of the parameter $\lambda = 1$, and in general case may be determined by the solution of system (1), supplemented by the corresponding inhomogeneous boundary conditions.

3 Method of Solution

By the assumption of heterogeneity of the subcritical state the proposed method is reduced to the sequential solution of two boundary value problems: (a) the problem of elasticity theory (1), in order to determine the subcritical state of the plate and calculate the values $N_{11}^0(x, y)$, $N_{22}^0(x, y)$, $N_{12}^0(x, y)$; (b) eigenvalue problem (2), in order to find the critical load and frequencies. Each of these problems is solved by the Ritz’s variational method and application of the R-function theory.

The variational formulation of the boundary value problem (1), is minimized to the following functional:

$$I(u, v) = \frac{1}{2} \iint_{\Omega} (N_{11}\varepsilon_{11} + N_{22}\varepsilon_{22} + N_{12}\varepsilon_{12}) d\Omega + \int_{\partial\Omega_1} P_{nagr} (u_1 \cos \alpha + v_1 \sin \alpha) ds, \tag{5}$$

where α is the angle between the outer normal to the boundary of the region and the axis Ox , P_{nagr} is function depending on loading way of the plate border. Forces $\{N\} = \{N_{11}, N_{22}, N_{12}\}$ in the case of symmetrical arrangement of the layers are defined as

$$\{N\} = [C] \{\varepsilon\}, \tag{6}$$

The deformations $\{\varepsilon\}^L = \{\varepsilon_{11}^L, \varepsilon_{22}^L, \varepsilon_{12}^L\}$ are determined by relations

$$\varepsilon_{11}^L = \frac{\partial u}{\partial x}, \quad \varepsilon_{22}^L = \frac{\partial v}{\partial x}, \quad \varepsilon_{12}^L = \frac{\partial v}{\partial x} + \frac{\partial u}{\partial y}, \tag{7}$$

In this paper, the critical load is determined by dynamic approach, that is, as a result of solving a sequence of eigenvalues problems provided P_0 is varied in the functional:

$$J = \frac{1}{2} \iint_{\Omega} [M_{11}\chi_{11} + M_{22}\chi_{22} + M_{12}\chi_{12} + (Q_1 \left(\frac{\partial w}{\partial x} + \psi_x\right) + Q_2 \left(\frac{\partial w}{\partial y} + \psi_y\right)) + P_0 \left(N_{11}^0 \left(\frac{\partial w}{\partial x}\right)^2 + N_{22}^0 \left(\frac{\partial w}{\partial y}\right)^2 + N_{12}^0 \frac{\partial w}{\partial x} \frac{\partial w}{\partial y}\right) - \Lambda^2 (m_1 w^2 + m_2 (\psi_x^2 + \psi_y^2))] dx dy. \tag{8}$$

The deformations $\{\chi\} = \{\chi_{11}, \chi_{22}, \chi_{12}\}$ in (8) are calculated as follows [7]:

$$\chi_{11} = \frac{\partial \psi_x}{\partial x}, \quad \chi_{22} = \frac{\partial \psi_y}{\partial y}, \quad \chi_{12} = \frac{\partial \psi_x}{\partial y} + \frac{\partial \psi_y}{\partial x}, \tag{9}$$

and moments $\{M\} = \{M_{11}, M_{22}, M_{12}\}$ are $\{M\} = [D]\{\chi\}$.

The transverse shear force resultants in (8) are defined as:

$$\begin{Bmatrix} Q_1 \\ Q_2 \end{Bmatrix} = \begin{bmatrix} C_{55} & C_{45} \\ C_{45} & C_{44} \end{bmatrix} \begin{Bmatrix} \varepsilon_{13} \\ \varepsilon_{23} \end{Bmatrix}, \tag{10}$$

where $\varepsilon_{13} = \left(\frac{\partial w}{\partial x} + \psi_x\right)$, $\varepsilon_{23} = \left(\frac{\partial w}{\partial y} + \psi_y\right)$, $C_{ij} = K^2 \sum_{s=1}^N \int_{h_s}^{h_{s+1}} B_{ij}^s dz$, $i, j = 4, 5$.

The shear correction factor is assumed to be equal 5/6 in this work. Changing the value of the parameter P_0 , we get a set of natural frequencies corresponding to different compression loads. The value of the parameter P_0 corresponding to the smallest value of the natural frequency will be critical parameter.

4 Numerical Results

There are existed many situations when subcritical state of a plate may be inhomogeneous: a plate has cut-out or complex form; external load acting along boundary is non-uniform and in other cases also. The proposed method allows to solve a wide class of similar problems, including plates with cut-outs. Below we present some results obtained by the proposed method.

4.1 Problem 1

Let us consider the laminated plate $(0^\circ/90^\circ)_s$ shown in Fig. 1. We assume that the thicknesses of the layers are the same. The plate is uniformly loaded along the edges parallel to the Oy axis.

Mechanical properties and geometric parameters are taken from paper [8]: $E_{11} = 141.0$ Gpa, $E_{22} = 9.23$ Gpa, $G_{12} = G_{13} = 5.95$ Gpa, $G_{23} = 2.96$ Gpa, $\nu_1 = 0.313$, $a = b = 0.5$ m, $h = 0.005$ m. Suppose that plate is simply supported on external border and free on cut-out. Comparison of the dimensionless parameter of the critical load $N_{cr} = \frac{N_x b^2}{E_2 h^3}$ with the results of work [8] is presented in Fig. 2.

The deviation of the results does not exceed 3%. From this it follows reliability of the proposed approach and the created software. Note that authors of paper [8] do not take into account the heterogeneous subcritical state of the plate, and the problem is solved by the finite element method.

The values of the natural frequencies for rectangular plate ($a / b = 2$) with cut-outs are presented in Table 1 for different values of the ratio p_0/p_{kr} .

As the cut-out increases, the frequencies increase, and when the load increases, frequencies decrease, which corresponds to the physical sense.

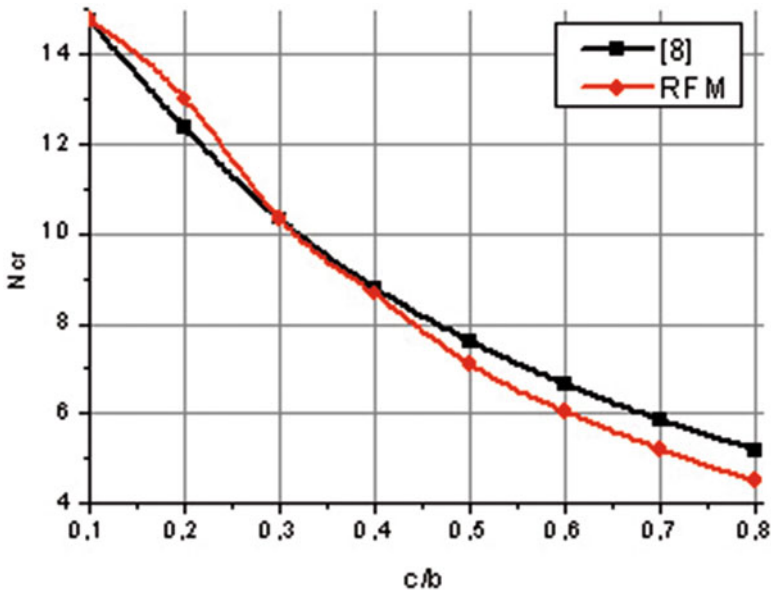


Fig. 2 Effect of the size cut-out on the critical load

Table 1 Effect of cut-out size and ratio p_0/p_{kr} on natural frequencies
 $\Lambda = \Omega_L a^2 \sqrt{\rho/E_2 h^2}$

p_0/p_{kr}	c/b			
	0.1	0.2	0.25	0.4
0	19.290	22.533	23.825	31.874
0.25	16.886	19.602	20.842	28.546
0.75	9.923	11.453	12.556	19.504

4.2 Problem 2

Consider symmetrically laminated ($0^\circ/90^\circ/0^\circ$) rectangular plate under parabolic edge compressions (Fig. 3). Parabolic load is defined by formula $P = P_0(1 - y^2/b^2)$

Material properties and plate dimensions are taken from paper [3]:

$$E_1 = 127.3 \text{ GPa}; E_2 = 11 \text{ GPa}; G_{12} = 5.5 \text{ GPa}; \nu_{12} = 0.34;$$

A comparison of the buckling coefficient $k = \frac{4\sigma_{cr} h b^2}{\sqrt{D_1 D_2}}$ for different value of the ratio a/b with results obtained in paper [3] is shown in Fig. 4. Obvious one can be seen from the graph, the best match of the results occurs when the aspect ratio varies from 0.75 to 2.25.

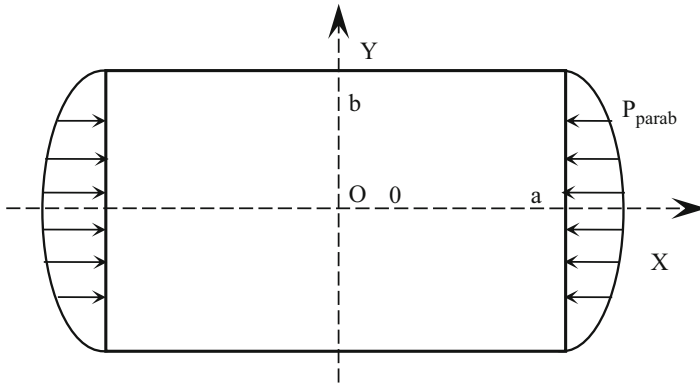


Fig. 3 Plate under parabolic load

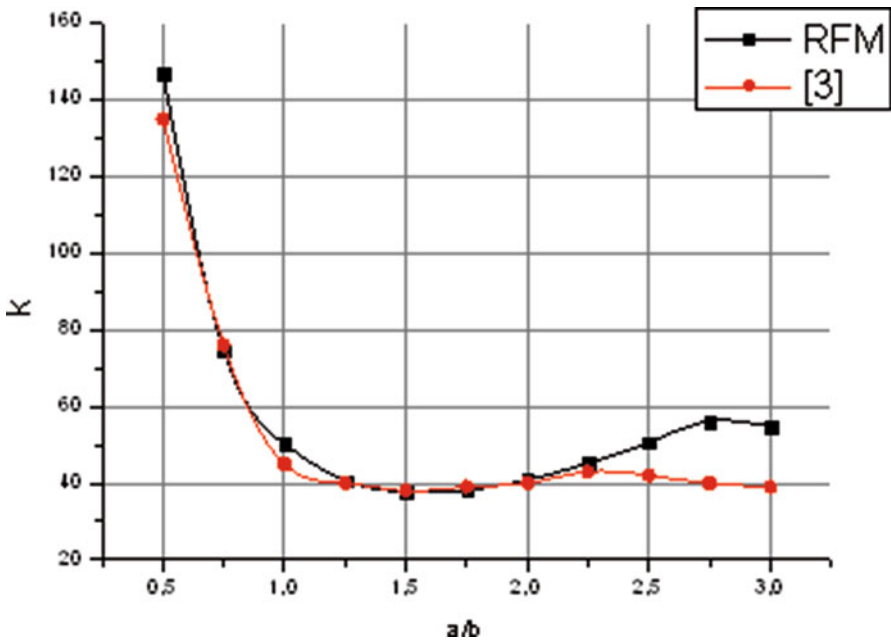


Fig. 4 Effect of ratio a/b on coefficient k

4.3 Problem 3

Consider laminated clamped plate ($0^\circ/90^\circ/0^\circ$) with shape shown in Fig. 5. Mechanical characteristics of layers are: $G/E_2 = 0.5$; $\nu_1 = 0.25$. And the relations of Young's modulus E_1/E_2 are changed as follows: $E_1/E_2 = 3; 10; 20; 30; 40$.

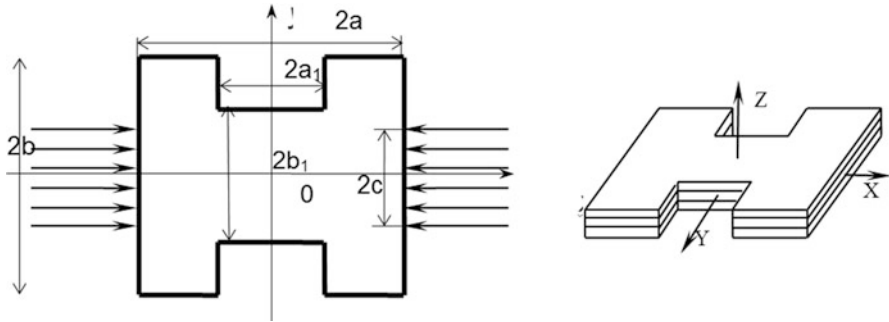


Fig. 5 Plate loaded on part of the border

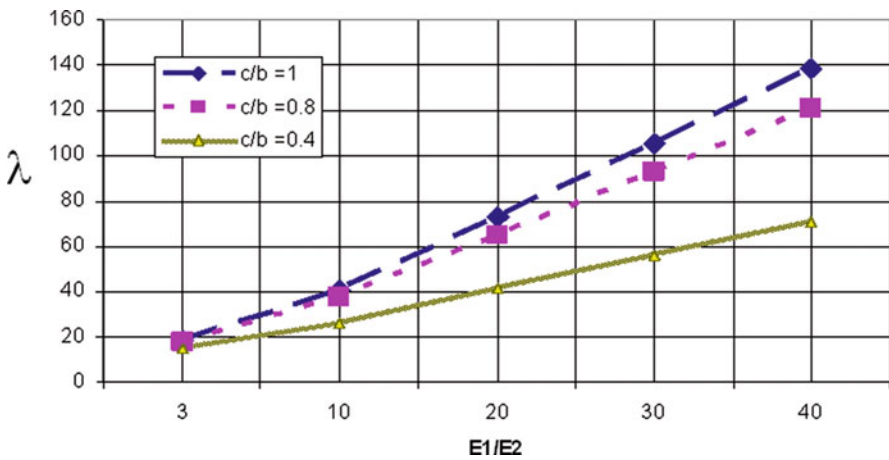


Fig. 6 Effect of the ratio modulus E_1/E_2 and loading area on dimensionless parameter of the critical load

Suppose that plate is loaded only on part of the border (Fig. 5). Geometric parameters are:

$$\frac{a}{b} = 1, \quad \frac{h}{2b} = 0,01, \quad \frac{a_1}{2b} = 0,3, \quad \frac{b_1}{2b} = 0,4.$$

Using the R-functions theory, we have constructed system of basic functions needed for minimizations of the corresponding functionals. The obtained results for dimensionless critical parameter $\lambda = \frac{4N_{cr}b^2}{E_2h^3}$ of the plate are presented in Fig. 6.

The qualitative effect of the ratio E_1/E_2 on critical parameter for the plates loaded along some part of the sides is the same as for the rectangular plate. In addition, it should be noted that critical parameter increases if the degree of orthotropic increases.

5 Conclusions

In the paper vibration and stability problems are studied for laminated composite plates under non-uniform edge compressions. The first-order theory of the symmetrically laminated plates is adopted to describe the mathematical formulation of the problem. The proposed approach is based on applications of the R-functions theory and variational Ritz's method. It takes into account inhomogeneous subcritical state and allows to consider the plates with different planform. The developed software is applied to investigation of the plates compressed in plane by uniform and non-uniform loading, that complex planform and cut-out.

References

1. Suleiman, O.M.E.: Bibliography and literature review on buckling of laminated plates. *Int. J. Sci. Eng.* **2**(8), 104–112 (2016)
2. Sayyad, A.S., Ghugal, Y.M.: Bending, buckling and free vibration of laminated composite and sandwich beams: A critical review of literature. *Compos. Struct.* **171**, 486–504 (2017)
3. Tang, Y., Wang, X.: Buckling of symmetrically laminated rectangular plates under parabolic edge compression. *Int. J. Mech. Sci.* **53**, 91–97 (2011)
4. Srivatsa, K.S., Krishna Murty, A.V.: Stability of laminated composite plates with cut-outs. *Comput. Struct.* **43**(2), 273–279 (1992)
5. Rvachev, V.L.: *The R-Functions Theory and Its Some Application*. Naukova Dumka, Kiev (1982). (in Russian)
6. Kurpa, L., Mazur, O., Tkachenko, V.: Dynamical stability and parametrical vibrations of the laminated plates with complex shape. *Lat. Am. J. Solids Struct.* **10**(1), 175–188 (2013). Rio de Janeiro
7. Reddy, J.N.: *Mechanics of Laminated Composite Plates and Shells: Theory and Analysis*. CRC Press, Boca Raton (2004). 856 p
8. Dash, S., Asha, A.V., Sahu, S.K.: Stability of laminated composite curved panels with cutout using finite element method. In: *Proceedings of the International Conference on Theoretical, Applied Computational and Experimental Mechanics (ICTACEM 2004)*, 28–31 December 2004 IIT, Kharagpur

Dynamical Systems and Stability in Fractional Solid Mechanics



Péter B. Béda 

Abstract The use of fractional calculus gets more and more importance in material modeling. It can take into account non-localities in both space and time domains. Quite simply, for example, by changing (local) conventional derivative to one of the non-local fractional derivatives, the effect of the time history (or of the values in a neighborhood) can “automatically” be taken into consideration. The reason is that such fractional derivative is a combination of a derivation and an integral operator. In stability analysis such models may cause problems starting from stability definitions to the complicated forms of characteristic equations. The selection of the fractional derivative (Caputo, Riemann-Liouville, Caputo-Fabrizio, Atangana-Baleanu etc.) has an important effect on that. The paper studies how the type of fractional derivatives effects the problems of stability investigation. From engineering point of view, the study aims constitutive modeling via instability phenomena. By observing the stability/instability behavior of some material we can be informed about the form of fractional derivative in its mathematical model.

Keywords Fractional calculus · Bifurcation · Dynamical system

1 Introduction

There are several ways to include non-locality into continuum mechanics. As a starting point two basic ways are presented for that. The first one could lead directly to the introduction of fractional derivatives, while it uses an integral in a general form and a more or less obvious consequence could be an expression of Caputo’s fractional derivative. The second approach adds gradient term to the constitutive equations. A third problem seems to be some different problem, the model of visco-elastic (-plastic) behavior. However, we will see that it can also

P. B. Béda (✉)

Budapest University of Technology and Economics, Budapest, Hungary
e-mail: bedap@kme.bme.hu

© Springer Nature Switzerland AG 2021

J. Awrejcewicz (ed.), *Perspectives in Dynamical Systems III: Control and Stability*,
Springer Proceedings in Mathematics & Statistics 364,
https://doi.org/10.1007/978-3-030-77314-4_22

269

be treated as a non-locality in time. This study concentrates on material instability problems for non-local cases, when fractional derivatives are used to model non-locality in constitutive equations. For reader's convenience a brief overview of elementary fractional calculus is included to show the basics. Fractional integral and differentials, the most important functions are presented there. In the following section non-local materials are treated with various types of fractional derivatives in bifurcation problems. Solid body is modeled by its basic equations. Then a dynamical system is defined and stability and bifurcation investigation could be performed as in the theory of dynamical systems.

2 Non-locality in Space and Time

Various concepts of non-localities are used. Most of them may lead to a more or less obvious generalization by using fractional derivatives as the non-local extension of derivation. This section serves as a kind of historical background.

2.1 Eringen's Approach to Non-locality

As a first impression, non-locality is related to some spatial neighbourhood of a point or a particle in mechanics. In such sense local stress is determined by the strain in a neighbourhood [1]. Then integration is used to encounter that

$$\sigma_{ij}(\mathbf{r}, t) = C_{ijkl} \varepsilon_{kl}(\mathbf{r}, t) + \int c_{ijkl}(\mathbf{r} - \mathbf{r}') \varepsilon_{kl}(\mathbf{r}', t) d\mathbf{r}', \quad (1)$$

by using the displacement field

$$\sigma = C \frac{\partial u(x)}{\partial x} + \int c(x - \xi) \frac{\partial u(\xi)}{\partial \xi} d\xi \quad (2)$$

is obtained. By specifying kernel $c(x - \xi)$ of the second term of (2) as in [2]

$$c(x - \xi) := \frac{(x - \xi)^{-\alpha}}{\Gamma(1 - \alpha)} \quad (3)$$

one has

$$\sigma = C \frac{\partial u(x)}{\partial x} + \int \frac{(x - \xi)^{-\alpha}}{\Gamma(1 - \alpha)} \frac{\partial u(\xi)}{\partial \xi} d\xi. \quad (4)$$

In (4) the second term on the right hand side is the so-called Caputo fractional derivative.

2.2 Gradient Materials

As it was done by Aifantis [3], let us introduce gradient term(s) into constitutive equations

$$\sigma_{ij} = C_{ijkl}\varepsilon_{kl} - l^2 C_{ijkl} \Delta \varepsilon_{kl}. \tag{5}$$

There are several explanations of the origin and use of formula (5). Sometimes it is called gradient regularization, because with (5) material instability studies avoid mesh-sensibility in numerical analysis.

However, there are lots of other, more physical interpretation including internal lengths, micro-structural effect theories. Early studies from the sixties of the last century use the notion of polar bodies [4] and couple stress effect and then gradient of deformation gradient appears, which can be interpreted as a constitutive equation containing first order strain gradient. The appearance of higher gradients can be explained as the property of multipolar materials: [5, 6].

At the end of this subsection one should remark that there are still a lot of controversies in the thermodynamics of gradient materials [7, 8].

2.3 Visco-Elastic Materials

Relaxation can be included into constitutive equations as Rabotnov treats them. In [9] relaxation of elastic materials is added by Volterra integral

$$\varepsilon(t) = \frac{1}{E} \left(\sigma(t) + \chi \int_0^t G(t - \tau) \sigma(\tau) d\tau \right), \tag{6}$$

where Volterra operator

$$K^*u = \int_{-\infty}^t K(t - \tau) u(\tau) d\tau \tag{7}$$

is a convolution integral with kernel K .

By searching for the solution of

$$K^*u = v \tag{8}$$

and assume, similarly to (3), that Abel operator I_α is used

$$K = I_\alpha \equiv \frac{t^\alpha}{\Gamma(1 + \alpha)}, \tag{9}$$

equation (8) is solved to

$$u = \frac{d}{dt} I_{-\alpha-1}^* v. \quad (10)$$

Here

$$\frac{d}{dt} I_{-\alpha-1}^* v \equiv \frac{1}{\Gamma(-\alpha)} \frac{d}{dt} \int_{-\infty}^t (t-\tau)^{-\alpha-1} u(\tau) d\tau \quad (11)$$

is called the Liouville fractional derivative. In the following section a short summary is presented of the basics of fractional calculus.

3 Elements of Fractional Calculus

Fractional order (say α th) generalization of an integral is a key element. When such operator is combined with an “ordinary”, first order, derivation the result is an $(1-\alpha)$ th order fractional derivative. In this section that way is followed to construct fractional derivatives. The most important functions used here are also briefly mentioned.

3.1 Two Important Functions

First Euler’s gamma function should be mentioned, being an integral of the two most important functions of analysis, power function and exponential functions:

$$\Gamma(\alpha) = \int_0^{\infty} \xi^{\alpha-1} e^{-\xi} d\xi \quad (12)$$

It can also be interpreted as a generalization of factorial to non-integers, because

$$\Gamma(n) = (n-1)!. \quad (13)$$

Mittag-Leffler function

$$E_{\alpha,\beta}(z) = \sum_{j=0}^{\infty} \frac{z^j}{\Gamma(j\alpha + \beta)} \quad (14)$$

can be considered as a generalized exponential function, because

$$E_{1,1} = \sum_{j=0}^{\infty} \frac{z^j}{\Gamma(j+1)} = \sum_{j=0}^{\infty} \frac{z^j}{j!} = \exp(z). \tag{15}$$

This function gets importance as eigenfunctions of fractional derivatives.

3.2 Integral Operators and Classical Fractional Derivatives

Construction of fractional derivatives starts with Cauchy’s original integral formula

$${}_a I_x^1 f(x) = \int_a^x f(\xi) d\xi. \tag{16}$$

For repeated integration its n th (integer) order generalization

$${}_a I_x^n f(x) = \frac{1}{(n-1)!} \int_a^x f(\xi) (x-\xi)^{n-1} d\xi \tag{17}$$

can be applied.

By using α th fractional order generalization, Riemann-Liouville integral operator can be defined

$${}_a I_x^\alpha f(x) = \frac{1}{\Gamma(\alpha)} \int_a^x f(\xi) (x-\xi)^{\alpha-1} d\xi. \tag{18}$$

In (18) integration goes from left to right, ($a < x$), it is called the left integral operator. By taking derivative of left Riemann-Liouville integral operator

$$\frac{d}{dx} {}_a I_x^\alpha f(x) = {}_a D_x^\alpha f(x) = \frac{1}{\Gamma(1-\alpha)} \frac{d}{dx} \int_a^x f(\xi) (x-\xi)^{-\alpha} d\xi \tag{19}$$

is a non-local derivative for interval $[a, x]$. Then right Riemann-Liouville derivative can also be defined as

$${}_x D_b^\alpha f(x) = -\frac{1}{\Gamma(1-\alpha)} \frac{d}{dx} \int_x^b f(\xi) (\xi-x)^{-\alpha} d\xi \tag{20}$$

for interval $[x, b]$.

By changing operators of derivation and integration in (19), Caputo’s derivative is defined

$${}_a I_x^\alpha \left(\frac{d}{d\xi} f \right) (x) = {}_a^C D_x^\alpha f(x) = \frac{1}{\Gamma(1-\alpha)} \int_a^x \frac{df(\xi)}{d\xi} (x-\xi)^{-\alpha} d\xi \tag{21}$$

for interval $[a, x]$. Hence right Caputo derivative

$${}_x^C D_b^\alpha f(x) = -\frac{1}{\Gamma(1-\alpha)} \int_x^b \frac{df(\xi)}{d\xi} f(\xi) (\xi-x)^{-\alpha} d\xi \tag{22}$$

is defined for interval $[x, b]$.

In non-local mechanics of small deformations, the kinematic equation will use uniaxial non-local strain:

$$\varepsilon_\alpha = \frac{\partial^\alpha u}{\partial x^\alpha}, \tag{23}$$

where $\frac{\partial^\alpha u}{\partial x^\alpha}$ should be some symmetric, non-local derivative. For example such derivative can be constructed from left and right Riemann-Liouville

$$\frac{\partial^\alpha u}{\partial x^\alpha} = \frac{1}{2} ({}_a D_x^\alpha u(x) - {}_x D_b^\alpha u(x)) \tag{24}$$

or Caputo derivatives

$$\frac{\partial^\alpha u}{\partial x^\alpha} = \frac{1}{2} ({}_a^C D_x^\alpha u(x) - {}_x^C D_b^\alpha u(x)) \tag{25}$$

or similarly from other types of left and right fractional derivatives.

In the last part of this subsection connection of symmetric Caputo derivative and Riesz derivative [10] is presented. Let us start from an equivalent forms of the left and right Caputo derivatives

$${}_a^C D_x^\alpha f(x) = \frac{1}{\Gamma(1-\alpha)} \frac{d}{dx} \int_a^x (f(\xi) - f(a)) (x-\xi)^{-\alpha} d\xi, \tag{26}$$

$${}_x^C D_b^\alpha f(x) = -\frac{1}{\Gamma(1-\alpha)} \frac{d}{dx} \int_x^b (f(\xi) - f(b)) (\xi-x)^{-\alpha} d\xi. \tag{27}$$

Then take “asymptotic case” ($a \rightarrow \infty, b \rightarrow \infty$) and combine them into a symmetric form

$${}_C D_+^\alpha f(x) - {}_C D_-^\alpha f(x) = \frac{1}{\Gamma(1-\alpha)} \frac{d}{dx} \int_{-\infty}^\infty f(\xi) |x-\xi|^{-\alpha} d\xi. \tag{28}$$

Derivative (28) is called the Riesz fractional derivative, \mathbf{D}^α .

3.3 Generalized Fractional Derivatives

Fractional derivatives are convolutions of two functions. In case of Caputo’s derivative

$$\frac{df(x)}{dx} * \frac{1}{x^\alpha} = \int_a^x \frac{df(\xi)}{d\xi} (x - \xi)^{-\alpha} d\xi \tag{29}$$

In (29) the second function is a power function and it is singular at zero. Caputo and Fabrizio suggest to use exponential function instead to construct an operator with a non-singular kernel

$${}^C D^\alpha f = \frac{M(\alpha)}{(1 - \alpha)} \int_a^t \frac{df(\xi)}{d\xi} \exp\left(-\frac{\alpha(t - \xi)}{1 - \alpha}\right) d\xi \tag{30}$$

where $M(0) = M(1) = 1$, defining a new fractional derivative [11].

A further generalization is done by Atangana and Baleanu [12] by changing exponential function to its version in fractional calculus, the Mittag-Leffler function

$${}^{AB} D^\alpha f = \frac{B(\alpha)}{1 - \alpha} \int_a^t \frac{df(\xi)}{d\xi} E_{\alpha,1}\left(-\frac{\alpha}{1 - \alpha}(t - \xi)^\alpha\right) d\xi. \tag{31}$$

4 Fractional Derivatives in Non-local Mechanics

In this section fractional calculus is applied to study stability and bifurcation problems in material instability investigations for non-local materials. First the set of basic equation is formed for a simple case and by using dynamical systems theory stability and bifurcation conditions are formed. The aim is to select constitutive equations, which lead to a generic bifurcation. In that cases at the loss of stability a non-trivial critical eigenspace can be found. Its basis vectors (functions) can be used to study post-bifurcation by projecting the equation on them. Thus the existence of such non-trivial critical eigenspace is essential in non-linear stability analysis.

In Sects. 4.1 and 4.2, a brief summary is presented for stability and bifurcation analysis via dynamical systems theory (details in [13]). Then the two basic non-locality concepts are studied by using the method described in Sects. 4.1 and 4.2 while constitutive equations and types of fractional derivatives are varied. Materials in Sect. 4.3 are referred as weakly non-local, while in Sect. 4.4 as strong non-locality. The investigation in both cases uses the whole set of basic equations of continua (see Sect. 4.1).

4.1 Dynamical Systems Approach

The classical description of continuum mechanics consists of the set of basic equations of continua:

- Cauchy's equations of motion
- kinematic equation
- constitutive equation.

In the simplest possible case (uniaxial problem with small deformations) such equations are

$$\rho \dot{v} = \sigma \nabla, \quad (32)$$

$$\dot{\varepsilon} = \frac{1}{2} (v \nabla + \nabla v), \quad (33)$$

$$F(\varepsilon, \sigma, \dot{\varepsilon}, \dot{\sigma}, \dots) = 0. \quad (34)$$

From the basic equations (32), (33), (34) a dynamical system can be defined

$$\frac{d}{dt} \begin{bmatrix} v \\ \varepsilon \\ \sigma \end{bmatrix} = \mathbf{F}(v, \varepsilon, \sigma), \quad (35)$$

where

$$\mathbf{F}(v, \varepsilon, \sigma) = \begin{bmatrix} \frac{1}{\rho} \sigma \nabla \\ \frac{1}{2} (v \nabla + \nabla v) \\ - \left(\frac{\partial F}{\partial \sigma} \right)^{-1} \left(\left(\frac{\partial F}{\partial \varepsilon} \right) \varepsilon + \left(\frac{\partial F}{\partial \sigma} \right) \sigma + \left(\frac{\partial F}{\partial \dot{\varepsilon}} \right) \frac{1}{2} (v \nabla + \nabla v) \right) \end{bmatrix}. \quad (36)$$

4.2 Stability and Bifurcation for Conventional Derivatives

Assume that $\mathbf{y}_0 = (v_0, \varepsilon_0, \sigma_0)$ is an equilibrium of (35). Then by introducing homogeneous perturbations

$$v = v_0 + \tilde{v}, \varepsilon = \varepsilon_0 + \tilde{\varepsilon}, \sigma = \sigma_0 + \tilde{\sigma} \quad (37)$$

the linearization of (35) and (36) is satisfied for the perturbations. As it is presented in [13], the eigenvalues and eigenvectors of linearized operator

$$\left(\frac{d}{dy} \mathbf{F} \right) \Big|_{\mathbf{y}=\mathbf{y}_0} \quad (38)$$

play the key role in stability and bifurcation analysis. For this reason the characteristic equation of (38) should be solved and stability conditions are formed for its solutions λ_i in a usual way.

State \mathbf{y}_0 of the material is stable, if $Re\lambda_i < 0$ for all solutions. Loss-of-stability happens, when at least for one i , $Re\lambda_i = 0$. Then two ways of instabilities can be distinguished, the static ($\lambda = 0$) and the dynamic ($Re\lambda = 0, Im\lambda \neq 0$) bifurcations. Non-linear analysis can be performed, if operator (38) has non-trivial critical eigenspace. Such case is referred as generic bifurcation and non-linearity should be projected to this eigenspace resulting bifurcation equations [14].

To show briefly how it works, let the constitutive equation be of a second gradient dependent material

$$\dot{\sigma} = c_1 \dot{\varepsilon} + c_2 \ddot{\varepsilon} - c_3 \frac{\partial^2 \dot{\varepsilon}}{\partial x^2}. \tag{39}$$

Its characteristic equation is

$$\lambda^2 y_1 - \lambda c_2 \frac{\partial^2}{\partial x^2} y_1 - \left(c_1 \frac{\partial^2}{\partial x^2} - c_3 \frac{\partial^4}{\partial x^4} \right) y_1 = 0. \tag{40}$$

The condition for static bifurcation is

$$\left(c_1 \frac{\partial^2}{\partial x^2} - c_3 \frac{\partial^4}{\partial x^4} \right) y_1 = 0. \tag{41}$$

For $c_1 = c_{1crit} < 0$ there exist critical eigenfunctions

$$y_{1crit} = \exp \left(ix \sqrt{-\frac{c_{1crit}}{c_3}} \right), \tag{42}$$

which can be used for projection in non-linear studies to derive bifurcation equations (see details in [13, 14]).

4.3 Non-local Strain

First, static bifurcation is studied at non-local strain as in [15]. A linear constitutive equation in form

$$\sigma = B\varepsilon_\alpha + D\dot{\varepsilon}_\alpha \tag{43}$$

is used, where non-local strain is

$$\varepsilon_\alpha = \frac{\partial^\alpha u}{\partial x^\alpha}. \tag{44}$$

At non-local strain the characteristic equation of (38) has the form

$$\rho\lambda^2 y_1(x) - D \frac{\partial}{\partial x} \lambda y_1(x) + B \frac{\partial}{\partial x} \frac{\partial^\alpha}{\partial x^\alpha} y_1(x) = 0 \quad (45)$$

and then static bifurcation condition reads

$$B \frac{\partial}{\partial x} \frac{\partial^\alpha}{\partial x^\alpha} y_1(x) = 0. \quad (46)$$

Second Gradient Dependent Materials In case of some generalized second gradient dependent material, the constitutive equation reads

$$\dot{\sigma} = B \dot{\varepsilon}_\alpha + C \frac{\partial^2}{\partial x^2} \dot{\varepsilon}_\alpha. \quad (47)$$

Having been transformed the basic equations to the velocity field

$$\rho \ddot{v} = B \frac{\partial^\alpha}{\partial x^\alpha} \frac{\partial}{\partial x} v + C \frac{\partial^\alpha}{\partial x^\alpha} \frac{\partial^3}{\partial x^3} v \quad (48)$$

is obtained.

Similarly to Sect. 4.2, for such constitutive equation a critical perturbation can be identified. The static bifurcation condition for periodic perturbations

$$y_1(x) = \exp(i\omega x) \quad (49)$$

is

$$\frac{\partial^\alpha}{\partial x^\alpha} \frac{\partial}{\partial x} \left((B - \omega^2 C) y_1(x) \right) = 0. \quad (50)$$

Equation (50) implies

$$B_{crit} = \omega^2 C. \quad (51)$$

Then critical perturbation frequency is

$$\omega = \sqrt{\frac{B_{crit}}{C}}, \quad (52)$$

and the non-trivial eigenfunction is

$$y_1(x) = \exp\left(i\sqrt{\frac{B_{crit}}{C}}x\right). \quad (53)$$

From (51), (52) and (53) we find no dependence on the type of fractional derivative.

Static and Dynamic Bifurcations Let the constitutive equation be the so-called Malvern-Cristescu equation

$$\sigma + D\dot{\sigma} = E\varepsilon_\alpha + H\dot{\varepsilon}_\alpha \tag{54}$$

Now the characteristic equation of the appropriate form of (38) is

$$- D\rho\lambda^3 y_1(x) - \rho\lambda^2 y_1(x) + H \frac{\partial}{\partial x} \frac{\partial^\alpha}{\partial x^\alpha} \lambda y_1(x) + E \frac{\partial}{\partial x} \frac{\partial^\alpha}{\partial x^\alpha} y_1(x) = 0. \tag{55}$$

Static bifurcation condition to (55) reads

$$E \frac{\partial}{\partial x} \frac{\partial^\alpha}{\partial x^\alpha} y_1(x) = 0, \tag{56}$$

while dynamic bifurcation condition requires the existence of a non-trivial solution of

$$\begin{aligned} & \left(\frac{E^2}{D^2 \rho^2} + \frac{H^2 \beta^2}{D^2 \rho^2} \right) \frac{\partial^{2\alpha+2}}{\partial x^{2\alpha+2}} y_1 + \left(\frac{2 E \beta^2}{D^2 \rho} \right. \\ & \left. + \frac{2 H \beta^4}{D \rho} \right) \frac{\partial^{\alpha+1}}{\partial x^{\alpha+1}} y_1 + \left(\beta^6 + \frac{\beta^4}{D^2} \right) y_1 = 0. \end{aligned} \tag{57}$$

Static Bifurcation for Non-local Strain As it was presented earlier in this section, for simple non-local strain static bifurcation condition in most cases contains

$$\frac{\partial}{\partial x} \frac{\partial^\alpha}{\partial x^\alpha} y_1(x) = 0. \tag{58}$$

To get non-trivial solution of (58) we need such a solution, which is a non-zero function satisfying homogeneous boundary conditions. Assume that Riesz derivative is used in non-local strain

$$\varepsilon_\alpha = \mathbf{D}^\alpha. \tag{59}$$

After integration and by using Fourier transform (58) implies

$$- 2B\omega^\alpha \sin\left(\frac{\pi\alpha}{2}\right) \mathcal{F}y_1 = \sqrt{2\pi} \delta(\omega), \tag{60}$$

which is solved to

$$\mathcal{F}y_1 = - \frac{\sqrt{2\pi} \delta(\omega)}{2B\omega^\alpha \sin\left(\frac{\pi\alpha}{2}\right)}. \tag{61}$$

The Use of Atangana-Baleanu Derivative A symmetric derivative can also be based on left and right Atangana-Baleanu derivatives. For such operators left and right derivatives differ only in sign [16], thus

$$\frac{\partial^\alpha}{\partial x^\alpha} = \frac{1}{2} \left(\left({}^A B D^\alpha u \right) (x) - \left(- \left({}^A B D^\alpha u \right) (x) \right) \right) = \left({}^A B D^\alpha u \right) (x). \tag{62}$$

In this case, static bifurcation condition (58) leads to

$$\left({}^A B D^\alpha u \right) (x) = C, \quad u(0) = 0. \tag{63}$$

Its solution is known [17]

$$u(t) = \frac{1}{B(\alpha)} \left((1 - \alpha) + C \left(1 + \frac{1}{1 - \alpha} \frac{1}{\Gamma(\alpha)} t^\alpha \right) \right). \tag{64}$$

Riesz Derivative in Carpinteri’s Equation By using a symmetric generalized version of Eringen’s integral non-locality (4) the constitutive equation, following Carpinteri’s idea [2] reads

$$\sigma = C\varepsilon + B \frac{\partial^\alpha}{\partial x^\alpha} u(x). \tag{65}$$

With Riesz derivative in case of Carpinteri’s equation the static bifurcation condition is

$$\frac{\partial}{\partial x} \left(C \frac{\partial}{\partial x} + B \frac{\partial^\alpha}{\partial x^\alpha} \right) y_1 = 0. \tag{66}$$

By using Fourier transform we have

$$\left(C\omega - 2B\omega^\alpha \sin\left(\frac{\pi\alpha}{2}\right) \right) \mathcal{F}y_1 = \sqrt{2\pi} \delta(\omega) \tag{67}$$

and its solution reads

$$\mathcal{F}y_1 = \frac{\sqrt{2\pi} \delta(\omega)}{C\omega - 2B\omega^\alpha \sin\left(\frac{\pi\alpha}{2}\right)}. \tag{68}$$

4.4 Fractional Gradient Material

In Aifantis-Tarasov material model [18] the idea is to use fractional derivative at gradient material

$$\dot{\sigma} = B\dot{\varepsilon} + C \frac{\partial^\alpha}{\partial x^\alpha} \frac{\partial^\alpha}{\partial x^\alpha} \dot{\varepsilon} \tag{69}$$

or simply

$$\dot{\sigma} = B\dot{\epsilon} + C \frac{\partial^\beta}{\partial x^\beta} \dot{\epsilon}. \tag{70}$$

Here a gradient material is selected, that is, on-locality is already involved. That makes the use of local fractional derivatives possible. Recently, in such cases the use conformable derivative [19], gets more and more importance [20]. Conformable derivative is defined by

$$D_\alpha (f) (x) = \lim_{\epsilon \rightarrow 0} \frac{f (x + \epsilon x^{1-\alpha}) - f (x)}{\epsilon}. \tag{71}$$

It has several beneficial properties:

$$D_\alpha (f) (x) = x^{1-\alpha} \frac{df (x)}{dx} \text{ and } D_\alpha \left(e^{\frac{1}{\alpha} x^\alpha} \right) = e^{\frac{1}{\alpha} x^\alpha} \dots \tag{72}$$

which make calculations much simpler.

As an application of conformable derivative let the constitutive equation be in form

$$\dot{\sigma} = B\dot{\epsilon} + C D_\alpha^2 \dot{\epsilon}. \tag{73}$$

In this case the characteristic equation for the appropriate form of (38) reads

$$\lambda^2 y_1 - \frac{\partial^2}{\partial x^2} \left(B + C D_\alpha^2 \right) y_1 = 0. \tag{74}$$

For perturbations $\sin \left(\frac{1}{\alpha} x^\alpha \right)$ the static bifurcation condition is

$$B_{crit} = C. \tag{75}$$

The basic function of the non-trivial kernel is (see in Fig. 1.)

$$y_1 = \sin \left(\frac{1}{\alpha} x^\alpha \right), \tag{76}$$

where α can be calculated from homogeneous perturbations, (for example $L = 1$, $\alpha = 0.318$).

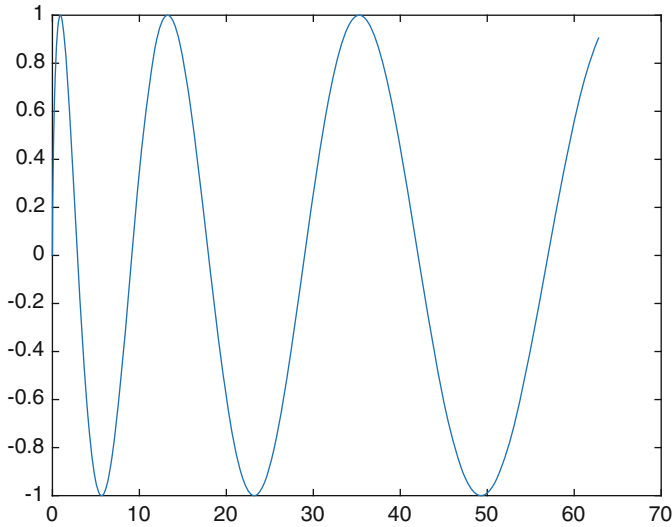


Fig. 1 Plot of $\sin\left(\frac{1}{\alpha}x^\alpha\right)$

5 Conclusions

The use of fractional calculus can be traced back to the origin of field theories of continuum mechanics, in visco-elasticity Liouville derivative appeared already in 1948. There are two ways to study non-locality in space. Strong non-locality concept includes an integral operator into the constitutive equation, which can easily and quite obviously be generalized to a fractional operator on displacement field. Weak non-locality adds gradient dependence. For such constitutive equations the type of fractional derivative has less effect on bifurcation conditions, than at strong non-locality. The presence of integral operator in fractional derivative adds more types of functions, because differentiability is not a condition for the field variables. Moreover the large variety of possible derivatives widens possibility of constitutive modeling.

References

1. Eringen, A.C.: *Nonlocal Continuum Field Theories*. Springer, New York (2002)
2. Carpinteri, A., Cornetti, P., Sapora, A.: A fractional calculus approach to nonlocal elasticity. *Eur. Phys. J. Spec. Top.* **193**, 193–204 (2011). <https://doi.org/10.1140/epjst/e2011-01391-5>
3. Aifantis, E.C.: On the role of gradients in the localization of deformation and fracture. *Int. J. Eng. Sci.* **30**, 1279–1299 (1992). [https://doi.org/10.1016/0020-7225\(92\)90141-3](https://doi.org/10.1016/0020-7225(92)90141-3)
4. Toupin, R.A.: Theories of elasticity with couple-stresses. *Arch. Rational Mech. Anal.* **17**, 85–112 (1964). <https://doi.org/10.1007/BF00253050>

5. Green, A.E., Rivlin, R.S.: Simple force and stress multipoles. *Arch. Rational Mech. Anal.* **16**, 325–353 (1964). https://doi.org/10.1007/978-1-4612-2416-7_113
6. Green, A.E., Rivlin, R.S.: Multipolar continuum mechanics. *Arch. Rational Mech. Anal.* **17**, 113–147 (1964). <https://doi.org/10.1007/BF00253051>
7. Maugin, G.A.: On the thermomechanics of continuous media with diffusion and/or weak nonlocality. *Arch. Appl. Mech.* **75**, 723–738 (2006). <https://doi.org/10.1007/s00419-006-0062-4>
8. Ván, P.: Weakly nonlocal irreversible thermodynamics - the Ginzburg -Landau equation. *Tech. Mech.* **22**, 104–110 (2002)
9. Rabotnov, Y.N.: Equilibrium of an elastic medium with after-effect. (in Russian) *Prikladnaya Matematika i Mekhanika (J. Appl. Math. Mech.)* **12**, 53–62 (1948)
10. Samko, S.G., Kilbas, A.A., Marichev, O.I.: *Fractional Integrals and Derivatives*. Gordon and Breach, Amsterdam (1993)
11. Caputo, M., Fabrizio, M.: A new definition of fractional derivative without singular kernel. *Prog. Fract. Differ. Appl.* **1**, 73–85 (2015). <https://doi.org/10.12785/pfda/010201>
12. Atangana, A., Baleanu, D.: New fractional derivatives with nonlocal and non-singular kernel: Theory and application to heat transfer model. *Thermal Science* **20**, 763–769 (2016). <https://doi.org/10.2298/TSCI160111018A>
13. Béda, P.B.: Dynamical systems, rate and gradient effects in material instability. *Int. J. Mech. Sci.* **42**, 2101–2114 (2000). <https://doi.org/10.1007/s00161-018-0633-y>
14. Béda, P.B.: Bifurcation and stability at finite and infinite degrees of freedom. In: Awrejcewicz, J. (ed.) *Dynamical Systems: Theoretical and Experimental Analysis*, pp. 1–13. Springer, Cham (2016). https://doi.org/10.1007/978-3-319-42408-8_1
15. Atanackovic, T.M., Stankovic, B.: Generalized wave equation in nonlocal elasticity. *Acta Mech.* **208**, 1–10 (2009). <https://doi.org/10.1007/s00707-008-0120-9>
16. Bahaa, G., Atangana, A.: Necessary and sufficient optimality conditions for fractional problems involving Atangana-Baleanu’s derivatives. In: Gomez, J.F., Torres, L., Escobar, R.F. (eds.) *Fractional Derivatives with Mittag-Leffler Kernel: Trends and Applications in Science and Engineering*, pp. 13–32. Springer, Cham (2019). https://doi.org/10.1007/978-3-030-11662-0_2
17. Al-Refai, M.: Fractional differential equations involving Caputo fractional derivative with Mittag-Leffler non-singular kernel: comparison principles and applications. Preprint (2017). <https://arxiv.org/abs/1710.03407>
18. Tarasov, V.E., Aifantis, E.C.: Non-standard extensions of gradient elasticity: Fractional non-locality, memory and fractality. *Commun. Nonlinear Sci. Numer. Simulat.* **22**, 197–227 (2015). <https://doi.org/10.1016/j.cnsns.2014.10.002>
19. Khalil, R., Horani, M.A., Yousef, A., Sababheh, M.: A new definition of fractional derivative. *J. Comput. Appl. Math.* **264**, 65–70 (2014). <https://doi.org/10.1016/j.cam.2014.01.002>
20. Rahimi, Z., Sumelka, W., Baleanu, D.: A mechanical model based on conformal strain energy and its application to bending and buckling of nanobeam structures. *ASME J. Comput. Nonlinear Dyn.* **14**, 061004 (2019). <https://doi.org/10.1115/1.4043085>

Stability of Coupled Systems of Stochastic Cohen-Grossberg Neural Networks with Time Delays, Impulses and Markovian Switching



Biljana Tojtovska  and Panche Ribarski 

Abstract This paper covers the topic of the p th moment ($p \geq 2$) stability of coupled systems of stochastic Cohen-Grossberg neural networks with time delays, impulses and Markovian switching. This model generalises many models in the literature and to the best of our knowledge has not been analysed before. The methods are based on results from graph theory, Lyapunov operator, Dini derivative and some known inequality techniques. Additionally, we consider the stability with respect to a general decay function which includes exponential, but also more general lower rate decay functions as the polynomial and the logarithmic ones. This fact gives us the opportunity to study general decay stability, even when the exponential one cannot be discussed. The presented theoretical results are supported by a numerical example.

Keywords Coupled stochastic neural networks · Time delays · Impulses · Markovian switching · Moment stability · General decay function

1 Introduction

Coupled networks consist of parts with individual dynamics which mutually interact based on some coupling structure. Examples of these complex networks can be seen both in nature and in engineering, among which maybe the most fascinating is the human brain [1]. Such networks can be studied with the methods from graph theory. This revolutionary approach was suggested by [2] and [3] in their work presented at the end of the last century. They have considered the systems as graphs, where each dynamical unit is represented by a node and the graph structure is defined by the interaction of the nodes. This powerful idea can be applied to different

B. Tojtovska (✉) · P. Ribarski
Faculty of Computer Science and Engineering, Ss. Cyril and Methodius University, Skopje,
North Macedonia
e-mail: biljana.tojtovska@finki.ukim.mk; pance.ribarski@finki.ukim.mk

models, which cover networks with time varying connections and directed weighted edges between the nodes. This includes also the models of networks where the nodes represent systems with nonlinear or stochastic dynamics. Thus, the theory of dynamical systems and stochastic differential equations are often a basic tool to study the properties of the networks.

One aspect of dynamical systems which received great attention since the ground breaking work of Lyapunov, is stability of the system and the stability of the synchronous state (complete synchronisation). Stability of the solution of a stochastic differential equation indicates that the system is not sensitive to small changes of the initial state or parameters of the model. However, it is known that dynamical systems may lose this property after coupling. In [4] the authors give an example which shows that the existence of Lyapunov functions for each vertex system is not sufficient for the existence of global Lyapunov function for the coupled system. The example shows that even if all the individual systems are stable, the coupled dynamical system may not be stable. Hence, it is important to give conditions on the network and the coupling structure which will imply existence of a global Lyapunov function, i.e. it will imply stability of the coupled system. For results on stability of coupled systems on networks, both deterministic and stochastic we refer to [4–10].

Stability has a practical importance in the case of neural networks, since it implies existence of thermal equilibrium, which is essential for the learning process. There are many results on stability of stochastic neural networks with different model characteristics. The literature on this topic is extensive and here we give only few references: [11–15] cover the analysis of mean-square, p th moment and almost sure exponential stability of stochastic neural network models with and without impulsive effects. The results presented in [16–19] are examples of stability analysis of models with time delays, and the models considered in [20–22] also include Markovian switching. In many cases, stability with respect to a general decay function is also of interest. Only few results in the literature consider this general decay in the case of neural networks—in [23–25] the authors analyze models of stochastic neural networks with and without time delay and impulses. However, to best of our knowledge, there are no results on stability analysis on a system of coupled stochastic Cohen-Grossberg neural networks, which include time delays, impulses and Markovian switching. This is a very general model and it includes as a special case many neural networks (see the cited papers and the references therein). The goal of this paper is to give sufficient conditions on p th moment general decay stability for this generalized model of coupled stochastic neural networks. The study of this paper is motivated by the results in [5, 23, 26]. In [5] the authors discuss p th moment exponential stability of coupled system of stochastic differential equations with Markovian switching. In [26] Li et al. extended the ideas from [5] and discussed stability of a system of coupled stochastic functional differential equations with no Markovian switching, defined on a graph. The authors also give sufficient conditions for the p th moment and almost sure exponential stability based on the M -matrix method and they extend their discussion to stochastic coupled systems with time-varying delays. However, the theory in both [5, 26] does not consider a model with

both time-varying delays and Markovian switching, and also impulsive effects have not been assumed in the systems. Even more, both [5, 26] base their models on one-dimensional Brownian motion. This is not very realistic, since the system may be influenced by different independent random sources and thus the model should include an n -dimensional Brownian motion. These results motivated us to extend the methods to a model of stochastic neural networks which includes these network characteristics. In [23] the authors discuss p th moment and almost sure general decay stability of a model of stochastic Cohen-Grosberg impulsive neural network with mixed time delays without Markovian switching, which is a special case from our model.

The important contribution of this paper is that we consider a general model—a system of n stochastic neural networks with a coupling given by interconnection functions, which represent the influence between two coupled neural networks. The model includes time varying delays, impulses and Markovian switching and additionally it is driven by n -dimensional Brownian motion. This leads to generalisation of many models in the literature. Even more, we discuss p th moment general decay stability which includes as a special case the exponential stability, and also allows us to discuss the p th moment stability even when results for exponential stability cannot be applied. The discussion in our paper is based on graph theory methods from [5, 26] and on the Lyapunov method and Dini derivative from [23].

The paper is organised as follows. In Sect. 2, we present the model and we introduce some notions from graph theory and results from the cited papers which will be used in the sequel. Additionally, we give assumptions about the parameters of the model. In Sect. 3, we give our main result, new criteria of a p th moment general decay stability for the equilibrium point. The theoretical results are supported by a numerical example which is presented in Sect. 4. We draw our conclusions in Sect. 5.

2 Formulation of the Problem and Preliminary Results

In this section, we study a network constructed by coupling of M neural networks which have own internal dynamics. We assume that the k th network, $k = 1, 2, \dots, M$ consists of l_k connected neurons. However, to simplify the notations, we define $n = \max\{M, l_1, l_2, \dots, l_M\}$ and assume that all the neural networks have dimension n and also that the whole system consists of n such networks. This can be achieved by adding “dead” neurons in the system which have zero dynamics modeled by functions which are constantly zero and do not affect the dynamics of the whole system. Such a system can be represented by a directed graph \mathcal{G} with n vertices, where each vertex represents one neural network from the system. The directed edge (k, j) exists if the k th network is connected to the j th network. The model is defined on a complete probability space $(\Omega, \mathcal{F}, \{\mathcal{F}_t\}_{t \geq t_0}, \mathbb{P})$ with a natural filtration $\{\mathcal{F}_t\}_{t \geq t_0}$ generated by a standard n -dimensional Brownian motion $W(t) = (W_1(t), W_2(t), \dots, W_n(t)), t \geq t_0$.

The dynamics of the i th neuron in the k th vertex, $k \in N = \{1, 2, \dots, n\}$, is given by the following stochastic differential equation with time delays, Markovian switching and impulses at times $t_m \in \mathbb{R}$:

For $t \geq t_0$, $t \neq t_m$, and $i, k \in N = \{1, 2, \dots, n\}$

$$\begin{aligned}
 dX_i^{(k)}(t) &= -h_i^{(k)}(X_i^{(k)}(t), r(t)) \left[c_i^{(k)}(t, X_i^{(k)}(t), r(t)) \right. \\
 &- \sum_{j=1}^n a_{ij}^{(k)}(t, r(t)) f_j^{(k)}(X_j^{(k)}(t), r(t)) - \sum_{j=1}^n b_{ij}^{(k)}(t, r(t)) g_j^{(k)}(X_{j, \tau_k}^{(k)}, r(t)) \\
 &- \left. \sum_{j=1}^n d_{ij}^{(k)}(t, r(t)) \int_{-\infty}^t l_{ij}^{(k)}(t-s) k_j^{(k)}(X_j^{(k)}(s), r(s)) ds \right] dt \\
 &+ \sum_{j=1}^n \eta_i^{(kj)}(t, X_i^{(k)}(t), X^{(j)}(t), r(t)) dt \\
 &+ \sum_{j=1}^n \sigma_{ij}^{(k)}(t, X_j^{(k)}(t), X_{j, \tau_k}^{(k)}, r(t)) dW_j(t) + \sum_{j=1}^n \zeta_i^{(kj)}(t, X_i^{(k)}(t), X^{(j)}(t), r(t)) dW_j(t) \\
 &\equiv \left(J_i^{(k)}(t, X^{(k)}(t), X_{\tau_k}^{(k)}(t), r(t)) + \sum_{j=1}^n \eta_i^{(kj)}(t, X_i^{(k)}(t), X^{(j)}(t), r(t)) \right) dt \\
 &+ \sum_{j=1}^n \left(\sigma_{ij}^{(k)}(t, X_j^{(k)}(t), X_{j, \tau_k}^{(k)}, r(t)) + \zeta_i^{(kj)}(t, X_i^{(k)}(t), X^{(j)}(t), r(t)) \right) dW_j(t), \tag{1a}
 \end{aligned}$$

and for $t = t_m > t_0$, $m \in \mathbb{N}$,

$$X_i^{(k)}(t) = \mathcal{I}_{im}(X_1^{(k)}(t^-), \dots, X_n^{(k)}(t^-)) + \mathcal{J}_{im}(X_1^{(k)}(t^- - \tau_k(t^-)), \dots, X_n^{(k)}(t^- - \tau_k(t^-))), \tag{1b}$$

$$X_i^{(k)}(t_0 + s) = \xi_i^{(k)}(s), \quad s \in (-\infty, t_0]. \tag{1c}$$

Here $X_i^{(k)} \in \mathbb{R}$ is the state stochastic process of the i th neuron in the k th vertex at time t . We denote that $X^{(k)}(t) = (X_1^{(k)}(t), X_2^{(k)}(t), \dots, X_n^{(k)}(t))^T \in \mathbb{R}^n$ is the process which describes the dynamics in the k th vertex and $X(t) = (X^{(1)}(t), \dots, X^{(n)}(t)) \in \mathbb{R}^{n \times n}$ is the stochastic process which describes the dynamics of the whole coupled system. $\xi_i^{(k)} \in C((-\infty, t_0]; \mathbb{R})$ is an initial condition for the corresponding neuron, and we also denote $\xi^{(k)} = (\xi_1^{(k)}, \dots, \xi_n^{(k)})^T$ and $\xi = (\xi_i^{(k)})_{n \times n}$. $X_{\tau_k}^{(k)} = (X_{1, \tau_k}^{(k)}, \dots, X_{n, \tau_k}^{(k)})^T \in \mathbb{R}^n$ is the delayed process in the k th vertex, where $X_{i, \tau_k}^{(k)} = X_i^{(k)}(t - \tau_k(t))$ is the delayed process of the corresponding neuron dependent on transmission delay $\tau_k(t)$. For simplification, we assume that the delay τ_k is the same for the whole vertex k and is such that $0 \leq \tau_k(t) \leq \tau$, where

τ is a constant. For the delayed process in the whole network, we use the notation $X_t = (X_{\tau_1}^{(1)}, \dots, X_{\tau_n}^{(n)})$.

The switching function $r(t)$ is a right-continuous Markov chain independent of the underlying Brownian motion, taking values in the finite space $\mathcal{P} = \{1, 2, \dots, m_0\}$, with $r(t_0) = \rho_0$ and with a generator matrix P given by (2)

$$\mathbb{P}(r(t + \Delta) = j | r(t) = i) = \begin{cases} \pi_{ij} + o(\Delta), & i \neq j, \\ 1 + \pi_{ij} + o(\Delta), & i = j, \end{cases} \quad (2)$$

where $\Delta > 0$, $\pi_{ij} \geq 0$ is the transition rate from i to j if $i \neq j$, while $\pi_{ii} = -\sum_{j \neq i} \pi_{ij}$.

To simplify the notation, we fix one mode $r(t) = \rho \in \mathcal{P}$ and write $X_i^{(k)}(t) = X_i^{(k)}$, $X^{(k)}(t) = X^{(k)}$, $h_i^{(k)}(X_i^{(k)}(t), \rho) = h_{i,\rho}^{(k)}$, $c_i^{(k)}(t, r(t)) = c_{i,\rho}^{(k)}$ and so on. Then, the equation (1) can be shortly written as

$$dX_i^{(k)} = \left(J_{i,\rho}^{(k)} + \sum_{j=1}^n \eta_{ij}^{(kj)} \right) dt + \sum_{j=1}^n \left(\sigma_{ij,\rho}^{(k)} + \zeta_{i,\rho}^{(kj)} \right) dW_j. \quad (3)$$

The meaning of the functions in the model is as following: $h_{i,\rho}^{(k)}$ are amplification functions at time t , $c_{i,\rho}^{(k)}$ are appropriately behaved functions dependent on t and on the state processes $X_i^{(k)}$, while $a_{ij,\rho}^{(k)}$, $b_{ij,\rho}^{(k)}$ and $d_{ij,\rho}^{(k)}(t)$ describe the strength of the neuron interconnections in the k th vertex network at times t , $f_{i,\rho}^{(k)}$, $k_{i,\rho}^{(k)}$ and $g_{i,\rho}^{(k)}$ are activation functions of the i th neuron in the k th vertex at time t and $t - \tau_k(t)$ respectively, and $l_{ij}^{(kj)}$ are delay kernel functions. The term $\sigma_{\rho}^{(k)}(t, X^{(k)}, X_{\tau_k}^{(k)}) = (\sigma_{ij,\rho}^{(k)}(t, X_j^{(k)}, X_{j,\tau_k}^{(k)}))_{n \times n}$ is a diffusion-coefficient matrix. New in this model are the interconnection functions $\eta_{\rho}^{(kj)} = (\eta_{1,\rho}^{(kj)}, \eta_{2,\rho}^{(kj)}, \dots, \eta_{n,\rho}^{(kj)})^T$ and $\zeta_{\rho}^{(kj)} = (\zeta_{1,\rho}^{(kj)}, \zeta_{2,\rho}^{(kj)}, \dots, \zeta_{\rho}^{(kj)})^T$ which represent the influence from the j th vertex to the k th vertex when $k \neq j$ and for $k = j$ we take $\eta_{\rho}^{(kj)} = \zeta_{\rho}^{(kj)} \equiv 0$. Here $\eta_i^{(kj)}, \zeta_i^{(kj)} : [t_0, \infty) \times \mathbb{R} \times \mathbb{R}^n \times \mathcal{P} \rightarrow \mathbb{R}$ depend on the time t , the state of the i th neuron in the k th vertex, the state of the vertex j and the switching function $r(t)$.

The impulses in the whole coupled network happen at fixed moments $t_m > t_0, m \in \mathbb{N}$ satisfying $t_1 < t_2 < \dots$ and $\lim_{m \rightarrow \infty} t_m = \infty$, $\mathcal{I}_{im}(X_1^{(k)}(t^-), \dots, X_n^{(k)}(t^-)) \in \mathbb{R}$ are impulsive perturbations of the i th neuron in the k th vertex at time t_m , where $X_j^{(k)}(t^-)$ is the left limit of $X_j^{(k)}(t)$, $\mathcal{J}_{im}(X_1^{(k)}(t^- - \tau_k(t^-)), \dots, X_n^{(k)}(t^- - \tau_k(t^-))) \in \mathbb{R}$ are impulsive perturbations of the i th neuron in the k th vertex at time t_m caused by transmission delays. We denote $\mathcal{I}_m = (\mathcal{I}_{1m}, \dots, \mathcal{I}_{nm})^T$ and $\mathcal{J}_m = (\mathcal{J}_{1m}, \dots, \mathcal{J}_{nm})^T$.

If we define $J_\rho^{(k)} := (J_{1,\rho}^{(k)}, \dots, J_{n,\rho}^{(k)})^T$ and $\zeta_\rho^{(k)} := (\zeta_{i,\rho}^{(kj)})_{n \times n}$ the system (1) can be represented in the matrix form,

$$dX^{(k)} = (J_\rho^{(k)} + \sum_{j=1}^n \eta_\rho^{(kj)})dt + (\sigma_\rho^{(k)} + \zeta_\rho^{(k)})dW, \quad t \geq t_0, \quad t \neq t_m, \quad k \in N, \quad (4a)$$

with impulsive perturbations

$$X^{(k)}(t) = \mathcal{I}_m(X^{(k)}(t^-)) + \mathcal{J}_m(X^{(k)}(t^-)), \quad t = t_m, \quad k \in N, \quad m \in \mathbb{N}, \quad (4b)$$

and initial condition

$$X^{(k)}(t_0 + s) = \xi^{(k)}(s), \quad s \in (-\infty, t_0]. \quad (4c)$$

We consider \mathbb{R}^n with the norm $\|x\| = \left(\sum_{i=1}^n |x_i|^p\right)^{\frac{1}{p}}$, for $p \geq 1$. We note that $C((-\infty, t_0]; \mathbb{R}^n)$ is the space of continuous functions φ , equipped with the norm $\|\varphi\| = \left(\sup_{s \in (-\infty, t_0]} \|\varphi(s)\|^p\right)^{\frac{1}{p}}$, and $\mathcal{L}_{\mathcal{F}_{t_0}}^p((-\infty, t_0]; \mathbb{R}^n)$ is the family of all \mathcal{F}_{t_0} -adapted $C((-\infty, t_0]; \mathbb{R}^n)$ -valued random variables φ satisfying $\mathbb{E}\|\varphi\|^p < \infty$.

For any interval $J \subset \mathbb{R}$ or for $J = \mathbb{R}$, we define the space

$$PC[J; \mathbb{R}^n] = \{X : J \rightarrow \mathbb{R}^n \mid X \text{ is continuous on } J \setminus J_0, \text{ where } J_0 \text{ is at most countable set and for } s \in J \setminus J_0, X(s^+), X(s^-) \text{ exist and } X(s^+) = X(s)\}.$$

For $X \in PC[\mathbb{R}; \mathbb{R}^n]$, let us take $\|X_t\| = \left(\sum_{i=1}^n \sup_{s \in [t-\tau, t]} |X_i(s)|^p\right)^{\frac{1}{p}}$, $t \geq t_0$. Also, for bounded functions $\phi \in C[J; \mathbb{R}^n]$ or $\phi \in PC[J; \mathbb{R}^n]$, we introduce the norm $\|\phi\| = \left(\sup_J |\phi(s)|^p\right)^{\frac{1}{p}}$.

For a given function $\lambda : \mathbb{R} \rightarrow \mathbb{R}^+$, we define the space

$$\wp(\lambda) = \{f : \mathbb{R}^+ \cup \{0\} \rightarrow \mathbb{R} \mid f \text{ is piecewise continuous and there are constants } 0 \leq \gamma_0^* < \gamma_1^* \text{ such that } \int_0^\infty |f(s)|\lambda^\gamma(s) ds < \infty \text{ for all } \gamma \in [\gamma_0^*, \gamma_1^*]\}. \quad (5)$$

Since our research is focused on stability problems, we assume with no emphasis on conditions that there exists a unique global solution $X(t; \xi, \rho)$ to the system (1) satisfying $\mathbb{E} \sup_{t \in \mathbb{R}} \|X(t; \xi, \rho)\|^p < \infty$, as well as that all the Lebesgue and Itô integrals employed further are well defined. The considered coupled system is in fact a large system of stochastic functional differential equations with impulses,

time delays and Markovian switching and because of that, we can use the known literature which discusses existence and uniqueness of a solution. For more details on stochastic functional differential equations with Markovian switching, we refer to the work by Mao et al. [27, 28].

For the stability purpose, we usually assume that $J_{\rho}^{(k)}(t, 0, 0) = \eta_{\rho}^{(kj)}(t, 0, 0) = \sigma_{\rho}^{(k)}(t, 0, 0) = \zeta_{\rho}^{(k)}(t, 0, 0) \equiv 0$ so that system (1) admits a trivial solution $X \equiv 0$. We additionally assume that if there exist “dead” neurons in the system, they are modeled by constant zero functions and have no influence on the dynamics on the other neurons.

The following definitions on the p th moment stability with a certain decay rate $\lambda(t)$ and stochastic Lyapunov operator will be used in the sequel.

Definition 1 Let $\lambda \in C(\mathbb{R}; \mathbb{R}^+)$ be a strictly increasing function on $[t_0 - \tau, \infty)$, with $\lambda(t) = 1$ for $t \in (-\infty, t_0 - \tau]$ and $\lim_{t \rightarrow \infty} \lambda(t) = \infty$. Additionally, we assume that it is differentiable on $[t_0, \infty)$, such that $\lambda'(t) \leq \lambda(t)$ and also let $\lambda(s + t) \leq \lambda(s)\lambda(t)$ for all s, t in its domain. Then, the system (1) (or equivalently, its trivial solution) is said to be *p th moment stable with a decay $\lambda(t)$ of order γ* if there exist a pair of constants $\gamma > 0$ and $c_{\xi} > 0$ such that

$$\mathbb{E} \|X(t; \xi, \rho)\|^p \leq c_{\xi} \lambda^{-\gamma}(t), \quad t \geq t_0,$$

holds for any $\xi \in \mathcal{L}_{\mathcal{F}_{t_0}}^p((-\infty, t_0]; \mathbb{R}^{n \times n})$ and $\rho \in \mathcal{P}$.

Clearly, this definition covers exponential, logarithmic and polynomial stability as its special cases.

Definition 2 For $V^{(k)}(t, x^{(k)}, \rho) \in C^{1,2}(\mathbb{R}^+ \times \mathbb{R}^n \times \mathcal{P}; \mathbb{R}^+)$, we define an operator $LV^{(k)}(t, x^{(k)}, \rho)$ associated with the k th vertex of system (1) by

$$\begin{aligned} LV^{(k)}(t, X^{(k)}, \rho) &= \sum_{j=1}^{m_0} \pi_{\rho j} V^{(k)}(t, X^{(k)}, j) + \frac{\partial V^{(k)}(t, X^{(k)}, \rho)}{\partial t} \quad (6) \\ &+ \frac{\partial V^{(k)}}{\partial x^{(k)}} \left[J^{(k)}(t, X^{(k)}, X_{\tau_k}^{(k)}, \rho) + \sum_{j=1}^n \eta^{(kj)}(t, X^{(k)}, X^{(j)}, \rho) \right] \\ &+ \frac{1}{2} \text{trace} \left\{ \left[\sigma^{(k)}(t, X^{(k)}, X_{\tau_k}^{(k)}, \rho) + \zeta^{(k)}(t, X^{(k)}, X^{(j)}, \rho) \right]^T \right. \\ &\quad \left. \times \frac{\partial^2 V^{(k)}}{\partial (x^{(k)})^2} \left[\sigma^{(k)}(t, X^{(k)}, X_{\tau_k}^{(k)}, \rho) + \zeta^{(k)}(t, X^{(k)}, X^{(j)}, \rho) \right] \right\}, \quad (7) \end{aligned}$$

where $\frac{\partial V^{(k)}}{\partial x^{(k)}}$ and $\frac{\partial^2 V^{(k)}}{\partial (x^{(k)})^2}$ are given by (8) and (9)

$$\frac{\partial V^{(k)}}{\partial x^{(k)}} = \left(\frac{\partial V^{(k)}(t, x^{(k)}, \rho)}{\partial x_1^{(k)}}, \dots, \frac{\partial V^{(k)}(t, x^{(k)}, \rho)}{\partial x_n^{(k)}} \right), \quad (8)$$

and

$$\frac{\partial^2 V^{(k)}}{\partial (x^{(k)})^2} = \left(\frac{\partial^2 V^{(k)}(t, x^{(k)}, \rho)}{\partial x_i^{(k)} \partial x_j^{(k)}} \right)_{n \times n}. \quad (9)$$

The global Lyapunov function will later be defined as a linear combination of the vertex Lyapunov functions.

The system of coupled neural networks (1) is built on a graph and thus it is important to introduce some basic concepts and notations from graph theory. For more details we refer to [5].

A *directed graph* or *digraph* $\mathcal{G} = (V_{\mathcal{G}}, E_{\mathcal{G}})$ consists of a set of vertices (nodes) $V_{\mathcal{G}} = \{1, 2, \dots, n\}$ and a set $E_{\mathcal{G}}$ of edges (arcs, links) (k, j) directed from initial vertex k to terminal vertex j . A subgraph \mathcal{S} of \mathcal{G} is *unicyclic* if it is a disjoint union of rooted trees whose roots form a directed cycle. A digraph \mathcal{G} is *weighted* if each edge (j, k) is assigned a nonnegative weight $a_{kj} \geq 0$, where $a_{kj} > 0$ if and only if $(j, k) \in E_{\mathcal{G}}$. We define the *weight of a subgraph* \mathcal{S} , denoted by $w(\mathcal{S})$, to be the product of the weights of all its edges, i.e. $w(\mathcal{S}) = \prod_{(j,k) \in E_{\mathcal{S}}} a_{kj}$. For a weighted graph \mathcal{G} , we define its *weight matrix* $A_{\mathcal{G}} = (a_{kj})_{n \times n}$ as a matrix whose entry a_{kj} equals the weight of the edge (j, k) , when such an edge exists, or it is 0 otherwise. We denote such a weighted digraph by $(\mathcal{G}, A_{\mathcal{G}})$. A weighted digraph $(\mathcal{G}, A_{\mathcal{G}})$ is said to be *balanced* if $w(\mathcal{C}) = w(-\mathcal{C})$ for all directed cycles \mathcal{C} , where $-\mathcal{C}$ is constructed by reversing the directions of all edges in \mathcal{C} .

For a weighted graph $(\mathcal{G}, A_{\mathcal{G}})$ we also define its *Laplacian matrix* $\mathcal{L}_{\mathcal{G}} = (l_{kj})_{n \times n}$ as follows

$$\mathcal{L}_{\mathcal{G}} = \begin{bmatrix} \sum_{j \neq 1} a_{1j} & -a_{12} & \cdots & -a_{1n} \\ -a_{21} & \sum_{j \neq 2} a_{2j} & \cdots & -a_{2n} \\ \vdots & \vdots & \ddots & \vdots \\ -a_{n1} & -a_{n2} & \cdots & \sum_{j \neq n} a_{nj} \end{bmatrix} = (l_{kj})_{n \times n} \quad (10)$$

i.e. $l_{kj} = -a_{kj}$ if $k \neq j$ and $l_{kk} = \sum_{j \neq k} a_{kj}$. The cofactor of the k th diagonal element of $\mathcal{L}_{\mathcal{G}}$ is denoted by $\zeta^{(k)}$.

The following result is used in our discussion of the p th moment stability of a coupled neural network presented in the next section. Its proof can be found in [4], where the authors discuss the global stability of coupled systems of differential equations on networks.

Lemma 1 *Let $n \geq 2$ and $\zeta^{(k)}, k = 1, 2, \dots, n$, be defined as before. Then, for any arbitrary functions $F_{kj}(x_k, x_j), G_k(x_k), k, j = 1, 2, \dots, n$, the following identities hold:*

- (i) $\sum_{k,j=1}^n \zeta^{(k)} a_{kj} F_{kj}(x_k, x_j) = \sum_{S \in \mathbb{S}} w(S) \sum_{(s,r) \in E_{C_S}} F_{rs}(x_r, x_s),$
- (ii) $\sum_{k,j=1}^n \zeta^{(k)} a_{kj} G_k(x_k) = \sum_{k,j=1}^n \zeta^{(k)} a_{kj} G_k(x_j);$

where $x = (x_1, x_2, \dots, x_n) \in \mathbb{R}^n, \mathbb{S}$ is the set of all spanning unicyclic graphs of $(\mathcal{G}, A_{\mathcal{G}})$ and C_S is the directed cycle of S with weight $w(S)$.

Next, we present two results from [23] which help us study the p th moment general decay stability of system (1).

Lemma 2 *Suppose that $\lambda \in C(\mathbb{R}; \mathbb{R}^+)$ is a decay function and $a, b, c \in C([t_0, \infty); \mathbb{R}^+)$. For $l \in \wp(\lambda)$, let us define $I := \max_{\gamma \in [\gamma_0^*, \gamma_1^*]} \int_0^\infty l(s)\lambda^\gamma(s) ds$. Also, let there exist constants $\alpha_0 > 0$ and $0 < \eta_0 < 1$ such that $a(t) - c(t)I \geq \alpha_0$ and $b(t) \leq \eta_0[a(t) - c(t)I]$ for $t \geq t_0$. Then, for every fixed $t \in [t_0, \infty)$, the equation*

$$\gamma = a(t) - c(t)I - b(t)\lambda^\gamma(t) \tag{11}$$

has a unique positive solution $\gamma = \gamma(t)$. In addition, $\gamma^* := \inf_{t \geq t_0} \gamma(t) > 0$.

The following lemma holds when $\gamma^* \in [\gamma_0^*, \gamma_1^*]$.

Lemma 3 *Suppose that λ is a decay function, $a, b, c \in C([t_0; \infty), \mathbb{R}^+), l \in \wp(\lambda)$, and that I, γ^* are defined as in Lemma 2. Moreover, let $\gamma^* \in [\gamma_0^*, \gamma_1^*]$ and let $u \in PC[\mathbb{R}; \mathbb{R}^+]$ satisfy the following inequality*

$$D^+u(t) \leq -a(t)u(t) + b(t) \sup_{\theta \in [t-\tau, t]} u(\theta) + c(t) \int_0^\infty l(s)u(t-s) ds, \quad t \geq t_0, \tag{12}$$

where $D^+u(t)$ is the upper-right Dini derivative of $u(t)$ defined by

$$D^+u(t) = \limsup_{\delta \rightarrow 0^+} \frac{u(t+\delta) - u(t)}{\delta}.$$

If

$$u(t) \leq c \frac{\lambda^{-\gamma^*}(t)}{\lambda^{-\gamma^*}(t_0)}, \quad t \in (-\infty, t_0] \tag{13}$$

for some positive constant c , then

$$u(t) \leq c \frac{\lambda^{-\gamma^*}(t)}{\lambda^{-\gamma^*}(t_0)}, \quad t \geq t_0. \tag{14}$$

In order to prove the main results, we introduce some additional assumptions for the coefficients of the coupled system (1). We generally assume that all the coefficients are Borel measurable on their domains. For a decay function $\lambda(t)$, $i, j, k \in N$ and $\rho \in \mathcal{P}$, we suppose that:

- (H₁) The functions $h_{i,\rho}^{(k)}(x)$ are locally Lipschitz continuous and there exist positive constants $\underline{h}_{i,\rho}^{(k)}$, $\bar{h}_{i,\rho}^{(k)}$ and $\underline{c}_{i,\rho}^{(k)}$ such that

$$0 < \underline{h}_{i,\rho}^{(k)} \leq h_{i,\rho}^{(k)}(x) \leq \bar{h}_{i,\rho}^{(k)}, \quad x \in \mathbb{R},$$

$$\underline{c}_{i,\rho}^{(k)} x^2 \leq x c_{i,\rho}^{(k)}(t, x), \quad (t, x) \in [t_0, \infty) \times \mathbb{R}.$$

- (H₂) The functions $c_{i,\rho}^{(k)}(t, x)$ are globally Lipschitz continuous, that is, there exist constants $\bar{c}_{i,\rho}^{(k)} > 0$ such that

$$|c_{i,\rho}^{(k)}(t, x) - c_{i,\rho}^{(k)}(t, y)| \leq \bar{c}_{i,\rho}^{(k)} |x - y|, \quad t \in [t_0, \infty), \quad x, y \in \mathbb{R}.$$

- (H₃) The activation functions $f_{i,\rho}^{(k)}(x)$, $g_{i,\rho}^{(k)}(x)$, $k_{i,\rho}^{(k)}(x)$ are globally Lipschitz continuous, that is, there exist positive constants $\bar{f}_{i,\rho}^{(k)}$, $\bar{g}_{i,\rho}^{(k)}$, $\bar{k}_{i,\rho}^{(k)}$ such that for all $x, y \in \mathbb{R}$,

$$|f_{i,\rho}^{(k)}(x) - f_{i,\rho}^{(k)}(y)| \leq \bar{f}_{i,\rho}^{(k)} |x - y|,$$

$$|g_{i,\rho}^{(k)}(x) - g_{i,\rho}^{(k)}(y)| \leq \bar{g}_{i,\rho}^{(k)} |x - y|,$$

$$|k_{i,\rho}^{(k)}(x) - k_{i,\rho}^{(k)}(y)| \leq \bar{k}_{i,\rho}^{(k)} |x - y|.$$

- (H₄) The functions $a_{ij,\rho}^{(k)}(t)$, $b_{ij,\rho}^{(k)}(t)$, $d_{ij,\rho}^{(k)}(t)$ are bounded, that is, there exist non-negative constants $\bar{a}_{ij,\rho}^{(k)}$, $\bar{b}_{ij,\rho}^{(k)}$, $\bar{d}_{ij,\rho}^{(k)}$ such that, for all $t \in [t_0, \infty)$,

$$|a_{ij,\rho}^{(k)}(t)| \leq \bar{a}_{ij,\rho}^{(k)}, \quad |b_{ij,\rho}^{(k)}(t)| \leq \bar{b}_{ij,\rho}^{(k)}, \quad |d_{ij,\rho}^{(k)}(t)| \leq \bar{d}_{ij,\rho}^{(k)}.$$

- (H₅) The drift functions $\sigma_{ij,\rho}^{(k)}(t, x, y)$ are globally Lipschitz continuous, uniformly in t , and there exist non-negative constants $\mu_{ij,\rho}^{(k)}$ and $\nu_{ij,\rho}^{(k)}$ such that

$$(\sigma_{ij,\rho}^{(k)}(t, x, y))^2 \leq \mu_{ij,\rho}^{(k)} x^2 + \nu_{ij,\rho}^{(k)} y^2, \quad (t, x, y) \in [t_0, \infty) \times \mathbb{R}^2.$$

(H6) For $l_{ij}^{(k)}(t), t \in [0, \infty)$, there exists a continuous function $l(t), t \in [0, \infty)$ with $l \in \wp(\lambda)$ such that

$$|l_{ij}^{(k)}(t)| \leq l(t), \quad t \in [0, \infty).$$

(H7) The connection functions $\eta_{i,\rho}^{(kj)}(t, x, y), \zeta_{i,\rho}^{(kj)}(t, x, y)$ are globally Lipschitz continuous and there exist positive constants $\bar{\eta}_\rho^{(kj)}, \bar{\zeta}_\rho^{(kj)}$ such that for all $i \in N$ and $(t, x, y) \in [t_0, \infty) \times \mathbb{R} \times \mathbb{R}^n$,

$$\begin{aligned} |\eta_{i,\rho}^{(kj)}(t, x, y)| &\leq \bar{\eta}_\rho^{(kj)}(|x| + \|y\|), \\ (\zeta_{i,\rho}^{(kj)}(t, x, y))^2 &\leq \bar{\zeta}_\rho^{(kj)}(|x|^2 + \|y\|^2). \end{aligned}$$

(H8) There exist non-negative matrices $\mathcal{I}_{(m)} = (\mathcal{I}_{ij,m})_{n \times n}$ and $\mathcal{J}_{(m)} = (\mathcal{J}_{ij,m})_{n \times n}$ such that for all $x = (x_1, \dots, x_n)^T \in \mathbb{R}^n$ and $y = (y_1, \dots, y_n)^T \in \mathbb{R}^n, i \in N, m \in \mathbb{N}$,

$$\begin{aligned} |\mathcal{I}_{im}(x) - \mathcal{I}_{im}(y)| &\leq \sum_{j=1}^n \mathcal{I}_{ij,m} |x_j - y_j|, \\ |\mathcal{J}_{im}(x) - \mathcal{J}_{im}(y)| &\leq \sum_{j=1}^n \mathcal{J}_{ij,m} |x_j - y_j|. \end{aligned}$$

The boundedness of the functions is not necessary for the methods presented further. These assumptions are made only to simplify the notations. More general conditions can be assumed, similar as in [23].

3 General Decay Stability

In this section, we present the main result of the paper, theorem which gives sufficient conditions under which the system (1) is p th moment stable with a decay $\lambda(t)$ of order $\underline{\gamma}$. The proof is based on the lemmas presented in the previous section, the defined Lyapunov operator and some important inequalities. To shorten the discussion, we introduce the following notations

$$\begin{aligned} p_{ij,\rho}^{(k)} &= \left(\bar{h}_{i,\rho}^{(k)} \bar{a}_{ij,\rho}^{(k)} \bar{f}_{j,\rho}^{(k)} + 2(p-1)\mu_{ij,\rho}^{(k)} \right), \quad i \neq j, \\ p_{i,\rho}^{(k)} &= \frac{1}{\theta_\rho^{(k)}} \sum_{j=1}^{m_0} \pi_{\rho j} \theta_j^{(k)} - p \bar{h}_{i,\rho}^{(k)} \bar{c}_{i,\rho}^{(k)} \end{aligned}$$

$$\begin{aligned}
 &+ (p-1)\bar{h}_{i,\rho}^{(k)} \sum_{j=1}^n \left(\bar{a}_{ij,\rho}^{(k)} \bar{f}_{j,\rho}^{(k)} + \bar{b}_{ij,\rho}^{(k)} \bar{g}_{j,\rho}^{(k)} + \bar{d}_{ij,\rho}^{(k)} \bar{k}_{j,\rho}^{(k)} \int_0^\infty |l_{ij}^{(k)}(s)| ds \right) \\
 &+ \bar{h}_{i,\rho}^{(k)} \bar{a}_{ii,\rho}^{(k)} \bar{f}_{i,\rho}^{(k)} + 2(p-1)\mu_{ii,\rho}^{(k)} + (p-1)(p-2) \sum_{j=1}^n (\mu_{ij,\rho}^{(k)} + \nu_{ij,\rho}^{(k)}) \\
 &+ \sum_{j=1}^n ((2p-1)\bar{\eta}_\rho^{(kj)} + 2(p-1)^2 \bar{\zeta}_\rho^{(kj)}), \\
 w_{ij,\rho}^{(k)} &= \bar{h}_{i,\rho}^{(k)} \bar{b}_{ij,\rho}^{(k)} \bar{g}_{j,\rho}^{(k)} + 2(p-1)\nu_{ij,\rho}^{(k)}, \\
 q_{ij,\rho}^{(k)}(t) &= \bar{h}_{i,\rho}^{(k)} \bar{d}_{ij,\rho}^{(k)} \bar{k}_{j,\rho}^{(k)} l(t), \quad t \in [0, \infty) \\
 \bar{\eta}_\rho^{(j)} &= \max_{k \in N} (\bar{\eta}_\rho^{(kj)} + 2(p-1)\bar{\zeta}_\rho^{(kj)}), \\
 p_\rho^{(k)} &= \max_{i \in N} \left(p_{i,\rho}^{(k)} + \sum_{j \neq i} p_{ji,\rho}^{(k)} \right), \\
 \epsilon_\rho^{(k)} &= p_\rho^{(k)} + n(n-1)\bar{\eta}_\rho^{(k)}, \\
 w_\rho^{(k)} &= \sum_{i=1}^n \max_{j \in N} w_{ij,\rho}^{(k)}, \\
 q_\rho^{(k)}(t) &= \sum_{i=1}^n \max_{j \in N} q_{ij,\rho}^{(k)}(t), \quad t \in [0, \infty).
 \end{aligned} \tag{15}$$

where $i, j, k \in N, \rho \in \mathcal{P}$ and $\theta_\rho^{(k)}$ are some positive constants.

Theorem 1 *Let us suppose that λ is a decay function, $\varphi \in \mathcal{L}_{\mathcal{F}_{t_0}}^p((-\infty, t_0]; \mathbb{R}^{n \times n})$ and that the assumptions **(H₁)** – **(H₈)** are satisfied for the coupled system (1). Also, let*

$$\begin{aligned}
 \epsilon_\rho &= \max_{k \in N} \epsilon_\rho^{(k)}, & q_\rho(t) &= \max_{k \in N} \sum_{i=1}^n \max_{j \in N} q_{ij,\rho}^{(k)}(t), \quad t \in [0, \infty), \\
 w_\rho &= \max_{k \in N} \sum_{i=1}^n \max_{j \in N} w_{ij,\rho}^{(k)}, & I_\rho &= \max_{\gamma \in [\gamma_0^*, \gamma_1^*]} \int_0^\infty q_\rho(s) \lambda^\gamma(s) ds.
 \end{aligned} \tag{16}$$

Additionally, let $\epsilon_\rho + I_\rho < 0$ and $\epsilon_\rho + I_\rho + nw_\rho < 0$ for any $\rho \in \mathcal{P}$ and some choice of the constants $\theta_\rho^{(k)}$, and define $\underline{\gamma} = \min_{\rho \in \mathcal{P}} \gamma_\rho$, where γ_ρ is the unique solution of the equation $\gamma_\rho = -\epsilon_\rho - nw_\rho \bar{\lambda}^{\gamma_\rho}(\tau) - I_\rho$, and let $\underline{\gamma} \in [\gamma_0^*, \gamma_1^*]$. Assume that for every $m \in \mathbb{N}$

$$2^{p-1} \sum_{i=1}^n \left[\left(\sum_{j=1}^n (\mathcal{I}_{ij,m})^{\frac{p}{p-1}} \right)^{p-1} + n \left(\sum_{j=1}^n (\mathcal{J}_{ij,m})^{\frac{p}{p-1}} \right)^{p-1} (\lambda(\tau))^{\underline{\gamma}} \right] \leq 1. \tag{17}$$

Then, the coupled system (1) is p th moment stable with a decay function λ of order $\underline{\gamma}$.

Proof Let $x^{(k)} = (x_1^{(k)}, \dots, x_n^{(k)})^T \in \mathbb{R}^n$ and $x = (x^{(1)}, \dots, x^{(n)}) \in \mathbb{R}^{n \times n}$. Let $V_{i,\rho}^{(k)}(x_i^{(k)}) = V_i^{(k)}(x_i^{(k)}, \rho) = \theta_\rho^{(k)} |x_i^{(k)}|^p$ be the Lyapunov function corresponding to the i th neuron in the k th vertex, where $\theta_\rho^{(k)} > 0$ are some constants. Also, let $V_\rho^{(k)}(x^{(k)}) = V^{(k)}(x^{(k)}, \rho) = \sum_{i=1}^n V_{i,\rho}^{(k)}(x_i^{(k)}) = \sum_{i=1}^n \theta_\rho^{(k)} |x_i^{(k)}|^p$. Then, for the coupled system (1) we have

$$\begin{aligned} L V_{i,\rho}^{(k)}(X_i^{(k)}) &= \sum_{j=1}^{m_0} \pi_{\rho j} V_{i,j}^{(k)}(X_i^{(k)}) + \frac{\partial V_{i,\rho}^{(k)}(X_i^{(k)})}{\partial t} + \frac{\partial V_{i,\rho}^{(k)}(X_i^{(k)})}{\partial x_i^{(k)}} \left(J_{i,\rho}^{(k)} + \sum_{j=1}^n \eta_{i,\rho}^{(kj)} \right) \\ &\quad + \frac{1}{2} \frac{\partial^2 V_{i,\rho}^{(k)}(X_i^{(k)})}{\partial (x_i^{(k)})^2} \sum_{j=1}^n \left(\sigma_{ij,\rho}^{(kj)} + \zeta_{i,\rho}^{(kj)} \right)^2 \\ &\leq \sum_{j=1}^{m_0} \pi_{\rho j} \theta_j^{(k)} |X_i^{(k)}|^p + p \theta_\rho^{(k)} |X_i^{(k)}|^{p-2} X_i^{(k)} J_{i,\rho}^{(k)} + p \theta_\rho^{(k)} |X_i^{(k)}|^{p-1} \sum_{j=1}^n |\eta_{i,\rho}^{(kj)}| \\ &\quad + p(p-1) \theta_\rho^{(k)} |X_i^{(k)}|^{p-2} \sum_{j=1}^n (\sigma_{ij,\rho}^{(kj)})^2 + p(p-1) \theta_\rho^{(k)} |X_i^{(k)}|^{p-2} \sum_{j=1}^n (\zeta_{i,\rho}^{(kj)})^2. \end{aligned}$$

Using **(H₁)**–**(H₇)**, Young’s inequality and the techniques presented in [23], we obtain the following estimate

$$\begin{aligned} L V_{i,\rho}^{(k)}(X^{(k)}) &\leq \theta_\rho^{(k)} \left(\frac{1}{\theta_\rho^{(k)}} \sum_{j=1}^{m_0} \pi_{\rho j} \theta_j^{(k)} - p h_{i,\rho}^{(k)} c_{i,\rho}^{(k)} \right) \\ &\quad + (p-1) \bar{h}_{i,\rho}^{(k)} \sum_{j=1}^n \left(\bar{a}_{ij,\rho}^{(k)} \bar{f}_{j,\rho}^{(k)} + \bar{b}_{ij,\rho}^{(k)} \bar{g}_{j,\rho}^{(k)} + \bar{d}_{ij,\rho}^{(k)} \bar{k}_{j,\rho}^{(k)} \int_0^\infty |l_{ij}^{(k)}(s)| ds \right) \\ &\quad + \bar{h}_{i,\rho}^{(k)} \bar{a}_{ii,\rho}^{(k)} \bar{f}_{i,\rho}^{(k)} + 2(p-1) \mu_{ii,\rho}^{(k)} + (p-1)(p-2) \sum_{j=1}^n \left(\mu_{ij,\rho}^{(k)} + \nu_{ij,\rho}^{(k)} \right) \\ &\quad + \sum_{j=1}^n \left((2p-1) \bar{\eta}_\rho^{(kj)} + 2(p-1)^2 \bar{\zeta}_\rho^{(kj)} \right) |X_i^{(k)}|^p \\ &\quad + \theta_\rho^{(k)} \sum_{j \neq i} \left(\bar{h}_{i,\rho}^{(k)} \bar{a}_{ij,\rho}^{(k)} \bar{f}_{j,\rho}^{(k)} + 2(p-1) \mu_{ij,\rho}^{(k)} \right) |X_j^{(k)}|^p \end{aligned}$$

$$\begin{aligned}
 & + \theta_\rho^{(k)} \sum_{j=1}^n \left(\bar{h}_{i,\rho}^{(k)} \bar{b}_{ij,\rho}^{(k)} \bar{g}_{j,\rho}^{(k)} + 2(p-1)v_{ij,\rho}^{(k)} \right) |X_{j,\tau_k}^{(k)}|^p \\
 & + \theta_\rho^{(k)} \bar{h}_{i,\rho}^{(k)} \sum_{j=1}^n \bar{d}_{ij,\rho}^{(k)} \bar{k}_{j,\rho}^{(k)} \int_0^\infty l(s) |X_j^{(k)}(t-s)|^p ds \\
 & + \theta_\rho^{(k)} \sum_{j \neq k} \left(\bar{\eta}_\rho^{(kj)} + 2(p-1)\bar{\xi}_\rho^{kj} \right) \|X^{(j)}(t)\|^p \\
 \leq & \theta_\rho^{(k)} p_{i,\rho}^{(k)} |X_i^{(k)}|^p + \theta_\rho^{(k)} \sum_{j \neq i} p_{ij,\rho}^{(k)} |X_j^{(k)}|^p + \theta_\rho^{(k)} \max_{j \in N} w_{ij,\rho}^{(k)} \|X_{\tau_k}^{(k)}\|^p \\
 & + \theta_\rho^{(k)} \int_0^\infty \max_{j \in N} q_{ij,\rho}^{(k)} \|X^{(k)}(t-s)\|^p ds + \theta_\rho^{(k)} \sum_{j \neq k} \bar{\eta}_\rho^{(j)} \|X^{(j)}\|^p \tag{18}
 \end{aligned}$$

where $p_{ij,\rho}^{(k)}, w_{ij,\rho}^{(k)}, q_{ij,\rho}^{(k)}$ and $\bar{\eta}_\rho^{(j)}, i, j, k \in N$ are given with equations (15).

Taking $V_\rho^{(k)}(x^{(k)}) = \sum_{i=1}^n V_{i,\rho}^{(k)}(x_i^{(k)})$ and summing (18) for all $i \in N$, we get

$$\begin{aligned}
 LV_\rho^{(k)}(X^{(k)}) & \leq \theta_\rho^{(k)} \sum_{i=1}^n \max_{i \in N} \left(p_{i,\rho}^{(k)} + \sum_{j \neq i} p_{ji,\rho}^{(k)} \right) |X_i^{(k)}|^p + \theta_\rho^{(k)} w_\rho^{(k)} \|X_{\tau_k}^{(k)}\|^p \\
 & + \theta_\rho^{(k)} \int_0^\infty q_\rho^{(k)}(s) \|X^{(k)}(t-s)\|^p ds + \theta_\rho^{(k)} \sum_{i=1}^n \sum_{j \neq k} \bar{\eta}_\rho^{(j)} \|X^{(j)}\|^p \\
 & = \theta_\rho^{(k)} \left(p_\rho^{(k)} + n(n-1)\bar{\eta}_\rho^{(k)} \right) \|X^{(k)}\|^p + \theta_\rho^{(k)} w_\rho^{(k)} \|X_{\tau_k}^{(k)}\|^p \\
 & + \int_0^\infty q_\rho^{(k)}(s) \|X^{(k)}(t-s)\|^p ds + \theta_\rho^{(k)} n \sum_{j \neq k} \left(\bar{\eta}_\rho^{(j)} \|X^{(j)}\|^p - \bar{\eta}_\rho^{(k)} \|X^{(k)}\|^p \right) \\
 & = \theta_\rho^{(k)} \epsilon_\rho^{(k)} \|X^{(k)}\|^p + \theta_\rho^{(k)} w_\rho^{(k)} \|X_{\tau_k}^{(k)}\|^p + \int_0^\infty q_\rho^{(k)}(s) \|X^{(k)}(t-s)\|^p ds \\
 & + n\theta_\rho^{(k)} \sum_{j \neq k} F^{(kj)}(X^{(k)}, X^{(j)}) \tag{19}
 \end{aligned}$$

where $p_\rho^{(k)}, \epsilon_\rho^{(k)}, w_\rho^{(k)}$ and $q_\rho^{(k)}$ are given by (15) and

$$F^{(kj)}(X^{(k)}, X^{(j)}) = \bar{\eta}_\rho^{(j)} \|X^{(j)}\|^p - \bar{\eta}_\rho^{(k)} \|X^{(k)}\|^p$$

For each $\rho \in \mathcal{P}$, let us denote by \mathcal{G}_ρ the corresponding complete directed graph \mathcal{G}_ρ and assign weight $\alpha_\rho^{(kj)} = \theta_\rho^{(k)}$ to each directed edge $(j, k), j \neq k$. Let $\mathcal{A}_{\mathcal{G}_\rho} = (\alpha_\rho^{(kj)})_{n \times n}$ represent the weight matrix of the graph \mathcal{G}_ρ . Then, the corresponding Laplacian matrix is given by

$$\mathcal{L}_{\mathcal{G},\rho} = \begin{bmatrix} (n-1)\theta_\rho^{(1)} & -\theta_\rho^{(1)} & \dots & -\theta_\rho^{(1)} \\ -\theta_\rho^{(2)} & (n-1)\theta_\rho^{(2)} & \dots & -\theta_\rho^{(2)} \\ \vdots & \vdots & \ddots & \vdots \\ -\theta_\rho^{(n)} & -\theta_\rho^{(n)} & \dots & (n-1)\theta_\rho^{(n)} \end{bmatrix}.$$

Let $\varsigma_\rho^{(k)}$ be the cofactor of the k th diagonal element of $\mathcal{L}_{\mathcal{G},\rho}$ and let us take $V_\rho(x) = \sum_{k=1}^n \varsigma_\rho^{(k)} V_\rho^{(k)}(x^{(k)})$ for $x \in \mathbb{R}^{n \times n}$ denoted as before. Then,

$$\begin{aligned} LV_\rho(X) &\leq \sum_{k=1}^n \varsigma_\rho^{(k)} \epsilon_\rho^{(k)} \theta_\rho^{(k)} \|X^{(k)}\|^p + \sum_{k=1}^n \varsigma_\rho^{(k)} w_\rho^{(k)} \theta_\rho^{(k)} \|X_{\tau_k}^{(k)}\|^p \\ &\quad + \sum_{k=1}^n \varsigma_\rho^{(k)} \int_0^\infty q_\rho^{(k)}(s) \theta_\rho^{(k)} \|X^{(k)}(t-s)\|^p ds \\ &\quad + n \sum_{k=1}^n \varsigma_\rho^{(k)} \theta_\rho^{(k)} \sum_{j=1}^n F^{(jk)}(X^{(j)}, X^{(k)}). \end{aligned}$$

Since each edge starting at vertex k has the same weight $\theta_\rho^{(k)}$, we conclude that the graph \mathcal{G}_ρ is a complete balanced graph. By Lemma 1, we have

$$\sum_{k,j=1}^n \varsigma_\rho^{(k)} \theta_\rho^{(k)} F^{(kj)}(X^{(k)}, X^{(j)}) = \sum_{\mathcal{S} \in \mathbb{S}} w(\mathcal{S}) \sum_{(s,r) \in E_{C_{\mathcal{S}}}} F^{(rs)}(X^{(r)}, X^{(s)}) = 0, \tag{20}$$

where \mathbb{S} is the set of all spanning unicyclic graphs \mathcal{S} of $(\mathcal{G}_\rho, \mathcal{A}_{\mathcal{G},\rho})$ with weight $w(\mathcal{S})$, whose unique cycle is denoted by $C_{\mathcal{S}}$. Thus

$$\begin{aligned} LV_\rho(X) &\leq \max_{k \in N} \epsilon_\rho^{(k)} \sum_{k=1}^n \varsigma_\rho^{(k)} \theta_\rho^{(k)} \|X^{(k)}\|^p + \max_{k \in N} w_\rho^{(k)} \sum_{k=1}^n \varsigma_\rho^{(k)} \theta_\rho^{(k)} \|X_{\tau_k}^{(k)}\|^p \\ &\quad + \sum_{k=1}^n \varsigma_\rho^{(k)} \int_0^\infty \left(\max_{k \in N} q_\rho^{(k)}(s) \right) \theta_\rho^{(k)} \|X^{(k)}(t-s)\|^p ds \\ &= \epsilon_\rho V_\rho(X(t)) + w_\rho \sum_{k=1}^n \varsigma_\rho^{(k)} \theta_\rho^{(k)} \|X_{\tau_k}^{(k)}\|^p + \int_0^\infty q_\rho(s) V_\rho(X(t-s)) ds, \end{aligned} \tag{21}$$

where ϵ_ρ , w_ρ and $q_\rho(t)$ are given by equations (16).

Next, we apply the Itô's formula and, similar to the proof in Theorem 1 in [23], we obtain

$$D^+ \mathbb{E}V_\rho(X(t)) \leq \epsilon_\rho \mathbb{E}V_\rho(X(t)) + nw_\rho \sup_{s \in [t-\tau, t]} \mathbb{E}V_\rho(X(s)) + \int_0^\infty q_\rho(s) \mathbb{E}V_\rho(X(t-s)) ds \tag{22}$$

Since $\epsilon_\rho + I_\rho < 0$ and $\epsilon_\rho + I_\rho + nw_\rho < 0$ hold for any $\rho \in \mathcal{P}$, it follows that the equation $\gamma_\rho = -\epsilon_\rho - nw_\rho \lambda^{\gamma_\rho}(\tau) - I_\rho$ has a unique positive solution for any $\rho \in \mathcal{P}$. This is a consequence of Lemma 2, if we take constant functions $a(t) = -\epsilon_\rho$, $b(t) = nw_\rho$, $c(t) = 1$ and $I = I_\rho$. For each ρ , we denote the solution by γ_ρ and we define $\underline{\gamma} = \min_{\rho \in \mathcal{P}} \gamma_\rho$ and $\bar{\gamma} = \max_{\rho \in \mathcal{P}} \gamma_\rho$.

Since $\xi \in \mathcal{L}_{\mathcal{F}_{t_0}}^p((-\infty, t_0]; \mathbb{R}^{n \times n})$ and $\lambda(t)$ is a non-decreasing function on $(-\infty, t_0]$, we find for $t \leq t_0$ and for any $\rho \in \mathcal{P}$ that

$$\mathbb{E}V_\rho^{(k)}(X^{(k)}(t)) \leq \sum_{i=1}^n \theta_\rho^{(k)} \mathbb{E} \|\xi_i^{(k)}\|^p \leq \max_{\rho \in \mathcal{P}} \theta_\rho^{(k)} \mathbb{E} \|\xi^{(k)}\|^p \frac{\lambda^{-\gamma_\rho}(t)}{\lambda^{-\gamma_\rho}(t_0)} \leq c_{\xi^{(k)}} \frac{\lambda^{-\underline{\gamma}(t)}}{\lambda^{-\bar{\gamma}(t_0)}}, \tag{23}$$

where $c_{\xi^{(k)}} = \max_{\rho \in \mathcal{P}} \theta_\rho^{(k)} \mathbb{E} \|\xi^{(k)}\|^p$. Hence, (22), (23) and Lemma 3 imply that

$$\mathbb{E}V_\rho(X(t)) \leq \max_{k \in N, \rho \in \mathcal{P}} S_\rho^k \theta_\rho^{(k)} \mathbb{E} \|\xi^{(k)}\|^p \frac{\lambda^{-\gamma_\rho}(t)}{\lambda^{-\gamma_\rho}(t_0)} \leq c_\xi \frac{\lambda^{-\underline{\gamma}(t)}}{\lambda^{-\bar{\gamma}(t_0)}}, \quad t \in [t_0, t_1), \tag{24}$$

where $c_\xi = \max_{k \in N, \rho \in \mathcal{P}} S_\rho^k \theta_\rho^{(k)} \mathbb{E} \|\xi^{(k)}\|^p$.

Let us suppose that for $i = 1, 2, \dots, m$ and all $k \in N$,

$$\mathbb{E}V_\rho^{(k)}(X^{(k)}(t)) \leq c_{\xi^{(k)}} \frac{\lambda^{-\underline{\gamma}(t)}}{\lambda^{-\bar{\gamma}(t_0)}}, \quad t \in [t_{i-1}, t_i).$$

Thus, for $i = 1, 2, \dots, m$,

$$\mathbb{E}V_\rho(X(t)) \leq c_\xi \frac{\lambda^{-\underline{\gamma}(t)}}{\lambda^{-\bar{\gamma}(t_0)}}, \quad t \in [t_{i-1}, t_i).$$

For $t = t_m$, by applying **(H8)** and the Jensen's inequality, we get

$$\begin{aligned} \mathbb{E}V_\rho^{(k)}(X^{(k)}(t_m)) &= \sum_{i=1}^n \theta_\rho^{(k)} \mathbb{E} \left| \mathcal{I}_{im}(X^{(k)}(t_m^-)) + \mathcal{J}_{im}(X_{\tau_k}^{(k)}(t_m^-)) \right|^p \\ &\leq \sum_{i=1}^n \theta_\rho^{(k)} \mathbb{E} \left[\sum_{j=1}^n |\mathcal{I}_{ij,m}| X_j^{(k)}(t_m^-) + \sum_{j=1}^n |\mathcal{J}_{ij,m}| X_{j,\tau_k}^{(k)}(t_m^-) \right]^p \\ &\leq 2^{p-1} \theta_\rho^{(k)} \sum_{i=1}^n \left[\mathbb{E} \left(\sum_{j=1}^n |\mathcal{I}_{ij,m}| X_j^{(k)}(t_m^-) \right)^p + \mathbb{E} \left(\sum_{j=1}^n |\mathcal{J}_{ij,m}| X_{j,\tau_k}^{(k)}(t_m^-) \right)^p \right]. \end{aligned}$$

Using the Hölder inequality and (17), we find that

$$\begin{aligned} &\mathbb{E}V_\rho^{(k)}(X^{(k)}(t_m)) \\ &\leq 2^{p-1} \theta_\rho^{(k)} \sum_{i=1}^n \left[\left(\sum_{j=1}^n |\mathcal{I}_{ij,m}|^{\frac{p}{p-1}} \right)^{p-1} \mathbb{E} \|X^{(k)}(t_m^-)\|^p + \left(\sum_{j=1}^n |\mathcal{J}_{ij,m}|^{\frac{p}{p-1}} \right)^{p-1} \mathbb{E} \|X_{\tau_k}^{(k)}(t_m)\|^p \right] \\ &\leq 2^{p-1} \sum_{i=1}^n \left[\left(\sum_{j=1}^n |\mathcal{I}_{ij,m}|^{\frac{p}{p-1}} \right)^{p-1} + \left(\sum_{j=1}^n |\mathcal{J}_{ij,m}|^{\frac{p}{p-1}} \right)^{p-1} \lambda^{\mathcal{Y}(\tau)} \right] c_{\xi^{(k)}} \frac{\lambda^{-\mathcal{Y}(t_m)}}{\lambda^{-\bar{\mathcal{Y}}(t_0)}} \\ &\leq c_{\xi^{(k)}} \frac{\lambda^{-\mathcal{Y}(t_m)}}{\lambda^{-\bar{\mathcal{Y}}(t_0)}}. \end{aligned}$$

Here we have used

$$\mathbb{E}V_\rho^{(k)}(X_{\tau_k}^{(k)}(t_m)) \leq c_{\xi^{(k)}} \frac{\lambda^{-\mathcal{Y}(t_m - \tau_k(t))}}{\lambda^{-\bar{\mathcal{Y}}(t_0)}} \leq c_{\xi^{(k)}} \lambda^{\mathcal{Y}(\tau)} \frac{\lambda^{-\mathcal{Y}(t_m)}}{\lambda^{-\bar{\mathcal{Y}}(t_0)}}.$$

Thus, (17) and Lemma 3, imply that

$$\mathbb{E}V_\rho^{(k)}(X^{(k)}(t)) \leq c_{\xi^{(k)}} \frac{\lambda^{-\mathcal{Y}(t_k)}}{\lambda^{-\bar{\mathcal{Y}}(t_0)}}, \quad t \in [t_m, t_{m+1})$$

and, therefore,

$$\mathbb{E}V_\rho(X(t)) \leq c_\xi \frac{\lambda^{-\mathcal{Y}(t)}}{\lambda^{-\bar{\mathcal{Y}}(t_0)}}, \quad t \in [t_m, t_{m+1}).$$

Hence, the last inequality holds by induction for every $t \geq t_0$. Finally,

$$\mathbb{E} \|X(t)\|^p \leq \frac{1}{\min_{k \in N, \rho \in \mathcal{P}} \varsigma_\rho^{(k)} \theta_\rho^{(k)}} \mathbb{E}V_\rho(X(t)) \leq \frac{c_\xi}{\min_{k \in N, \rho \in \mathcal{P}} \varsigma_\rho^{(k)} \theta_\rho^{(k)}} \frac{\lambda^{-\mathcal{Y}(t)}}{\lambda^{-\bar{\mathcal{Y}}(t_0)}} = \bar{c}_\xi \frac{\lambda^{-\mathcal{Y}(t)}}{\lambda^{-\bar{\mathcal{Y}}(t_0)}}, \quad (25)$$

where \bar{c}_ξ is a generic constant. Thus, the trivial solution of the coupled system (1) is p th moment stable with a decay function $\lambda(t)$ of order $\underline{\gamma}$.

Remark 1 We note again that the boundedness of the model functions (as defined in the assumptions **(H₁)**–**(H₇)**) is not necessary for the presented result. Also, it is not necessary to choose equal values for the constants $\theta_\rho^{(k)}$ and the time delays $\tau_k(t)$ for the k th network. Similar as in [23], more general conditions can be assumed. We also remark that with some additional assumptions, the result on almost sure general stability from [23] can be extended to system (1).

4 Numerical Example (General Decay Stability)

Let us consider the 4th moment general decay stability of the coupled system of stochastic Cohen-Grossberg neural network represented by (1), where $t_0 = 2$, $x_0 = \xi \in \mathcal{L}_{\mathcal{F}_0}^4((-\infty, 2]; \mathbb{R}^2)$, $W(t)$ is a two-dimensional Brownian motion, $\tau_1(t) = 1 + |\sin(t)|$, $\tau_2(t) = 1 + |\cos(t)|$ are delay functions, $\tau = 2$, $x = (x_1, x_2)^T$, $y = (y_1, y_2)^T \in \mathbb{R}^2$, $z = [z_{ij}]_{2 \times 2} \in \mathbb{R}^{2 \times 2}$ and $t_m = 2(m + 1)$, $k \in \mathbb{N}$ are the impulsive moments. The two state Markov chain has the following generator matrix $P = \begin{pmatrix} 2 & 2 \\ 2 & 2 \end{pmatrix}$.

For $\rho = 1$ the model functions are given by

$$h_{1,1}^{(1)}(x_1) = 1.75 + 0.25 \sin x_1, \quad h_{2,1}^{(1)}(x_2) = 1.6 + 0.1 \cos x_2,$$

$$h_{1,1}^{(2)}(x_1) = 2.75 + 0.25 \sin x_1, \quad h_{2,1}^{(2)}(x_2) = 2.2 + 0.5 \cos x_2,$$

$$c_{1,1}^{(1)}(t, x_1) = \left(400 + \frac{4}{1+t}\right)x_1, \quad c_{2,1}^{(1)}(t, x_2) = \left(420 + \frac{5}{1+t}\right)x_2,$$

$$c_{1,1}^{(2)}(t, x_1) = \left(800 + \frac{3}{1+t}\right)x_1, \quad c_{2,1}^{(2)}(t, x_2) = \left(820 + \frac{2}{1+t}\right)x_2,$$

$$a_{11,1}^{(1)}(t) = 0.4 + \frac{0.1}{1+t}, \quad a_{21,1}^{(1)}(t) = 0.1 + \frac{0.2}{1+t}, \quad a_{12,1}^{(1)}(t) = 0.2 + \frac{0.1}{1+t}, \quad a_{22,1}^{(1)}(t) = 0.3 + \frac{0.3}{1+t},$$

$$a_{11,1}^{(2)}(t) = 0.4 + \frac{0.4}{1+t}, \quad a_{21,1}^{(2)}(t) = 0.5 + \frac{0.2}{1+t}, \quad a_{12,1}^{(2)}(t) = 0.9 + \frac{0.1}{1+t}, \quad a_{22,1}^{(2)}(t) = 0.2 + \frac{0.1}{1+t},$$

$$b_{11,1}^{(1)}(t) = \frac{0.1}{1+t}, \quad b_{21,1}^{(1)}(t) = b_{12,1}^{(1)}(t) = 1.5 + \frac{0.5}{1+t}, \quad b_{22,1}^{(1)}(t) = 0.3,$$

$$b_{11,1}^{(2)}(t) = \frac{0.6}{1+t}, \quad b_{21,1}^{(2)}(t) = b_{12,1}^{(2)}(t) = 0.7 + \frac{0.8}{1+t}, \quad b_{22,1}^{(2)}(t) = 1.8,$$

$$f_{1,1}^{(1)}(x_1) = 0.2 \tanh(x_1), \quad f_{2,1}^{(1)}(x_2) = 0.4 \tanh(x_2),$$

$$f_{1,1}^{(2)}(x_1) = 0.5 \tanh(x_1), \quad f_{2,1}^{(2)}(x_2) = 0.7 \tanh(x_2),$$

$$g_{1,1}^{(1)}(y_1) = 5 \tanh(y_1), \quad g_{2,1}^{(1)}(y_2) = 7 \tanh(y_2),$$

$$g_{1,1}^{(2)}(y_1) = 2 \tanh(y_1), \quad g_{2,1}^{(2)}(y_2) = 2 \tanh(y_2),$$

$$\begin{aligned}
 d_{11,1}^{(1)}(t) &= \frac{1}{6e^t}, \quad d_{21,1}^{(1)}(t) = \frac{1}{9(1+t)}, \quad d_{12,1}^{(1)}(t) = \frac{0.3}{1+t^2}, \quad d_{22,1}^{(1)}(t) = \frac{\cos t}{12e^t}, \\
 d_{11,1}^{(2)}(t) &= \frac{1}{6e^t}, \quad d_{12,1}^{(2)}(t) = \frac{0.2}{1+t^2}, \quad d_{21,1}^{(2)}(t) = \frac{5}{9(1+t)}, \quad d_{22,1}^{(2)}(t) = \frac{\sin t}{10e^t}, \\
 k_{1,1}^{(1)}(x_1) &= \frac{x_1}{3}, \quad k_{2,1}^{(1)}(x_2) = \frac{x_2}{2}, \quad k_{1,1}^{(2)}(x_1) = \frac{x_1}{3}, \quad k_{2,1}^{(2)}(x_2) = \frac{x_2}{4}, \\
 \eta_{1,1}^{(21)}(t, x_1, y) &= \frac{2.5}{1+t^2}(x_1^2 + y_1^2 + y_2^2), \quad \eta_{2,1}^{(21)}(t, x_2, y) = \frac{2.5}{1+t^2}(x_2^2 + y_1^2 + y_2^2), \\
 \eta_{1,1}^{(12)}(t, x_1, y) &= 0.8|\sin t|(x_1^2 + y_1^2 + y_2^2), \quad \eta_{1,1}^{(12)}(t, x_2, y) = 0.8|\sin t|(x_2^2 + y_1^2 + y_2^2), \\
 \zeta_{1,1}^{(21)}(t, x_1, y) &= \frac{\sqrt{1.35}x_1 + \sqrt{0.675}(y_1 + y_2)}{e^{2t}}, \quad \zeta_{2,1}^{(21)}(t, x_2, y) = \frac{\sqrt{1.35}x_2 + \sqrt{0.675}(y_1 + y_2)}{e^t}, \\
 \zeta_{1,1}^{(12)}(t, x_1, y) &= \frac{2|x_1|^{\frac{1}{2}}|8y_1y_2|^{\frac{1}{4}}}{1+t^2}, \quad \zeta_{2,1}^{(12)}(t, x_2, y) = \frac{2|x_2|^{\frac{1}{2}}|8y_1y_2|^{\frac{1}{4}}}{e^t}, \\
 \sigma_{11,1}^{(1)}(t, x_1, z_{11}) &= \frac{\sqrt{20}x_1 + \sqrt{3}z_{11}}{\sqrt{1+t^2}}, \quad \sigma_{21,1}^{(1)}(t, x_1, z_{21}) = \sqrt{8}x_1 + \sqrt{2.5}z_{21}e^{-\frac{t}{2}}, \\
 \sigma_{12,1}^{(1)}(t, x_2, z_{12}) &= 2\sqrt{|x_2z_{12}|}\sin t, \quad \sigma_{22,1}^{(1)}(t, x_2, z_{22}) = \frac{2x_2 \sin t + z_{22}}{\sqrt{1+t^2}}, \\
 \sigma_{11,1}^{(2)}(t, x_1, z_{11}) &= \frac{3\sqrt{2}x_1 + \sqrt{2}z_{11}}{1+t^2}, \quad \sigma_{21,1}^{(2)}(t, x_1, z_{21}) = \sqrt{12|x_1z_{21}|}\exp^{-2t}, \\
 \sigma_{12,1}^{(2)}(t, x_2, z_{12}) &= x_1 + \sqrt{0.5}z_{12}e^{-t}, \quad \sigma_{22,1}^{(2)}(t, x_2, z_{22}) = \frac{\sqrt{7}x_2 + z_{22} \cos t}{\sqrt{2(1+t^2)}},
 \end{aligned}$$

For $\rho = 2$ the model functions are given by

$$\begin{aligned}
 h_{1,2}^{(1)}(x_1) &= 1.95 + 0.25 \sin x_1, \quad h_{2,2}^{(1)}(x_2) = 1.8 + 0.1 \cos x_2, \\
 h_{1,2}^{(2)}(x_1) &= 2.9 + 0.3 \sin x_1, \quad h_{2,2}^{(2)}(x_2) = 2.4 + 0.5 \cos x_2, \\
 c_{1,2}^{(1)}(t, x_1) &= \left(450 + \frac{10}{1+t}\right)x_1, \quad c_{2,2}^{(1)}(t, x_2) = \left(430 + \frac{2}{1+t}\right)x_2, \\
 c_{1,2}^{(2)}(t, x_1) &= \left(850 + \frac{1}{1+t}\right)x_1, \quad c_{2,2}^{(2)}(t, x_2) = \left(830 + \frac{3}{1+t}\right)x_2, \\
 a_{11,2}^{(1)}(t) &= 0.1 + \frac{0.8}{1+t}, \quad a_{21,2}^{(1)}(t) = 0.2 + \frac{0.4}{1+t}, \quad a_{12,2}^{(1)}(t) = 0.3 + \frac{0.3}{1+t}, \quad a_{22,2}^{(1)}(t) = 0.4 + \frac{0.1}{1+t}, \\
 a_{11,2}^{(2)}(t) &= 0.8 + \frac{0.3}{1+t}, \quad a_{21,2}^{(2)}(t) = 0.1 + \frac{0.5}{1+t}, \quad a_{12,2}^{(2)}(t) = 0.1 + \frac{0.5}{1+t}, \quad a_{22,2}^{(2)}(t) = 0.2 + \frac{0.1}{1+t}, \\
 b_{11,2}^{(1)}(t) &= \frac{0.2}{1+t}, \quad b_{21,2}^{(1)}(t) = b_{12,2}^{(1)}(t) = 1.6 + \frac{0.2}{1+t}, \quad b_{22,2}^{(1)}(t) = 0.6, \\
 b_{11,2}^{(2)}(t) &= \frac{1.2}{1+t}, \quad b_{21,2}^{(2)}(t) = b_{12,2}^{(2)}(t) = 0.6 + \frac{0.2}{1+t}, \quad b_{22,2}^{(2)}(t) = 2, \\
 f_{1,2}^{(1)}(x_1) &= 0.3 \tanh(x_1), \quad f_{2,2}^{(1)}(x_2) = 0.5 \tanh(x_2), \\
 f_{1,2}^{(2)}(x_1) &= 0.6 \tanh(x_1), \quad f_{2,2}^{(2)}(x_2) = 0.8 \tanh(x_2),
 \end{aligned}$$

$$\begin{aligned}
g_{1,2}^{(1)}(y_1) &= 6 \tanh(y_1), \quad g_{2,2}^{(1)}(y_2) = 8 \tanh(y_2), \\
g_{1,2}^{(2)}(y_1) &= 3 \tanh(y_1), \quad g_{2,2}^{(2)}(y_2) = 3 \tanh(y_2), \\
d_{11,2}^{(1)}(t) &= e^{-t}/3, \quad d_{21,2}^{(1)}(t) = \frac{1}{3(1+t)}, \quad d_{12,2}^{(1)}(t) = \frac{0.6}{1+t^2}, \quad d_{22,2}^{(1)}(t) = e^{-t} \cos t/4, \\
d_{11,2}^{(2)}(t) &= e^{-t}/2, \quad d_{21,2}^{(2)}(t) = \frac{1}{9(1+t)}, \quad d_{12,2}^{(2)}(t) = \frac{0.6}{1+t^2}, \quad d_{22,2}^{(2)}(t) = e^{-t} \sin t/2, \\
k_{1,2}^{(1)}(x_1) &= x_1, \quad k_{2,2}^{(1)}(x_2) = \frac{x_2}{7}, \quad k_{1,2}^{(2)}(x_1) = \frac{x_1}{3}, \quad k_{2,2}^{(2)}(x_2) = \frac{2x_2}{3}, \\
\eta_{1,2}^{(21)}(t, x_1, y) &= \frac{2.5}{1+t^2}(x_1^2 + y_1^2 + y_2^2), \quad \eta_{2,2}^{(21)}(t, x_2, y) = \frac{2.5}{1+t^2}(x_2^2 + y_1^2 + y_2^2), \\
\eta_{1,2}^{(12)}(t, x_1, y) &= 0.8|\sin t|(x_1^2 + y_1^2 + y_2^2), \quad \eta_{1,2}^{(12)}(t, x_2, y) = 0.8|\sin t|(x_2^2 + y_1^2 + y_2^2), \\
\zeta_{1,2}^{(21)}(t, x_1, y) &= \frac{\sqrt{0.75}x_1 + \sqrt{0.375}(y_1 + y_2)}{1 + e^t}, \quad \zeta_{2,2}^{(21)}(t, x_2, y) = \frac{\sqrt{0.75}x_2 + \sqrt{0.375}(y_1 + y_2)}{1 + t^3}, \\
\zeta_{1,2}^{(12)}(t, x_1, y) &= \frac{x_1 + 2^{-\frac{1}{2}}(y_1 + y_2)}{1 + t^2}, \quad \zeta_{2,2}^{(12)}(t, x_2, y) = \frac{x_1 + 2^{-\frac{1}{2}}(y_1 + y_2)}{e^t}, \\
\sigma_{11,2}^{(1)}(t, x_1, z_{11}) &= \frac{7\sqrt{2}x_1 + \sqrt{7}z_{11}}{2\sqrt{1+t^2}}, \quad \sigma_{21,2}^{(1)}(t, x_1, z_{21}) = \frac{3x_1 + \sqrt{3}z_{21}}{e^t}, \\
\sigma_{12,2}^{(1)}(t, x_2, z_{12}) &= 24^{\frac{1}{4}}\sqrt{|x_2z_{12}|} \sin 2t, \quad \sigma_{22,2}^{(1)}(t, x_2, z_{22}) = \frac{\sqrt{10}x_2 \cos t + z_{22}}{\sqrt{2(1+t^2)}}, \\
\sigma_{11,2}^{(2)}(t, x_1, z_{11}) &= \frac{2\sqrt{5}x_1 + 2z_{11}}{\sqrt{1+t^2}}, \quad \sigma_{21,2}^{(2)}(t, x_1, z_{21}) = \sqrt{6}x_1 \cos(t) + \sqrt{3}z_{21}, \\
\sigma_{12,2}^{(2)}(t, x_2, z_{12}) &= 40^{\frac{1}{4}}\sqrt{|x_2z_{12}|} \exp^{-2t}, \quad \sigma_{22,2}^{(2)}(t, x_2, z_{22}) = \frac{\sqrt{10}x_2 \sin t + z_{22}}{\sqrt{2+t^2}}.
\end{aligned}$$

For the delay kernel functions which do not depend on the state of the Markov chain, we have: for $k \in \{1, 2\}$

$$l_{11}^{(k)}(t) = \frac{4}{(1+t^2)^2}, \quad l_{12}^{(k)}(t) = \frac{\cos t}{e^{4t}}, \quad l_{21}^{(k)}(t) = l_{22}^{(k)}(t) = \frac{\arctg t}{(1+t^2)^2} \quad \text{and} \quad l(t) = \frac{4}{1+t^4}.$$

In the impulsive moments t_m , $m \in \mathbb{N}$, we assume that $I_{1m}(x) = x_1/4$, $I_{2m}(x) = x_2/4$, $J_{1m}(y) = 2^{-(m+2)}y_1$, $J_{2m}(y) = 2^{-(m+2)}y_2$.

Using the simple inequality $(a+b)^2 \leq 2(a^2+b^2)$, we can easily calculate the following parameters and verify the assumptions **(H₁)** – **(H₈)**.

For $\rho = 1$

$$\begin{aligned}
\underline{h}_{1,1}^{(1)} &= 1.5, \quad \bar{h}_{1,1}^{(1)} = 2, \quad \underline{h}_{2,1}^{(1)} = 1.5, \quad \bar{h}_{2,1}^{(1)} = 1.7, \quad \underline{h}_{1,1}^{(2)} = 2.5, \quad \bar{h}_{1,1}^{(2)} = 3, \quad \underline{h}_{2,1}^{(2)} = 1.7, \quad \bar{h}_{2,1}^{(2)} = 2.7, \\
\underline{c}_{1,1}^{(1)} &= 400, \quad \underline{c}_{2,1}^{(1)} = 420, \quad \underline{c}_{1,1}^{(2)} = 800, \quad \underline{c}_{2,1}^{(2)} = 820, \\
\bar{a}_{11,1}^{(1)} &= 0.5, \quad \bar{a}_{21,1}^{(1)} = 0.3, \quad \bar{a}_{12,1}^{(1)} = 0.3, \quad \bar{a}_{22,1}^{(1)} = 0.6, \quad \bar{a}_{11,1}^{(2)} = 0.8, \quad \bar{a}_{21,1}^{(2)} = 0.7, \quad \bar{a}_{12,1}^{(2)} = 1, \quad \bar{a}_{22,1}^{(2)} = 0.3,
\end{aligned}$$

$$\begin{aligned} \bar{b}_{11,1}^{(1)} &= 0.1, \bar{b}_{21,1}^{(1)} = 2, \bar{b}_{12,1}^{(1)} = 2, \bar{b}_{22,1}^{(1)} = 0.3, \bar{b}_{11,1}^{(2)} = 0.6, \bar{b}_{21,1}^{(2)} = 1.5, \bar{b}_{12,1}^{(2)} = 1.5, \bar{b}_{22,1}^{(2)} = 1.8, \\ \bar{f}_{1,1}^{(1)} &= 0.2, \bar{f}_{2,1}^{(1)} = 0.4, \bar{f}_{1,1}^{(2)} = 0.5, \bar{f}_{2,1}^{(2)} = 0.7, \bar{g}_{1,1}^{(1)} = 5, \bar{g}_{2,1}^{(1)} = 7, \bar{g}_{1,1}^{(2)} = 2, \bar{g}_{2,1}^{(2)} = 2, \\ \bar{d}_{11,1}^{(1)} &= \frac{1}{6}, \bar{d}_{21,1}^{(1)} = \frac{1}{9}, \bar{d}_{12,1}^{(1)} = 0.3, \bar{d}_{22,1}^{(1)} = \frac{1}{12}, \bar{d}_{11,1}^{(2)} = \frac{1}{6}, \bar{d}_{21,1}^{(2)} = \frac{5}{9}, \bar{d}_{12,1}^{(2)} = 0.2, \bar{d}_{22,1}^{(2)} = 0.1, \\ \bar{k}_{1,1}^{(1)} &= \frac{1}{3}, \bar{k}_{2,1}^{(1)} = 0.5, \bar{k}_{1,1}^{(2)} = \frac{1}{3}, \bar{k}_{2,1}^{(2)} = 0.25, \\ \bar{\eta}_1^{(11)} &= 0, \bar{\eta}_1^{(21)} = 2.5, \bar{\eta}_1^{(12)} = 0.8, \bar{\eta}_1^{(22)} = 0, \bar{\zeta}_1^{(11)} = 0, \bar{\zeta}_1^{(21)} = 2.7, \bar{\zeta}_1^{(12)} = 4, \bar{\zeta}_1^{(22)} = 0, \\ \mu_{11,1}^{(1)} &= 40, \mu_{21,1}^{(1)} = 16, \mu_{12,1}^{(1)} = 4, \mu_{22,1}^{(1)} = 8, \mu_{11,1}^{(2)} = 36, \mu_{21,1}^{(2)} = 12, \mu_{12,1}^{(2)} = 2, \mu_{22,1}^{(2)} = 7, \\ \nu_{11,1}^{(1)} &= 6, \nu_{21,1}^{(1)} = 5, \nu_{12,1}^{(1)} = 1, \nu_{22,1}^{(1)} = 2, \nu_{11,1}^{(2)} = 4, \nu_{21,1}^{(2)} = 3, \nu_{12,1}^{(2)} = 1, \nu_{22,1}^{(2)} = 1. \end{aligned}$$

For $\rho = 2$

$$\begin{aligned} \underline{h}_{1,2}^{(1)} &= 1.7, \bar{h}_{1,2}^{(1)} = 2.2, \underline{h}_{2,2}^{(1)} = 1.7, \bar{h}_{2,2}^{(1)} = 1.9, \underline{h}_{1,2}^{(2)} = 2.6, \bar{h}_{1,2}^{(2)} = 3.2, \underline{h}_{2,2}^{(2)} = 1.9, \bar{h}_{2,2}^{(2)} = 2.9, \\ \underline{c}_{1,2}^{(1)} &= 450, \bar{c}_{2,2}^{(1)} = 430, \underline{c}_{1,2}^{(2)} = 850, \bar{c}_{2,2}^{(2)} = 830, \\ \bar{a}_{11,2}^{(1)} &= 0.9, \bar{a}_{21,2}^{(1)} = 0.6, \bar{a}_{12,2}^{(1)} = 0.6, \bar{a}_{22,2}^{(1)} = 0.5, \bar{a}_{11,2}^{(2)} = 1.1, \bar{a}_{21,2}^{(2)} = 0.6, \bar{a}_{12,2}^{(2)} = 0.6, \bar{a}_{22,2}^{(2)} = 0.3, \\ \bar{b}_{11,2}^{(1)} &= 0.2, \bar{b}_{21,2}^{(1)} = 1.8, \bar{b}_{12,2}^{(1)} = 1.8, \bar{b}_{22,2}^{(1)} = 0.6, \bar{b}_{11,2}^{(2)} = 1.2, \bar{b}_{21,2}^{(2)} = 0.8, \bar{b}_{12,2}^{(2)} = 0.8, \bar{b}_{22,2}^{(2)} = 2, \\ \bar{f}_{1,2}^{(1)} &= 0.3, \bar{f}_{2,2}^{(1)} = 0.5, \bar{f}_{1,2}^{(2)} = 0.6, \bar{f}_{2,2}^{(2)} = 0.8, \bar{g}_{1,2}^{(1)} = 6, \bar{g}_{2,2}^{(1)} = 8, \bar{g}_{1,2}^{(2)} = 3, \bar{g}_{2,2}^{(2)} = 3, \\ \bar{d}_{11,2}^{(1)} &= \frac{1}{3}, \bar{d}_{21,2}^{(1)} = \frac{1}{3}, \bar{d}_{12,2}^{(1)} = 0.6, \bar{d}_{22,2}^{(1)} = 0.25, \bar{d}_{11,2}^{(2)} = 0.5, \bar{d}_{21,2}^{(2)} = \frac{1}{9}, \bar{d}_{12,2}^{(2)} = 0.6, \bar{d}_{22,2}^{(2)} = 0.5, \\ \bar{k}_{1,2}^{(1)} &= 1, \bar{k}_{2,2}^{(1)} = \frac{1}{7}, \bar{k}_{1,2}^{(2)} = \frac{1}{3}, \bar{k}_{2,2}^{(2)} = \frac{2}{3}, \\ \bar{\eta}_2^{(11)} &= 0, \bar{\eta}_2^{(21)} = 0.5, \bar{\eta}_2^{(12)} = 0.4, \bar{\eta}_2^{(22)} = 0, \bar{\zeta}_2^{(11)} = 0, \bar{\zeta}_2^{(21)} = 1.5, \bar{\zeta}_2^{(12)} = 2, \bar{\zeta}_2^{(22)} = 0, \\ \mu_{11,2}^{(1)} &= 49, \mu_{21,2}^{(1)} = 18, \mu_{12,2}^{(1)} = 6, \mu_{22,2}^{(1)} = 10, \mu_{11,2}^{(2)} = 40, \mu_{21,2}^{(2)} = 12, \mu_{12,2}^{(2)} = 5, \mu_{22,2}^{(2)} = 10, \\ \nu_{11,2}^{(1)} &= 7, \nu_{21,2}^{(1)} = 6, \nu_{12,2}^{(1)} = 1, \nu_{22,2}^{(1)} = 1, \nu_{11,2}^{(2)} = 8, \nu_{21,2}^{(2)} = 6, \nu_{12,2}^{(2)} = 2, \nu_{22,2}^{(2)} = 1. \end{aligned}$$

Let $V_\rho^{(k)}(x^{(k)}) = \theta_\rho^{(k)} |x_1^{(k)}|^4 + \theta_\rho^{(k)} |x_2^{(k)}|^4$, where $\theta_1^{(1)} = \theta_2^{(2)} = 1$ and $\theta_2^{(1)} = \theta_1^{(2)} = 2$. Using the calculated parameters, and equations (15) and (16), we obtain

$$\begin{aligned} \epsilon_1 &= -1547.12, & q_1(t) &= \frac{2.667}{1+t^4}, & w_1 &= 84, \\ \epsilon_2 &= -2104.5, & q_2(t) &= \frac{8.9867}{1+t^4}, & w_2 &= 102.48, \end{aligned}$$

The choice of the decay function depends straightforwardly on the kernel functions. Since $l_{ij}^{(k)}(t) \leq l(t) = \frac{4}{1+t^4}$ for $i, j, k = 1, 2$ and since $\int_0^\infty \frac{4e^{\gamma s}}{1+s^4} ds$ does not converge for any $\gamma > 0$, condition **(H₆)** is not fulfilled and, therefore, we cannot discuss exponential stability.

Let $\lambda(t) = 1$ for $t < 0$ and $\lambda(t) = 1 + t$ for $t \geq 0$ be a decay function. Since $\lambda(\tau) = \lambda(2) = 3$ and $\int_0^\infty \frac{4(1+s)^\gamma}{1+s^4} ds < \infty$ for all $\gamma \in [0, 3)$, we can take $[\gamma_0^*, \gamma_1^*] = [0, 2.9]$ and compute $I_1 = \max_{\gamma \in [0, 2.9]} \int_0^\infty q_1(s)\lambda^\gamma(s)ds = 42.992$ and $I_2 = \max_{\gamma \in [0, 2.9]} \int_0^\infty q_2(s)\lambda^\gamma(s)ds = 144.884$. Next, we can easily check that for $\rho = 1, 2$ the equations

$$\gamma_\rho + \epsilon_\rho + n w_\rho \lambda^{\gamma_\rho}(\tau) - I_\rho = 0$$

have unique solutions $\gamma_1 = 1.992$ and $\gamma_2 = 2.054$. Also, $\underline{\gamma} = \min\{\gamma_1, \gamma_2\} = 1.992 \in [0, 2.9]$.

For the impulsive moments $m \in \mathbb{N}$, in view of **(H₈)**, we take $I_{11,m} = I_{22,m} = \frac{1}{4}$, $J_{11,m} = J_{22,m} = 2^{-(m+2)}$ and $I_{12,m} = I_{21,m} = J_{12,m} = J_{21,m} = 0$. The condition **(17)** holds, since it is in the form

$$8(I_{11,m}^4 + I_{22,m}^4 + 2(J_{11,m}^4 + J_{22,m}^4)3^{\underline{\gamma}}) = \frac{1}{2^4}(1 + 2^{1-4m}3^{\underline{\gamma}}) \leq 1$$

Thus, by virtue of Theorem 1 we conclude that the system is 4th moment polynomially stable with Lyapunov exponent $\underline{\gamma} = 1.992$.

Remark 2 With a different choice of the delay kernel functions $l_{ij}^{(k)}(t)$, we can also give a suitable example for p th moment exponential stability. Due to the space constraint, we chose to give an example only on p th moment general decay stability, to illustrate the importance of the generalized approach.

5 Conclusions

In this paper, we study the p th moment stability ($p \geq 2$) on a general decay rate for a model of coupled systems of stochastic Cohen-Grossberg neural networks with time delays, impulses and Markovian switching. The results are based on methods from graph theory, the Lyapunov functional method, Dini derivative and some famous inequalities. Additionally, we extend the usual notion on the general decay function. The presented techniques allow us to discuss the p th moment stability even if the exponential stability cannot be shown. The new results improve the results in earlier publications and since the considered model is very general, the results could be applied to different models in the literature and they can be extended to some other types of coupled networks and dynamical systems. A numerical example is given to support the theoretical results.

Acknowledgments This research was partially supported by the Faculty of Computer Science and Engineering at Ss. Cyril and Methodius University, Skopje, Republic of North Macedonia.

References

1. Strogatz, S.H.: Exploring complex networks. *Nature* **410**(6825), 268–276 (2001)
2. Watts, D.J., Strogatz, S.H.: Collective dynamics of ‘small-world’ networks. *Nature* **393**(6684), 440–442 (1998)
3. Barabási, A.L., Albert, R.: Emergence of scaling in random networks. *Science* **286**(5439), 509–512 (1999)
4. Li, M.Y., Shuai, Z.: Global-stability problem for coupled systems of differential equations on networks. *J. Differ. Equ.* **248**(1), 1–20 (2010)
5. Li, W., Song, H., Qu, Y., Wang, K.: Global exponential stability for stochastic coupled systems on networks with Markovian switching. *Syst. Control Lett.* **62**(6), 468–474 (2013)
6. Li, W., Su, H., Wang, K.: Global stability analysis for stochastic coupled systems on networks. *Automatica* **47**(1), 215–220 (2011)
7. , Kao, Y., Wang, C.: Global stability analysis for stochastic coupled reaction–diffusion systems on networks. *Nonlinear Anal. Real World Appl.* **14**(3), 1457–1465 (2013)
8. Lin, Z.: Coupled dynamic systems: from structure towards stability and stabilizability. Ph.D. Thesis, University of Toronto (2006)
9. Guo, Y., Ding, X.: Razumikhin method to global exponential stability for coupled neutral stochastic delayed systems on networks. *Math. Methods Appl. Sci.* **40**(15), 5490–5501 (2017)
10. Liu, Y., Li, W., Feng, J.: The stability of stochastic coupled systems with time-varying coupling and general topology structure. *IEEE Trans. Neural Networks Learn. Syst.* **29**(9), 4189–4200 (2018)
11. Huang, C., He, Y., Chen, P.: Dynamic analysis of stochastic recurrent neural networks. *Neural Process. Lett.* **27**(3), 267–276 (2008)
12. , Huang, C., Cao, J.: Stochastic Dynamics of Nonautonomous Cohen–Grossberg Neural Networks, *Abstract and Applied Analysis*, vol. 2011, pp. 1–17. Hindawi Publishing Corporation (2011)
13. Wang, X., Guo, Q., Xu, D.: Exponential p -stability of impulsive stochastic Cohen–Grossberg neural networks with mixed delays. *Math. Comput. Simul.* **79**(5), 1698–1710 (2009)
14. Peng, S., Zhang, Y.: Razumikhin-type theorems on p th moment exponential stability of impulsive stochastic delay differential equations. *IEEE Trans. Autom. Control* **55**(8), 1917–1922 (2010)
15. Zhu, E., Zhang, H., Wang, Y., Zou, J., Yu, Z., Hou, Z.: p th moment exponential stability of stochastic Cohen–Grossberg neural networks with time-varying delays. *Neural Process. Lett.* **26**(3), 191–200 (2007)
16. He, Q., Liu, D., Wu, H., Ding, S.: Robust exponential stability analysis for interval Cohen–Grossberg type BAM neural networks with mixed time delays. *Int. J. Mach. Learn. Cybern.* **5**(1), 23–38 (2014)
17. Senan, S.: An analysis of global stability of Takagi-Sugeno fuzzy Cohen-Grossberg neural networks with time delays. *Neural Process. Lett.* **48**(3), 1693–1704 (2018)
18. Zhou, X., Zhou, W., Dai, A., Yang, J., Xie, L.: Asymptotical stability of stochastic neural networks with multiple time-varying delays. *Int. J. Control* **88**(3), 613–621 (2015)
19. Song, Q., Wang, Z.: Stability analysis of impulsive stochastic Cohen–Grossberg neural networks with mixed time delays. *Phys. A Stat. Mech. Appl.* **387**(13), 3314–3326 (2008)
20. Liu, L., He, X., Wu, A.: p th moment exponential input-to-state stability of non-autonomous delayed Cohen–Grossberg neural networks with Markovian switching. *Neurocomputing* **349**, 44–51 (2019)

21. Li, Z., Liu, L., Zhu, Q.: Mean-square exponential input-to-state stability of delayed Cohen–Grossberg neural networks with Markovian switching based on vector Lyapunov functions. *Neural Networks* **84**, 39–46 (2016)
22. Liu, Y., Wang, Z., Liu, X.: Stability analysis for a class of neutral-type neural networks with Markovian jumping parameters and mode-dependent mixed delays. *Neurocomputing* **94**, 46–53 (2012)
23. Tojtovska, B., Janković, S.: General decay stability analysis of impulsive neural networks with mixed time delays. *Neurocomputing* **142**, 438–446 (2014)
24. Tojtovska, B., Janković, S.: On a general decay stability of stochastic Cohen–Grossberg neural networks with time-varying delays. *Appl. Math. Comput.* **219**(4), 2289–2302 (2012)
25. Hu, Y., Huang, C.: LaSalle method and general decay stability of stochastic neural networks with mixed delays. *J. Appl. Math. Comput.* **38**(1–2), 257–278 (2012)
26. Li, W., Qi, X., Pan, M., Wang, K.: Razumikhin-type theorems on exponential stability of stochastic functional differential equations on networks. *Neurocomputing* **131**, 278–285 (2014)
27. Mao, X.: Stochastic functional differential equations with Markovian switching. *Funct. Differ. Equ.* **6**(3–4), 375–396 (1999)
28. Mao, X., Matasov, A., Piunovskiy, A.B.: Stochastic differential delay equations with Markovian switching. *Bernoulli* **6**(1), 73–90 (2000)

Stability of Steady States with Complex Behavior in Time



Yuri V. Mikhlin  and Nataliia S. Goloskubova 

Abstract A stability of the NNMs and standing or traveling waves is analyzed by two approaches. One of them is the method of Ince algebraization (IA), when a new independent variable associated with the unperturbed solution is used as independent one. In this case equations in variations transform to equations with singular points. A problem of determination of solutions, corresponding to boundaries of the stability/ instability regions, is reduced here to problem of determination of ones that have singularity at the mentioned points. An advantage of the IA is that in the stability problem we do not need in use of the unperturbed solution time-presentation. Other approach of the steady states stability investigation is associated with the classical Lyapunov definition of stability. An implementation of this definition permits to obtain boundaries between the stability/instability regions in the system parameter space. Such analytical-numerical test can be used in stability problem for periodic vibrations or waves with complex behavior in time when the stability problem has no analytical solution.

Keywords Stability of steady states · Ince algebraization · Lyapunov definition

1 Introduction

Concept of nonlinear normal modes (NNMs), first proposed by Kauderer and Rosenberg [1, 2], is an important step of investigation of the nonlinear systems behavior. In regime of NNM a nonlinear n-DOF system behaves like to the conservative single DOF system. Principal fundamentals of the NNMs theory and different applications of the theory are presented in some books and reviews [3–5]. Stationary standing or traveling waves can be considered as generalization of the NNMs to chains or continuous structures [3, 6].

Y. V. Mikhlin (✉) · N. S. Goloskubova
National Technical University “Kharkiv Polytechnic Institute”, Kharkiv, Ukraine

Different approaches can be used to solve a problem of the vibration modes or stationary waves stability. We refer here only few of numerous books on this subject [7–10]. The stability can be effectively analyzed by the so-called *Algebraization by Ince* [11]. This approach is performed by choosing a new independent variable associated with the solution under consideration. An advantage of this approach is that we do not need to use a specific form of the solution in analysis of the stability problem. This approach was successfully used in a problem of the NNMs stability in some nonlinear conservative systems [3, 4, 12]. The Ince algebraization (IA) can be used also in a problem of stability of nonlinear stationary traveling waves.

The NNMs concept can be used not only for periodic vibrations. In particular, the NNMs having smooth trajectories in configuration space and chaotic in time behavior can be found in some non-conservative systems. Such vibration modes are observed in post-buckling dynamics of elastic systems that have lost stability under external compressive force. The energy transfer from some vibration mode to another one is possible in such systems. Thus one can formulate a problem of the stability of periodic/ chaotic vibration mode in the higher-dimensional spaces. Taking into account that analytical approaches in a case of chaotic motions are absent, moreover, an analysis of stability of stationary states with complex behavior in time, is difficult, the numerical-analytical test which is based on the known Lyapunov definition of stability [7] is used in such stability problem [13]. This test can be used also in a problem of the nonlinear standing waves stability.

The paper is organized as follow. The method of IA is presented in Sect. 2 for the stability of stationary states, in particular, in a problem of stability of NNMs in the so-called sonic vacuum system (Sect. 2.1), and in a problem of the traveling waves stability in the Klein-Gordon equation (Sect. 2.2). The numerical-analytical test of stability (Sect. 3) is used both for problems of stability of NNM in the so-called stochastic absorber (Sect. 3.1), and for standing waves in the model of DNK by Peyrard, Bishop and Dauxois (Sect. 3.2).

2 The Ince Algebraization of Equations in Variations for Nonlinear Normal Modes and Traveling Waves

2.1 Stability of Nonlinear Normal Modes

Consider a problem of stability of the so-called similar NNMs by Rosenberg [2], that is, NNMs with rectilinear trajectories in configuration space. The IA presupposes that in corresponding equations in variations the variable t is replaced by the variable x which defines motion along the rectilinear trajectory. In particular, a use of the IA permits to transfer equations in variations for the homogeneous systems which potential energy is a homogeneous function of generalized coordinates, to the form

of the known hypergeometric equations with two singular points, $z = 0$ and $z = 1$ [3, 4, 12]:

$$z(1-z)v_{zz} + \left[\frac{r}{r+1} - \frac{3r+1}{2(r+1)}z \right] v_z + \lambda v = 0; \tag{1}$$

here λ is eigenvalue of the stability problem. Indexes of the singular point $z = 0$ are equal to 0 and $1/(r + 1)$, indexes of the singular point $z = 1$ are equal to 0 и $1/2$. Solutions corresponding to boundaries of the stability/ instability regions are named as degenerate solutions of the equation [14] and can be presented as

$$v = z^{\mu_1}(1-z)^{\mu_2}q_n(z), \tag{2}$$

where $q_n(z)$ are polynomials, μ_1, μ_2 are indexes of the singular points. These solutions are so-called Gegenbauer polynomials [14]. Values of the parameter λ , corresponding to change of stability, can be obtained in closed form [3, 4, 12]:

One considers now a stability of NNMs in the system of connected oscillators on grounding elastic support under conditions of the so-called sonic vacuum [15, 16]. The system dynamics is described by the following equations:

$$\begin{cases} \mu \frac{d^2 v_1}{dt^2} + v_1^3 + \frac{\mu}{6} [v_1^2 + (v_2 - v_1)^2 + v_2^2] (2v_1 - v_2) = 0 \\ \mu \frac{d^2 v_2}{dt^2} + v_2^3 + \frac{\mu}{6} [v_1^2 + (v_2 - v_1)^2 + v_2^2] (2v_2 - v_1) = 0 \end{cases}, \tag{3}$$

where the parameter μ presents an influence of the elastic support. After the following transformation, $z_1 = \frac{v_1+v_2}{\sqrt{2}}, z_2 = \frac{v_1-v_2}{\sqrt{2}}$, the Eq. (3) can be rewritten as

$$\begin{cases} \mu \frac{d^2 z_1}{dt^2} + 0.5(z_1^2 + 3z_2^2)z_1 + \frac{\mu}{3}[z_1^2 + 3z_2^2]z_1 = 0 \\ \mu \frac{d^2 z_2}{dt^2} + 0.5(z_2^2 + 3z_1^2)z_2 + \mu[z_1^2 + 3z_2^2]z_2 = 0 \end{cases} \tag{4}$$

The system (4) allows two similar nonlinear normal modes, namely,

1. $z_2 = 0, z_1 = z_1(t)$; where an equation in variations in direction which is orthogonal to the NNM, is the following:

$$\mu \frac{d^2 u}{dt^2} + (1.5 + \mu) z_1^2 u = 0 \tag{5}$$

2. $z_1 = 0, z_2 = z_2(t)$; where an equation in variations in direction which is orthogonal to the NNM, is the following:

$$\mu \frac{d^2 u}{dt^2} + \left(1.5 + \frac{\mu}{3}\right) z_2^2 u = 0 \tag{6}$$

Integral of energy for the first NNM is the following:

$$\frac{\mu}{2} \left(\frac{dz_1}{dt} \right)^2 + \left(0.5 + \frac{\mu}{3} \right) \frac{z_1^4}{4} = h \quad (7)$$

Equation of motion along the first NNM is presented as

$$\mu \frac{d^2 z_1}{dt^2} + \left(0.5 + \frac{\mu}{3} \right) z_1^3 = 0 \quad (8)$$

We use the IA introducing a new independent variable z_1 instead of t . After some transformations using relations (7) and (8), one obtains the equation in variations in the form of the following equation with singularities:

$$\frac{d^2 u}{dz_1^2} \left(2h - \left(0.5 + \frac{\mu}{3} \right) \frac{z_1^4}{2} \right) - \frac{du}{dz_1} \left\{ \left(0.5 + \frac{\mu}{3} \right) z_1^3 \right\} + u \left(1.5\mu + \mu^2 \right) z_1^2 = 0 \quad (9)$$

The singularities are calculated from the equation

$$2h - \left(0.5 + \frac{\mu}{3} \right) \frac{\Phi_0^4}{2} = 0, \quad (10)$$

Indices of these singularities are equal to $r_1 = 0$ and $r_2 = \frac{1}{2}$. It is known [7–10] that T - and $2T$ -periodic solutions of the equation in variations determine boundaries of the stability/instability regions for the NNM under consideration in the system parameter space, where T is a period of the equation coefficients. In the equation with singularities such “boundary” solutions are determined by the following expansions [10, 12]:

$$u = z^r (a_0 + a_1 z + \dots), \quad (11)$$

where r is one of two indices of the singularity point; $z = z_1 - \Phi_0$; here Φ_0 is a root of the Eq. (10). Introducing the series (11), corresponding to zero index, to Eq. (9), and equating coefficients of the same degree by z , one obtains the following infinite recurrent system of linear homogeneous algebraic equations to determine coefficients of the series (11):

$$\begin{aligned} z_0 : & \quad a_0 [1.5\mu + \mu^2] \Phi_0^2 + a_1 \left(0.5 + \frac{\mu}{3} \right) \Phi_0^3 + a_2 \left\{ 4h - \left(0.5 + \frac{\mu}{3} \right) \right\} \Phi_0^4 = 0; \\ z_1 : & \quad a_0 \{ 3\mu + 2\mu^2 \} \Phi_0 + a_1 (1.5 + 2.5\mu + \mu^2) \Phi_0^2 - a_2 (3 + 2\mu) \Phi_0^3 = 0; \\ z_2 : & \quad a_1 \{ (1.5 + 4\mu + 2\mu^2) \Phi_0 + [1.5\mu + \mu^2] \} + a_2 [-2 - 2.5\mu + \mu^2] \Phi_0^2 = 0, \end{aligned} \quad (12)$$

etc.

The system (12) has non-trivial solution if determinant of the system equal to zero. This determinant is calculated up to the 5-th order inclusively, and, thus, relations connecting the system parameters are obtained; so, boundaries of the stability/instability regions in the system parameter space can be constructed. Note that boundaries obtained by calculation of determinants of the 4-th and 5-th orders are close, thus, we did not calculate determinants of the highest order than five.

Substituting the expansion (11), corresponding to the second index r_2 , to the equation in variations (9) and equating coefficients of the same degree by z , one obtains the following infinite recurrent system of linear homogeneous algebraic equations to determine coefficients of the series (11):

$$\begin{aligned}
 z^{-\frac{1}{2}} : 0.75a_1 (2h - (0.25 + \frac{\mu}{2}) \Phi_0^4) &= 0; \\
 z^{\frac{1}{2}} : a_0 \{1.25\mu - 0.375 + \mu^2\} \Phi_0^2 - a_1 (1 + \frac{2}{3}\mu) \Phi_0^3 + a_2 \frac{15}{4} (2h - (0.25 + \frac{\mu}{2}) \Phi_0^4) &= 0; \\
 z^{\frac{3}{2}} : a_0 (2.5\mu + 2\mu^2 - 0.5) \Phi_0 - a_1 (3.375 + 0.75\mu - \mu^2) \Phi_0^2 - a_2 (5 + \frac{10\mu}{3}) \Phi_0^3 &= 0
 \end{aligned}
 \tag{13}$$

etc.

Thus, it is obtained one more system of linear homogeneous algebraic equations, which has non-trivial solution if the system determinant equal to zero. This determinant is calculated up to the 5-th order inclusively, and, thus, relations connecting the system parameters are obtained; so, boundaries of the stability/instability regions in the system parameter space can be constructed. Similar transformations are made in Eq. (6) for variations which are orthogonal to the second NNM.

In Fig. 1 boundaries between regions of the both NNMs stability/ instability on place of the system energy h and the parameter μ are shown. In Fig. 1a the boundary is shown for the first NNM; one has from Eq. (10) that here $\Phi_0 \in [0.941; 1.682]$. The boundary is the same for both indices r_1 and r_2 . In Fig. 1b the boundary is shown for the second NNM; one has from Eq. (10) that here $\Phi_0 \in [0.404; 1.185]$. Boundary is coinciding for both indices r_1 and r_2 too. Regions of stability here are situated from the left of the boundary in Fig. 1a, and from the right in Fig. 1b.

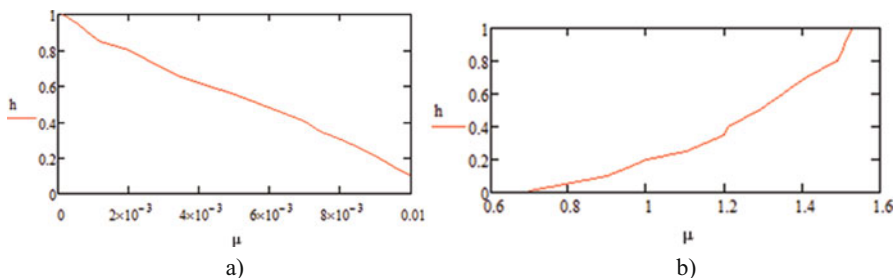


Fig. 1 Boundaries of regions of stability/ instability on place (h, μ) for the first NNM of the system under consideration **(a)** and for the second one **(b)**

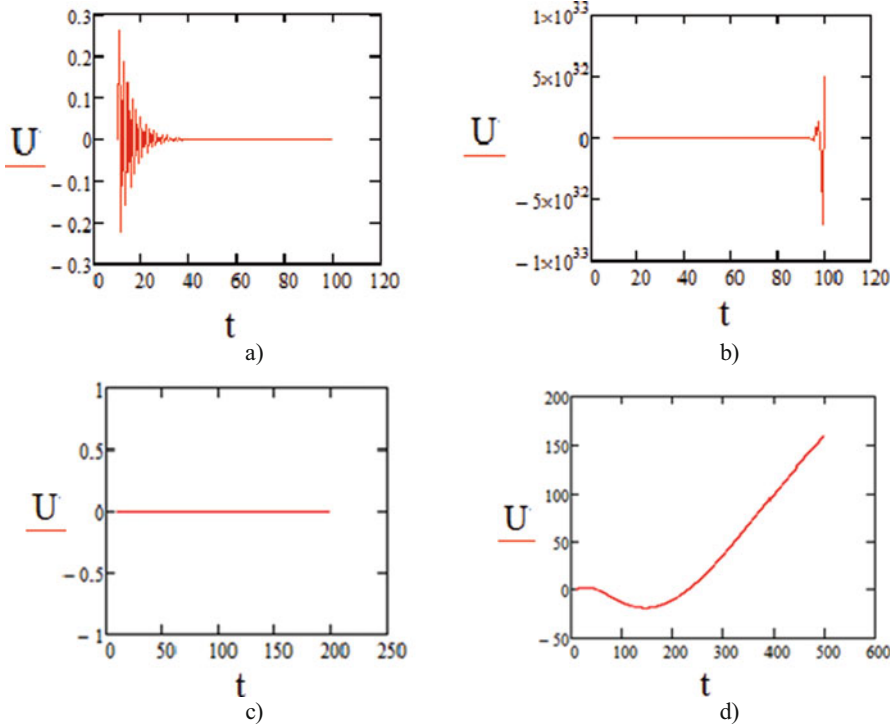


Fig. 2 Limited and unlimited solutions of the equation in variations; (a) $h = 0.2, \mu = 0.008$; (b) $h = 0.9, \mu = 0.002$; (c) $h = 0.6, \mu = 0.002$; (d) $h = 0.4, \mu = 0.009$

As illustration of the obtained results, limited and unlimited solutions of the equations in variations are constructed by the Runge-Kutta method. Parameters μ and h for the calculations are chosen from regions of stability/ instability presented in Fig. 1. In particular, in Fig. 2 such solutions are chosen from regions of stability or instability, shown in Fig. 1a, for the following cases: (a) $h = 0.2, \mu = 0.008$; (b) $h = 0.9, \mu = 0.002$; (c) $h = 0.6, \mu = 0.002$; (d) $h = 0.4, \mu = 0.009$. In Fig. 3 such solutions are chosen from regions of stability or instability, shown in Fig. 1b, for the following cases: (a) $h = 0.2, \mu = 1.25$; (b) $h = 0.6, \mu = 1$; (c) $h = 0.05, \mu = 1$; (d) $h = 0.5, \mu = 1.2$.

2.2 Stability of Traveling Waves in the Klein-Gordon Equation

One considers the Klein-Gordon equation [17] with cubic nonlinearity:

$$\frac{\partial^2 u}{\partial t^2} - c_0^2 \frac{\partial^2 u}{\partial x^2} + \omega_0^2 u = -qu^3 \tag{14}$$

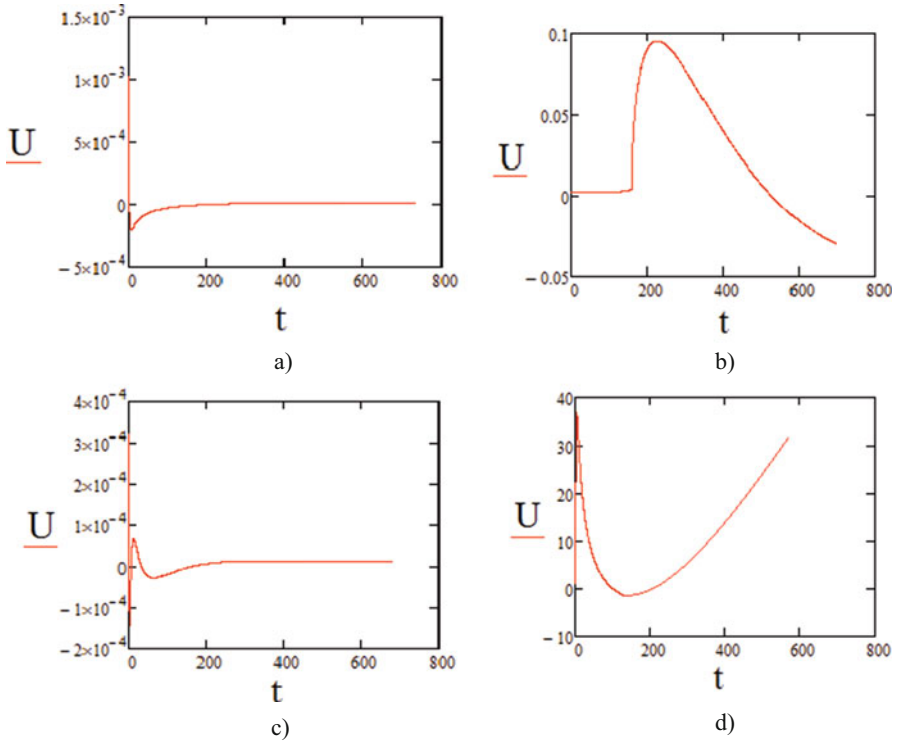


Fig. 3 Limited and unlimited solutions of the equation in variations; (a) $h = 0.2, \mu = 1.25$; (b) $h = 0.6, \mu = 1$; (c) $h = 0.05, \mu = 1$; (d) $h = 0.5, \mu = 1.2$

Stationary traveling waves are presented here in the following form:

$$u = \Phi(\varphi), \varphi = kx - \omega t \tag{15}$$

where φ is the wave phase. Substituting (15) into Eq. (14), we obtain the following ordinary differential equation to describe the traveling waves:

$$\frac{d^2\Phi}{d\varphi^2} (\omega^2 - c_0^2 k^2) + \omega_0^2 \Phi + q \Phi^3 = 0 \tag{16}$$

The energy integral can be written here as

$$\frac{1}{2} \left(\frac{d\Phi}{d\varphi} \right)^2 (\omega^2 - c_0^2 k^2) + \omega_0^2 \frac{\Phi^2}{2} + q \frac{\Phi^4}{4} = h \tag{17}$$

In addition, from Eq. (16), (17) we can obtain the following relations, which will be used later in analysis of the traveling waves stability:

$$\frac{d^2\Phi}{d\varphi^2} = \frac{-\omega_0^2\Phi - q\Phi^3}{\omega^2 - c_0^2k^2}, \left(\frac{d\Phi}{d\varphi}\right)^2 = \frac{2\left(h - \omega_0^2\frac{\Phi^2}{2} - q\frac{\Phi^4}{4}\right)}{\omega^2 - c_0^2k^2}. \quad (18)$$

To study the stability of stationary waves, we write out, first of all, the linearized equation in variations $V(t, x)$ obtained for the solution (15). One has from the Eq. (14) the following:

$$\frac{\partial^2 V}{\partial t^2} = c_0^2 \frac{\partial^2 V}{\partial x^2} - V(\omega_0^2 + 3q\Phi^2), \quad (19)$$

where the function $\Phi(\varphi)$ is determined by the Eq. (16).

As the first step, we now introduce the independent variables φ, t instead of the variables x, t . The Eq. (19) in the new variables is presented as follows:

$$\frac{\partial^2 V}{\partial \varphi^2} (\omega^2 - c_0^2k^2) - 2\omega \frac{\partial^2 V}{\partial \varphi \partial t} + \frac{\partial^2 V}{\partial t^2} = -V(\omega_0^2 + 3q\Phi^2). \quad (20)$$

Then we use the separation of variables as $V = e^{st} \check{z}(\varphi)$ and the transformation, $\check{z}(\varphi) = e^{A\varphi} W$, where $A = \frac{s\omega}{\omega^2 - c_0^2k^2}$. As a result, the Eq. (20) can be presented as

$$\frac{d^2 W}{d\varphi^2} (\omega^2 - c_0^2k^2) = -W(B - \omega_0^2 - 3q\Phi^2), \quad (21)$$

where $B = \frac{s^2}{c_0^2k^2 - \omega^2}$. Note that since namely the parameter s^2 is presented in Eq. (16), in the case of real values of the parameter s , values of the parameter can be both positive and negative. In view of the preceding transformation, it leads to increase of the variations, that is, to instability. Thus, stability can be observed only if $s^2 < 0$. One has from here that for the stability there should be the following inequalities:

$$B > 0, \text{ if } c_0^2k^2 - \omega^2 < 0 \text{ and } B < 0, \text{ if } c_0^2k^2 - \omega^2 > 0. \quad (22)$$

Then, as a new independent variable, the variable Φ , determining the traveling wave under consideration, is chosen instead of φ . Use of the relations (18) permits to present the equation of variations as the following equation:

$$2\frac{d^2 W}{d\Phi^2} \left(h - \omega_0^2\frac{\Phi^2}{2} - q\frac{\Phi^4}{4}\right) - \frac{dW}{d\Phi} (\omega_0^2\Phi + 3q\Phi^3) + W(B - \omega_0^2 - 3q\Phi^2) = 0, \quad (23)$$

whose singular points can be obtained from the equation

$$h - \omega_0^2 \frac{\Phi^2}{2} - q \frac{\Phi^4}{4} = 0 \quad (24)$$

The transformation of the equation in variations to the form of Eq. (23) corresponds to the IA of the stability problem. Here we do not need in use of the specific form of the solution $\Phi(\varphi)$. According to the preceding sub-Section boundaries of the stability/instability regions in the parameter space of the equation in variations with singular points are connected with solutions presented by the following series:

$$W = z^r (a_0 + a_1 z + \dots). \quad (25)$$

Here r is one of two indices of singularity of the equation in variations; $z = (\Phi - \Phi_0)$; Φ_0 is some root of the Eq. (24). One has $r_1 = 0$ and $r_2 = -\frac{2q\Phi_0^2}{\omega_0^2 + q\Phi_0^2}$.

Substituting then the series (25) corresponding to the zero index to the equation in variations (23) and equating coefficients with the same degrees by z , we get the infinite recurrent system of linear homogeneous algebraic equations to determine coefficients of the series, which are not presented here. Such systems allow a non-trivial solution if their determinants are equal to zero. The determinants are calculated up to the 5-th order inclusively, and, thus, relations connecting the system parameters are obtained; so, boundaries of the stability/ instability regions in the system parameter space can be constructed. Note that boundaries obtained by calculation of determinants of the 4-th and 5-th orders are close, thus, we did not calculate determinants of the highest order than five. Similar transformations are made for the index r_2 .

Obtained boundaries of the stability/ instability regions in the place of the parameters B , h are presented in Fig. 4 for both indices. Here we fix the traveling wave amplitude, namely, it is assumed that $\Phi_0 = 1$; thus, the frequency $\omega = 1.5$; $c_0 = 1$; $k = 0.1$. Here the parameter q is calculated from the Eq. (24); thus, one has $c_0^2 k^2 - \omega^2 = -2.24$. In Fig. 4 region of instability is situated between the boundaries.

The Runge-Kutta test for the equation in variations (23) is used to show limited/unlimited solutions when parameters are chosen from the stability/ instability regions presented in Fig. 4. Such limited solutions are shown in Fig. 5. Here the system energy $h = 0.4$ and the parameter $B = 2$ are used for Fig. 2a; $h = 14$ and $B = 3$ are used for Fig. 2b. Other parameters correspond to ones used for Fig. 4. Unlimited solutions of the equation in variations are presented when the parameters are chosen in the instability region showed in Fig. 4, where $h = 1$, $B = 2$ (Fig. 2c); $h = 5$, $B = 1$ (Fig. 2d).

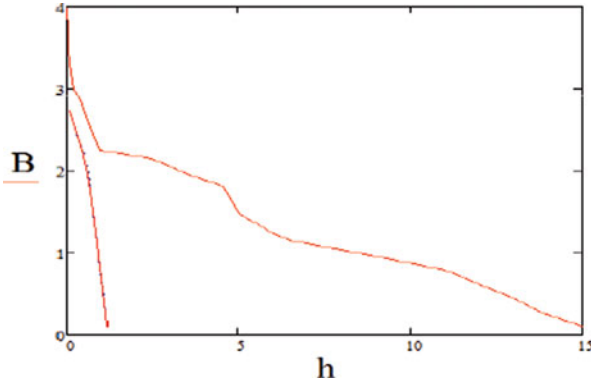


Fig. 4 Boundaries of the stability/ instability regions in the place (B, h) for the index r_1 (right boundary) and for the index r_2 (left boundary)

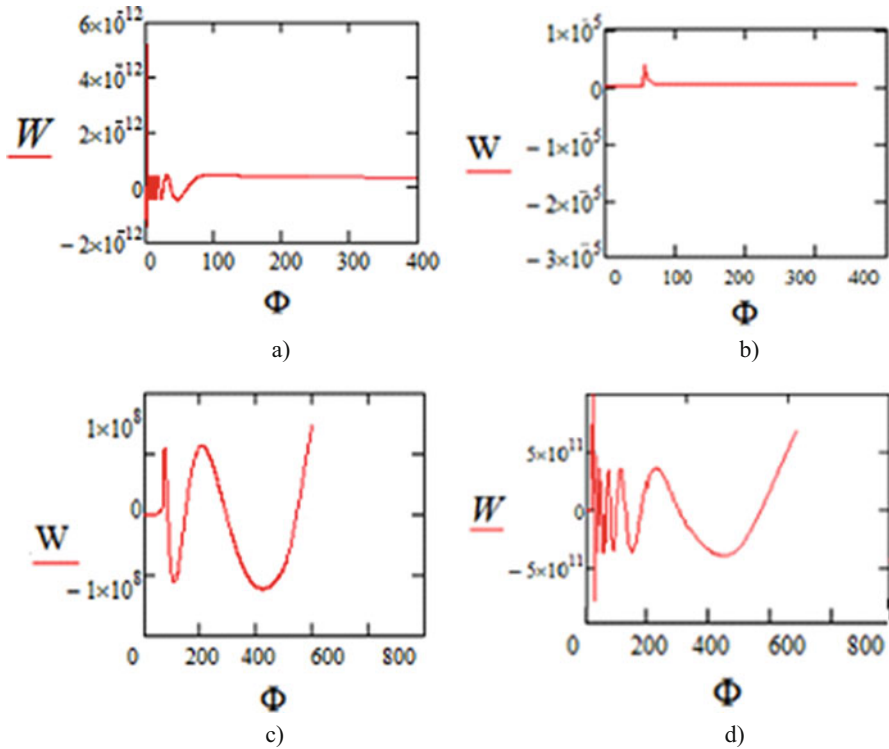


Fig. 5 Limited and unlimited solutions of the equation in variations chosen in regions of stability/instability. Calculations are made for $h = 0.4, B = 2$ (a); $h = 10, B = 2$ (b); $h = 1, B = 2$ (c); $h = 5, B = 1$ (d)

3 Analytical-Numerical Criterion of Stability for Nonlinear Normal Modes and Traveling Waves

3.1 Stability of Nonlinear Normal Mode with Complex Behavior in Time

Often a problem of stability of modes or stationary waves with complex behavior in time has no analytical solution. In particular, it concerns to stability problem in post-buckling behavior of elastic systems, such as roads, plates, shells, when chaotic in time behavior can be observed [18, 19]. The stability of NNMs with complex behavior in time is considered here by use of the numerical-analytical approach based on the known Lyapunov definition of stability [7]. One has the following test for the system under consideration [18]. Instability of the solution $y = 0$ is fixed if

$$|y(t)| \geq \rho |y(0)| \quad (0 \leq t \leq T) \quad (26)$$

In contrast to the Lyapunov definition a time of calculations T is limited in the test (26). We discuss now a choice of the constant T . All concrete calculations are made at points of some chosen mesh of the system parameter space. Calculations are conducted as long as boundaries of stability/instability regions in a chosen scale on the system parameter space are variable. This is a principal criterion for the choice of the calculation time T [18]. There is also some arbitrariness in a choice of the value ρ . In fact, in the instability region the variations leave the solution ε -neighborhood under increase of t for any choice of the parameter ρ . We can choose, in particular, $\rho = 10$.

One considers now a stability of horizontal vibration mode in model of the so-called stochastic absorber. Such model exhibiting one-directional long-term trends in energy exchange flows is introduced in [20]. The stochastic absorber is shaped as a typical contour of the potential energy determining interactions with one or few inner particles with the container wall. The container is attached with massive well by linearly elastic spring (Fig. 6). Equations of motion of the single particle for the system in a small neighborhood of the NNM $y = 0$ are the following [20]:

$$\ddot{x} + x^{2n-1} = \frac{\mu}{1 + \mu} + \left[\ddot{x} + \frac{(\alpha - \beta)^2}{\gamma} X \right]$$

$$\ddot{y} + \lambda x^{2n} y = 0 \quad (27)$$

$$\ddot{X} + \mu (\ddot{X} + \ddot{x}) + X = 0$$

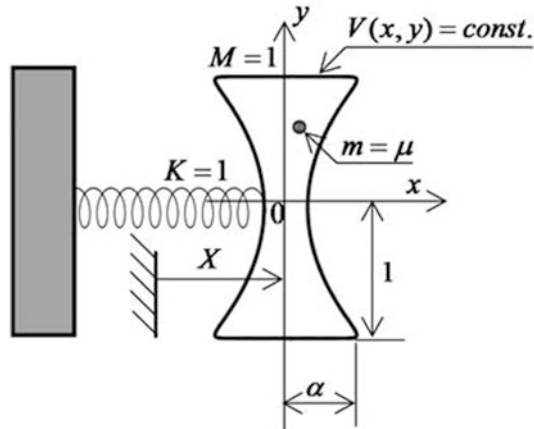


Fig. 6 Model of the stochastic absorber

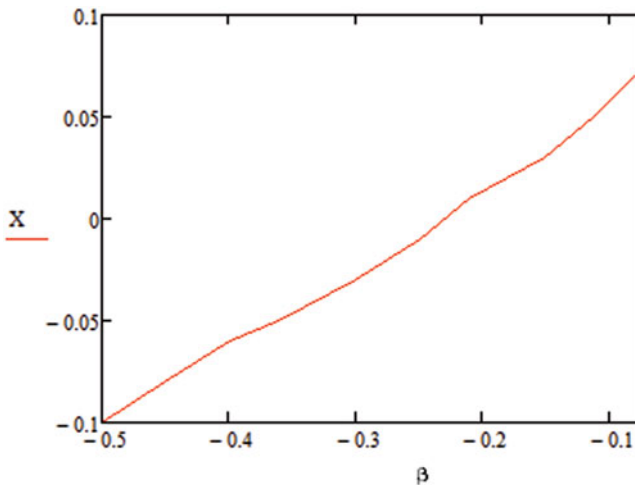


Fig. 7 Boundary of stability/ instability regions for the mode $y = 0$

Here β is the main geometrical parameter determining the contour's curvature κ in the rigid-body limit $n \rightarrow \infty$; α and μ are shown in Fig. 6; $\lambda = -2\beta(\alpha - \beta)$. The second equation of the system (27) is the equation in variations for the vibration mode $y = 0$. The test (26) is used. It permits to obtain boundary of the stability/ instability regions in the place $(X(0), \beta)$. This boundary is shown in Fig. 7 for $\alpha = 0.5$ $\mu = 0.01$, $n = 10$. The stability region is disposed on the right in the Fig. 7. Trajectories of particle inside the container during the time interval $t \leq 3000$ are shown in Fig. 8 for parameters corresponding to stability/ instability regions presented in Fig. 7. Here $\alpha = 0.5$, $\gamma = 1$, $n = 10$. Different forms of the contour are chosen, namely, Fig. 8: (a) $\beta = -0.3$, $X = -0.03$; (b) $\beta = -0.1$, $X = 0.09$; (c) =

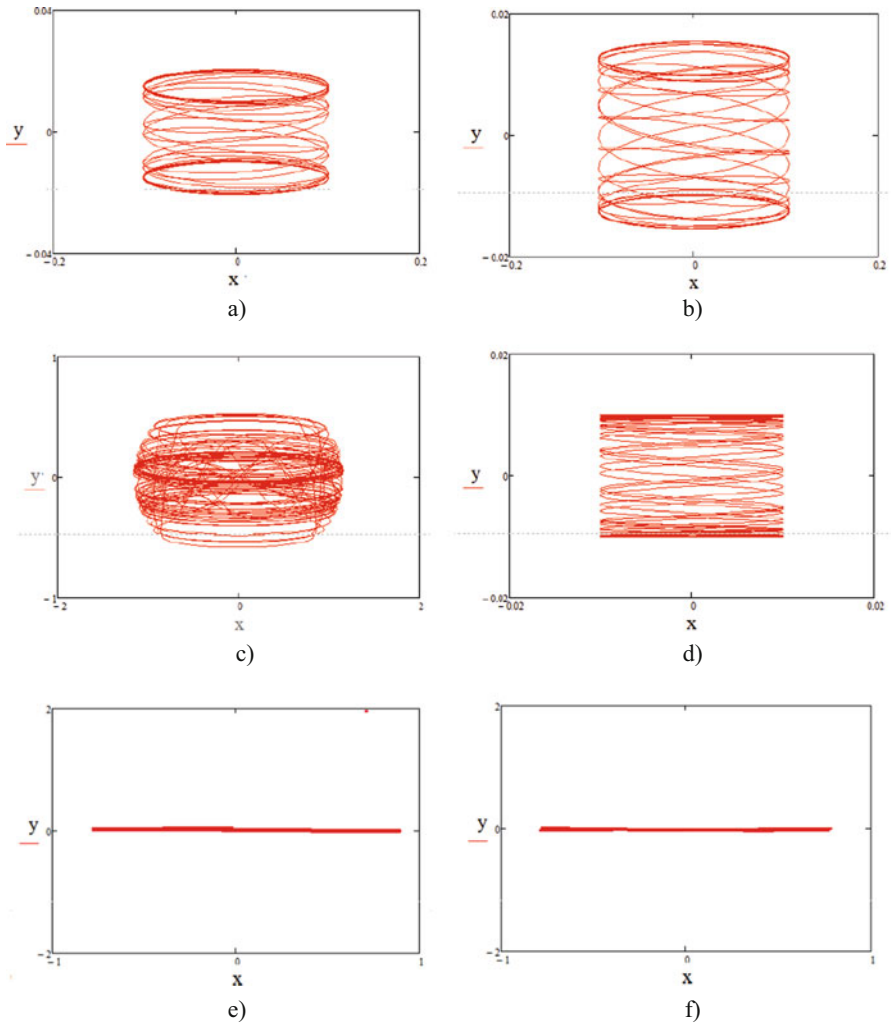


Fig. 8 Trajectories of particle inside the container during the time interval $t \leq 3000$, obtained for $\alpha = \frac{1}{2}$, $\gamma = 1$, $n = 10$ and different forms of the contour, namely, (region of instability) **(a)** = -0.3 , $X = -0.03$; **(b)** = -0.1 , $X = 0.09$; **(c)** = -0.15 , $X = 0.08$; **(d)** = -0.05 , $X = 0.094$; (region of stability) **(e)** = -0.2 , $X = -0.04$; **(f)** = -0.1 , $X = 0.04$

-0.15 , $X = 0.08$; **(d)** = -0.05 , $X = 0.094$; **Fig. 9:** **(a)** = -0.2 , $X = -0.04$; **(b)** = -0.1 , $X = 0.04$. Here $X \equiv X(0)$. For all cases initial position of the particle is $(x, y) = (0.0, 0.01)$ with zero velocities.

3.2 Stability of Localized Standing Waves in the Peyrard-Bishop-Doksua DNA Model

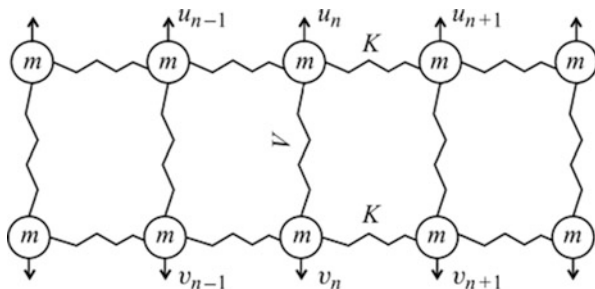
Many recent works are devoted to study of wave processes in the DNA molecule. One of the most successful models of the DNA molecule dynamics is the model developed by Peyrard, Bishop and Dauxois (the PBD model) [21, 22] which is considered here. In the PBD model two strands of the DNA are represented by linked chains of hard disks, where the bonds within base pairs are described by the anharmonic potential and the interaction between opposite discs of different chains is represented by the Morse potential. In this model, the transfer of the DNA duplex in space as a whole is not considered, and only a divergence of different chains is studied.

The PBD model is presented in Fig. 9. A mass of the discs is assumed as $m = 1$. An interaction between opposite discs of different chains is represented by the Morse potential, $V = d(\exp(-a(u_n - v_n)) - 1)^2$. Introducing new coordinates as $z_n = \frac{u_n + v_n}{\sqrt{2}}$, $y_n = \frac{u_n - v_n}{\sqrt{2}}$, one describes so-called staking interaction between nodes of the same chain by using the anharmonic potential,

$$W(y_n, y_{n+1}) = \frac{k}{a^2} \left(1 + \rho e^{-\gamma(y_{n+1} + y_n)} (y_{n+1} - y_n)^2 \right) \tag{28}$$

Here γ is the damping coefficient for the staking interaction, ρ is a parameter of anharmonicity, which characterizes a nonlinearity in the chain; d is an energy of dissociation of the polynucleotide chains, a is a parameter inversed to distance between disks, k is a constant which characterizes an interaction between bonds within chain. As it was written above, only a divergence of different chains, which is described by variables y_n , is considered. Passing on to unidimensional time and displacement, $\tau = t\sqrt{\frac{da^2}{m}}$, $u = ay_n$, then returning to initial notations of variables, $\tau \rightarrow t$, $u \rightarrow y$, one presents, as a result, the system of equations describing a divergence of chains in the PBD model as follows:

Fig. 9 Model DNK by Peyrard, Bishop and Dauxois



$$\frac{d^2 y_n}{dt^2} = \frac{k}{a^2} (y_{n+1} - 2y_n + y_{n-1}) + \frac{k}{a^2} \rho \left\{ e^{-\gamma(y_{n+1}+y_n)} (y_{n+1} - y_n) \left[\frac{1}{2}\gamma (y_{n+1} - y_n) + 1 \right] \right. \\ \left. + e^{-\gamma(y_n+y_{n+1})} (y_n - y_{n-1}) \left[\frac{1}{2}\gamma (y_n - y_{n-1}) - 1 \right] \right\} - 2\sqrt{2}De^{-\sqrt{2}y_n} \left[1 - e^{-\sqrt{2}y_n} \right] \quad (29)$$

Localized standing waves are excited by either the initial displacement y_n , describing the divergence of the chosen opposite discs of two chains, or the corresponding initial velocity.

The stability of the localized standing waves in the PBD model is investigated here by using the numerical-analytical procedure presented in preceding sub-Section.

Here we compare values of initial value of the kinetic energy of the excited disk y_n and current values of kinetic energies of the neighboring elements of the chain. Instability of localized standing wave is fixed if more than 10% of the initial kinetic energy is transferred to neighboring discs. We consider a chain consisting of nine elements. Calculations are made in nodes of some mesh in chosen domain of the system parameters with mesh width equal to $h = 0.1$. As it was pointed out above, calculations are stopped when boundaries of the stability / instability regions are stabilized in the chosen mesh. This is a principal criterion of the choice of the calculation time. Results are presented in Fig. 10, where boundaries of the stability/ instability regions are shown in places of some chosen parameters. It is assumed that $\alpha = 0.65$, $\gamma = 0.577$. Besides, in Fig. 10a the parameter $d = 0.9$ (eV); the parameter k ($eV/\text{\AA}^2$) changes on the interval $[0; 0.025]$; the unidimensional parameter ρ changes on the interval $[0; 6]$. For Fig. 10b the parameter $d = 0.33$ (eV); k changes on the interval $[0; 0.023]$; the parameter ρ belongs to the interval $[0; 6]$. For Fig. 10c the parameter $\rho = 0.5$; k belongs to the interval $[0.011; 0.051]$; d changes on the interval $[1.25; 3.1]$. For Fig. 10d the parameter $\rho = 1$; k changes on the interval $[0.01; 0.1]$; d changes on the interval $[0.1; 1.75]$. Here regions of stability are situated on the left side of the obtained boundaries.

To illustrate obtained results calculations of the considered chain dynamics (9 nodes) are made using the Runge-Kutta method of the 4-th order. Let $\alpha = 0.65$, $\gamma = 0.577$. The following parameters are chosen for region of stability: $= 0.001 eV/\text{\AA}^2$; $\rho = 0.01$, $d = 0.9 eV$ (Fig. 11), and for region of instability: $= 0.1 eV/\text{\AA}^2$; $\rho = 0.1$, $d = 0.9 eV$ (Fig. 12). Here only the single central disc in the model under consideration is excited, $y_5(0) = 0.782$; initial displacements of other nodes and all initial velocities are equal to zero, that is, the localized standing wave is excited. Displacements in time for each of nine nodes of the model are presented both for the stable localized wave (Fig. 11), and for the unstable one (Fig. 12).

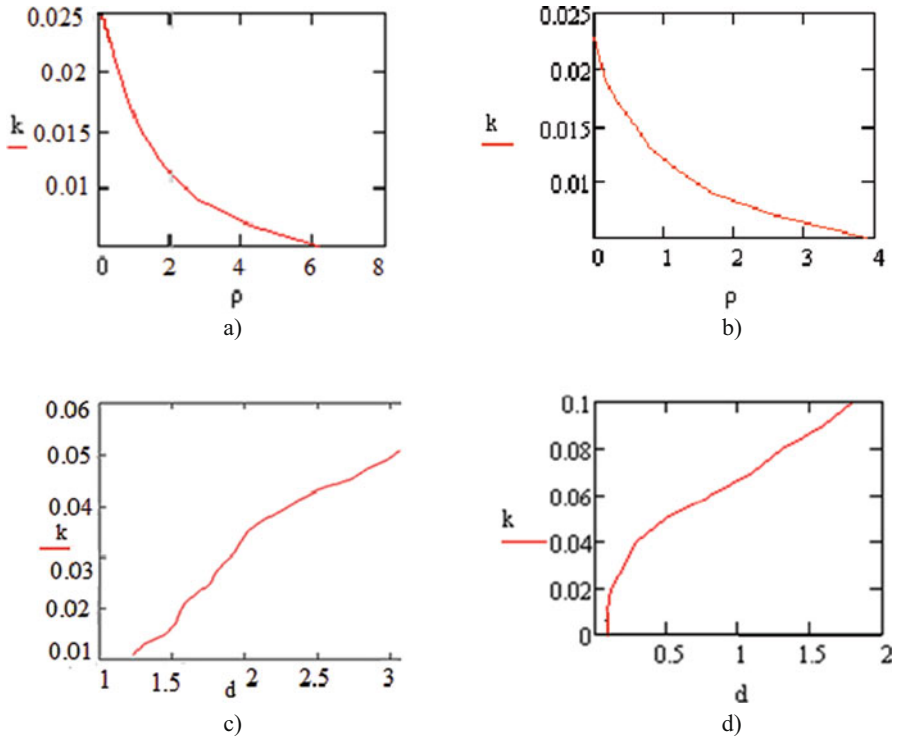


Fig. 10 Boundaries of the stability/ instability regions for the system (29): in place (k, ρ) for $d = 0.9$ (a) and $d = 0.33$ (b); boundaries in place (k, d) for $\rho = 0.5$ (c) and $\rho = 1$ (d)

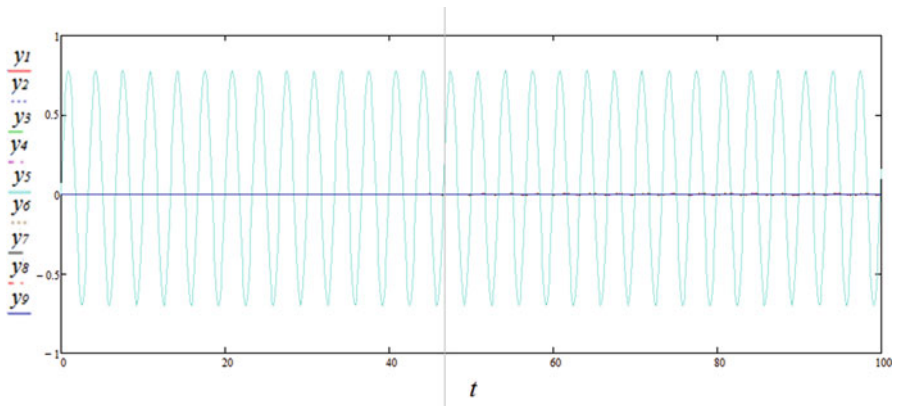


Fig. 11 Stable standing localized wave for $k = 0.001$; $\rho = 0.01$; $d = 0.9$

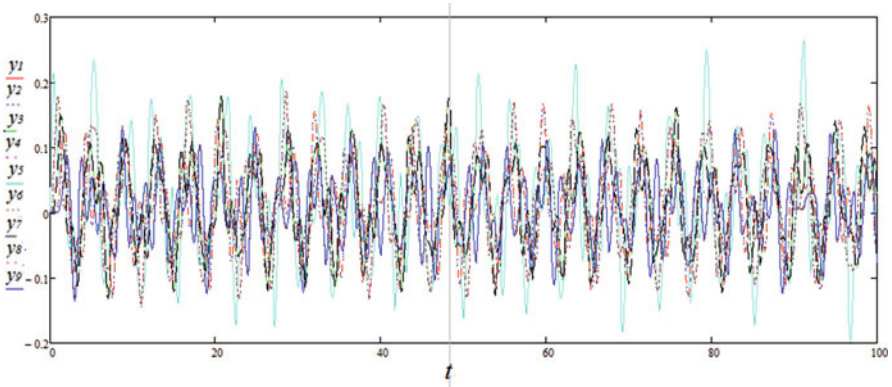


Fig. 12 Unstable standing localized wave for $k = 0.1$; $\rho = 0.1$; $d = 0.9$

4 Conclusions

It is shown that both the method of Ince algebraization, and the numerical-analytical procedure which is a consequence from the classical Lyapunov definition of stability, can be successfully used in a problem of stability of steady states. An advantage of the IA is that we do not need in use of the unperturbed solution time-presentation. Limitation of the IA consists in that only conservative systems must be considered, and that the stability problem must be reduced to a single equation in variations. Investigation of stability of traveling nonlinear waves in nonlinear media is possible too. The second numerical-analytical approach permits to analyze a stability of NNMs, including modes with complex in time behavior when analytical solution of the stability problem is absent. Investigation of stability of traveling or standing nonlinear waves in nonlinear chains can be also realized by the approach.

References

1. Kauderer, H.: *Nichtlineare Mechanik*. Springer, Berlin (1958)
2. Rosenberg, R.M.: Nonlinear vibrations of systems with many degrees of freedom. *Adv. Appl. Mech.* **9**, 156–243 (1966)
3. Vakakis, A.F., Manevitch, L.I., Mikhlin, Y.V., Pilipchuk, V.N., Zevin, A.A.: *Normal Modes and Localization in Nonlinear Systems*. Wiley, New York (1996)
4. Mikhlin, Y.V., Avramov, K.V.: Nonlinear normal modes for vibrating mechanical systems. Review of theoretical developments. *Appl. Mech. Rev.* **63**(6), 060802 (2010)
5. Avramov, K.V., Mikhlin, Y.V.: Review of applications of nonlinear normal modes for vibrating mechanical systems. *Appl. Mech. Rev.* **65**(2), 020801 (2013)
6. Vakakis, A.F., Gendelman, O.V., Bergman, L.A., McFarland, D.M., Kerschen, G., Lee, Y.S.: *Nonlinear Targeted Energy Transfer in Mechanical and Structural Systems Solid mechanics and its applications*, vol. 156. Springer Netherlands (2008)
7. Lyapunov, A.M.: *Stability of Motion*. Academic, New York (1966)

8. Cesari, L.: *Asymptotic Behavior and Stability Problems in Ordinary Differential Equations*. Springer, New York (1971)
9. LaSalle, J.P.: *The Stability of Dynamical Systems*. SIAM, Philadelphia (1976)
10. Glendinning, P.: *Stability, Instability and Chaos*. Cambridge University Press, New York (1994)
11. Ince, E.L.: *Ordinary Differential Equations*. Longmans Green, London (1926)
12. Mikhlin, Y.V., Zhupiev, A.L.: An application of the Ince algebraization to the stability of non-linear normal vibration modes. *Int. J. Non-Linear Mech.* **32**(2), 393–409 (1997)
13. Mikhlin, Y.V., Shmatko, T.V., Manucharyan, G.V.: Lyapunov definition and stability of regular or chaotic vibration modes in systems with several equilibrium positions. *Comput. Struct.* **82**, 2733–2742 (2004)
14. Bateman, H., Erdelyi, A.: *Higher Transcendental Functions*, vol. 3. McGraw-Hill, New York (1955)
15. Kikot, I.P., Manevich, L.I.: Weakly coupled oscillators in the presence of elastic support in the conditions of acoustic vacuum. *Nelineinaya Dinamika [Russian Journal of Nonlinear Dynamics]*, **10**(3), 245–263. (in Russian) (2014)
16. Koroleva (Kikot), I., Manevitch, L., Vakakis, A.F.: Non-stationary resonance dynamics of a nonlinear sonic vacuum with grounding supports. *J. Sound Vib.* **357**, 349–364 (2015)
17. Whitham, G.B.: *Linear and Nonlinear Waves*. Wiley, New York (1999)
18. Mikhlin, Y.V., Shmatko, T.V., Manucharyan, G.V.: Lyapunov definition and stability of regular or chaotic vibration modes in systems with several equilibrium positions. *Comp. Struct.* **82**, 2733–2742 (2004)
19. Awrejcewicz, J., Krysko, V.A.: *Chaos in Structural Mechanics*. Springer, New York (2008)
20. Pilipchuk, V.: Stochastic energy absorbers based on analogies with soft-wall billiards. *Nonlinear Dyn.* **98**, 2671–2685 (2019)
21. Dauxois, T., Peyrard, M., Bishop, A.R.: Entropy-driven DNA denaturation. *Phys. Rev. E.* **47**, R44–R47 (1993)
22. Peyrard, M.: Nonlinear dynamics and statistical physics of DNA. *Nonlinearity.* **17**, R1–R40 (2004)

Modelling of Torsional Vibrations in a Motorcycle Steering System



Andrzej Dębowski  and Dariusz Żardecki 

Abstract Torsional vibrations of steering systems are significant problems for the active safety of motorcycles. These vibrations may occur even with slight disturbances of the steady state motion, and their causes result from the improper mechanical parameters and characteristics of the steering system affecting the dynamic properties of the vehicle. In many cases, full elimination of torsional vibrations requires the use of special dampers acting as mechatronic systems. Identifying the causes of vibrations and finally the proper synthesis of the active damper requires research studies using mathematical modelling and computer simulation. Due to the complex nature of motorcycle dynamics, which prompts the creation of complex forms of the mathematical model, and at the same time the obvious paradigm of the relative simplicity of the model used in mechatronic systems, the synthesis of such a model requires a special approach. The paper presents a method of model synthesis including determination of nonlinear equations of motion in an extreme “expanded” version, then their linearization, Laplace transformation and determination of the transfer functions, frequency analysis based on Bode plots, reduction of the transfer functions and finally calculation of state equations allowing a synthesis of the active damper algorithm.

Keywords Wobble · Steering system · Motorcycle · Vibrations · LabVIEW · Bode plots · Shimmy

1 Introduction

Dynamic peculiarities occurring in the movement of a motorcycle are a significant problem of motorcyclist safety. The behavior of the motorcycle results from the complex dynamic properties of the driver-vehicle-road system as well as internal

A. Dębowski (✉) · D. Żardecki
Military University of Technology, Warsaw, Poland
e-mail: andrzej.debowski@wat.edu.pl

© Springer Nature Switzerland AG 2021
J. Awrejcewicz (ed.), *Perspectives in Dynamical Systems III: Control and Stability*,
Springer Proceedings in Mathematics & Statistics 364,
https://doi.org/10.1007/978-3-030-77314-4_25

327

and external interactions disturbing steady motion. The source of these disturbances may be balancing, steering control, acceleration and braking. Stimulation of vibrations can also come from wheel imbalance or from uneven roads. The variety of peculiar behavior of motorcycles is demonstrated by their classifications emphasizing the specificity of non-oscillation processes and the vibrations of the vehicle and its components [2]. Vibration in the motorcycle steering system can be counteracted by proper selection of parameters, as well as by introducing special dampers (especially electronically controlled dampers) [4].

Modeling of motorcycle motion dynamics (including vibrations) was undertaken by many researchers and has significantly changed after the spread of MBS-type software. The most important achievements in terms of testing vibrations in motorcycles from the last 50 years are presented in Table 1 (based on works [2, 5, 7–9, 11–15]), and a broader historical perspective can be found in [4, 6].

Modeling of torsional vibrations in the steering system of a motorcycle is discussed in this paper. The presented models are used to analyze the vibration sensitivity to changes in motorcycle parameters (the initial model, then linearized and transformed to the transmittance form) and to synthesize the control of the vibration damper (the reduced model resulting from the transmittance model).

Table 1 Major works related to motorcycle vibrations testing

Year	Author	The most important report
1971	Sharp	Stability analysis of rectilinear motorcycle movement including tire properties
1974	Sharp	Study on the effect of frame flexibility on lateral stability of a motorcycle.
1974	Jennings	Observing the relationship between the lateral movement of the motorcycle and weave-type vibrations.
1976	Sharp	Presentation of the relationship between motorcycle lateral movement and weave-type vibrations at high speeds.
1978	Kane	Analysis of the impact of frame flexibility on weave-type vibrations at high speeds.
1983	Koenen	Investigations of motorcycle vibrations in steady state conditions for a cornering case and a model taking into account suspension compliance.
1994	Sharp	Taking into account current reports in the field of studying the dynamics of motorcycles in a single model.
1994	Sharp	Review of modeling methods for multi-body systems and their application to mathematical modeling of vehicles
2002	Cossalter	The first book on motorcycle dynamics
2004	Evangelou	Torsional vibration damper for sports motorcycles due to their poor stability at high speeds.

2 Mathematical Model and Its Application in Sensitivity Analysis

The physical model corresponding to the steering system of the motorcycle mounted in a special drum test stand is shown in Fig. 1.

The model takes into account the key features of the motorcycle's steering system and is in accordance with the fundamental development of Cossalter [2]. This model has five degrees of freedom, which are vertical movement of the wheel and body, rotational movement of the wheel relative to the wheel axis and angular movement of the steering wheel and wheel around the axis of the steering head frame (see Fig. 2). The model includes longitudinal suspension work and its torsional flexibility. Due to the fact that the analysis of dynamics concerns vibrations in the range of small amplitudes, small deformations and displacements, the impact of the lateral tilt of the suspension (considered around the X axis) is ignored. The model includes the gyroscopic effect. Between the steering wheel and the head of the frame there is a spring-damping element representing the driver's hands and a damping element representing the torsional vibration damper. In the field of tire modeling, works [2, 10, 16] were used. Therefore, a simplified wheel-road cooperation model was adopted, with passing over the phenomenon of tire dynamics and with a simplified description of the stabilizing moment (due to the large overtaking distance, it has a small share in the total stabilizing moment [11, 16]).

Due to small angular movements and constant wheel speed, all characteristics of the elements are linear (in particular, this also applies to the description of wheel/road interaction). The model's non-linearity results only from geometric conditions.

Fig. 1 Test stand of motorcycle steering system



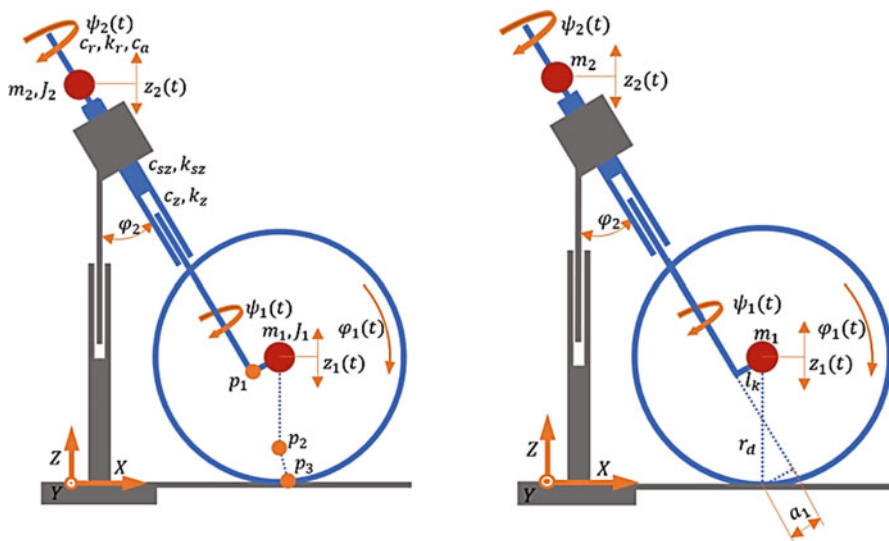


Fig. 2 Physical model of motorcycle steering system

List of variables and parameters (examples of parameter values are presented in this list):

- ψ_1, ψ_2 – the steering angle of the wheel and steering wheel, respectively,
- φ_1 – wheel rotation angle,
- z_1, z_2 – vertical displacement of elements associated with the wheel and frame,
- φ_2 – head angle (24 degrees),
- m_1, m_2, m – reduced mass of elements associated with the wheel (15 kg) and frame (200 kg) respectively, and the sum of the mass m_1 i m_2 ,
- J_1, J_2 – the equivalent moment of inertia of the elements associated with the wheel (0.21 kgm^2) and steering handlebar (0.4 kgm^2),
- $c_r, c_a, c_{sz}, c_z, C_o$ – damping coefficient of the driver's hands (10 Nms/rad), vibration damper (0–3 Nms/rad), torsional suspension (1 Nms/rad), longitudinal suspension (2.6 kNs/m), tire damping coefficient (150 Ns/m) respectively,
- k_r, k_{sz}, k_z, K_z - stiffness coefficient of the driver's hands (0.8 kN/rad), torsional suspension (7 kNm/rad), longitudinal suspension (14 kN/m), radial tires (190 kN/m) respectively,
- p_1, p_2, p_3 – point of suspension end, wheel rim and wheel contact with the road, respectively,
- X, Y, Z – axes of the coordinate system,
- r_d – dynamic radius of the wheel (0.3 m),
- l – wheelbase of road wheels (1.35 m),
- l_1 – distance between the center of mass and the axis of the front wheel (0.6 m),
- l_k – offset the wheel axis from the steering head axle (0.03 m),
- w_{po} – tire tread height (0.08 m),

- a_1 – actual overtaking distance (0.1 m),
- $M_{nk}, M_b, M_{or}, M_{sk}$ – the moment stimulating vibrations, driving from the drum and resistance to movement, steering wheel turning, respectively,
- W_0 – excitation from the road surface.

To write the equations of motion, Lagrange equations of the second type were used and a system of non-linear differential equations (initial model) was obtained with the general structure expressed by relations (1–5).

$$f_1 (\ddot{z}_1, \ddot{\psi}_1, \dot{\psi}_1, \dot{z}_2, \dot{z}_1, \psi_1, z_1, z_2; W_0) = 0 \quad (1)$$

$$f_2 (\ddot{z}_2, \ddot{\psi}_1, \dot{\psi}_1, \dot{z}_2, \dot{z}_1, \psi_1, z_1, z_2) = 0 \quad (2)$$

$$f_3 (\ddot{\varphi}_1, \ddot{\psi}_1; M_b, M_{or}) = 0 \quad (3)$$

$$f_4 (\ddot{\psi}_1, \ddot{\psi}_2, \dot{z}_1, \dot{z}_2, \dot{\varphi}_1, \dot{\psi}_1, \dot{\psi}_2, \dot{z}_1, \dot{z}_0, \psi_1, \psi_2; M_{sk}, M_{nk}) = 0 \quad (4)$$

$$f_5 (\ddot{\psi}_2, \dot{\psi}_1, \dot{\psi}_2, \psi_1, \psi_2) = 0 \quad (5)$$

The initial mathematical model has a complicated non-linear form. For example, the form of Eq. (1) is as follows.

$$\begin{aligned} \ddot{z}_1 = & \frac{1}{lm_1} (lK_z (r_k - w_{po}) \cos(\varphi_2 \sin(\psi_1)) - \varphi_2 l \cos(\psi_1) \dot{\psi}_1 C_o (r_k - w_{po}) \sin(\varphi_2 \sin(\psi_1))) \\ & + \sin(\varphi_2) \sin(\psi_1) l_k m_1 \ddot{\psi}_1 l + \sin(\varphi_2) \dot{\psi}_1^2 \cos(\psi_1) l_k m_1 l + C_o l_k \dot{\psi}_1 \sin(\psi_1) \sin(\varphi_2) l \\ & - l (C_o + c_z) \dot{z}_1 + c_z \dot{z}_0 l + c_z \dot{z}_2 \cos(\varphi_2) l - K_z l_k \cos(\psi_1) \sin(\varphi_2) l \\ & + l_k l (K_z + k_z) \sin(\varphi_2) + k_z z_2 \cos(\varphi_2) l - l (K_z + k_z) z_1 + K_z z_0 l - g (lm_2 - l_1 m) \end{aligned} \quad (6)$$

Linearization of the initial mathematical model would lead to extremely complex records. That is why model linearization and then determination of Laplace transmittances was “automated” using the Maple programming tool, which, however, requires the numerical form of the model. The model was linearized assuming a work point:

$$z_1 = 0 \quad (7)$$

$$z_2 = 0 \quad (8)$$

$$\dot{\varphi}_1 = 15.9 \text{ rad/s} \quad (9)$$

$$\dot{\varphi}_2 = 0.42 \text{ rad/s} \quad (10)$$

For a system with two inputs and five outputs, ten different transmittances can be obtained that describe the steering system in question. However, from the perspective of further analysis, the most important is the transmittance between the steering angle $\Psi_2(s)$ the stimulating moment $M_{nk}(s)$. The steering model will then be of the transmittance form given by the following equation:

$$\frac{\Psi_2(s)}{M_{nk}(s)} = \frac{b_1s + b_0}{a_4s^4 + a_3s^3 + a_2s^2 + a_1s + a_0}. \quad (11)$$

Assuming the example values of parameters (in accordance with the list presented earlier), the numerical form of this transmittance is as follows:

$$\frac{\Psi_2(s)}{M_{nk}(s)} = \frac{4.37 \bullet 10^{-4} \bullet (s + 1)}{5.52 \bullet 10^{-9}s^4 + 2.25 \bullet 10^{-7}s^3 + 5.48 \bullet 10^{-4}s^2 + 5.16 \bullet 10^{-4}s + 1}. \quad (12)$$

For transmittance (12), the logarithmic characteristics of the module and phase have a graph, as in Fig. 3.

The next stage, which facilitates the analysis of system dynamics, is the distribution of transmittance (having fourth order polynomial) on the sum of two more simple transmittances (having second order polynomials). After such

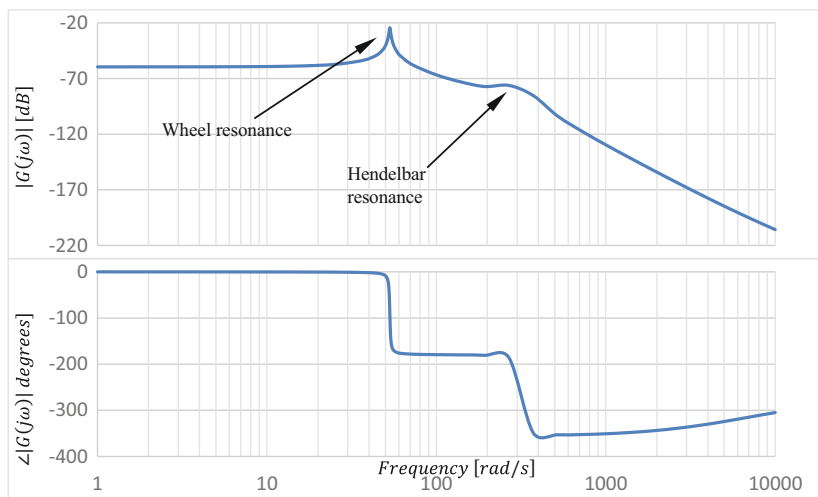


Fig. 3 Amplitude and phase characteristics of transmittance (12)

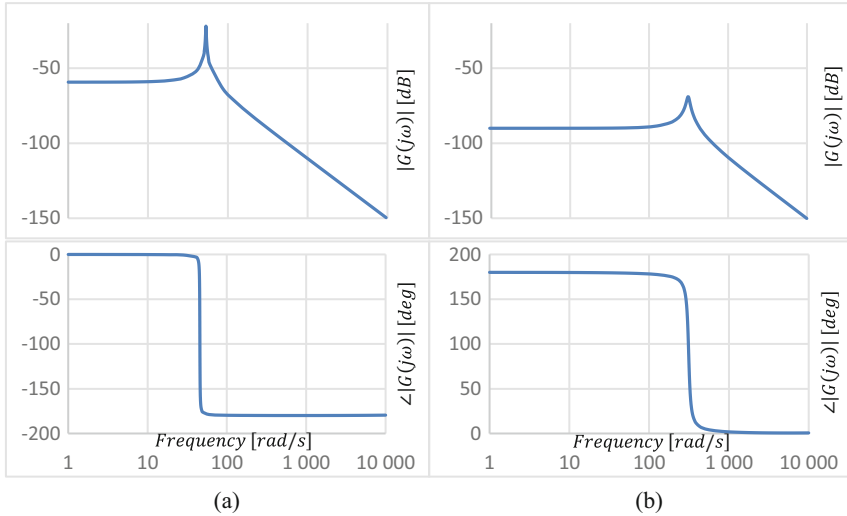


Fig. 4 Amplitude and phase characteristics of the transmittance elements $G_1(s)$ i $G_2(s)$. **(a)** Wheel resonance. **(b)** Hendelbar resonance

decomposition, it is possible to do the frequency analysis of these components and reveal the dynamic features that will be assigned in this case to the vibrations associated with the steering handlebar and the wheel. Applying the decomposition method to simple fractions described, among others in [3] one obtains:

$$\frac{\Psi_2(s)}{M_{nk}(s)} = G_1(s) + G_2(s) = \frac{1.7 \cdot 10^{-5}s + 3.1}{s^2 + 0.18s + 1857.0} + \frac{-9.55 \cdot 10^{-6}s - 3.1}{s^2 + 40.6s + 97380.9} \tag{13}$$

In this way, values were obtained for individual resonance frequencies, where for the steering wheel it is 314 rad/s (50 Hz) (left side on Fig. 4), and for the wheel 47 rad/s (7.5 Hz) (right side on Fig. 4).

Stability analysis was also carried out using Routh and Hurwitz methods, on the basis of which it was found that the steering system is on the limit of stability, which requires the use of additional damping systems.

Using the previously presented method of separating two resonance frequencies, it is possible to assess the impact of selected steering system parameters. Examples of them are presented below (Figs. 5 and 6).

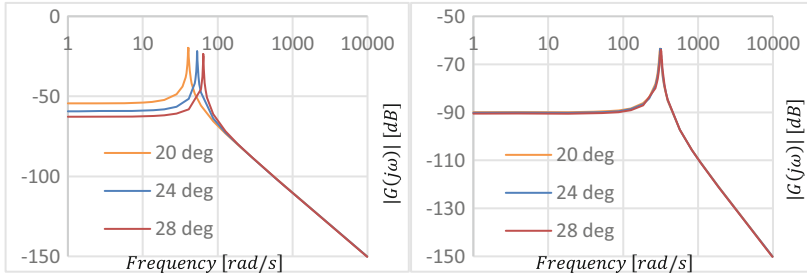


Fig. 5 Impact of suspension angle on steering vibration φ_2

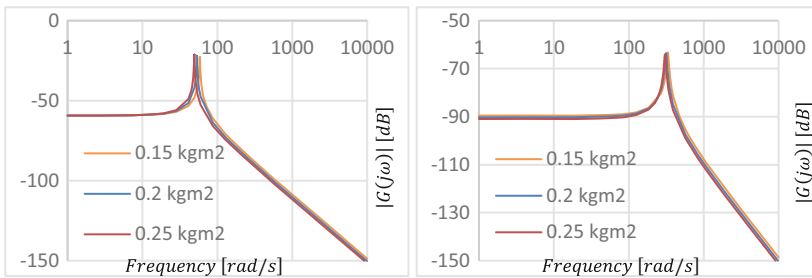


Fig. 6 Impact of the moment of inertia of the upper steering system I_{2z}

3 The Reduced Model and Its Application in the Synthesis of the Algorithm by a Vibration Damper

Based on the distribution of higher order transmittance to the sum of two lower order transmittances, it can be seen that the essence of the problem of torsional vibration in the steering system is represented by the transmittance of the reduced form:

$$\frac{\Psi_2(s)}{M_{nk}(s)} = \frac{b_0}{a_2s^2 + a_1s + a_0}. \tag{14}$$

This form is useful to project a control system for active vibration damper using modern methods of the optimal control theory. One of them is the LQR method dedicated to synthesis linear regulators [1]. It requires the model in the state equation form and quadratic optimized functional.

If the object description is done by vector state equation:

$$\dot{x} = Ax + bu, \tag{15}$$

and optimized functional is

$$J(u) = \frac{1}{2} \int_0^{\infty} (x^T Qx + u^T Ru) dt, \tag{16}$$

where A, B, Q, R are given matrices.

The optimal control signal fulfills equations

$$\hat{u}(t) = -R^{-1} B^T Kx(t), \tag{17}$$

where:

$$-KA - A^T K + KBRB^T K = 0 \tag{18}$$

In our case: $X1 = \psi$, $X2 = \dot{\psi}$, $u = M_{nk}$, $A = \begin{bmatrix} 0 & 1 \\ -a_0 & -a_1 \end{bmatrix}$, $b = \begin{bmatrix} 0 \\ b_0 \end{bmatrix}$, $Q = \begin{bmatrix} q_1 & 0 \\ 0 & q_2 \end{bmatrix}$, $R = r$. where: r – control signal weight, q_1, q_2 – object condition weights.

After solving the non-linear algebraic Riccati equation, the optimal regulator is obtained, which is the PD regulator, and the optimal LQR control is obtained as:

$$M_{nk}(t) = Kx(t) = K_{11}\psi(t) - K_{22}\dot{\psi}(t) \tag{19}$$

In the case, when $r = 1$, $q_1 = 0.05$, $q_2 = 0.087$, one calculates $K_{11} = 5.37$ and $K_{22} = 0.14$.

Based on the synthesis of the regulator presented above, the damper control system was obtained (Fig. 7):

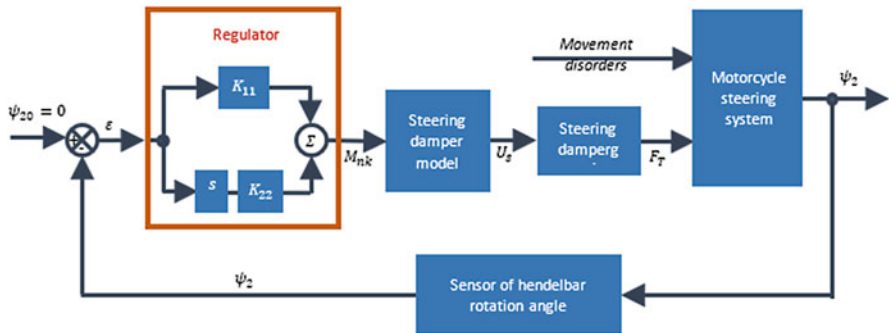


Fig. 7 Diagram of the vibration damping regulation system in the motorcycle steering system. Notation: ψ_{20} – reference value, ψ_2 – current value of the steering wheel angle, ε – control error, M_{nk} – optimal value of damping force, U_s – control voltage, F_T – actual damping force

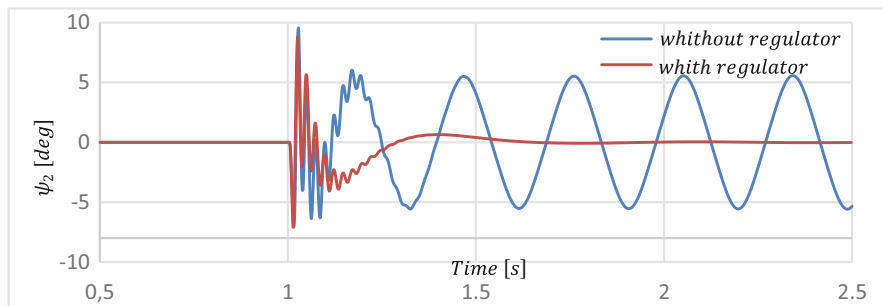


Fig. 8 Comparison of the steering wheel rotation angle ψ_2 courses with and without the regulator (here motorcycle speed is 20 km/h)

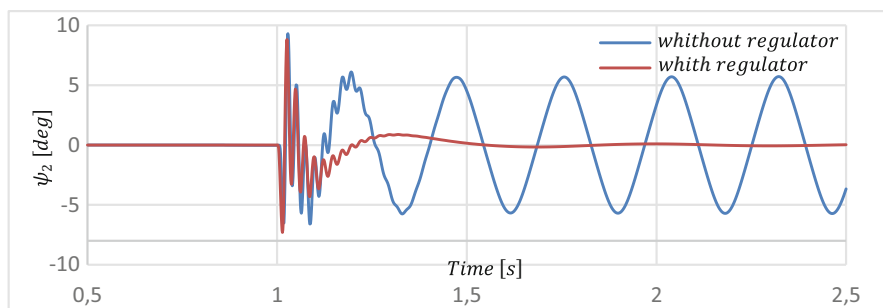


Fig. 9 Comparison of the course of the steering wheel rotation angle ψ_2 with an operating regulator and without it after increasing the driving speed to 30 km/h

The developed regulator was tested using computer simulation, in which typical traffic conditions were varied (e.g. vehicle speed, see Figs. 8 and 9).

4 Conclusion

The paper presented a method of model synthesis including determination of nonlinear equations of motion in an extreme “expanded” version, then their linearization, Laplace transformation and determination of the transfer functions, frequency analysis based on Bode plots, reduction of the transfer functions and finally calculation of state equations allowing a synthesis of the active damper control algorithm. Based on the simulation investigations, it was found that the developed damper’s regulator works correctly in various traffic conditions. Additionally, it can be stated that the time needed to reduce the impact of a disorder is similar to the basic driver response time. And this time is crucial, because then wobble vibrations may occur if the damping in the motorcycle steering system does not increase quickly

enough. Typical driver response time is much longer than the response time of actuators, and therefore the use of a damper with a regulator in the steering system is justified.

References

1. Athans, M., Falb, P.L.: *Sterowanie optymalne. Wstęp do teorii i jej zastosowania*, Wydawnictwo Naukowo-Techniczne, Warszawa (1966)
2. Cossalter, V.: *Motorcycle Dynamics*. LULU (2006)
3. Czemplik, A.: *Modele dynamiki układów fizycznych dla inżynierów. Zasady i przykłady konstrukcji modeli dynamicznych obiektów automatyki*, Wydawnictwo Naukowo-Techniczne, Warszawa (2017)
4. Dębowski, A.: *Analiza możliwości ograniczenia drgań skrętnych w układzie kierowniczym motocykla*. Doctoral thesis, Military University of Technology, 2019
5. Evangelou, S., Limebeer, D.J., Sharp, R.S., Smith, M.C.: Steering compensation for high-performance motorcycles. In: *Decision and Control*, 2004. CDC. 43rd IEEE Conference on, vol. 1, pp. 749–754. IEEE (2004)
6. Giner, D.M.: *Symbolic-numeric tools for the analysis of motorcycle dynamics. Development of a virtual rider for motorcycles based on model predictive control*. Doctoral thesis, Universidad Miguel Hernández, 2016
7. Jennings, G.: A study of motorcycle suspension damping characteristics. SAE, Technical Paper No. 740628, 1974
8. Kane, T.R.: The effect of frame flexibility on high speed weave of motorcycles. SAE, Technical Paper 780306, 1978
9. Koenen, C.: *The dynamic behaviour of a motorcycle when running straight ahead and when cornering*. PhD thesis, Delft University, 1983
10. Pacejka, H.: *Tyre and Vehicle Dynamics*. Elsevier, Waltham (2012)
11. Sharp, R.S.: The stability and control of motorcycles. *J. Mech. Eng. Sci.* **13**(5), 316–329 (1971)
12. Sharp, R.S.: The influence of frame flexibility on the natural stability of motorcycles. *J. Mech. Eng. Sci.* **16**(2), 117–120 (1974)
13. Sharp, R.: The influence of the suspension system on motorcycle weave-mode oscillations. *Veh. Syst. Dyn.* **5**(3), 147–154 (1976)
14. Sharp, R.: Vibrational modes of motorcycles and their design parameter sensitivities. In: *Institution of Mechanical Engineers Conference Publications*, vol. 3, pp. 107–107 (1994)
15. Sharp, R.: The application of multi-body computer codes to road vehicle dynamics modelling problems. *Proc. Inst. Mech. Eng Part D J. Automob. Eng.* **208**(1), 55–61 (1994)
16. Ślusarczyk, P.: Analiza modelowa stateczności pojazdu jednośladowego, *Czasopismo Techniczne*, Wyd. PK, Zeszyt 7-M, Kraków, 2004, 165–173

Free Vibration Frequencies of Simply Supported Bars with Variable Cross Section



Olga Szlachetka , Jacek Jaworski, and Marek Chalecki 

Abstract Using the Rayleigh method, the authors developed a procedure for determination of higher natural frequencies and derived formulas for frequencies of first three modes of free (transverse) vibrations of simply supported bars having the shape of truncated cone and truncated wedge. The bars are made of a homogeneous and elastic material and are considered as Bernoulli-Euler beams. It was assumed that the shape of the bar axis deflected during vibration corresponds to a deflection line resulting from action of a specific continuous static load. Dimensionless frequency parameters for bars with various truncation factors, obtained as a result, were compared to those known from literature and to results of application of FEM. High concordance of results was found for the first natural frequency. For the second and third frequencies, however, the results acceptable from engineer's point of view (i.e. burdened with an error lower than 6%) were obtained only for bars with the truncation factor not lower than 0.6 (for the truncated cone) and 0.4 (for the truncated wedge). It means that the hypothesis assumed in the study for the shape of a beam axis deflection line during vibrations, enabling determination of higher frequencies of free vibrations and being proper for bars having shapes close to a solid cylinder or cuboid, loses its appropriateness for bars approaching the shape of cone or wedge.

Keywords Simple supported bar · Non-uniform section · Natural frequencies

1 Introduction

Variable cross-section beams can ensure a better mass and strength distribution than the constant cross-section ones what makes them more popular in common application in building and machine constructions. Higher natural frequencies of

O. Szlachetka (✉) · J. Jaworski (retired) · M. Chalecki
Warsaw University of Life Sciences – SGGW, Warsaw, Poland
e-mail: olga_szlachetka@sggw.edu.pl; marek_chalecki@sggw.edu.pl

© Springer Nature Switzerland AG 2021
J. Awrejcewicz (ed.), *Perspectives in Dynamical Systems III: Control and Stability*,
Springer Proceedings in Mathematics & Statistics 364,
https://doi.org/10.1007/978-3-030-77314-4_26

339

such beams can be determined from the differential equation of Bernoulli-Euler beam. An analytical solution of this equation for truncated cone and truncated wedge beams, obtained with use of the Bessel functions of the first kind, was presented by Conway and Dubil [4]. Naguleswaran [8] obtained the exact solution using Frobenius method and presented (in tables) first three dimensionless natural frequencies for 16 combinations of supporting schemes and various values of truncation factors. Many researchers extended the analysis to beams with other shapes of the cross-section. For example, Ece, Aydogdu and Taskin [5] investigated a bar with exponentially varying width, Caruntu [3] analyzed a bar with circular cross-section and parabolic variability of radius, Keshmiri, Wu and Wang [7] studied exponentially and trigonometrically tapered cone beams with different taper ratios.

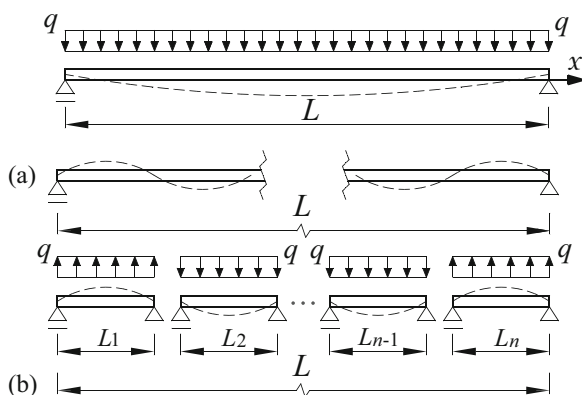
In some papers (e.g. [6]) it was proven that the application of the Rayleigh’s method for determination of first natural frequency of transverse vibrations of variable cross-section cantilever bars – with assumption that the shape of the bar axis deflected during vibration corresponds to a deflection line resulting from action of a uniform continuous static load – gives results which can be acknowledged as accurate for practical engineering calculations. Bagdasaryan et al. [1] checked that the differences between frequencies calculated in such way and results obtained in FEM did not exceed 1.7% for truncated cone beams and 0.5% for truncated wedge beams, supported in any form. For simply supported beams, these differences did not exceed 0.6%.

For a beam with length L and constant bending stiffness ($EJ = \text{const}$), higher natural frequencies can be also calculated using the assumption mentioned in the previous paragraph. The deflection of the beam (Fig. 1a) is described by the equation:

$$u(x) = \frac{q}{24EJ} (x^4 - 2Lx^3 + L^3x) \tag{1}$$

The potential energy in the deflected position of the beam is equal to

Fig. 1 (a) Uniformly loaded, simply supported beam. (b) Scheme for determination of an n -th natural frequency



$$E_p = \int_0^L \frac{1}{2} q u(x) dx = \frac{1}{2} \frac{q^2 L^5}{120 E J} \quad (2)$$

whereas the kinetic energy in the non-deflected position

$$E_k = \int_0^L \frac{1}{2} \omega^2 u^2(x) \rho A dx = \frac{1}{2} \rho A \omega^2 \frac{31 q^2 L^9}{24^2 \cdot 630 (E J)^2} \quad (3)$$

where q – continuous static load, ρ – mass density, A – cross-section area, ω – natural frequency.

Comparing both energies, one obtains the frequency for the first mode:

$$\omega_1 = 12 \sqrt{\frac{21}{31}} \frac{1}{L^2} \sqrt{\frac{E J}{\rho A}} \quad (4)$$

Higher frequencies can be obtained considering a shape of the vibrating beam as in Fig. 1b. If a simply supported beam with the length L is replaced by n simply supported beams with the length L/n , then – as it results from (4) – the n -th frequency will be n^2 times greater than the first one:

$$\omega_2 = 4\omega_1; \omega_3 = 9\omega_1; \omega_n = n^2\omega_1 \quad (5)$$

The comparison of these results to the well-known solution for the first natural frequency of the transversal vibrations of a simply supported beam (cf. e.g. [2])

$$\omega_1 = \frac{\pi^2}{L^2} \sqrt{\frac{E J}{\rho A}}, \omega_n = n^2\omega_1 \quad (6)$$

allows to state that the difference (relative error) of the simplified solution amounts

$$\frac{\left| \pi^2 - 12 \sqrt{\frac{21}{31}} \right|}{\pi^2} 100\% = 0.0715\% \quad (7)$$

The aim of this work is an attempt to apply the aforementioned method of calculation of higher natural frequencies for beams with variable cross-section. The detailed description of the approach will be presented on the example of a simply supported truncated cone beam.

2 Materials and Methods

2.1 Truncated Cone Beam – Deflection and First Natural Frequency

Assume that a truncated cone beam is subjected to a continuous load with a constant value q (Fig. 2). The diameter δ , cross-section area A and second area moment J in any cross section of the beam are functions of the coordinate x :

$$\delta(x) = d + \frac{D - d}{L}x = \alpha x + \beta; A(x) = \frac{\pi \delta(x)^2}{4}; J(x) = \frac{\pi \delta(x)^4}{64} \tag{8}$$

where

$$\alpha = \frac{D - d}{L}, \beta = d \tag{9}$$

The differential equation of a deflected neutral axis of the beam can be written as

$$E J(x) \frac{d^2 u(x)}{dx^2} = \frac{q}{2} (x^2 - Lx) \tag{10}$$

Arranging this equation and putting $J(x)$, one obtains

$$\frac{\pi E}{32q} \frac{d^2 u(x)}{dx^2} = \frac{x^2 - Lx}{(\alpha x + \beta)^4} \tag{11}$$

The integration yields a slope angle (12) and deflection (13) of the section:

$$\frac{\pi E}{32q} \frac{du(x)}{dx} = C_1 - \frac{1}{\alpha^3 (\alpha x + \beta)} + \frac{2\beta + \alpha L}{2\alpha^3 (\alpha x + \beta)^2} - \frac{\beta (\alpha L + \beta)}{3\alpha^3 (\alpha x + \beta)^3} \tag{12}$$

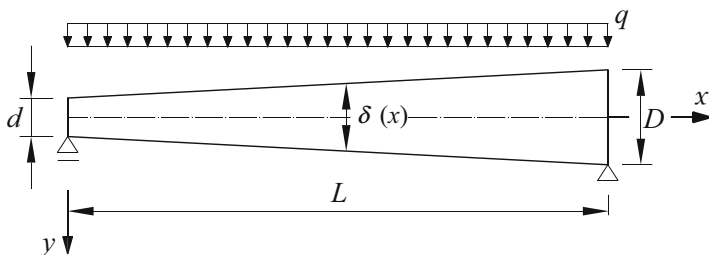


Fig. 2 Simply supported, truncated cone beam

$$\frac{\pi E}{32q} u(x) = C_1 x + C_2 - \frac{1}{\alpha^4} \ln(\alpha x + \beta) - \frac{2\beta + \alpha L}{2\alpha^4(\alpha x + \beta)} + \frac{\beta(\alpha L + \beta)}{6\alpha^4(\alpha x + \beta)^2} \quad (13)$$

where C_1, C_2 - integration constants:

$$C_1 = -\frac{1}{\alpha^4 L} \ln \frac{\beta}{\alpha L + \beta} - \frac{2\alpha\beta + \alpha^2 L^2}{3\alpha^4 \beta L(\alpha L + \beta)}; C_2 = \frac{1}{\alpha^4} \ln \beta - \frac{5\beta + \alpha L}{6\alpha^4 \beta} \quad (14)$$

The comparison of the potential and kinetic energy yields a formula for the first natural frequency of the beam which can be transformed into a form

$$\omega_1 = 3\sqrt{\frac{5}{2} \frac{D}{L^2}} \sqrt{\frac{E}{\rho}} \sqrt{\frac{(\eta - 1)^5 \eta (P_1 - 6\eta(1 + \eta) \ln[\eta])}{P_2 - 3\eta \ln[\eta] (P_3 - P_4 \ln[\eta])}} \quad (15)$$

where

$$\begin{aligned} \eta &= \frac{d}{D} \\ P_1 &= \eta^3 + 9\eta^2 - 9\eta - 1 \\ P_2 &= 4\eta^8 + 9\eta^7 + 36\eta^6 + 311\eta^5 - 720\eta^4 + 311\eta^3 + 36\eta^2 + 9\eta + 4 \\ P_3 &= 8\eta^6 + 13\eta^5 + 80\eta^4 - 80\eta^2 - 13\eta - 8 \\ P_4 &= 12\eta(1 + \eta + \eta^2 + \eta^3 + \eta^4) \end{aligned} \quad (16)$$

2.2 Truncated Cone Beam – The Second Natural Frequency

The slope angle of the left end ($x = 0$) of the beam from Fig. 2 fulfils the equation:

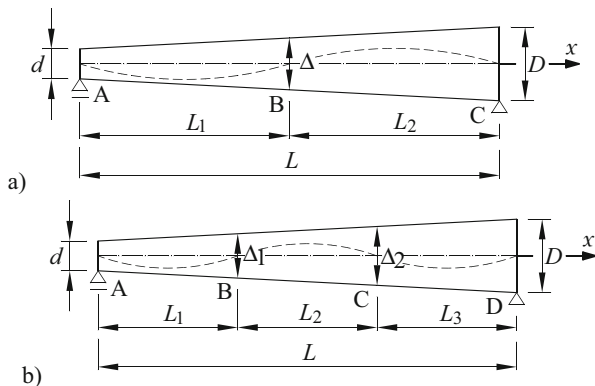
$$\frac{\pi E}{32q} \frac{du(x)}{dx} = \frac{1}{\alpha^4 L} \left(-\ln \frac{\beta}{\alpha L + \beta} - \frac{2\alpha\beta + \alpha^2 L^2}{3\beta(\alpha L + \beta)} - \frac{2\alpha\beta L - \alpha^2 L^2}{6\beta^2} \right) \quad (17)$$

and that of the right end ($x = L$) – the equation:

$$\frac{\pi E}{32q} \frac{du(x)}{dx} = \frac{1}{\alpha^4 L} \left(-\ln \frac{\beta}{\alpha L + \beta} - \frac{2\alpha\beta + \alpha^2 L^2}{3\beta(\alpha L + \beta)} - \frac{\alpha L}{\alpha L + \beta} - \frac{4\alpha\beta L + 3\alpha^2 L^2}{6(\alpha L + \beta)^2} \right) \quad (18)$$

Considering the shape of the beam in the second vibration mode, as it is presented in Fig. 3a, one can determine the position of an inflection point B of the deflection curve using the condition of equality of the slope angles of the beam on both sides of the point B and knowing that the point B is in the distance of L_1 from the support A and the beam diameter in the point B is equal to Δ . On the right end of the left

Fig. 3 Scheme of a beam for determination of an inflexion point of the deflection curve: (a) for the second natural frequency, (b) for the third natural frequency



part of the beam (Fig. 3a – in the point B⁻), using Form. (18) with an appropriate sign and assuming that $L \rightarrow L_1$, $d \rightarrow d$, $D \rightarrow \Delta$, $\alpha \rightarrow \frac{\Delta-d}{L_1}$ one obtains

$$\varphi_{B^-} = -\frac{32q}{\pi E} \frac{L^3}{(\Delta - d)(D - d)^3} \left[-\ln \frac{d}{\Delta} - \frac{(\Delta - d)(\Delta + 4d)}{3d\Delta} + \frac{(\Delta - d)(3\Delta + d)}{6\Delta^2} \right] \tag{19}$$

In analogical way, on the left end of the right part of the beam (in the point B⁺), using Form. (17) and assuming that $L \rightarrow L - L_1$, $d \rightarrow \Delta$, $D \rightarrow D$, $\alpha \rightarrow \frac{D-\Delta}{L-L_1}$, the slope angle in the point B⁺ is equal to

$$\varphi_{B^+} = \frac{32q}{\pi E} \frac{L^3}{(D - \Delta)(D - d)^3} \left[-\ln \frac{\Delta}{D} - \frac{D^2 - \Delta^2}{3d\Delta} - \frac{(D - \Delta)(3\Delta - D)}{6\Delta^2} \right] \tag{20}$$

It has been used a connection:

$$L_1 = \frac{\Delta - d}{D - d} L \tag{21}$$

The condition $\varphi_{B^-} = \varphi_{B^+}$ yields dependence:

$$\begin{aligned} &-\frac{D - \Delta}{\Delta - d} \left[\ln \frac{d}{\Delta} + \frac{(\Delta - d)(\Delta + 4d)}{3d\Delta} - \frac{(\Delta - d)(3\Delta + d)}{6\Delta^2} \right] \\ &= \left[\ln \frac{\Delta}{D} + \frac{D^2 - \Delta^2}{3\Delta D} + \frac{(D - \Delta)(3\Delta - D)}{6\Delta^2} \right] \end{aligned} \tag{22}$$

which allows calculation of Δ and then, using (21), L_1 . Knowing that the length L is divided into two parts L_1 and $L_2 = L - L_1$, one can write energy expressions and compare them (23), what enables to determine the second natural frequency:

$$E_p^{AB} + E_p^{BC} = E_k^{AB} + E_k^{BC} \tag{23}$$

2.3 Truncated Cone Beam – Higher Natural Frequencies

A similar approach concerns determination of higher natural frequencies, what is presented on the example of the third natural frequency. The bar of length L has been divided into three parts and their lengths L_1, L_2, L_3 have been determined from the condition of equality of slope angles on both sides of the points B and C (Fig. 3b). The expression for the slope angle in the point B⁻ has been written with use of (18), where

$$L \rightarrow L_1, d \rightarrow d, D \rightarrow \Delta_1, \alpha \rightarrow \frac{\Delta_1 - d}{L_1} :$$

$$\varphi_{B^-} = -\frac{32q}{\pi E} \frac{L_1^3}{(\Delta_1 - d)^3} \left[-\frac{1}{\Delta_1 - d} \ln \frac{d}{\Delta_1} - \frac{\Delta_1 + d}{3d\Delta_1} - \frac{1}{\Delta_1} + \frac{3\Delta_1 + d}{6\Delta_1^2} \right] \quad (24)$$

whereas in the point B⁺ – with use of (17), where $L \rightarrow L_2, d \rightarrow \Delta_1, D \rightarrow \Delta_2, \alpha \rightarrow \frac{\Delta_2 - \Delta_1}{L_2}$:

$$\varphi_{B^+} = \frac{32q}{\pi E} \frac{L_2^3}{(\Delta_2 - \Delta_1)^3} \left[-\frac{1}{\Delta_2 - \Delta_1} \ln \frac{\Delta_1}{\Delta_2} - \frac{\Delta_2 + \Delta_1}{3\Delta_1\Delta_2} - \frac{3\Delta_1 - \Delta_2}{6\Delta_1^2} \right] \quad (25)$$

Comparison of these angles, after simplification, yields:

$$-\frac{1}{\Delta_1 - d} \ln \frac{d}{\Delta_1} - \frac{\Delta_1 + d}{3d\Delta_1} - \frac{1}{\Delta_1} + \frac{3\Delta_1 + d}{6\Delta_1^2} = \frac{1}{\Delta_2 - \Delta_1} \ln \frac{\Delta_1}{\Delta_2} + \frac{\Delta_2 + \Delta_1}{3\Delta_1\Delta_2} + \frac{3\Delta_1 - \Delta_2}{6\Delta_1^2} \quad (26)$$

In similar way, from the condition of equality of slope angles on both sides of the point C, one obtains:

$$-\frac{1}{\Delta_2 - \Delta_1} \ln \frac{\Delta_1}{\Delta_2} - \frac{\Delta_1 + \Delta_2}{3\Delta_1\Delta_2} - \frac{1}{\Delta_2} + \frac{3\Delta_2 + \Delta_1}{6\Delta_2^2} = \frac{1}{D - \Delta_2} \ln \frac{\Delta_2}{D} + \frac{\Delta_2 + D}{3D\Delta_2} + \frac{3\Delta_2 - D}{6\Delta_2^2} \quad (27)$$

The values of Δ_1 and Δ_2 can be determined from the set of equations (26) and (27) and then, after calculation of values of $L_1 = \frac{\Delta_1 - d}{D - d} L, L_2 = \frac{\Delta_2 - \Delta_1}{D - d} L, L_3 = L - L_1 - L_2$, one can write equations of the deflection lines for each part of the beam what allows to calculate the energies and the third natural frequency.

In aim to calculate an n -th natural frequency, one must divide the beam into n parts and obtains $n - 1$ equations which serve to determine the beam diameters on the ends of each part and the lengths of these parts. Finally, the comparison of the energies yields the n -th natural frequency.

2.4 Truncated Wedge Beam

For a simply supported truncated wedge beam, subjected to a continuous load with constant value q and having a constant width B (Fig. 4a) as well as variable height κ , cross-section area and second area moment for any given cross section described by formulas

$$\kappa(x) = h + \frac{H - h}{L}x, A(x) = B\kappa(x), J(x) = \frac{B\kappa^3(x)}{12} \tag{28}$$

the first natural frequency can be determined analogically as in Form. (15):

$$\omega_1 = 6\sqrt{2} \frac{H}{L^2} \sqrt{\frac{E}{\rho}} \sqrt{\frac{(\phi - 1)^5 (3 - 3\phi^2 + (1 + 4\phi + \phi^2) \ln[\phi])}{R_1 + R_2 \ln^2[\phi] - R_3 \ln[\phi]}} \tag{29}$$

where

$$\begin{aligned} \phi &= \frac{h}{H} \\ R_1 &= 551\phi^5 - 783\phi^4 + 232\phi^3 + 232\phi^2 - 783\phi + 551 \\ R_2 &= 72\phi^5 + 360\phi^4 + 648\phi^3 + 648\phi^2 + 360\phi + 72 \\ R_3 &= 396\phi^5 + 744\phi^4 - 312\phi^3 + 312\phi^2 - 744\phi - 396 \end{aligned} \tag{30}$$

Then, using the methodology described in the previous chapter consisting in comparison of the slope angles on both sides of the point B (Fig. 4b)

$$\left(\frac{2H + K}{H - K} \ln \frac{K}{H} + \frac{5K + H}{2K} \right) = - \left(\frac{K + 2h}{K - h} \ln \frac{h}{K} + \frac{5K + h}{2K} \right) \tag{31}$$

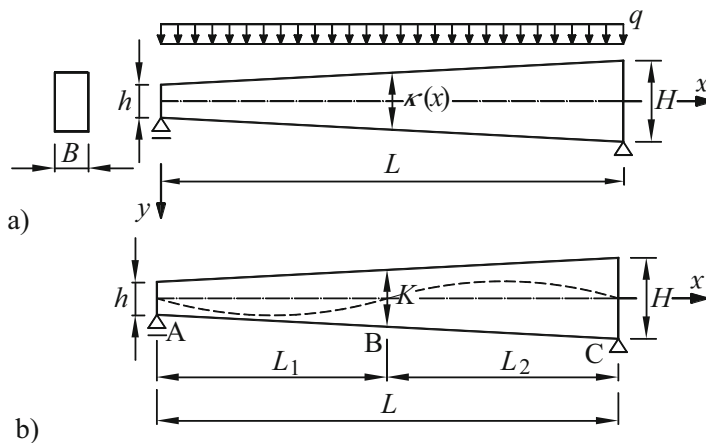


Fig. 4 (a) Simply supported, truncated wedge beam. (b) Scheme for determination of an inflection point of the deflection curve for the second natural frequency

one can determine the value of the beam height K in this point and then the distance $L_1 = \frac{K-h}{H-h}L$, what – after consideration of an expression analogical to (23) – enables to determine the second natural frequency.

In aim to determine the third natural frequency one must solve the following set of equations:

$$\begin{aligned}
 -\left(\frac{2h+K_1}{K_1-h} \ln \frac{h}{K_1} + \frac{h+5K_1}{2K_1}\right) &= \frac{K_1+2K_2}{K_2-K_1} \ln \frac{K_1}{K_2} + \frac{K_2+5K_1}{2K_1} \\
 -\left(\frac{2K_1+K_2}{K_2-K_1} \ln \frac{K_1}{K_2} + \frac{K_1+5K_2}{2K_2}\right) &= \frac{K_2+2H}{H-K_2} \ln \frac{K_2}{H} + \frac{H+5K_2}{2K_2}
 \end{aligned}
 \tag{32}$$

It enables to determine the cross section heights K_1 and K_2 in the inflection points of the deflection curve which allow to establish the bar division into three parts with lengths $L_1 = \frac{K_1-h}{H-h}L$, $L_2 = \frac{K_2-K_1}{H-h}L$, $L_3 = L - L_1 - L_2$, what finally allows to calculate the third natural frequency from the condition of equality of sums of potential and kinetic energies from each parts.

3 Validation of Results

Data for calculation of frequencies for the first three modes of free transversal vibrations of simply supported beams are presented in Tables 1 and 2. The simply supported beams have various truncation factors of lateral faces η and ϕ , defined

Table 1 Comparison of the authors’ results (A) to the benchmark solution (N) and the FEM results for truncated cone beam

Ω_m	η				
	0.2	0.4	0.6	0.8	1
$\Omega_1^{(A)}$	4.3761	6.2259	7.6423	8.8326	9.8767
$\Omega_1^{(N)}$	4.3527	6.2086	7.6314	–	9.8696
$\Omega_1^{(FEM)}$	4.3779	6.2121	7.6223	8.8032	9.8340
$\delta^{(N)}[\%]$	0.54	0.28	0.14	–	0.07
$\delta^{(FEM)}[\%]$	0.04	0.22	0.26	0.33	0.43
$\Omega_2^{(A)}$	14.904	23.16	29.7951	35.1812	39.5066
$\Omega_2^{(N)}$	21.9379	26.8518	31.2871	–	39.4784
$\Omega_2^{(FEM)}$	22.1738	26.9419	31.2094	35.1454	38.7934
$\delta^{(N)}[\%]$	32.06	13.75	4.77	–	0.07
$\delta^{(FEM)}[\%]$	32.79	14.04	4.53	0.10	1.84
$\Omega_3^{(A)}$	32.0626	51.2924	66.6978	72.533	88.8899
$\Omega_3^{(N)}$	48.4030	59.9914	–	–	88.8264
$\Omega_3^{(FEM)}$	49.4424	60.2383	68.9557	74.7285	86.9421
$\delta^{(N)}[\%]$	33.76	14.50	–	–	0.07
$\delta^{(FEM)}[\%]$	35.15	14.85	3.27	2.94	9.42

Table 2 Comparison of the authors' results (A) to the benchmark solution (N) and the FEM results for truncated wedge beam

Ω_m	ϕ				
	0.2	0.4	0.6	0.8	1
$\Omega_1^{(A)}$	4.9292	6.4743	7.73622	8.8527	9.8767
$\Omega_1^{(N)}$	4.9198	6.4666	7.7295	–	9.8696
$\Omega_1^{(FEM)}$	4.9265	6.4627	7.7144	8.8175	9.8246
$\delta^{(N)}[\%]$	0.19	0.12	0.09	–	0.07
$\delta^{(FEM)}[\%]$	0.05	0.18	0.28	0.40	0.53
$\Omega_2^{(A)}$	18.1676	25.1138	30.6347	35.179	39.5066
$\Omega_2^{(N)}$	21.3445	26.6002	31.1937	–	39.4784
$\Omega_2^{(FEM)}$	21.4544	26.5600	30.9313	34.8649	38.4471
$\delta^{(N)}[\%]$	14.88	5.59	1.79	–	0.07
$\delta^{(FEM)}[\%]$	15.32	5.45	0.96	0.90	2.76
$\Omega_3^{(A)}$	40.2265	56.1797	68.7985	79.4622	88.8899
$\Omega_3^{(N)}$	47.4820	59.5969	67.5630	–	88.8264
$\Omega_3^{(FEM)}$	48.2732	58.4444	65.0345	66.7546	92.6655
$\delta^{(N)}[\%]$	15.28	5.73	1.83	–	0.07
$\delta^{(FEM)}[\%]$	16.65	3.87	5.79	7.56	4.07

in formulas (16) and (30), respectively, what corresponds to various values of diameters d (for the truncated cone beam) or heights h (for the truncated wedge beam). Results of authors' calculations are compared to the results of a benchmark solution given by Naguleswaran [8] in Table 1 for truncated cone beam and in Table 2 for truncated wedge beam. A dimensionless frequency parameter Ω_m , presented in these tables, is described by:

$$\Omega_m = \omega_m L^2 \sqrt{\frac{A_L}{J_L}} \sqrt{\frac{\rho}{E}} \tag{33}$$

where A_L and J_L are cross-section area and second area moment for $x = L$, respectively. In Tables 1 and 2, δ is a relative error of authors' calculations in relation to the benchmark solution ($\delta^{(N)} = \frac{|\Omega_m^{(N)} - \Omega_m^{(A)}|}{\Omega_m^{(N)}} \cdot 100\%$) and results obtained in FEM

$$(\delta^{(FEM)} = \frac{|\Omega_m^{(FEM)} - \Omega_m^{(A)}|}{\Omega_m^{(FEM)}} \cdot 100\%).$$

The value of $\Omega_m^{(FEM)}$ has been obtained from (33) once the frequencies for the analyzed steel beams had been calculated with use of the finite element method (in ANSYS).

It must be emphasized that the derived formulas for natural frequencies do not concern a beam with constant cross section – the values of the parameter $\Omega^{(A)}$ for

$\eta = 1$ (cylinder) and $\phi = 1$ (cuboid) have been calculated from the formulas (4) and (5).

As it has been mentioned in Introduction, application of the Rayleigh method for calculation of first natural frequency of beams with assumption that the shape of the bar axis deflected during vibration corresponds to a deflection line resulting from action of a uniform continuous static load leads to well approximated results. The relative error between the parameters $\Omega^{(A)}$ and $\Omega^{(N)}$ does not exceed 0.3% for truncated wedge beams and 0.6% for truncated cone beams.

For second and third natural frequencies of transversal vibrations, if the beam shape approaches cylinder or cuboid, the differences between the solutions are satisfactory from engineer's point of view, whereas for $\eta < 0.6$ (for truncated cone beam) and $\phi < 0.4$ (for truncated wedge beam) the results obtained with use of the proposed approach are unacceptable.

It is worth to notice that, for small truncation factors, the second and third natural frequencies were lower than those in the reference solutions. In this case, the error magnitude depends mainly on the beam type (cone or wedge) and the truncation factor value, whereas the error magnitudes for second and third natural frequencies are of similar order.

4 Conclusions

The Rayleigh's method can be applied with good accuracy for calculations of the first natural frequency of transverse vibrations of non-prismatic bars, but for calculations of the second, third or higher natural frequencies this method can be successfully applied only for beams with the truncation factor of the walls $\eta \geq 0.6$ for truncated cone beam and $\phi \geq 0.4$ for truncated wedge beam. It probably means that the assumed shape of the neutral axis resulting during vibrations does not correspond to the real deflection line. It is interesting that the error of the obtained results strongly increases along with the increase of the truncation factor, however the errors for the second and third frequencies are similar.

Acknowledgements The authors would like to express their sincere thanks to Jan Grudziński, Ph.D. Eng., for his help in the FEM calculations in the ANSYS.

References

1. Bagdasaryan, V., Chalecki, M., Gierasimiuk, M., Jaworski, J., Szlachetka, O.: First natural transverse frequency of truncated cone and wedge beams. *Acta Sci. Pol. Archit.* **17**(1), 3–12 (2018)
2. Bijak-Żochowski, M. (ed.): *Mechanika materiałów i konstrukcji. Tom 2*. Oficyna Wydawnicza Politechniki Warszawskiej (2006)

3. Caruntu, D.I.: Dynamic modal characteristics of transverse vibrations of cantilevers of parabolic thickness. *Mech. Res. Commun.* **36**(3), 391–404 (2009)
4. Conway, H.D., Dobil, J.F.: Vibration frequencies of truncated-cone and wedge beams. *J. Appl. Mech. (ASME)*. **32**(4), 932–934 (1965)
5. Ece, M.C., Aydogdu, M., Taskin, V.: Vibration of variable cross-section beam. *Mech. Res. Commun.* **34**, 78–84 (2007)
6. Jaworski, J., Szlachetka, O.: Free vibrations of cantilever bars with linear and nonlinear variable cross-section. *Discontinuity Nonlinearity Complexity*. **6**(4), 489–501 (2017)
7. Keshmiri, A., Wu, N., Wang, Q.: Free vibration analysis of a nonlinearly tapered cone beam by Adomian decomposition method. *Int. J. Struct. Stab. Dyn.* **18**(07), 1850101 (2018)
8. Naguleswaran, S.: A direct solution for the transverse vibration of Euler-Bernoulli wedge and cone beams. *J. Sound Vib.* **172**(3), 289–304 (1994)

On Dynamics of a Rigid Block on Visco-Elastic Foundation



Yury D. Selyutskiy , Rinaldo Garziera , and Luca Collini 

Abstract We consider a rigid block installed on a viscoelastic foundation in such a way that the foundation interacts both with bottom and lateral sides (partially) of the block. The foundation is modeled using distributed springs and dashpots. It is supposed that oscillation amplitudes are small, so that the bottom of the block always remains in contact with the foundation. Oscillations of the system induced by horizontal harmonic motion of the foundation are studied. The influence of parameters of the system, as well as of the amplitude and frequency of the excitation, upon characteristics of such oscillations is analyzed.

Keywords Rocking · Stability · Rigid block · Viscoelastic foundation

1 Introduction

Dynamics of slender bodies installed on an oscillating foundation has been of theoretical and technical interest for many years. This problem involves development of approaches to describe the contact between body and supporting surface; besides, it is related with prevention of overturning of structures (monuments, towers, chimneys, oil or water tanks, etc.) during earthquakes.

The first model of rocking of a rigid block on moving horizontal rigid plane was proposed in [1]. Later this topic attracted attention of many researchers (for example, [2–6]). In these works, an extensive study was performed of behavior of rocking rigid blocks, both free and forced, and ways to damp such rocking were discussed.

Y. D. Selyutskiy
Lomonosov Moscow State University, Institute of Mechanics, Moscow, Russia
e-mail: seliutski@imec.msu.ru

R. Garziera (✉) · L. Collini
Department of Engineering and Architecture, University of Parma, Parma, Italy

Different approaches were used to simulate the contact interaction between the block and the foundation. In [7], such interaction is simulated using vertical and horizontal springs in contact points, in order to take into account the compliance. In [8], only vertical springs are used, and non-linear analysis of body dynamics is performed. In [9], the interaction with the supporting plane is described using the Hunt-Crossley nonlinear impact force model. In both last works, the center of mass of the block is constrained to the vertical motion only.

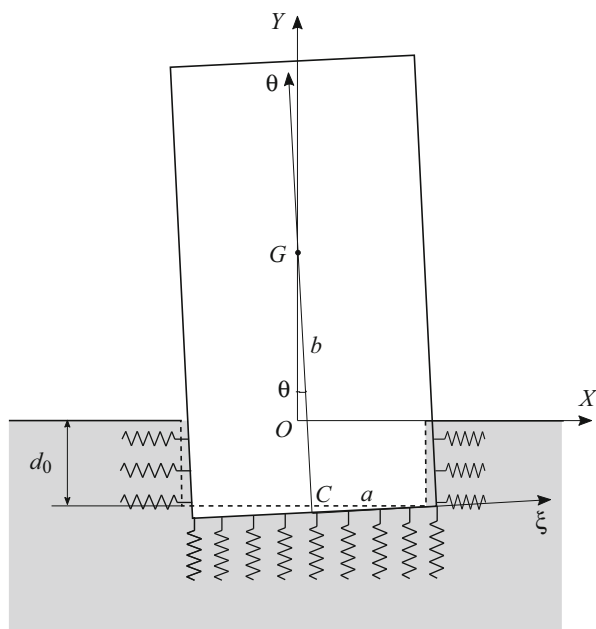
Rocking of blocks partly embedded into elastic foundation was studied in [10]. In [11], the flexibility of foundation is described with a system of horizontal and spiral springs.

In this paper, we consider planar dynamics of a rigid block partly embedded into a visco-elastic foundation, and simulate elastic properties of the foundation with a system of distributed horizontal and vertical springs.

2 Equations of Motion

Consider a rigid block installed on a visco-elastic foundation (see Fig. 1). Suppose that there is a rectangular cut in the foundation (shown with dashed line in Fig. 1), the width of which equals to the width of the block $2a$, and the depth is equal to d_0 . The block is installed into this cut and, as the foundation is elastic, it can move horizontally and vertically, as well as rotate. We assume that the block base always

Fig. 1 Rigid block on visco-elastic foundation



remains in contact with the foundation (no bouncing takes place), and there is a perfect bond between the sides of the block and the foundation. The foundation can move translationally along horizontal axis.

We introduce a coordinate system OXY fixed to the foundation so that OX axis is horizontal and directed along the foundation surface, and OY axis coincides with the symmetry axis of the cut. In order to determine position of the block with respect to the foundation, we use generalized coordinates x, y , and theta (the angle between the base and the horizontal axis OX , or tilt angle). We assume that the center of mass G of the block is located on the line normal to the base and passing through the point C , and denote the distance GC with b .

The interaction between the foundation and the block is simulated with independent springs and dashpots (horizontal and vertical). If only vertical springs would be considered, this would correspond to the well-known Winkler foundation.

When the block is installed into the cut, the cut is deformed. We assume that it remains rectangular, and its deformation is constrained to deepening, so that the new coordinate of the cut bottom in OXY system becomes $-d_0 + y_0$ (thus, $y_0 < 0$ is deformation caused by the block weight). We suppose also that lateral springs in this position are non-deformed.

We also introduce another coordinate system $C\xi\eta$ linked to the block itself; the axis $C\xi$ is directed along the base.

The horizontal and vertical forces acting on an element of the base are given by the following formulae:

$$\begin{aligned} f_{xb} &= -k(x + \xi \cos \theta - \xi) - c(\dot{x} - \xi \dot{\theta} \sin \theta), \\ f_{yb} &= -k(y + \xi \sin \theta + d_0) - c(\dot{y} + \xi \dot{\theta} \cos \theta). \end{aligned} \tag{1}$$

Here ξ is the coordinate of the element, k (units of force per unit width per unit deformation) is the stiffness coefficient, c (unit of force per unit width per unit deformation velocity) is the damping coefficient.

The horizontal and vertical forces acting on an element of the side of the block are given by the following formulae:

left-hand side:

$$\begin{aligned} f_{xl} &= -k(x - a \cos \theta - \eta \sin \theta + a) - c(\dot{x} + a \dot{\theta} \sin \theta - \eta \dot{\theta} \cos \theta), \\ f_{yl} &= -k(y - a \sin \theta + d_0 - y_0 - \eta) - c(\dot{y} - a \dot{\theta} \cos \theta - \eta \dot{\theta} \sin \theta); \end{aligned} \tag{2}$$

right-hand side:

$$\begin{aligned} f_{xr} &= -k(x + a \cos \theta - \eta \sin \theta - a) - c(\dot{x} - a \dot{\theta} \sin \theta - \eta \dot{\theta} \cos \theta), \\ f_{yr} &= -k(y + a \sin \theta + d_0 - y_0 - \eta) - c(\dot{y} + a \dot{\theta} \cos \theta - \eta \dot{\theta} \sin \theta). \end{aligned}$$

Here ξ and η are coordinates of the element in the $C\xi\eta$ coordinate system, and a is half width of the base.

Hence, expressions for components of the integral elastic force acting on the block are as follows:

$$\begin{aligned} F_x &= \int_{-a}^a f_{xb} d\xi + \int_0^{\eta_l} f_{xl} d\eta + \int_0^{\eta_r} f_{xr} d\eta, \\ F_y &= \int_{-a}^a f_{yb} d\xi + \int_0^{\eta_l} f_{yl} d\eta + \int_0^{\eta_r} f_{yr} d\eta. \end{aligned} \tag{3}$$

Here η_l and η_r are ordinates of intersection of the corresponding sides of the block with OX axis in $C\xi\eta$ coordinate system:

$$\eta_l = \frac{-y+a \sin \theta}{\cos \theta}, \quad \eta_r = \frac{-y-a \sin \theta}{\cos \theta}. \tag{4}$$

It is also necessary to find the integral moment of elastic forces about the center of mass of the block:

$$\begin{aligned} M_z &= - \int_{-a}^a f_{xb} (\xi \sin \theta - b \cos \theta) d\xi + \int_{-a}^a f_{yb} (\xi \cos \theta + b \sin \theta) d\xi \\ &- \int_0^{\eta_l} f_{xl} (-a \sin \theta - (b - \eta) \cos \theta) d\eta + \int_0^{\eta_l} f_{yl} (-a \cos \theta + (b - \eta) \sin \theta) d\eta \\ &- \int_0^{\eta_r} f_{xr} (a \sin \theta - (b - \eta) \cos \theta) d\eta + \int_0^{\eta_r} f_{yr} (a \cos \theta + (b - \eta) \sin \theta) d\eta. \end{aligned} \tag{5}$$

Now, using relations (1)–(5), we can write down equations of motion of the block using the momentum theorem and the theorem of angular momentum about the center of mass:

$$\begin{aligned} m(\ddot{x} - b\ddot{\theta} \cos \theta + b\dot{\theta}^2 \sin \theta) &= F_x - m\ddot{X}, \\ m(\ddot{y} - b\ddot{\theta} \sin \theta - b\dot{\theta}^2 \cos \theta) &= F_y - mg, \\ m\rho^2\ddot{\theta} &= M_z. \end{aligned} \tag{6}$$

Here m is the block mass, ρ is the radius of inertia of the block about its center of mass, g is the gravity acceleration, \ddot{X} is the horizontal acceleration of the foundation.

“Normal” position of the block (i.e., $x = 0$, $y = -d_0 + y_0$, $\theta = 0$) is equilibrium, hence,

$$y_0 = -\frac{mg}{2ka}.$$

In order to simplify the notation, we introduce the following non-dimensional variables and parameters:

$$\begin{aligned} \tau &= t\sqrt{\frac{g}{b}}, \quad \bar{a} = \frac{a}{b}, \quad \bar{x} = \frac{x}{b}, \quad \bar{y} = \frac{y}{b}, \quad \bar{d}_0 = \frac{d_0}{b}, \\ \bar{\rho} &= \frac{\rho}{b}, \quad \bar{k} = \frac{kb^2}{mg}, \quad \bar{c} = \frac{cb}{m}\sqrt{\frac{b}{g}}. \end{aligned}$$

Hereinafter, we omit bars over non-dimensional values and denote derivatives with respect to τ with dots.

3 Stability and Free Oscillations

First, we discuss the question of stability of the “normal” equilibrium.

Characteristic polynomial of equations of motion (6) linearized in the vicinity of this equilibrium is rather cumbersome, and we don’t show it here. Its constant term looks as follows:

$$\begin{aligned}
 &16(ka)^4 \left(4a^2 - 2a^2\sqrt{3} + 2d_0a + d_0^2\right) \left(4a^2 + 2d_0a + 2a^2\sqrt{3} + d_0^2\right) \\
 &\quad + 32(ka)^3 (a + d_0) \left(4a^2 + 2ad_0 + d_0^2 - 3a\right) \quad (7) \\
 &\quad + 24(ka)^2 \left(2a^2 + 2ad_0 + d_0^2 - 2a\right) + 8ka (a + d_0) + 1.
 \end{aligned}$$

Evidently, under some conditions expression (7), which represents a quartic polynomial in k , can have positive solutions. In such case, there will exist ranges of values of the stiffness coefficient, where the equilibrium in question will be unstable. Note that for block on an absolutely rough rough rigid plane such equilibrium is always stable.

Domains of instability obtained by numerical calculations are shown in Fig. 2 in plane (k, a) with grey colors for different values of d (for $\rho = 0.5$ and $c = 10$).

One can readily see that increase in cut depth d results in decrease of the instability area. Increase in a (base width) leads also leads to stabilization. These results are quite natural.

As for k , it is interesting to note that, under certain conditions, the equilibrium is stable both for small and large values of stiffness, while being unstable for “intermediate” k . This looks somewhat unexpected.

However, it is necessary to mention that, for small k , the value y_0 , as well as η_l and η_r become large. This means that the height of the block also must be large. Otherwise, there would appear segments of the side walls of the cut that are not in contact with the block, and our scheme for calculation of elastic forces would not be applicable.

In Fig. 3, time histories of the tilt angle θ are shown for $k = 10,000$, $c = 500$, and different values of the cut depth d_0 and base half-width a .

Note that increase in d_0 , as could be expected, results in quicker decay of oscillations. Besides, the frequency of oscillations also increases.

The effect of a is similar. Efficient damping and frequency of free oscillations of more slender blocks (i.e., blocks with smaller a) is lower.

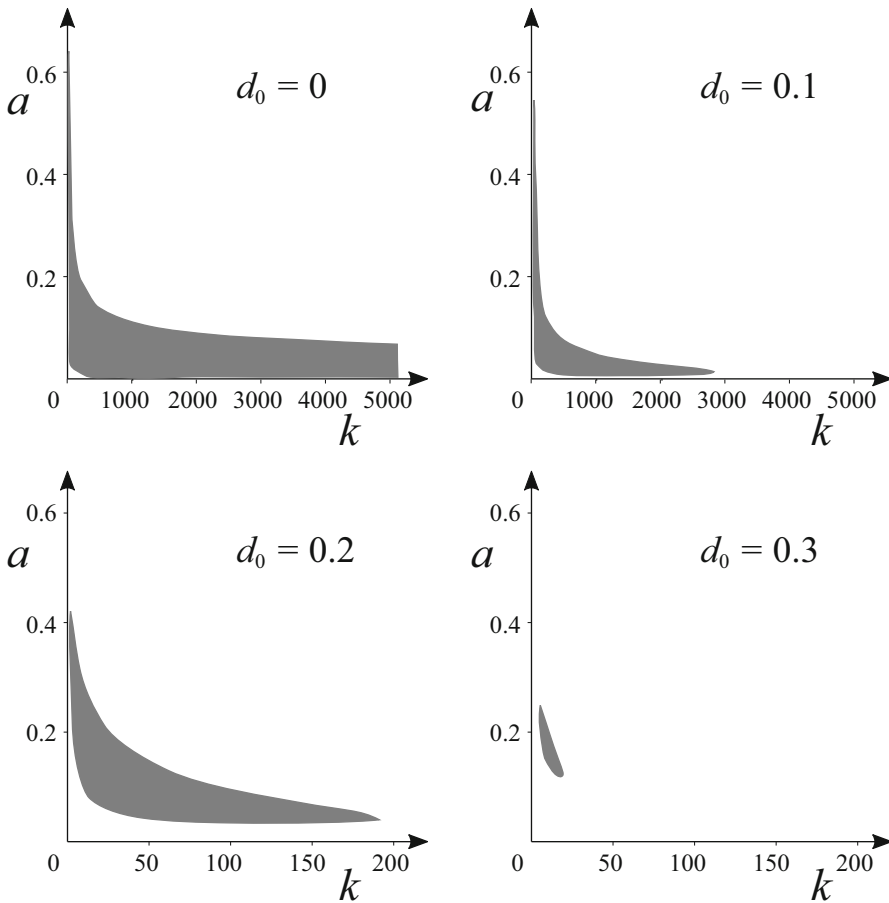


Fig. 2 Domains of instability (grey color)

4 Response to Excitation

First, let us consider the oscillations of the block induced by a single-sine excitation. For computations, we select the following values of non-dimensional parameters:

$$c = 100, \quad \rho = 0.5, \quad d_0 = 0.1, \quad \ddot{X} = \begin{cases} \sin(2\pi\tau), & \tau \leq 1 \\ 0, & \tau > 1 \end{cases}$$

We suppose that, at $\tau = 0$, the block is in its “normal” position: $\theta = 0, x = 0, y = -d_0 + y_0$.

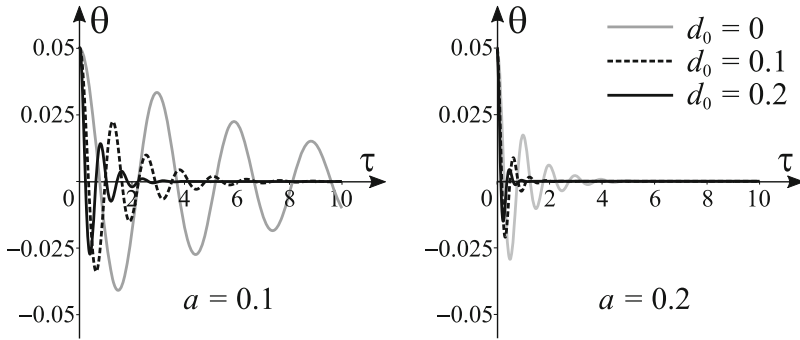


Fig. 3 Tilt angle time history for different a and d_0

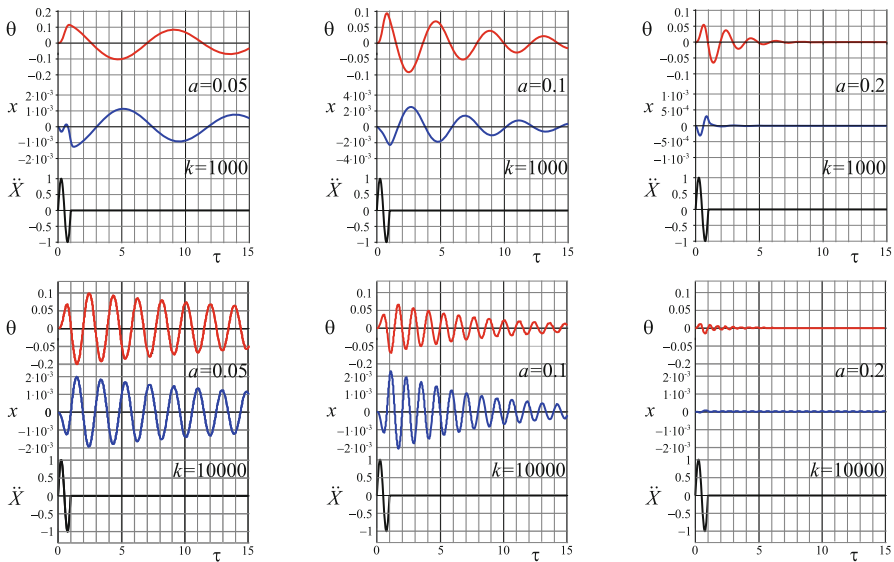


Fig. 4 Response of the block to a one-sine pulse for different a

In Fig. 4, time histories of the tilt angle θ and block horizontal displacement x are shown for different values of a and k . Parameters are chosen in such a way that the equilibrium position is asymptotically stable.

It is interesting to note that the maximum displacement of the center of the bottom x depends on the body width a in a non-monotonic way. However, this non-monotonicity becomes less pronounced with the increase in k . In the same time, the maximum tilt angle monotonically decreases, as a gets larger.

Besides, increase in the body width results in larger efficient damping, and larger rate of decay of oscillations.

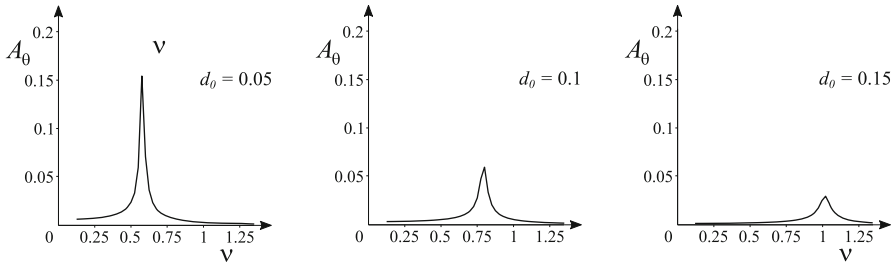


Fig. 5 Block tilt angle amplitude vs. excitation frequency

Now, let us discuss the response of the system to purely harmonic excitation:

$$\ddot{X} = 0.1 \sin(2\pi \nu \tau)$$

In Fig. 5, dependence of the amplitude A_θ of the tilt angle upon the excitation frequency ν is shown for different values of the cut depth. In calculations, the following values of the other parameters were taken: $a = 0.1$, $k = 10,000$, $c = 100$.

One can readily see the resonance peak. It should be noted that the resonance frequency increases as the cut depth d_0 increases. The rocking amplitude monotonically decreases with the decrease in d_0 , which is quite natural.

5 Conclusions

Rocking of a rigid block partly embedded into a viscoelastic foundation is considered. Interaction between the block and the foundation is described with a system of distributed horizontal and linear springs.

Stability of the “nominal” position of the block is analyzed depending on stiffness of the springs.

Rocking response of the body to single-sine and harmonic excitation of the foundation is studied for different values of parameters.

As a future work, it is supposed to perform experiments in order to devise the way to identify parameters of the model and to identify the area of applicability of this approach to description of rocking of a rigid block on visco-elastic foundation.

References

1. Housner, G.W.: The behaviour of inverted pendulum structures during earthquake. Bull. Seismol. Soc. Am. **53**(2), 403–417 (1963)
2. Hogan, S.J.: On the dynamics of rigid block motion under harmonic forcing. Proc. R. Soc. Lond. A. **425**(1869), 441–476 (1989). <https://doi.org/10.1098/rspa.1989.01146>

3. Ishiyama, Yu.: Motions of rigid bodies and criteria for overturning by earthquake excitations. *Earthq. Eng. Struct. Dyn.* **10**, 635–650 (1982). <https://doi.org/10.1002/eqe.4290100502>
4. Lipscombe, P., Pellegrino, S.: Free rocking of prismatic blocks. *J. Eng. Mech.* **119**(7), 1387–1410 (1993). [https://doi.org/10.1061/\(ASCE\)0733-9399\(1993\)119:7\(1387\)](https://doi.org/10.1061/(ASCE)0733-9399(1993)119:7(1387))
5. Peña, F., Prieto, F., Lourenço, P.B., Campos-Costa, A., Lemos, J.V.: On the dynamics of rocking motions of single rigid-block structures. *Earthq. Eng. Struct. Dyn.* **36**, 2383–2399 (2007). <https://doi.org/10.1002/eqe.739>
6. Collini, L., Garziera, R., Karapetyan, A.V., Munitsyna, M.A., Tasora, A.: Oscillations of a rocking block with an added pendulum. *J. Syst. Contr. Eng.* **230**(2), 104–114 (2016). <https://doi.org/10.1177/0959651815616715>
7. Andreaus, U., Casini, P.: On the rocking-uplifting motion of a rigid block in free and forced motion: influence of sliding and bouncing. *Acta Mech.* **138**(3), 219–241 (1999). <https://doi.org/10.1007/BF01291846>
8. Palmeri, A., Makris, N.: Response analysis of rigid structures rocking on viscoelastic foundation. *Earthq. Eng. Struct. Dyn.* **37**(8), 1039–1063 (2008). <https://doi.org/10.1002/eqe.800>
9. Spanos, P.D., Di Matteo, A., Pirrotta, A., Di Paola, M.: Nonlinear rocking of rigid blocks on flexible foundation: analysis and experiments. *Proc. Eng.* **199**, 284–289 (2017). <https://doi.org/10.1016/j.proeng.2017.09.032>
10. Beredugo, Y.O., Novak, M.: Coupled horizontal and rocking vibration of embedded footings. *Can. Geotech. J.* **9**(4), 477–497 (1972). <https://doi.org/10.1139/t72-046>
11. Jaimes, M.A., Arredondo, C., Fernández-Sola, L.: Coupled Horizontal and Rocking Vibration of Embedded Footings. *J. Earthq. Eng.* **22**(8), 1509–1536 (2018). <https://doi.org/10.1080/13632469.2017.1286620>